

Development of sensors and non-destructive techniques to determine the performance of coatings in construction

By
Timothy John Savill

A Thesis

Presented to Swansea University

In fulfilment of the requirements for the degree of
Engineering Doctorate (EngD) in Materials Engineering



Swansea University
Prifysgol Abertawe

College of Engineering, Swansea University, 2023

© Timothy J. Savill 2023

Author Declarations

STATEMENT 1

This work has not previously been accepted in substance for any degree and is not being concurrently submitted in candidature for any degree.

Signed: Tim Savill 

Date: 11/05/2023

STATEMENT 2

This thesis is the result of my own investigations, except where otherwise stated. Other sources are acknowledged by footnotes giving explicit references and a bibliography is appended.

Signed: Tim Savill 

Date: 11/05/2023

STATEMENT 3

I hereby give consent for my thesis, if accepted, to be available for photocopying and for inter-library loan, and for the title and summary to be made available to outside organisations.

Signed: Tim Savill 

Date: 11/05/2023

STATEMENT 4

I confirm that the University's ethical procedures have been followed and, where appropriate, that ethical approval has been granted.

Signed: Tim Savill 

Date: 11/05/2023

Abstract

The primary objective of this work was to examine and develop techniques for monitoring the degradation of Organically Coated Steel (OCS) in-situ. This included the detection of changes associated with the weathering to both the organic coating and metallic substrate. Initially, a review of current promising techniques was carried out however many were found to be unsuitable for this application and the adaptation of current techniques and the development of new techniques was considered. A brief concept investigation, based on initial testing and considerations, was used to determine a number of sensing techniques to examine. These included embedded, Resonant Frequency Identification (RFID), Magnetic Flux Leakage (MFL) and dielectric sensing. Each of these techniques were assessed for the application, prototyped, and tested against a range of samples to determine the accuracy and sensitivity of degradation detection provided. A range of poorly and highly durable coated samples were used in conjunction with accelerated weathering testing for this aim.

Track based electronic printed sensors were presented as both a cut edge corrosion tracking and coating capacitance measurement method. While suffering somewhat from electrical paint compatibility issues both concepts showed merit in initial trials however the capacitive sensor ultimately proved insufficiently responsive to coating changes. The embedded, progressive failure-based, cut edge corrosion sensor was produced and tested in modern coating systems with moderate success. Novel applications of RFID and MLF techniques were considered and proved capable of detecting large changes in substrate condition due to significant corrosion. However, there was a lack of sufficient sensitivity when considering early-stage corrosion of durable modern OCS products. Finally, it was shown that a chipless antenna could be designed and optimised for novel monitoring the changes to the dielectric properties of a paint layer due to degradation. However, ultimately this test, due to equipment requirements, lent itself more to lab testing than in-situ.

Due to some of these limitations a different approach was considered in which the environmental factors influencing degradation were examined with the aim of relating these to performance across a building. It was observed that a combination of high humidity and the build-up of aggressive natural deposits contributed to high degradation rates in sheltered regions, such as building eaves, where microclimates were created. The build-up of deposits and their effect was presented as a key degradation accelerant during in-use service. A unique numerical simulation approach was developed to predict the natural washing, via rain impact and characteristics of the building analysed. This approach showed promise for determining areas unlikely to be naturally washed, and therefore subjected to a degradation accelerating, build-up of deposits. Given these understandings coated wetness sensors were considered as a realistic live-monitoring device capable of determining deposit build up and ultimately OCS lifetime.

Table of Contents

Abstract	III
Acknowledgements	XII
List of Figures	XIII
List of Tables	XXI
List of Symbols/Abbreviations	XXII
List of Publications	XXIII
Chapter 1: Introduction	1
1.1 Background	1
1.2 Coating basics.....	2
1.3 Coating Compositions	3
1.3.1 Metallic Coatings	4
1.3.2 Organic Coatings.....	4
1.3.2.1 Resin/Binder	4
1.3.2.2 Solvent/Carrier	4
1.3.2.3 Pigments	5
1.3.2.4 Additives and Fillers.....	5
1.4 Coating layers.....	6
1.4.1 Metallic layers.....	6
1.4.2 Organic layers	6
1.4.2.1 Pre-treatment	6
1.4.2.2 Primer	7
1.4.2.3 Topcoat.....	7
1.4.2.4 Clear coat.....	8
1.5 Tata Steel Colors Coated Construction Products	8
1.5.1 Colorcoat Prisma®.....	8
1.5.2 Colorcoat HPS200 Ultra®	9
1.6 The Colorcoat Line.....	9
1.7 The Confidex® guarantee	10
1.8 Drivers changing industry	11
1.9 Thesis aims and objectives	11
1.10 References	12
Chapter 2: Literature Review	14
2.1 Introduction	14
2.2 Organically coated steel performance	14
2.2.1 Basics of corrosion.....	14
2.2.1.1 Definition of Corrosion	14

2.2.1.2	Gibbs Energy Changes	14
2.2.1.3	Redox reactions and the electrode potential	15
2.2.1.4	Aqueous Corrosion	16
2.2.2	Corrosion control through coatings.....	18
2.2.2.1	Metallic Coatings.....	18
2.2.2.2	Organic Coatings	18
2.2.3	Coating Failure.....	19
2.2.3.1	How coatings fail.....	20
2.2.3.2	Why coatings fail.....	21
2.2.4	Factors affecting constructional OCS coating failure	21
2.2.4.1	Light	21
2.2.4.2	Temperature.....	22
2.2.4.3	Mechanical action.....	23
2.2.4.4	Chemicals	24
2.2.4.5	Biological	25
2.2.4.6	Corrosion under coatings.....	26
2.3	Sensing Technologies	30
2.3.1	Non-destructive testing	32
2.3.1.1	Acoustic emission.....	32
2.3.1.2	Ultrasonic	33
2.3.1.3	Terahertz waves.....	36
2.3.1.4	Magnetic flux leakage	37
2.3.1.5	Magnetic adaptive testing.....	38
2.3.1.6	Magnetic memory method.....	39
2.3.1.7	Eddy current testing.....	39
2.3.1.8	Infrared thermography	41
2.3.1.9	Pulsed Thermal NDT.....	42
2.3.1.10	Eddy current pulsed thermography	43
2.3.2	Optical Techniques	44
2.3.2.1	Corrosion indicating paint	44
2.3.2.2	Stressed optical fibres	46
2.3.2.3	Bragg gratings	47
2.3.2.4	Corrosion product detection	49
2.3.2.5	Interferometry.....	49
2.3.3	Gravimetric Techniques	50
2.3.3.1	Corrosion coupons.....	50
2.3.4	Electrical Techniques	51
2.3.4.1	Galvanic.....	51
2.3.4.2	Zero resistance ammetry (ZRA)	51
2.3.4.3	Electrical resistance (ER)	53
2.3.4.4	Induction resistance probes.....	54

2.3.4.5	Capacitive sensors	55
2.3.4.6	Electrical field signature method (FSM)	56
2.3.5	Electrochemical Techniques	57
2.3.5.1	Potentiodynamic polarization techniques	57
2.3.5.2	Harmonic analysis	59
2.3.5.3	Electrochemical impedance spectroscopy (EIS).....	60
2.3.5.4	Electrochemical noise.....	62
2.3.5.5	Scanning electrochemical microscopy (SECM)	65
2.3.6	Other sensors.....	66
2.3.6.1	Embedded strain gauges	66
2.3.6.2	MEMs Based Systems	68
2.3.6.3	Nuclear thin layer activation.....	69
2.3.6.4	RFID Technology	69
2.3.6.5	NFC	72
2.3.6.6	Biological sensors.....	73
2.3.6.7	pH sensors	73
2.3.6.8	Chemical sensors	74
2.3.6.9	Simulations	75
2.3.7	Current technique Review Conclusions	76
2.4	References	77
Chapter 3: Materials and Methods		88
3.1	Introduction	88
3.2	Materials used.....	88
3.2.1	Pre-produced samples	88
3.2.2	Substrates	88
3.2.3	Coatings	89
3.3	Laboratory characterisation methods	89
3.3.1	FTIR.....	89
3.3.2	EDX/S.....	90
3.3.3	XRD	90
3.3.4	Colour Measurements	91
3.3.5	Gloss Measurements	91
3.3.6	Water Contact Measurement.....	92
3.3.7	Coating Adhesion.....	92
3.3.8	Scratch resistance.....	93
3.3.9	Coating thickness	94
3.4	Accelerated Degradation Methods	94
3.4.1	Salt spray.....	94
3.4.2	UV condensation testing	95

3.4.3	MEK Rubs	95
3.5	Development of a device to monitor localised conditions	95
3.6	Conclusions	99
3.7	References	99
Chapter 4: Concept Investigation.....		101
4.1	Introduction	101
4.2	Sensor positioning	102
4.3	Feasibility of embedded sensors.....	104
4.3.1	Manufacturing Feasibility – Line Applicability.....	105
4.3.1.1	Comparison of line and hand coated PU system	105
4.3.1.2	Comparison of line and hand coated PVC system.....	108
4.3.1.3	Outcome of line and hand comparison	110
4.3.2	Manufacturing Feasibility – Size Constraints	110
4.3.3	Manufacturing Feasibility – Survivability	111
4.3.4	Powering and Communication.....	111
4.3.4.1	Concept 1 – Semi-Embedded System (Wired)	111
4.3.4.2	Concept 2 – Fully-Embedded System (Wired).....	112
4.3.4.3	Concept 3 – PCB Coated System (Wired).....	113
4.3.4.4	Concept 4 – Fully-Embedded System (Wireless).....	114
4.3.5	Wireless powering and communication	115
4.3.5.1	Challenges surrounding RFID use near metals.....	116
4.3.5.2	Current solutions and their applicability	120
4.3.5.3	Low Frequency RFID	121
4.3.5.4	Wireless communication conclusions.....	122
4.3.6	Embedded sensor conclusions	123
4.4	Sensor concepts investigated.....	123
4.5	References	124
Chapter 5: Embedded Sensors		127
5.1	Introduction	127
5.2	Embedded sensor concepts.....	128
5.2.1	Connection based cut edge corrosion sensor	128
5.2.2	Capacitive coating sensor for coating degradation	129
5.3	Materials and methods.....	131
5.4	Paint compatibility	132
5.4.1	PU System compatibility	133
5.4.2	PVC System compatibility.....	135
5.4.2.1	Compatibility conclusions	136
5.5	Cut edge corrosion sensor	136

5.5.1	Initial proof of concept.....	136
5.5.2	Further proof of concept	138
5.5.3	Embedding in actual paint system.....	141
5.5.4	Cut edge sensor conclusions	145
5.6	Capacitive coating sensor	145
5.6.1	Initial proof of concept.....	145
5.6.2	Embedding in actual paint system.....	149
5.6.2.1	Immersion testing	151
5.6.2.2	MEK Rubs	153
5.6.2.3	UV Testing	154
5.6.2.4	Salt Spray Testing.....	156
5.7	Discussion	157
5.8	Conclusions	158
5.9	References	159
Chapter 6: RFID Blocking Sensor		161
6.1	Introduction	161
6.2	Background and application of the technique	161
6.3	Methods and materials.....	162
6.4	Development of the concept.....	166
6.5	Determination of blocker size	170
6.5.1	Initial size comparisons.....	170
6.6	Artificial defect detection	172
6.6.1	PVC coated samples.....	173
6.6.2	PU coated samples	176
6.6.3	Overall comparison.....	179
6.7	Corrosion based testing	180
6.7.1	Blackplate substrate samples	180
6.7.2	Lacquered samples.....	183
6.7.3	Metallically coated samples	186
6.7.4	Tata Steel Coated Samples.....	188
6.8	Improved Corrosion Testing	192
6.9	Conclusions	196
6.10	References	197
Chapter 7: Chipless RFID Sensor		199
7.1	Introduction	199
7.2	Theory and Background	200
7.3	Methodology	202

7.3.1	Simulations	202
7.3.2	Production of the Antenna	205
7.3.3	Antenna Measurement	206
7.4	Results	207
7.4.1	Simulations	207
7.4.1.1	Antenna Radius Optimisation.....	207
7.4.1.2	Initial system simulations	209
7.4.1.3	Effect of sample size.....	211
7.4.1.4	Simulated Changes in Dielectric Constant	212
7.4.1.5	Simulated Aging/Degradation	214
7.4.2	Experimental	216
7.4.2.1	Initial test of the system.....	216
7.4.2.2	Detection of Artificial Weathering	217
7.5	Discussion	221
7.6	Conclusions	222
7.7	References	223
	Chapter 8: Magnetic Flux Leakage Sensor	225
8.1	Introduction	225
8.2	Background and application of the technique	225
8.3	Methods and materials.....	228
8.4	Prototype 1	230
8.4.1	Prototype 1 – Detection of metal presence/absence.....	231
8.4.2	Prototype 1 – Detection of smaller zones of metal absence.....	235
8.4.3	Prototype 1 – Effect of non-metallic layer on response.....	236
8.4.4	Prototype 1 – Detection of corrosion defects.....	238
8.4.5	Prototype 1 – Sensor interference check.....	241
8.4.6	Prototype 1 – Conclusions	242
8.5	Prototype 2	242
8.5.1	Prototype 2 – Small defect detection	243
8.5.2	Prototype 2 – Corrosion detection	245
8.5.3	Prototype 2 – Galvanised steel corrosion detection	251
8.5.4	Prototype 2 – Coated steel corrosion detection.....	254
8.5.5	Prototype 2 – Conclusions	257
8.6	Prototype 3	258
8.6.1	Prototype 3 – Coated Steel Corrosion Detection	258
8.7	Conclusions	259
8.8	References	260
	Chapter 9: Understanding and Predicting OCS Degradation.....	261

9.1	Introduction	261
9.2	Background	261
9.3	Methodology	262
9.3.1	The Building: Materials and Locational Climate Data	263
9.3.2	Experimental Tests.....	265
9.3.2.1	Measurement of Degradation	265
9.3.2.2	Collection of Highly Localised Microclimatic Data.....	266
9.3.2.3	Collection, Measurement, and Analysis of Accumulated Natural Deposits	267
9.3.2.4	Creation of Laboratory-Fouled Samples and Analysis of Moisture-Related Properties	269
9.3.3	Numerical Simulation of Rainfall	270
9.4	Results—Physical Experimental Work	275
9.4.1	Degradation Variations Across the Building	275
9.4.2	Environmental Condition Variations Across the Building	276
9.4.2.1	Temperature.....	276
9.4.2.2	Humidity.....	277
9.4.2.3	UV Exposure	278
9.4.2.4	Time of Wetness.....	278
9.4.2.5	Airborne Particulate Concentration	279
9.4.3	Variations in Natural Deposit Build-Up Across the Building.....	280
9.4.4	Analysis of the Naturally Occurring Deposit.....	282
9.4.5	Effect of Deposit Weight on Wetting Angle.....	284
9.4.6	Effect of Deposit Weight on Water Absorption and Retention	285
9.5	Results—Simulated Measurements	288
9.5.1	Single Building Only—‘Visual’ Analysis	288
9.5.2	Single Building Only—Semi-Quantitative Analysis	290
9.5.3	Adjacent Building Model—‘Visual’ Analysis.....	293
9.5.4	Adjacent Building Model—Semi-Quantitative Analysis.....	293
9.5.5	Using the Simulation to Predict Degradation Rates.....	295
9.6	Discussion	296
9.7	Conclusions	299
9.8	References	299
	Chapter 10: Wetness Sensing.....	303
10.1	Introduction	303
10.2	Current Wetness Sensing.....	303
10.3	Wetness Sensor Design	305
10.3.1	Concept	305
10.3.2	PCB Designs	306
10.4	Paint Compatibility.....	307

10.4.1	Three-layer PU system.....	307
10.4.2	Two-layer PVC system.....	309
10.4.3	Durability assessment	311
10.4.4	Compatibility Conclusions.....	312
10.5	Initial proof of concept	313
10.6	Testing of actual paint system.....	316
10.7	Conclusions	317
10.8	References	318
Summary, Conclusions and Recommendations		319
	Conclusions	319
	Recommendations for further work.....	322
Appendix.....		324

Acknowledgements

Firstly, I would like to thank the M2A, Tata Steel Colors and the various other funders (UKRI, EPSRC, European Social Fund and the Welsh Government) that allowed me to carry out this work. I would also like to say thanks to the whole M2A team for their general support of the project.

I am also very grateful for the fantastic support, mentoring and supervision provided by Dr Eifion Jewell over the last 5 years. The advice, knowledge and often humour, he provided is a key reason this thesis exists. A thanks also to those in Swansea University who helped me with training, experimentation and testing along the way, particularly to Dr Chris Griffiths, but also those in Baglan, WCPC, the Smart Cities group and the Corrosion and Coatings group.

My thanks also to Peter Barker, Neil Metherall and Ian Clarke from Tata Steel for their guidance and help from an industrial point of view throughout the project. Without the ideas, and samples, they provided, much of this work would not have been possible.

Finally, a big thank you to my family and friends for their continued support.

List of Figures

Figure 1.1. Generic Organic Coating Layers	6
Figure 1.2. Colorcoat Prisma Layer Composition [22].....	9
Figure 1.3. The Colorcoat Line (simplified).....	10
Figure 2.1. Gibbs Energy Diagram for a Metal Lifetime.....	15
Figure 2.2. The effect of an aqueous environment on the activation energy for oxidation ...	16
Figure 2.3. Undercutting of a Coating [14].....	21
Figure 2.4. UV Degradation of Polymer Coatings [14].....	22
Figure 2.5. Osmotic blistering [14].....	27
Figure 2.6. Blister Formation in Coatings [13].....	27
Figure 2.7. Formation of Anodic (right) and Cathodic (left) Blisters [12]	28
Figure 2.8. Example of cathodic disbondment mechanism [15].....	29
Figure 2.9. Example of anodic undermining mechanism [10].....	30
Figure 2.10. Example of anodic undercutting leading to formation of a differential aeration cell [14].....	30
Figure 2.11. Acoustic emission detection [21].....	32
Figure 2.12. Ultrasonic testing principle [26].....	34
Figure 2.13. Application of ultrasonic testing to coating layers. On the right the numbers refer to the calculated polymer layer thicknesses measured by considering the different reflections provided by each layer [27].....	35
Figure 2.14. The use of acoustic waves to measure coating thickness [29].....	36
Figure 2.15. Example magnetic flux leakage device [28].....	37
Figure 2.16. The principles of eddy current testing [40].....	40
Figure 2.17. Use of eddy current testing on organic coatings [43]	40
Figure 2.18. The principles of thermography [47].....	42
Figure 2.19. The principle of eddy current thermography for use in (left) corrosion detection and (right) generic defect detection [50] [51]	43
Figure 2.20. The effect on the measured thermal energy of different coating failure modes: (a) corrosion, (b) under coating corrosion, (c) blistering, (d) coating failure [51].....	44
Figure 2.21. The principle of a smart release pH triggered microcapsule [54].....	45
Figure 2.22. The principle of corrosion triggered fluorescent microcapsules [55].....	45
Figure 2.23. The basic principle of a corrosion fuse [57][56]	46
Figure 2.24. The response of a Bragg grating to an applied strain [60].....	48
Figure 2.25. Detection of corrosion blister forming under a coating by a Bragg's grating [59]	48
Figure 2.26. Optical fibre interferometer [57]	50
Figure 2.27. Effect of corrosion on path length of light used in interferometry [62].....	50
Figure 2.28. A common circuit for a zero-resistance ammeter [67]	52
Figure 2.29. An ER probe [73]	54
Figure 2.30. Capacitive sensing set up [80].....	56
Figure 2.31. Basic principles of the FSM technique.....	57
Figure 2.32. An example of a potentiodynamic experiment set up	58
Figure 2.33. Example Bode (left) and Nyquist (right) plots for a coated metal electrode under EIS testing modelled on the equivalent circuit for a coated metal electrode (top) [98].....	61
Figure 2.34. Example SECM [117]	65
Figure 2.35. Example of a screen printed strain gauge embedded in an organic coating. Layers 1, 2, 3 and 4 represent the substrate, primer, electronics and topcoat layers respectively [119].....	67
Figure 2.36. A basic description of the RFID system [131]	70
Figure 2.37. Classification of RFID technologies by frequency [129].....	71
Figure 2.38. Design of a potentiometric chlorine sensor [140].....	74

Figure 2.39. COMSOL example simulation of potential distribution over time at a specific time period 2A [143].....	75
Figure 3.1. Formation of characteristic x-rays as a result of electron beam analysis [2].....	90
Figure 3.2. Principle of XRD in determining spacing of atomic planes [3]	91
Figure 3.3. Spectrophotometer working principle [4].....	91
Figure 3.4. Principle of gloss measurements [5].....	92
Figure 3.5. Examples of contact angles [6].....	92
Figure 3.6. Process of a tape adhesion test [8].....	93
Figure 4.1. Remaining grouped techniques	102
Figure 4.2. Two automated scanning sensor (shown in red) ideas; an extendable arching pole (left) and a more typical XY CNC positioner (right).....	103
Figure 4.3. Comparison between required layer thicknesses (dry film thickness) for line coated PU and the measured thickness of the hand coated sample.....	106
Figure 4.4. Microscopy comparison of line and hand PU samples.....	106
Figure 4.5. Surface topography comparison between line (left) and hand (right) coated PU samples.....	107
Figure 4.6. Comparison between required layer thicknesses (dry film thickness) for line coated PVC and the measured thickness of the hand coated sample	108
Figure 4.7. Microscopy comparison of line and hand PVC samples	109
Figure 4.8. Surface topography comparison between line (left) and hand (right) coated PVC samples.....	109
Figure 4.9. Demonstration of a partially embedded wired system.....	112
Figure 4.10. Application of the partially embedded sensor connection concept	112
Figure 4.11. Demonstration of a fully embedded wired sensor system	113
Figure 4.12. Application of the fully embedded sensor connection concept	113
Figure 4.13. Demonstration of a PCB based embedded sensor system	114
Figure 4.14. Types of wireless transfer [2]	115
Figure 4.15. Equivalent circuit of Monza R6 chip.....	117
Figure 4.16. Dogbone RFID tag as produced in CST Studio.....	118
Figure 4.17. Simulation set up in CST Studio	118
Figure 4.18. Simulated S11 response of the tag in free space.....	119
Figure 4.19. Simulated S11 response of the tag on different substrates	119
Figure 4.20. Simulated S11 response of the tag on coated steel substrates	120
Figure 4.21. Techniques remaining after initial testing	123
Figure 4.22. The techniques investigated in this work.....	124
Figure 5.1. Concept 1 - A cut edge corrosion sensor based on detecting electrical connection breaks. Embedded tracks are broken as corrosion spreads from the cut edge (bottom) of the sample upwards.....	128
Figure 5.2. Concept 2 – a fully embedded capacitive sensor (A) that could detect changes in coating condition (B)	129
Figure 5.3. Coplanar capacitor field lines (right) compared to parallel plate [7].....	130
Figure 5.4. Visual appearance of each coating system with an embedded conductive paint layer	132
Figure 5.5. Appearance of the embedded electrical paint under the PU system at 5x magnification lens	133
Figure 5.6. Resulting appearance of the PU samples after the crosshatch tape test.....	134
Figure 5.7. Appearance of the embedded electrical paint under the PVC system at 5x magnification lens	135
Figure 5.8. Resulting appearance of the PVC samples after the crosshatch tape test.....	136
Figure 5.9. Condition of the sample during each test showing dissolution of track once exposed	138
Figure 5.10. Measurement of track connection during each test	138
Figure 5.11. The epoxy coated sensors both before and after wire connection and sealing	139
Figure 5.12. Condition of the epoxy covered cut edge corrosion sensors during the test....	140

Figure 5.13. The new test sample composed of a tape covered sensor and utilising casting resin to protect the connections and uncoated substrate	140
Figure 5.14. Condition of the PTFE tape covered cut edge corrosion sensors during the test including close up of the sensing element broken as a result of cut edge defect spread.....	141
Figure 5.15. The cut edge corrosion sensors produced for testing. Green discoloration around the wires is from epoxy glue used to hold the wires in place before encapsulation.	142
Figure 5.16. The cut edge corrosion sensors after 4 weeks exposure	143
Figure 5.17. Close up of the PU systems sensing element.....	143
Figure 5.18. The cut edge corrosion sensors after 8 weeks exposure	144
Figure 5.19. Reference PU sample (left) and cut edge close up (right)	144
Figure 5.20. Printed capacitive sensor design and corresponding dimensions	145
Figure 5.21. Examples of the printed capacitive coating sensor produced using carbon (left) and silver (right) paints	146
Figure 5.22. Measured capacitance (raw data) over time during the application and drying of PVB over a carbon (left) and silver (right) embedded sensor.....	147
Figure 5.23. Epoxy coated carbon (left) and silver (right) paint sensors	148
Figure 5.24. Effect of steam exposure (left) and acetone immersion (right) on the epoxy embedded sensors	149
Figure 5.25. FTIR analysis of the epoxy coated carbon (left) showing an increase in the magnitude of the OH peak as a result of steam exposure (arrow) and comparison of the trend between peak area and measured capacitance for both samples (right).....	149
Figure 5.26. The embedded capacitive sensors produced using the two industrial coatings	150
Figure 5.27. Examples of samples prepared for degradation testing	151
Figure 5.28. Post immersion testing sample appearance including close up	152
Figure 5.29. Measured capacitance of the embedded sensors during the immersion test....	152
Figure 5.30. Example FTIR spectrum for the PU sample (left) and the calculated OH peak area for each sample (right)	153
Figure 5.31. Post MEK testing sample appearance (left) and measured gloss (right)	153
Figure 5.32. Measured capacitance of the embedded sensors during the MEK test.....	154
Figure 5.33. Post UV testing sample appearance.....	154
Figure 5.34. Effect of UV testing on sample colour (left) and gloss (right)	155
Figure 5.35. Measured capacitance of the embedded sensors during the UV test (left) and example FTIR with no obvious OH peak change (right).....	155
Figure 5.36. Post salt spray testing sample appearance including close up of PU blisters ..	156
Figure 5.37. Measured capacitance of the embedded sensors during the salt spray test	157
Figure 6.1. Example of an RFID based corrosion sensing system.....	162
Figure 6.2. The RFID tags used in this work	163
Figure 6.3. The developed test rig used in this work	164
Figure 6.4. The two possible implementation concepts	166
Figure 6.5. Initial reasoning behind choice of second concept. The top of the image shows how attaching RFID tags behind large cladding pieces leads to likely poor detection of cut edge corrosion. The bottom of the image shows how by covering the tag with a small representative sample the whole sample is monitored and detection of cut edge corrosion is far more likely.....	167
Figure 6.6. Comparison of the SR/s at each angle for the system with no backing metal (left) and a 100cm ² backing metal (right)	168
Figure 6.7. Comparison of the RSSI at each angle for the system with no backing metal (left) and a 100cm ² backing metal (right)	168
Figure 6.8. Resulting average RSSI values (left) and SR/s (right) recorded during the BM size and interrogation distance test	169
Figure 6.9. Key dimensions of RFID tag and blockers used in this work	170
Figure 6.10. Comparison of the three metrics when measuring differences in tag response due to increases in blocker length (width=5mm).....	172
Figure 6.11. Example of one sample showing how 2mm holes were punched through the blocking layer.....	173

Figure 6.12. Average RSSI recorded for each PVC blocker size under the artificial damage test.....	174
Figure 6.13. Average SR/s recorded for each PVC blocker size under the artificial damage test.....	175
Figure 6.14. The MinPow recorded for each PVC blocker size under the artificial damage test.....	176
Figure 6.15. Average RSSI recorded for each PU blocker size under the artificial damage test	177
Figure 6.16. Average SR/s recorded for each PU blocker size under the artificial damage test	178
Figure 6.17. The MinPow recorded for each PU blocker size under the artificial damage test	178
Figure 6.18. Comparison of the average change in metric compared to the value recorded for 5 holes. Note the difference in scale for the positive and negative axis	180
<i>Figure 6.19. Blackplate sample condition during testing at each measurement interval....</i>	181
Figure 6.20. Average RSSI recorded during the corrosion test for the blackplate substrate samples.....	182
Figure 6.21. Average SR/s recorded during the corrosion test for the blackplate substrate samples.....	183
Figure 6.22. The MinPow recorded during the corrosion test for the blackplate substrate samples.....	183
Figure 6.23. Lacquered blackplate sample condition during testing at each measurement interval	184
Figure 6.24. Average RSSI recorded during the corrosion test for the lacquered blackplate samples.....	185
Figure 6.25. Average SR/s recorded during the corrosion test for the lacquered blackplate samples.....	185
Figure 6.26. The MinPow recorded during the corrosion test for the lacquered blackplate samples.....	185
Figure 6.27. Galvanised sample condition during testing at each measurement interval	186
Figure 6.28. Average RSSI recorded during the corrosion test for the galvanised steel substrate samples	187
Figure 6.29. Average SR/s recorded during the corrosion test for the galvanised steel substrate samples	187
Figure 6.30. The MinPow recorded during the corrosion test for the galvanised steel substrate samples	188
Figure 6.31. Actual coated product sample condition during testing at each measurement interval. The front and back of the sample is shown for each week.	189
Figure 6.32. Average RSSI recorded during the corrosion test for the PU samples	190
Figure 6.33. Average SR/s recorded during the corrosion test for the PU samples	190
Figure 6.34. The MinPow recorded during the corrosion test for the PU samples	190
Figure 6.35. PVC sample week 10 (left) with identified blister locations (right).....	191
Figure 6.36. Side view of RFID tag with virgin (top) and corroded blocking layers (bottom). Note the gap produced in the corroded sample between blocking layer and tag	192
Figure 6.37. Samples used in the new corrosion test	193
Figure 6.38. Examples of the appearance of the samples during the test	194
Figure 6.39. Average RSSI recorded during the corrosion test for the hole punched samples: PVC (left) and PU (right).....	195
Figure 6.40. Average SR/s recorded during the corrosion test for the hole punched samples: PVC (left) and PU (right).....	195
Figure 6.41. The MinPow recorded during the corrosion test for the hole punched samples: PVC (left) and PU (right).....	196
Figure 7.1. Types of chipless RFID tags [3]	200
Figure 7.2. A basic CMPA.....	200
Figure 7.3. Basic working principle of an RCS backscattered RFID tag.....	201

Figure 7.4. Two tag systems NS, no substrate, (left) and S, substrate, (right) showing the copper sensor (C), the substrate layer (S), the paint system (P) the zinc galvanized layer (Z) and the steel metal substrate layer (M).	202
Figure 7.5. Tag systems showing key dimensions.....	203
Figure 7.6. Simulation set up in CST Studio Suite	205
Figure 7.7. The manufactured Chipless RFID Tag deployed onto the same without (left) and with (right) the substrate layer.	206
Figure 7.8. The OCS samples used in this study.....	206
Figure 7.9. VNA and horn antennas used to interrogate the sample.....	207
Figure 7.10. RCS response of each antenna radius (left) and the measured RCS drop (right)	208
Figure 7.11. Percentage change in resonant frequency as a result of dielectric constant change from 3.5	208
Figure 7.12. Simulated RCS response of sensors mounted directly on coated system (NS, left) and sensors mounted on an additional substrate (S, right).	209
Figure 7.13. Simulated surface current distribution on each system at resonant frequency	211
Figure 7.14. The effect of sample size on the simulated RCS response	212
Figure 7.15. The effect of changes in the dielectric constant of the paint layer on the simulated RCS response	213
Figure 7.16. The effect of changes in the dielectric constant of the paint layer on the resonant frequency and the RCS at resonant frequency of each system	213
Figure 7.17. The effect of simulated aging on the simulated RCS response of each system	215
Figure 7.18. The effect of simulated aging on the resonant frequency and the RCS at resonant frequency of each system	215
Figure 7.19. Comparison of the simulated and measured RCS response of sensors mounted directly on coated system (NS, right) and sensors mounted on an additional substrate (S, left). Identifiable peaks are matched between simulated and experimental results with designators A and B.	217
Figure 7.20. Sample appearance after no testing (control) (top), chemical (middle) and salt (bottom) exposure testing.	218
Figure 7.21. Resulting FTIR spectra for an example PVC sample (left) and example PU sample (right).	219
Figure 7.22. Measured RCS for a PVC coating system (left) and a PU coating system (right) samples exposed to salt and chemical degradation.	220
Figure 7.23. Measured resonant frequency for each PVC (left) and PU (right) sample tested and the associated standard error.	220
Figure 8.1. Effect of ferromagnetic iron on magnetic field lines [2]	225
Figure 8.2. Demonstration of magnetic field testing on uncorroded (top) and corroded (bottom) coated steel.....	226
Figure 8.3. Different MFL testing methods including commercially available handheld (top left) roller (bottom left) and research-based CNC (right) [7,8]	227
Figure 8.4. Suggested adaptation to the technique for this application.....	227
Figure 8.5. Sensor output to value relationship	229
Figure 8.6. The initial test rig.....	230
Figure 8.7. Test sample 1 image (left) and dimensions (right)	231
Figure 8.8. Test 1 sensor values.....	232
Figure 8.9. Test 1 average sensor values for each position.....	232
Figure 8.10. Average sensor deviation for each position (Left) and 2D Plot of the average deviation (Right)	233
Figure 8.11. Test sample 2 image (left) and dimensions (right)	234
Figure 8.12. Test 2 2D Plot of the average sensor deviation for each position.....	234
Figure 8.13. Test sample 3 image (left) and layout (right)	235
Figure 8.14. Test 3 2D Plot of the average sensor deviation for each position.....	236
Figure 8.15. Test sample 4 image (left) and dimensions (right)	237
Figure 8.16. Test 4 2D Plot of the average sensor deviation for each position.....	237

Figure 8.17. Test samples 5 Reference, A, B, C, D	238
Figure 8.18. Test 5 samples after exposure/cleaning	239
Figure 8.19. Test 5 Gauss deviations after 8 days for the uncleaned and cleaned samples .	240
Figure 8.20. Deviation analysis for test 7	242
Figure 8.21. The second test rig design	243
Figure 8.22. Test sample 2.1 image (left) and layout (right)	244
Figure 8.23. Measured Gauss percentage deviation (left) and likely defect locations based on a 5% threshold value (right).....	245
Figure 8.24. Test sample 2.2 dimensions A (left) and B (right)	245
Figure 8.25. Sample condition at each week exposure	247
Figure 8.26. Resulting Gauss Deviation maps for samples A and B	249
Figure 8.27. Likely defect locations based on the recorded data using a threshold value of 5%	250
Figure 8.28. Polyester coated galvanised steel with artificial scribed cross in the centre....	251
Figure 8.29. Condition of the sample during the test from 1 week exposure (far left), 2-week exposure, 4-week exposure and 6-weeks exposure (far right).....	252
Figure 8.30. Examples of the data captured in this test for weeks 2 and 6	253
Figure 8.31. Modified data for the test period with sensor 1 and 6 removed and a new threshold of 2%	254
Figure 8.32. Sample outline and example used for testing the coated products	255
Figure 8.33. Condition of the coated steel samples during the test.....	256
Figure 8.34. Detection pattern for the PU sample.....	257
Figure 8.35. Prototype 3.....	258
Figure 8.36. Sample used for the 3rd prototype testing	259
Figure 9.1. Building viewed from the (a) northwest, (b) southeast, and (c) location of the building and the façade names used for reference.	264
Figure 9.2. Examples of the two main types of cut edge degradation observed: blistering (left) and white rust (right).....	266
Figure 9.3. Location of the five sensing boxes on the building. The building is coloured according to materials with green indicating PVDF cladding, red indicating integrated PV roofing, blue indicating windows and doors, and dark purple indicating the soffit region composed of PVC cladding material.	267
Figure 9.4. Initially clean PVDF sample (left), PVDF sample with wet-applied 4000 mgm^{-2} of deposit (middle), and observed natural deposit on the building (right).	269
Figure 9.5. Experimental setup of the humidity testing chamber	270
Figure 9.6. Droplet test used to measure drying/water retention.	270
Figure 9.7. Building model (left) and actual building (right).	271
Figure 9.8. Dual building model (left) and actual buildings (right).....	272
Figure 9.9. The computation domain for the single (left) and dual building (right) models. The black arrows signify an inlet boundary condition whereas the blue arrows show an open boundary condition.	273
Figure 9.10. Example of façade sectioning for the east (top) and south (bottom) façades. .	275
Figure 9.11. Variation in cut edge defect size and type across the building.	276
Figure 9.12. Comparison of air (left) and panel (right) temperatures recorded at each location.....	277
Figure 9.13. Comparison of the relative humidity recorded at each location.	278
Figure 9.14. Comparison of UVA (left) and UVB (right) intensity recorded at each location.	278
Figure 9.15. Comparison of % wetness recorded at each location.	279
Figure 9.16. Comparison of particulate concentration recorded at each location.	280
Figure 9.17. Variation in the amount of deposit present across the building.....	281
Figure 9.18. Comparison of the cut edge defect distance to the measured deposit weight in each location (left) and a demonstration of the logarithmic trend between the two factors (right).	281
Figure 9.19. EDS analysis of the SP sample (left) and the P sample (right).....	282

Figure 9.20. XRD analysis of the SP sample (left) and the P sample (right).....	283
Figure 9.21. Likely constituents of the analysis of the SP sample (left) and the P sample (right).	283
Figure 9.22. The effect of increased deposit build-up on the wetting angle measurements for the three different coating systems.....	285
Figure 9.23. Water adsorption as a result of deposit weight and time in a humidity chamber for the PVDF-coated samples.	286
Figure 9.24. Water adsorption per mgm^{-2} of deposit weight as a result of time in the humidity chamber for each coating system.....	286
Figure 9.25. Effect of deposit weight on the drying of applied water droplets for the PVDF-coated samples.	287
Figure 9.26. Effect of deposit weight on the drying of applied water droplets for all coating systems.	288
Figure 9.27. Predicted rain impact density for the east elevation under 2 (A), 4 (B), 6 (C), and 8 (D) ms^{-1} wind speed applied normal to the east elevation.	289
Figure 9.28. Predicted rain impact density for the south elevation under 2 (A), 4 (B), 6 (C), and 8 (D) ms^{-1} wind speed applied normal to the south elevation.....	290
Figure 9.29. Predicted rain impact density for the north elevation under 2 (A), 4 (B), 6 (C), and 8 (D) ms^{-1} wind speed applied normal to the north elevation.....	290
Figure 9.30. Measured average rain volume fraction at each location for the east (top left), south (top right), and north (bottom) façade.	291
Figure 9.31. Wind-speed probability distribution used (left) to calculate wind-speed weighted averaged rain fraction for each panel on each façade (right).	292
Figure 9.32. Comparison between measured deposit fouling intensity and model predicted rain impact density.	292
Figure 9.33. Effect of the semi-shielding building on the predicted rain impact density for the north elevation under 2 (A), 4 (B), 6 (C), and 8 (D) ms^{-1} wind speed applied normal to the north elevation.	293
Figure 9.34. (Left) Measured average rain volume fraction at each location for the north façade in the dual building model. The dashed line represents the maximum volume fraction achieved in the single building model. (Right) Comparison between the wind-speed-weight	294
Figure 9.35. Comparison of the fitting of north façade data from each model to the trend given by the east and south façade data.	295
Figure 9.36. Comparison of measured cut edge defect distance and the model-predicted rain impact density.	296
Figure 10.1. Examples of wetness sensors with elements that prevent flush mounting and wetting from water run off.....	304
Figure 10.2. Corrosion of resistive sensors after just 6 months of exposure	304
Figure 10.3. Contact angle measurements of two commercial coating systems and a number of commercial sensors.....	305
Figure 10.4. An embedded wetness sensor (A) for detecting moisture levels (B & C).....	305
Figure 10.5. A PCB based wetness sensor (A) for detecting moisture levels (B & C).....	306
Figure 10.6. The designed PCB boards including designs (A/B) and produced boards on FR-4 (1/2) and aluminium (1a)	307
Figure 10.7. Appearance of sample 1 after application and curing of each PU coating layer	308
Figure 10.8. Appearance of the traces after primer application and cure for samples 1 (top) and 2 (bottom).....	308
Figure 10.9. Appearance of the PU PCB samples under microscope focussing on the end of a trace.....	309
Figure 10.10. Appearance of sample 1 during the PVC coating process.....	310
Figure 10.11. Appearance of the PVC PCB samples under microscope focussing on the end of a trace.....	310
Figure 10.12. Appearance of the samples after the salt spray test	312

Figure 10.13. Comparison of the water contact angle of the produced wetness sensor and commercial sensors to line and hand produced samples.....	313
Figure 10.14. The epoxy coated wetness sensors	313
Figure 10.15. Each test condition for the moisture test, the blue regions indicate de-ionised water was placed in these regions	314
Figure 10.16. Measured capacitance (left) and average values (right) for each condition during the epoxy coated PCB moisture test	315
Figure 10.17. Measured capacitance of the coated PCB sensors during the moisture test (left) and the average value for each condition (right).....	317

List of Tables

Table 2.1. Current Techniques.....	31
Table 2.2. Potentiodynamic polarisation tests.....	58
Table 3.1. Design requirements of the system.....	96
Table 3.2. Sensors used in the multifunctional sensing device.....	97
Table 3.3. Design specification analysis on further improvements.....	98
Table 4.1. Initially discarded methods.....	101
Table 4.2. Comparison between the properties of the hand and line coated PU samples....	107
Table 4.3. Comparison between the properties of the hand and line coated PVC samples .	110
Table 4.4. Equivalent circuit values.....	117
Table 4.5. Resonant frequency bands for the simulated tag in free space.....	119
Table 4.6. Resonant frequency bands for the simulated tag on different substrates.....	120
Table 4.7. Resonant frequency bands for the simulated tag on coated steel substrates.....	120
Table 5.1. Effect of the electrical paint embedding on the coating properties of the PU system.....	134
Table 5.2. Effect of the electrical paint embedding on the coating properties of the PVC system.....	135
Table 5.3. Calculated parameters for different gap sizes.....	146
Table 6.1. Antenna properties.....	163
Table 6.2. The range of materials used in this work.....	165
Table 6.3. Measured RSSI, SR/s and MinPow (MP) for each size PVC blocking layer at 25cm. For reference the RFID tag measures 15mm by 75mm.....	171
Table 6.4. Measured RSSI, SR/s and MinPow for each size PU blocking layer at 25cm. For reference the RFID tag measures 15mm by 75mm.....	171
Table 7.1. Simulation parameters.....	203
Table 7.2. Simulation material properties.....	204
Table 7.3. Results of initial simulations.....	209
Table 7.4. Calculated optimum range of dielectric height.....	210
Table 7.5. Parameters used for each aging severity level.....	214
Table 9.1. Building material characteristics.....	263
Table 9.2. Average weather data for this location.....	264
Table 9.3. Sensing box locations and their properties.....	266
Table 9.4. Simulation scenarios.....	274
Table 9.5. Identified compounds and their likely sources.....	283
Table 9.6. Measured conductivity of different electrolytes.....	284
Table 10.1. Examples of four commercially available wetness sensors.....	303
Table 10.2. Comparison of the PCB PU coated samples to the line sample.....	309
Table 10.3. Comparison of the PCB PVC coated samples to the line sample.....	311

List of Symbols/Abbreviations

Symbols/Abbreviations

ISO	International Standards Organization
ΔG	Gibbs Energy Change
ΔG^*	Gibbs Activation Energy
E	Electrode Potential
E^0	Standard Electrode Potential
F	Charge on one mole of electrons
R	Gas Constant
OCS	Organically Coated Steel
NDT	Non-Destructive Testing
MFL	Magnetic Flux Leakage
SMFL	Self-Magnetic Flux Leakage
FCS	Fluorescent Correlation Spectroscopy
BOTDA	Brillouin Optical Time Domain Analysis
FBG	Fibre Bragg Grating
ZRA	Zero Resistance Ammetry
ER	Electrical Resistance
RFID	Resonant Frequency IDentification
FSM	Field Signature Method
ASTM	American Society for Testing and Materials
EIS	Electrochemical Impedance Spectroscopy
EPN	Electrochemical Potential Noise
ECN	Electrochemical Current Noise
SECM	Scanning ElectroChemical Microscopy
SVET	Scanning Vibrating Electrode Technique
MEMs	Micro-ElectroMechanical system
LF	Low Frequency
HF	High Frequency
UHF	Ultra-High Frequency
NFC	Near Field Communication
OCS	Organically Coated Steel
PU	Polyurethane
PVC	Poly-Vinyl Chloride
PVB	Poly-Vinyl Butyral
FTIR	Fourier Transform Infrared Spectroscopy
EDX/S	Energy Dispersive X-Ray Spectroscopy
XRD	X-Ray Diffraction
PCB	Printed Circuit Board
RCP	Right Hand Circular Polarisation
MEK	Methyl Ethyl Ketone
RSSI	Received Signal Strength Indication
SR/s	Successful Reads per Second
MinPow	Minimum Interrogation Power

BM	Backing Metal
CMPA	Circular Micro Patch Antenna
RCS	Radar Cross Sectio
NS	No Substrate
S	Substrate
VNA	Vector Network Analyser
TX	Transmission Antenna
RX	Receiving Antenna
ECCA	European Coil Coating Association
PVDF	PolyVinylidene Fluoride
PV	PhotoVoltaic
CFD	Computational Fluid Dynamics

List of Publications

Techniques for In Situ Monitoring the Performance of Organic Coatings and Their Applicability to the Pre-Finished Steel Industry: A Review

T. Savill & E. Jewell

Published: Sept 2021 Journal: *Sensors* Doi: 10.3390/s21196334

Design of a Chipless RFID Tag to Monitor the Performance of Organic Coatings on Architectural Cladding

T. Savill & E. Jewell

Published: Apr 2022 Journal: *Sensors* Doi: 10.3390/s22093312

Understanding and Predicting Localised Variations in the Degradation Rate of Architectural, Organically Coated, Steel Cladding

T. Savill & E. Jewell

Published: Jan 2023 Journal: *Buildings* Doi: 10.3390/buildings13020270

Chapter 1: Introduction

1.1 Background

The cost of corrosion is extremely extensive and can be broken down into the direct cost and the indirect cost. The direct costs include costs incurred due to damage of structures, products and services [1]. The indirect costs include costs due to lost productivity, delays, litigations, taxes, outages [1]. The direct cost of corrosion has been estimated by several studies to be approximately 3-4% of a countries GDP [1–3] and a 1998 NACE study suggested that a the direct cost of corrosion can be used as a conservative estimate of the indirect cost of corrosion. Hence, a rough, minimum estimate of the total cost of corrosion would be 6-8% of GDP [1].

This means, with an projected global GPD of \$88 trillion, a global total estimated cost of corrosion of \$5,280 billion or £4,066 billion at the time of writing [4]. The construction industry represents a large share of this cost and it was reported that the cost due to infrastructure corrosion was estimated to be \$50 billion in the US in 1998, £250 million in the UK in 1970 and \$8 billion in India in 2011 [2].

In part, this is due to the high demand and use of steel in the construction industry. For example, of all sectors that consumed finished steel in 2017, the construction sector is by far the largest, demanding 35% of the total finished steel demand; approximately 4 million metric tonnes a month [5]. Construction has also increased finished steel usage by 4.8% from 2016 to 2017 [5] which is one of the largest increases seen by an industry. It has been estimated by several sources that a potential of 15-35% of the cost of corrosion across all sectors could be saved by using practises that increase corrosion protection [1–3]. This translates to a potential saving of approximately £1,400 billion pounds worldwide.

One commonly used method of protection is the use of organic coatings [1]. In fact, in 2017 the EU produced 153 million metric tonnes of hot rolled steel of which 4 million metric tonnes was organically coated [5]. However, despite this, it has been suggested by some studies that the reason for the high cost of corrosion is due, in part, to poor selection of protective measures [6]. Hence, one widely suggested strategy for corrosion protection is to ‘develop advanced life-prediction and

performance-assessment methods' and to move to a greater degree of corrosion monitoring [1].

It is important to note that such an approach aims to detect corrosion intensity and propagation rate rather than being a preventative solution. However, their application should, in theory, allow far better understanding as to the health of an asset and hence reduce failure rate and minimize costs if used appropriately. The oil and gas industry have long been aware of the benefits of corrosion monitoring of pipelines and are the most advanced sector when it comes to corrosion monitoring [7]. Some of the stated benefits include the ability to verify lifetime estimations and better plan maintenance and repair due to awareness of defect size and severity measurement. It also offers an easy way to optimise conditions, processes and any inhibitors that may be used to prevent corrosion as well as showing willingness to safety and conformation to legal and insurance requirements.

Currently, however, they are the only significant industry with commonly used, commercially viable, in-situ monitoring methods. This is despite the realisation of the importance of corrosion monitoring by other sectors such as the construction industry. For example, a report from a large chemical company stated that bad inspection led to 10% of their corrosion failures and 36% of failures were due to lack of proving (new material) and 16% due to lack of or wrong specification [8]. Monitoring devices in this company could offer a solution which could help prevent failure and assess performance.

However, at the point of writing there is little commercially available sensor technology aimed at in-situ monitoring the performance of organically coated steel. This is of high importance to companies such as TATA Steel who have committed to certain guarantees for a variety of their coated construction products with no maintenance or inspection required [9].

1.2 Coating basics

A coating is defined by ISO 4618 [10] to be a 'layer formed from a single or multiple applications of a coating material to a substrate'. This coating material is said to be a 'product, in liquid, paste or powder form, that, when applied to a substrate, forms a layer possessing protective, decorative and/or other specific properties'. The substrate is simply the 'surface to which a coating material is applied to'.

A number of types of coatings exist with different definitions. For example, a lacquer is a paint containing a solid binder dissolved in a solvent that dries via solvent evaporation. This means it is possible for re-dissolution if the solvent is reintroduced [11]. In comparison an emulsion is a water-borne paint containing dispersed polymer particles that dries by coalescence. Once the bulk of the water has evaporated off the small amounts of other, ‘coalescing’, solvents evaporate and in doing so form a permanent structure of merged polymer particles [11].

In the context of this project the substrate will be the TATA Steel produced steel coil to which the coating layers are subsequently applied. The coatings are composed a mixture of both metallic and organic coating (paint) layers and the overall properties are produced by the combination of these corresponding components.

A number of reasons exist as to why a coating may be applied to a substrate. For example, coatings can also offer protective properties such as resistance to corrosion, wear, chemical and general weathering. Coatings can also offer improved mechanical properties or other additional functionality through smart coatings as well as producing a pleasing aesthetic finish which is often key for consumer products [12].

Often a manufacturer will have to carry out a delicate balancing act of all these factors in order to achieve the most commercially effective coating. For example, for consumer goods, such as car panels and building cladding, the manufacturer has to balance aesthetic appearance with environmental protection. Although a coating may be superior in terms of protective qualities if the coating appearance is non-desirable the coating will not be commercially viable. Hence, when considering the overall effectiveness of a coating, it is as important to consider aesthetic failures as other, perhaps more damaging, mechanical or chemical failure modes.

Although a wide range of coatings exist, the following sections focus on the metallic and organic coatings used in the scope of this project.

1.3 Coating Compositions

Both metallic and organic coatings can be composed of a mixture of components in order to best optimise the functionality.

1.3.1 Metallic Coatings

Whilst coating of a pure metal onto a substrate does still occur, more commonly alloys of a number of metals, specifically chosen for their combined properties, are used. A wide range of alloys exist for the coating of metallic substrates and their applications vary depending on the intended use of the product. Often sacrificial metals such as zinc and tin are used to provide cathodic protection to the substrate. A common problem with zinc however is the formation of intermetallics with the iron substrate and hence metals such as aluminium and silicon are often added to control this. Other metals such as nickel, magnesium, titanium and chromium are also often alloyed into metallic coatings for reasons ranging from temperature performance to adhesion and corrosion inhibition.

1.3.2 Organic Coatings

An organic coating (paint) is a complex chemical mix of a variety of components of specific properties, each of which facilitate certain paint functions. The most common components present in paints are the resin (binder), solvent (carrier), pigments, filler and additives [12][13][11]. However, these are not a requirement of all paint systems and it is possible one or more of these may be absent in a coating for a number of reasons.

1.3.2.1 Resin/Binder

Generally, resins are organic polymers and they provide the backbone and structure of the coating system [13]. This is a required component of any paint system [11] as it facilitates the formation of a continuous film. Often the precursor is called the resin and the binder is the cured product [14]. This component has a large influence on the mechanical properties of the system such as weathering, flexibility, toughness, adhesion and curing time [12][11][14].

1.3.2.2 Solvent/Carrier

Often this component is used to vary the viscosity of the coating to ensure the coating has the correct properties to allow it to be applied via the chosen coating method. The solvent acts as a medium to dissolve the resin into for coating and is then removed as part of a curing process. The combination of solvent and binder is sometimes called the vehicle and control of this property is required to make the coating fluid enough for use [14]. It is reported that the type and amount of solvent

used can directly affect the durability and adhesion of the final coating layer even once the solvent is removed [12] [13]. While crucial for some applications, solvent may be absent in others which do not rely on the fluidity of the coatings, such as powder coating [11]. Finally, the solvent helps allows the even dispersion of any particles, that may be included in the paint, across the substrate [11].

1.3.2.3 Pigments

One of the main functions of the pigments is to provide the colour of the paint and they can be functional, for example UV protective and anticorrosive, or inert [12] [13]. Pigments remain after the curing process and often provide the required opacity to the coating film [14]. Three main types of anticorrosion pigments exist; sacrificial, inhibitive and barrier. Sacrificial pigments act as anodic regions and hence cathodically protect the substrate. Inhibitive pigments, e.g. phosphates, promote the formation of protective layers on the metal surface if corrosion begins [13]. Barrier pigments aim to, through a variety of methods, decrease the permeability of the coating and hence prevent key electrochemical components [13]. Some pigments may fall into more than one category, such as zinc dust, which is both a sacrificial and barrier pigment. The dispersion and the quantity of pigment used are both important factors in the suitability of a pigment, as is the wettability in the selected binder [13]. Sometimes dyes are used instead of pigments in order to achieve the desired colour but these can have the drawback of changing the hardness or viscosity of the system [11].

1.3.2.4 Additives and Fillers

Fillers are commonly used for commercial and economic reasons to increase coating volume and are usually cheap compounds such as talc or lime [11]. Additives are components that can perform a variety of tasks such as ensuring coating uniformity and changing the permeability properties. They can also be used to decrease the cost of the coating or alter the properties of the resin or solvent if required [12] [13]. Some examples of additives are, surfactants, antifoaming agents, stabilizers and wetting agents [11]. These additives all have their specific functions which falls outside the scope of this project but is well documented elsewhere.

1.4 Coating layers

The coating of a steel product can be simply achieved by applying a high weight molecular polymer film. Depending on the application this is known as lamination (if coated by a solid film) or a lacquer or paint (if coated by liquid precursor). However, in order to achieve the best mechanical and protective properties, coatings are composed of a number of layers, each with their own specific functionality. This is shown below in Figure 1.1.



Figure 1.1. Generic Organic Coating Layers

Most organically coated products also include coatings on the reverse of the substrate for aesthetic reasons and further protection. Generally speaking however, these are either identical to the front face or only include pre-treatment and a single backing coat due to the decreased environmental requirements [15].

1.4.1 Metallic layers

The substrate is coated with a metallic layer through either an electroplating or hot dipping process. The method used depends on the composition of the metallic layer being produced and is not considered in detail here. Historically the metallic layer was a ‘galvanised’ layer of zinc which provided sacrificial protection of the substrate improving corrosion performance. More recently there has been development into binary and tertiary alloy compositions which aim to improve the corrosion resistance of the substrate. This is described in detail in [16] but this falls outside the scope of the project.

1.4.2 Organic layers

1.4.2.1 Pre-treatment

Historically, these were often either phosphate or chromate-based layers and are only produced at a thickness of approximately $1\mu\text{m}$ or less. However, due to the toxicity

and carcinogenic properties of chromate there was a significant effort to discover alternative pre-treatments, but this falls outside the scope of this project. Since 2017, Tata Steel Colors has stopped using chromate-based pre-treatments in their products and instead use a more environmentally friendly titanium hexafluoride technology. An exact characterization of this system is not explained in any detail here but is described in [17].

The pre-treatment layer acts as a corrosion barrier and inhibitor and also provides better adhesion and mechanically keying of the subsequent paint layers.

1.4.2.2 Primer

Generally, this is a relatively thin layer of 5-15 μ m and is applied onto the pre-treatment. Primers are a family of coatings that are used to improve the adhesion of subsequently applied layers, compared to the bare substrate, and can also increase functionality of the coating. They provide a level of corrosion resistance but mostly aim to produce a homogeneous smooth layer for subsequent layers to be deposited on and reduce the effects of topographical defects in the metallic coating [18]. These effects are achieved by increasing the substrate surface energy and improving the wetting of the surface specifically for the following coating layers while also removing contaminants and impurities and adding reactive chemical sites [19].

Pigments that provide corrosion inhibition and protection are present in this layer and hence this is a significant protective layer. The primer lacks the aesthetic quality to be considered as a final coat and as such this requires further coating by the top coat [18].

Examples of some such pigments commonly used in a primer are chromates such as strontium or calcium chromate and phosphates such as zinc and calcium phosphate. As previously mentioned, due to health concerns there is significant current work to develop new chromate free primer pigments.

1.4.2.3 Topcoat

Apart from coating systems using an additional clear coat, this is the layer that forms the final finish of the coating and hence is subject to the largest aesthetic requirements. Compared to the other paint layers, the topcoat is much thicker and can be up to 200 μ m thick. However, the topcoat must also provide sufficient environmental resistance in order to prevent rapid degradation under chemical or

physical conditions. Gloss and colour imparting pigments are heavily used in this coating to provide the required visual appearance of the end product and various finishes may be achieved through careful compositional control [18]. This layer is also important because it aims to provide protection against the ingress of water into the other coating layers [15].

1.4.2.4 Clear coat

In some cases, the topcoat is not the final coat but is covered by a final 'clear' coat. This is becoming increasingly more prominent in applications for car parts and other consumer goods due to the creation of aesthetically pleasing, high gloss finishes.[20] Clear coats are also often considered for use if additional protective qualities are required such as further protection from environmental effects or from mechanical scratches and abrasion. Although it may be coloured, the clear coat is usually transparent, hence its name, and the lack of pigments allows other properties, such as scratch resistance, to be optimised [21]. As shown by Tata Steels product range the use of a clear coat may allow similar protection to be achieved with lower overall coating thicknesses when compared to a thicker system without a clear coat.

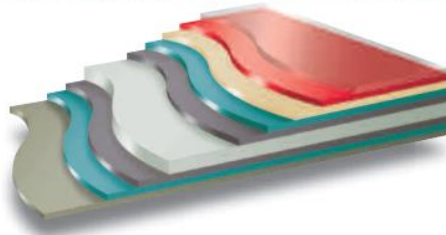
1.5 Tata Steel Colors Coated Construction Products

Tata Steel Colors produces a range of branded, pre-finished, coated steels which are used by the construction industry. Two of their flagship and most advanced products are Colorcoat Prisma® and HPS200 Ultra® which can be used for a variety of finishing and cladding purposes. This study will mainly focus on these systems as many of the other Tata Colors are designed for specialist applications such as Colorfarm® for agricultural use or Advantica® for clean room use.

1.5.1 Colorcoat Prisma®

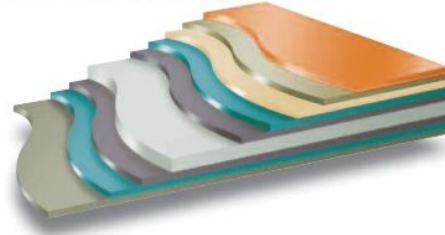
This organic coating system has a total thickness between 40 (elements) and 65 (solids, metallics and matts) microns. In the case of Prisma Elements this is composed of a 10µm clear coat, a 20µm topcoat and a 10µm primer. The other Prisma products are composed of a 15µm clear coat, a 25µm topcoat and a 25µm primer. In all Prisma systems the metallic coating is a Galvalloy® layer; this is a 95% zinc 5% aluminium alloy layer which is applied via a hot dipping process [22]. The layers present in the Prisma® products are shown in Figure 1.2.

Colorcoat Prisma® Solid, Metallic & Matts



Key	
15µm additional protective clear layer	Base steel substrate
25µm coloured layer with polyamide beads	Galvalloy® metallic coating
25µm corrosion resistant primer	Pre-treatment
Pre-treatment	High performance backing coat
Galvalloy® metallic coating	

Colorcoat Prisma® Elements



Key	
10µm additional protective clear or coloured layer	Base steel substrate
20µm coloured or base polymer layer	Galvalloy® metallic coating
10µm corrosion resistant primer	Pre-treatment
Pre-treatment	High performance backing coat
Galvalloy® metallic coating	

Figure 1.2. Colorcoat Prisma Layer Composition [22]

Prisma® products have a stated corrosion resistance of RC5 and CP15 (to EN13523-8 standards) and salt spray 1000h and humidity 1500h. Their UV resistance category is classed as Ruv4 (to EN 10169 standards). They have a stated maximum operating temperature of 90°C [22].

1.5.2 Colorcoat HPS200 Ultra®

This organic coating system has a total thickness of 200 microns. The metallic layer present is the same 95% zinc 5% aluminium Galvalloy® layer used in the Prisma products and is similarly applied by hot dipping [23].

HPS200 Ultra® has a stated corrosion resistance of RC5 (to EN10169:2015 standards) and of salt spray (1000h) and humidity (1500h). It also has the highest internal environment rating of CP15 (to EN10169:2010 standards). The UV resistance category is classed as Ruv4 (to EN 10169:2015 standards) and the stated maximum operating temperature is 60°C [23].

1.6 The Colorcoat Line

For reasons of efficiency, high production rate and lower production costs, coated steel products are made in a roll-to-roll continuous process known as coil coating. During this process the steel substrate known as the ‘web’ is passed through a number of processes to produce the end product; coated steel [24]. Although there is a large capital requirements for the development of coil coating lines they provide a high level of automation and potential for high production rates of approximately 28 to 66 meters per minute [24] [25].

The Tata Steel Colorcoat line, based in Shotton UK, receives pre-galvanised coils of steel of a gauge thickness between 0.68 and 1.5mm and aims to coat them as efficiently and as accurately as possible in order to increase product throughput and quality [25]. Production of Colorcoat steel, however, is a complex multistage process and a typical coating coil line will follow the diagram in Figure 1.3.

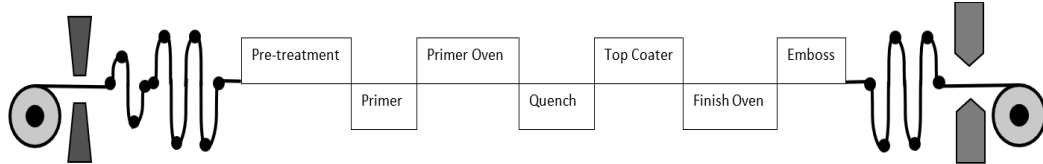


Figure 1.3. The Colorcoat Line (simplified)

First, the galvanised steel coil is unwound and welded to the end of the previous coil; this ensures the line is always fed. At this stage the web is also monitored for defects. In order to facilitate a line change the web enters into an accumulator which stores and releases material to allow for stationary welding. Upon exit of the accumulator the web is steered and tensioned to ensure it follows a smooth and aligned path. The web is cleaned of any grease or contaminates, and the pre-treatment coating layer is applied before the primer coating is applied and cured in the primer oven. In the primer oven the temperature of the web is between 204 and 370°C [25]. After quenching, to cool the web, the top coat and optional clear coat is applied, cured and quenched and then the coating is embossed. In the main oven the temperature of the web is between 138 and 370°C [25]. An inspection camera checks the quality of the coating and there is the option for customer oils to be applied to the web if this has been requested. The web is then fed into an exit accumulator which stores material to allow the cutting and changing of finished rolls to be facilitated. Finally, the web passes through another set of tensioning rolls before being wound back into coil form and cut by shears.

1.7 The Confidex® guarantee

This is Tata Steels flagship guarantee which is stated to be the ‘longest and most comprehensive guarantee for pre-fished steel available in Europe’ [23]. Up to 40 years is guarantee for both Prisma® and HPS200 Ultra® products. This guarantee is reduced for coastal locations (within 1km of any coast) and generally roof panels have a stated guarantee which is 5 years shorter than wall panels. There is also a locational variation on the guarantee by up to 10 years when comparing, for example,

application in the UK to that in Portugal. It covers cut edges and allows the whole building envelope to be covered by the same guarantee [22][23]. This guarantee has proved popular with the market and led to commercial benefits.

1.8 Drivers changing industry

Manufacturers of building materials have often offered guarantees on their product for customers. The demand on this guarantee is only increasing as building designs adapt, architects often find novel ways to use materials in ways that may subject them to harsher conditions than previously. For example, cladding is now often perforated to create aesthetic designs increasing the quantity of exposed cut edge and access for rain penetration into the rear cavity. Furthermore, to justify building construction economically and environmentally clients expect longer building lifespans and degradation of building materials is more of a pollutant concern than ever before.

1.9 Thesis aims and objectives

This project aims to research and develop methods that allow performance monitoring of coated steel construction products.

Currently, coatings are rarely monitored in-situ and expected performance of the overall building envelope is often only estimated from lab-based accelerated corrosion testing. Monitoring could allow more accurate estimates of building cladding lifespan and required maintenance schedules and provide customers with active performance data. Furthermore, introduction of these sensors may be the next step for so called ‘smart buildings’; a sustainability concept increasingly sought after.

Development of techniques to assess the ‘aggressivity’ of an environment will also be considered as another potential method of determining coating performance and to allow selection of the most suitable coatings for local environmental requirements. For example, the requirements of a protective coating may change based on the location of a project geographically, or across different areas of a building. Hence, more appropriate coatings or coating weights could be more accurately selected for a project, offering economic benefits.

The major challenge of this project is developing techniques that work in the field; there are many techniques that can assess coating performance in the laboratory

however adapting these for in-situ monitoring poses several difficulties. These issues include, powering of the module, extraction of data, the requirement to not affect the coating performance, to be non-destructive and to be resistant to environmental conditions and noise.

1.10 References

1. Koch G, Brongers MP., Thompson N., Virmani Y., Payer J. Corrosion Costs and Preventative Strategies in the United States. U.S. Department of Transport. 1998.
2. Koch G, Varney J, Thopson N, Moghissi O, Gould M, Payer J. International Measures of Prevention , Application , and Economics of Corrosion Technologies Study. NACE IMPACT Rep. 2006;1–216.
3. Koch G. 1 - Cost of corrosion [Internet]. Trends in Oil and Gas Corrosion Research and Technologies. Elsevier Ltd; 2017. 3-30 p. Available from: <http://dx.doi.org/10.1016/B978-0-08-101105-8.00001-2>
4. International_Monetary_Fund_(IMF). World Economic Outlook Database, October 2018 [Internet]. 2018 [cited 2019 May 13]. Available from: <https://www.imf.org/external/pubs/ft/weo/2018/02/weodata/weorept.aspx?pr.x=60&pr.y=8&sy=2019&ey=2019&ssd=1&sort=country&ds=.&br=1&c=512%2C668%2C914%2C672%2C612%2C946%2C614%2C137%2C311%2C546%2C213%2C962%2C911%2C674%2C314%2C676%2C193%2C548%2C122%2C556%2C912>
5. Eurofer. European Steel in Figures 2008-2017. 2018.
6. Biezma M., Cristobal RJ. Methodology to Study Cost of Corrosion. Int J Corros Process Corros Control. 2005;40(4).
7. Singh R. Corrosion and Corrosion Protection. In: Pipeline Integrity Handbook. 2nd ed. 2017. p. 241–70.
8. Roberge P. Handbook of Corrosion Engineering. McGraw-Hill; 1999.
9. TATASteel. THE CONFIDEX® GUARANTEE [Internet]. 2022 [cited 2022 Jul 4]. Available from: <https://www.tatasteeleurope.com/construction/services/guarantees/confidex>
10. Standard I. ISO 4618 Paints and varnishes — Terms and definitions [Internet]. 2014. Available from: <https://www.iso.org/obp/ui/#iso:std:iso:4618:ed-2:v1:en%0D>
11. McKeen LW. The Components of Paint. Fluorinated Coatings Finish Handb [Internet]. 2016;51–8. Available from: <http://linkinghub.elsevier.com/retrieve/pii/B9780323371261000035>
12. Popov B. Organic Coatings. In: Corrosion Engineering. Elsevier; 2015. p. 557–79.
13. Knudsen O., Forsgren A. Corrosion Control Through Organic Coatings. 2nd ed. Schweitzer P, editor. CRC Press; 2017.
14. Wicks Z., Jones F., Pappas S., Wicks D. Organic Coatings. Third. Wiley, editor. 2007.
15. Littlehales AW. Optimisation of organic coating layers to improve corrosion resistance on next generation galvanised steels. Swansea University; 2014.
16. Cooze N. The use of a novel time-lapse microscopy technique to study the corrosion

- effects of zinc magnesium aluminium alloys in aqueous salt solutions. Swansea University; 2010.
17. Saarimaa V, Markkula A, Arstila K, Manni J, Juhanoja J. Effect of Hot Dip Galvanized Steel Surface Chemistry and Morphology on Titanium Hexafluoride Pretreatment. *Adv Mater Phys Chem* [Internet]. 2017;07(02):28–41. Available from: <http://www.scirp.org/journal/doi.aspx?DOI=10.4236/ampc.2017.72004>
 18. Fraunhofer JA Von. Paint Technology. In: *Basic Metal Finishing*. London: Science, Elek; 1976. p. 151–70.
 19. Dunn T. Primers. In: *Flexible Packaging* [Internet]. Elsevier; 2015. p. 239–43. Available from: <https://linkinghub.elsevier.com/retrieve/pii/B9780323264365000291>
 20. Jalili MM, Moradian S, Dastmalchian H, Karbasi A. Investigating the variations in properties of 2-pack polyurethane clear coat through separate incorporation of hydrophilic and hydrophobic nano-silica. *Prog Org Coatings*. 2007;59(1):81–7.
 21. Yari H, Moradian S, Ramazanzade B, Kashani A, Tahmasebi N. The effect of basecoat pigmentation on mechanical properties of an automotive basecoat/clearcoat system during weathering. *Polym Degrad Stab* [Internet]. 2009;94(8):1281–9. Available from: <http://dx.doi.org/10.1016/j.polymdegradstab.2009.04.008>
 22. Tata_Steel. Colorcoat Prisma ® Colour Card. Vol. 2019. 2019.
 23. Tata_Steel. Colorcoat HPS200 Ultra ® Colour Card. Vol. 2014. 2014.
 24. McKeen LW. Application of Liquid Coatings. *Fluorinated Coatings Finish Handb*. 2008;2:135–46.
 25. TATA_Steel. Tata Communication. 2019;

Chapter 2: Literature Review

2.1 Introduction

This chapter first explores the methods of, and factors that contribute to, the failure of organically coated steel used in construction. This allows an understanding of the changes that occur during degradation as well as the conditions that lead to degradation occurring. Secondly a review of the current techniques that are or could be used for the monitoring of organically coated steel is presented to give the foundation of the current state of technology and research in this area.

2.2 Organically coated steel performance

The performance of organically coated steel used in the construction industry is ultimately determined by how well the two components, substrate and coating, resist degradation. The product is deemed to be performing poorly if corrosion occurs or the required coating properties are deemed to have failed.

2.2.1 Basics of corrosion

2.2.1.1 Definition of Corrosion

The ISO 8044 standard defines corrosion as ‘Physiochemical interaction (usually of an electrochemical nature) between a metal and its environment which results in changes in the properties of the metal and which often leads to impairment of the functions of the metal, the environment, or the technical system of which this forms a part’ [1][2]. Other definitions include; ‘the deterioration of a metal due to chemical or electrochemical reactions with its environment’ [3] and ‘the reaction of a metal with components of its environment’[4].

2.2.1.2 Gibbs Energy Changes

Corrosion occurs because the majority of metals are at a state of higher energy when they are in their pure, or ‘refined’, form compared to when they exist as oxides or ores. This is why production of metals requires energy and hence why corrosion of metals is inevitable; there is thermodynamic driving force for the metal to oxide.

Figure 2.1 diagrammatically shows this process, displaying the required energy of

extraction and the driving force for corrosion ΔG and the activation energy for these processes ΔG^* [5].

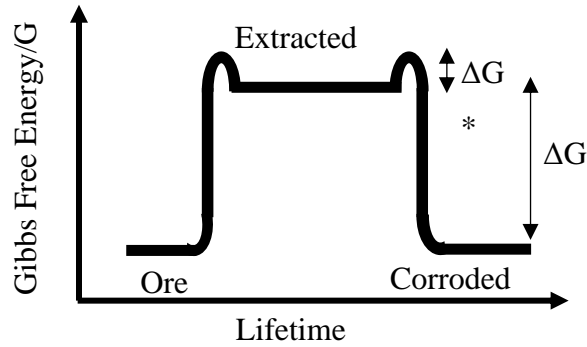


Figure 2.1. Gibbs Energy Diagram for a Metal Lifetime

2.2.1.3 Redox reactions and the electrode potential

The Gibbs diagram represents redox half reactions that the metal undergoes during its lifetime. In extraction, the metal is reduced in a reduction reaction to produced metal from the respective ions present in the ore. As the metal is corroded it undergoes an oxidation reaction in which the metal is oxidised back to ions. An example of the half reactions for copper are given:

Reduction, extraction of metal from ions requires ΔG_{Copper} energy



Oxidation, return of metal to ions via corrosion; driven by ΔG_{Copper}



Each metal system has a specific ΔG associated with its redox reactions. This value for any system can be calculated using the following equation:

$$\Delta G = -nFE \quad (2.3)$$

Where n is the number of electrons transferred, F is the charge, in coulombs, on one mole of electrons and E is the electrode potential. The electrode potential is formed as a result of the electron transfer between reacting species and is specific to individual reaction conditions. The standard electrode potential (E^0), however, is a standardised measure of the electrode potential of the reduction of a species compared to a controlled hydrogen reduction half reaction; which is set as 0V. The electrode potential of a species is used to determine reaction favourability with a more positive value indicating higher favourability. For example, copper and iron reduction have values of E^0 of +0.34V and -0.44V respectively. Hence, under

standard conditions, it would be expected that copper would be reduced, and iron oxidised, in a redox reaction.

For conditions that are not standard the Nernst equation can be used to calculate the non-standard electrode potential:

$$E = E^{\circ} - \frac{RT}{nF} \ln \left(\frac{[products]}{[reactants]} \right) \quad (2.4)$$

Where R is the gas constant, T is the temperature.

Corrosion of a metal can occur in dry conditions if a metal is sufficiently hot and is exposed to oxygen, but the more common, and destructive, form of corrosion is aqueous corrosion. This occurs when there is the presence of an electrolyte, such as water containing salts, and is particularly damaging. This is because, under these conditions, the activation energy for corrosion ΔG^* is reduced, as shown in Figure 2.2 . Consequently, corrosion can occur, thermodynamically speaking, more easily.

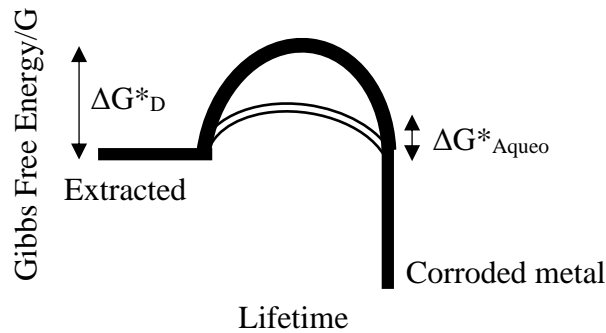
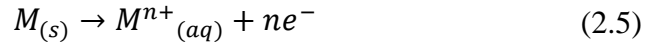


Figure 2.2. The effect of an aqueous environment on the activation energy for oxidation

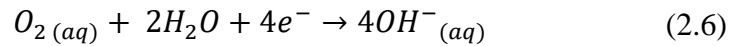
2.2.1.4 Aqueous Corrosion

The simplest demonstration of aqueous corrosion is the wet corrosion cell, which consists of four components and is an example of an electrochemical cell. This system is composed of two electrodes, the anode and cathode, an electrolyte and an electrical connection. An electrode can be defined as ‘the boundary between a solid phase (metal) and a liquid phase (aqueous environment)’ [5]. The electrolyte can be any solution that is able to conduct electrically and a direct electrical connection between anode and cathode is required for the flow of electrons from anode to cathode [5][6].

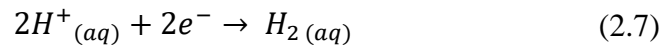
The anode is the electrode at which the net reaction is anodic i.e. it is a net electron producing region. It is at the anode that metal dissolution occurs as the metal is oxidised in the following reaction.



The metal ions produce diffuse into the electrolyte where they often react to form corrosion products such as iron oxide (rust). The electrons produced flow to the cathode electrode where the net reaction is cathodic i.e. is a net electron consuming region. The most common reaction that occurs at this electrode in aqueous corrosion is the reduction of oxygen.



However, in certain conditions, such as low concentration of oxygen or low pH conditions, another reduction reaction can occur, namely the evolution of hydrogen.



It is important to note that the electrodes could be two different, electrically connected materials or two separate regions of the same material. The former is the case in galvanic corrosion in which the material with the more negative electrode potential will be the focus of anodic attack. The latter can be observed in differential aeration, a corrosion cell set up as a result of oxygen deficiency in a certain location leading to localised domination of the anodic reaction.

A founding principle of corrosion protection is that if any one of the four components of the corrosion cell is absent, corrosion will not occur [5]. There are various methods of providing corrosion protection and each aim to remove one or more of the components required [7]. Examples include the use of inhibitors or coatings and or making changes to the environment, materials used or the design. However, for the purposes of this project, corrosion control and protection through the use of coatings is considered only. The other methods fall outside the scope of this project and hence are not described in any detail here.

2.2.2 Corrosion control through coatings

Both metallic and organic coatings can be used for corrosion protection, and both have their uses, advantages and disadvantages. Often, to provide the best possible protection, they are used in conjunction with each other.

2.2.2.1 Metallic Coatings

Metallic coatings can offer galvanic protection of a substrate. Perhaps the most common example of this involves applying a zinc coating to a steel substrate, carried out in a process called galvanising. Zinc is more electroactive than iron so corrodes preferentially to the steel, but it also forms an insoluble corrosion product which provides a further layer of protection. This layer is regarded as ‘self-healing’ as if breached through mechanical damage the zinc will corrode producing further insoluble product that can repair the zinc layer. This type of protection is often called sacrificial protection and can be incorporated into organic paint systems through the use of metal powders [8].

Other metals that are not more electroactive than iron may also be used as coatings such as nickel or chromium. These are used commonly for aesthetic reasons and solely provide a barrier to the environment. Materials that are very inert such as tin or that form inert oxide layers such as aluminium are also often used to provide durable coating barrier layers.

2.2.2.2 Organic Coatings

Organic coatings, or paints, protect a substrate by removing one or more of the four components required for aqueous corrosion [8] and hence prevent the electrochemical reaction. This can be achieved through a variety of ways. At the most basic level they are barriers between an aggressive environment and a metal to be protected [9].

Some organic coatings act solely as a barrier coating as they are impermeable to water and hence remove the required electrolyte for ionic current to flow and corrosion to occur [8]. Other coatings can prevent current flow between anode and cathode by acting as ‘high resistivity dielectric layers’ and usually this involves disrupting the ionic current [8] that usually flows in the electrolyte. It can also be the case the paint contains additives that contribute to corrosion protection, e.g. inhibiting chromate pigments [8] or phosphates for passivation of the surface [10]. In

these cases, corrosion is arrested through removal of one of the components of the electrochemical cell via some chemical reaction between the additive and the product of corrosion. Furthermore, it is also possible that, by using various paint additives for example zinc dust, a paint system can provide a level of cathodic protection of the metal [10].

However, it is important to note that most commercial organic coatings are permeable to oxygen and water and therefore the coatings do not simply act as a barrier [10].

It is suggested in [10] that the coating protects the substrate by protecting the oxide layer that is formed on any newly exposed metal surface. Often this oxide layer is removed through dissolution into an aggressive environment, such as that present in aqueous corrosion, allowing further fresh attack. If a paint coating is present, dissolution of the oxide layer is prevented, and a level of protection is provided attributable to the decreased ease of electron transfer through it. In order for the anodic reaction beneath the oxide to continue, electrons must pass out through the oxide layer and ions must pass in through the oxide layer. If oxide integrity is maintained both these processes are slowed and hence the rate of corrosion is slowed. This mechanism explains the corrosion resistance of metals such as aluminium and stainless steel which form stable adherent oxides naturally, so are corrosion resistant. However, these metals will still corrode if the environment is sufficiently aggressive that the oxide stability is affected, as predicted by this mechanism [10].

More simply, oxygen and water will diffuse through an organic coating allowing the growth of a thick oxide on the substrate which is protected by the coating. As long as the paint integrity is maintained the oxide layer will be suitable to provide corrosion protection [10]. The ability of the paint to maintain this protection depends on the components used in the coating system

2.2.3 Coating Failure

For a coating to be effective it must perform without failure for the intended lifespan as there are large financial costs of paint failure due to cost of repair, loss of time and repainting [11]. Due to the complex chemistries involved in coating systems and the complexity of the environments they are placed in, the subject of coating failure and

performance analysis is vast. It has, however, been reported that coating performance can be affected by a number of factors [9]. This includes the coating composition such as the type of system used, any additives or inhibitors that may be present as well as the way this coating is used for example the thickness. Furthermore, the preparation may also have an effect as it will determine important parameters such as the adhesion and effectiveness of pre-treatment and subsequent layers. Finally, the coating chemistry can affect the performance depending on coating permeability to oxygen, water and ions.

2.2.3.1 How coatings fail

Coatings may fail in a number of different ways however it has been reported that coating failure and damage generally follows the following sequence[8]:

1. Formation of defect – Defects may be present because of poor preparation, for example lack of sufficient cleaning can leave dirt or grease on the substrate pre-coating. Alternatively, they may be formed as a result of mechanical action or degradation by, for example, temperature or UV light exposure. Finally, chemical defects may form because of reactions with acids or other chemical species that the coating may be exposed to in some environments [8].
2. Oxygen and ion uptake from surrounding environment – This process is dependent on the pore space of a coating which defines the amount of space between the molecular chains of a coating. The permeability of the coating, which may change with the increased presence of defects, will also determine the ease and rate of this step.
3. Coating adhesion loss – The coating begins to de-adhere from either the substrate or another coating layer. This may occur through the formation of a blister or may involve the delamination of large sections of the coating [8].
4. Electrolyte penetration to substrate surface – In some environments, electrolytes may be able to penetrate through the, now significant, defects in the coating. This can lead to increased adhesion loss [8].

5. Corrosion initiation on substrate – If electrolyte penetration occurs then corrosion is very likely to initiate. However, even though the coating is no longer intact, ion transport is still reduced by its presence. This can, hence, prevent corrosion somewhat by reducing the availability of charge balancing ions reaching the active corroding site. Unfortunately this effect can also increase the rate of corrosion through the retention of ions that are aggressive such as chloride by restricting their diffusion away from active sites [8].

2.2.3.2 Why coatings fail

There are a number of reasons why a coating may fail in use but the most common reason is due to lack of or poor preparation, poor application conditions or incorrect formulation, mixing or composition of the coating [12][11][13]. This can either provide a pre-existing defect or more rapidly promote defect formation beginning the previously described failure process. Other common reasons for coating failure include improper coating selection or poor design of components leading to inadequate protection from the environment. Coatings may also fail because of substrate exposure due to cut edges, adhesion failure, mechanical damage or surface roughness which can lead to corrosion and undercutting as shown in Figure 2.3.

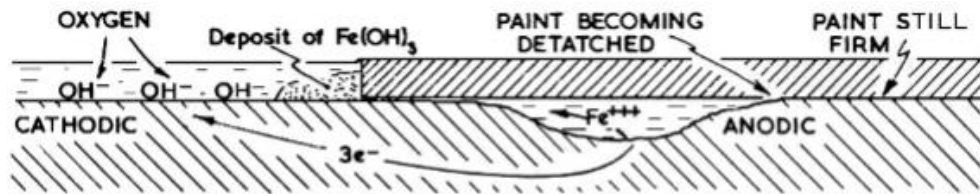


Figure 2.3. Undercutting of a Coating [14]

Defining the point of coating failure is difficult as it is widely accepted that all paints will deteriorate over time and, under exposure to aggressive environments, lose protective and aesthetic qualities leading to a perceived ‘failure’[12]. Failures can be caused by issues with formulation, adhesion, substrate or physical defects [11][13].

2.2.4 Factors affecting constructional OCS coating failure

2.2.4.1 Light

High energy photons in the UV spectrum are known to have the ability to degrade organic coatings through a variety of methods such as photooxidation and bond scission [8]. Near UV and blue light are the biggest contributors to polymeric degradation [12] as the less energetic, long wavelengths, do not have the energy

required and the more energetic wavelengths are blocked by the earth's atmosphere [12].

Changes in properties crucial to the protectiveness of a coating can occur because of exposure to UV ($\lambda=30\text{-}300\text{nm}$). An increase in the permeability of the coating and resin degradation are common under the effects of UV exposure and can both lead to an increased rate of failure [8]. Furthermore, many paint pigments are semiconductors; the most obvious example of this is being TiO_2 . Under exposure of UV light these semiconductors can produce an electron-hole pair. The hole that is formed is a strong oxidising agent and can go on to react with organic compounds such as the coating resin or any organic dyes in the coating. In the reaction the organic component can be mineralised to carbon dioxide. As a result, the pigment causes degradation of the coating leading to the creation of a large number of pores accelerating final coating failure. The pores reduce the effectiveness of the coating to preventing the ion transport reducing the corrosion protection. This is shown in Figure 2.4.

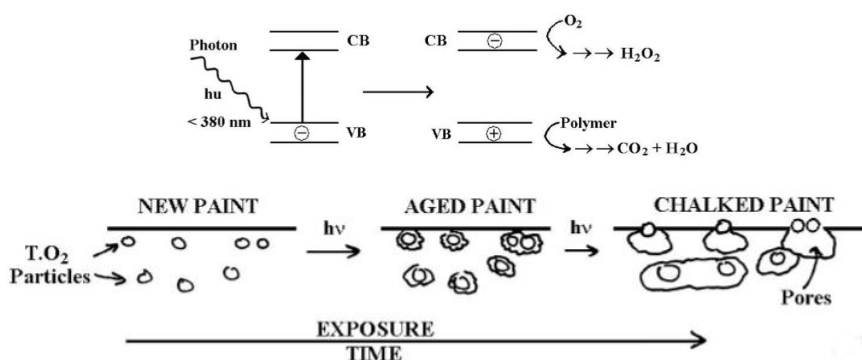


Figure 2.4. UV Degradation of Polymer Coatings [14]

UV exposure can also lead to a reduction in the molecular weight through chain scission and this can result in a reduction of the strength of the coating leading to adhesion failure [12]. It is well known that fading and embrittlement is very prominent in coatings exposed to high UV environments [12].

2.2.4.2 Temperature

Certain organic coatings such as thermoplastics are susceptible to softening at high temperatures and changes in the coating permeability and cracking are also possible. Cold temperatures can also be damaging as they often introduce brittleness to a coating leading to increased chance of mechanical damage. Large fluctuations in temperature can also lead to coating failure through the effects of thermal expansion. As the substrate and coating will often be composed of materials that expand at

different rates there is a high chance that cracking or delamination may occur depending on the organic coating used [8][12]. As mentioned previously because of this temperature fluctuations generally affect thicker paints to a greater extent [12].

If sufficient heat is applied then bond vibration can be such that bonds are broken [12]. This leads to formation of free radicals and degradation of the polymer through their reactions. Temperature is also known to increase the rate of penetration of liquids into coatings and the result of this is that water or other chemicals that can lead to deterioration of the coating are more readily absorbed [12].

2.2.4.3 Mechanical action

General wear of the coating can occur overtime due to abrasion by wind driven particles, solvent driven particles or accidental damage [8]. Mechanical deterioration of coatings can be considered in the following categories.

Internal stresses

During the drying and curing of a coating it is common for there to be some shrinkage in the coating as the solvent is lost. This, amongst other factors, can cause residual stresses to be retained in the coating. Furthermore, further residual stresses may be formed as the substrate is coiled or processed or by variations in coating thickness. As any areas of high internal stresses are thermodynamically preferential for defect formations these often form sites for the initiation of peeling or cracking of the coating overtime [12].

Abrasion

This is the name for any particle driven deterioration of the sample and so be prominent in buildings in dusty or sandy locations. This is usually more damaging for brittle paint systems, however by embedding hard particles or making the coating more elastomeric the effect is reduced. It is possible for the coating to be removed from the substrate by abrasion if the coating has poor resistance [12].

Erosion

This is a general term for the wear of the coating. It can be considered an extension of the chalking process. Although different to abrasion of coating it is increased in adverse weather and also is more damaging to brush coatings [11][13].

Impact

This is as simple as the coating being dropped or hit. Generally, this occurs in the installation of coated panels or in areas with moving parts or high traffic. This causes damage especially when the coating is below its glass transition temperature or is inherently brittle [12]. Often this is due to poor design, human error or lack of care and leads to exposure of the underlying substrate which can allow corrosion to begin.

2.2.4.4 Chemicals

Organic coatings are susceptible to attack from a variety of chemical groups depending on their composition. Certain solvents may attack them, or they may be penetrated by other chemicals which can have adverse effects on the components of the paint or the resin itself. There are many sources of potential chemical damage such as acid rain or pollution and all of these have the potential to degrade the coating in some way [8].

Water

Due to its small molecular size and polar charge, water molecules can easily penetrate into pores and cracks if they are present in a coating system. If the coating has a charge applied to it this penetration can increase through a process named electroendosmosis. This charging can occur if an electrochemical reaction such as a corrosion reaction is occurring hence the penetration of a coating by water could be considered a autocatalytic process in some circumstances [12].

Water ingress is damaging as it can separate loose bonds and cause expansion of the coating. Furthermore, hydrolysis of ester linkage groups can occur producing acids and alcohols. It is important to note that the rainwater composition varies geographically and hence other potentially damaging ions may be present depending on the location [12].

Solvents

Usually these are present due to their use in the coating process or formulation. However, problems can occur if the solvent is not totally evaporated off during drying or curing as the solvent molecules can separate the resin molecules leading to softening. Furthermore, certain solvents may encourage water penetration into the coating leading to the aforementioned problems [12].

Acids and alkalis

Acids can be directly present or can form as a result of gaseous species condensation or precipitation. Examples include acid rain or NO_x gases and both of these attack susceptible bonds which are common in organic coatings, such as urethane. Alkalis can attack coatings through a variety of methods but perhaps most commonly observed is saponification which degrades oil-based coatings by attacking the ester linkage groups present. Both acids and alkalis can also attack the constituents of the coating such as the pigments or any dyes if these components are susceptible.

Generally, however, due to the low ion permeability of the vast majority of coatings, chemicals do not penetrate easily unless the coating is very porous [12].

Gases

Oxygen molecules are a requirement for the reaction that results in the degradation via UV light of coatings. They allow the formation of ozone molecules which are a strong oxidising agent and aggressively attack the organic coating. Oxygen is also a contributor to degradation through heat as it can react with generated free radicals to rapidly produce more. This leads to loss of flexibility and increased permeability through depolymerization and chain fragmentation [12]. It is agreed, however, that ion permeation is far slower than that of oxygen which is far slower than that of water [12] which suggests that oxygen permeation is more likely to be damaging than ions but less likely than water.

2.2.4.5 Biological

Biological products that form or accumulate on the surface of coated metal products can hold moisture or a variety of chemicals inside them. These can lead to deterioration of the coating via the previous methods. For example by holding moisture close to the coating the likelihood of water penetration increases [12]. Some microorganisms produce acids or contribute to the reduced aeration of a section of material which leads to a more aggressive form of corrosive attack. Some bacterial will effectively feed of coatings [13] but this is often a geographically issue rather than coating composition problem with areas of low sunlight usually being the worst affected [13]. A significant issue with biological corrosion is the formation of unsightly black areas as a result of biological matter [11][13].

Mildew

This is a form of fungi that grows in humid environments. Certain coatings such as oil-based and coatings containing fatty acids can undergo direct attack from such a fungus. Also some components of coating systems can also be a food source for the mould and these are either directly consumed or degraded by production of an enzyme [12].

Marine fouling

This is caused when microorganisms or animals that attach themselves to a submerged sample. These often do not directly attack the coating but cause abrasion to the coating by changing fluid flow and can contribute to the formation of a differential aeration cell [12].

2.2.4.6 Corrosion under coatings

Under film corrosion causes significant damage to coatings and is provides the largest requirement for coating repair on constructed metal [10]. Three of the most commonly seen under film corrosion phenomenon are; blistering cathodic disbondment, corrosion creep and filiform [10].

Blistering

Blistering is a process that has been defined as ‘local separation of the coating from the substrate’ [8]. Generally, it refers to a phenomenon when a region of a coating fills with fluid, leading to swelling. The most common driving force for this process is the osmotic pressure due to the differences in concentrations between the coating and the environment. This is called osmotic blistering and is shown in Figure 2.5. In this case the coating is acting as the permeable membrane required for osmosis. Often blisters form because of substrate corrosion and gas blisters are possible if the reaction involves the evolution of a gas for example if hydrogen reduction is occurring [8]. Blistering will occur if the adhesion strength of the coating is less than that produced by the pressure of gasses or liquids and bursting of the blister can occur once the tensile strength of the coating layer is exceeded. It is important to note that increased adhesion strength reduces chances of blisters forming regardless of the conditions the coating is placed in [13].

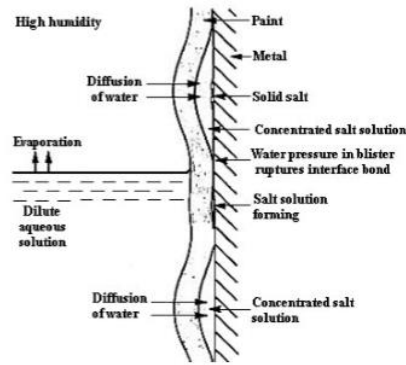


Figure 2.5. Osmotic blistering [14]

Blisters can also form due to contaminants that may be present on the substrate as a result of the surface preparation. For example, salt particles or some oils left of the substrate will encourage the diffusion of water though osmosis from a surrounding aqueous environment. Interestingly osmotic blistering is less prominent in highly concentrated environments such as saltwater as the osmotic driving force is from coating to environment. Often blisters become focal points for anodic dissolution, driven by the cathodic activity on areas of intact coating.

If the substrate is cold compared to the outside environment there is the possibility of vapour condensation forming blisters as shown in Figure 2.6 [13]. Electroendosmosis from overly cathodically protected structures can also cause greater blistering [13].

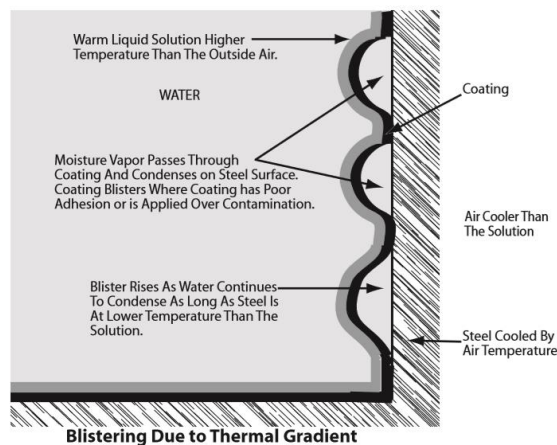


Figure 2.6. Blister Formation in Coatings [13]

Anodic and cathodic blistering

Figure 2.7 shows the formation process for an anodic and cathodic blister. In the case of anodic the blister is formed as a result of the iron ions forming iron oxide. In the case of the cathodic the blister is formed by the attraction of water by the OH^- group and the electroendosmosis effect [12].

There are three postulated methods for the effect of coating disbonding at the cathodic regions of a steel coated sample. Hydrolysis of the coating due to the alkaline conditions, oxide layer dissolution from the substrate and failure of the coating substrate interface. Furthermore, water is attracted by the OH⁻ groups present leading to an increased chance of blistering [12].

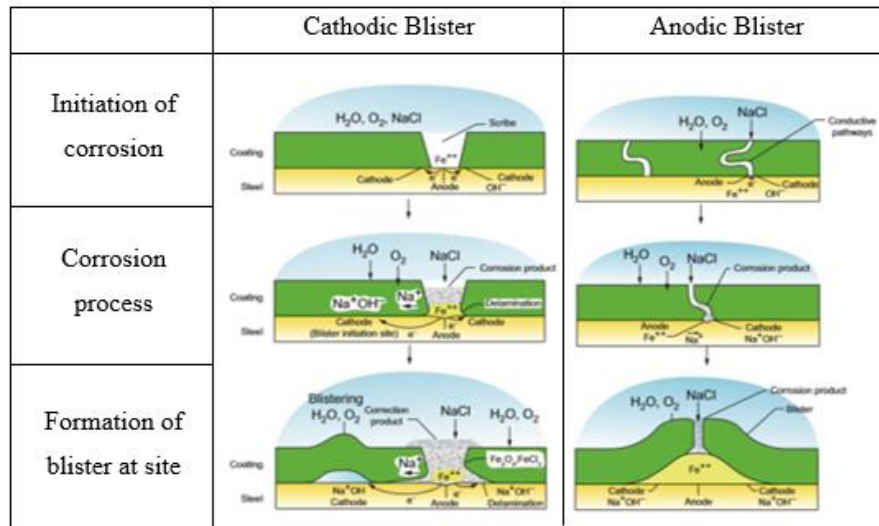


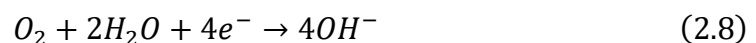
Figure 2.7. Formation of Anodic (right) and Cathodic (left) Blisters [12]

Filiform corrosion

This form of undercoating corrosion can be distinguished as small tendril like patterns on the surface of a sample, often radiating out from a defect such as a scratch. This is formed due to the action of an active acidic head which proceeds under a coating causing delamination. The ‘tail’ of the corrosion is highly aerated and alkaline. This is more of an aesthetic problem that one that can cause significant degradation of the substrate although degradation of the coating adhesion does occur [8]. Filiform corrosion is a more specialized mechanism mainly seen on aluminium products although sometimes on other metals [10].

Cathodic disbondment

Generally speaking, cathodic disbondment is the main failure method for coated steel that is either buried or submerged during use. However, it can form part of the corrosion creep propagation method. Cathodic disbondment is caused when a cathodic reaction of corrosion, oxygen reduction, is concentrated under the coating and the production of hydroxide and other species occurs.



These species react with the adhesion layer between the coating to the substrate and hence cause the coating to detach and peel away [10]. The build-up of OH^- ions leads to a localised pH increase and in salty solutions sodium ions diffuse into the delaminating front to maintain charge neutrality [10]. An example of this mechanism is shown in Figure 2.8. This can be seen where cut edges are submerged; the cut edge acts as the anodic site and cathodic activity takes place under the coating. Although commonly seen in lab-based testing this mechanism is less frequent in real applications where corrosion, indicative of anodic undercutting, is seen at the degradation front.

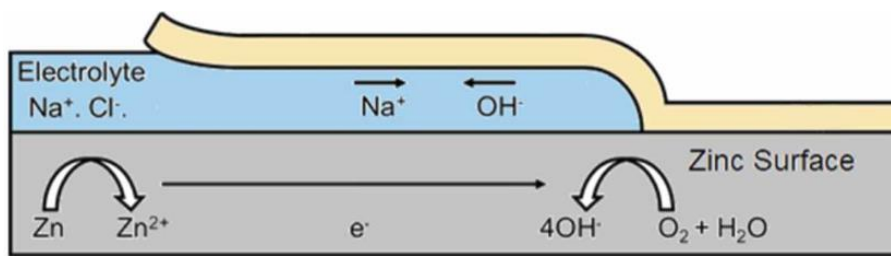


Figure 2.8. Example of cathodic disbondment mechanism [15]

Corrosion creep

Corrosion creep occurs where part of the underlying metal is exposed to atmospheric conditions be it at a defect in the paint or a cut edge. Initially only the exposed metal corrodes however with time the corrosion begins to creep under the coating hence the name of this degradation method. It can also be called anodic undermining, under cutting and under film corrosion [10]. Three of the most recognised mechanisms of corrosion creep are cathodic disbondment, wedging and anodic undercutting.

However more than one mechanism can be present at once [10].

Consider the previous example however if the cut edge dries or is in atmospheric conditions anodic undermining also known as undercutting becomes more prominent and this is often the dominant method that is seen in field testing [10] [16]. This is when the substrate under an intact coating becomes the focal anode and corrodes and hence the coating loses adhesion to it [13]. Often this process leads to the formation of a differential aeration cell leading to aggressive anodic attack. Examples are shown in Figure 2.9 and Figure 2.10. Furthermore, to balance the production of iron II ions negative ions migrate into the anodic site and in marine environments this is commonly chloride ions. Hydrolysis of the product, iron chloride produce low

local pH values and turn this may lead to increased corrosion rates through initiation of hydrogen evolution [10].

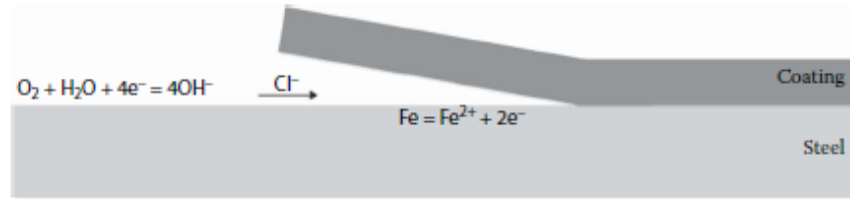


Figure 2.9. Example of anodic undermining mechanism [10]

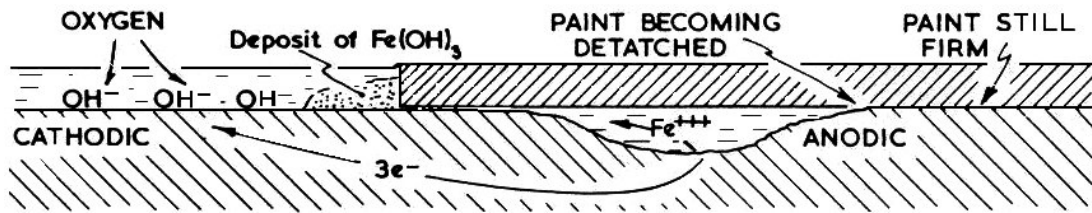


Figure 2.10. Example of anodic undercutting leading to formation of a differential aeration cell [14]

The final mechanism of anodic undermining, wedging, causes the coating to be forced away from the metal substrate by the production of corrosion product which exposes further metal for atmospheric corrosion [10][17]. This is because the products of corrosion occupy a greater volume than the initial metal and hence it is an expansive process [12]. Unless the adhesion of the coating to the substrate is poor or there is poor preparation of the surface prior to painting, this is not a dominant mechanism [10]. Often this is described as a mechanical process of coating failure [17].

2.3 Sensing Technologies

Coating failure and corrosion has long been recognised as a serious potential route to the failure of components in many different sectors. Hence a wide variety of techniques have been developed and exist that aim to detect the development and severity of defects. In this chapter some of the most promising and prominent current techniques are briefly introduced and their applicability to pre-finished coated steel is explored. The techniques have been split into a number of categories as shown in Table 2.1.

Table 2.1. Current Techniques

Family	Family/Technique	Technique
Non-Destructive	Wave based	Acoustic emission Ultrasonic Terahertz waves
	Magnetic	Magnetic flux leakage Magnetic adaptive testing Magnetic memory method
	Thermal	Pulsed thermal NDT Infrared thermography Eddy current pulsed thermography
Optical	Visual	Corrosion indicating paint Stressed optical fibres
	Fibre based	Braggs gratings Corrosion product detection Interferometry
Mass		Corrosion coupons
Electrical		Galvanic Zero resistance ammetry Electrical resistance Induction resistance probes
	Resistance	Capacitive sensor Electrical field signature method
Electrochemical		Potentiodynamic polarisation Harmonic analysis Electrical impedance spectroscopy Electrochemical noise Scanning electrochemical microscopy
Other		Embedded strain gauges MEMs based sensors Nuclear thin layer activation
	RF Based	RFID technology NFC technology
	Conditions	Biological detectors pH sensors Chemical sensors Simulations

2.3.1 Non-destructive testing

2.3.1.1 Acoustic emission

The basic principle of this technique is to determine the condition of a structure by detecting sound waves emitted from it due to the sudden redistribution of stress and associating this with damage or defects [18]. Usually, cracks are the defect responsible for the generation of the sound detected and the waves generated are often dependant on the geometry of the crack [19]. Hence, this is a so called ‘passive method’, the sensor simply tells you when the sample fails in some way rather than how it is performing [20]. The basic working principle of this technique is shown in Figure 2.11.

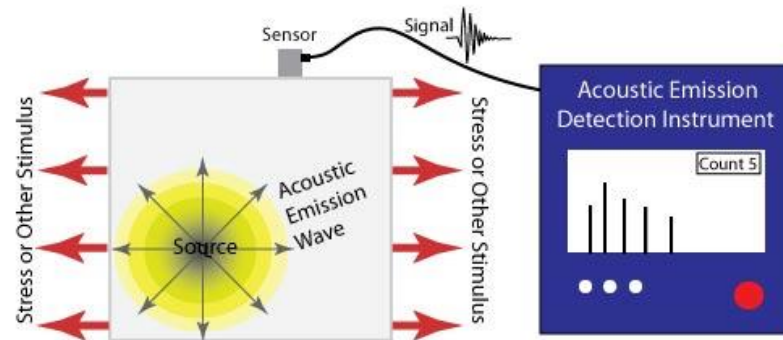


Figure 2.11. Acoustic emission detection [21]

Generally, the sensors are piezoelectric and are connected to the surface of the test material. They produce signals which can be easily amplified, filtered and computationally analysed [18, 21]. It is important that the frequency spectrum of the sensor corresponds to the test medium, the scale of the sample and the expected defect that will be generated. Normally higher frequencies are expected from smaller specimens and vice versa [19].

A benefit of this technique is that it allows a cumulative calculation of defects and damage and hence an estimate of the remaining lifetime until failure. Use of multiple detectors can allow spatial determination of a defect location and hence propagation and severity indications [20]. It has also been reported that it can distinguish between flaws that are active (are increasing in size/severity) and those that are not [18].

A disadvantage of this technique is the required sensitivity. For example, if the sample examined is very small the acoustic emission will be of a similarly small magnitude, so detection may be difficult. There is also high possibility of noise from

the surround and a difficulty in determining the size of the defect without further testing using additional techniques.

Perhaps the simplest application of this method is in determining the damage to bridge cables by measuring the sound waves generated when individual wires break. The number of emissions and the frequency of their detection can be easily corresponded to the lifetime of the cable [23].

There has been some success in using this technique for coating monitoring, most notably analysis of thermal barrier coatings when subjected to thermal cycling [22]. In this work [24] cracking of an approximately 100 μm thick coating due to thermal fluctuation was detected and an estimation of coating condition was possible. However, it is considered that while this specific application, in which the most likely coating failure method is via cracking, is useful the technique may be less applicable to detecting failure from general weathering of samples.

2.3.1.2 Ultrasonic

This technique utilises ultrasonic sound waves. Sound waves are the propagation of mechanical or elastic energy through materials via the mechanical vibration of particles about a fixed point [20,25].

Ultrasonic waves refer to high frequency soundwaves of 20,000 Hz and higher, representing the highest of the three regions of the sound spectrum: the others being audio and infrasonic [25]. The short wavelength associated with high frequency ultrasonic waves gives better resolution than, for example, infrasonic waves which are used for the detection of earthquakes [25].

This non-destructive technique uses the time difference between ultrasonic vibration generation and detection in order to allow accurate distance measurements to be made. Frequencies between 1 and 6 MHz are common testing frequencies used [25] and the probe is often piezoelectric. When ultrasonic waves passing through a medium encounter a different medium they are partially or totally reflected; this is due to their short wavelength, not dissimilar to the wavelength of light [25]. These reflections are picked up by a detector and a simple calculation is used to determine the distance travelled by the vibration and hence the location of defects can be determined. The basic principle is shown in Figure 2.12; Case 1 shows ultrasonic testing of a defect free specimen in which ultrasonic waves propagate through the

material and reflect off the base and return to the sensor. This gives rise to two peaks separated by the time taken for the waves to reach the base and return, distance D . In Case 2 there is a defect which causes reflection of some of the ultrasonic waves giving rise to an additionally detected peak at a closer defect distance DD .

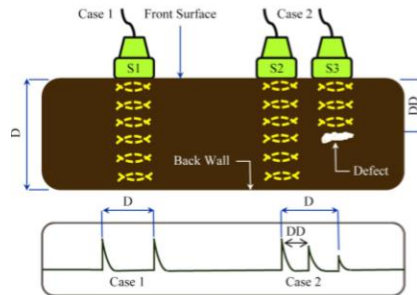


Figure 2.12. Ultrasonic testing principle [26]

There are two main methods for ultrasonic testing, straight and angled beam. In straight beam the ultrasonic vibration is not continuous, and the vibration is directed in a straight beam into the sample. This is effective at detecting defects parallel to the surface of the sample. Angled beam testing is more common in weld analysis and uses vibrations at an angle to the surface to allow better detection of defects that are not parallel to the surface. This makes angled beam a more complex, but often more accurate, method [26].

Currently, the technology exists for easy affordable and reliable measurement of coatings of several mm in thickness [27]. This technique is already extensively used in the oil and gas industry for a variety of testing including measuring pipe thickness and condition of welds [26].

Unfortunately, the quality of results is affected by surface condition and dirty or rough surfaces will produce a significant quantity of noise and hence reduced likelihood to easy detection [28].

Limitations in detection due to noise are best avoided when the medium tested is homogenous in nature due to a reduction in the presence of reflections due to porosity or inclusions [19].

It is known that the accuracy of this technique is directly corresponding to the speed of sound in the measured medium [27]. Testing is also required in order to determine accurate quantitative measurements: a test piece of known thickness should be used

as a reference. However, an advantage of this method is that temperature is not usually a significant variable [25].

A probe that could generate and detect ultrasonic vibrations could determine thickness measurements of coatings. It is possible that, with sufficient calibration, the determination could be made between different coating layers, as shown in Figure 2.13 [27]. It is important, however, to note that as these layers are decreased in thickness limitations in distinguishing layers occur due to noise and that these layers require distinct properties for accurate detection.

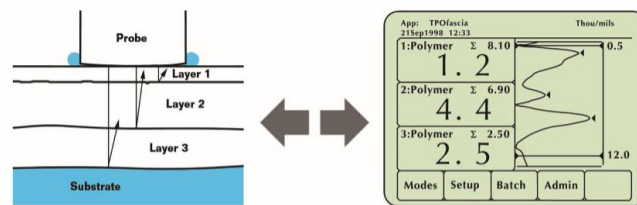


Figure 2.13. Application of ultrasonic testing to coating layers. On the right the numbers refer to the calculated polymer layer thicknesses measured by considering the different reflections provided by each layer [27]

The potential of this technique cannot be understated as there is a great deal of information that could be determined by such testing. For example, by carrying out thickness measurements over a set time period, the rate of paint degradation could be measured, and the expected lifetime estimated. Furthermore, it may be possible to detect otherwise difficult to see defects, such as individual layer delamination or osmotic blistering by comparing the expected thicknesses of each layer to measured. Finally, the fact that this is a spatially resolvable procedure is very important; flaws are not only detected but their location and size can precisely be measured [20].

There has been success using other waves such as acoustic waves in the same way [29]. An example looked at lacquers on food beverage cans with the aim of detecting blisters and deformation of the coating [29]. An example of the equipment used, and the measurement method is shown in Figure 2.14.

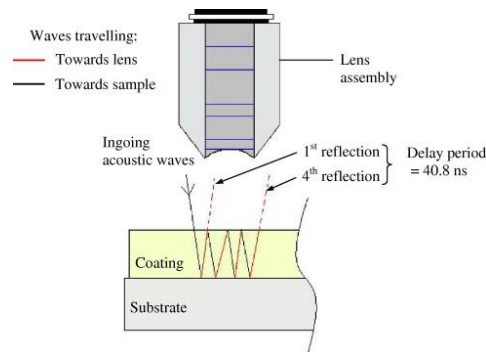


Figure 2.14. The use of acoustic waves to measure coating thickness [29]

However, there is concern that at the thickness that is required for some coating systems this method becomes far too sensitive to noise for in situ measurements. Furthermore, the requirement for a clean sample that is easy to access to scan a probe may limit feasibility. There is also an argument that this type of testing is too reliant on human involvement as the scanning of the probe would be difficult to automate across a complex building geometry.

2.3.1.3 Terahertz waves

This is a technique similar to that of ultrasonic testing but that involves using terahertz waves, which are electromagnetic waves with a frequency between that of light and radio waves [30]. By measuring the time delay of returning reflected waves the thickness of the sample can be measured accurately if the refractive index is known [30]. Photoconductive antennas can and have been used for both detection and generation of terahertz waves and thickness measurements of 300 μm have been achieved [30].

This technique has been successfully used to measure the thickness of ceramic topcoats used in thermal coatings as it is better than ultrasonic testing at analysing thicker coatings which are more defect prone [30]. There has also been success in measuring the thickness of marine protective coatings [31].

Further benefits of this technique are that it is better for analysing coatings that are opaque or that heavily scatter visible or infra-red light, when compared to ultrasonic [31]. Changes in thickness, refractive index or absorption coefficient can be detected [31] all of which may be affected by degradation of a coating or corrosion.

2.3.1.4 Magnetic flux leakage

This is the most common, non-destructive, electromagnetic technique for determining metal loss and damage due to corrosion [32]. It relies on the basic principle that the direction and strength of a magnetic field surrounding a magnet can be defined by magnetic flux lines [32].

In this technique a magnet is used to saturate an area of a sample with magnetic flux. A sensor then measures deviations in the expected flux lines of the magnet; these deviations can be attributed to defects in a sample which cause the flux to ‘leak’ out of the sample due to the change in relative magnetic permeability. An example of a standard set up and the working principle is shown in Figure 2.15 [28].

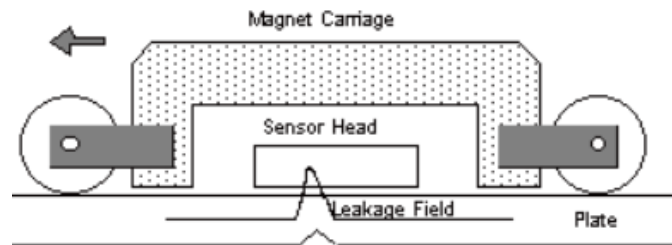


Figure 2.15. Example magnetic flux leakage device [28]

There are two main types of sensors used for the detection of leakage field, these are Hall effect devices and coils [28]. Both produce a voltage dependent on the strength of the magnetic field passed through them based on the principles of Faradays law of induction.

This technique is used extensively in the pipeline industry where ‘pigs’, cylindrical units composed of magnetic flux leakage sensors, are sent down the inside of pipes frequently with a 90–95% detection rate for defects greater than 10% of the pipe thickness [32].

When used on clean surfaces up to 10 mm there is reliable detection of 10–20% thickness changes and scan speeds of 0.5 m/s are possible [28], however, the cleanliness of the sample is crucial in reducing noise and hence samples are often cleaned before measurement.

It should be noted that MFL can still maintain sensitivity when the test sample is surface coated [28] and hence is expected to be able to give useful data of the condition of the substrate and hence the effectiveness of the coating. This is proven in [33] where a MFL device is used to detect artificial defect cracks down to 1.4 mm

in a steel sheet even when various composition coatings up to 30 mm are used. Although organic coatings were not used in this work it is expected to behave similarly.

However, it is evident that this technique is limited to ferrous materials for obvious reasons and calibration to the specific magnetic permeability of the specimen is also required [28].

A variation of magnetic flux leakage, known as magnetic particle testing (MPT), uses a magnetic powder to visually detect the defects. The magnetic powder is attracted to the flaw regions as where 'escaped' magnetic flux is strongest and hence indicate the presence of flaws. Despite common use in NDT testing, it is unlikely to be easily automated as a method of testing due to complications in cleaning and applying the test medium [34].

2.3.1.5 Magnetic adaptive testing

This is a fairly newly developed technique which is based upon the principle that structural defects in a ferromagnetic material will affect the magnetisation of that sample [35]. It has been suggested that different flaws will have unique effects on the magnetisation process [35]. The magnetisation of an object is often considered by examining the hysteresis loop, the relationship between the magnetisation of a material with an applied magnetic field intensity. Hence, it is expected that, by analysing a large number of subsequent hysteresis loops for a sample, the health of the sample can be calculated. This is done by measuring the voltage induced in a pickup coil as the magnetising field changes [35].

It is accepted that a large amount of experimentation will be required in order to determine the type of defect or to be able to determine severity. This method has been suggested for use in nuclear reactor pressurised containers, however, fatigue testing of samples is also thought to be an application.

The applicability of this technique is limited as it has mainly been applied to measuring strain in metal samples, which may be difficult to relate to corrosion of the sample. Furthermore, measuring the magnetic properties of the material in situ would be complex.

2.3.1.6 Magnetic memory method

This method developed by A.A Dubov determines stress concentration zones by detecting changes in the residual magnetisation field [36]. This has been described as ‘the measurement of self-magnetic flux leakage’ (SMFL) [37]. It relies on the detection of abnormal magnetic fields without magnetisation or stimulation. These are developed as a result of stress concentration zones and hence allow predictions of lifetime of a sample [37].

Stress concentration zones accumulate as irreversible changes in the magnetic domain of structures under load in ambient geomagnetic conditions. This means that the magnetic state of a sample at any point is related to the concentration of stress through structural damage. Hence, measurement of SMFL and its distribution can give information about structural health [37]. These measurements are made using a magnetometer which detects ‘places of maximum inhomogeneity’ shown by describing changes in magnetic field components at any point [36].

The disadvantage of this method is that its practicality outside a theoretical assessment has yet to be proved and therefore it may not be as accurate or quantitative as other techniques [37]. Furthermore, this technique has only currently been applied in any detail to pressure pipes and pipelines [37]. The lack of quantitative data received implies that this technology can only accurately be used to determine points of interest for further testing and there is difficulty in relating measurements to the actual level of damage present [37].

However, it does have the benefits of early failure detection and ease of use and it does not necessarily require application of an external magnetic field. With sufficiently sensitive measurement sensors ambient magnetic fields can be used instead leading to less equipment demand than, for example, magnetic flux leakage. Other benefits include good resolution, up to mm level, that can be measured at a speed in the order of meters a second [37].

2.3.1.7 Eddy current testing

This is a form of electromagnetic testing based on the principle of electromagnetic induction [38,39]. By passing an alternating current through a coil a magnetic field is produced and this in turn produces eddy currents in a sample when placed in close proximity to it; these eddy currents then produce their own magnetic field which

opposes the primary field. Defects cause a change in these secondary magnetic fields and hence produce a shift of impedance on the primary coil [40]. These impedance changes or simply changes in the secondary magnetic field are measured [40,41]. Hence, changes in conductivity and permeability are measured and these can be related to corrosion effects [40]. Frequencies between 50 Hz and 1 MHz are commonly used [38] and an example of this principle is shown in Figure 2.16.

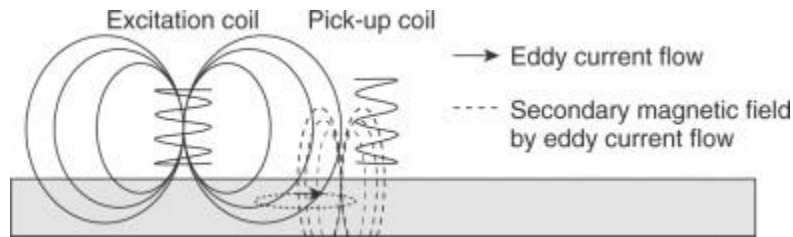


Figure 2.16. The principles of eddy current testing [40]

Although often used for metal substrates it can also be used to measure organic layer thicknesses as shown in Figure 2.17. This is possible by monitoring the feedback effect produced when the probe is placed near a coated substrate as described in [42].

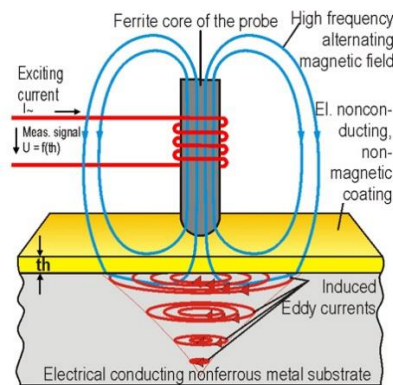


Figure 2.17. Use of eddy current testing on organic coatings [43]

Advantages of this technique include good sensitivity and the ability to penetrate through layers on top of the substrate. These could be coating layers or accumulated dirt which means that pre-cleaning of the substrate is not as crucial as with other testing, such as magnetic flux leakage [38]. It has also been reported that coatings of up to 5 mm thickness can be penetrated which is far thicker than the coatings for the scope of this work [38]. There are also benefits of easier automation and portability when compared to other non-destructive techniques [38] such as ultrasonic. It has also been suggested that under coating corrosion (of few mm) can be detected in early stage, independent of thickness of coating (300–1000 μm) or presence of corrosion product [41].

Disadvantages include accuracy issues, caused by natural variation of permeability values of the substrate and coating, and the complexity and difficulty in signal interpretation [38]. Furthermore, it has been suggested that defects out of the plane of view are often not detected and those scans of geometries that are complex is difficult to implement [38].

Insulating coatings for storage tanks have been analysed using eddy current testing with success. These were an epoxy glass reinforced phenolic coating and a modified epoxy on steel substrate as documented in [41]. There has also been some success using eddy currents to measure the integrity of thermal barrier coatings on gas turbine blades [44]. Example of developed sensors such as [42] exist as do the use of eddy current testing for measurement of non-conductive coatings such as [39,45]. Heterogeneities in the coating can lead to a phenomenon ‘lift-off variation’ [41] and this lift off effect can be used for thickness measurements for thicknesses of 0.5–25 μm

Furthermore, a technique called ECCPC (eddy current co planar coil configuration) has been developed for measuring thickness of non-conducting layers and is documented in [45]. However, summarily to ultrasonic testing these devices suffer in terms of ease of automation, scanning complex large geometries with human interaction may be difficult.

2.3.1.8 Infrared thermography

This is a technology that relies on the principle that the thermal signature produced by a component will be dependent on the presence and severity of defects in that sample [46]. There are two types of infrared thermography: active and passive. In active thermography the sample is stimulated with a fixed quantity of infrared energy and the resulting thermal signature, when the infrared source has been removed, is measured. In passive thermography the sample is not stimulated with any infrared energy, the ambient thermal signature is simply monitored [47].

It is generally agreed that using active thermography allows much better characterisation and detection of defects [47]. Hence, a commonly used experimental set up will be composed of a heat source and a detector [46]. Often the detector is simply a sensitive infrared camera, however, a variety of heat sources can be used

from a simple heat gun to devices using electromagnetic radiation and electromagnetic effects to heat the sample [46,47].

Advantages of this technique are that it can be used on any material, but effectiveness does depend on factors such as the thickness and the material thermal properties [46]. It can also be used to analyse a large area rapidly on a variety of sample shapes [46] and no contact to the sample is required so it is often easier to implement than another non-destructive testing method [46]. Finally, the equipment is relatively safe and simple [47].

The main disadvantage of this technology is that it requires very sensitive infrared sensors. It is also of crucial importance that the stimulating infrared source supplies an even reproducible quantity of energy to the sample. Due to the sensitive nature of this method, external factors present in situ, such as sunlight and other weather features, could drastically reduce the accuracy of measurement.

There has been some success of detecting corrosion under coating, blisters, ruptured blisters and filliform [48]. There is also some evidence to suggest that this technology can allow the size and severity of the corrosion to be determined [48]. An example of active thermography operation is shown in Figure 2.18 below [47].

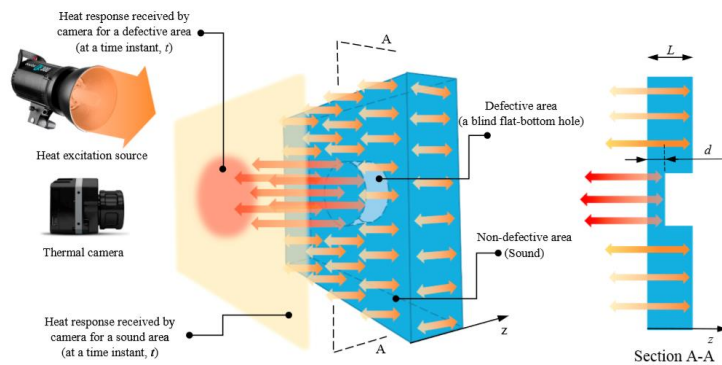


Fig. 7. Schematic of heat diffusion and response through a defective solid.

Figure 2.18. The principles of thermography [47]

2.3.1.9 Pulsed Thermal NDT

This is a form of thermography testing in which the sample is thermally stimulated using a series of pulses of thermal energy and the resulting thermal field is analysed [49]. Stimulation can be through a variety of methods including mechanical waves, optical radiation, microwaves, inductive methods, electrical or eddy currents or

through heated gasses [49]. As the stimulating source can be more finely controlled, temperature deviations should theoretically only occur at areas where there are defects [49]. The benefit of this specific version of thermography is that it can be used over large areas, using a linear or on a point-by-point test basis, and produces spatial determination of defects. For all stimulation methods the distance between the sample and source/detector are important factors in the overall sensitivity of the method [49].

2.3.1.10 Eddy current pulsed thermography

This is a variation of thermography technology that has been used in [50,51] to detect corrosion blisters in coated substrates. It involves heating a substrate through a coating using electromagnetic induction and analysing the resulting thermal patterns created [50]. Hence two steps are involved: through coating heating and through coating imaging [50]. Eddy currents that are generated in the substrate, by application of a magnetic field, generate heat through resistive heating and joule heating [51]. This heat then conducts through the material until there is a thermal balance set up and infrared radiation is then emitted from the sample [51]. An example of this process is shown in Figure 2.19.

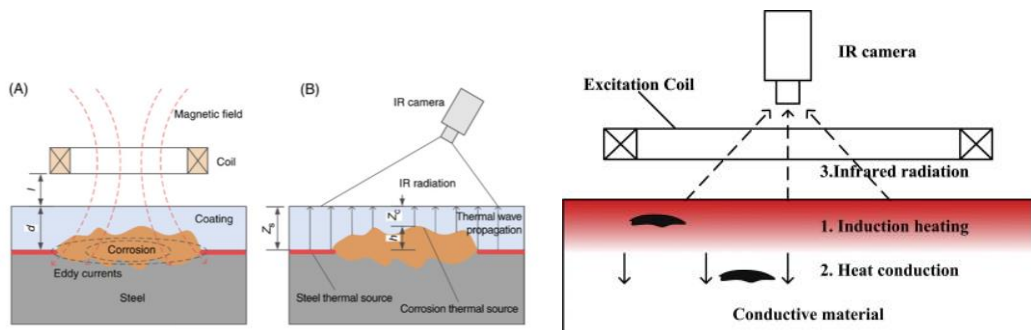


Figure 2.19. The principle of eddy current thermography for use in (left) corrosion detection and (right) generic defect detection [50] [51]

At areas where the coating is deteriorated a hot spot is detected due to the reduced insulating effect given by a deteriorated or thinner coating. Experimentation has shown that corrosion on a non-coated sample shows as a hot spot, as does corrosion under a coating although this effect is reduced by the coating present. A blister in a coating will show as a cold spot due to the increased distance and material that the infrared radiation has to penetrate to be detected. As expected, a crack or broken coating will show as a hot spot [51]. This is displayed in Figure 2.20.

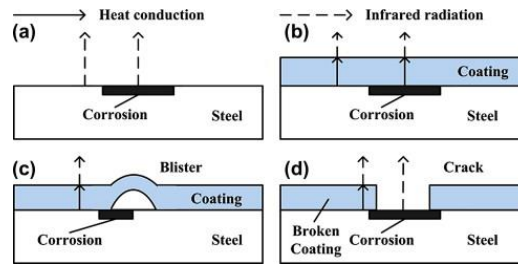


Figure 2.20. The effect on the measured thermal energy of different coating failure modes: (a) corrosion, (b) under coating corrosion, (c) blistering, (d) coating failure [51]

This technology combines the benefits of eddy current testing with the large scale, rapid imaging of thermograms [50]. Non-uniform heating is the main barrier to accurate measurements with this technology. The sensitivity previously mentioned is also a potential limitation of this method and it requires experimentation on each coating used in order to determine the thermal barrier contribution of different compositions [51].

2.3.2 Optical Techniques

2.3.2.1 Corrosion indicating paint

This works on the principle that there is some component present in the paint layer which can signal the onset of corrosion by way of some reaction with a component of corrosion.

There has been some success with redox and metal ion complex fluorescent materials; these either become fluorescent when oxidised (redox) or fluoresce as a result of forming complexes with metal ions produced through corrosion (metal ion). An example is Oxine which fluoresces when reacted with corroded aluminium, or Fluorescein [52].

Another approach involves detecting changes in pH as, in localised corrosion, it has been shown that there can be large changes in acidity or alkalinity. pH triggered microcapsules can be made from 1 micron in diameter upwards with a release time of approximately 4 h in pH 8–10 or 1–4. An example of these microcapsules is shown in Figure 2.21. They can either contain dyes to indicate where this localised corrosion is occurring or healing agents to arrest the corrosion. Current work includes making the paint itself a fluorescent dye capable of responding to pH changes [53].

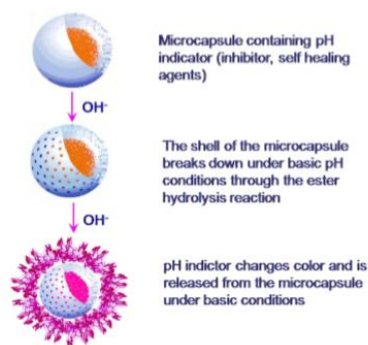


Figure 2.21. The principle of a smart release pH triggered microcapsule [54]

A recent example of this approach is given in [55] which describes the development of a nano-sensor composed of dispersed mesoporous silica shells filled with organic molecules. These molecules undergo a reaction with iron ions present due to metal dissolution during corrosion causing fluorescence as shown in Figure 2.22.

Alternatively the shell of these capsules can be composed of ester or thioester groups which undergo hydrolysis under high pH conditions releasing the indicator [53]. It was reported that these particles allowed corrosion detection before visual detection of corrosion products (iron oxide) and has also been successfully implemented in an organic coating. Measurement of the fluorescence was carried out with a fluorescent microscope and FCS (fluorescent correlation spectroscopy) [55].

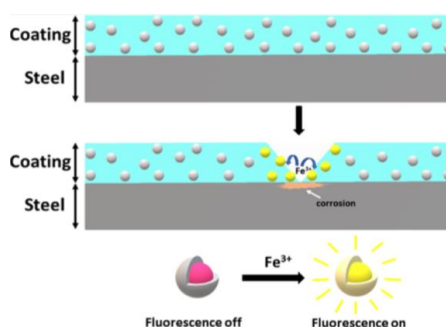


Figure 2.22. The principle of corrosion triggered fluorescent microcapsules [55]

Although using a dye directly would be easier to implement, by using microcapsules issues such as dye solubility in the paint system can be avoided [53]. It has been reported that oil core capsules were compatible with water-based paints and solvent based paint compatible with water core capsules [54]. Furthermore, adhesion testing and basic corrosion testing has shown that there was little effect of the addition of these microcapsules on the coatings' properties [54].

The advantages of this technology are that, theoretically, the capsules can contain anything including liquids and solids. Hence a wide range of indicators may be used,

or the capsules could facilitate implementation of new inhibitor systems without having to modify paint characteristics. Furthermore, as the mechanism of release does not require mechanical breaking these capsules can be used to detect or combat corrosion under a film [54].

A potential disadvantage is that the microcapsules sit in the paint system and could potentially interfere with the adhesion or protective qualities although some testing by Li et al. has suggested this is limited for certain coatings [53]. However, the potential of capsules to rupture during the coating process or to disrupt current methods of painting and curing are as yet not fully documented. It may well be the case that these capsules may be unsuitable for current coating methods leading to decreased ease of implementation. Furthermore, it may be considered undesirable to have visual indicators of corrosion as it could lead to unsightly patches of colour change on a façade.

2.3.2.2 Stressed optical fibres

In the literature these are also referred to as a corrosion fuse [56]. This technology involves embedding stressed glass optical fibres in the medium to be monitored. As the medium is corroded or begins to fail the stressed optical fibre is gradually exposed until the medium no longer supports the fibre and it fails. By passing light through the fibre and measuring the intensity, it can be determined when the fibre has failed [56,57]. A visual description of this process is shown in Figure 2.23 [57][56].

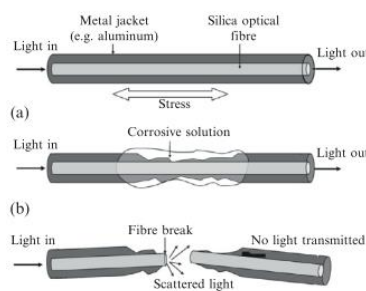


Figure 2.23. The basic principle of a corrosion fuse [57][56]

By embedding fibres at different depths, there is the potential that the rate of penetration can be calculated, and a lifetime estimate, or maintenance schedule could be determined. Alternatively, by having several optical fibres coated in differing quantities of metal a rate of corrosion could be estimated.

There has been some evidence suggesting that aluminium coated fibres under testing show results that correlate with expected corrosion times [56] suggesting the technique provides accurate results. There are also some commercially available wire sensors (Cosasco) which allow monitoring by passing a current through them reducing the requirement to use thin brittle glass fibres.

Fan [58] used optical fibres to measure the expansion due to corrosion of steel fibres in reinforced concrete. In this case BOTDA (Brillouin optical time domain analysis) was used to measure the strain imparted on the optical fibres. It was reported that strains as small as $100\mu\epsilon$ could be recorded [58].

The advantage of this technique is that it is very easy to analyse the data produced and directly relate that to the coating condition. A potential disadvantage of this technology is that it may, itself, reduce the coating protective properties by decreasing adhesion or increasing the likelihood of defects forming. Additionally, it is difficult to imagine how this could be scaled up to factory levels of production considering the fibres are extremely brittle and thin. Depending on the coating thickness there may also be aesthetic issues created by using embedded fibres and there are limitations to how thin the fibres can be made and handled.

2.3.2.3 Bragg gratings

A Fibre Bragg Grating (FBG) is an optical fibre that has periodic changes in refractive index along certain lengths of their fibre. This has the effect of creating an optical filter that reflects certain wavelengths and only transmits others [57]. The effect of this is that any changes in pitch length of the fibre can be measured by relating these variables to back reflection at certain wavelengths [57]. This is given by the formula:

$$\lambda_B = 2n_{eff}\Lambda \quad (2.8)$$

where λ_B is the resonant wavelength, n_{eff} effective refractive index, Λ pitch length of the grating [57].

These changes could be induced by deformation, induced by corrosion, or could be down to a coating failure type that involves deformation of the coating; for example, osmotic blistering. Therefore these sensors could potentially be used to measure and determine corrosion related strains as well as coating issues, such as delamination [59]. As changes in strain occur in the coating, due to corrosion or failure, the Bragg

grating wavelength changes and the corrosion rate can be calculated [59]. The effect of strain on a Bragg grating is shown in Figure 2.24.

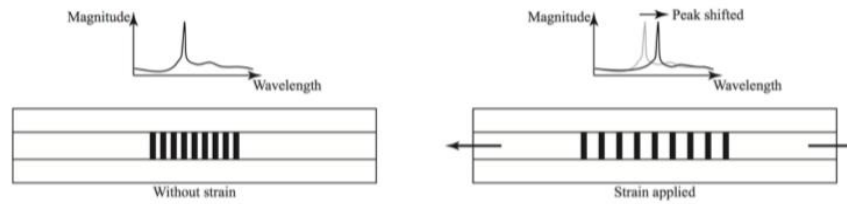


Figure 2.24. The response of a Bragg grating to an applied strain [60]

Many companies have developed this technology and there has been some implementation success in the civil industry using integrated FBGs to monitor static building structures [57]. There has also been some success in embedding these sensors into coatings (polymeric and metallic) on top of steel [59,60]. These studies showed that results from FBGs could give readings that correlated with electrochemical tests carried out simultaneously. Furthermore, FBGs have been deployed into concrete rebar structures to measure corrosion [59] and it was reported that the FBG method was within 1% of the calculated electrochemical corrosion rate [59] (for a metallic coating). An example of a Bragg grating detecting the formation of a blister in a coated product is shown in Figure 2.25.

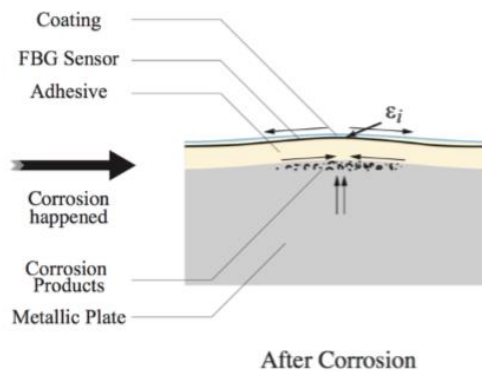


Figure 2.25. Detection of corrosion blister forming under a coating by a Bragg grating [59]

Potential advantages of using this technology include the ability to determine damage to the coating as well as movement of the coating due to delamination or blistering. Their high sensitivity, low cost and ease of installation are further benefits of FBGs. It has also been shown that the Bragg fibre is capable of surviving thermal metal coating deposition so it is expected to be able to survive application of a paint system [60]. Finally as they are a well-developed sensor technique they are available

commercially at high quality and it has been suggested that measurement of crack initiation and corrosion rate under polymeric coating is possible [59].

The main disadvantage of the Bragg's grating is that it is affected by temperature so a temperature reference sensor is required [59]. Furthermore, the coating may fail via a method that does not induce large strains in the coating, for example UV degradation, and the effect on embedding these systems on the lifetime of the coating is not well documented.

2.3.2.4 Corrosion product detection

It has been suggested that it may be possible to optically view the product of corrosion using optical fibres [61].

One study looked at the production of Al ions when airframes begin to corrode [61]. In this test, aluminium ions were made to react with a compound to form a fluorescent metal ion complex. By passing UV light down a fibre, it was possible to detect the presence of Al ions by detecting the presence and intensity of fluorescent light. Some factors such as pH and water absorption were observed to affect the ease with which the chemistry could be controlled [61]. Although experimental and subject to complex manufacturing requirements, it offers an insight into other ways optical fibres may be used.

2.3.2.5 Interferometry

This is a device that measures distances by comparing the phase change achieved between light that has reflected off the front and back interfaces of a sample. This phase change can be related to the thickness between the two interfaces of the cavity by the equation: [57]

$$\delta = \frac{2\pi}{\lambda} 2nl \cos\theta \quad (2.9)$$

where δ is the phase shift, λ is the wavelength, n is refractive index of cavity, l is thickness of cavity and θ is angle of the light. An example of a device made of an optical fibre used to measure coating thicknesses is shown in Figure 2.26.

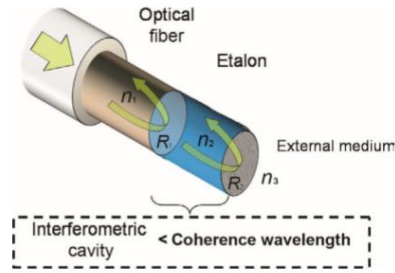


Figure 2.26. Optical fibre interferometer [57]

These devices are used for measuring a variety of variables such as strain, pressure and displacement [57]. There has also been some success in using this technique to monitor ABS coated copper by detecting changes in distances [62] and it has been reported that 2D and 3D microscopic profiles may be constructed from testing. In this case, the difference in the sample thickness before and after corrosion was measured as shown in Figure 2.27.

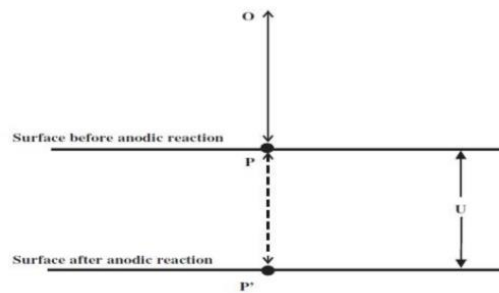


Figure 2.27. Effect of corrosion on path length of light used in interferometry [62]

A commonly used method, the Michelson interferometer, involves using a beam splitter and two light paths and precise measurements can be made through analysis of the interference pattern. Advantages of this method include very accurate distance measurements; disadvantages include the large quantity of equipment and the sensitivity. Furthermore, the high likelihood of noise may limit in situ suitability and poor durability that may mean the sensor is damaged during panel installation or maintenance.

2.3.3 Gravimetric Techniques

2.3.3.1 Corrosion coupons

Possibly the simplest of all the sensor technologies, these are samples that are weighed, exposed to an environment for a set amount of time and then cleaned and reweighed to calculate the rate of mass lost [63,64]. Quicker and more accurate readings can be achieved by using coupons with larger exposed surface areas and

hence coupons come in a variety of shapes and sizes depending on the requirements of the situation [63].

Often coupons are used as an indicator of the corrosivity of an environment and how this varies across a building envelope. Coated corrosion coupons are used to allow measurement of paint integrity, but similarly these require manual testing or inspection at periodic intervals.

Advantages of corrosion coupons include their low cost and ease of use. They are durable, compared to some other techniques, and there are no complicated electronic control systems or power requirements [63]. They can also be used in any environment and be made out of virtually any material required [65].

The disadvantages are that they can take time to produce data and it is possible the sample does not reflect the bulk material being measured. Furthermore, readings are time consuming and prone to human error and the often localised nature of corrosion is neglected by solely testing with coupons [63]. There is also a requirement that the coupon is not interfered with by any external effects during testing [65].

Despite very common use in civil and the oil and gas industry there is little evidence that they have been applied to the determining of in situ performance of organically coated steel. The main issue with this technology is that it just shifts the item to be monitored from the building to this coupon, manual inspection and testing is still required however now the sample may be less representative.

2.3.4 Electrical Techniques

2.3.4.1 Galvanic

This is a similar technique in some respects to corrosion coupons, however, relies on the principle of galvanic corrosion. The system is composed of two metals, one which is more electronegative and hence becomes the preferential anodic site. The current of the produced galvanic cell is measured and can be directly related to the corrosivity of the environment [66]. Often measurements are taken using the ZRA method [66].

2.3.4.2 Zero resistance ammetry (ZRA)

A standard ammeter will allow the determination of a current by conversion of measured voltage across a resistor by Ohms law [67]. Zero resistance ammeters

reduce the chance of interfering with the measured experiment by using a feedback loop to reduce the potential difference at the input terminals to zero [67]. The current required to do this is then converted into the voltage between the outputs [67]. A common circuit design of a zero-resistance ammeter is shown in Figure 2.28.

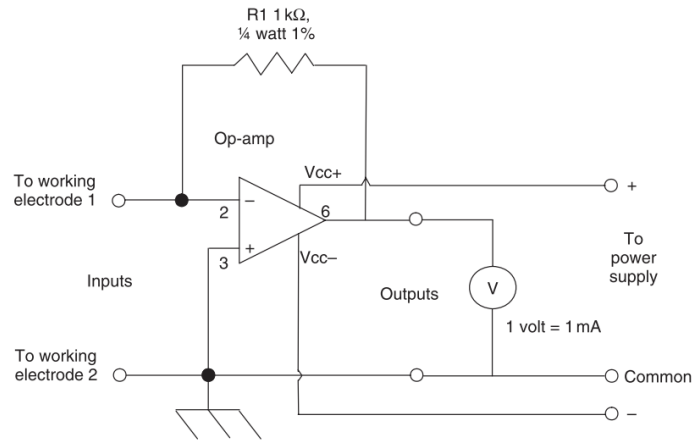


Figure 2.28. A common circuit for a zero-resistance ammeter [67]

Hence, by exposing two electrodes to a medium the current required to null the resulting voltage can be measured and related to the corrosion rate of the active electrode [65].

Examples of this principle include atmospheric corrosivity measurements. In this case, by measuring the voltage between two electrodes exposed to the atmosphere a measurement of corrosivity can be made. However, it is known that these sensors usually underestimate corrosivity compared to other sensors and have been seen to observe changes in measurement even in a stable environment [67]. There has been some experimenting to develop a ZRA method of directly measuring a coated sample; this is a relatively poorly developed technology but is documented somewhat in [68].

A technique for monitoring rebar in concrete, using the ZRA approach, involves monitoring the rebar as the working electrode and the concrete as the reference, however, it was seen that unless the active and passive regions are physically separate it is difficult to determine between the two [69].

Advantages of ZRA include simplicity and low cost. It has also been shown to be effective at monitoring localised corrosion events [67], however, it does not produce as much useful data as EIS, a similar technology. It is also difficult to integrate into coatings in order to measure coating integrity and the effect of integration would

have to be considered. Perhaps this technology would be useful for measuring where on the building envelope is more or less corrosive and hence where the focus of other sensors should be.

2.3.4.3 Electrical resistance (ER)

This is also referred to as an electronic coupon [70]. The working principle is to monitor mass lost due to corrosion via the electrical resistance of an electrode [70]. Corrosion will cause the cross sectional area of an electrode to decrease and this decrease is measured as a resulting increase in electrical resistance of the electrode [70].

The resistance of the probe is calculated via Ohms law by measuring the voltage produced when a small current is applied to the electrode; this is compared to a reference electrode which is shielded from the environment [70].

Sensors based on this principle have been implemented in the oil and gas industry, amongst others [70]. Although it depends on the size and design of the probe, previous work has shown that the smallest change in thickness that can be detected is 1 μm [71].

This technique can provide information as to corrosion rate by monitoring the decrease of the thickness of the test piece [72]. Generally, it is agreed this technique is much more useful than corrosion coupons as there is no assumption of uniform corrosion rate and hence a much better indication of the corrosion rate and how this is varying is produced [70].

Advantages of this method include low maintenance, reliability and easy interpretation of data. ER sensors can also provide real time data and, compared to other technologies, are relatively easy to operate [70]. They can also be used to give corrosion rate data by calculating rate of thickness decrease [72]. Furthermore, they do not rely on the medium having certain characteristics; it can be used in any medium and gives simpler data analysis due to a lesser influence of solution resistance [72]. Finally, they can be used in aqueous and non-aqueous electrolytes, thin films and are, due to improved sensitivity, better suited for atmospheric measurements [70].

Disadvantages of ER sensors include the requirement to ensure the environmental conditions faced by the electrode are the same as the sample being studied, i.e., not shielded or fouled to a greater extent. There are also limits on the temperature and pressure at which they can be used with 100 bar and 500 °C quoted [70]. The sensitivity is often too low for rapid changes to be detected and this method also assumes uniform corrosion over the entirety of the electrode. Finally, precipitates or other fouling can form on the electrode leading to underestimates of corrosion rate [70].

Diler [73] concluded that the time to failure of coating could be accurately determined using this method and that electrical resistance probes can be used with both organic and metallic coatings [73]. An example of an ER probe for organically coated samples is shown in Figure 2.29.

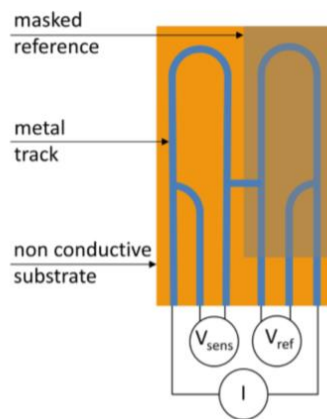


Figure 2.29. An ER probe [73]

2.3.4.4 Induction resistance probes

This is a variation of the ER method in which inductive resistance is used to determine the quantity of metal loss [70]. The principle is that a decreased thickness leads to a change in the magnetic permeability of the electrode and hence mass changes can be measured by detecting changes in the inductive resistance of an internal coil [74].

Compared to standard electrical resistance probes, sensitivity is greatly increased as greater changes in magnetic permeability are seen for the same thickness change. There can also be a decrease in the response time of up to 2500 times compared to electrical resistance probes [70]. The main disadvantages of this method are that magnetic materials must be used and shorter probe lives are seen [70].

2.3.4.5 Capacitive sensors

Capacitance is an indication of a capacitor's ability to hold charge. Applying a voltage to two conductors separated by a medium allows negative and positive charge to accumulate on the plates [75]. If the voltage is alternated the resulting alternating current formed by the alternating charge is proportional to capacitance [75].

The advantages of capacitive sensors is that they can be used for a number of measurements such as displacement or strain [76] and they can be high resolution. It is also possible to create low power sensors that are cheap and recent development has looked at feasibility for RFID compatibility [76]. It has also been reported that these sensors are better than inductive, magnetic or eddy current methods [77] and it has also been shown by Zang [77] that coating thickness can be measured.

Capacitance can also be used to measure other features, such as the rate of water diffusion through a coating, to determine the extent to which the coating has degraded [78]. The following equation is derived:

$$D = \frac{L^2 \pi}{4t} \left[\frac{\lg \left(\frac{C_t}{C_o} \right)}{\lg \left(\frac{C_\infty}{C_o} \right)} \right]^2 \quad (2.10)$$

where D is the diffusion coefficient, L is thickness of coating, t is time C is capacitance at time (t), start (o) and fully saturated (∞) [78].

The main disadvantage of capacitive sensors is interference which causes noise and difficulty in producing accurate measurements [76]. However, it has also been shown that the penetrability of a coating is calculatable [78] and capacitive sensors have also been shown to be able to be printed inside organic coatings [79].

Capacitance theory can also be used to carry out what is known as capacitive imaging. This is a form of non-destructive testing in which two capacitor electrodes are placed near a surface a set distance away from each other, as shown in Figure 2.30. An electrostatic field is formed between the two electrodes which passes through the sample to be monitored.

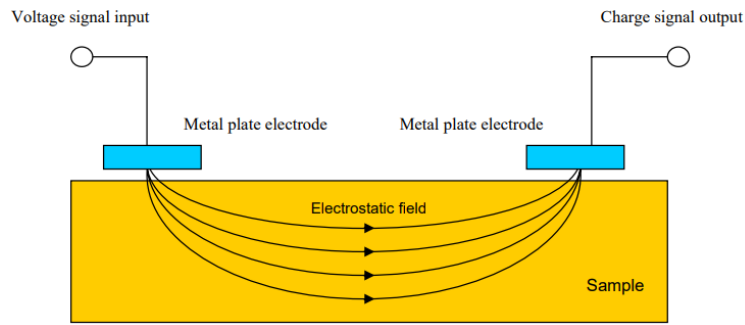


Figure 2.30. Capacitive sensing set up [80]

In effect a capacitor is formed in which, by moving the electrodes, changes in substrate can be monitored. Defects in both conductive and non-conductive substrates are detectable as are changes in dielectric constants due to, for example, water absorption into a coating [80]. However, it has been stated that only surface defects may be detected in conductive specimens [81].

Compared to eddy current testing, changes in magnetic properties of the sample do not affect the measurement principles of capacitive imaging [80]. This method does, however, decrease in accuracy if the surface of the sample is contaminated or there is high moisture content. This is due to the effect of these conditions on the dielectric properties and hence may limit the feasibility to use this method in situ.

2.3.4.6 Electrical field signature method (FSM)

The basic principle of this technique involves passing a current through the test piece which is under observation and measuring the resulting potential difference field to determine the electric field pattern. By monitoring changes to this electric field pattern, corrosion information such as thickness and metal loss can be determined [82]. Measurement of the potential difference field is achieved using pick-up pins which are permanently installed along the length of the sample. An example of the principle of FSM is shown in Figure 2.31. For the same current input, I_0 , a different voltage, V_1 , is detected between pick up pins when the sample has damage compared to the initial damage free state, V_0 .

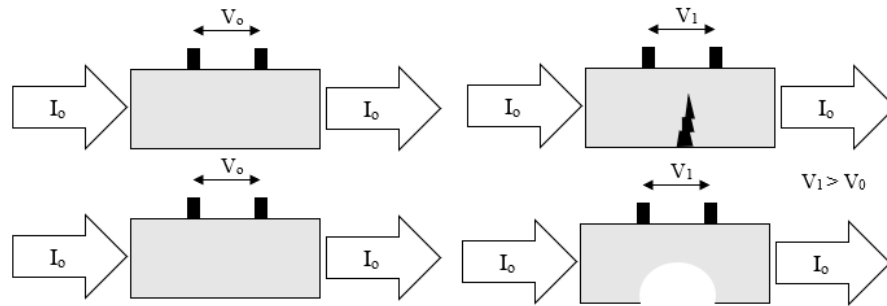


Figure 2.31. Basic principles of the FSM technique

The ‘signature’ relates to the first measurement that determines the base-line potential difference pattern that all other measurements are compared to in order to estimate the change experienced by the sample [83]. This unique, ‘signature’, potential field is set up in the sample based on the geometry and several other parameters.

Metal loss or other structural damage will cause an increase in electrical resistance at that point due to a decrease in thickness. Hence the potential difference measured between two points will change.

Advantages of this technique include the ability to monitor large structures with an ability to control resolution; increased resolution can be achieved by increased number of pins per meter. Furthermore, it is a technique that can distinguish between localised and general corrosion and allows detection of corrosion in real time, often quicker than other methods [82]. It has also been shown to be effective at detecting cracks forming in bridge components [84].

Unfortunately, as this technique relies on electrical measurements it would only be applicable to the underlying substrate as the coating is non-conductive. Connection to the substrate during measurement is also required which, therefore, would require penetration of the coating layer. This would likely have a negative impact on the coating performance.

2.3.5 Electrochemical Techniques

2.3.5.1 Potentiodynamic polarization techniques

This title covers a number of techniques which, although are mainly used in lab-based testing, can occasionally be applied to in situ measurements. They allow determination of highly important corrosion parameters and are often used for analysing passivating metals. In potentiodynamic polarisation three electrodes are

used. The voltage of interest is measured between a working and reference (often a saturated calomel) electrode whereas the current of interest is measured between the working electrode and a counter (often platinum) electrode. It is important that the counter electrode is larger than the working electrode so as to not be a limiting factor in the kinetics of the process. A standard set up is shown in Figure 2.32 and a list of tests that can be carried out is given in Table 2.2.

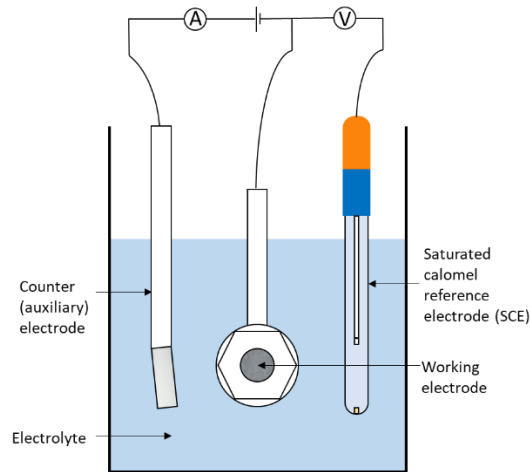


Figure 2.32. An example of a potentiodynamic experiment set up

Table 2.2. Potentiodynamic polarisation tests.

Test Type	Brief Explanation	Used for	Procedure	References
Anodic polarisation	Sample is forced to become anode	Determining pitting, galvanic and localised corrosion behaviour in active-passive metals	ASTM G5	[85,86]
Cathodic polarisation	Sample is forced to become cathode	Likely rates of corrosion and kinetics of the system	ASTM G59	[87]
Cyclic polarisation	Sample potential is increased until the current is 5 mA then reversed	Tendency of pitting and determining breakdown, passivation and protection potentials	ASTM G61	[88]
Cyclic voltammetry	As above but a set voltage is scanned to rather than current	Tendency of pitting and determining breakdown, passivation and protection potentials		[89]
(Cyclic) Galvanostaircase	Current is increased then decreased in steps	Determining protection potential.	ASTM G100	[88]

				Gives qualitative, quick sensitive data	
Electrochemical reactivation	Potential is varied and current measured	In situ corrosion, sensitisation of stainless steels			[90]
Potentiostatic polarisation	A single potential is applied, and current measured	Resistance to pitting	ASTM G150 ASTM F746		[88]
Tafel extrapolation	Analysis of potentiodynamic tests	Corrosion potential, corrosion current density	ASTM G5		[88]
Linear polarisation	Current is measured as voltage is varied linearly	Free corrosion current, polarisation resistance	ASTM G217		[63,65,72]
Galvanostatic pulse	Pulsed current is applied galvanostatically and potential is measured	Polarisation resistance, free corrosion current polarisation potential			[91,92]

2.3.5.2 Harmonic analysis

A limitation of the polarisation methods, and other methods that make use the Stern–Geary equation, is that it is dependent on the accuracy of the Stern–Geary coefficient, B . This introduces some inherent uncertainty in any corrosion rate calculation as this coefficient is not a constant but is often taken to be one [93,94].

Several methods described by [93] exist that can reduce this uncertainty, but the harmonic analysis technique is unique in that it directly measures, for the system being investigated, the Stern–Geary coefficient [93].

In harmonic analysis a sine wave is applied to a corroding electrode and the distortion due to corrosion results in production of harmonics of this sine wave; the Tafel constants and hence the Stern–Geary coefficient can be determined by analysis of the amplitudes of the harmonics produced [93,94].

The Stern–Geary equation with derived coefficient from Tafel lines [95] is given by:

$$i_{corr} = \frac{\beta_a \beta_c}{2.303(\beta_a + \beta_c)} \frac{1}{R_p} \quad (2.11)$$

where β_a is the anodic Tafel slope and β_c is the cathodic Tafel slope. Hence, the advantages of this method are that it does not presume values for the Tafel constants and it is also reported that measurements can occur quicker than other electrical techniques [95].

The disadvantages are that more complex methods of stimulating and measuring the test sample are required and hence more equipment and control systems are required. It is also the case that data analysis is more complicated.

2.3.5.3 Electrochemical impedance spectroscopy (EIS)

EIS is an AC technique and uses small potential excitation amplitudes to cause minimal perturbation of the sample [91]. It can provide information on both electrode capacitance and resistance and allows more easy resolution of variables than DC techniques. It involves the measurement of impedance between corroding metal and a reference across a wide frequency range [72] and is ‘one of the main methods to evaluate performance of coatings’ [96]. Impedance is the Alternating Current (AC) equivalent of resistance. Hence, can be stated in a way similar to Ohm’s Law [91]:

$$\hat{E} = \hat{I}Z \quad (2.12)$$

where \hat{E} is the amplitude of potential sine wave, \hat{I} the amplitude of current sine wave and Z is the impedance (Ω hms)

Often EIS is used to model an electrochemical cell as an electronic circuit in order to use established circuit theory to analyse it [97]. Examples of physical electrochemical properties able to be represented in EIS are electrolyte resistance, polarisation resistance, coating capacitance and double layer capacitance. Through analysis of the plots gained by EIS experimentation these properties can all be calculated for the test piece. An understanding of the performance of the system can then be obtained. There are two main plots used in EIS analysis, Nyquist and Bode [91] and examples of these plots from analysis of a coated metal is shown in Figure 2.33.

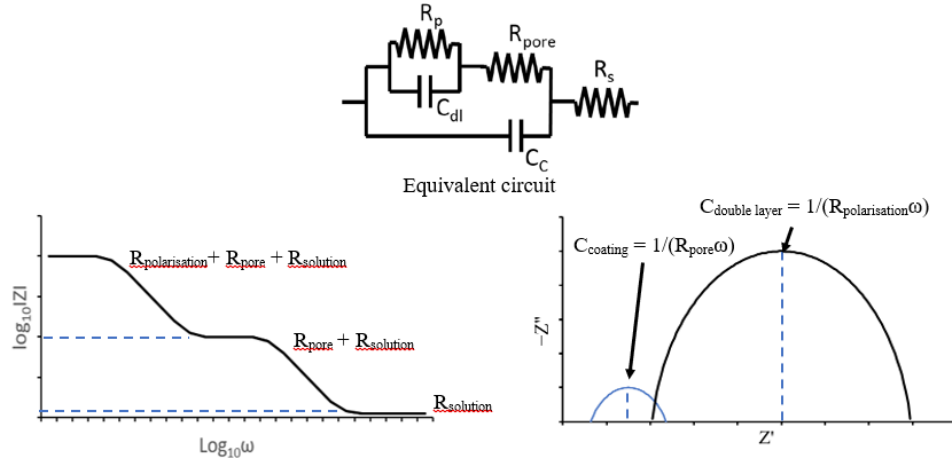


Figure 2.33. Example Bode (left) and Nyquist (right) plots for a coated metal electrode under EIS testing modelled on the equivalent circuit for a coated metal electrode (top) [98].

Nyquist plots show imaginary impedance component ($-Z''$) against the real impedance component (Z') whereas Bode plots the log of impedance magnitude ($\log(Z)$) against log of the frequency ($\log(\omega)$) where [91]:

$$\omega = 2\pi f \quad (2.13)$$

where f is frequency in Hz. EIS uses three electrodes; working, counter and reference, and the polarisation applied to the working electrode is a small amplitude sine wave. By varying the frequency of the sine wave and measuring the current flowing, the impedance of the electrode as a function of frequency can be determined. This is the electrochemical impedance spectrum.

Calculation of the polarisation resistance can allow calculation of the corrosion rate, via the Stern–Geary equation, in a similar way to that in linear polarisation resistance. However, other properties of significant interest can be calculated such as the coating capacitance; this exists when two conducting materials are separated by a non-conducting material and is defined as [97]:

$$C = \frac{\epsilon_0 \epsilon_r A}{d} \quad (2.14)$$

where C is capacitance, ϵ_0 is permittivity of free space, ϵ_r is a dielectric constant, A is surface area of one plate, d is distance between plates. Coating capacitance is a useful parameter for establishing the condition of a coating and monitoring degradation as it allows measurement of the thickness of the organic coating. Furthermore, the change of a substrate over time can be measured such as the absorption of water through a change in the capacitance due to a change in ϵ_r . Pore

resistance is another variable that can be calculated by the EIS method; this is able to give information about the integrity of organic coatings.

Hence the main advantage of EIS is the quality and amount of information that can be gathered as to the condition of the coating and substrate in a relatively quick manner. It has also been the subject of extensive research and therefore is well developed and optimised for several different situations. For example, EIS can be used to analyse blister formation, permeability to water, coating swelling, delamination and corrosion [97,99].

The disadvantages of EIS are that it requires three electrodes and immersion in an electrolyte [96]. Although there have been efforts to produce in situ, electrolyte free kits [100], complexity in design still exists. Furthermore, the majority of EIS calculations use the non-linear least squares fitting algorithm to fit the data to the expected spectrum. This has some limitations caused by incorrect modelling poor data fittings, poor initial values and noise.

There has been development of specific sensors for diagnosis of polyurethane organic coatings [96]. A miniature battery powered sensor example is given in [96] and this was shown to be a sensitive and effective method of determining coating performance on an in situ basis [96].

The authors of [101] have proposed a design for an EIS which functions in atmospheric conditions negating the immersion requirement. This has been shown to give consistent data when measuring a coated sample [101]. Other designs have also been suggested that allow long range, low cost remote monitoring [102,103].

It has also been shown that EIS can use two embedded sensors as the working and reference electrodes. This has the benefit of not requiring electrical contact to the substrate and hence does not fully penetrate the protection, offered by the coating, with wires [104]. This also allows different parts of a coating system to be analysed separately [105].

2.3.5.4 Electrochemical noise

Electrochemical noise refers to the fluctuations in potential and current that occur during corrosion of an electrode [72,93]. Theoretically, by studying the ‘noise’ created by a corroding element, information can be gathered as to the corrosion

process itself [93]. For monitoring applications results are analysed statistically. The authors of [106] concluded that this technique could ‘offer much promise for the detection of corrosion’.

During testing it is possible to measure both potential noise and current noise. EPN (electrochemical potential noise) is either measured between one electrode and a reference or two electrodes. ECN (electrochemical current noise) is measured between two electrodes or by holding a fixed potential of a single electrode [93]. Alternatively, it is possible to simultaneously measure both with a three electrode setup [93].

Directly related to the fluctuation amplitude is the standard deviation; this is the most commonly used statistical analysis technique. Eden suggested the following relationship between standard deviation and a quantity electrochemical noise resistance [93,107]:

$$R_n = \frac{\sigma_E A}{\sigma_I} \quad (2.15)$$

where R_n is the electrochemical noise resistance, A is the area of the sample, σ_E is the standard deviation associated with the potential and σ_I is the standard deviation associated with current [93]. Further work has shown that the linear polarisation resistance, R_p , is comparable to the value of R_n [93]. Hence, using the Stern–Geary equation, i_{corr} can be calculated (assuming R_p is approximately equal to R_n):

$$i_{corr} = \frac{B}{R_p} = \frac{B}{R_n} \quad (2.16)$$

where B is the Stern–Geary coefficient and i_{corr} is the free corrosion current [93]. It is possible to estimate the tendency for localised corrosion to occur, using a method which estimates the true coefficient of variation, which was developed by Kane [93,108]

$$TCR = \frac{\sigma_I}{I_{corr}} \quad (2.17)$$

where TCR is termed for the true coefficient of variation. Using several assumptions, Schottky demonstrated theoretically that [93,109]

$$\sigma_I = \sqrt{2qIb} \quad (2.18)$$

where q is the charge on an electron, I is the average current and b is the bandwidth of the material [93]. Hence it can be shown that:

$$q = \frac{\sigma_I \sigma_E}{Bb} \quad (2.19)$$

The advantages of EN include the ability to determine the type of corrosion occurring, although this is dependent on certain conditions [93]. Furthermore, noise measurements have been shown to be well correlated with EIS when determining corrosion resistance of organic coatings [110]. The technique is a non-interfering method and hence does not affect the corrosion process unlike some DC techniques [110]. Unlike EIS, EN can give an indication as to the localisation or uniformity of the corrosion which is often useful [110]. Finally, Woodcock et al. (2004) developed a no connection to substrate (NOCS) method leading to easier measurement of coatings [110].

The disadvantages of this technique are that it requires a high sensitivity measuring system or amplification of signals. Both of these solutions have errors associated with them [93]. Additionally, it is difficult to conclude with confidence how corrosion is occurring, even though the rate of corrosion can be measured with reasonable accuracy [93]. Often, other techniques involving measurement of R_p are more reliable and produces less noise and this technique is also very sensitive to interference [93].

Several reviews into EN have been carried out and it has been concluded that EN is a versatile, quick and simple technique for determining the defects present in coatings and the level of protection afforded [111,112]. However, it is suggested that in systems with passivity and inhibition the data analysis is more difficult and that data collection and analysis methods are crucial to the effectiveness of the technique [111,112].

Mills [113] examined Alkyd and Polyurethane coatings using the NOCS technique. It was suggested that areas may be able to be resolved in terms of their resistances allowing spatially resolved data points. By using copper pads the requirement to attach other reference electrodes such as a SCE (saturated caramel electrode) was avoided [113].

2.3.5.5 Scanning electrochemical microscopy (SECM)

This is a technique that has been described to ‘provide spatially resolved (electro)chemical information about a sample under investigation’ [114]. The working principles and methods are well described by Wittstock [115]. It relies on measuring, at the surface of a sample, the rate of redox reactions in order to determine corrosion properties [114]. Unlike SVET (the scanning vibrating electrode technique) it can determine the nature of chemical species involved in the process and there are examples of it being used for coated metallic products documented in [116]. The cathodic reaction can be measured in situ within the coating defect [116] and it allows the determination of the reactivity of a point giving an indication of the degradation present at that position [117]. The experimental set up is shown in basic form in Figure 2.34.

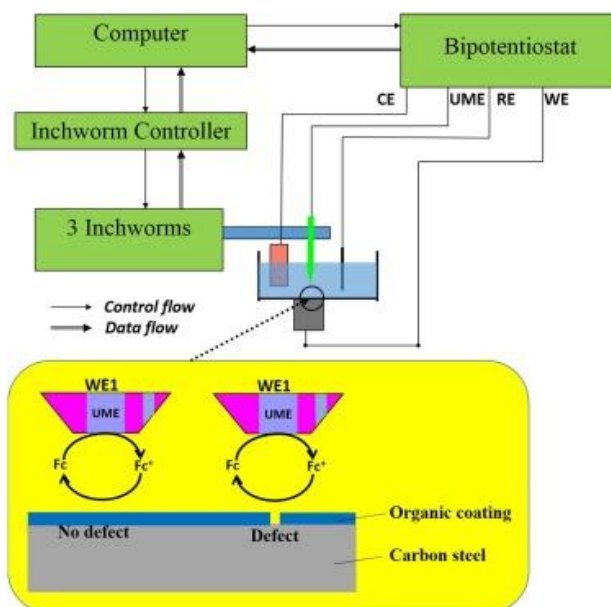


Figure 2.34. Example SECM [117]

Whilst this technology has the potential to provide a large quantity of useful data at high accuracy, it is difficult to consider how in situ measurements may be made outside of a laboratory. Furthermore, automation and the likelihood of disturbance from other factors leads to the conclusion that this technique may not be useful for the specific application at the heart of this work.

2.3.6 Other sensors

2.3.6.1 Embedded strain gauges

These are commonly used to measure force, or strain, and are sensors that can be made from a variety of substrates [118]. They allow measurement of strain through a corresponding change in their electrical resistance, known as piezoresistivity. Hence, measurement of deformation or movement can be determined [118].

It can be shown that:

$$\frac{\Delta R}{R_0} = GF\varepsilon \quad (2.20)$$

where $\Delta R = R - R_0$ where R is the resistance at strain ε and R_0 is the resistance at strain zero (initial conditions). GF is the gauge factor which defines the sensitivity of a change in resistance with strain [118,119]. The strain in the device can be calculated by:

$$\varepsilon(x) = \frac{3hx\delta}{2l^3} \quad (2.21)$$

where l is length, w is width, h is thickness, δ is vertical displacement, longitudinal strain is ε at position x [118].

Strain gauges have the advantage that they can be screen printed, as described by [118], and hence they could be placed on any layer of the coating such as the topcoat or primer [118]. This gives a potentially easy route to deployment at a large scale. Design and printing considerations are given in [79] in which it was concluded that organically coated steel ‘can be used as a substrate for printed electronics’. Screen and inkjet printing were both considered by [79] but it was reported that screen printing was more appropriate for thicker conductors, due to larger depositions. An example of a printed strain gauge under an organic coating is shown in Figure 2.35.

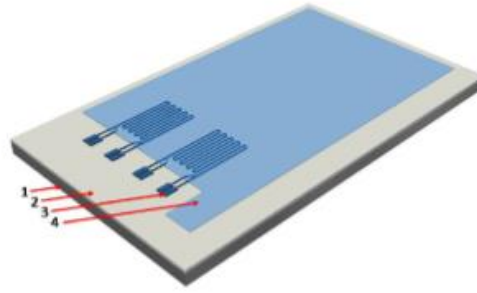


Figure 2.35. Example of a screen printed strain gauge embedded in an organic coating. Layers 1, 2, 3 and 4 represent the substrate, primer, electronics and topcoat layers respectively [119]

The conductive inks used [119] in the studies carried out were a Loctite EDAG PR 406B E&C (a carbon black thermoset resin) and an EDAG PF 050 E&C (a silver thermoplastic). These have cure times of 30 min at 150 °C and 3 min at 140 °C and flash points of 54 and 74 °C, respectively [120,121]. However, even when the top coat was applied to these strain gauges and cured at 250 °C for 90 s, there was no suggestion that this excessive temperature affected the strain gauge operation [119].

A full report by Enser in 2018 [122] describes the feasibility of integrating capacitive, strain and piezo and pyro electric sensors into organic coatings on steel products. Perhaps optimistically, this reports that ‘the concept has the potential to introduce additional functionality [] without the need of significant changes to associated production processes’ [122]. It is possible that one or more the of the sensors described in this report may provide significant coating integrity information.

There is also significant current development of conductive inks; one notable ink is a conductive epoxy which contains silver flake pigment. One manufacturer (XYMOX) states that although having a cure condition of 130 °C for 10 min, the flash point is much higher at 212 °C suggesting that the survivability of the electronics may be increased [123].

The advantages of this technology are that it is relatively simple, however, when embedded in a coat, can provide a good indication of the coating condition. Unfortunately, it is unknown if embedding the sensor reduces the protective properties of the coating and it is difficult to consider how to make an electrical connection to the sensor.

2.3.6.2 MEMs Based Systems

A MEMs is a micro-electromechanical system; these are tiny devices that can be used as a sensor or control factors on a scale much larger than their own. They are composed of a mixture of electrical and mechanical components [124] and they use mechanical motion to influence an electrical signal.

The basic design is a silicon chip composed of microsensors and microelectronics and these sensors can be configured to measure chemical, electromagnetic or mechanical changes [124]. They have a high diversity of potential uses due to their small size and volume and some examples of in-use application include accelerometers, data storage and air bag deployment [124].

Domains that can be measured include:

Mechanical—force, pressure, velocity, acceleration, position;

Thermal—temperature, entropy, heat, heat flow;

Chemical—concentration, composition, reaction rate;

Radiant—electromagnetic wave intensity, phase, wavelength, polarisation reflectance, refractive index, transmittance;

Magnetic—field intensity, flux density, magnetic moment, permeability;

Electrical—voltage, current, charge, resistance, capacitance, polarisation.

The advantages of using these sensors is that they have high sensitivity and a long life. They are also rugged, small and are relatively inexpensive [125]. Additionally, many are commercially available and can be bought tailor made to measure a number of features to a stated degree of accuracy. Some MEMs have been developed which measure the diffusion rate of a corrosive species through a sensor and as the sensor corrodes its resistivity changes and this can be detected [125]. It is assumed a sensor based on measuring several factors could be developed and it may be the case that a previously mentioned technology could be facilitated through the use of MEMs.

The disadvantage of these systems is that they are often complex to design, and communication and powering of the device may be complicated in situ. In order to detect certain features, the device may have to have an electrical connection to the substrate which would require penetration of the coating.

2.3.6.3 Nuclear thin layer activation

For this technique a small section of material is exposed to a high energy beam of charged particles, to produce a radioactive surface layer. The loss of material, as a result of corrosion of this layer, is measured by considering the corresponding decrease in radiation intensity [126,127]. Radiation levels are low enough for safe handling with only basic precautions, although this technique is often viewed with concern [127].

The direct relationship between thickness reduction and measured radioactivity allows calculation of the thickness, however, complicated calibration is required and it is a so called ‘non-direct method’ [126]. An example of this principle in use is a study where a gamma radiation detector was used to monitor changes in a carbon steel irradiated with a high energy proton beam. The isotope formed was Cobalt 56 [126].

Carbon and stainless steels have also been tested with this method and the results are stated to have correlated with gravimetric testing [127]. However, some samples’ radioactivity change was below the sensitivity threshold, leading to a lack of measurement. The conclusion of this work was that this is a method that is viable for the measurement of material loss and measurement of specific locations to give insight into the areas most affected [127].

If irradiating larger areas of samples, it is of crucial importance to ensure that the level of activation is uniform throughout the sample in order to have repeatable readings [128]. A scanning beam may achieve this and some work has been done using TLA on a macroscopic level; the advantage of this technique is the ability to use it on curved surfaces [128]. The measurement can also be carried out without damaging the coating in any way.

Consideration of the half-life is important, if long term measurement is required, as is the penetrating power of the radiation, should the sample be imbedded in such coating [128].

2.3.6.4 RFID Technology

Typically, RFID technology is composed of an antenna, a reader and a tag [129]. The tag or chip contains the memory, energy harvesting unit, microcontroller, and response generator [129]. The components of an RFID system function as a coupling

device, an interrogator and a transponder, respectively [130]. The tag receives an electromagnetic wave from the interrogator via the antenna. Data in the form of, for example, an identifier code can then be supplied by the tag via the electromagnetic wave [130]. This process is shown in Figure 2.36.

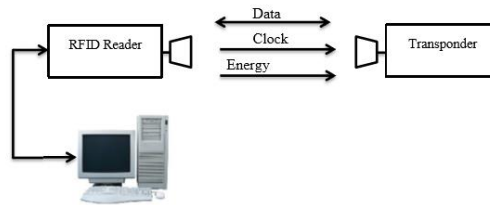


Figure 2.36. A basic description of the RFID system [131]

RFID is similar to a barcode technology, in terms of the data transferred, but does not require line of sight. The reader has a microcontroller, signal generator and a signal receiver/detector and an antenna for each. Passive tag systems have an antenna, a transponder, rectifier circuit, controller and memory. LF (Low Frequency), HF (High Frequency) and UHF (Ultra High Frequency) frequencies can all be used for the operation of the tag depending on various requirements. The higher the frequency the greater the distance of detection and depending on the frequency the type of coupling that is employed changes.

LF and HF works on inductive coupling (near field coupling) where the reader powers the tag, synchronisation of clock and a carrier for return data. The field emitted by the reader couples with the tag and a voltage is induced; this is used as power for memory access. When a load is connected the impedance can be used to change current and hence the rate of change of current can be used to create a voltage. The load can be controlled and switched on and off to create binary communication and hence changes voltage across tag coil affecting the carrier wave of the reader. High frequency can be read from approximately 0.8 m but is generally a cheaper solution [131].

UHF uses far field coupling and has a range of up to several meters. The reader sends a continuous signal to tag and the tag sends weak signal (backscattered signal) back. Depending on the load matching across coil, the intensity of backscattered signal changes. By changing load condition, the intensity of backscattered signal can be controlled. This is known as a backscattered modulation/coupling technique and in

order for this to be effective the initial signal from reader is required to be strong. UHF can be read from approximately 15 m away but is generally higher cost [131].

These different systems are shown in Figure 2.37.

Family	Range	Coding capacity	Access	Level of confidentiality	Susceptibility	Positioning	Tag cost
LF, HF	<1 m	Some kbits	Read/write	High	Metal at 13.56 MHz	Polarization independent	>0.4 euros
UHF, SHF	1-100 m	Some kbits	Read/write	Low	Metal and liquids	Polarization dependent	>0.1 euros
UWB	<60 m	Some bits	Read/write	Good	Metal and liquids	Polarization dependent	>0.3 euros
Chipless	<1 m	256 bits	Read/write	None	Metal and liquids	Polarization dependent	>0.005 euros

Figure 2.37. Classification of RFID technologies by frequency [129]

Three types of tag also exist:

A passive tag has no internal power and is solely powered by harvesting the reader’s electromagnetic field [129]. With an effective range of approximately 20 feet they are often cheaper than active tags and hence are often disposed with the product [130]. Passive tags vary the load impedance connected to the antenna. This affects the amplitude of the signal reflected back to the reader allowing communication through load modulation [132]. A semi passive tag uses harvested energy to respond to the reader [129]. A reader is used to wake a battery powered tag and hence there is extended battery life over an active tag [130]. An active tag has its own power source in the form of a battery and uses this to emit radio waves to a reader [129]. This allows larger range and a better degree of accuracy in detection. However, there is the obvious disadvantages that the tags are generally larger and more expensive and also have a finite lifetime [130].

There are three types of data storage:

RO or read-only is a system where there is stored data that cannot be changed or removed [130]. RW or read-write is a system where the stored data can be edited or removed [130]. WORM or write once, read many is a system where the data can be changed or removed once only [130].

Various corrosion based radio frequency devices have been developed, often for measuring the diffusion of water through concrete, and they work on the principle that the sensors electromagnetic performance will vary as a result of the quantity of

water surrounding it [133,134]. This process is based on the principle that the permittivity of a medium can be determined through analysis of the impedance of an antenna that is embedded in that medium. Capdevila [133] describes the methodology behind this technique in detail.

Use of RFID technology to determine the water diffusion through a coating has also been considered. Khalifeh et al. (2016) suggested that to overcome the sensitivity of a thin layer coating a new approach is required, such as the use of ‘microstrip planar resonators’ which have a smaller field of electromagnetic influence. It was shown that an RFID tag can be embedded in the coating and that, with background testing, chemical and physical changes can be detected [134]. It was concluded that this is ‘a promising and reliable tool for the monitoring of protective properties of coatings’ [134].

The benefit of these is that they are passive devices and hence complex issues involved with powering the device are negated. It is also reported that a standard RFID reader can be used with these sensors reducing the technical demand [133].

The disadvantage of RFID based systems are that they are heavily affected by metal interference and require complex design to ensure optimum range. Furthermore, complexities exist in combining the communication system into a sensing system.

2.3.6.5 NFC

Near field communication (NFC) is an RFID compatible interface and protocol which was developed with the aims of simplifying the RFID system [135]. This allows communication wirelessly between devices at a distance of approximately 10 cm or less, making it one of the shortest range wireless communication protocols [131]. It uses RFID technology and hence communication is based on the principle of magnetic coupling and can involve passive or active tags.

The main advantages of NFC, over RFID, are that reading devices are relatively simple and are now commonplace in mobile phones unlike RFID readers which are more complex. Data sharing is also relatively simple via the protocol [131].

An NFC device is classed as active if, similar to the RFID system, it is capable of generating a radio frequency field. If this is not the case it is classed as passive and hence transfers data via the inductive coupling method [131]. Communication is

active if achieved by two active devices and passive if one is passive and one active. Instead of being called the reader and tag, as in RFID, the devices are known as the initiator and target.

2.3.6.6 Biological sensors

The aim of these sensors is to detect the formation of biological films on the surface of coatings. As previously mentioned, these are detrimental to coating life. There has been some success in detecting biofilms by using a hydrogen peroxide-based detector which reacts with biofilms if present to form bubbles. There has also been some success in using a colouring in this peroxide in order to increase the ease of detection [136].

2.3.6.7 pH sensors

A number of options exist for detecting changes in pH. There are, for example, standard electrodes which could be used for comparison, such as glass electrodes, yttria stabilised zirconia, metal oxides. These are all explained in detail in [137]. However, while commonplace in laboratory testing, their suitability for in-field coating monitoring is very limited.

Some corrosion specific sensors have emerged from research. For example, Behnood et al. (2016) discuss an embedded potentiometric electrode and fibre optic sensors for monitoring alkalinity in concrete structures [138]. To overcome the issue of electrodes involving glass, there have been a number of developments such as solid state, hydrogel film and fibre optical sensors. Metal–metal oxide sensors which calculate pH based on the redox reaction reversibility show some promise as in situ sensors and a variety of fibre optic techniques exist as well; these use a variety of factors such as refractive index, absorbance or fluorescence to determine pH values. These methods are described further in [138].

Potentiometric thick film sensors are presented in [139]. Similar to the chemical sensors explained below, these are screen printed sensors for measuring pH in which a silver–silver oxide ($\text{Ag}/\text{Ag}_2\text{O}$) sensor is used. Good response time and repeatability was seen with these sensors which were developed for monitoring concrete environments [139].

While pH monitoring could be a suitable method for monitoring corrosion the difficulties involved in using this, usually aqueous reference comparison technique, make it less suited to this specific application.

2.3.6.8 Chemical sensors

A potentiometric chlorine thick film sensor for concrete monitoring is outlined in [140]. These are small sensors with a number of silver/silver chloride sensors attached, as shown in Figure 2.38. Ag/AgCl is used as it can be used to detect changes in variations in Cl⁻ concentration [140]. It was shown these sensors could be screen printed and provide reasonable accuracy at low cost and ease of manufacturing [140].

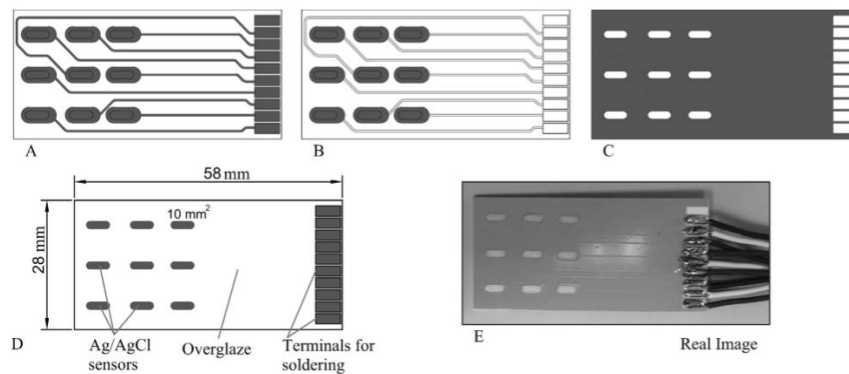


Figure 2.38. Design of a potentiometric chlorine sensor [140]

A wireless chlorine sensor for monitoring of concrete structures is described by [141]. This involves using a silver/silver chloride reference electrode with a wireless interface. As the concentration of chlorine ions changes, the half-cell potential of the electrode changes, and this is measured by the circuitry.

The main disadvantages of these techniques are that they currently require a reference and working electrode set up in an electrolyte. Whilst in-lab results, and monitoring, are therefore possible, and ‘accurate’, it is difficult to reproduce these results in situ and the equipment complexity increases dramatically. Additionally, they only provide an understanding of the environmental conditions rather than the actual current performance of the coating.

A range of other chemicals are able to be detected using various methods which are summarised in [142] although not explained in any detail here.

2.3.6.9 Simulations

As computing techniques and power has developed the field of corrosion and coatings has incorporated computer modelling and simulation alongside physical measurements and observations.

Corrosion modelling software, such as COMSOL-Modelling Corrosion and Corrosion Protection, is commercially available [143]. This uses thermodynamics, kinetics, and transport phenomena to govern the chemical reactions occurring at a surface. By calculating concentrations of specific species, electrical potentials and currents, and a range of other parameters the electrochemical process of corrosion can be modelled. This software can be used to model the expected severity of corrosion of complex systems such as those involving galvanic corrosion, stress corrosion cracking and cathodic protection. One such example created in the software models the potential distribution in a cathodically protected structure over time as shown in Figure 2.39 [143].

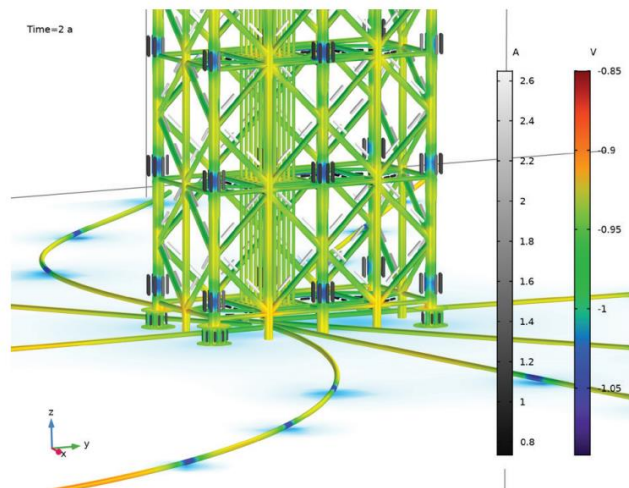


Figure 2.39. COMSOL example simulation of potential distribution over time at a specific time period

2A [143]

Other software development companies are understanding the benefit of modelling building performance and corrosion with BEASLY recently introducing the concept of digital twin software onto which degradation is modelled to assess and predict areas of required maintenance [144].

While a great deal of the simulation work carried out is in the area of coating formation, application and curing there are developments of techniques for monitoring coating lifetime and degradation. Perhaps unsurprisingly the most

progress has been made in modelling mechanical degradation of organic coatings such as the modelling of the removal of paint through particle impact [145] and lifetime predictions of organic coatings under alternating pressure [146]. There has also been some research around simulating UV degradation of organic coatings such as the work in [147] and [148] and models produced on water uptake by organic coatings such as [149]. However, while models may exist for certain mechanisms this does not necessarily lend itself to simulation of expected real life exposure results.

The main disadvantage of these techniques, therefore, is that the degradation of organic coatings and the substrates they are on is an immensely complex problem that would have to combine many different degradation mechanisms. It is for this reason perhaps that current research focuses on modelling individual mechanisms and there is not a great deal of work on the prediction of general weathering via simulations. Combining coating degradation and substrate corrosion would further complicate matters with additional parameters and mechanisms present.

The potential advantages of a simulation-based approach are huge as it could be used early in the design and specification stage of a building's lifespan to ensure the correct product is used in the correct way. Furthermore, it would allow targeting of sensing, inspection and maintenance.

2.3.7 Current technique Review Conclusions

There is no doubt that corrosion is a big problem for the construction industry. However, whilst the industry understands the benefits of protecting metal components against corrosion, there appears to be little in-situ monitoring of the most common protective method; organic coatings. Reinforced concrete has been shown to be the current main focus of in-situ testing development and it seems that for many companies a solution involving a human operated probe, such as regular ultrasonic testing, is currently sufficient. Despite this, there is a clear appetite for smart solutions that allow monitoring of larger, building scale, organically coated components. Embedded sensors in paint systems are being considered however there is a realisation that the embedding of systems may lead to a decreased coating performance. A serious complication is that many techniques, that are effective in the lab, require either complex and delicate reference electrode systems or electrical

connection to both the substrate and surface, producing a potential coating breach. Furthermore, difficulties exist in powering and collecting data from a device without significantly penetrating the barrier produced by the coating. It is perhaps because of these features, passive sensors such as corrosion indicating paints and RFID style sensors as well as computer simulation-based techniques are emerging as a promising new area of research.

Unfortunately, there seems to exist an inevitable dilemma in current research in which a technology fits into one of the following categories:

- Simple and non-intrusive to the coating. In this case the data received is equally basic in nature and is often only reactive to failure offering little or none of the expected benefits of in-situ monitoring. An example is corrosion indicating paint.
- Complex and expensive. The sensor requires a high-resolution or other expensive component or is complex to automate. An example would be infrared thermography.
- Simple and cheap. Although easy to implement and use, the sensor does not provide sufficient quality or depth of data to allow confident analysis. An example would be corrosion coupons.
- Complex and intrusive to the coating. Whilst the data produced is very useful, the coating integrity is affected by the sensor and hence overall the sensor decreases the effectiveness of the coating. Examples of these technologies include capacitance and EIS sensors.

Therefore, a clear motive exists to develop or refine a technique that produces the quality of data of a complex, expensive or intrusive technique but does not suffer from the limitations currently posed.

2.4 References

1. Javaherdashti R. *Microbiologically Influenced Corrosion*. 1st ed. Springer, editor. 2008.
2. Mattsson E. *Basic corrosion technology for scientists and engineers*. 1st ed. Institute of Materials; 2001.
3. Balan KP. Corrosion. *Metall Fail Anal* [Internet]. 2018;155–78. Available from: <https://linkinghub.elsevier.com/retrieve/pii/B9780128143360000093>
4. Lycett RW, Hughes AN. Corrosion. *Met Ceram Biomater Vol II Strength Surf*. 2018;91–118.

5. Trethewey K, Chamberlain J. Corrosion for Science and engineers. Longman Group; 1995.
6. Scully J. The fundamentals of corrosion. 3rd ed. Pergamon Press; 1990.
7. Singh R. Corrosion and Corrosion Protection. In: Pipeline Integrity Handbook. 2nd ed. 2017. p. 241–70.
8. Buchheit RG. Corrosion resistant coatings and paints [Internet]. Third Edit. Handbook of Environmental Degradation of Materials. Elsevier Inc.; 2005. 367-385 p. Available from: <http://dx.doi.org/10.1016/B978-0-323-52472-8.00022-8>
9. Popov B. Organic Coatings. In: Corrosion Engineering. Elsevier; 2015. p. 557–79.
10. Knudsen O., Forsgren A. Corrosion Control Through Organic Coatings. 2nd ed. Schweitzer P, editor. CRC Press; 2017.
11. Bayer GT, Zamanzadeh M. Failure Analysis of Paints and Coatings. Pigment Resin Technol. 2014;35(5):1–37.
12. Tator KB. Coating Deterioration. In: Protective Organic Coatings [Internet]. ASM International; 2015. p. 462–73. Available from: <https://dl.asminternational.org/books/book/13/chapter/143061/coating-deterioration>
13. Munger CG. Causes and Prevention of Paint Failure. In: Good Painting Practice, Steel Structures Paint Manual. 2014. p. 1–21.
14. Sullivan JH. EG-387 Protection and Corrosion of Metals. Swansea Univ. 2018;
15. Griffiths CM, Wint N, Williams G, McMurray HN. The contribution of Zn(II) and phosphate anions to the inhibition of organic coating cathodic disbondment on galvanised steel by zinc phosphate pigment. Corros Sci [Internet]. 2022;198(January):110111. Available from: <https://doi.org/10.1016/j.corsci.2022.110111>
16. Nazarov A, Thierry D. Influence of electrochemical conditions in a defect on the mode of paint corrosion delamination from a steel surface. Corrosion. 2010;66(2):0250041–02500410.
17. Dickie RA. Paint adhesion, corrosion protection, and interfacial chemistry. Prog Org Coatings. 1994;25(1):3–22.
18. Faisal N, Droubi G, Steel I. Acoustic Emission Techniques in Corrosion Monitoring. 2017;2017(January).
19. Verstrynge E. Acoustic emission testing [Internet]. Long-term Performance and Durability of Masonry Structures. Elsevier; 2019. 287-307 p. Available from: <https://linkinghub.elsevier.com/retrieve/pii/B9780081021101000108>
20. Payan C, Abraham O, Garnier V. Ultrasonic Methods. Non-destructive Test Eval Civ Eng Struct. 2017;21–85.
21. NDTResourceCentre. Introduction to Acoustic Emission Testing [Internet]. NDT Resource Center. [cited 2019 Apr 9]. Available from: http://www.nde-ed.org/EducationResources/CommunityCollege/Other Methods/AE/AE_Intro.htm
22. Bose S, Bose S. Nondestructive Inspection (NDI) of Coatings. High Temp Coatings [Internet]. 2018;301–18. Available from: <http://linkinghub.elsevier.com/retrieve/pii/B9780128046227000085>
23. Li D, Ou J, Lan C, Li H. Monitoring and failure analysis of corroded bridge cables

- under fatigue loading using acoustic emission sensors. *Sensors*. 2012;12(4):3901–15.
24. Voyer J, Gitzhofer F, Boulos MI. Study of the Performance of TBC under Thermal Cycling Conditions using an Acoustic Emission Rig. *J Therm Spray Technol*. 1998;7(2):181–90.
 25. Ooka N, Ishii T. Ultrasonic testing. *Keikinzoku Yosetsu/Journal Light Met Weld Constr*. 1998;36(5):216–21.
 26. Alobaidi WM, Alkuam EA, Al-Rizzo HM, Sandgren E. Applications of Ultrasonic Techniques in Oil and Gas Pipeline Industries: A Review. *Am J Oper Res [Internet]*. 2015;05(04):274–87. Available from: <http://www.scirp.org/journal/doi.aspx?DOI=10.4236/ajor.2015.54021>
 27. Beamish D. Using Ultrasonic Coating Thickness Gauges. *Mater Perform*. 2004;(September):2–5.
 28. Drury JC, Marino A. Comparison of the Magnetic Flux Leakage and Ultrasonic Methods in the detection and measurement of corrosion pitting in ferrous plate and pipe. In: 15th World Conference on Nondestructive Testing Roma (Italy). 2000.
 29. Doherty M, Sykes JM. A quantitative study of blister growth on lacquered food cans by scanning acoustic microscopy. *Corros Sci [Internet]*. 2008;50(10):2755–72. Available from: <http://dx.doi.org/10.1016/j.corsci.2008.03.020>
 30. Fukuchi T, Fuse N, Okada M, Fujii T, Mizuno M, Fukunaga K. Measurement of refractive index and thickness of topcoat of thermal barrier coating by reflection measurement of terahertz waves. *Electron Commun Japan*. 2013;96(12):37–45.
 31. Tu W, Zhong S, Shen Y, Incecik A. Nondestructive testing of marine protective coatings using terahertz waves with stationary wavelet transform. *Ocean Eng [Internet]*. 2016;111:582–92. Available from: <http://dx.doi.org/10.1016/j.oceaneng.2015.11.028>
 32. Bubenik T. Electromagnetic methods for detecting corrosion in underground pipelines: Magnetic flux leakage (MFL) [Internet]. *Underground Pipeline Corrosion: Detection, Analysis and Prevention*. Woodhead Publishing Limited; 2014. 215-226 p. Available from: <http://dx.doi.org/10.1533/9780857099266.2.215>
 33. Tamhane D. Detection of Defect in Steel Sheets Under Coatings by Magnetic Flux Leakage Detection of Defect in Steel Sheets Under Coatings by Magnetic Flux Leakage Durgesh Tamhane. 2019.
 34. Singh R. Magnetic particle testing. In: *Applied Welding Engineering*. 3rd ed. 1998. p. 220–1.
 35. Tomas I, Vertesy G. Magnetic Adaptive Testing. In: *Nondestructive Testing Methods and New Applications [Internet]*. InTech; 2012. Available from: <http://www.intechopen.com/books/nondestructive-testing-methods-and-new-applications/magnetic-adaptive-testing>
 36. Dubov AA. A study of metal properties using the method of magnetic memory. *Met Sci Heat Treat*. 1997;39(9–10):401–5.
 37. Bao S, Fu M, Hu S, Gu Y, Lou H. A Review of the Metal Magnetic Memory Technique. In: *Volume 4: Materials Technology [Internet]*. ASME; 2016. p. V004T03A006. Available from: <http://proceedings.asmedigitalcollection.asme.org/proceeding.aspx?doi=10.1115/OMAE2016-54269>

38. Singh R. Eddy Current Testing. In: Applied Welding Engineering [Internet]. Elsevier; 2016. p. 357–8. Available from: <http://www.emeraldinsight.com/doi/10.1108/eb036252>
39. García-Martín J, Gómez-Gil J, Vázquez-Sánchez E. Non-destructive techniques based on eddy current testing. *Sensors*. 2011;11(3):2525–65.
40. Heuer H, Schulze MH, Meyendorf N. Non-destructive evaluation (NDE) of composites: eddy current techniques. In: Non-Destructive Evaluation (NDE) of Polymer Matrix Composites [Internet]. Elsevier; 2013. p. 33–55. Available from: <https://linkinghub.elsevier.com/retrieve/pii/B9780857093448500038>
41. Margarit-Mattos ICP, Pacheco CJ, Soares SD, Arenas MP, Pereira GR, Grosso M, et al. Eddy current and inspection of coatings for storage tanks. *J Mater Res Technol* [Internet]. 2018;7(3):356–60. Available from: <https://doi.org/10.1016/j.jmrt.2018.05.006>
42. Yanling FU, Haiqing X, Hui M, Xing W, Hong BAI, Hongmei YU. A new coating thickness measuring instrument based on eddy current sensor. In: ECNDT 2014 Session: Eddy Current and Electromagnetic Testing. 2014.
43. FisherTechnology. Eddy Current Method [Internet]. [cited 2019 Apr 9]. Available from: <http://www.fischer-technology.com/en/united-states/knowledge/methods/coating-thickness-measurement/eddy-current-method-amplitude-sensitive/>
44. Yong L, Chen Z, Mao Y, Yong Q. Quantitative evaluation of thermal barrier coating based on eddy current technique. *NDT E Int* [Internet]. 2012;50:29–35. Available from: <http://dx.doi.org/10.1016/j.ndteint.2012.04.006>
45. Pedersen LB, Magnusson K, Zhengsheng Y. Eddy current testing of thin layers using co-planar coils. *Res Nondestruct Eval*. 2000;12(1):53–64.
46. Perez I, Kulowitch P. Thermography for Characterization of Corrosion Damage. 2000.
47. Doshvarpassand S, Wu C, Wang X. An overview of corrosion defect characterization using active infrared thermography. *Infrared Phys Technol* [Internet]. 2019;96(December 2018):366–89. Available from: <https://doi.org/10.1016/j.infrared.2018.12.006>
48. Han JS, Park JH. Detection of corrosion steel under an organic coating by infrared photography. *Corros Sci*. 2004;46(4):787–93.
49. Vavilov VP, Burleigh DD. Review of pulsed thermal NDT: Physical principles, theory and data processing. *NDT E Int* [Internet]. 2015;73:28–52. Available from: <http://dx.doi.org/10.1016/j.ndteint.2015.03.003>
50. He Y, Gao B, Sophian A, Yang R. Through Coating Imaging of Early Marine Corrosion Using ECPPT. *Transient Electromagn Nondestruct Test*. 2017;241–55.
51. He Y, Tian GY, Pan M, Chen D, Zhang H. An investigation into eddy current pulsed thermography for detection of corrosion blister. *Corros Sci* [Internet]. 2014;78:1–6. Available from: <http://dx.doi.org/10.1016/j.corsci.2013.09.001>
52. Johnson RE, Agarwala VS. Fluorescence Based Chemical Sensors For Corrosion Detection. In: *Corrosion 97*. 1997.
53. Li W, Calle LM. Micro-Encapsulation for Corrosion Detection and Control. 2007;(April):1–10.

54. Li W, Hintze P, Calle LM, Buhrow J, Curran J. Smart coating for corrosion indication and prevention: recent progress. *Corrosion*. 2009;NACE(Paper No: 09499):1–17.
55. Exbrayat L, Salaluk S, Uebel M, Jenjob R, Rameau B, Koynov K, et al. Nanosensors for Monitoring Early Stages of Metallic Corrosion. *ACS Appl Nano Mater* [Internet]. 2019;2(2):812–8. Available from: <http://pubs.acs.org/doi/10.1021/acsnm.8b02045>
56. Wade SA, Wallbrink CD, McAdam G, Galea S, Hinton BRW, Jones R. A fibre optic corrosion fuse sensor using stressed metal-coated optical fibres. *Sensors Actuators, B Chem*. 2008;131(2):602–8.
57. Zamarreño CR, Rivero PJ, Hernaez M, Goicoechea J, Matías IR, Arregui FJ. Optical Sensors for Corrosion Monitoring. *Intell Coatings Corros Control*. 2014;603–40.
58. Fan L, Bao Y, Meng W, Chen G. In-situ monitoring of corrosion-induced expansion and mass loss of steel bar in steel fiber reinforced concrete using a distributed fiber optic sensor. *Compos Part B Eng* [Internet]. 2019;165(February):679–89. Available from: <https://doi.org/10.1016/j.compositesb.2019.02.051>
59. Deng F, Huang Y, Azarmi F. Corrosion Behavior Evaluation of Coated Steel Using Fiber Bragg Grating Sensors. *Coatings*. 2019;9(1):55.
60. Deng F, Huang Y, Azarmi F, Wang Y. Pitted Corrosion Detection of Thermal Sprayed Metallic Coatings Using Fiber Bragg Grating Sensors. *Coatings*. 2017;7(3):35.
61. McAdam G, Newman PJ, McKenzie I, Davis C, Hinton BRW. Fiber optic sensors for detection of corrosion within aircraft. *Struct Heal Monit*. 2005;4(1):47–56.
62. Uruchurtu J, Mayorga Cruz D, Uribe D, Guardian Tapia R, Menchaca C. ELECTROCHEMICAL AND OPTICAL INTERFEROMETRIC CORROSION EVALUATION OF ABS COATED COPPER IN A SULPHATE/CHLORIDE SOLUTION. 2016.
63. Maaß P. Corrosion and Corrosion Protection. *Handb Hot-Dip Galvaniz*. 2011;1–19.
64. Brossia S. Laboratory Assessment of Corrosion. 2018;27–50.
65. Speight J. Corrosion. In: *Subsea and Deepwater Oil and Gas Science and Technology* [Internet]. 2015. p. 213–56. Available from: <https://doi.org/10.1016/B978-1-85617-558-6.00008-8%0A>
66. Aiello L, Colavita M, Agarwala VS. Galvanic Sensor for Monitoring Structural Damage. *Corros Rev* [Internet]. 2007 Jan;25(1–2):1–10. Available from: <https://www.degruyter.com/view/j/correv.2007.25.1-2/correv.2007.25.1-2.39/correv.2007.25.1-2.39.xml>
67. Klassen R., Roberge P. Zero resistance ammetry and galvanic sensors. In: Yang L, editor. *Techniques for corrosion monitoring* [Internet]. Florida: Woodhead Publishing Limited; 2008. p. 111–26. Available from: <http://www.sciencedirect.com/science/article/pii/B9781845691875500261>
68. Tsaprailis H, Kovacs W, Tuggle J, Garfias L. Corrosion Resistance of Stainless Steels Exposed to Aggressive Environments With Particles And Water. 2019;
69. Gonzalez J, Benito M, Feliu S, Rodriguez P, Andrade C. Suitability of Assessment Methods for Identifying Active and Passive Zones in Reinforced Concrete. *Corrosion*. 1995;51(2):145–52.
70. Brossia C. Electrical resistance techniques. In: Yang L, editor. *Techniques for*

- corrosion monitoring. Woodhead Publishing Limited; 2008. p. 277–93.
71. Clarke M. Industrial Corrosion. 1991. 11 p.
 72. Cristiani P. Corrosion monitoring in microbial environments. In: Yang L, editor. Techniques for corrosion monitoring. Woodhead Publishing Limited; 2008. p. 347–88.
 73. Diler E, Lédan F, LeBozec N, Thierry D. Real-time monitoring of the degradation of metallic and organic coatings using electrical resistance sensors. *Mater Corros.* 2017;68(12):1365–76.
 74. Panayotova M, Garbatov Y, Guedes Soares C. Corrosion of steels in marine environment, monitoring and standards. In: *Safety and Reliability of Industrial Products, Systems and Structures*. 2010. p. 269–417.
 75. Christenson J. Sensors and Transducers. In: *Handbook of Biomechanics* [Internet]. Elsevier; 2019. p. 74. Available from: <http://dx.doi.org/10.1016/B978-0-12-812539-7.00003-9>
 76. Ferrari V, Prudenziati M. Printed thick-film capacitive sensors. *Print Film Mater Sci Appl Sensors, Electron Photonics*. 2012;193–220.
 77. Zhang RJ, Dai SG, Mu PA. A spherical capacitive probe for measuring the thickness of coatings on metals. *Meas Sci Technol*. 1997;8(9):1028–33.
 78. Kolek Z. Characterization of water penetration inside organic coatings by capacitance measurements. *Prog Org Coatings*. 1997;30(4):287–92.
 79. Sell JK, Enser H, Jakoby B, Schatzl-Linder M, Strauss B, Hilber W. Printed Embedded Transducers: Capacitive Touch Sensors Integrated Into the Organic Coating of Metallic Substrates. *IEEE Sens J* [Internet]. 2016 Oct;16(19):7101–8. Available from: <http://ieeexplore.ieee.org/document/7529214/>
 80. Diamond GG, Hutchins DA. A New Capacitive Imaging Technique for NDT. *ECNDT 2006 - Poster 229*. 2006;1–8.
 81. Yin X, Hutchins DA, Chen G, Li W. Detecting surface features on conducting specimens through an insulation layer using a capacitive imaging technique. *NDT E Int* [Internet]. 2012;52:157–66. Available from: <http://dx.doi.org/10.1016/j.ndteint.2012.08.004>
 82. Wold K. The electric field. 2010;35–7.
 83. Clarida DR, Scanlan RJ, Boothman RM. Corrosion Monitoring Experience in the Refining Industry Using the FSM Technique [Internet]. *CORROSION 2003*. San Diego, California: NACE International; 2003. p. 14. Available from: <https://doi.org/>
 84. Kawakam Y, Kanaji H, Oku K. Study on application of Field Signature method (FSM) to fatigue crack monitoring on steel bridges. In: *Procedia Engineering* [Internet]. Elsevier B.V.; 2011. p. 1059–64. Available from: <http://dx.doi.org/10.1016/j.proeng.2011.07.133>
 85. Popov B. Passivity. In: *Corrosion Engineering*. 2015. p. 143–79.
 86. Technology FHAR and. An FHWA Special Study: Post-Tensioning Tendon Grout Chloride Thresholds. 2014.
 87. Enos DG. The Potentiodynamic Polarization Scan. Solartron Instruments Technical Report 33. Charlottesville; 1997.

88. Papavinasam S. Electrochemical polarization techniques for corrosion monitoring. In: *Techniques for Corrosion Monitoring* [Internet]. Elsevier; 2008. p. 49–85. Available from: <https://linkinghub.elsevier.com/retrieve/pii/B9781845691875500030>
89. Elgrishi N, Rountree KJ, McCarthy BD, Rountree ES, Eisenhart TT, Dempsey JL. A Practical Beginner's Guide to Cyclic Voltammetry. *J Chem Educ.* 2018;95(2):197–206.
90. Cíhal V, Lasek S, Blahetová M, Kalabisová E, Krhutová Z. Trends in the electrochemical polarization potentiodynamic reactivation method - EPR. *Chem Biochem Eng Q.* 2007;21(1):47–54.
91. Poursaeed A. Corrosion measurement and evaluation techniques of steel in concrete structures [Internet]. *Corrosion of Steel in Concrete Structures*. Elsevier Ltd; 2016. 169-191 p. Available from: <http://dx.doi.org/10.1016/B978-1-78242-381-2.00009-2>
92. Frølund T, Jensen FM, Bassler R. Determination of Reinforcement Corrosion Rate By. *First Int Conf Bridg Maintenance, Saf Manag.* 2002;14–7.
93. Cottis R. Electrochemical noise for corrosion monitoring. In: Yang L, editor. *Techniques for corrosion monitoring*. Woodhead Publishing Limited; 2008. p. 86–109.
94. Vedalakshmi R, Manoharan S, Song HW, Palaniswamy N. Application of harmonic analysis in measuring the corrosion rate of rebar in concrete. *Corros Sci* [Internet]. 2009;51(11):2777–89. Available from: <http://dx.doi.org/10.1016/j.corsci.2009.07.014>
95. Slepski P, Gerengi H, Bereket G, Samandar A. HARMONIC ANALYSIS FOR CORROSION MONITORING. 2009;2–5.
96. Cai G, Wang H, Jiang D, Dong Z. Impedance sensor for the early failure diagnosis of organic coatings. *J Coatings Technol Res* [Internet]. 2018;15(6):1259–72. Available from: <https://doi.org/10.1007/s11998-018-0072-5>
97. Hinton AJ. Determination of coating adhesion using electrochemical impedance spectroscopy. *Solartron Anal* [Internet]. 2010;2(1):18–23. Available from: http://www.ameteksi.com/-/media/ameteksi/download_links/documentations/library/solartronanalytical/electrochemistry/technical_note_impedance_spectroscopy_for_coatings.pdf?la=en
98. Hallam * D, Thurrowgood D, Otieno-Alego V, Creagh D. An EIS Method for assessing thin oil films used in museums. *ABN* [Internet]. 2004;592:967. Available from: www.nma.gov.au
99. van Westing EPM, Ferrari GM, de Wit JHW. The determination of coating performance with impedance measurements—II. Water uptake of coatings. *Corros Sci* [Internet]. 1994 Jun;36(6):957–77. Available from: <https://linkinghub.elsevier.com/retrieve/pii/0010938X9490197X>
100. Davis GD. In-situ corrosion sensor for coating testing and screening. *Mater Perform.* 2000;39(2):46–50.
101. Simpson TC, Moran PJ, Hampel H, Davis GD, Shaw BA, Arah CO, et al. Electrochemical monitoring of organic coating degradation during atmospheric or vapor phase exposure. *Corrosion.* 1990;46(4):331–6.
102. Davis GD, Ross RA, Dunn RC. Wireless, Battery-Powered Coating Health Monitor (CHM). *NACE Int.* 2010;(January 2010):1–9.
103. Shi Y, You C. A sensor system designed for remote coating degradation detection. In:

- 2010 IEEE Sensors Applications Symposium (SAS) [Internet]. IEEE; 2010. p. 257–60. Available from: <http://ieeexplore.ieee.org/document/5439388/>
104. Allahar K, Su Q, Bierwagen G. Non-substrate EIS monitoring of organic coatings with embedded electrodes. *Prog Org Coatings*. 2010;67(2):180–7.
105. Kittel J, Celati N, Keddani M, Takenouti H. New methods for the study of organic coatings by EIS. *Prog Org Coatings* [Internet]. 2001 Mar;41(1–3):93–8. Available from: <http://linkinghub.elsevier.com/retrieve/pii/S0300944000001557>
106. Iverson W. Transient Voltage Changes Produced in Corroding Metals. *J Electrochem Soc*. 1968;115:617–8.
107. Eden D., John D., Dawson J. *Corrosion Monitoring*. UK; 8611518, 1986.
108. Kane R., Eden D., Eden D. Evaluation of Potable Water Corrosivity using Real Time Monitoring Methods. In: *Corrosion/2003*. 2003. p. 03271.
109. Schottky W. Über spontane Stromschwankungen in verschiedenen Elektrizitätsleitern. *Ann Phys (N Y)*. 1918;362(23):541–67.
110. Jamali SS, Mills DJ, Sykes JM. Measuring electrochemical noise of a single working electrode for assessing corrosion resistance of polymer coated metals. *Prog Org Coatings* [Internet]. 2014;77(3):733–41. Available from: <http://dx.doi.org/10.1016/j.porgcoat.2013.12.014>
111. Mills DJ, Mabbutt S. Investigation of defects in organic anti-corrosive coatings using electrochemical noise measurement. *Prog Org Coatings*. 2000;39(1):41–8.
112. Jamali SS, Mills DJ. A critical review of electrochemical noise measurement as a tool for evaluation of organic coatings. *Prog Org Coatings* [Internet]. 2016;95:26–37. Available from: <http://dx.doi.org/10.1016/j.porgcoat.2016.02.016>
113. Mills D, Picton P, Mularczyk L. Developments in the electrochemical noise method (ENM) to make it more practical for assessment of anti-corrosive coatings. *Electrochim Acta* [Internet]. 2014;124:199–205. Available from: <http://dx.doi.org/10.1016/j.electacta.2013.09.067>
114. Schuhmann W, Bron M. Scanning electrochemical microscopy (SECM) in proton exchange membrane fuel cell research and development [Internet]. *Polymer Electrolyte Membrane and Direct Methanol Fuel Cell Technology: In Situ Characterization Techniques for Low Temperature Fuel Cells*. Woodhead Publishing Limited; 2012. 399-424 p. Available from: <http://dx.doi.org/10.1533/9780857095480.3.399>
115. Wittstock G, Burchardt M, Pust SE, Shen Y, Zhao C. Scanning electrochemical microscopy for direct imaging of reaction rates. *Angew Chemie - Int Ed*. 2007;46(10):1584–617.
116. González-García Y, Mol JMC, Muselle T, De Graeve I, Van Assche G, Scheltjens G, et al. SECM study of defect repair in self-healing polymer coatings on metals. *Electrochem Commun* [Internet]. 2011;13(2):169–73. Available from: <http://dx.doi.org/10.1016/j.elecom.2010.12.005>
117. Xia DH, Wang J, Wu Z, Qin Z, Xu L, Hu W, et al. Sensing corrosion within an artificial defect in organic coating using SECM. *Sensors Actuators, B Chem* [Internet]. 2019;280(October 2018):235–42. Available from: <https://doi.org/10.1016/j.snb.2018.10.051>
118. Enser H, Kulha P, Sell JK, Jakoby B, Hilber W, Strauß B, et al. Printed Strain Gauges

- Embedded in Organic Coatings. *Procedia Eng* [Internet]. 2016;168:822–5. Available from: <http://dx.doi.org/10.1016/j.proeng.2016.11.282>
119. Enser H, Kulha P, Sell JK, Schatzl-Linder M, Strauß B, Hilber W, et al. Printed strain gauges embedded in organic coatings - Analysis of gauge factor and temperature dependence. *Sensors Actuators A Phys* [Internet]. 2018 Jun;276:137–43. Available from: <https://doi.org/10.1016/j.sna.2018.03.042>
120. Sheet TD. Loctite EDAG PR 406B E&C. 2014;20–1.
121. Sheet TD. Loctite EDAG PF 050 E&C. 2014;20–1.
122. Enser H, Sell JK, Kulha P, Hilber W, Jakoby B. Printed transducers embedded in polymer coatings. *e i Elektrotechnik und Informationstechnik* [Internet]. 2018 Oct 23;135(6):401–7. Available from: <http://dx.doi.org/10.1007/s00502-018-0637-0>
123. Sheet TD. Conductive Epoxy Data Sheet.
124. PRIME_Faraday_Partnership. An Introduction to MEMS. Prime Faraday Technology Watch- Wolfson School of Mechanical and Manufacturing Engineering. 2002. 1-51 p.
125. Pan F. Development of MEMS-based Corrosion Sensor. Shandong University; 2012.
126. Saxena RC, Biswal J, Pant HJ, Samantray JS, Sharma SC, Gupta AK, et al. Application of thin layer activation technique for monitoring corrosion of carbon steel in hydrocarbon processing environment. *Appl Radiat Isot* [Internet]. 2018;135(February):201–6. Available from: <https://doi.org/10.1016/j.apradiso.2018.01.044>
127. Laguzzi G, Luvidi L, De Cristofaro N, Stroosnijder MF. Corrosion monitoring of different steels by thin layer activation. *J Radioanal Nucl Chem*. 2004;262(2):325–30.
128. Ditrói F, Takács S, Tárkányi F, Reichel M, Scherge M, Gervé A. Thin layer activation of large areas for wear study. *Wear*. 2006;261(11–12):1397–400.
129. Vena A, Perret E, Tedjini S. Introduction to RFID Technologies. In: *Chipless RFID based on RF Encoding Particle* [Internet]. Elsevier; 2016. p. 1–26. Available from: <https://linkinghub.elsevier.com/retrieve/pii/B978178548107950001X>
130. Dewi LM. Rfid: Theory, Implementation and Critics. Bina Ekon [Internet]. 2010;(January 2010). Available from: <http://journal.unpar.ac.id/index.php/BinaEkonomi/article/view/732>
131. Motlagh NH. Near Field Communication (NFC) - A technical Overview [Internet]. 2012. Available from: https://www.researchgate.net/publication/283498836_Near_Field_Communication_NFC_-_A_technical_Overview
132. Garbati M, Perret E, Siragusa R. Introduction to Chipless RFID Technology. In: *Chipless RFID Reader Design for Ultra-Wideband Technology* [Internet]. Elsevier; 2018. p. 1–20. Available from: <https://linkinghub.elsevier.com/retrieve/pii/B978178548292250001X>
133. Capdevila S, Roqueta G, Guardiola M, Jofre L, Romeu J, Bolomey JC. Water infiltration detection in civil engineering structures using RFID. In: *2012 6th European Conference on Antennas and Propagation (EUCAP)* [Internet]. IEEE; 2012. p. 2505–9. Available from: <http://ieeexplore.ieee.org/document/6206147/>
134. Khalifeh R, Lescop B, Gallée F, Rioual S. Development of a radio frequency resonator for monitoring water diffusion in organic coatings. *Sensors Actuators, A*

- Phys [Internet]. 2016;247:30–6. Available from:
<http://dx.doi.org/10.1016/j.sna.2016.05.024>
135. Bilginer B, Ljunggren P. Near Field Communication. Lunds Universitet; 2011.
136. Ripolles-Avila C, Ríos-Castillo AG, Rodríguez-Jerez JJ. Development of a peroxide biodetector for a direct detection of biofilms produced by catalase-positive bacteria on food-contact surfaces. *CYTA - J Food* [Internet]. 2018;16(1):506–15. Available from: <https://doi.org/10.1080/19476337.2017.1418434>
137. Hall DM, Beck JR, Lvov SN, Ziomek-Moroz M. Review of pH and Reference Electrodes for Monitoring Corrosion in HPHT Extreme Environments. *Corrosion*. 2015;(January 2015):1–15.
138. Behnood A, Van Tittelboom K, De Belie N. Methods for measuring pH in concrete: A review. *Constr Build Mater* [Internet]. 2016;105:176–88. Available from: <http://dx.doi.org/10.1016/j.conbuildmat.2015.12.032>
139. Gandía-Romero JM, Campos I, Valcuende M, García-Breijo E, Marcos MD, Payá J, et al. Potentiometric thick-film sensors for measuring the pH of concrete. *Cem Concr Compos* [Internet]. 2016 Apr;68:66–76. Available from: <https://linkinghub.elsevier.com/retrieve/pii/S095894651630018X>
140. Gandía-Romero JM, Bataller R, Monzón P, Campos I, García-Breijo E, Valcuende M, et al. Characterization of embeddable potentiometric thick-film sensors for monitoring chloride penetration in concrete. *Sensors Actuators, B Chem* [Internet]. 2016;222:407–18. Available from: <http://dx.doi.org/10.1016/j.snb.2015.07.056>
141. ten Have B, de Bruijn D, Olthuis W, Abbas Y, Hoekstra GI, van den Berg A, et al. Connecting to Concrete: Wireless Monitoring of Chloride ions in Concrete structures. *Procedia Eng* [Internet]. 2015;120:965–8. Available from: <http://dx.doi.org/10.1016/j.proeng.2015.08.827>
142. Kassal P, Steinberg MD, Steinberg IM. Wireless chemical sensors and biosensors: A review. *Sensors Actuators, B Chem*. 2018;266:228–45.
143. Fontes BE, Nistad B, Story U, Fontes E. Modeling Corrosion and Corrosion Protection MODELING CORROSION AND CORROSION PROTECTION 2 Further Resources Contact Information About the Authors. 2012;
144. Peratta C. Supporting Integrity Management with a CP Digital Twin. In: *CORROSION 2021*. 2021.
145. Zouari B, Touratier M. Simulation of organic coating removal by particle impact. *Wear*. 2002;253(3–4):488–97.
146. Tian W, Meng F, Liu L, Li Y, Wang F. Lifetime prediction for organic coating under alternating hydrostatic pressure by artificial neural network. *Sci Rep* [Internet]. 2017;7(January):1–12. Available from: <http://dx.doi.org/10.1038/srep40827>
147. Hunt FY. Modeling and Simulation of Weathering of Organic Coatings [Internet]. 1996. Available from: <https://math.nist.gov/mcsd/Reports/96/yearly/node20.html>
148. Kiil S. Mathematical modeling of photoinitiated coating degradation: Effects of coating glass transition temperature and light stabilizers. *Prog Org Coatings* [Internet]. 2013;76(12):1730–7. Available from: <http://dx.doi.org/10.1016/j.porgcoat.2013.05.008>
149. Duarte RG, Castela AS, Ferreira MGS. A new model for estimation of water uptake of an organic coating by EIS: The tortuosity pore model. *Prog Org Coatings*

[Internet]. 2009;65(2):197–205. Available from:
<http://dx.doi.org/10.1016/j.porgcoat.2008.11.007>

Chapter 3: Materials and Methods

3.1 Introduction

A description of the materials used and where they were procured from is given in this chapter. Furthermore, the various methods used, in subsequent chapters, for the characterisation of samples are provided, along with a brief description of their principles and details of the specific equipment used. To provide a reasonable level of degradation of the samples during the relatively short experimental timescale a number of common accelerated degradation techniques were used during this work. The methods and details of exposure parameters are given in this chapter. In the previous chapter it was shown that a number of environmental factors can contribute to the degradation of OCS in service. In order to measure locational variations in these factors a multi-functional sensing device was developed. The design requirements, building, development, and testing of this device is described in detail in this section.

3.2 Materials used

3.2.1 Pre-produced samples

Small Tata Steel line produced organically coated steel samples measuring approximately 15x7.5cm were used in this study. These samples, which included both a 3-layer PU coating system and a 2-layer PVC coating system, were provided by Tata Steel Colors. A wide range of colours of sample were used and these are discussed further in each section of work.

3.2.2 Substrates

The main substrates used in this work were steel blackplate, galvanised and Galvalloy coated steel. Blackplate is a low carbon steel that was provided by Tata Steel Packaging with a gauge thickness of 0.2mm. The galvanised steel was provided by Tata Steel Colors and had a gauge thickness of 0.86mm and a 20 μ m Zn – 0.15% wt. Al galvanising layer applied via hot dipping which had been pre-treated ready for application of the primer layer. Tata Steel Colors also provided metallically, 95% wt. Zn – 5% wt. Al, coated steel with a gauge thickness of 0.86mm.

All substrates were provided in sheets of approximately A4 size and cut to the required sizes using a Clarke sheet metal guillotine.

3.2.3 Coatings

Several coatings and coating systems were used in this work. Industrial paint systems were provided by Beckers (3-layer polyurethane-based system) and AkzoNobel (2-layer polyvinyl chloride-based system). A generic polyester-based system from Beckers was also used for some small-scale testing. A PVB 15% w/w solution was produced in the lab from ethanol and polyvinyl butyral-co-vinyl alcohol-co-vinyl acetate (PVB), obtained from Sigma-Aldrich Chemical Co. Loctite EA double bubble epoxy manufactured by Henkel Adhesives and Lacomit Varnish manufactured by Agar Scientific were also used as a coating for some samples.

3.3 Laboratory characterisation methods

3.3.1 FTIR

Fourier Transform Infrared (FTIR) Spectroscopy is a commonly used analytical technique in which the absorption and/or emission spectrum of the sample under test is measured. The technique works on the principle that molecular bonds can be excited into oscillation during exposure to infrared radiation. This leads to absorption of the wavelengths of infrared radiation, usually between 4000 cm^{-1} to 500 cm^{-1} , for which oscillation occurs. Molecular bonds will oscillate in different ways and at different wavelength due to varieties in bonding molecules, size, and types of bonding and hence it is possible to characterize the absorption wavelengths for specific functional groups. Therefore, when a spectrum is produced the absorption peaks can be compared to known peak locations for different functional groups to allow a determination of the groups present in the sample. The area of the peak can be, and is often, calculated to give a semi-quantitative measurement of group presence. For example, an increase in peak area from one sample to another would suggest increased concentration of that group. FTIR as a technique is commonly used for the characterization and failure analysis of organic coatings [1]. The machine used in this work was a Perkin Elmer Spotlight 400 in Attenuated Total Reflectance (ATR) mode.

3.3.2 EDX/S

Energy Dispersive X-Ray Spectroscopy (EDX/S) is quantitative and qualitative analytical technique that is commonly used in conjunction with SEM and can be used to characterize the elements present in a sample. EDX/S detects x-rays produced when an electron beam removes an electron from an atom present in the sample. The produced hole is then filled by another electron moving down from a higher energy orbital during which the additional energy is released as an X-ray as shown in Figure 3.1 [2]. Because of the different energy levels of orbitals in atoms of different elements the energy released in the x-ray is unique to each element. By analysing and comparing the x-rays released from a sample to known standards, the elements present can be determined along with their relative concentrations.

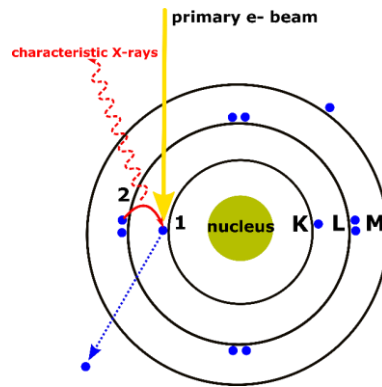


Figure 3.1. Formation of characteristic x-rays as a result of electron beam analysis [2]

3.3.3 XRD

X-Ray Diffraction is common technique for analysing the crystalline structure and/or composition of a material. During XRD testing x-rays are emitted towards the sample from a variety of angles which are then scattered by the regular arrangement of the atoms. The scattered x-rays interfere with each other before reaching the detector and at certain angles the constructive interference occurs leading to maxima. The angle of constructive interference can be associated to the crystallographic spacing of the atoms by Braggs law as shown in Figure 3.2 [3]. This spacing is dependent on the atoms present in different compounds. Therefore, compounds can be identified by comparing the resulting plot to a database of compounds to assess matching peaks. The machine used in this work was a Bruker D8 Discover with a 1600w copper radiation source and a 1D detector.

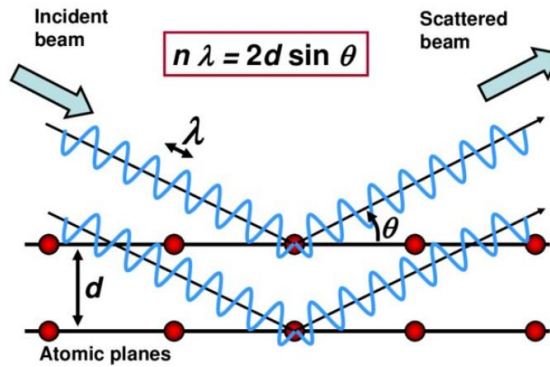


Figure 3.2. Principle of XRD in determining spacing of atomic planes [3]

3.3.4 Colour Measurements

Sample colour was measured using $L^*a^*b^*$ values in which L^* defines how white (100) or black (0), a^* defines how green (-a) to red (+a) and b^* defines how blue (-b) to yellow (+b) the sample is. The measurement device used in this work was an X-rite Ci62 spectrophotometer which was calibrated before each use by measuring a standard white plaque and black trap. This measures colour by observing the quantity of each light wavelength absorbed by the sample of interest as shown in Figure 3.3.

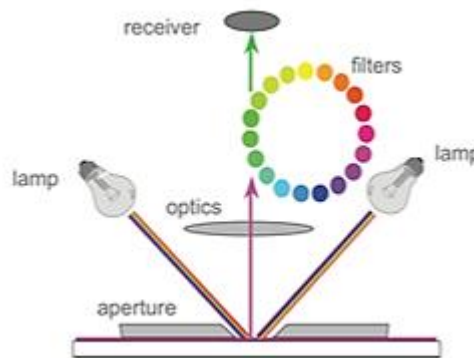


Figure 3.3. Spectrophotometer working principle [4]

3.3.5 Gloss Measurements

Sample gloss is defined as the ability of a sample to reflect incident light and is calculated by applying light at a specific angle to the sample and measuring the specular reflectance. This principle is shown in Figure 3.4. For the analysis of coatings 20, 65 and 80° are commonly used as the angle of test with 65° being the most common. The gloss meter used for this work was a Sheen Glossmaster 260 capable of measuring gloss at 20, 65 and 80°.

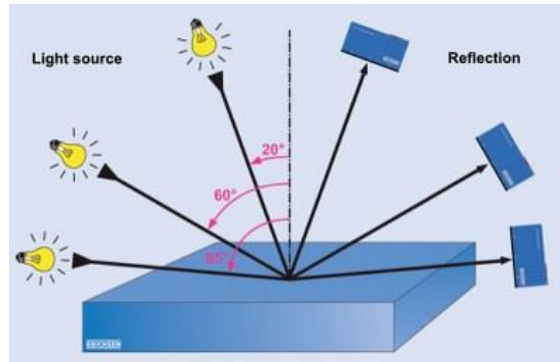


Figure 3.4. Principle of gloss measurements [5]

3.3.6 Water Contact Measurement

The water contact angle of a sample is a commonly used measurement to determine the wettability of a surface. While there are several possible measurement methods it is often measured by placing a droplet of a solution onto the surface and observing the angle produced between surface the droplet as shown in Figure 3.5. A larger contact angle is indicative of a more hydrophobic surface and low wetting whereas a smaller angle suggests hydrophilic surface properties and a high degree of wetting. The contact angle can also be related to the surface energy. In this work the static sessile drop method was used to measure contact angle and was carried out using a contact angle measurement system composed of a mounted pipette and camera. A single droplet of de-ionised water was dispensed from a pipette and the camera was used to photograph the resulting droplet on the surface of the test sample. FTA32 software was then used to calculate the contact angle.

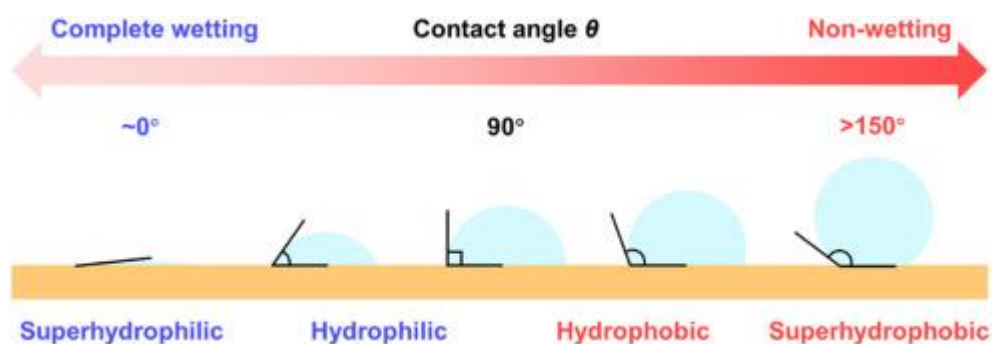


Figure 3.5. Examples of contact angles [6]

3.3.7 Coating Adhesion

Coating adhesion is a measure of the strength of the bond between coating and substrate or between each coating layer in a multicoating system. Poor adhesion implies that layers of a coating or the whole coating can be removed mechanically

with little force or may peel naturally over time. In this work adhesion was measured following techniques described in BS EN 13523-6 [7]. The first method was the crosshatch tape test in which two sets of 6 parallel 50mm lines, separated by 1mm were scribed at 90° to each other. Adhesive tape with a strength of 10N per 25mm width was then applied to the crosshatched area and then quickly removed at approximately 60° angle. The resulting surface was then examined to determine the quantity of coating removed which was recorded as a percentage. The general principle of this method is shown in Figure 3.6.

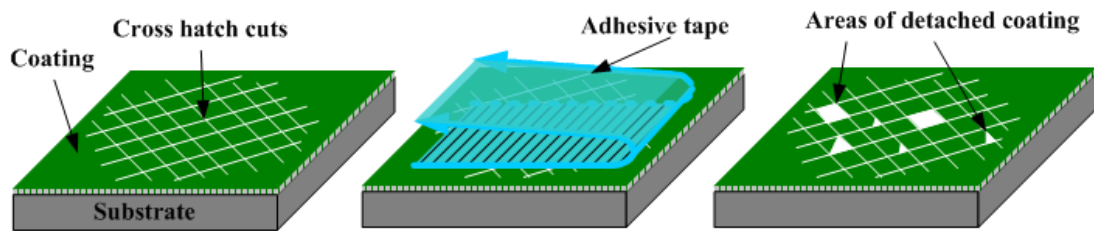


Figure 3.6. Process of a tape adhesion test [8]

The second method used was the cupping test method. A similar set of crosshatched lines were produced on a sample which was then placed into a manual Erichsen dome testing device. This device, which met BS EN 13523-6 standards, was used to produce a uniform dome of deformation centered on the crosshatch by forcing a xmm ball bearing into the sample. After 10mm of deformation the sample was removed, and the crosshatched area examined for evidence of paint removal or loss of adhesion. The approximate area of the cross hatch observed to show loss of adhesion was then recorded as a percentage.

3.3.8 Scratch resistance

Scratch resistance is considered another test of coating adhesion however can also be used to gauge the resistance to wear and accidental damage [9]. In this work an automatic mechanical scratch tester produced by Sheen was used to measure the scratch resistance. The machine allows the test sample to be clamped in place and then a stylus is drawn over the sample. The machine monitors the connection between stylus and sample and when a scratch to the substrate is made a connection is completed and visible on the readout. During testing weights are incrementally added to the stylus to increase the force upon it and the maximum weight that can be added before breakthrough of the coating occurs is recorded. Each scratch was made

on a fresh sample area and the stylus was inspected before and after each scratch to ensure it was free from any debris from previous tests.

3.3.9 Coating thickness

The thickness of individual coating layers as well as the overall coating system is a key parameter to ensure repeatable and representable samples are produced. A Elcometer 456 coating thickness gauge was used in this work to measure the thickness of coating layers. For measurements on steel substrates the device uses an electromagnetic induction-based technique with a stated accuracy of $\pm 1-3\%$ and a resolution of $0.1\mu\text{m}$ [10]. The device measures the distance between the probe and substrate by comparing the detection of a magnetic field generated on a central coil by an upper and lower coil. As the probe moves closer to the substrate the lower coil measures increased magnetic field strength compared to the upper. The distance between probe and substrate, therefore the coating thickness, is then calculated based on the degree of this discrepancy [10]. The device was used according to the manufacturer's instructions and calibrated before each use using the two-point calibration mode by measuring the thickness of two standard films of a thickness less than and greater than that of the sample measured. This device, or devices of similar function and capabilities have widespread use for the measurement of coating thickness in published research [11].

3.4 Accelerated Degradation Methods

3.4.1 Salt spray

Salt spray or fog testing is a well-established accelerated corrosion and aging testing method used to determine corrosion resistance of coated and uncoated metal samples. While there are several standards and methods of testing, testing similar to the ASTM B117 standard [12] was used for this work. In this work samples were subjected to an environment composed of an ambient temperature of 35°C and a pH 6.5-7.2 5% NaCl atmosphere. The 5% NaCl solution was produced in the lab using 95% pure NaCl from Fisher Scientific and de-ionised water with a resistance greater than $1\text{M}\Omega$. The solution was neutralised to pH 7 using small amounts of either hydrochloric acid or sodium hydroxide as required. The duration of the test was carried out in 24-hour blocks. The advantage of this testing is that it promotes very rapid corrosion of the samples allowing results to be generated quickly.

3.4.2 UV condensation testing

UV condensation testing was also used to rapidly degrade samples. Samples underwent cyclic testing involving exposure to 1.9 W/m^2 of UV exposure at 80°C and exposure to condensation at 50°C . These two cycles were run continuously for 8 and 4 hours respectively for blocks of 250 hours. The lamps used for the UV irradiation were type II UVA-340 as defined by BS EN ISO 11507 [13] and the overall testing was carried out in a Q-Lab QUV accelerated weathering tester which meets and can test to a number of standards including BS EN ISO 11507.

3.4.3 MEK Rubs

Chemical stability and degree of cure of organic coatings is often tested by carrying out ‘rubs’ with a solvent until coating breakthrough occurs. While a range of solvents can be used one of the most commonly used is Methyl ethyl ketone (MEK) also known as 2-butanone and this was used in this work and was procured from Fisher Scientific at a 99% purity. The MEK rubs were applied using a clean cheesecloth with one forward and reverse rub counted as one double rub.

3.5 Development of a device to monitor localised conditions

As covered in the literature review coating degradation and corrosion are complex processes which are affected by a large number of environmental parameters. To establish how these parameters vary across a building a device was required to measure as many of these factors as accurately as possible. Such a system would also be required to have certain features to facilitate use and to simplify this process the required specification of hypothetical best-case system, shown in Table 3.1, was drawn up.

Table 3.1. Design requirements of the system

Requirements	Justification
Easy secure mounting to building facades	The system must allow non-intrusive attachment to a variety of building envelope geometries to avoid damaging panels and allow all area monitoring. Mounting must be secure enough to ensure safety.
Ability to change components easily if required	In the case that components become uncalibrated or less accurate with time these can be changed without affecting the overall system to lower costs and decrease downtime.
Long term weather resistance	The system will be exposed outdoors for long durations and hence will require considerable resistance to water ingress as well as temperatures ranging from sub-zero to 40°C+.
Data acquisition rate of several points per hour	A datalogging style of results is required to have meaningful long-term data acquisition.
Long term battery life	Mains power will not always be easily available on building exteriors and hence the system should have a battery which is suitable for long term measurements.
Live data monitoring and acquisition	Live data allows instantaneous analysis and would allow better monitoring of the system effectiveness.
Easy interface to commercial sensors	Commercially available sensors for measuring certain parameters will be incorporated into the system.
Compact size	The requirement to be placed in a variety of building locations means the system should be smaller than A4

Measurements	Justification and Requirements
Ambient temperature	A number of temperature driven failure methods were mentioned previously. Higher temperature often leads to accelerated rates of reactions however can allow better drying.
Ambient humidity	Humidity often accelerates corrosion rate and leads to greater prevalence of moisture to produce moisture driven coating failure methods.
Panel temperature	The temperature of the panel will likely vary from ambient and hence is important to consider when determining temperature effects.
UV intensity	UV is known to attack organic coatings leading to colour fade and other more damaging effects.
Time/cycle of wetness	Moisture presence can cause coating failure via a number of methods and facilitates aqueous corrosion. Cyclic wetting however can reduce contaminant build up protecting the coating.
Contaminant build up	Soiling of the coating surface can produce differential aeration cells and may lead to aggressive compounds being held close to the coating.
Contaminant composition	Some contaminants are far more damaging than others for example the presence of acidic or saline compounds.
Aqueous conditions	The conditions present, such as concentration of salts or other dissolved compounds, can affect the rate of coating degradation and failure.
Gaseous conditions	Different concentrations of local gases, for example oxygen, can cause greater likelihood of some failure modes.
Local pH	Both acidic and alkaline conditions attack coatings and can be important in establishing corrosion.
Windspeed	Erosion of coatings can occur by wind driven particles
Biological build up	The build-up of biological matter can directly damage coatings or can cause products that lead to degradation. Ideally measurement of the different rate of build-up of contaminant in both area and mass would be possible.

The development and testing process of producing the device is explained in detail in Appendix A. The final device was composed of an Arduino pro mini along with multiple sensors to provide low cost, easily manufacturable devices capable of measuring a diverse range of atmospheric conditions, which are given in Table 3.2.

While the absolute calibration of each device to relevant SI standards is not quantified, the repeatability of each sensor type provides satisfactory relative measurement.

Table 3.2. Sensors used in the multifunctional sensing device.

Parameter	Sensor	Operational Principle	Quoted Repeatability
Air temperature	Adafruit BME 680	Diode Voltage	+/- 1 °C [14]
Humidity	Adafruit BME 680	Capacitive	+/- 3% [14]
Panel temperature	Adafruit TMP 006	IR Thermopile	+/- 1 °C [15]
UVA	Adafruit VEML 6075	Photodiode	+/- 3 μWcm^{-1} [16]
UVB	Adafruit VEML 6075	Photodiode	+/- 3 μWcm^{-1} [16]
Particulate concentration	Grove PPD42NS	Low Pulse Occupancy	+/- 50% [17]
Time of wetness	Grove Capacitive Moisture Sensor	Capacitive	+/- 5%

The comparison of the features of the final device are also compared to the original specification in Table 3.3. It is shown that the requirements of the system were mainly fulfilled and although the system could of course be improved it was considered to meet the specification sufficiently. Although there were, however, still measurement criteria that were not met by the current system, the specification was viewed as an ideal system that may not be feasible.

Table 3.3. Design specification analysis on further improvements

Requirements	Met	Current solution	Possible improvements
Easy secure mounting to building facades	Yes	Smaller lighter design with more secure mounting	None Required
Ability to change components easily if required	Yes	As before	None Required
Long term weather resistance	Yes	More secure box sealing and better component fitting	None Required
Data acquisition rate of several points per hour	Yes	As before	None Required
Long term battery life	Yes	Redesigned control system with new battery system of up to 40-day life.	Further remove non-essential components.
Live data monitoring and acquisition	No	No longer considered a key requirement	None Required
Easy interface to numerous commercial sensors	Yes		
Compact size	Yes	Current 3D box is approximately	None Required

Measurements	Met	Solution/Justification
Ambient temperature	Yes	Measured to a stated instrument accuracy of $\pm 1^{\circ}\text{C}$. Agreement with calibration testing.
Ambient humidity	Yes	Measured to a stated instrument accuracy of $\pm 3\% \text{RH}$. Agreement with calibration testing.
Panel temperature	Yes	Measured to a stated instrument accuracy of $\pm 1-3^{\circ}\text{C}$. Agreement with calibration testing.
UV intensity	Yes	UVA, UVB and UVI measured with agreement to calibration testing.
Time/cycle of wetness	Yes	Capacitive moisture sensor which provides % wetness output.
Contaminant build up	Yes	Dust sensor Measurement of actual contaminant build up via manual measurement
Contaminant composition	Yes	Accurate in-situ measurement considered too complicated so will be carried out in the lab post collection.
Aqueous conditions	No	Not considered possible to automate due to the complication of collecting, analysing and releasing liquids. Human measurement at discrete intervals would be far easier and more efficient as it is not expected to vary on an hourly basis.
Gaseous conditions	Yes	Accurate in-situ measurement considered too complicated to automate however VOC measurement (indication) facilitated.
Local pH	No	No considered possible to automate due to the complication of collecting, analysing and releasing liquids. Human measurement at discrete intervals would be far easier and more efficient as it is not expected to vary on an hourly basis.
Windspeed	No	Although possible the size of the system would be adversely affected. Human measurement at discrete intervals would be far easier and more efficient.
Biological build up	Yes	Difficult to distinguish biological matter from other contaminants and classify automatically. Measurement can be taken via manual analysis if required.

The remaining measurements that were not been considered possible were aqueous conditions, pH and windspeed. Windspeed could be easy measured with a handheld commercial device held in close proximity to the test site, if needed. pH, if also

needed could be measured with a standard lab-based probe by either collecting rainwater coming off the test site or washing the test site with pH 7 deionised water and collecting the resulting liquid.

The aqueous conditions of each location are more complicated but essentially what was required was some sort of device that can determine which locations of a building are most susceptible to aqueous corrosion and one way to achieve this is through the detection of the conductivity which is indicative of the dissolved salts in an aqueous system. By creating a standalone device many of the complications to the initial system is removed human operation removes complication of liquid management. Such a device was produced which could measure the electrical conductivity of solutions. The design, testing and production of said device is detailed in Appendix B.

3.6 Conclusions

In this section the materials and laboratory methods used in the following sections have been detailed. The development of custom measurement devices that are used in this work and an assessment of their accuracy as well as the rationale behind their production has also been given. It has been shown that the automatic measurement of a number of environmental factors is possible accurately however, if other, more complex factors, are required to be measured then some level of human collection/analysis is required. The following chapter investigates the basic requirements of sensing technology for the monitoring of OCS performance in-situ in an attempt to narrow down the large number of possible approaches to several distinct and promising avenues to research.

3.7 References

1. Poliskie M, Clevenger JO. Fourier transform infrared (FTIR) spectroscopy for coating characterization and failure analysis. *Met Finish*. 2008;106(5):44–7.
2. Nanakoudis A. EDX Analysis with SEM: How Does it Work? *Accelerating Science* [Internet]. 2019; Available from: <https://www.thermofisher.com/blog/materials/edx-analysis-with-sem-how-does-it-work/#:~:text=The way EDX analysis works,shell to fill the vacancy.>
3. Nasir S, Hussein MZ, Zainal Z, Yusof NA, Mohd Zobir SA, Alibe IM. Potential valorization of by-product materials from oil palm: A review of alternative and sustainable carbon sources for carbon-based nanomaterials synthesis potential valorization of by-product materials from oil palm: A review of alternative and sustainable. *BioResources*. 2019;14(1):2352–88.

4. Mike Huda. What is a Spectrophotometer? X-rite Color Blog [Internet]. 2015; Available from: <https://www.xrite.com/blog/what-is-a-spectrophotometer>
5. Erichsen. Gloss measurement - high gloss to matt gloss [Internet]. [cited 2022 Nov 21]. Available from: <https://www.erichsen.de/en-gb/service/test-methods/surface-testing/gloss-measurement-high-gloss-to-matt-gloss>
6. Song JW, Fan LW. Temperature dependence of the contact angle of water: A review of research progress, theoretical understanding, and implications for boiling heat transfer. *Adv Colloid Interface Sci* [Internet]. 2021;288:102339. Available from: <https://doi.org/10.1016/j.cis.2020.102339>
7. BSI. Coil coated metals-Test methods-Part 6: Adhesion after indentation (cupping test). 2002.
8. Kopeliovich D. Adhesion tests. SubsTech [Internet]. 2014; Available from: https://www.substech.com/dokuwiki/doku.php?id=adhesion_tests
9. Jennett NM. Good Practice Guide The Scratch Test : Calibration , Verification and the Use of a Certified. National Physical Laboratory. (54).
10. Elcometer. Elcometer 456 Coating Thickness Gauge [Internet]. 2022 [cited 2022 Nov 22]. Available from: <https://www.elcometer.com/en/coatings-inspection/all-coatings-inspection/dry-film-thickness/digital/elcometer-456-separate-coating-thickness-gauge.html>
11. Rodger J, Bartlett S, Atrens A. Corrosion of the galvanizing of galvanized-steel electricity transmission towers. *Mater Corros*. 2017;68(8):902–10.
12. ASTMInternational. ASTM B117-19 Standard Practice for Operating Salt Spray (Fog) Apparatus [Internet]. 2019. Available from: <https://www.astm.org/b0117-19.html>
13. InternationalOrganizationforStandardization. ISO 11507:2007 Paints and varnishes — Exposure of coatings to artificial weathering — Exposure to fluorescent UV lamps and water [Internet]. 2007. Available from: <https://www.iso.org/standard/37489.html>
14. Adafruit. Adafruit BME680 - Temperature, Humidity, Pressure and Gas Sensor [Internet]. [cited 2020 Apr 7]. Available from: <https://www.adafruit.com/product/3660>
15. Texas Instruments. Infrared Thermopile Sensor in Chip-Scale Package. 2012;(December). Available from: <http://www.ti.com/product/TMP006/description>
16. vishay. VEML6075 Vishay Semiconductors Not for New Designs UVA and UVB Light Sensor with I 2 C Interface. 2019;1–11. Available from: www.vishay.com/doc?91000
17. Shinyei Corporation. Particle Sensor Model PPD42NS. 2010;2010:3. Available from: http://www.seeedstudio.com/wiki/images/4/4c/Grove_-_Dust_sensor.pdf

Chapter 4: Concept Investigation

4.1 Introduction

As shown in Chapter 2 there is a number of existing techniques for the monitoring of corrosion control through coatings. Given the number of potential methods, quantities of measurement and ways of measurement it is not possible to explore every possible option. From the initial literature search the following methods were easily discarded, Table 4.1.

Table 4.1. Initially discarded methods

Method	Reasons For Discarding
Nuclear Thin Layer Activation	Requires specific conditions such as applied stress or nuclear activation that are not attractive
Acoustic emission	
pH Sensors	Often difficult to relate provided data to actual asset condition. Are well-established techniques for analysing corrosiveness of environments that are difficult to expand on
Chemical Sensor	
Bio-Detectors	
Corrosion Coupons	
Galvanic	
Potential dynamic polarisation	Complex to implement when considering reference probes, control systems and often aqueous conditions are required
Hamonic Analysis	
SECM	
EIS	
EN	
Magnetic memory method	Relatively untested new concept that requires significant fundamental development
Magnetic adaptive testing	
Corrosion Product Detection	
Corrosion Indicating Paint	Likely to require significant changes to the product and or manufacturing methods
Corrosion Fluorescent Paint	

This still left a number of additional methods although these were grouped into 11 main techniques which are summarised in Figure 4.1. Of these remaining techniques a number are concepts that would be affixed onto the surface of the OCS (shown in blue), techniques that require embedding in the coating and/or connection to the substrate (shown in green) and techniques that could be embedded and/or connected to the substrate but do not require it (shown in orange).

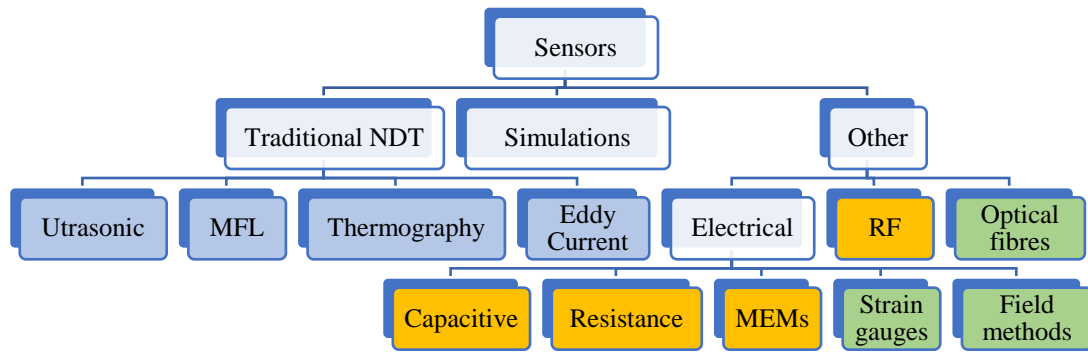


Figure 4.1. Remaining grouped techniques

This chapter aims to briefly investigate feasibility of some broad potential options for sensor concepts and to further narrow down and determine the best possible lines of research to carry forward.

In order to best achieve this, it is important to consider the characteristics that an optimum solution would give. Ideally a sensor produced would be sensitive enough to determine coating condition before failure and detect corrosion and any defect formation as early as possible. Furthermore, the sensor ideally would be self-maintained, requiring minimal or no power or human interaction and have a long-life span. Finally, the sensor itself must not reduce the lifespan of the coating itself and present a relatively easy route of installation.

As there are no current techniques that exist that are optimal for this application, basic concepts of the sensor were considered in terms of feasibility. This was in an attempt to narrow down on the basics of the design of the sensor system. In this chapter two key factors are considered; whether the sensor should be composed of a number of discrete stationary units or fewer scanning units and whether the sensor should be embedded into the coating or affixed onto it. A discussion of possible sensor concepts is then presented to provide the background of the techniques investigated in the thesis.

4.2 Sensor positioning

A key property of the sensor device is how the sensor will be positioned in relation to the coating, steel substrate and overall building. It was considered whether the sensor should be static and only monitors the area directly surrounding it or a movable sensor capable of providing monitoring across an area should be developed.

A movable sensor was an attractive principle as it would allow a large area to be scanned repeatedly and require only one sensor to provide significant area coverage rather than a number of static sensors set up in a discrete array. The resolution of a moving sensor would be far easier to control and adjust and the sensor can afford to be more sophisticated and expensive as there would be fewer required to install and maintain. This is the approach taken by pipeline monitoring, a movable intelligent ‘pig’ is sent through the pipeline and MFL is carried out across the cross-sectional area [1]. Ultrasonic testing is also usually carried out with one movable sensor which is manually operated by a technician to scan over small areas; for large-scale application, this option would be far too human resource intensive. If a movable sensor were to be used it would have to be autonomous in nature otherwise it would not offer significant advantages over pre-existing non-destructive methods. Initially this seemed to be a viable option with a system such as an arcing extendable pole or a CNC style frame which could fit round a rectangular building façade as shown in Figure 4.2.

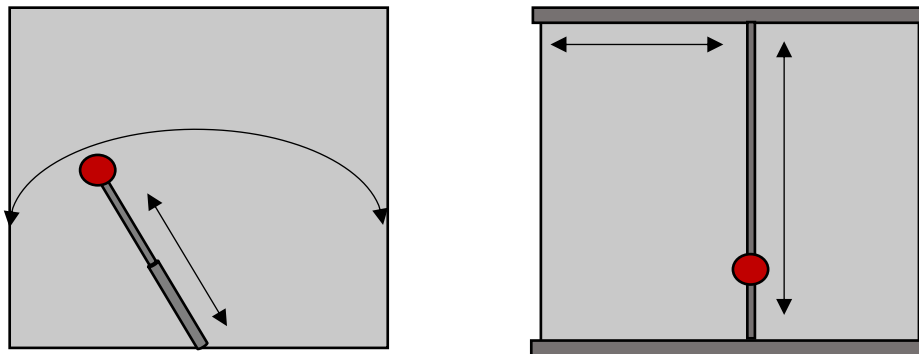


Figure 4.2. Two automated scanning sensor (shown in red) ideas; an extendable arching pole (left) and a more typical XY CNC positioner (right)

However, while this style of system is highly effective for an application where the scanned surface is consistent in size over a large area, such as a pipeline, it is more complicated on an irregular building façade. Areas such as windows, pipework, doorways, shelters and changing geometries would prove difficult to scan over or around and it would be the case that a bespoke solution may be required for almost every building deployed onto. This is perhaps why documented systems such as these are usually limited to simple flat surfaces such as bridge undersides or roads [2]. Furthermore, unless the surface is very well orientated along a flat plane maintaining consistent sensor distance, or contact, to the coated panel would be

extremely difficult. This may limit the quality of results possible from any sensing device. While simple in principle, the system of motors and control systems required to run a system like this would be complicated to design and install and may limit the sensor complexity, weight, and other factors. With these considerations it was decided that an autonomous scanning system would not be taken forward as a concept and that the project would focus on a discrete array style of sensors.

The outcome of this decision is that techniques that rely on very accurate, and therefore large and/or expensive, measurement systems would likely be unsuitable. This is because in order to sample a reasonable area in a discrete array it would require significant investment, calibration, and mounting. Therefore, the following techniques were discarded.

Method	Reasons For Discarding
Thermography	Unsuitable for discrete array sensing, either require too expensive equipment or manual operation
Ultrasonic	

4.3 Feasibility of embedded sensors

The other initial area of consideration was whether the sensor is embedded into coated layers of the panel itself or is mounted externally onto the product. There are several benefits to the sensor being embedded such as better protection to the environment and therefore a likely longer lifespan and less sensitivity to external noise also due to limited exposure [3]. Furthermore, it allows determination of more measurements such as capacitance of individual coating layers rather than the coating as a whole and would not affect the aesthetics or geometries of the panels compared to a sensor attached to the outside. A non-embedded sensor could also potentially shield the area of interest from the environment meaning that the sampled area is not representative of the bulk.

However, the disadvantages of a method like this are that the sensor is limited to a thin form and has to be inlaid during the manufacturing process without deteriorating or disturbing the coating performance. There is also an inherent problem powering and communicating with the device if they are embedded in the coating system [4].

To fully determine the feasibility of embedded sensors their use was considered and tested with regards to manufacturing, durability, powering, and communication.

4.3.1 Manufacturing Feasibility – Line Applicability

Considering the speed at which the substrate travels on the coating line, it is not considered possible that embedded sensors could be applied to line produced product. Even if the sensor were extremely simple in design, it is difficult to imagine a method of placing it onto the substrate and would require significant changes to the coating line itself. Therefore, any embedded sensor system would have to be produced on smaller, hand coated samples. It is therefore important to consider how representative a hand coated sample is of the line coated sample to consider the usefulness of the sensor data for determining the condition of the bulk. To determine this samples of two common coating systems, based on Polyurethane (PU) and Polyvinyl Chloride (PVC) chemistries, were produced via bar coating, and tested to compare their properties to similar line coated product.

4.3.1.1 Comparison of line and hand coated PU system

PU systems are often composed of three layers and can range in total thickness from approximately 40-65 μm . For this work, the system produced was a 65 μm coating composed of a 25 μm primer, 25 μm topcoat and 15 μm clear coat layer. This gave a final product comparable to that of a Tata Steel Colors' PU product produced on the line. For lab scale production, each of these paint layers were deposited onto a pre-treated galvanised steel sample using both black and green wire bars. These produce a coating wet film thickness of 40 μm and 24 μm which were expected to provide the required dry film thicknesses of 25 μm and 15 μm . All the coating layers were cured in accordance with the manufacturer's (Beckers) guidelines.

To verify that the correct coating layer thicknesses were being produced, each layer was measured using an Elcometer 456. These measurements are shown in Figure 4.3 where the measured hand coated thicknesses are compared to the line coated thickness tolerances. It can be seen that generally the layers deposited to produce the hand coated sample match well with the manufacturing requirements of a line coated PU samples. Therefore, it can be concluded that the system is well replicated physically using the process described above.

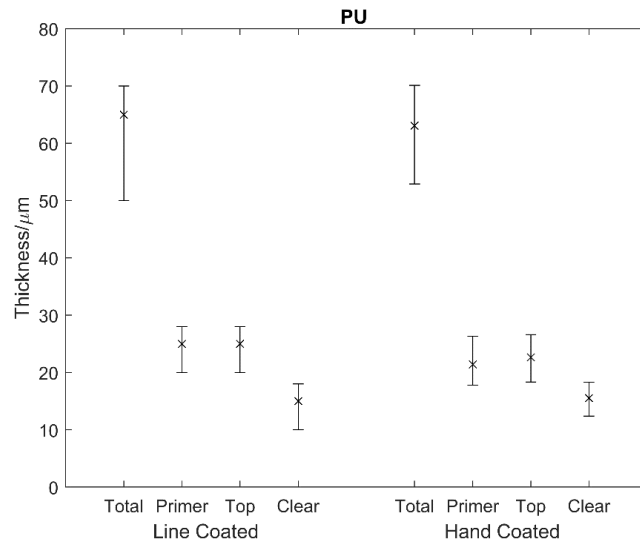


Figure 4.3. Comparison between required layer thicknesses (dry film thickness) for line coated PU and the measured thickness of the hand coated sample

The hand and line samples were also compared via optical microscopy as shown in Figure 4.4. It is observed that the two systems generally appear similar however there is perhaps a slightly rougher surface finish, with what appears to be larger peaks, to the hand coated samples.

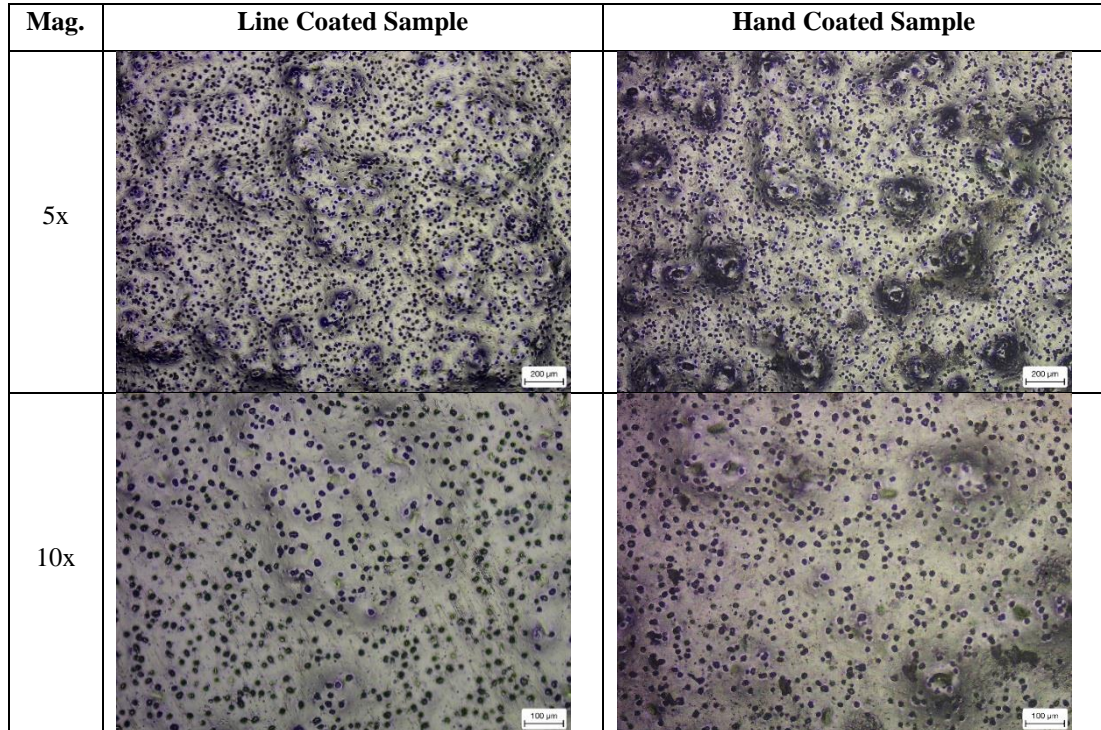


Figure 4.4. Microscopy comparison of line and hand PU samples

In order to compare the surface roughness of each sample 3D depth profiles were produced using a Keyence optical microscope. This was then used to calculate a

surface roughness for each sample. the depth profiles, shown in Figure 4.5 show similar characteristics and the calculated average surface roughness (S_a) of the hand sample was only slightly larger than that of the line sample; $5.6\mu\text{m}$ compared to $4.6\mu\text{m}$.

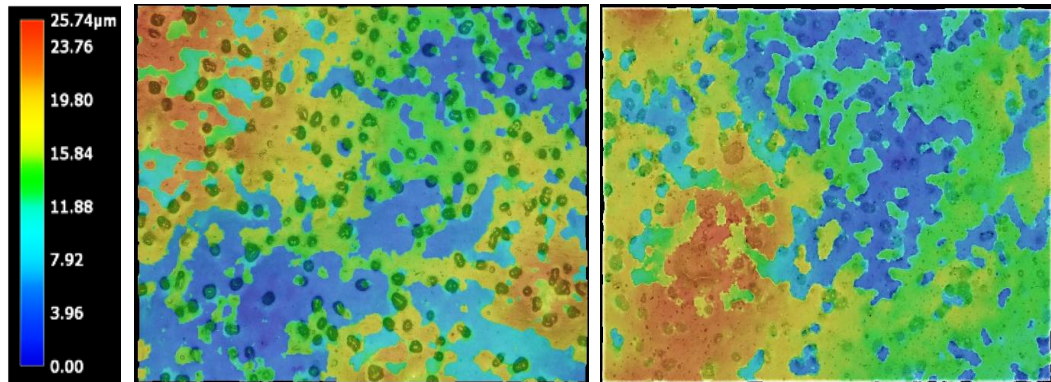


Figure 4.5. Surface topography comparison between line (left) and hand (right) coated PU samples

A number of other coating properties, Table 4.2, were also tested for the hand and line produced samples and the results were compared to the required specification. The results of these tests are shown in and show that there were similar properties between the two samples and that the hand sample meets the required specifications. Although the water contact angle was different between the two samples this was thought to be due to the fact that the hand samples had just been produced so had little exposure to the elements.

Table 4.2. Comparison between the properties of the hand and line coated PU samples

Property	Measurement Method	Specification	Line Coated	Hand Coated
Colour (L*)	Elcometer 6085	RAL 7016*	36.4 ± 0.0	36.6 ± 0.1
Colour (a*)	Elcometer 6085	RAL 7016*	-1.5 ± 0.0	-1.6 ± 0.0
Colour (b*)	Elcometer 6085	RAL 7016*	-2.6 ± 0.0	-2.4 ± 0.0
Colour difference (ΔE^*_{ab})	Elcometer 6085	$<1^{**}$	0.3	
Scratch Resistance	Sheen Scratch Tester	$>3000\text{g}$	3200g	3600g
Gloss @ 60°	Sheen Tri Gloss Meter	25-35%	$28.8 \pm 0.5 \%$	$24.7 \pm 0.8 \%$
Water Contact Angle	FTA 241	N/A	$70.3 \pm 0.1^\circ$	$76.9 \pm 0.2^\circ$
Adhesion Cross Hatch	Tape method	100%	100%	100%
Adhesion Cross Hatch	Erichson dome method	100%	100%	100%

*Closest RAL (Reichsausschuß für Lieferbedingungen und Gütesicherung) colour to actual colour

** $\Delta E^*_{ab} < 1$ corresponds to no noticeable difference for the human eye where:

$$\Delta E_{ab} = \sqrt{(L_{*2} - L_{*1})^2 + (a_{*2} - a_{*1})^2 + (b_{*2} - b_{*1})^2} \quad (4.1)$$

4.3.1.2 Comparison of line and hand coated PVC system

In comparison to the PU system, the PVC coating system produced was composed of only two layers, a primer of 5µm and a topcoat of 195µm. Again, these parameters gave a final product comparable to that of a Tata Steel Colors' PVC product produced on the line. The hand samples were produced on the same pre-treated galvanised steel substrate but 6µm and 200µm wet film thickness k-bars were used to produce the required thicknesses. As before the coatings were cured as specified by the manufacturer (Akzo Nobel). It is important to note that the PVC line samples were embossed but this was not carried out on the hand coated samples.

As before, the thickness of the coating layers was measured and compared to the line coated manufacturing requirements as shown in Figure 4.6. Again, it was shown that the hand produced sample matched well with the physical dimensions of coating system produced on the line.

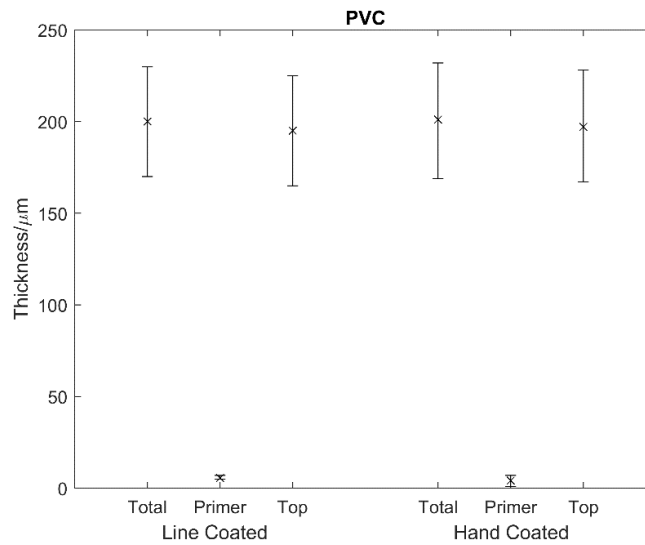


Figure 4.6. Comparison between required layer thicknesses (dry film thickness) for line coated PVC and the measured thickness of the hand coated sample

Microscopy of the two samples did show a lot more variation than the PU samples, as shown in Figure 4.7 however this can be attributed to the lack of embossing which will change the surface appearance greatly. It is worth noting, however, that larger features appeared to exist on the hand coated samples.

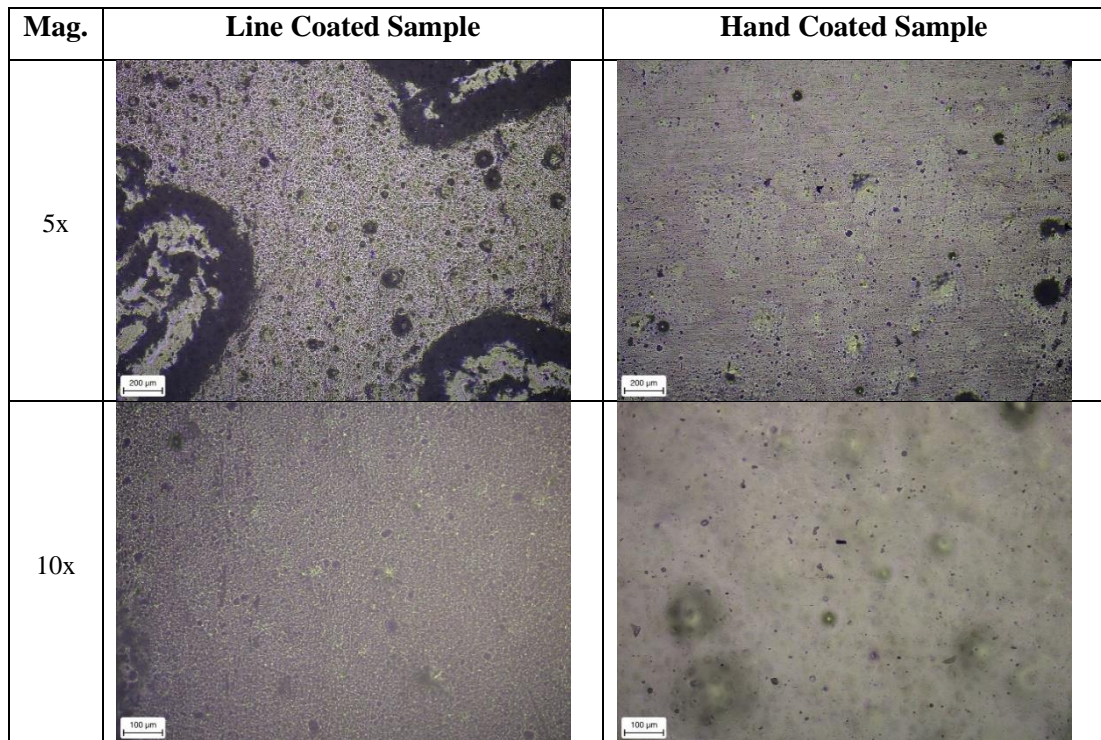


Figure 4.7. Microscopy comparison of line and hand PVC samples

Compared to the two PU samples, the PVC samples showed a far greater surface topography difference under a 3D height scan. The hand sample showed a far less uniform surface although it is highly likely this difference is due to the lack of embossing. As a result, the average surface roughness of the hand sample, $2.8\mu\text{m}$, was higher than that of the line sample, $1.1\mu\text{m}$. However, these values were still reasonably similar.

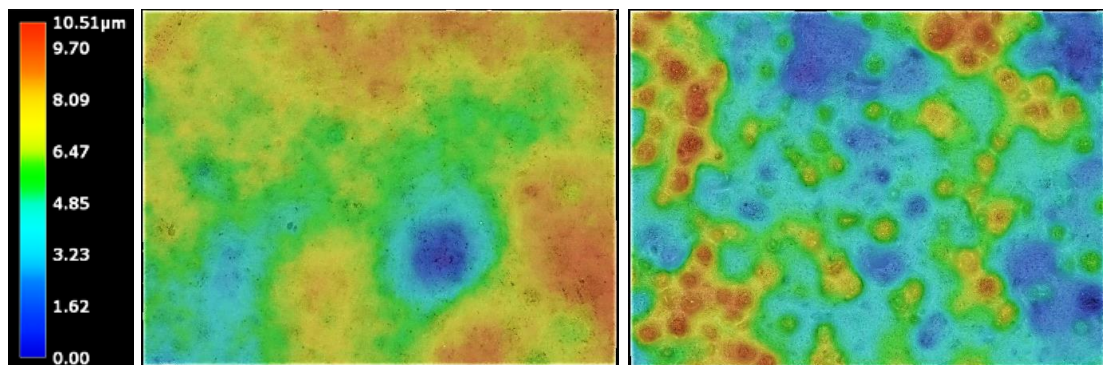


Figure 4.8. Surface topography comparison between line (left) and hand (right) coated PVC samples

The properties of the hand coated PVC samples were also shown to be similar to the line coated samples and also met the required specifications, Table 4.3. Therefore, performance is expected to be similar in terms of lifetime and rates of degradation.

Table 4.3. Comparison between the properties of the hand and line coated PVC samples

Property	Measurement Method	Specification	Line Coated	Hand Coated
Colour (L*)	Elcometer 6085	RAL 7038*	72.8 ± 0.1	72.3 ± 0.1
Colour (a*)	Elcometer 6085	RAL 7038*	-1.0 ± 0.0	-1.1 ± 0.0
Colour (b*)	Elcometer 6085	RAL 7038*	3.8 ± 0.0	3.9 ± 0.0
Colour difference (ΔE^*_{ab})	Elcometer 6085	<1**	0.6	
Scratch Resistance	Sheen Scratch Tester	>5000g	>4200g	>4200g
Gloss @ 60°	Sheen Tri Gloss Meter	20-40	31.7 ± 0.2 %	36.9 ± 0.6 %
Water Contact Angle	FTA 241	N/A	70.9 ± 1.3 °	71.0 ± 2.4 °
Adhesion Cross Hatch	Tape method	100%	100%	100%
Adhesion Cross Hatch	Erichson dome method	100%	100%	100%

4.3.1.3 Outcome of line and hand comparison

It is shown above that it is possible to produce lab samples that match well with the properties of line coated samples. This is important for this project as it means that small scale coated sections can be produced with relevancy to the real product allowing the use of technology such as embedded sensors, which would be difficult to implement into line-based manufacturing, to be explored.

4.3.2 Manufacturing Feasibility – Size Constraints

Another limitation of the embedded sensor concept is the requirements for the electronics to reasonably fit between the layers of the coatings. As previously discussed, the thicknesses can vary from 15µm to 200µm depending on the layer and product. While a thicker layer could be used this would require extrapolation of results to relate measurements to the actual coating performances which could reduce relevance. Hence the sensor system thickness cannot feasibly exceed 200µm, removing a large quantity of possible options. Even some of the smallest surface mount varieties of basic components such as resistors exceed this suggesting that the use of physical componentry is unlikely to be possible. In fact, the thickness requirements are so stringent the only likely technology that could be embedded is that of electrical tracks which could be deposited a number of ways for example via screen printing. Previous work have achieved thicknesses of approximately 4-10µm using screen printing techniques and 100nm using evaporation of gold [5] showing track based sensors could be achieved within the required range. Certainly, track based sensors appear to be at least a viable approach to an embedded sensor. This removes the possibility of using embedded optical fibres and MEMs.

Method	Reasons For Discarding
Optical Fibres	Unsuitable for embedding due to the thin coating layers used
Embedded MEMs	

4.3.3 Manufacturing Feasibility – Survivability

A final manufacturing consideration is that the sensing system has to survive overcoating by one or more coating layers. These layers are cured with a peak metal temperature around 210-240°C. The printed sensor system would have to be able to withstand not only this curing process but also be resistant to solvents in the paint system overcoating it. However, this is not perhaps such a large problem as many different electrical paint systems now exist with PU, water and epoxy based available with good temperature stability [6,7].

4.3.4 Powering and Communication

This is perhaps one of the biggest drawbacks of using an embedded sensor design. While a wired system could be used this would have to directly penetrate the coating and hence the barrier afforded by the coating. Attaching wired connections post embedding would be difficult and require careful removal of one or more coating layers however coating over a pre-established wired connection is not without difficulties in terms of how a consistent thickness of coating can be applied and correctly cured. This is perhaps why a lot of the research into embedded sensors, such as strain gauges, simply do not coat over the electrical tracks required allowing them to easily connect to them. While this is adequate for lab testing protection of the electrical tracks would be required for actual monitoring use.

4.3.4.1 Concept 1 – Semi-Embedded System (Wired)

To attempt to solve this issue several concepts were considered. The first concept that was considered was to simply use the bottom half of a sample as the ‘sensing’ element and to only coat this to mimic the real product. Printed electrical connections could be extended up into the uncoated section, connected to the required wires and then this top section could be overcoated in a thick protective layer. Therefore, the entry and exit connections would not affect the coating of interest but still be protected from the environment. This concept is shown in Figure 4.9.

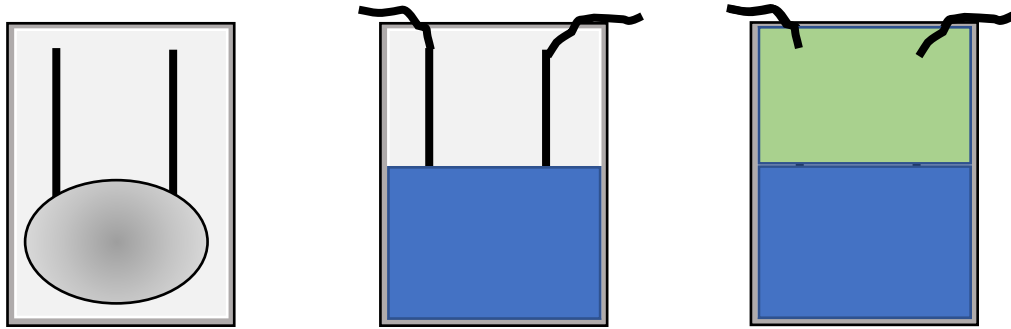


Figure 4.9. Demonstration of a partially embedded wired system

This concept was tested as shown in Figure 4.10 and was found to be a relatively easy method to use at small scale. In this test the ‘sensing’ element was composed of an electrical paint deposited onto galvanised steel pre-coated with a primer via bar coating using a masking tape mask. This was then coated with a PVB layer containing yellow dye for ease of visual identification. The exposed contacts were then sealed off using an epoxy glue dyed orange. While the more complex paint systems would require more complex processing the idea of connecting to the embedded sensor via an extended protected track does seem, from this test, a viable concept.



Figure 4.10. Application of the partially embedded sensor connection concept

4.3.4.2 Concept 2 – Fully-Embedded System (Wired)

The second concept was to connect the wires to the back of the sample using small holes in the sample. These holes would be isolated to prevent shorting on the substrate but provide access to any electrical connections. The top layer of the sample could then be coated as required with no interference from the connection as shown in Figure 4.11.

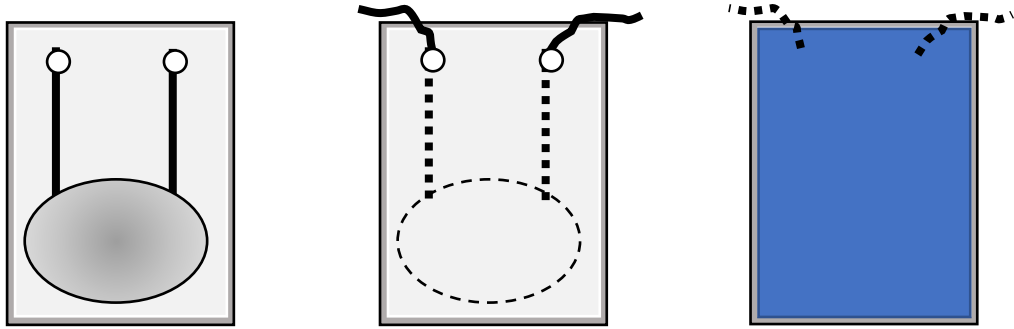


Figure 4.11. Demonstration of a fully embedded wired sensor system

This concept was similarly tested, as shown in Figure 4.12 on pre-primed galvanised steel. Firstly, the uncoated rear of the sample was electrically insulated with masking tape holes in the sample were created using a hole punch and sealed by thin application of a lacquer. The connecting wires were then glued into place flush with the holes using epoxy glue. Electrical paint was then bar coated onto the front of the sample and the paint filled the wells created by the holes, wires, and epoxy glue, creating a sealed connection. This system was then overcoated with the simulative ‘topcoat’ of dyed PVB. While more complex than the previous method the benefit of these additional steps was that the finished product would be fully coated with the system to be tested with no exposed wires.

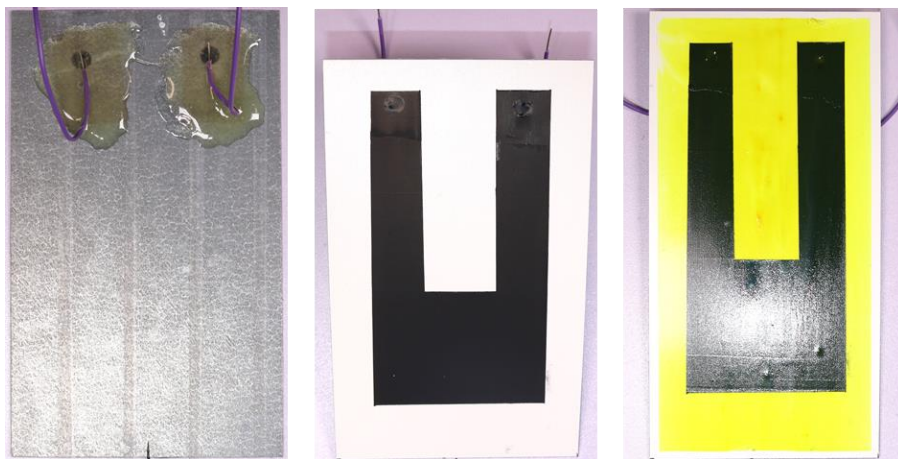


Figure 4.12. Application of the fully embedded sensor connection concept

4.3.4.3 Concept 3 – PCB Coated System (Wired)

A third concept was to not use a steel substrate but instead overcoat a PCB sensor with the coating system. This idea has the benefit of not requiring complicated printing of the sensor as PCB traces can be used to similar effect, however, would only be able to detect changes to the coating layers. As the metal substrate would no

longer be present corrosion-based failure methods would not be present and there are questions as to whether the coating system would adhere and perform similarly when applied to the PCB compared to a steel substrate. However, this concept has been used before to monitor coating performance most notably in [8] where the effectiveness of anticorrosion pigments in paints were assessed by overcoating PCB based resistance and EIS style sensors. Connection to the substrate could then be made as in concept 1 by wiring into the PCB and then protecting this connection with a thick coating layer. A demonstration of this concept is shown in Figure 4.13.

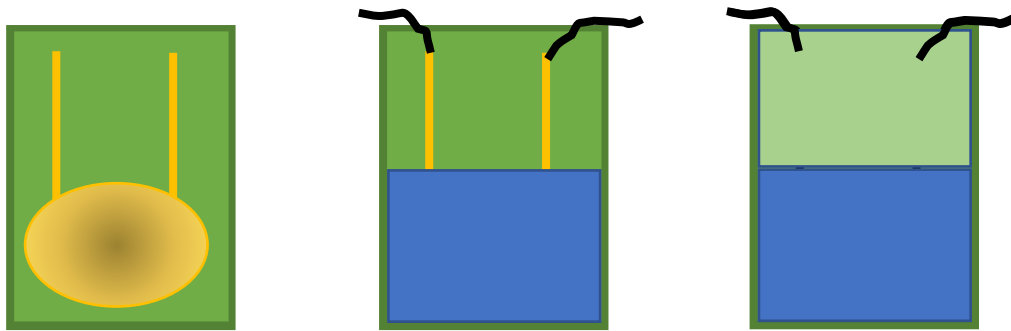


Figure 4.13. Demonstration of a PCB based embedded sensor system

For this concept to be possible it is important that the PCB system can withstand the temperature required to cure the overcoating paint systems. Most PCBs are fabricated from an FR-4 glass reinforced epoxy laminate which generally are stated to have a maximum operating temperature of 130-170°C due to their glass transition temperature of approximately 150-170°C. Aluminium based PCBs are also available which provide the ability to withstand higher temperatures. However, testing showed that a normal PCB was able to withstand 30 seconds in a paint curing oven with a peak PCB temperature of 241°C. The only effect on the PCB was softening of the substrate although this returned to the original state upon cooling. An aluminium PCB also survived the same temperatures but showed no change in mechanical properties. Although it is stated that electrical properties can degrade due to high temperatures both PCBs showed no real change in the measured electrical properties of the present tracks. This suggests that this is a viable concept for a semi-representative embedded coating sensor.

4.3.4.4 Concept 4 – Fully-Embedded System (Wireless)

The final solution was to consider using a wireless-based system so that no connection through the coating is required. The concept of wireless powering of

devices has existed since conception in the 19th century by both Tesla and Hertz [9] although has recently become an area of high research interest due to the move to a greater quantity of consumer electronics and electric vehicles. Wireless charging of some mobile phones is now commercially offered as is the ability to wirelessly charge some electric cars. It is suggested by Bomber [9] that there are two key circumstances requiring wireless powering; to allow power transfer over or through ‘an impossible or impractical barrier for wires’, and long range powering where generators are insufficient i.e. disaster relief. The former is the clearly the case in this specific application. Despite this complication, the potential benefit of an embedded sensor warrants further examination of this concept.

4.3.5 Wireless powering and communication

The ideal solution for a sensing device would be a true passive system independent on any external input. While this is potentially possible using thermal, mechanical, or solar energy harvesting methods paired with built in communication the development of IOT devices solely powered through energy harvesting is complex. This is compounded by the embedded nature of the sensor removing exposure to certain energy sourced. Hence, it was concluded a form of wireless power transfer would be required to activate the device. There are several types of power and communication transfer and these are shown in Figure 4.14 below [10] and include; (A) Radiofrequency, (B) Optical, (C) Ultrasonic, (D) Capacitive, (E) Inductive (tightly coupled) and (F) Inductive (loosely coupled).

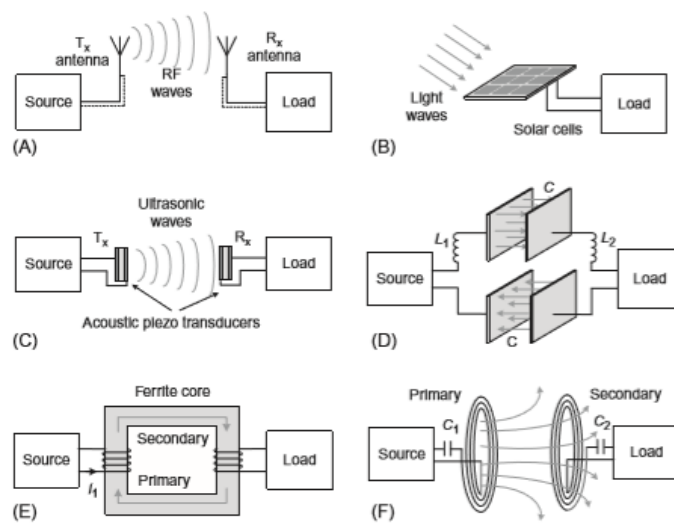


Figure 4.14. Types of wireless transfer [2]

It is easy to discount several of these methods (B, C, E) due to the thickness constraints of a potential embedded sensor; any technology used would have to fit within a maximum 45 - 200 μ m coating. A capacitive based solution would be difficult to imagine due to interference from the metal substrate. Therefore, the only possible way an embedded tag could work for this application would be by RF or loosely coupled inductive; with a loosely coupled inductive effectively being a low frequency RF system. This technology is commonly used commercially in UHF RFID tags for tracking inventory and NFC tags which are used for short range digital consumer communication. Due to the increased range, a decreased tag thickness and more wide scale use of these systems, compared to LF RFID, they were initially targeted as the potential solution. However, these techniques are further complicated by the use of the RFID tag in such close proximity to a metal substrate.

4.3.5.1 Challenges surrounding RFID use near metals

It is well known that a traditional RFID or NFC tag perform poorly when mounted in close proximity or directly upon metal substrates [11]. Park 2011 suggests this is due to ‘reactance variation on the antenna impedance’ due to the reflection of RF off the metal.

These effects have been reported [12][13][14] to be due to the deformation of a magnetic field near a non-perfect conductor, as predicted by Maxwell’s electricity and magnetism equations, and formation of eddy currents in the metal which interact in a number of ways with the tag. The magnitude of these eddy currents increases with a decrease in the skin depth (δ) (the distance required for an incidence wave to be attenuated to 37% [15]) which is given (in mm) by [16][17]:

$$\delta = \frac{65.23 \times 10^3}{(\sigma_r \mu_r f)^{\frac{1}{2}}} \quad (4.2)$$

Another effect of this is that the antenna becomes detuned to the frequency of the reader and hence can no longer communicate. Detuning of antennas can be understood by considering the antenna and reader as a circuit model, each with a resonant frequency (f) given by the Thomson formula[13]:

$$f = \frac{1}{2\pi\sqrt{L \times C}} \quad (4.3)$$

Where L is the inductance and C is the capacitance of the reader or tag, respectively. In order for the most efficient power and communication transfer between reader and tag the two should be tuned, that is operating at the same resonant frequency.

However, in close proximity to metal, magnetic fields interact with the antenna leading to, usually, a reduction in the inductance as described in [13]. Hence the frequency of the antenna tag is shifted and no longer matches that of the reader; the two are detuned and efficient transfer does not occur. Furthermore the tag is shielded by the metal which absorbs the RF radiation which greatly reduces the power harvested by the tag [13].

The effect of different substrates was studied using simulations which were carried out using CST Studio Suite 2019. Firstly, a commercial UHF tag was modelled in CST. In order to represent the Monza R6 chip circuit two lumped elements were used to match the equivalent circuit of the chip, shown in Figure 4.15. The equivalent circuit parameters given by the manufacturer [18] are listed in Table 4.4 and were represented with a 1.44pF lumped element capacitor and a 1560 Ω lumped element resistor. This approach is commonly used in antenna design.

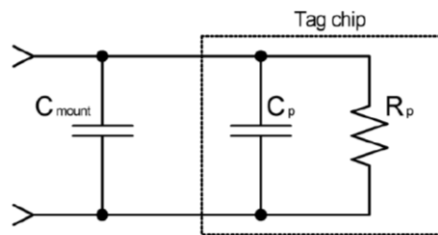


Figure 4.15. Equivalent circuit of Monza R6 chip

Table 4.4. Equivalent circuit values

Parameter	Symbol	Value [18]
Represents energy conversion/absorption of RF circuit	R_p	1.56 k Ω
Intrinsic chip capacitance	C_p	1.23 pF
Typical capacitance due to adhesive mounting	C_{mount}	0.21pF
Auto Tune capacitance	C_p (add)	-100, -40, 40, 100fF

The autotune capacitance (C_p) is an internal feature of the chip that allows automatic adjustment of the intrinsic chip capacitance to ensure the best matching of the chip and antenna at the resonant frequency. It has 5 possible values as shown in Table 4.4 and, although small, can vary simulation results greatly so has been considered in the following work.

The tag designed in CST is shown in Figure 4.16 which is matched to the dimensions of the real-life tag. For the simulation, a plane wave excitation source was used with right hand circular polarisation (RCP) and propagation in the -z direction at a reference frequency of 868MHz. The plane wave was set 300mm away from the tag surface in the z direction. All the boundaries were set as open (add space), and the frequency range observed was 500-1200MHz and a discrete s parameter (scattering parameter representing the relationship between incident, reflected and transmitted waves) port in place of the chip was used for the determination of results. This set up is shown in Figure 4.17.

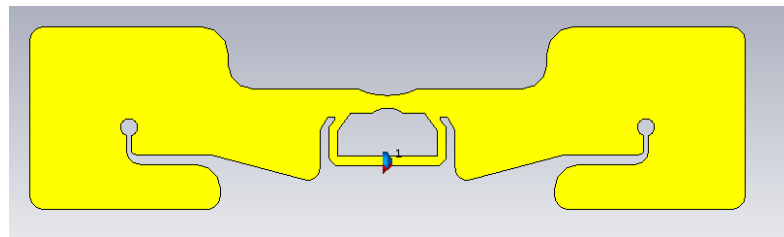


Figure 4.16. Dogbone RFID tag as produced in CST Studio

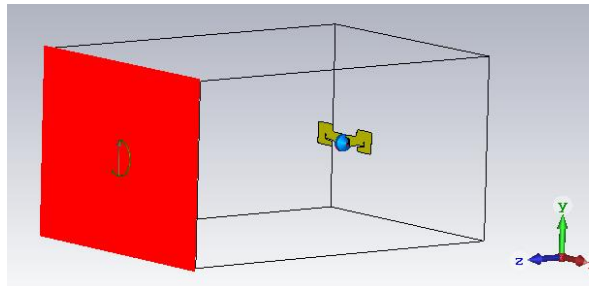


Figure 4.17. Simulation set up in CST Studio

In simulations where a backing material was used this was a 10x10 cm block with a thickness relative to the material being tested for example a paper backing material was given a thickness of 0.1 mm. Simulation of the tag in free space are shown in Figure 4.18 and the calculated 2dB and 5dB bands are shown in Table 4.5. The effect of modifying the autotuned capacitance value is shown to be a decreased resonant frequency, as predicted by the Thomson formula, and a decreased S_{11} magnitude. It is important to note that the simulated antenna system does not include the inlay mounting system which is usually composed of a thin adhesive layer to allow antenna attachment. Antennas are usually designed to resonate at a slightly higher frequency than their band would suggest so that once the effects of the inlay are included the resonant frequency is decreased to the correct value [19][20]. As the

simulation does not include the inlay layer due to difficulties in determining the material properties it is expected results may show resonance at higher frequencies as is the case in these results.

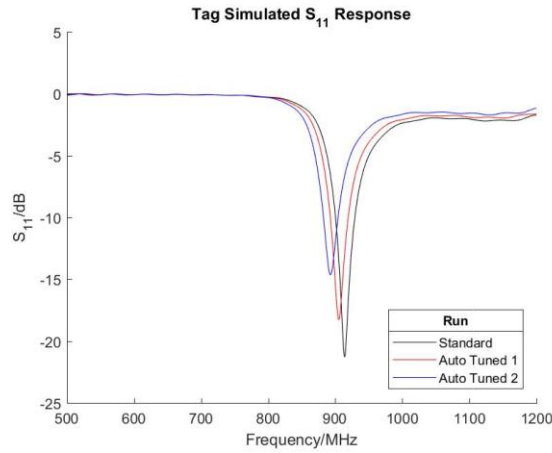


Figure 4.18. Simulated S11 response of the tag in free space

Table 4.5. Resonant frequency bands for the simulated tag in free space

Run	Autotune/fF	Capacitance	-2dB Band/MHz	-5dB Band/MHz
Standard	0	1.44pF	868-1036	887-950
Auto Tuned 1	+40	1.48pF	862-1009	880-939
Auto Tuned 2	+100	1.54pF	853-972	870-923

The effect of different substrate mounting is shown in Figure 4.19 and this demonstrates the issue of on metal mounting. Whilst the paper and wood substrates both provide an adequate response the metal provides no response due to the aforementioned problems. The bandwidth measured for each substrate is shown in Table 4.6.

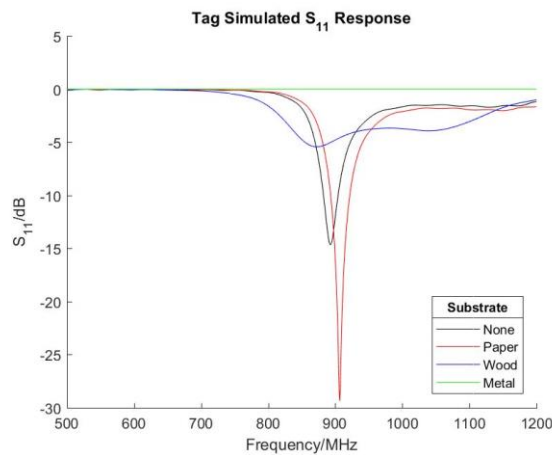


Figure 4.19. Simulated S11 response of the tag on different substrates

Table 4.6. Resonant frequency bands for the simulated tag on different substrates

Substrate	Thickness/mm	Central Frequency/MHz	-2dB Band/MHz	-5dB Band/MHz
None	0	893	853-972	870-923
Paper	0.125	907	863-1011	881-940
Wood	10	872	808-1139	854-893
Metal	10	N/A	N/A	N/A

If the results of both wood and paper are compared to that of the coated steel substrates, as shown in Figure 4.20, it can be seen that the coated steel substrate does not provide an adequate frequency response even when placed on top of the surface of the sample. This commercial tag on its own will not provide any response as outlined by the frequency ranges shown in Table 4.7.

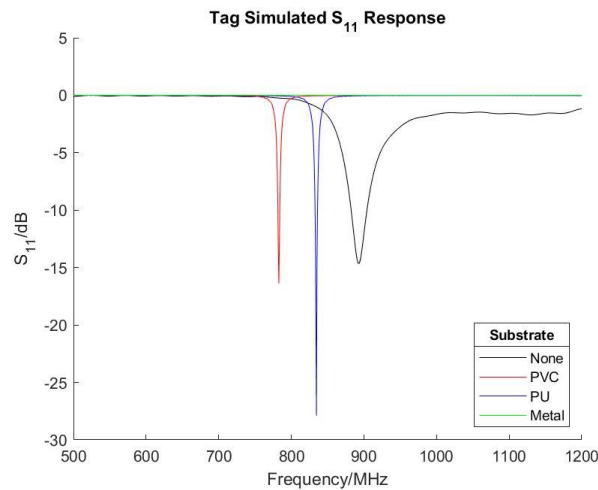


Figure 4.20. Simulated S11 response of the tag on coated steel substrates

Table 4.7. Resonant frequency bands for the simulated tag on coated steel substrates

Substrate	Thickness/mm	Central Frequency/MHz	-2dB Band/MHz	-5dB Band/MHz
None	0	893	853-972	870-923
Metal	10*	N/A	N/A	N/A
PVC System	*+0.211	783	777-788	780-786
PU System	*+0.040	835	828-841	831-838

4.3.5.2 Current solutions and their applicability

The easiest and most common solution to the problem of metal mounting is the insertion of a spacer between metal and the RFID tag which acts as a ‘electromagnetic band gap ground plate’[11]. It is important that this spacer is made of a material with a high magnetic permittivity or impedance [21]. Alternatively, the effect of the metal can be reduced by integrating a conductive ground plate to the

antenna [21]. Unfortunately, these solutions are easily implementable into the required parameters of this application as a spacer will likely increase the thickness of the device beyond acceptable limits. While the substrate could theoretically act as a ground plane, making a connection to it would be difficult and almost impossible to scale up as a manufacturing process.

Several so called 'on metal' RFID and NFC tags are now commercially available which are composed of an RFID tag with said spacer, usually in the form of an adhesive backing layer. [11] The spacer level in these products is simply a layer of electromagnetic interference sheet which is often composed of a suspension of magnetic particles in a polymer. It is important that these particles are coated by an insulating di-electric layer to reduce the effect of eddy-currents.[22] However even the thinnest of these are still approaching 600 μ m which is still three times the coating thickness.

There are areas of research that are investigating modifying the antenna physics and design to overcome the issue of mounting on metal which could reduce the thickness or quantity of the required spacer. Examples include [21], [23] and [24] but these are experimental and currently too thick for embedding in a coating system.

While it is certainly not impossible that a metal resistant RFID tag could be designed to fit into the coating within the thickness constraints to just reach the point where communication and powering of such a tag is achieved would be a significant endeavour. Therefore, a different approach was required, and Low Frequency RFID was considered.

4.3.5.3 Low Frequency RFID

Low Frequency (LF) RFID systems typically operate between 30 and 500 MHz and offer the lowest read range of the RFID family. 125kHz is a common frequency used for tracking and security cards. Although these tags also have comparatively low rates of data transfer and unregulated bands, they do offer better resistance to on-metal mounting. This is due to the tag coupling with the reader which occurs inductively in the near field compared to backscattering in the far field as is the case with UHF which removes some effects. Furthermore, by decreasing the frequency used, the skin depth, which is given previously, is increased. It has been reported that a larger skin depth reduces the magnitude and hence effect of generated eddy

currents and therefore better on-metal resilience is seen [12]. Finally, due to the lower frequency requirements, readers of LF RFID tags are significantly less complex and expensive with small handheld devices far more common and custom-made readers far easier to design and test on a small scale.

The immediate benefit of the LF RFID is that an unaltered commercially available tag placed on a metal substrate can easily be read by a commercially available reader with little issue. This suggests communication and powering of an embedded device would, albeit at a small range of 1-3cm, be possible. It must be considered, though, if the device would be able to be implanted into the coating layer without affecting the performance of the coating.

However, LF RFID tags require a far longer antenna length when compared to higher frequency tags. This is to compensate for the far larger wavelength of lower frequency signals. Hence, in order to make LF tag antenna of sufficient length while still being compact in size they are often composed of many circular loops of thin wire. This method of manufacturing means that LF tags are often thicker than UHF tags, which are die cut from extremely thin metal sheets. In fact, the minimum thickness of commercially available LF appears to be in the range of 400-600 μ m however this does include a polyester surrounding layer. Considering that this would then have to be somehow integrated with a sensor it is highly likely that the full system would be too thick to allow embedding fully into even the thicker 200 μ m coating system without causing significant issues.

4.3.5.4 Wireless communication conclusions

The idea of a wireless communication system allowing full embedding of a sensor into a coating system would be extremely useful. However, due to the restrictive thickness limitations and close proximity of to a metal substrate, developing a wireless system would be non-trivial. It is therefore concluded that the work following will only focus on ‘wired’ embedded systems and non-embedded systems. Therefore, the idea of an embedded RF sensor system was discarded.

Method	Reasons For Discarding
Embedded RF	Unable to facilitate communication without significant fundamental research

4.3.6 Embedded sensor conclusions

Using an embedded sensor has several benefits but is not without its drawbacks. From a feasibility standpoint, it is clear that such a device would be possible but would have to be produced as a small lab-based sample and most likely be composed of a printed electronics sensor. This sensor would have to be able to survive high temperature environments to allow overcoating, and would have to be connected to via a wired solution, such as those presented earlier. Despite these restrictions, they still appear an attractive way to monitoring coating performance by offering several potential applications and should not be immediately discarded. However, it does appear that their use and design would be more complex than a system where the sensor is not embedded.

4.4 Sensor concepts investigated

From the initial assessment work the techniques given in Figure 4.21 remained as potential avenues.

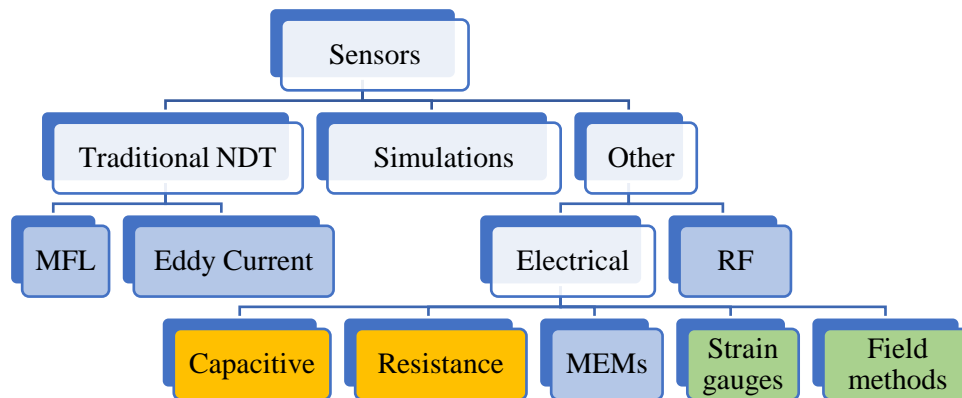


Figure 4.21. Techniques remaining after initial testing

It had been concluded that discrete stationary sensors would be focused on, and any embedded sensor technology investigated would have to be of a simple printed electronic track design with no physical componentry. It was therefore assumed that a simple resistive or capacitive sensor would likely be the best embedded option. While embedded strain gauges have previously been examined, the design and measurement principles are far more complex and some of the field methods can be somewhat implemented by resistance-based sensing methods.

The non-embedded sensing ideas generated broadly fell into two categories; those which measured for corrosion and those which measured for coating deterioration.

For each of these categories two techniques were chosen for investigation with one being better established and researched, and one more novel and requiring development. The techniques investigated are displayed in Figure 4.22.

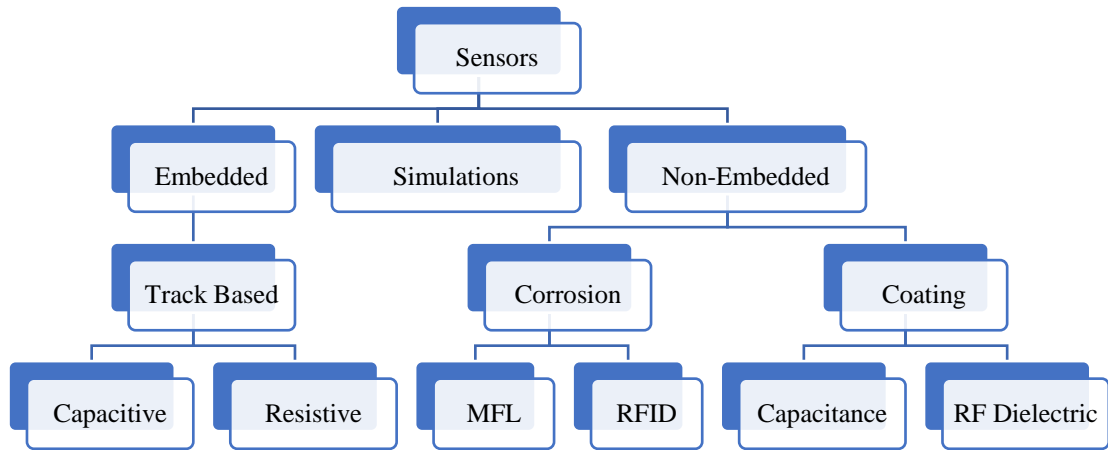


Figure 4.22. The techniques investigated in this work

For the detection of corrosion, magnetic flux leakage was chosen due to its simplicity, ease of modification. An RFID blocking method inspired by recent works [25,26] was the second corrosion monitoring method investigated and was chosen due to its wireless, semi-remote monitoring nature.

Capacitive sensing was chosen for a coating monitoring sensor due to its good balance of simplicity, ease of application and usefulness of information. A novel dielectric sensing method inspired by chipless RFID research in [27] was developed as the second coating sensor due to its wireless, semi-remote monitoring nature.

4.5 References

1. Bubenik T. Electromagnetic methods for detecting corrosion in underground pipelines: Magnetic flux leakage (MFL) [Internet]. *Underground Pipeline Corrosion: Detection, Analysis and Prevention*. Woodhead Publishing Limited; 2014. 215-226 p. Available from: <http://dx.doi.org/10.1533/9780857099266.2.215>
2. Wiggerhauser H, Niederleithinger E. Innovative ultrasonic techniques for inspection and monitoring of large concrete structures. *EPJ Web Conf.* 2013;56(January 2016).
3. Ferreira PM, Machado MA, Carvalho MS, Vidal C. Embedded Sensors for Structural Health Monitoring: Methodologies and Applications Review. *Sensors.* 2022;22(21):8320.
4. Frias-Cacho X, Castro M, Nguyen DD, Grolleau AM, Feller JF. A Review of In-Service Coating Health Monitoring Technologies: Towards “Smart” Neural-Like Networks for Condition-Based Preventive Maintenance. *Coatings.* 2022;12(5).
5. Enser H, Kulha P, Sell JK, Schatzl-Linder M, Strauß B, Hilber W, et al. Printed strain

- gauges embedded in organic coatings - Analysis of gauge factor and temperature dependence. *Sensors Actuators A Phys* [Internet]. 2018 Jun;276:137–43. Available from: <https://doi.org/10.1016/j.sna.2018.03.042>
6. Graphene_Lab. High -temperature silver-graphene electrically conductive epoxy (Data Sheet). New York; 2022. p. 5–6.
 7. MGChemicals. 842-UR Technical data sheet. Vol. 1.01. Ontario, Canada; 2019. p. 1–6.
 8. Zajec B, Bajt Leban M, Lenart S, Gavin K, Legat A. Electrochemical impedance and electrical resistance sensors for the evaluation of anticorrosive coating degradation. *Corros Rev*. 2017;35(2):65–74.
 9. Bomber A. Wireless Power Transmission : An Obscure History , Possibly a Bright Future. *Phys 464 Appl Opt*. 2006;
 10. Etemadrezai M. Wireless Power Transfer [Internet]. 4th ed. *Power Electronics Handbook*. Elsevier Inc.; 2018. 711-722 p. Available from: <http://dx.doi.org/10.1016/B978-0-12-811407-0.00024-6>
 11. Park CR, Eom KH. RFID Label Tag Design for Metallic Surface Environments. *Sensors* [Internet]. 2011 Jan 17;11(1):938–48. Available from: <http://www.mdpi.com/1424-8220/11/1/938>
 12. Alamin M. Passive Low Frequency RFID for Detection and Monitoring of Corrosion under Paint and Insulation. Newcastle University; 2013.
 13. Ciudad D, Cobos P, Sanchez P, Aroc C. RFID in Metal Environments: An Overview on Low (LF) and Ultra-Low (ULF) Frequency Systems. In: *Radio Frequency Identification Fundamentals and Applications Design Methods and Solutions* [Internet]. InTech; 2010. p. 181–96. Available from: <http://www.intechopen.com/books/radio-frequency-identification-fundamentals-and-applications-design-methods-and-solutions/untitrfid-in-metal-environments-an-overview-on-low-lf-and-ultra-low-ulf-frequency-systems>
 14. Balanis CA. *Antenna theory : analysis and design*. Third edit. 2005.
 15. Dhawan SK, Ohlan A, Singh K. Designing of Nano Composites of Conducting Polymers for EMI Shielding. In: *Advances in Nanocomposites - Synthesis, Characterization and Industrial Applications* [Internet]. InTech; 2011. Available from: <http://www.intechopen.com/books/advances-in-nanocomposites-synthesis-characterization-and-industrial-applications/designing-of-nano-composites-of-conducting-polymers-for-emi-shielding>
 16. He YL, McLaughlin S, Lo JSH, Shi C, Lenos J, Vincelli A. Radio frequency identification (RFID) based corrosion monitoring sensors Part 1 – Component selection and testing. *Corros Eng Sci Technol*. 2015;50(1):63–71.
 17. D.D.L. Chung. *Materials for Electromagnetic Interference Shielding*. *J Mater Eng Perform*. 2000;9(3):350–4.
 18. Impinj. Monza R6 datasheet. 2017; Available from: <https://support.impinj.com/hc/en-us/articles/202765328-Monza-R6-Product-Brief-Datasheet>
 19. Oyeka DO, Batchelor JC, Ziai AM. Effect of skin dielectric properties on the read range of epidermal ultra-high frequency radio-frequency identification tags. *Healthc Technol Lett*. 2017;4(2):78–81.
 20. Dobkin D. *The RF in RFID* [Internet]. Newens, editor. Elsevier; 2008. Available

from: <https://linkinghub.elsevier.com/retrieve/pii/B9780750682091X50013>

21. Chen S-L, Kuo S-K, Lin C-T. A METALLIC RFID TAG DESIGN FOR STEEL-BAR AND WIRE-ROD MANAGEMENT APPLICATION IN THE STEEL INDUSTRY. *Prog Electromagn Res* [Internet]. 2009;91:195–212. Available from: <http://www.jpier.org/PIER/pier.php?paper=09021304>
22. Kuo S-K, Hsu J-Y, Hung Y-H. A performance evaluation method for EMI sheet of metal mountable HF RFID tag. *Measurement* [Internet]. 2011 Jun;44(5):946–53. Available from: <http://dx.doi.org/10.1016/j.measurement.2011.02.018>
23. Chen SL, Lin KH. A slim RFID tag antenna design for metallic object applications. *IEEE Antennas Wirel Propag Lett*. 2008;7:729–32.
24. Son H-W, Choi G-Y, Pyo C-S. Design of wideband RFID tag antenna for metallic surfaces. *Electron Lett* [Internet]. 2006;42(5):263. Available from: https://digital-library.theiet.org/content/journals/10.1049/el_20064323
25. He YL, McLaughlin S, Lo JSH, Shi C, Lenos J, Vincelli A. Radio frequency identification (RFID) based corrosion monitoring sensors Part 2 – Application and testing of coating materials. *Corros Eng Sci Technol*. 2014;49(8):695–704.
26. He Y. Wireless Corrosion Monitoring Sensors Based on Electromagnetic Interference Shielding of RFID Transponders. 2020;76(4):411–23.
27. Marindra AMJ, Tian GY. Chipless RFID Sensor Tag for Metal Crack Detection and Characterization. *IEEE Trans Microw Theory Tech* [Internet]. 2018 May;66(5):2452–62. Available from: <https://ieeexplore.ieee.org/document/8307772/>

Chapter 5: Embedded Sensors

5.1 Introduction

The investigation carried out in the previous chapter displayed that certain, simple, embedded sensor systems may offer more accurate ways of monitoring coating systems. It was concluded that printed electronic tracks would be the most appropriate form of these sensors and that connection to the tracks could be achieved in potentially three different ways. Furthermore, it was decided that line production of embedded sensors would not be possible; they would be limited to lab produced, small scale, representative samples. Two possible, wired, embedded sensor concepts were found from the literature, resistive and capacitive, and developed to be used to determine the condition of the paint and steel on the panel over time. These were examined in turn with the aim of determining whether they met following hierarchical requirements:

1. The sensor must not impact the primary function painted surface and be compatible with current paint material sets.
2. The sensor must not act as point failure and thus accelerate failure.
3. The sensor must be capable of withstanding the harsh environment on the building envelope and provide reliable data over the primary panel lifetime.
4. The sensor must be sufficiently sensitive to provide information data of condition which precedes visual changes in the panel.

Each technology was pursued using laboratory manufactured prototypes through a test procedure in the order of the criteria set out above. When a failure occurred, the testing process was stopped, and the merits of the sensor was evaluated. In each case, wiring connections to the sensors were made manually and protected by a suitable encapsulant. This was considered appropriate as industrial connection technologies for PV, lighting and security can be obtained with a 25-year lifetime.

5.2 Embedded sensor concepts

5.2.1 Connection based cut edge corrosion sensor

Cut edge corrosion is a generic term for the degradation of coated steel products at locations where the initially sheet material has been cut. Most coated steel products are produced on a roll-to-roll manufacturing line which produces rolls with many continuous hundreds of meters. When this coil is cut down to make the final products it exposes a small cross section of the substrate. This is unavoidable in the manufacturing process, and it is not common to recoat these sections. As a result, steel is exposed to the environment, and this makes these sites common initiation points for under film corrosion effects [1]. In fact, cut edge corrosion is one of the most common routes of degradation for organically coated cladding [2] and hence the ability to detect and track the severity of it would be significant.

The novel concept developed in the present work was inspired by techniques used to measure crack propagation by successive mechanical failure of electrical track/tracks [3–5] and the use of corrosion fuses [6]. For this application, electrical tracks embedded in the paint layer would allow the monitoring of cut edge corrosion through their progressive failure. The principle of this idea, Figure 5.1, is to print a number of electrical tracks at different distances from a cut edge. As corrosion progresses into the sample, from the cut edge, it will reach a connection and cause severing of that connection either via mechanical action or exposure of the electrical track to environmental degradation. By monitoring the connections in a number of electrical tracks spaced at set distances from a cut edge, it was thought that the distance and also rate of cut edge corrosion in the sample could be inferred.

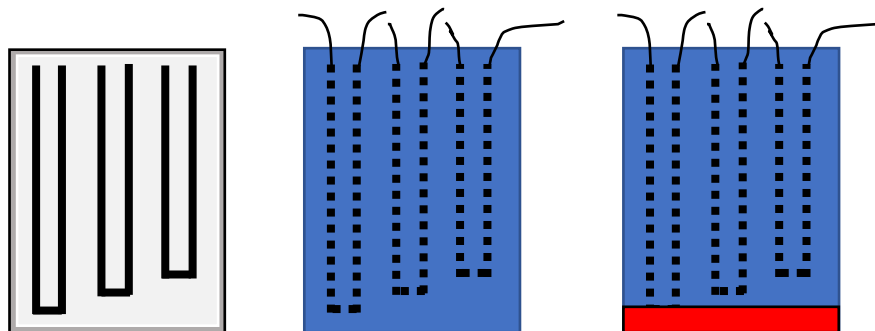


Figure 5.1. Concept 1 - A cut edge corrosion sensor based on detecting electrical connection breaks. Embedded tracks are broken as corrosion spreads from the cut edge (bottom) of the sample upwards.

As corrosion is the metric to be monitored this concept can only be achieved using a metal substrate and hence of the three methods mentioned in the previous chapter only the semi and fully embedded wired sensor would be possible. Using a PCB would remove the metallic substrate and hence no corrosion would occur.

5.2.2 Capacitive coating sensor for coating degradation

Coating degradation, especially due to UV exposure, can also be another method by which coated steel cladding is deemed to have failed. This, however, is often not a structural failure, but an aesthetic one, with colour change and or blistering occurring. The second embedded sensor concept developed here aimed to detect changes in the coating condition via capacitance measurement. As outlined in the literature review previously, if a coating is placed between two electrodes the distance between electrodes, area of overlap and dielectric constant ϵ_r of the paint will determine the capacitance. If the electrodes are fixed, then any measured changes in capacitance can be inferred to be as a result of a change in the dielectric properties of the coating. These changes may include water uptake, leading to an increased ϵ_r , or UV degradation, likely to cause a decrease in ϵ_r due to material removal. It was thought that by embedding electrodes in the paint system a capacitive measurement may be possible. To achieve this, two electrical tracks are printed onto the primer layer of small samples and then overcoated with the top and, if required, clear coats. This would then allow, as shown in

Figure 5.2, coating capacitance to be measured between the two embedded electrical tracks.

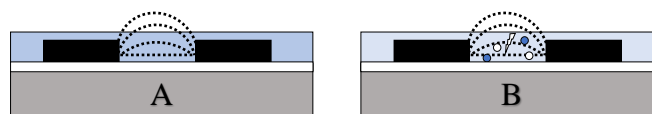


Figure 5.2. Concept 2 – a fully embedded capacitive sensor (A) that could detect changes in coating condition (B)

In this case a specific type of capacitor, a coplanar capacitor is created. The capacitance is still governed by the electrode separation and dielectric constant however the area of overlap is no longer solely used due to the requirement to consider fringing effects as well as direct fields, Figure 5.3.

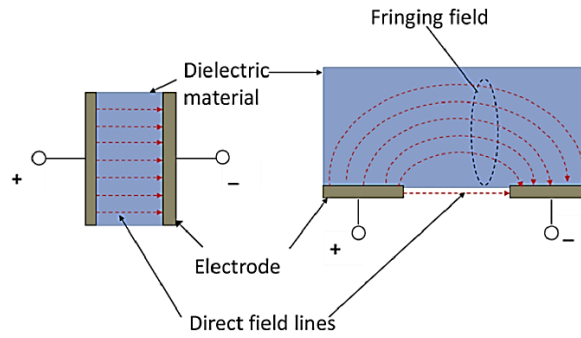


Figure 5.3. Coplanar capacitor field lines (right) compared to parallel plate [7]

Hence the equation for coplanar capacitance is less trivial and can be given by [8]:

$$C = \frac{\epsilon_r \cdot l \cdot \ln \left(-\frac{2}{\sqrt[4]{1 - \frac{s^2}{(s+2w)^2}} - 1} \left(\sqrt[4]{1 - \frac{s^2}{(s+2w)^2}} + 1 \right) \right)}{377 \cdot \pi \cdot v_0} \quad (5.1)$$

or:

$$C = \frac{\epsilon_r \cdot l}{120 \cdot v_0 \cdot \ln \left(-\frac{2}{\sqrt{1 - \frac{s}{(s+2w)}} - 1} \left(\sqrt{1 - \frac{s}{(s+2w)}} + 1 \right) \right)} \quad (5.2)$$

for

$$0 < \frac{s}{s+2w} \leq \frac{1}{\sqrt{2}} \quad \text{and} \quad \frac{1}{\sqrt{2}} < \frac{s}{s+2w} \leq 1 \quad (5.3)$$

respectively, in which s is the electrode separation, w the electrode width, l the electrode length, ϵ_r the dielectric constant and v_0 the speed of light.

Despite a more complicated derivation, changes due to UV degradation, moisture uptake, or other factors should be detectable via the respective change in the measured capacitance of a coating embedded capacitor. To this end, coplanar capacitors, such as these, have been previously proposed and shown to measure changes in a surrounding dielectric layer [9–11]. However, it is not thought that this type of embedded application for steel coating condition sensing has been considered despite the promise offered.

5.3 Materials and methods

The steel samples used were galvanised and had received a pre-treatment and were provided by Tata Steel UK.

Two different electrical paint systems were used in this study. The first was a conductive carbon filled (5-20%) water-based paint from Bare Conductive. This is a convenient, low cost, non-toxic paint which dries at room temperature in 15 minutes [12]. As it is water based it was thought to be less likely to be dissolved in subsequent paint layer solvents and the low curing temperature was unlikely to affect previously deposited layers. However, the main choice in using this was its water solubility as it was thought this could be used to facilitate the breaking of the connection in the cut edge corrosion sensor. The second electrical paint was a polyurethane-based paint containing 30% wt. silver produced by MG Chemicals. Although this had a higher required cure temperature of 140°, this is lower than the curing temperatures of subsequent layers so thought unlikely to affect the previous layers [13]. This was chosen due to its stated excellent adhesion, environmental stability, and high temperature resistance [13]. Printing of the electrical paints was achieved by taping off the design area and applying the electrical paint with the drawdown of a thin glass rod.

Several different non-conductive paint systems were investigated as the surrounding layers. These were provided by Becker's (Polyurethane (PU) primer, topcoat and clearcoat) and Akzo Nobel (PVC primer and topcoat). The 15% w/w solution of ethanol and polyvinyl butyral-co-vinyl alcohol-co-vinyl acetate (PVB), obtained from Sigma-Aldrich Chemical Co, was produced in the lab. The epoxy used was a Loctite EA Double Bubble manufactured by Henkel Adhesives. The casting resin used was KLEER-SET which is a 2-part polyester cold mounting resin manufactured by MetPrep Ltd.

Capacitive and resistive measurements were taken with a variety of equipment. For discrete measurements, a Tenma Inductance Capacitance Meter was used and for continuous measurements an Arduino was used to output to Excel.

Initial testing of the sensing concepts used an acetone and steam exposure test. In the acetone test the sample was left submerged in acetone and removed and measured at 5, 15, 25, 40 and 180 minutes of immersion. During the steam test the sample was

placed over a beaker of de-ionised water kept at 95°C by a hotplate. This was then removed, dried, and measured at 10 and 20 minutes of exposure. After 20 minutes of exposure the sample was placed on a hot plate at 60°C for 10 minutes to drive off any potential moisture and given a ‘dried’ sample measurement.

Degradation testing of the industrial coatings was carried out using a number of recognised techniques including testing similar to ASTM B117 Salt Spray [14] and BS EN ISO 11507:2007 UV condensation [15]. Furthermore, immersion in 5% NaCl solution pH7 was used as was double rubs using MEK. For the salt spray and immersion tests the samples were tested each week for 5 weeks, for the UV test samples were tested every 250 hours for 1000 hours and for the MEK rub test samples were tested every 50 double rubs for 200 rubs.

5.4 Paint compatibility

While it has been shown in the previous chapter that hand produced samples are representative of line produced product the effect of embedding the electrical paint systems needs also to be considered. If the embedding of the conductive paint leads to significantly different properties, then it is questionable whether an embedded sensor would be representative of the actual system and hence the usefulness may be limited. To assess the effect of the additional layer on the overall system properties, an approximately 7x4cm square of each conductive paint was deposited onto the primer layer of both paint systems. This was then overcoated with the required top and, in the case of the PU system, clear coat layers. The resulting samples are shown in Figure 5.4.

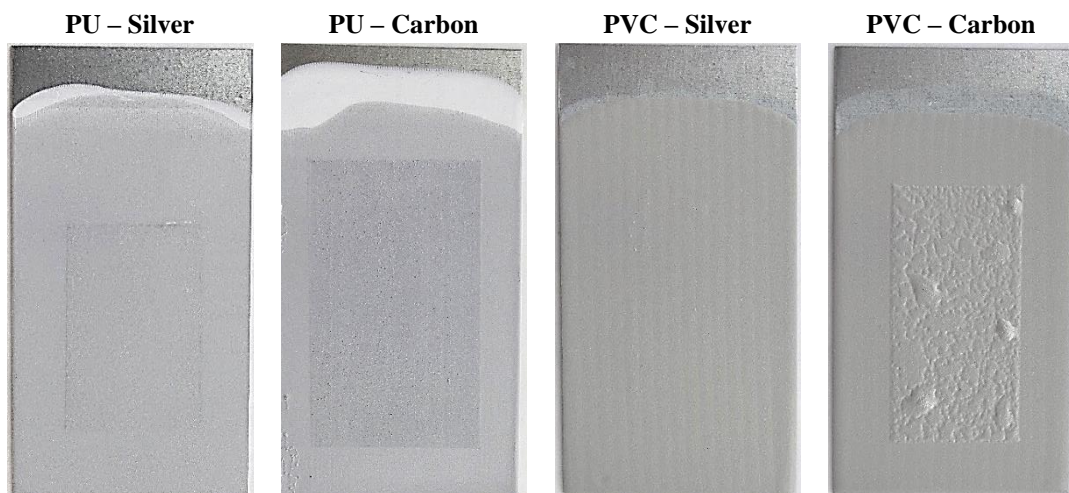


Figure 5.4. Visual appearance of each coating system with an embedded conductive paint layer

Just from a visual analysis it appeared that carbon paint system was not compatible with the PVC system leading to significant defects during the curing process. The resulting surface had an appearance similar to an orange peel defect and the topcoat had delaminated away from the substrate in a number of positions. It is likely that this was caused by the poor adherence of the PVC coating to the carbon paint and hence is an unsuitable pairing for producing embedded sensors.

From initial analysis the conductive paint appeared to have not affected the other samples significantly. Due to the thinner nature of the PU system the square of conductive paint was easily seen and did not appear to alter the appearance and topography of the sample however the latter did appear to be minimal, and it was promising there was no large defects at the conductive paint boundaries. Due to the increased thickness the PVC system seemed to fully encapsulate the silver paint leaving little evidence of its presence.

5.4.1 PU System compatibility

The conductive paint boundaries were examined under a microscope, Figure 5.5, to observe the difference, if any, in the surface with conductive paint present as well as the appearance of the boundary. While a raised surface was observed where the conductive paint was present the overall appearance of this region was similar to that without the conductive paint. Perhaps, however, there was a slight increase in the number of distinguishable features suggesting increased surface roughness. The boundary between the two regions appears to be free of any significant defects.

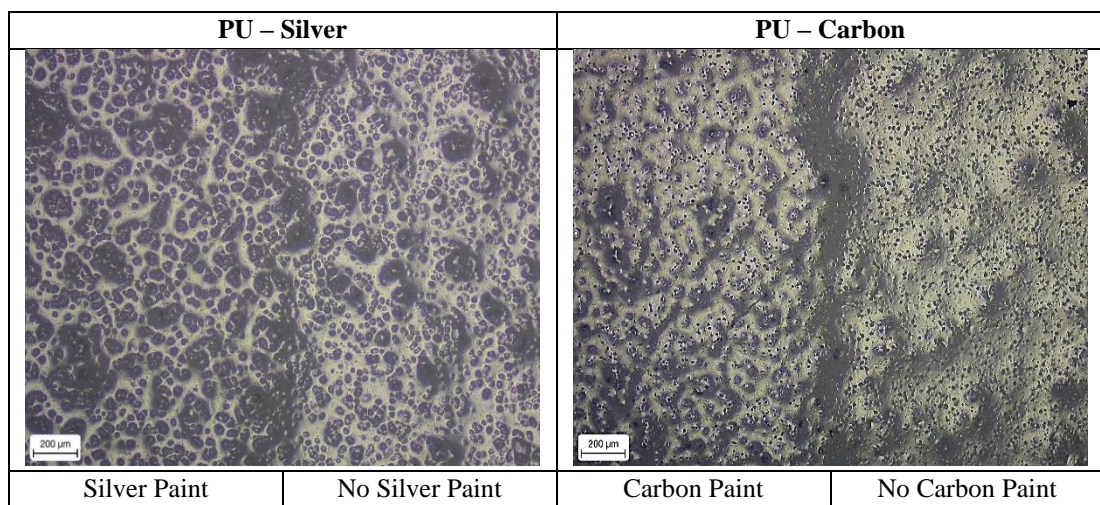


Figure 5.5. Appearance of the embedded electrical paint under the PU system at 5x magnification lens

The properties of the coating with each electrical paint embedded are shown in Table 5.1 and are compared to that of the line sample described previously. It was observed that there is a noticeable colour change as a result of embedding the electrical paints in this system with the black carbon paint giving the greatest change in colour to the end coating. There was also a significant decrease in gloss, most likely due to increased roughness, but the water contact angle was comparable to the line sample suggesting similar surface wetting properties.

Table 5.1. Effect of the electrical paint embedding on the coating properties of the PU system

Property	Line Sample	Silver	Carbon
Colour (L*)	77.8 ± 0.3	76.3 ± 0.1	74.5 ± 0.1
Colour (a*)	-1.7 ± 0.0	-1.5 ± 0.0	-2.0 ± 0.0
Colour (b*)	-2.6 ± 0.0	-2.5 ± 0.0	-3.7 ± 0.1
Colour difference (ΔE^*_{ab})	N/A	1.5	3.5
Scratch Resistance	3200g	3000g	3600g
Gloss @ 60°	28.8 ± 0.5 %	18.7 ± 0.1 %	16.8 ± 0.1 %
Water Contact Angle	70.3 ± 0.1 °	71.3 ± 2.7 °	70.4 ± 1.7°
Adhesion Cross Hatch (T)	100%	95%	85-95%
Adhesion Cross Hatch (ED)	100%	95%	85-95%

There was a notable effect on coating adhesion as a result of the additional conductive layer with the carbon paint sample showing a significant increase in coating removed in the crosshatch test with sections of topcoat and clear coat being totally removed from the carbon layer, Figure 5.6. The silver paint system showed less of a decrease in adhesion, but a level of peeling was observed at the corners of the cross hatched, Figure 5.6.

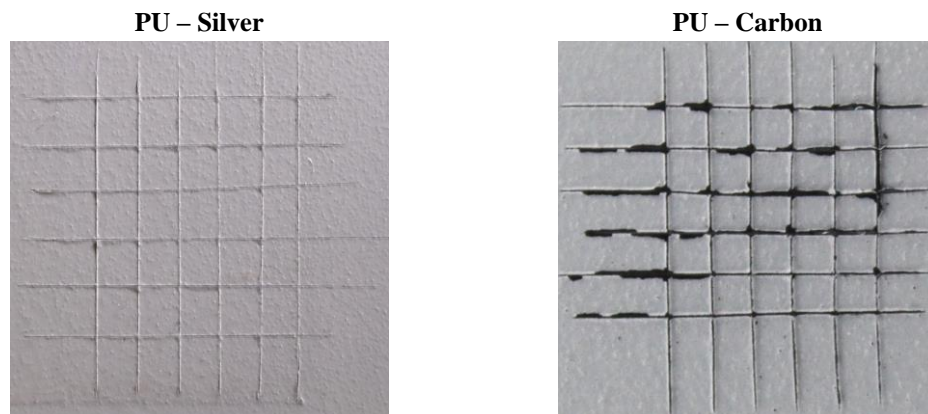


Figure 5.6. Resulting appearance of the PU samples after the crosshatch tape test

5.4.2 PVC System compatibility

In comparison to the previous system the thicker PVC system fully encapsulated the silver conductive paint leading to no visible boundary under microscope examination, Figure 5.7. There was no observed change in the surface of the coating applied to the silver paint suggesting no immediate compatibility issues. As previously mentioned, the carbon paint seemed to be in-compatible with the curing of the PVC paint and hence a mottled surface was produced with large sections where the PVC coating had de-adhered completely from the carbon paint during curing.

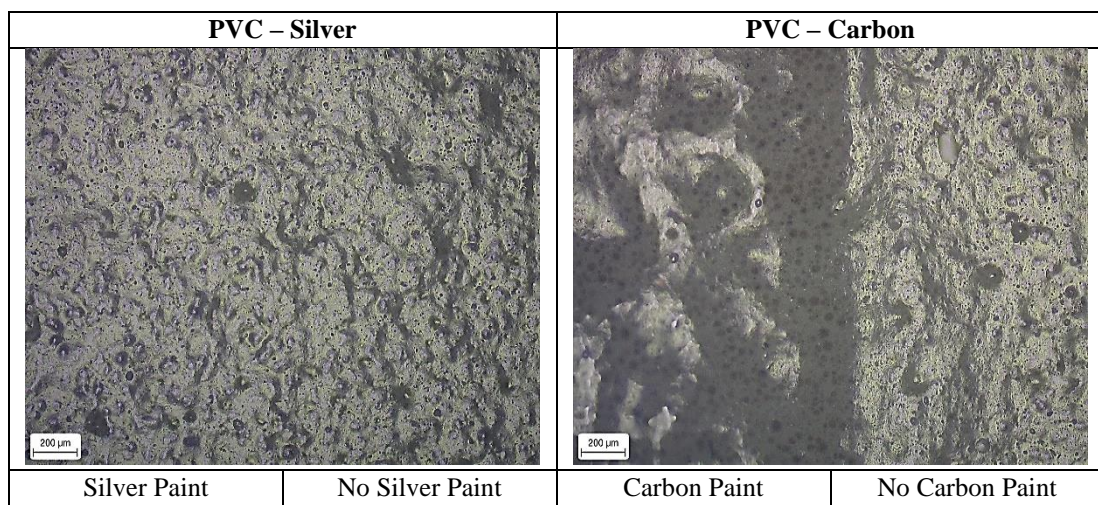


Figure 5.7. Appearance of the embedded electrical paint under the PVC system at 5x magnification lens

The properties shown by the PVC system with embedded conductive paints are given in Table 5.2. Due to the increased thickness of the coating, there was little colour deviation between the samples compared to the line sample. The gloss was also similar for the silver paint sample and only thought to be less for the carbon sample due to the surface roughness. The water contact angle was similar for the silver system suggesting similar wetting properties; the carbon system showed a lower contact angle due to the mottled surface.

Table 5.2. Effect of the electrical paint embedding on the coating properties of the PVC system

Property	Line Sample	Silver	Carbon
Colour (L*)	72.8 ± 0.1	72.4 ± 0.1	72.3 ± 0.1
Colour (a*)	-1.0 ± 0.0	-1.1 ± 0.0	-1.2 ± 0.0
Colour (b*)	3.8 ± 0.0	4.1 ± 0.0	3.6 ± 0.0
Colour difference (ΔE^*_{ab})	N/A	0.4	0.6
Scratch Resistance	>4200g	>4200g	>4200g

Gloss @ 60°	31.7 ± 0.2 %	32.1 ± 0.4 %	26.7 ± 2.4 %
Water Contact Angle	70.9 ± 1.3 °	73.48 ± 1.0 °	66 ± 3.8 °
Adhesion Cross Hatch (T)	100%	100%	0%
Adhesion Cross Hatch (ED)	100%	100%	N/A

The lack of adhesion of the carbon sample was apparent from the tape test with all the paint being completely removed but the silver conductive paint, in comparison showed good adhesion with no removal or peeling, Figure 5.8.

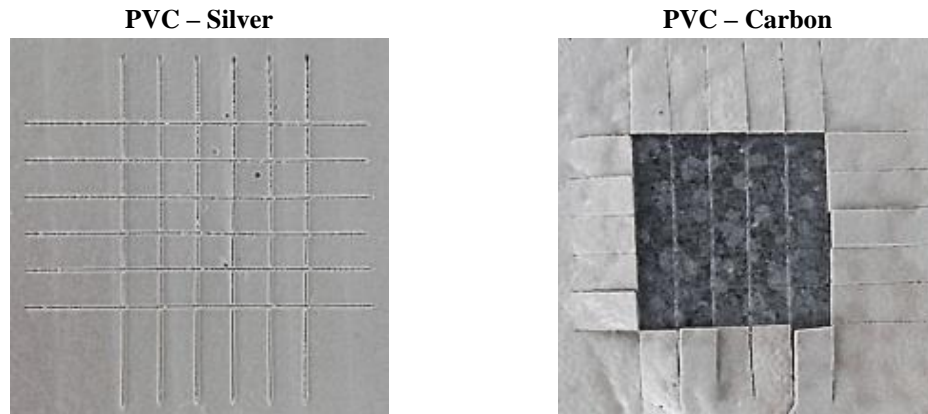


Figure 5.8. Resulting appearance of the PVC samples after the crosshatch tape test

5.4.2.1 Compatibility conclusions

Two different conductive inks were analysed for embedding between the primer and topcoat layers of two industrial paint systems. Both conductive inks had a small effect on the colour and gloss of thinner coatings, but this effect was reduced as topcoat thickness increased. The water-based carbon ink had poor compatibility with the PVC topcoat leading to extremely poor adhesion. The PU – carbon combination had better adhesion, but it was still lower than that of the silver paint or the line sample. From this work the carbon-based paint is clearly unsuitable for embedding in the PVC coating but may be suitable in the PU system. The silver, polyurethane based conductive paint appeared to embed well into both systems with minimal impact on the mechanical properties.

5.5 Cut edge corrosion sensor







5.5.1 Initial proof of concept

Work on the embedded cut edge corrosion sensor involved the use of both electrical paint systems. The key feature required of the electrical paint system was that, once exposed to the environment, it would begin to degrade relatively quickly breaking the connection. For the water-based paint this would be as a result of dissolution

whereas for the polyurethane it would most likely be as a result of more complex weathering and degradation. Because of this, the water-based paint was considered the best option for an initial test due to an increased ease of removal once exposed to environmental conditions as a result of cut edge corrosion.

The first sample produced used a galvanised steel substrate of approximately 15cm x 7.5cm. To prevent shorting of the electrical tracks on the galvanised substrate the steel was first coated with a thin layer of masking tape. This acted as the insulating primer paint layer that the electrical track would be printed on. Onto this masking tape, the electrical paint was deposited by masking off the sample with electrical tape and drawing the paint over the sample using a thin glass rod. This gave an approximate wet film thickness of 50µm. The masking tape was removed, and the electrical paint allowed to dry as per the manufacturer’s instructions. The sample was then coated with a thin layer of PVB using a glass rod and two pieces of electrical tape placed on either side as a thickness guide; providing a similar approximately wet film thickness. The PVB was then allowed to dry at ambient conditions.

To prove the concept of dissolution upon exposure, the sample was mounted at a 45° angle and tap water was gently run over the sample at a rate of 5L/min. The PVB coating was then peeled back to expose the lower track first and then subsequently both tracks. While test was more representative of paint delamination than cut edge corrosion the test did show that the electrical tracks were sufficiently protected when coated (Test 1) yet dissolution of the lower and upper tracks occurred once exposed (Test 2 and 3) as shown in Figure 5.9.

Test	Condition (time under flow increasing left to right)		
	0 seconds	10 seconds	20 seconds
1			
2			

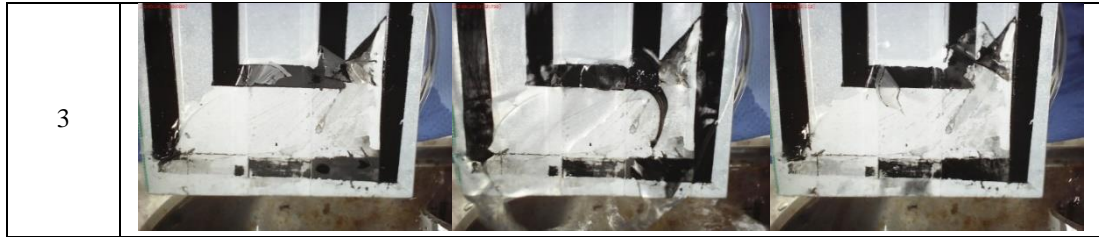


Figure 5.9. Condition of the sample during each test showing dissolution of track once exposed

As dissolution occurred the connection was easily measured to have decreased as shown in Figure 5.10. It did not measure zero response however due to the conductivity of the water that, when present, allowed a small signal to pass between the two, now unconnected ends. The outcome of these results is that a clear indication of track breakage is given by monitoring the connection. Therefore, the technique shows promise at detecting the sort of defects that occur at the cut edge.

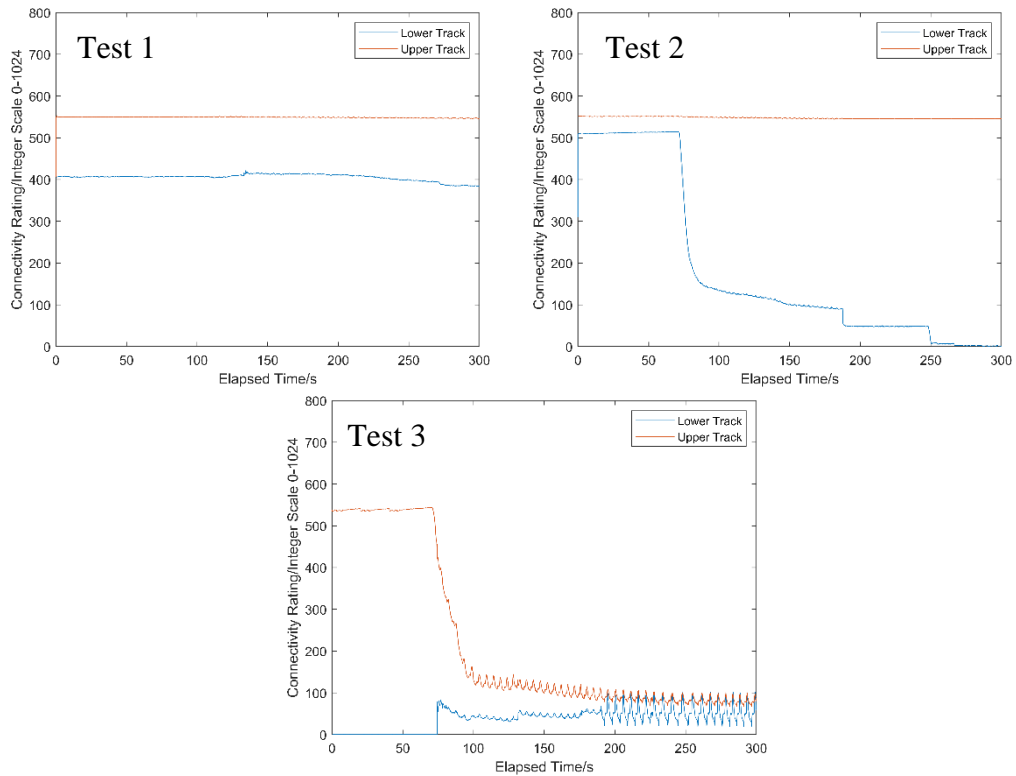


Figure 5.10. Measurement of track connection during each test

5.5.2 Further proof of concept

While the previous experiment displayed some proof of concept it did so in a fairly artificial way. In order to further validate the concept additional samples were made to be tested in a more representative way. The aim would be to determine if actual cut edge corrosion up to the sensor would lead to connection breaking as well as

investigating the use of the polyurethane electrical paint. The substrate for this test was galvanised steel which had been coated with a 25um thick polyurethane primer layer onto which electrical tracks were painted using the method described previously. These tracks were then overcoated with an approximately um thick epoxy resin layer. Wires were connected to the tracks with small amounts of electrical paint and then sealed with further epoxy resin. To prevent coating failure PTFE tape was then applied around the whole sample up to the base of the longest track. The bottom edge of the sample was then cut so that the exposed cut edge was approximately 2mm from the bottom of the longest sensing track. This production process for both paint systems is shown in Figure 5.11.

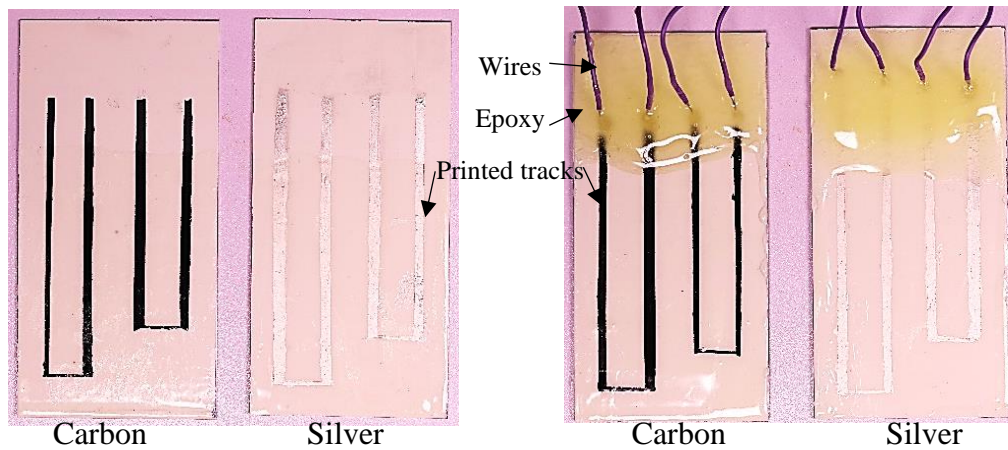


Figure 5.11. The epoxy coated sensors both before and after wire connection and sealing

The finished samples were placed in a salt spray chamber operating at ASTM B117 conditions. The sensors were examined weekly to view the extent of the corrosion and measurements were made to check the connection between each track. Unfortunately, the epoxy did not perform well under the influence of the high humidity in the chamber and was rapidly delaminated from the surface as can be seen in Figure 5.12. As a result of this delamination, however, the electrical tracks were broken, and communication was lost. While there is no obvious visual breaking of the tracks they have been sufficiently attacked/dissolved to allow a lack of connection to be measured. This suggests that the theory of track removal is viable, but this test did not provide full validation of the technique due to the rapid delamination which is un-representative of the sort of cut edge features this technique was designed to measure.

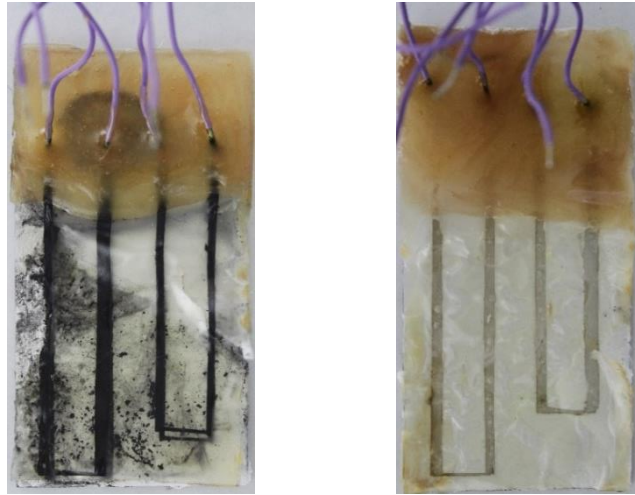


Figure 5.12. Condition of the epoxy covered cut edge corrosion sensors during the test

In order to produce more useful validation results, identical samples were produced however instead of using an epoxy coating, PTFE tape was used as a ‘coating layer’. This was placed over all the sample except a small 1mm section along the cut edge. It was thought this would better produce cut edge corrosion while protecting the bulk of the sample as an industrial coating would. Due to the poor protection offered to the environment by the epoxy the exposed wires and tracks were sealed using casting resin to provide better protection. An example of the new sample is shown in Figure 5.13.

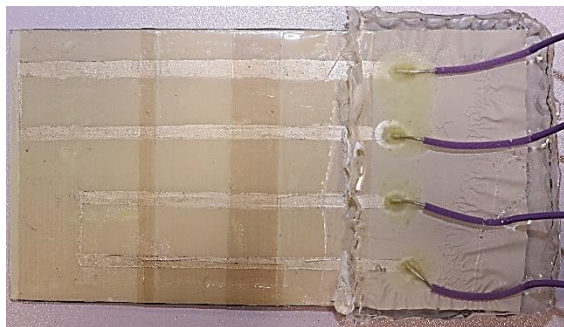


Figure 5.13. The new test sample composed of a tape covered sensor and utilising casting resin to protect the connections and uncoated substrate

After several weeks in the salt spray chamber the sample began to show cut edge corrosion and defects on the exposed test edge as shown in Figure 5.14. It was observed that once corrosion product reached the lower of the two sensing elements connection was lost for that element however remained for the higher element. The method of electrical connection severing was not discernible however it was though

that it was a combination of dissolution, environmental attack, and mechanical stress due to blistering and corrosion product production. What was evident though, was that at the distance of spread of blistering, cut edge corrosion and or water uptake from the cut edge had been detected by this method. More accurate results would be ascertained by the use of the actual coating system, but this proved the overall concept.

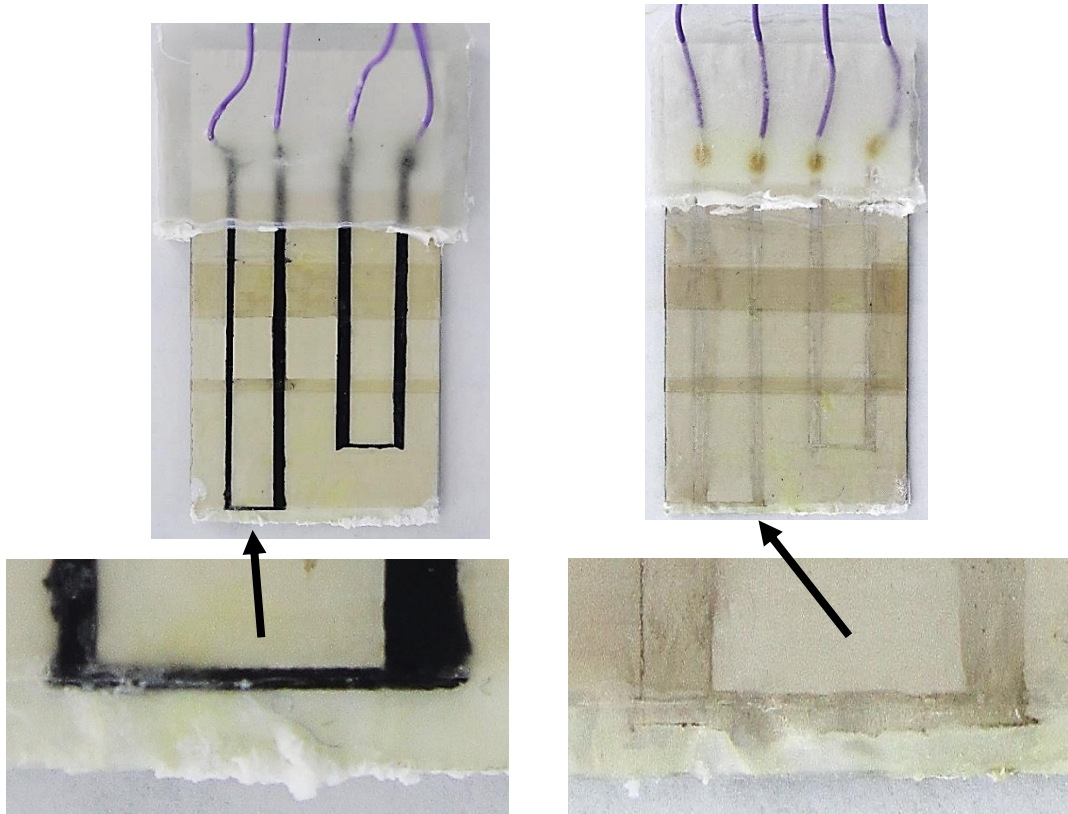


Figure 5.14. Condition of the PTFE tape covered cut edge corrosion sensors during the test including close up of the sensing element broken as a result of cut edge defect spread

5.5.3 Embedding in actual paint system

After the previous successful proof of concept of the system samples were made using the actual Tata Steel Colors coating systems. The procedure for making these samples was fairly similar to that of the previous samples. First the pre-treated galvanised steel was coated with the correct primer layer and thickness for the system and then the electrical tracks were painted as described previously. These were allowed to cure as recommended and then overcoated with the required thickness of top and, in the case of the PU system, clear coats. Although the PVC system has previously shown poor compatibility with the water-based carbon ink it

was still used to see if a smaller area of paint would reduce compatibility issues. In order to allow connection to the tracks the top and clear coats were carefully applied to leave exposed track ends.

The required connections were then made to these samples and protected with casting resin. Furthermore, the uncoated rear of the sample was also protected using PTFE tape. Finally, the bottom edge of the sample was cut using a guillotine to provide a fresh cut edge 5mm from the lower sensing tracks. The samples, Figure 5.15, were then placed under the same salt spray test as the previous samples and periodically examined and the sensing element connection tested.

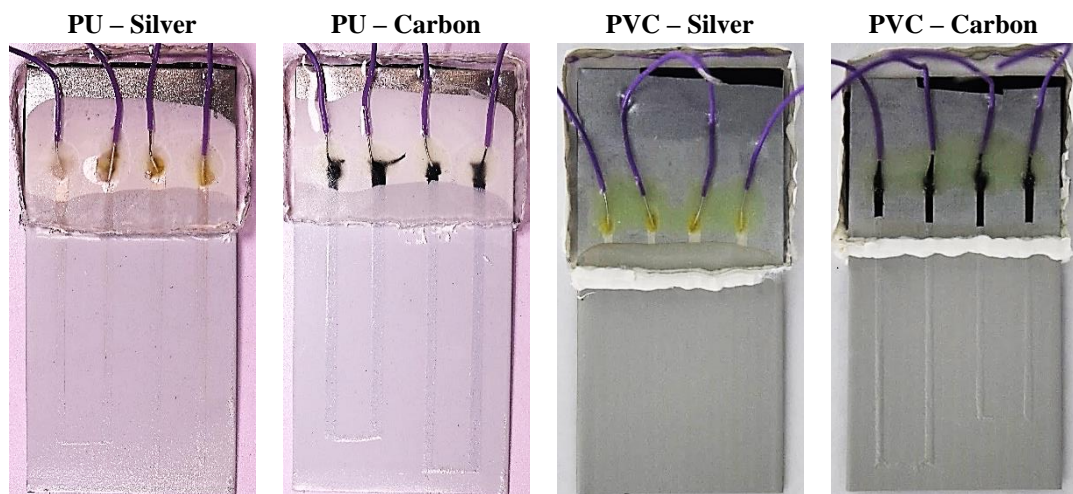


Figure 5.15. The cut edge corrosion sensors produced for testing. Green discoloration around the wires is from epoxy glue used to hold the wires in place before encapsulation.

After approximately 4 weeks cut edge corrosion and defects were present on the exposed edge as is shown in Figure 5.16. However, as the defect has not reached the sensing element, Figure 5.17, it there was no change in the connection between sensing tracks and hence it was undetected.

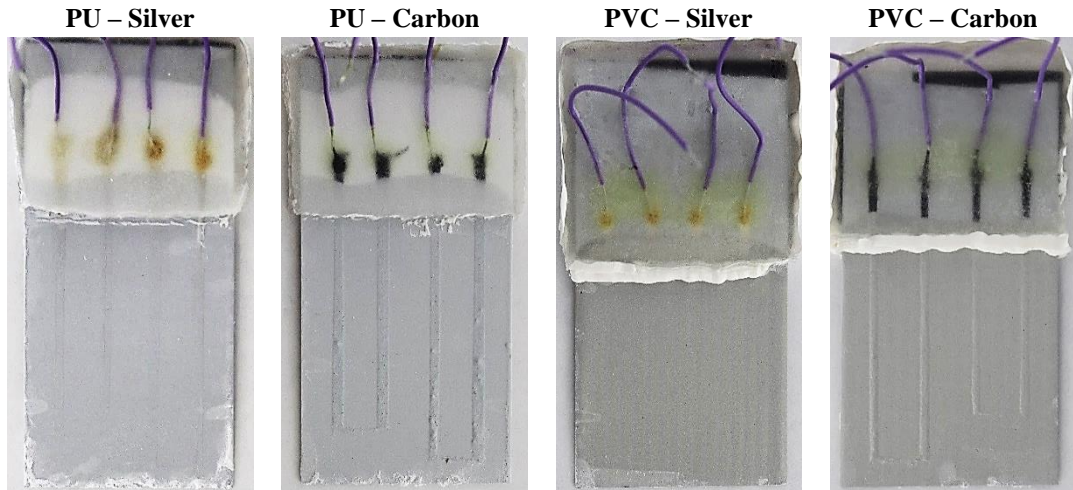


Figure 5.16. The cut edge corrosion sensors after 4 weeks exposure

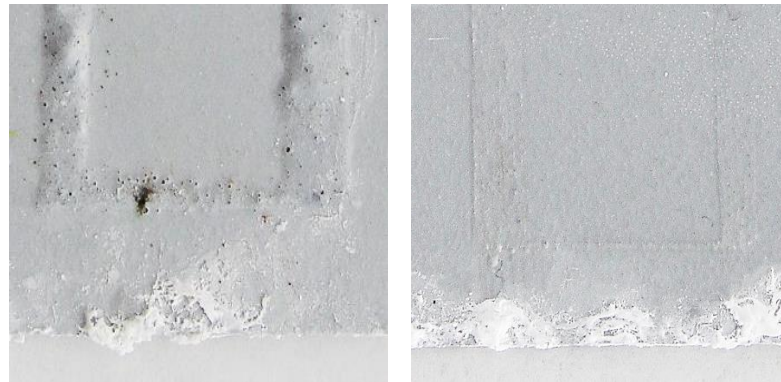


Figure 5.17. Close up of the PU systems sensing element

By week 8 more significant cut edge corrosion and defects were observed to have developed in the PU samples, Figure 5.18. Unfortunately, it appeared that the PU-Carbon sample had experienced blistering across the sensor element which was thought to be due to the reduced adhesion between the carbon and topcoat leading to decreased blister resistance. Although the longer sensing tracks were more blistered, both were affected, and this led to broken connections of both sensing elements. This suggests the PU-Carbon sensor is not suitable as failure can occur without being a direct result of cut edge corrosion. The PU-Silver sensor also showed this behaviour but to a much lesser extent with blisters mainly forming around the resin protective layer and near the cut edge corrosion sections. In fact, it appears somewhat that blisters have only formed at regions where defect spread inwards from an edge. This suggests this system is far more durable to the conditions and better for cut edge detection. Arguably the PU-Silver sensor may function far better in real-life conditions where the sample would not be subjected to as constantly aggressive

environments and blistering is less likely. Due to the poorer performance and adhesion of the PU-Carbon sample however this is unlikely to ever be as suitable. Both systems have shown however, that connection is lost as a result of degradation, in this case blister formation.

Less significant corrosion was observed on the PVC samples and in fact the sensing element was still providing connection, Figure 5.18. The extra protection offered by the thick coating required further exposure to determine the effectiveness of the sensing element.

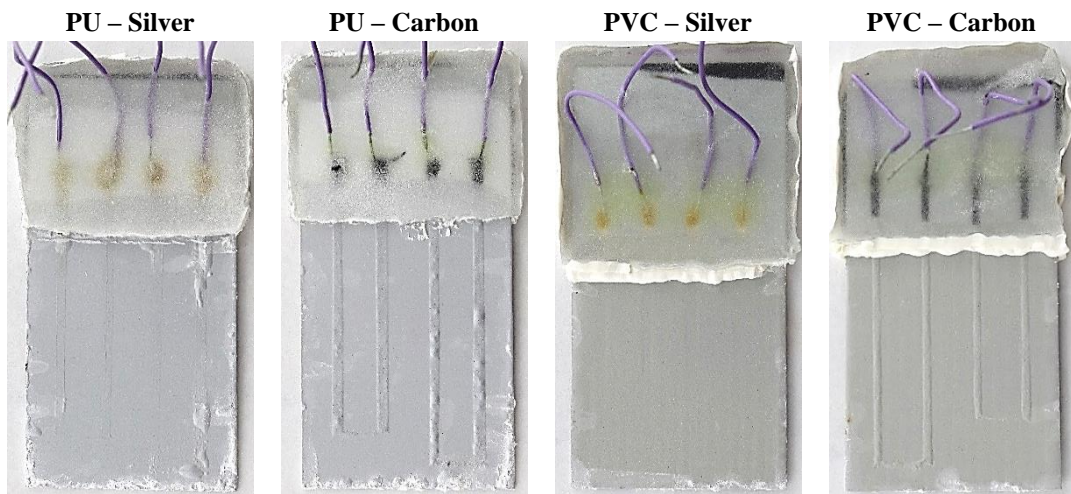


Figure 5.18. The cut edge corrosion sensors after 8 weeks exposure

Control samples of line manufactured material, with no embedded sensing elements, were also exposed to 8 weeks of salt spray exposure. Similar cut edge performance was observed for both PU and PVC samples; PU sample shown in Figure 5.19.



Figure 5.19. Reference PU sample (left) and cut edge close up (right)

5.5.4 Cut edge sensor conclusions

The cut edge corrosion sensing concept explored shows some promise in that the concept of a number of progressive failure sensing elements seems feasible from both a manufacturing and principal standpoint. While the water-soluble carbon-based paint seems to provide the easiest track failure mechanism it appears to drastically affect the durability of the coating and hence seems unsuitable. The silver-based paint appeared to affect durability less, however the coating system as a whole still performed worse as a result of the sensor addition. While it is suggested this discrepancy would be less for natural exposure durability, further, long term, experimentation would be required to confirm this. It is concluded therefore, that although the sensor concept is valid, application is limited by the effect on durability of the sensor presence. It is possible that experimentation with different electrical paint systems, or sensor thickness, could solve this problem.

5.6 Capacitive coating sensor

5.6.1 Initial proof of concept

To test the concept of a capacitive coating sensor, a simple printed design, shown in Figure 5.20, was used. This was composed of two 1cm tracks which were separated by 1cm. The sensing part of the tracks were 5cm long and there was a thinner 2cm track extending off the sensing part to allow the connection of wires for measurements.

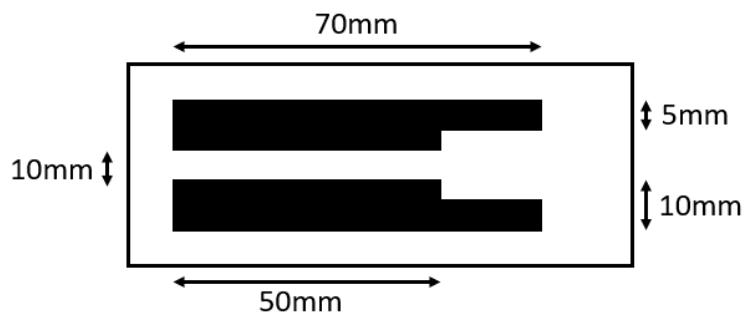


Figure 5.20. Printed capacitive sensor design and corresponding dimensions

Compared to other capacitive sensors, which can have gaps between tracks that range from microns to 2-3mm [16,17] the sensor design used had a larger gap. Partly this was due to the method of printing, as it was found that a gap of 5mm or less was difficult to accurately produce and often paint crept under the tape mask leading to poorly defined, and often connected, coating tracks. Furthermore, calculation of the

expected capacitance for a realistic paint dielectric constant of 3.5 [18,19] and the expected sensitivity of different sensor separations showed only a slight difference, Table 5.3. While in reality these calculations, due to negation of the metal substrate and other assumptions, are unlikely to accurately predict these parameters the trends provided should be reflected. Therefore, for the principle aim of testing this concept to determine feasibility of embedded sensing, ease of manufacturing was initially preferred over optimised sensing especially given that, initially, very large changes in dielectric constant were tested.

Table 5.3. Calculated parameters for different gap sizes

Gap/mm	Calculated C ($\epsilon_r = 3.5$) /pF	Calculated Sensitivity for ($1 \leq \epsilon_r \leq 6$) /pF ϵ_r^{-1}
1	4.4	0.62
2	3.7	0.53
5	2.9	0.42
10	2.4	0.35

The sensor was printed onto pre-primed galvanised steel samples of approximately 12x6cm allowing approximately 15mm between the edges of the sample and the printed sensor. Examples of the printed sensor in both conductive inks are shown in Figure 5.21.



Figure 5.21. Examples of the printed capacitive coating sensor produced using carbon (left) and silver (right) paints

In order to test the ability to detect changes in a coating placed over the sensor a continuous measurement was taken during the application, and curing, of a PVB topcoat. PVB was chosen as it will air dry within a short period and the solvent used is ethanol which was not expected to disrupt the water-soluble carbon paint. It was expected that as the PVB layer is applied the capacitance should increase as predicted by Equation 5.1 and 5.2 due to the presence of ethanol (dielectric constant $\epsilon_r \approx 25$ [19]). As the coating dries and the ethanol evaporates a decrease in capacitance is expected until drying is complete, and the capacitance stabilises.

The resulting measurements of capacitance with time are shown in Figure 5.22 and follow the expected trends well. There was an initial increase in capacitance as the coating is applied which gradually decreased with time as the coating underwent drying. At the end of the test the capacitance stabilized at a reading slightly higher than the uncoated sample. Both sensor systems responded similarly although generally the sensitivity was fairly low considering that a large change in dielectric constant had occurred. This was not unsurprising given the indications from the calculated sensitivity, but it did further suggest that changes in the coating were detectable but may be limited to large changes dielectric properties. Both systems showed capacitance measurements far higher than expected from the calculations however this was thought to be due to the metal substrate contributing additional factors not considered in those calculations.

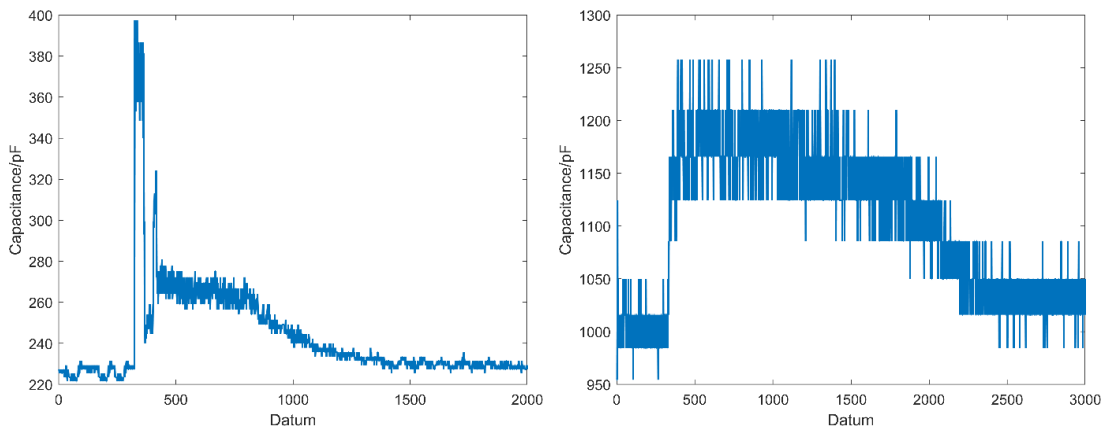


Figure 5.22. Measured capacitance (raw data) over time during the application and drying of PVB over a carbon (left) and silver (right) embedded sensor

To further investigate the sensor systems a second set of sensors were produced which were overcoated using epoxy resin, Figure 5.23. These sensors were then subjected to both steam and immersion in acetone and the capacitance was measured at set intervals. FTIR measurements were also taken in order to correlate any changes in capacitance to changes in the coating chemical structure.

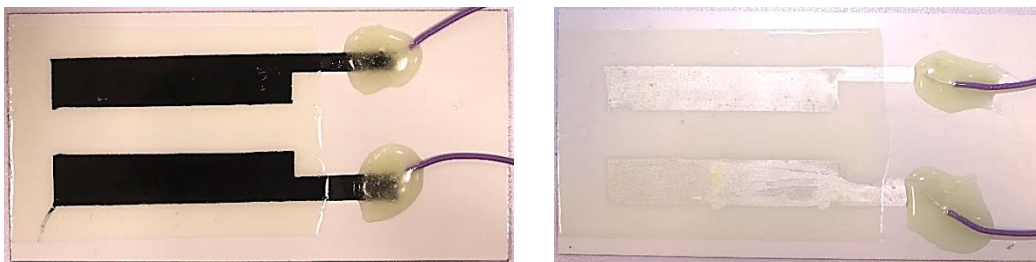


Figure 5.23. Epoxy coated carbon (left) and silver (right) paint sensors

It was observed, as shown in Figure 5.24, that both systems showed an increase in measured capacitance as a result of exposure to steam. This was expected as water has a high dielectric constant ($\epsilon_r \approx 80$ at 20°C [19]) and hence the uptake of water into the coating would increase the relative dielectric constant of the layer and increase the capacitance. This was confirmed to be the cause of the increase from FTIR analysis which showed an increase in the intensity of the OH peak (broad peak at $\lambda \approx 3000 - 3500 \text{ cm}^{-1}$ [20]) as a result of steam exposure during the test, Figure 5.25.

In comparison the acetone shows a similar increase in capacitance for the first 40 minutes but a significant decrease capacitance at the 180-minute measurement. This, however, is also explainable from theory. It was thought that up to the 40-minute mark a small amount of acetone was absorbed into the coating which was not fully evaporated when measured leading to an increased capacitance. At 180 minutes the epoxy coating had begun to blister and slightly delaminate from the substrate explaining the decrease in capacitance as the coating ($\epsilon_r \approx 3.5$) is somewhat removed and replaced with air ($\epsilon_r \approx 1$). It was not clear why the capacitance increase, as a result of the testing, was larger for the carbon sample compared to silver.

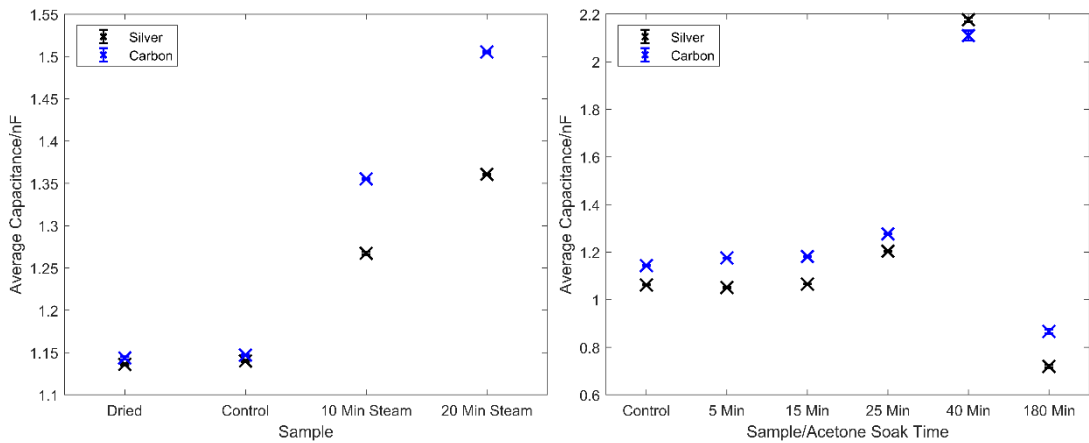


Figure 5.24. Effect of steam exposure (left) and acetone immersion (right) on the epoxy embedded sensors

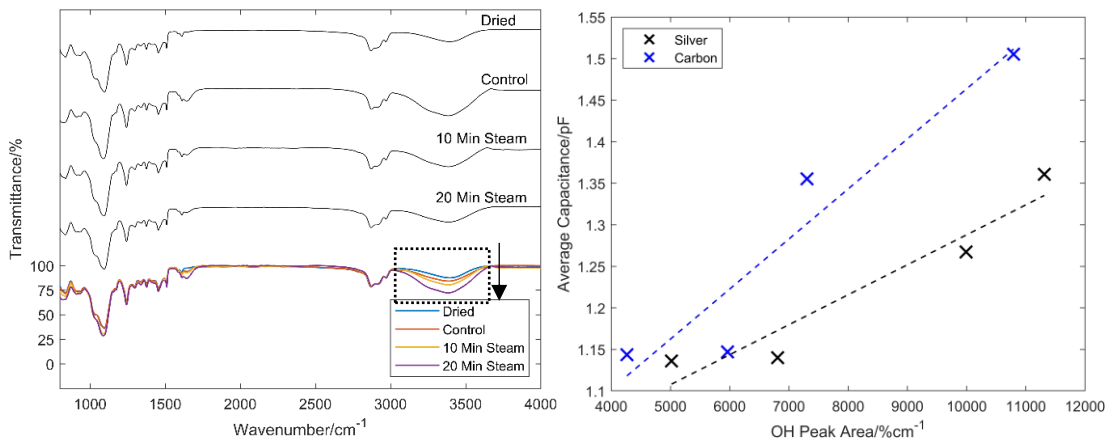


Figure 5.25. FTIR analysis of the epoxy coated carbon (left) showing an increase in the magnitude of the OH peak as a result of steam exposure (arrow) and comparison of the trend between peak area and measured capacitance for both samples (right)

Hence, it was shown that for a simple coating system, such as epoxy, changes in the coating were able to be detected as a direct result of capacitance changes measured from the embedded sensor. While some interpretation of results was required this allowed an understanding of the coating condition. For more representative results this sort of test would have to be verified by using the actual industrial coating system.

5.6.2 Embedding in actual paint system

To embed the capacitive sensor in the coating system a similar manufacturing process was followed to the previous epoxy system. First galvanised, pre-treated steel samples of 12x6cm were coated with the required primer and cured. Onto this primer the electrical paints were applied creating the capacitive sensor. The same

design was used due to the positive results in previous tests and the increased ease at which samples could be produced. Once the electrical paint was correctly cured this was overcoated with the top and, if required, clear coat. This gave the samples shown in Figure 5.26. At this point the PVC-Carbon sample was discarded due to the poor compatibility of the two systems leading to a heavily defective coated product not though to be representable of the actual system. Furthermore, due to the results of the cut edge corrosion sensor the PU-Carbon sample was also discarded due to poor stability in aggressive environments due to low adhesion. This therefore left the two silver paint samples.

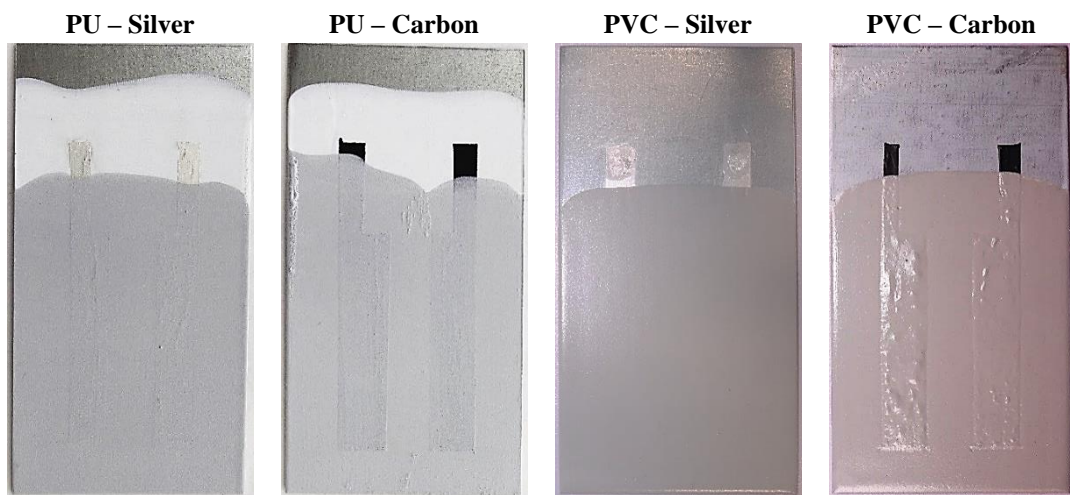


Figure 5.26. The embedded capacitive sensors produced using the two industrial coatings

Once fully coated, wires were connected with small amounts of electrical paint to the remaining three samples via the exposed track ends and then this was sealed with epoxy resin to protect the connection during the degradation testing. For the samples undergoing MEK rubs and UV testing, this was considered sufficient protection as the exposed ends would not be greatly exposed to the test conditions. For the immersion and salt spray tested samples, tape was used to seal off the exposed tops of the samples to attempt to protect it more fully from the environment. Finally, the reverse, uncoated side of the sample was protected from corrosion using PTFE tape to give the final sample ready for testing. Examples of the final samples produced for degradation testing are shown in Figure 5.27.

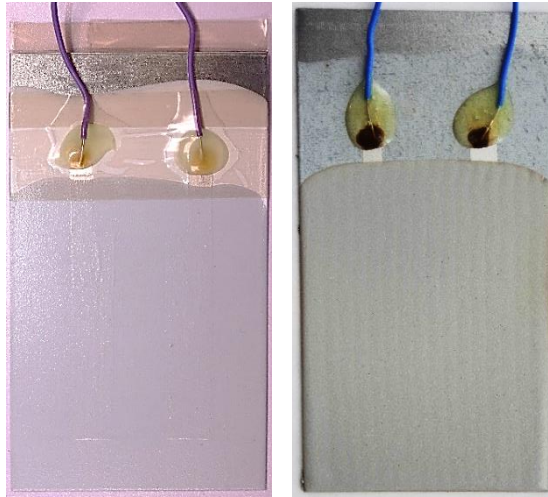


Figure 5.27. Examples of samples prepared for degradation testing

Exposing the samples to the accelerated degradation testing had two main objectives. Firstly, while the effect on the initial physical and mechanical properties has been explored, it was important to ascertain whether the embedding of the electrical tracks detrimentally affect the coating durability. Secondly, these tests were used to determine if the capacitive measurement provided by the embedded tracks is suitable for detecting coating degradation as a result of exposure.

5.6.2.1 Immersion testing

During immersion testing the PVC sample appeared to change little in appearance however the PU sample did experience a small amount of blister formation from week 3-5, Figure 5.28. These blisters mainly formed on the regions where conductive paint was or the boundaries of the conductive paint. It is possible this is due to the slightly decreased adhesion shown by the embedded areas. While this may suggest a reduced durability of the embedded samples the immersion test is not well representative of real-life conditions and hence not an immediate cause for concern.

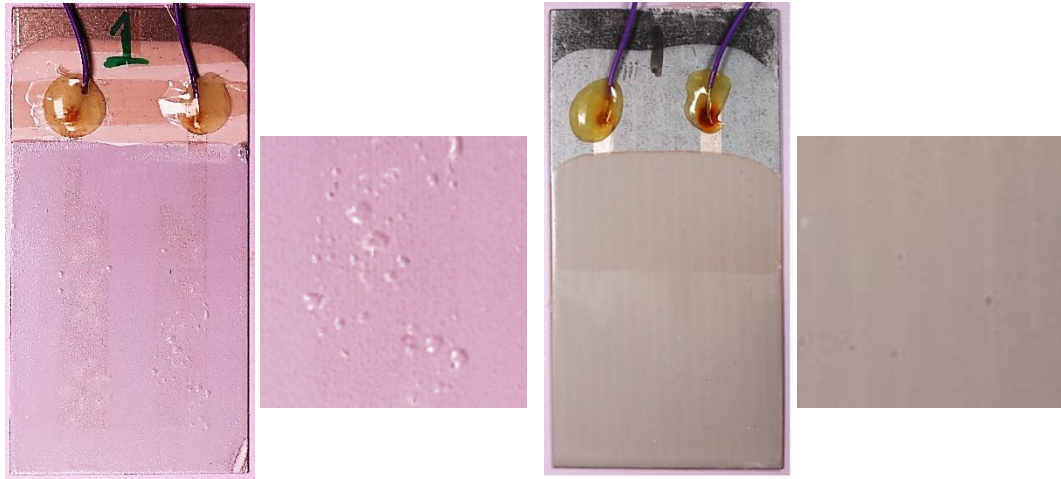


Figure 5.28. Post immersion testing sample appearance including close up

The appearance of the sample may explain somewhat the difference in measured capacitance trends for both samples, Figure 5.29. Both samples show a gradual increase in capacitance with immersion time however the PU sample does show a rapid increase from week 3 onwards. A gradual increase in capacitance was expected as water is up taken into the coating and water uptake was verified to be occurring via FTIR measurements and calculation of the OH peak area, Figure 5.30. While this did not show an exactly linear increase the general trend was increased OH area with immersion time and therefore this was concluded to be detected for both samples. It is possible that the change in capacitance behaviour in the PU sample is due to the formation of the water filled blisters more rapidly increasing the capacitance between the tracks.

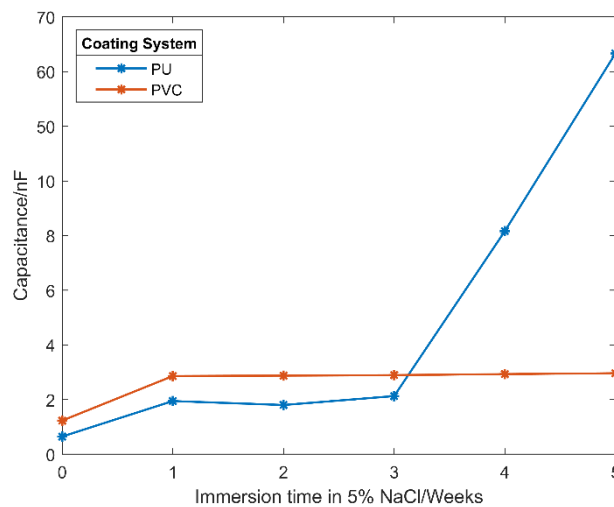


Figure 5.29. Measured capacitance of the embedded sensors during the immersion test

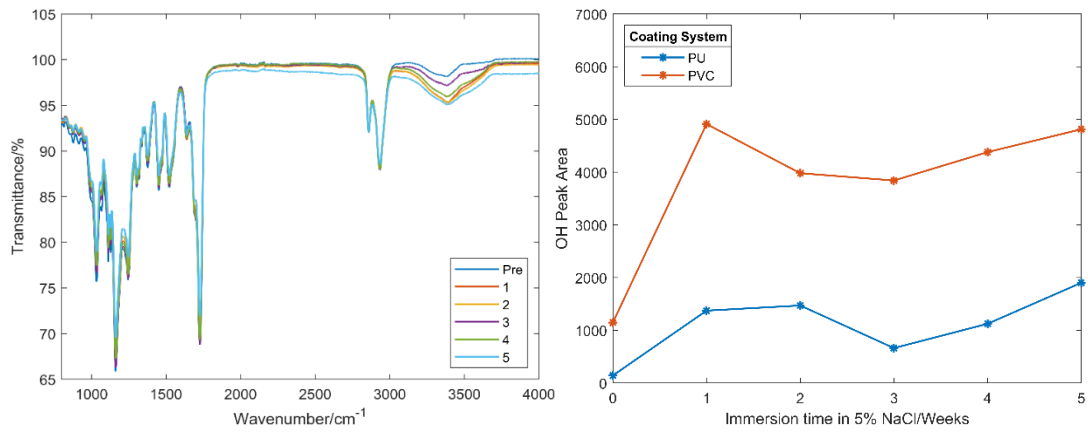


Figure 5.30. Example FTIR spectrum for the PU sample (left) and the calculated OH peak area for each sample (right)

5.6.2.2 MEK Rubs

As a result of subsequent MEK rubs both samples did not change in appearance drastically but were observed to lose a small amount of their gloss, as is expected from this test, and a small amount of the PVC coating was observed to be removed onto the cheesecloth. However, generally both samples showed good resistance to the MEK rubs suggesting that a good degree of cure was achieved.

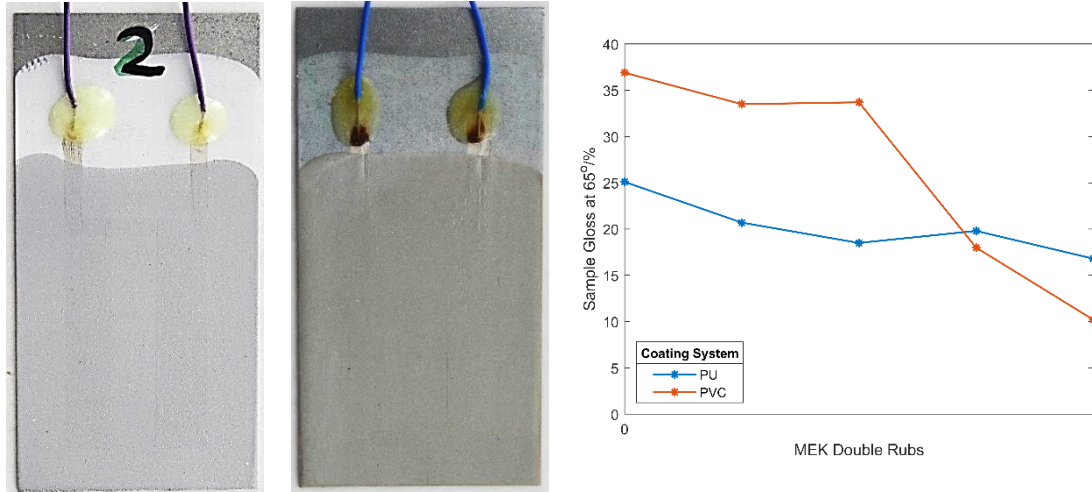


Figure 5.31. Post MEK testing sample appearance (left) and measured gloss (right)

The measured capacitance during the test is given in Figure 5.32. For this test it was not easy to determine what the expected result of MEK rubs on capacitance should be. This is because it is possible for a number of outcomes to occur that may affect the capacitance differently such as removal of coating, uptake of MEK and breakdown of the coating bonds. The results show that the capacitance initially increase up to 100 rubs with the PVC system showing a continuing increase in

capacitance for the remainder of the rubs whereas the PU system showed a decreased capacitance.

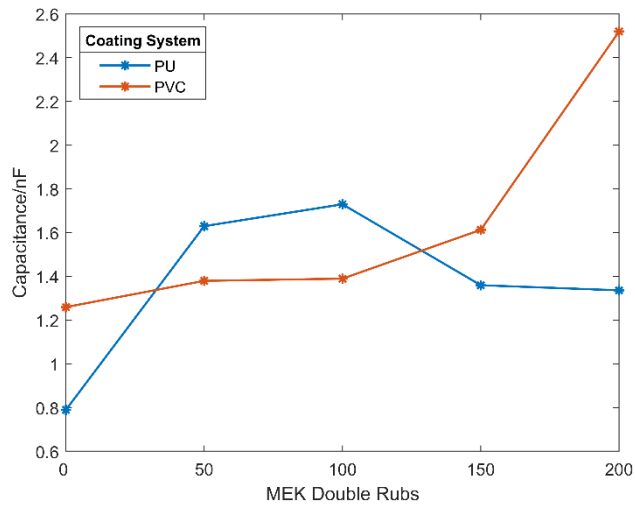


Figure 5.32. Measured capacitance of the embedded sensors during the MEK test

5.6.2.3 UV Testing

The samples underwent the smallest visual change during the UV-condensation testing with no obviously detectable impact on the samples, Figure 5.33. Further analysis showed that both samples maintained similar gloss levels however both did show an increase in ΔE^* with time however only the PVC sample colour change was considered significant ($\Delta E^* > 1$), Figure 5.34.

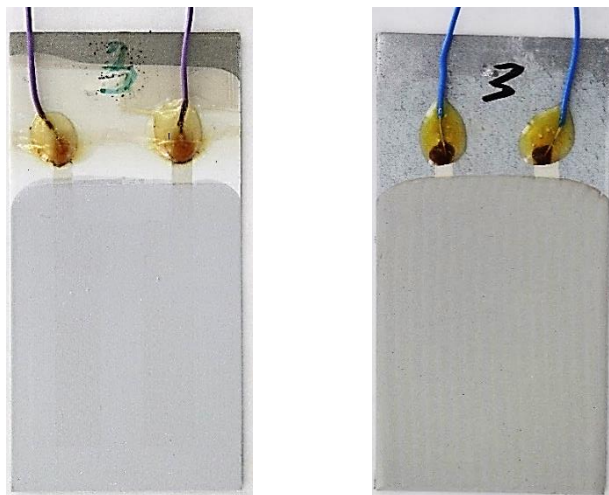


Figure 5.33. Post UV testing sample appearance

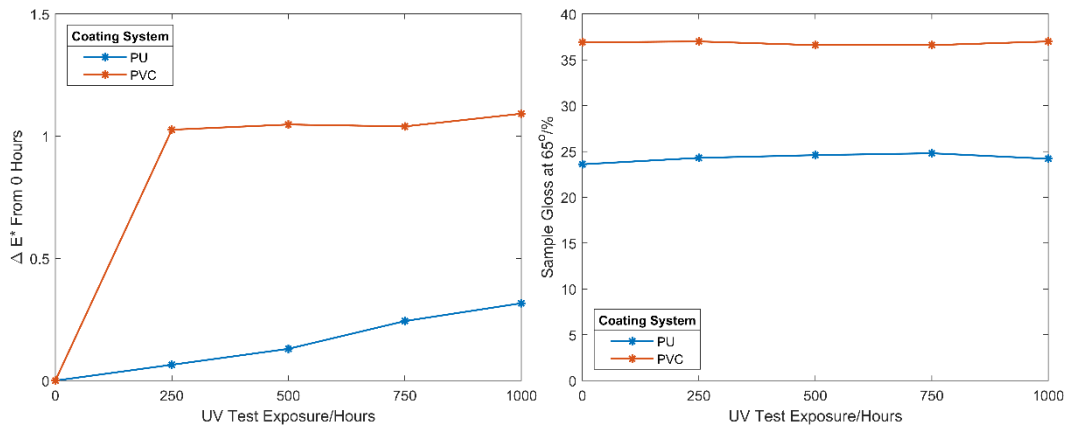


Figure 5.34. Effect of UV testing on sample colour (left) and gloss (right)

In terms of the measured capacitance during the test, shown in Figure 5.35, both samples showed a similar pattern of an increased capacitance up to 500 hours before capacitance decreased to pre-exposure levels at 1000 hours. For the PVC sample the 500 hours showed an exceptionally large increase. It is likely that any increases in capacitance are due to water uptake and any decrease would be due to coating degradation and breakdown via UV. It was thought that perhaps the reason for an increase up to 500 hours is that water uptake is dominating the capacitance changes whereas after 500 hours some coating degradation is occurring leading to a decrease. However, considering changes in sample appearance due to degradation were low and there was no significant change in OH peak areas across the test period, Figure 5.35, it was concluded that the results were due to natural variation rather than detection of any particular changes. The PVC result at 500 hours was considered due to improper drying of the sample before test.

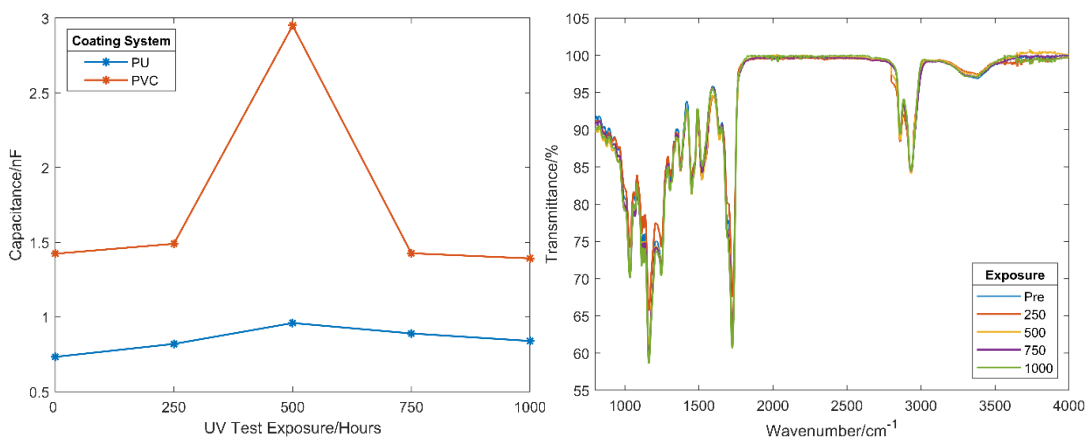


Figure 5.35. Measured capacitance of the embedded sensors during the UV test (left) and example FTIR with no obvious OH peak change (right)

5.6.2.4 Salt Spray Testing

During exposure to salt spray, both samples showed a small amount of cut edge corrosion and a very small amount of blistering around the cut edge. Unlike the immersion test, no significant blistering was observed on the embedded section suggesting good resistance of these areas to this test. However, the PU sample did experience some larger blistering around the top of the sample where the topcoat/clearcoat ended due to poor protection from the tape. This is shown, along with the samples, in Figure 5.36. This has formed as a result of poor sealing of the topcoat/clearcoat end rather than poor performance of the coating.

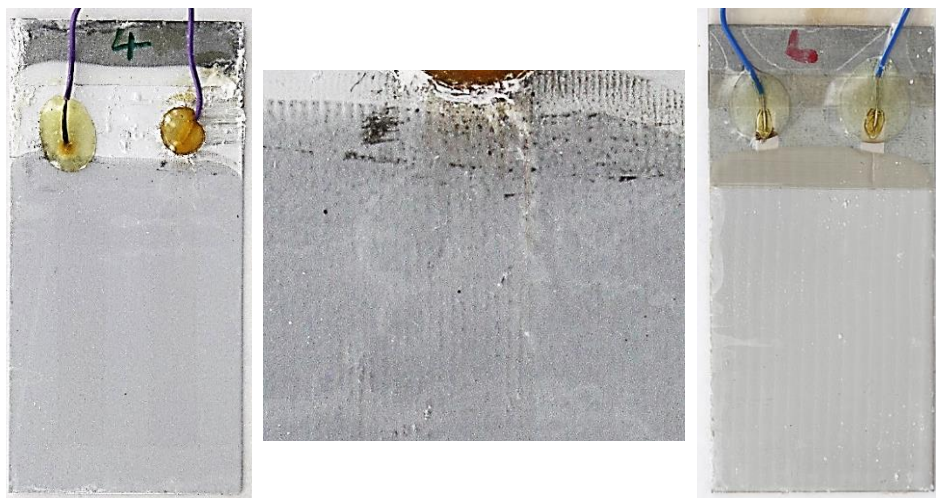


Figure 5.36. Post salt spray testing sample appearance including close up of PU blisters

The measured capacitance of each sensor is shown in Figure 5.37 and show that both samples recorded a slight increase in capacitance with exposure time however the PU did experience a rapid increase in weeks 4 and 5. As this coincided with the bulk of the blister formation at the top of the sample this was considered the cause of this. It is not expected for the samples to be degraded, or to uptake water, significantly as a result of this test so the fact the PVC sample recorded similar values throughout and the PU sample recorded similar values until the blister formed is reasonable.

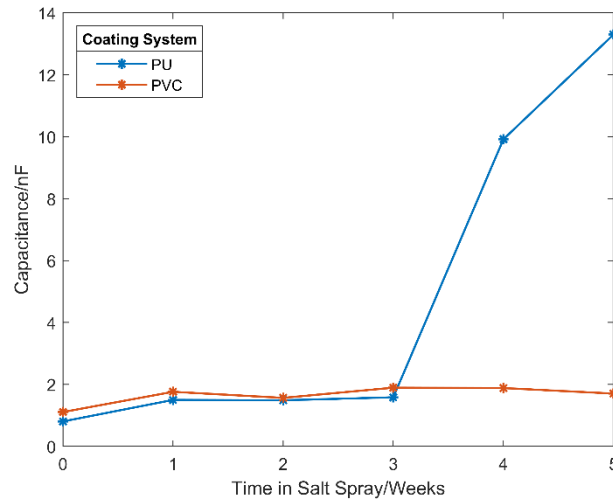


Figure 5.37. Measured capacitance of the embedded sensors during the salt spray test

5.7 Discussion

Embedded sensors offer a promising way to detect changes and degradation of coated steel samples without affecting the exposure of these samples to an environment. The production of small, representative, lab scale samples which can then be attached to facades for representative monitoring also present an easy route for the installation of sensors during or post construction. These types of sensors would be especially useful for deployment in hard, or dangerous, to reach, areas of a building such as rainscreen cavities or on tall structures. The control system could then be internally wired such as that of a security camera.

It has been shown that there can be significant compatibility issues with embedding electrical paints in the systems, but it seems at least some options are available that provide representative coating properties. Considering the recent growth of printed electronics, it is highly likely that other electrical paints and methods of printing exist which affect the end product to a far lesser extent. Furthermore, due to advances in paint manufacturing, it would not be unreasonable to suggest that specific formations could be developed solely for this aim. Therefore, while compatibility is identified as a key issue surrounding embedded sensor development it was not thought to be a limiting one.

The use of simple embedded tracks as a failure based embedded cut edge corrosion sensor has been proposed and appears a promising technique which benefits from the simplicity of operation and measurement. While it was limited to a binary result in

this work, the use of multiple elements would allow a quantitative estimate of defect spread from the cut edge inwards. This, however, assumes that degradation is consistent across the length of the sample and failure is not influenced by the embedding of the sensor system. Further work is required to ensure confidence that the failure rate of the sensor laden section is comparable to the bulk product during extended natural weathering. Also, the connection system from embedded sensor to control system must be further verified to be robust for the expected lifespan of the sensor so that any recorded connection loss can be assumed to solely arise as a result of sensor element failure.

Embedding of coplanar electrodes is an interesting concept for in-situ measuring the capacitance of the coating, and the theory of operation is well supported by literature. However, much of the published work revolves around sensing effects that will lead to large changes in the dielectric constant under examination, such as the presence/absence of water [7,9]. It is perhaps unsurprising, therefore, that large changes in coating properties were easily detected, however smaller changes, as will be present with gradual degradation over years, were more challenging. This may limit the ability of the technique to function accurately in-situ. For example, changes in capacitance due to moisture from humidity or measurement drift may drown out the small changes directly caused by degradation. Use of this technique is further complicated as it is difficult to extract information as to the coating condition based solely on the capacitance. This is because some methods of degradation may increase the capacitance whereas others may decrease it simultaneously. While it is sometimes possible to extract information in lab conditions, in real-life situations, where multiple coating degradation methods will likely be present, this may be harder.

5.8 Conclusions

Two embedded sensor concepts were developed and investigated in this work and tested in terms of feasibility and accuracy. The cut edge corrosion sensor appears the most effective of the two concepts, and shows promise, however, is ultimately a failure reactive measurement. Although more promising for monitoring, the capacitive sensor concept appears to lack the applicability and sensitivity for effective use. It is clear that substantial further work is also required to determine the

optimum electrical paint and method of printing to minimise the effect of an embedded sensor on the durability of the end coating product. Ultimately, as well, the sample under monitoring is only a representation of the bulk. Hence, while embedded sensors show some promise from a feasibility perspective, the following work focuses on sensing technology which can be more easily deployed onto, or near, the actual in-service product.

5.9 References

1. Ogle K, Baudu V, Garrigues L, Philippe X. Localized Electrochemical Methods Applied to Cut Edge Corrosion. *J Electrochem Soc.* 2000;147(10):3654.
2. Ryan PA, Wolstenholme RP, Howell DM. Durability of Cladding, A State of the Art Report. 1994.
3. Kurnyta A, Baran M, Kurnyta-Mazurek P, Kowalczyk K, Dziendzikowski M, Dragan K. The experimental verification of direct-write silver conductive grid and ARIMA time series analysis for crack propagation. *Sensors.* 2021;21(20).
4. Ashrafi B, Johnson L, Martinez-Rubi Y, Martinez M, Mrad N. Single-walled carbon nanotube-modified epoxy thin films for continuous crack monitoring of metallic structures. *Struct Heal Monit.* 2012;11(5):589–601.
5. Althens. FAC Series Crack Detection Strain Gauges [Internet]. 2022 [cited 2022 Dec 30]. Available from: <https://www.althensensors.com/sensors/strain-sensors-strain-gauges/special-application-straingauges/4478/fac-series-crack-detection-strain-gauges/>
6. Wade SA, Wallbrink CD, McAdam G, Galea S, Hinton BRW, Jones R. A fibre optic corrosion fuse sensor using stressed metal-coated optical fibres. *Sensors Actuators, B Chem.* 2008;131(2):602–8.
7. Nguyen T. Capacitive Sensing of Water Level. Helsinki Metropolia University of Applied Sciences; 2016.
8. EMI_Analyst_Software. Coplanar Capacitance Model [Internet]. 2021 [cited 2023 Feb 16]. Available from: <https://www.emisoftware.com/calculator/coplanar-capacitance/>
9. Martinez-Lopez AG, Guzmán-Caballero DE, Mejia I, Tinoco JC. Silicon based coplanar capacitive device for liquid sensor applications. *Sensors.* 2021;21(17).
10. Khan RR, Kang SW. Highly sensitive multi-channel IDC sensor array for low concentration taste detection. *Sensors (Switzerland).* 2015;15(6):13201–21.
11. Pouchias A, Cunningham PR, Stein J, Kazilas M. Development of a flexible dielectric sensor for flow monitoring of the liquid resin infusion process. *Sensors (Switzerland).* 2019;19(23).
12. BareConductive. Bare Paint Technical Data Sheet. London UK; 2012. p. 1–4.
13. MGChemicals. 842-UR Technical data sheet. Vol. 1.01. Ontario, Canada; 2019. p. 1–6.
14. ASTMInternational. ASTM B117-19 Standard Practice for Operating Salt Spray (Fog) Apparatus [Internet]. 2019. Available from: <https://www.astm.org/b0117->

19.html

15. International Organization for Standardization. ISO 11507:2007 Paints and varnishes — Exposure of coatings to artificial weathering — Exposure to fluorescent UV lamps and water [Internet]. 2007. Available from: <https://www.iso.org/standard/37489.html>
16. Cleary F; MTI. Capacitive touch sensor design guide [Internet]. Microchip AN2934. 2020. Available from: <http://ww1.microchip.com/downloads/en/DeviceDoc/AN2934-Capacitive-Touch-Sensor-Design-Guide-00002934A.pdf>
17. Rivadeneyra A, López-Villanueva JA. Recent advances in printed capacitive sensors. *Micromachines*. 2020;11(4).
18. MatWeb. Overview of materials for Thermoset Polyurethane [Internet]. 2020 [cited 2020 Jun 4]. Available from: <http://www.matweb.com/search/DataSheet.aspx?MatGUID=26606798bc9d4538a7c7eadf78ab082b>
19. KAB_ELECTRO_ACOUSTICS. Dielectric Constants [Internet]. [cited 2020 Jun 4]. p. 1–52. Available from: <https://www.kabusa.com/Dilectric-Constants.pdf>
20. Merck. IR Spectrum Table [Internet]. Technical Data Sheet. 2022 [cited 2022 Feb 21]. Available from: <https://www.sigmaaldrich.com/GB/en/technical-documents/technical-article/analytical-chemistry/photometry-and-reflectometry/ir-spectrum-table>

Chapter 6: RFID Blocking Sensor

6.1 Introduction

RFID communication is often used for sensing networks as it offers the ability to produce wireless, passive (via energy harvesting) sensors for a range of domains. Examples include humidity, temperature, and pH sensors [1–5]. Often these sensors require intricate circuit design and/or interrogation equipment depending on their mode of operation. This increases the development required to tailor these types of systems to specific measurement domains and reduces the ease of field deployment. However, recently, for corrosion sensing, RFID technology has been utilised more simply to directly detect corrosion due to the effect metals can have on the communication between tag and reader. This chapter presents application of a technique that uses this effect to monitor the degradation of organically coated, steel blocking layers placed over RFID tags.

6.2 Background and application of the technique

Recently, there have been advances in using RFID technology for corrosion monitoring based on the principle of shielding. Put simply, this concept involves placing a piece of metal in front of an RFID tag, which partially or fully blocks the ability of the tag to communicate with a reader. The extent to which the metal blocks the RFID tag can be estimated by considering the effective shielding which is given by [6][7][8]:

$$E_s = 168.2 + 10 \log_{10} \left(\frac{\sigma_r}{\mu_r f} \right) + 131.4 \times 10^{-6} t (\sigma_r \mu_r f)^{\frac{1}{2}} \quad (6.1)$$

Where σ_r is the conductivity of the shielding material relative to copper, f is the frequency of the electromagnetic radiation μ_r is the relative permeability of the shielding material and t is the thickness of the layer in μm . Hence as corrosion occurs, the conductivity of the metal decreases through the production of an oxide layer, resulting in a reduced shielding effect. Furthermore, as material is lost via corrosion the thickness of the blocking layer also decreases further reducing the effective shielding. Therefore, as the metal ‘blocking layer’ corrodes, the shielding

effect is reduced allowing reestablishment of communication or an increased quality of communication.

Corrosion monitoring via RFID blocking was introduced as a concept by He et al. [8] with a proof of concept experiment monitoring the corrosion of thin foils and metal based conductive paints. This technique, however, has since been expanded to monitor sheet metal ‘blocking layers’ up to 250µm in thickness [9]. It has been shown in both these studies that there is a strong correlation between mass lost through corrosion and the received signal strength. The concept has previously been explored for use as corrosion sensors in concrete [10] and atmospheric aggressivity sensors [11]. However, it is not believed that this approach has been used to monitor coated steel products. A simplified visual demonstration of the proposed use of this concept to monitor coated steel is shown below in Figure 6.1.

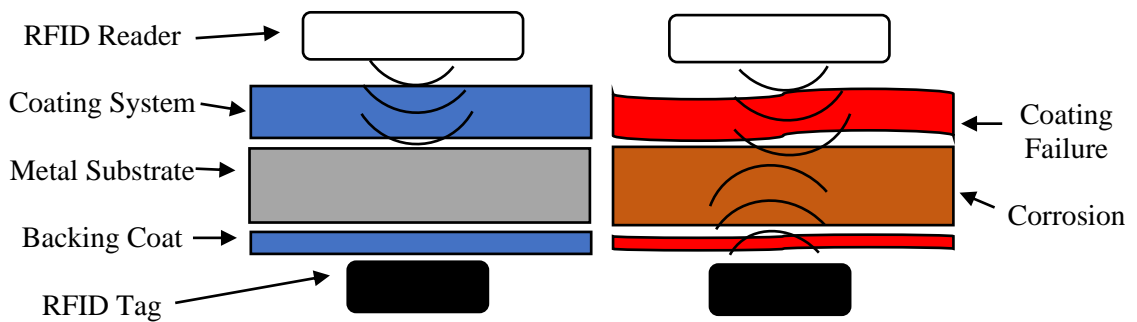


Figure 6.1. Example of an RFID based corrosion sensing system

A potential disadvantage of this method is that the metal may have to significantly corrode before a significant improvement or detection in signal is received from the RFID tag. Despite this, installation and durability of the system would be expected to be significantly easier than other methods given the passive nature of the tags which can simply be attached to a building. Measurements could be taken manually with a handheld reader or automatically using a fixed permanent reader to interrogate several tags.

6.3 Methods and materials

All the RFID tags used in this work were on-metal UHF RFID tags. Initial experimentation and proof of concept used UHF on metal RMT75 tags which are a fairly basic, small tag with a footprint of 15mm by 75mm by 2mm. The specific tags

used, shown in Figure 6.2, came pre-mounted on a metal strip with magnets to allow easy attachment to metal substrates.



Figure 6.2. The RFID tags used in this work

The RFID reader used to interrogate the tags was an Impinj Revolution Speedway R140, which was chosen as it could provide sufficient data to consider tag communication. This was paired with a Times7 compact ETSI antenna the details of which are shown in Table 6.1 below.

Table 6.1. Antenna properties

Name	Times7 SlimLine A5020
Type	Right Hand Circular Polarized
Range	865-868 MHz
Antenna Gain	5.5 dBi Circular

The reader-antenna combination was controlled using the Impinj ItemTest software.

The quality of the communication between a reader and tag can be measured using a few different metrics of which three of the easiest and most common were used in this work. The first was the average number of successful reads per second (SR/s) which was manually calculated using the outputted file containing the tag read information produced by the RFID Reader.

The Received Signal Strength Indication (RSSI) was another metric used which is a measure of the power of the tags backscattered signal and usually ranges from approximately -30dBm (very strong signal received) to -85 dBm (very weak signal received) for UHF RFID tags. This metric was automatically measured by the reader and provided in the outputted results file.

The final metric used was the minimum interrogation power required for a response (MinPow) which was measured by increasing the reader signal strength incrementally until the tag responds. This can be considered the ease at which communication can be established with a lower reader signal strength suggesting increased ease of communication.

A test rig was developed to allow testing of the effect of range and tag orientation. This was produced from laser cut 5mm plywood and contained two stepper motors to control the distance of the antenna from the tag and the orientation of the tag relative to the antenna. The test rig is shown in Figure 6.3.

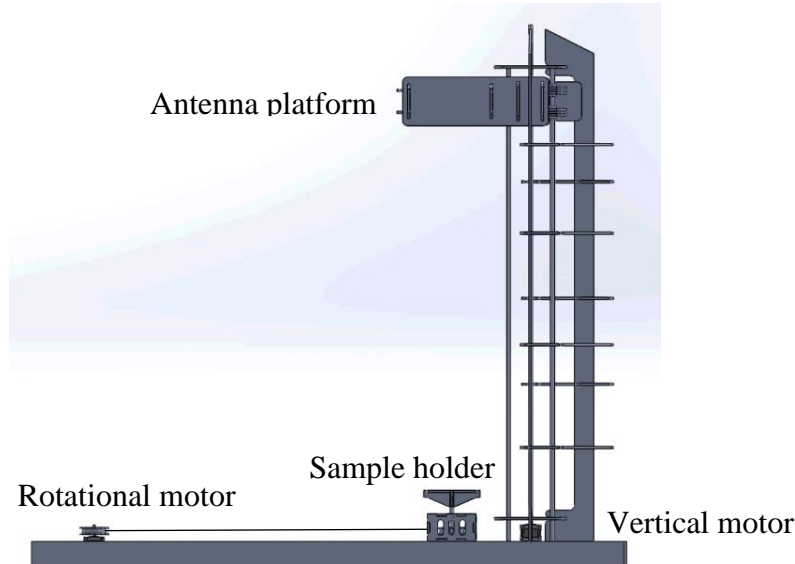


Figure 6.3. The developed test rig used in this work

Tests were conducted in a number of different ways depending on the metric to be measured. To examine the effect of tag orientation the tag was turned through 360° in 18° increments. At each orientation the reader was activated for 20 seconds at the maximum interrogation power of 30dBm. The average RSSI and SR/s were calculated using the recorded results across all orientations. In order to measure the MinPow, a margin test was used during which the reader strength was increased from 10 to 30 dBm in 0.5 dBm steps. At each power level the reader was activated for 20 seconds. During the margin test the tag was not rotated.

A range of materials were used as blocking layers in this work, and these are summarised in Table 6.2 below.

Table 6.2. The range of materials used in this work

Material	Description	Source
Blackplate	≈0.2 mm thick steel	Tata Steel
PVB Coated Blackplate	≈0.2 mm thick steel with an approximately 20μm PVB coating	Lab made
Lacquered Blackplate	≈0.2 mm thick steel with an approximately 50μm Lacomit varnish coating	Lab made
Galvanised Steel	≈0.9mm galvalloy coated steel	Tata Steel Colors
Polyester Coated Steel	≈0.9mm galvanised coated steel with polyester system on front side and backing coat on rear side	Lab made
PU Coated Steel	≈0.9mm galvalloy coated steel coated with 3-layer PU system on front side and backing coat on rear side	Tata Steel Colors
PVC Coated steel	≈0.9mm galvalloy coated steel coated with 2-layer PVC system and backing coat on rear side	Tata Steel Colors

Initial corrosion samples were composed of steel blackplate both uncoated and coated with an approximately 20μm PVB coating layer. The reverse of the PVB coated blackplate sample was covered with electrical tape to prevent corrosion of the rear. The blackplate sample was used as it was expected it would corrode quickly giving results within a few weeks or even days and similarly the PVB coated blackplate to allow results for coated sample to be quickly assessed.

The blackplate samples were expected to corrode across the entirety of the sample due to the lack of, or poor quality of the coating system used. In reality, the samples of interest will include a durable coating system that, in the absence of defects, will initially limit corrosion to the cut edge. To quickly attempt to assess this methods' capability on detecting cut edge corrosion blackplate samples coated with Lacomit varnish were also used. This is a far more durable coating which should limit corrosion to the exposed edges from which it should then spread inwards. The reverse side of these varnished samples were coated with tape to protect it from corrosion.

Further testing involved the use of metallicly coated steel samples, polyester coated metallicly coated steel samples, and Tata Steel coated samples. These were used to represent increased levels of corrosion protection up to the actual product. Due to the additional coating the steel samples would corrode far slower than the blackplate and better represent the metallicly coated steel substrates that are the focus of this work.

Therefore, this would allow an understanding of the degree of corrosion required for a measurable change in the blocking properties. It is important to note that Tata Steel coated, and the uncoated steel substrates were produced with a 20 μ m Zinc + Aluminium (95% wt. Zn 5%wt. Al) coating whereas the polyester coated samples were produced with a 20 μ m galvanised coating (Zn \approx 0.15% Al). Furthermore, the polyester coating on the galvanised steel is inferior to the actual coating products and hence should allow a more rapid assessment of a coated system. Finally, industrial style coated systems would be tested to directly determine the effectiveness of the technique if the previous tests were successful.

6.4 Development of the concept

When considering RFID Blocking as a potential monitoring system there were two concepts that were possible. The first was to simply use the panel that is part of the building as the measured object and place the RFID tag behind this; this has the advantage that the actual asset is monitored but, due to the size of the panel, may require significant degradation to occur to receive a signal. The second option was to use a small representative sample of the same specification as the bulk and attach this and the RFID tag to the outside of the panel; this has the advantage that less damage may be required for a signal but that the test piece is in a slightly different plane to the actual asset to be monitored. Both these concepts are shown in Figure 6.4.

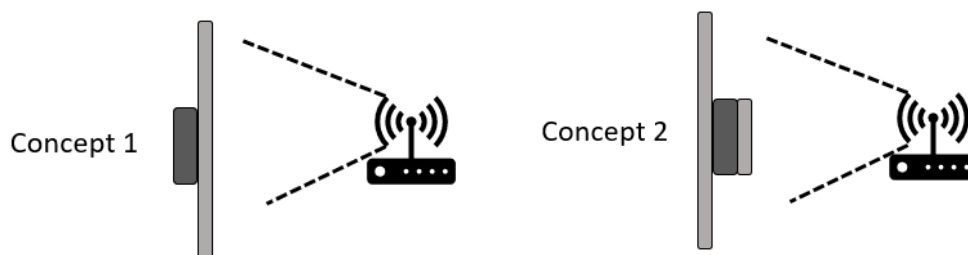


Figure 6.4. The two possible implementation concepts

Initial testing and discussion quickly lead to the second concept being more favourable as it was determined that placing the RFID tag behind such a large piece of façade cladding would be far less effective and more difficult. The tag would have to be placed during construction and, in cladding systems utilizing close fitting insulation, there may not be sufficient space. However, most importantly, it was thought that concept 2 would be more appropriate for detecting in-service corrosion.

With modern coatings, through coating corrosion in the centre of a façade panel is very unlikely and the majority of corrosion will occur at the cut edge. Therefore, it would be inappropriate to centrally place a relatively small RFID tag behind a large piece of cladding as corrosion in this region would be unlikely. Placing a tag near the cladding edge would be more suitable but could present problems due to fixings and joins getting in the way and would still require a significant amount of cut edge corrosion to occur before the tag signal is likely affected.

By placing a small representative sample over the tag and attaching both of these to the outside building far more cut edge area is exposed and being monitored likely allowing greater detection. This is visually shown in Figure 6.5. Furthermore, the tag and sample can be added post-construction and be less limited in terms of locations of deployment.

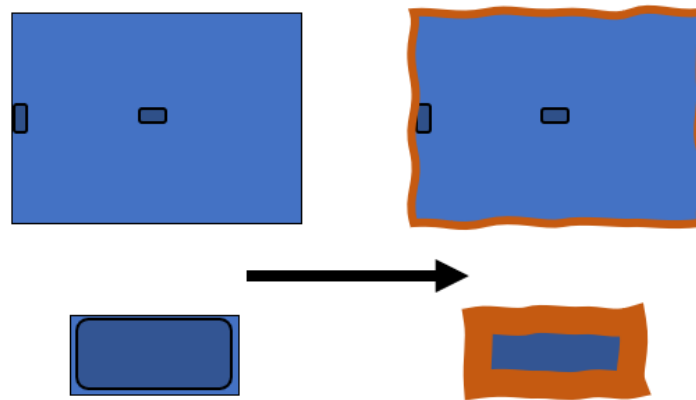


Figure 6.5. Initial reasoning behind choice of second concept. The top of the image shows how attaching RFID tags behind large cladding pieces leads to likely poor detection of cut edge corrosion. The bottom of the image shows how by covering the tag with a small representative sample the whole sample is monitored and detection of cut edge corrosion is far more likely.

Furthermore, the second concept would likely improve the performance of the tag as previous work and manufacturers guidelines state that on-metal tags have the greatest range when placed onto a large piece of backing metal. This was verified for the initial tags used by comparing the tag metrics measured for a naked tag (not mounted on metal) and a tag mounted onto a 10x10cm galvanised steel backing metal (BM) at 25cm. A comparison of the measured RSSI and SR/s is shown in Figure 6.6 and Figure 6.7.

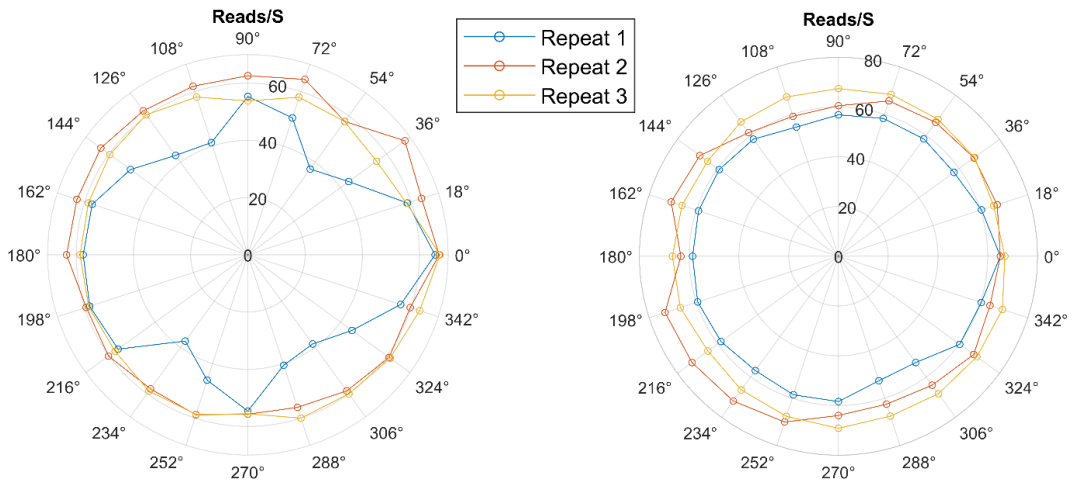


Figure 6.6. Comparison of the SR/s at each angle for the system with no backing metal (left) and a 100cm² backing metal (right)

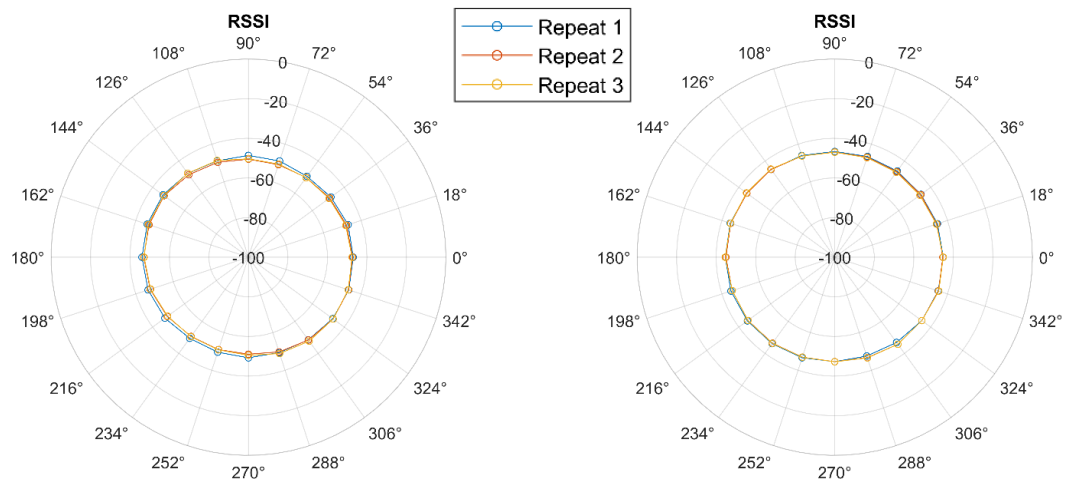


Figure 6.7. Comparison of the RSSI at each angle for the system with no backing metal (left) and a 100cm² backing metal (right)

It was observed that the average, minimum and maximum SR/s and RSSI for the tag mounted on the backing metal was on average improved compared to the tag without backing metal suggesting improved tag performance across all directions.

Furthermore, the standard deviation of the BM system was lower than the no BM system suggesting that more repeatable results were gained by using a BM. It was also observed that for the BM system the orientation of the tag had a relatively small effect on the RSSI and SR/s, hence polar plots are discontinued from here onwards in favour of the orientation averaged RSSI and SR/s.

In reality a system like this would be deployed onto a building façade and hence the BM would be far larger than 100cm² and it would be beneficial if the interrogation

distance was far larger than 25cm. To determine the effect of BM size and interrogation distance three systems were tested at a distance of 5, 10, 25 and 50cm. The three systems were no BM, a 100cm² BM and a 225cm² BM as this was the largest size possible to fit in the testing rig. Although still far smaller than the likely deployment BM this test was designed just to give an indication on how the results may change. The resulting average RSSI and SR/s are shown in Figure 6.8.

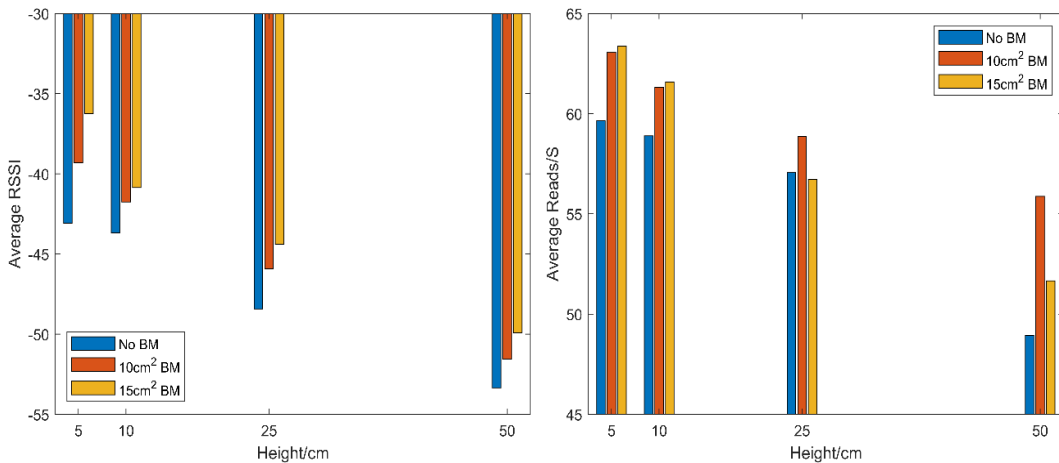


Figure 6.8. Resulting average RSSI values (left) and SR/s (right) recorded during the BM size and interrogation distance test

As expected, both measurement metrics show that as the interrogation distance increases, the signal strength received decreases. This suggests that there would be a limit to how far measurements can be taken from the sensor and that it would be important to ensure that this distance is kept constant during repeat measurements. Although measurements at 50cm still showed reasonable signal strength and SR/s it is important to note that this is the tag with no blocking layer. Comparing the two metrics, RSSI showed that for every distance a larger BM improved the signal strength suggesting that the size of the building façade should not degrade detection range. This trend was not always observed in the SR/s, but it is thought this may be due to the much larger inherent deviations in the reads/s measurement. It is still important to note, however, that both systems utilising a BM performed better than just the naked tag alone and this further suggests concept 2 is a better proposal.

6.5 Determination of blocker size

6.5.1 Initial size comparisons

Having chosen concept 2 as the deployment method, the blocker size became an important consideration. Previous work, [8,9], has often simply used a blocking layer of the same dimensions of the tag however it was not always clear how this decision had been reached. Therefore, a range of blocking layer sizes were first examined to determine the effect of their size on tag response as well as the detection of defects. To understand this blocking layers were produced out of the PVC and PU samples ranging in size from 5mm by 65mm to 20mm by 80mm in increments of 5mm. The smallest tag size, therefore, fitted on the tag with 5mm of space in all directions whereas the largest overlapped the tag by 2.5mm in all directions, as shown in Figure 6.9.

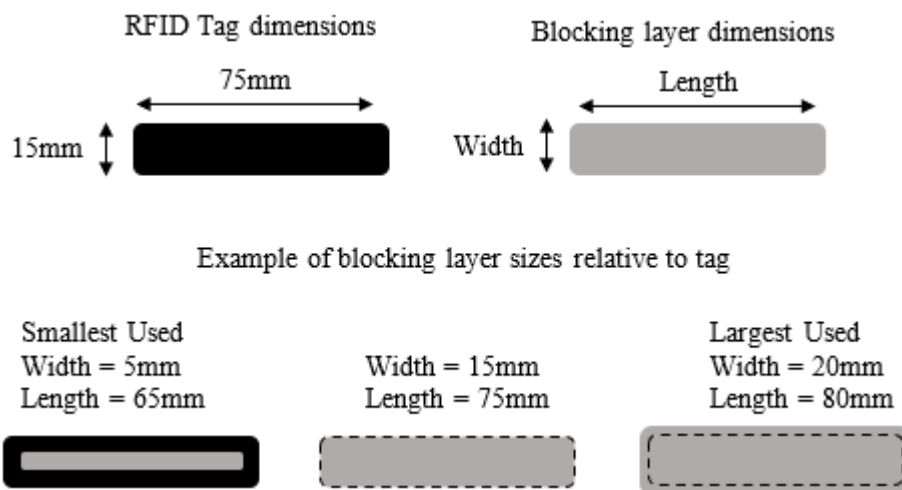


Figure 6.9. Key dimensions of RFID tag and blockers used in this work

It was thought that this would give a good indication of how a range of width and length tags performed. Also, the relative performance of each size blocking layer was thought to give an indication on the likely detectability of cut edge corrosion if we very simply model cut edge corrosion as decreasing the sample in size.

Measurements were taken at 25cm with a 100cm² backing metal and the results are given in Table 6.3 and Table 6.4.

Table 6.3. Measured RSSI, SR/s and MinPow (MP) for each size PVC blocking layer at 25cm. For reference the RFID tag measures 15mm by 75mm

PVC Metric	Width = 5mm			Width = 10mm			Width = 15mm			Width = 20mm		
	RSSI	SR/S	MP	RSSI	SR/S	MP	RSSI	SR/S	MP	RSSI	SR/S	MP
L = 65mm	-44	66	22.5	-44	66	27	NR	NR	NR	NR	NR	NR
L = 70mm	-44	64	23.5	NR	NR	NR	NR	NR	NR	NR	NR	NR
L = 75mm	-44	66	24.5	NR	NR	NR	NR	NR	NR	NR	NR	NR
L = 80mm	-47	64	28	NR	NR	NR	NR	NR	NR	NR	NR	NR

Table 6.4. Measured RSSI, SR/s and MinPow for each size PU blocking layer at 25cm. For reference the RFID tag measures 15mm by 75mm

PU Metric	Width = 5mm			Width = 10mm			Width = 15mm			Width = 20mm		
	RSSI	SR/S	MP	RSSI	SR/S	MP	RSSI	SR/S	MP	RSSI	SR/S	MP
L = 65mm	-44	67	24	-46	62	27	NR	NR	NR	NR	NR	NR
L = 70mm	-44	64	24	NR	NR	NR	NR	NR	NR	NR	NR	NR
L = 75mm	-45	66	27	NR	NR	NR	NR	NR	NR	NR	NR	NR
L = 80mm	-48	67	29	NR	NR	NR	NR	NR	NR	NR	NR	NR

From these results it was observed, as expected, that blocker size does have a significant effect on the tags response. However, it appeared that width seems to be the key dimension when considering the blocking power of a sample. For example, a sample with a sufficiently thin width will allow communication even when the length is larger than the RFID tag itself. It is promising that, generally, as the blocking layer decreased in size the RSSI and SR/s improved suggesting detection of a gradual decrease in size over time may be possible. However, the MinPow metric displayed this trend far better than the RSSI or SR/s; this was shown by comparing the % change in measured metric for each increase in length for the 5mm wide samples, Figure 6.10.

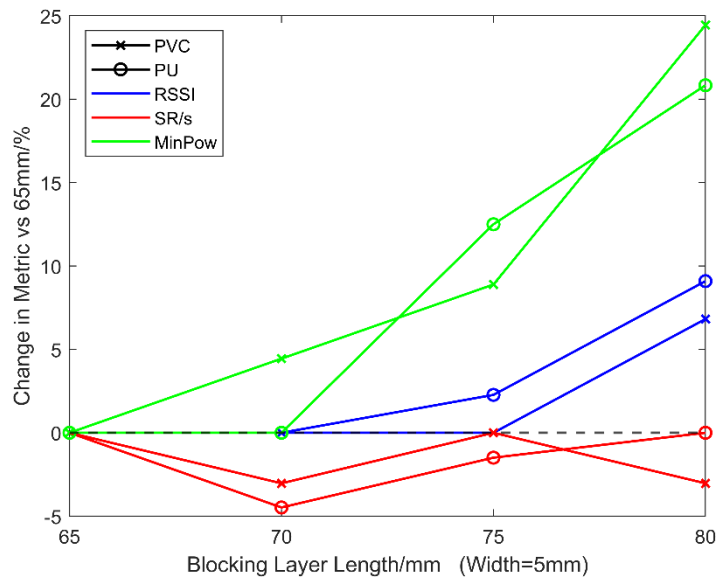


Figure 6.10. Comparison of the three metrics when measuring differences in tag response due to increases in blocker length (width=5mm)

This suggested that actually the SR/s metric was a fairly poor indicator of blocker layer size and therefore may not be particularly suitable for the detection of corrosion driven changes. The RSSI was a better indicator although was far less responsive to the changes in length when compared to the MinPow metric. Not only did the MinPow seem able to detect smaller changes to the blocker layer length it also produced a far greater response increasing 20-25% in magnitude compared to just 5-10% for the RSSI. The conclusion of this was that MinPow should be the metric of choice for further testing and the SR/s should be viewed with caution. The RSSI appears to compliment the MinPow but appears to have decreased sensitivity for an application such as this.

6.6 Artificial defect detection

To further assess the ability of this technique to detect changes in the blocking layer, 5 lots of 2mm holes were incrementally punched in the samples, Figure 6.11, to see how the loss of small amounts of metal from the blocking layer affected the response. While this was not particularly representative of the changes that would occur as a result of corrosion it was used to gain an understanding of how the size of the tag affects the response to changes. All these tests were carried out at 25cm with a 100cm² BM as used in the previous tests. The test was carried out on all the samples in the previous test with the exception of the 5mm wide samples as these were too thin to punch the holes in without causing significant bending and

disforming of the blocking layer. All three metrics; average RSSI and SR/s and the MinPow were measured at each stage.








Example Tag W=15 L=75m	5 Holes	10 Holes
 +  = 		
	15 Holes	20 Holes
		

Figure 6.11. Example of one sample showing how 2mm holes were punched through the blocking layer

6.6.1 PVC coated samples

The resulting RSSI measurements for the PVC samples are shown in Figure 6.12 from which it was observed that a general trend of improvement of signal with increased artificial damage exists. However, it was also concluded that the accumulation of damage is not well detected. For example, there was a large signal improvement for most blocking layers when comparing 0 to 20 holes however the transition from 5 to 10 to 15 was not fully represented as incremental improvements in signal for many of the samples. This may be due to the metric itself being unsuitable for detecting changes such as those imposed in this test. Certainly it seemed that once the RSSI has reached a level of approximately -40 to -45 the addition of more holes had little effect. It is important to note that the two largest size blocking layers produced no response at all confirming that if the blocking layer is too large, even significant material removal will not facilitate communication. When comparing the other sizes of blocking layer there appeared to be no significant difference in the levels of detection.

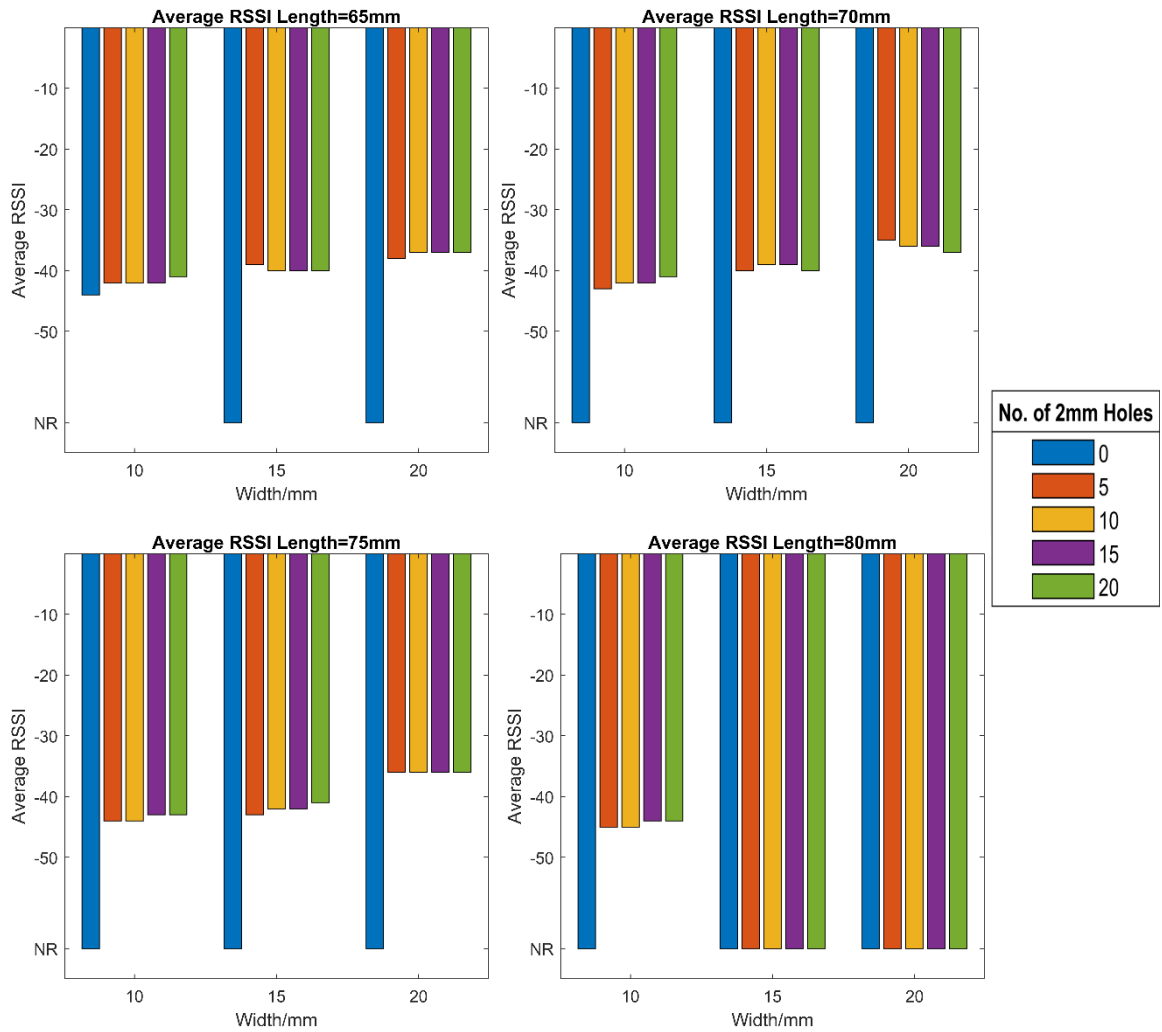


Figure 6.12. Average RSSI recorded for each PVC blocker size under the artificial damage test

Similar results are seen when considering the SR/s metric, shown in Figure 6.13. Again, there was an obvious increase in successful reads when comparing 0 and 20 holes however the 5, 10 and 15 results do not always provide gradual improvements in reads as would be optimal. Certain samples, such as 70mm by 15mm, did appear to better detect the accumulation of damage but on the whole the metric provides little confidence in the ability to do this. It was thought a similar issue to the RSSI metric existed where, once the damage is sufficient, the SR/s cannot increase significantly with further damage. This was observed in the Length = 65mm samples; a rough maximum of approximately 63-65 SR/s was reached once 5 holes are present which was not increased even with the addition of another 15 holes. This provided evidence that the size of the blocker layer is crucially important to what is being detected. A small blocking layer will detect smaller amounts of damage but be poorer at indicating accumulation of further damage whereas a larger blocking layer

may be poor at detecting very slight damage but better at detecting accumulation of significant damage.

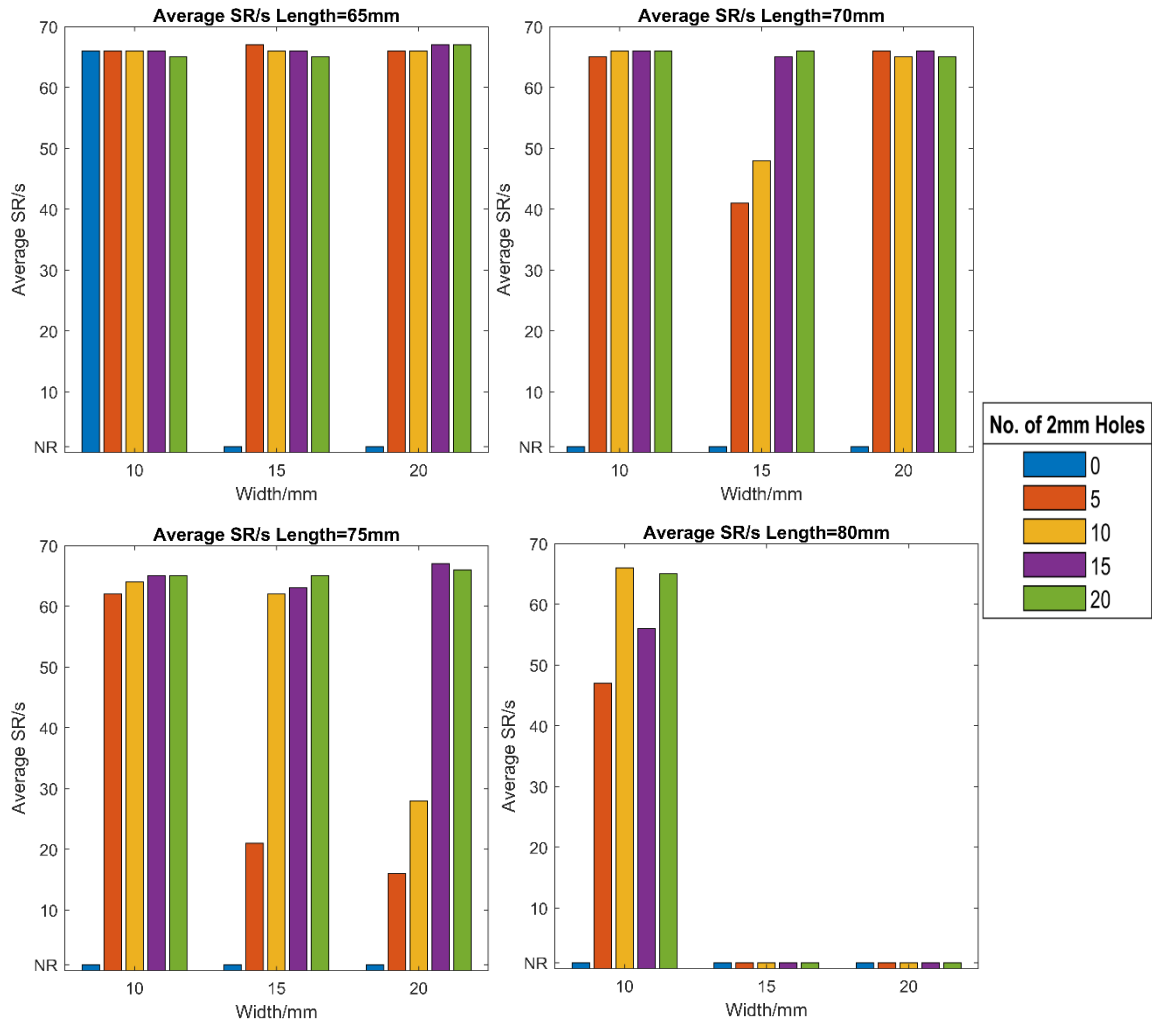


Figure 6.13. Average SR/s recorded for each PVC blocker size under the artificial damage test

In comparison to the previous two metrics, the measured MinPow for each PVC sample during the test, shown in Figure 6.14 provided far more promising results. For those samples of sufficient size to show a change, the change in MinPow between a sample with 0 and 20 holes was significant, and there was a gradual decrease in the MinPow as damage is accumulated. This implied that this metric can not only detect between intact and damaged but an assessment of the quantity of damage may be possible. Interestingly the sample where the levels of damage were most easily distinguished; and therefore, the sensitivity of the metric was highest, appears to be the 75mm by 15mm blocking layer which corresponds to the dimensions of the RFID tag. However, it was difficult to conclude that this is the best

blocking layer size on this single test result especially when considering that the holes were punched randomly on each sample.

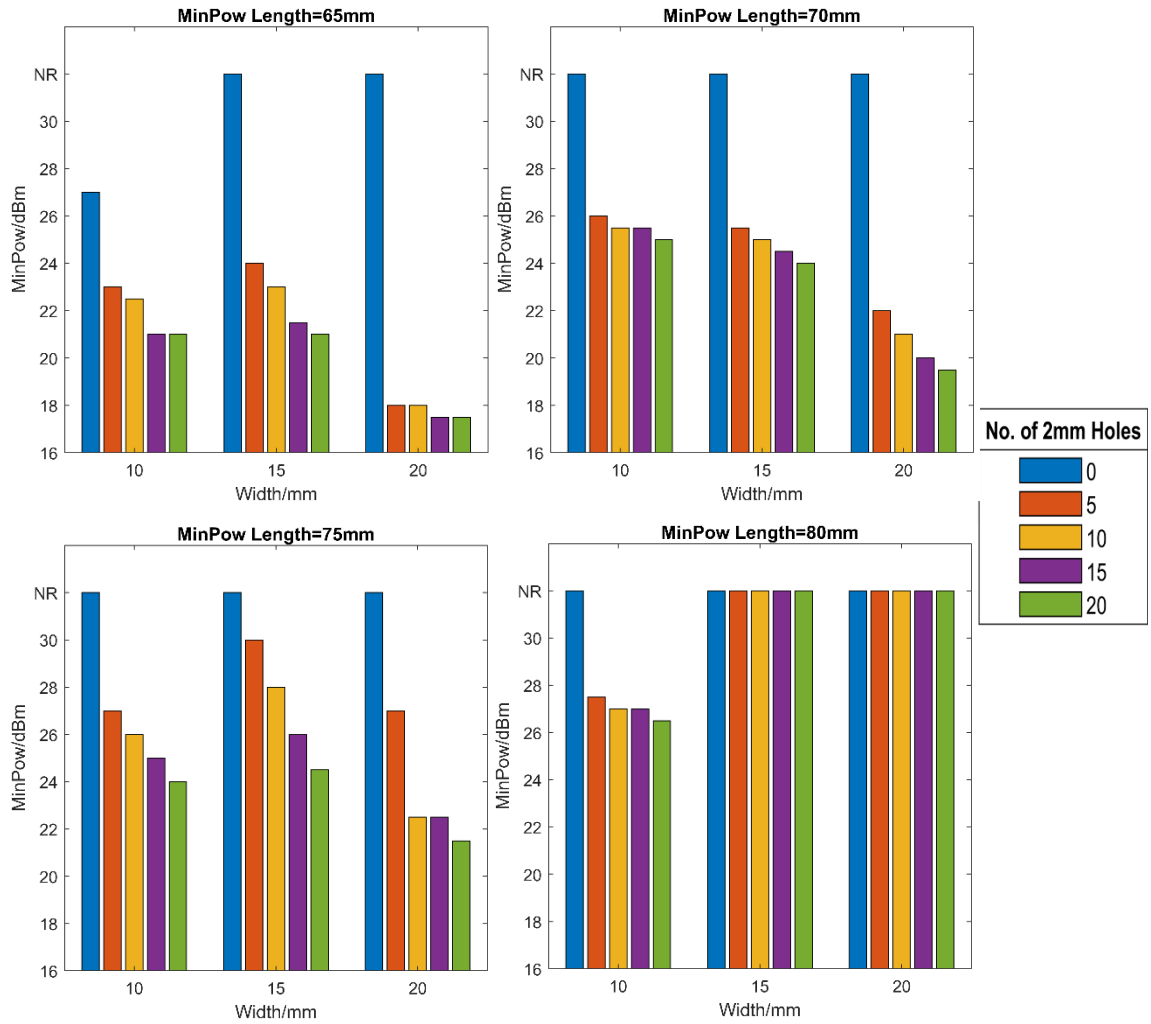


Figure 6.14. The MinPow recorded for each PVC blocker size under the artificial damage test

6.6.2 PU coated samples

The results from the three metrics for the PU samples are very consistent with the PVC samples so are not each described in considerable detail. All the metrics showed the ability to detect a significant change in tag response when comparing 0 to 20 holes however it was only the MinPow that provided the ability to consistently detect the small incremental changes between each level of artificial damage. The SR/s metric did perform better for this test, tracking the increase in holes more accurately for more of the samples, although perhaps this just suggests that while this metric has the ability to detect damage accumulation it cannot be relied upon to do so consistently. Similarly, to the PVC samples, the two largest blocking layers provided no response during the test. From both these sets of samples, it would be concluded

that this method can be used to detect artificial damage and metal removal and that the MinPow metric shows promise at displaying the degree of the damage sustained.

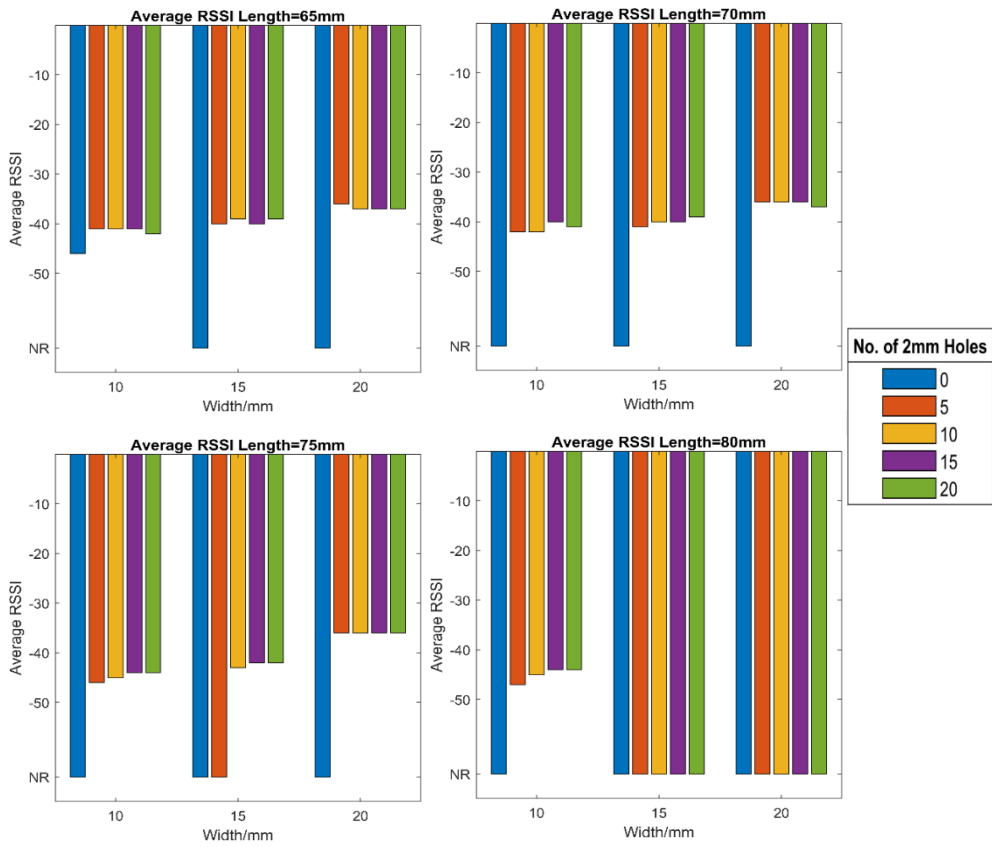


Figure 6.15. Average RSSI recorded for each PU blocker size under the artificial damage test

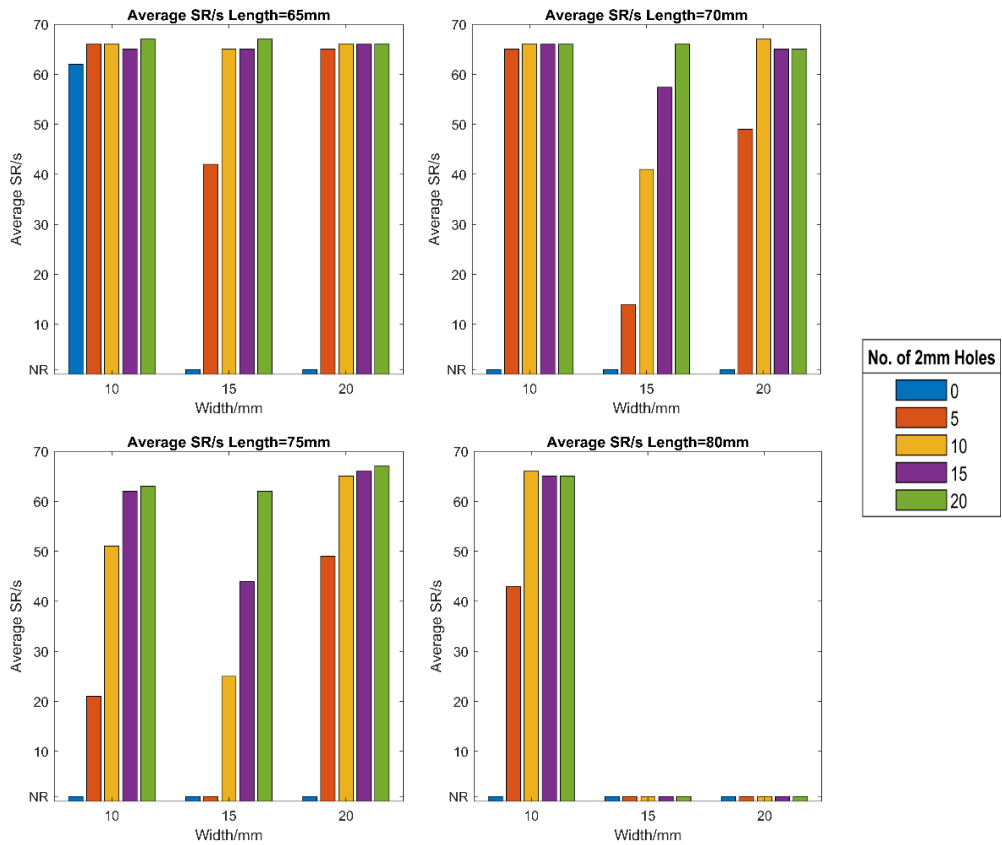


Figure 6.16. Average SR/s recorded for each PU blocker size under the artificial damage test

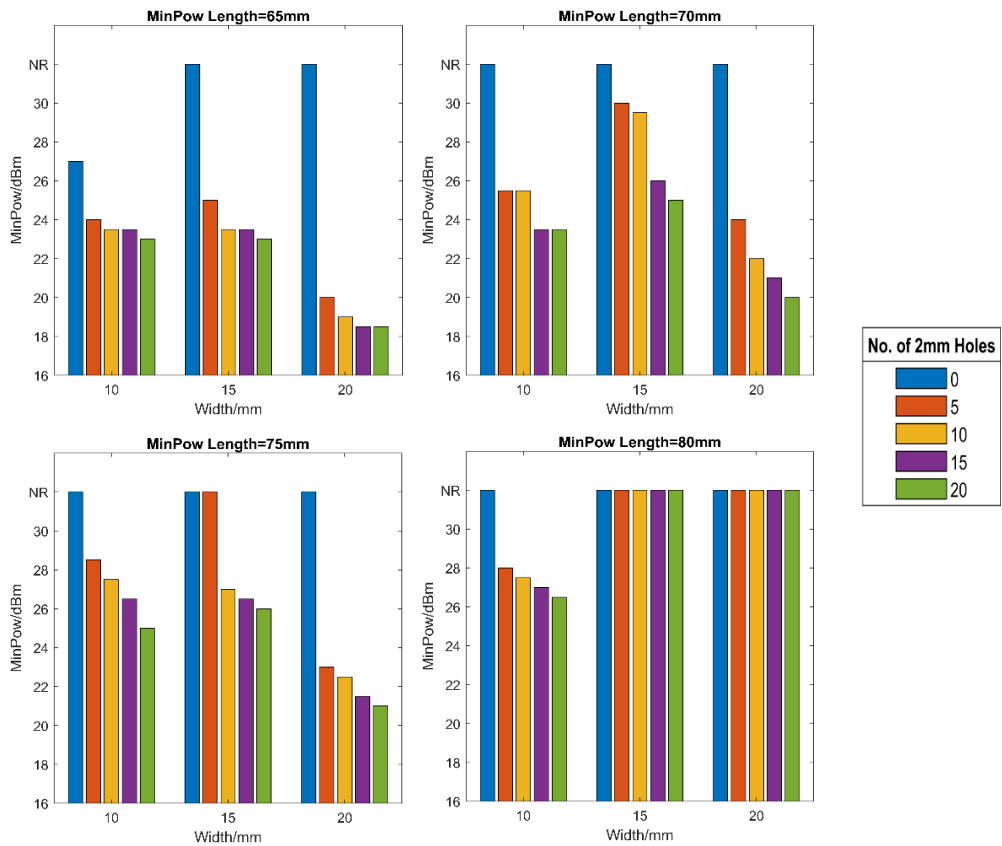


Figure 6.17. The MinPow recorded for each PU blocker size under the artificial damage test

6.6.3 Overall comparison

An overall comparison of the measured percentage change in each metric as a result of the increase in the number of holes is shown in Figure 6.18. To create this comparison, an average of the percentage change per incremental step was taken across all the sizes of sample that showed a response. Comparison was made to the 5 holes sample as many of the 0 holes samples showed no response. From this analysis it was confirmed that all metrics recorded the expected changes as a result of an increased number of holes. The RSSI decreased, the SR/s increased and the MinPow decreased.

The RSSI was shown to have very little sensitivity, however, to this specific test and showed a maximum change of approximately 2% across the test. It did, however, have the lowest variance when considering the average changes measured. This shows that the RSSI provided a repeatable, yet insensitive method of measurement for this test.

The SR/s showed a far greater average increase of approximately 60-80% when comparing the 20 holes sample to the 5 holes, however the associated error with this average value was considerable. This shows that the SR/s provided a sensitive method of measurement but not a repeatable one.

The MinPow appears to provide a middle ground of measurement with reasonable sensitivity (approximately 10% change in value from 5 to 20 holes) while remaining repeatable. Furthermore, the fact the MinPow provided a fairly linear trendline confirms its ability to detect incremental change far more accurately than the other methods. This method is confirmed therefore to likely be the best measurement method moving forwards.

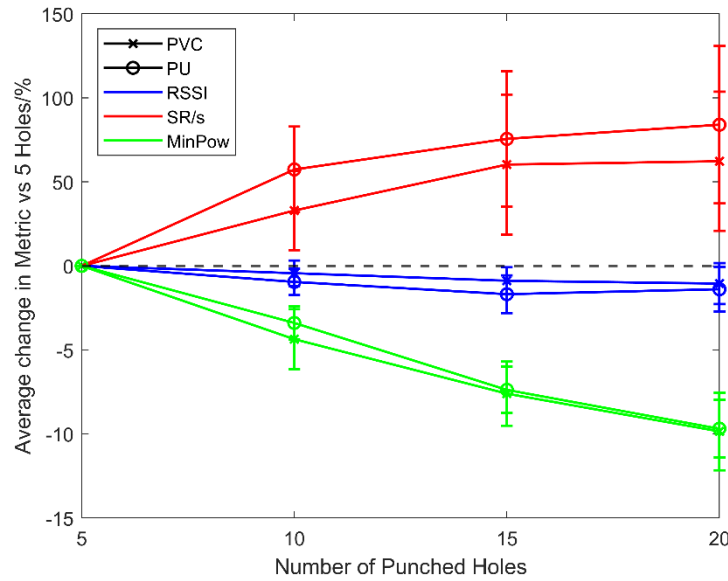


Figure 6.18. Comparison of the average change in metric compared to the value recorded for 5 holes.

Note the difference in scale for the positive and negative axis

6.7 Corrosion based testing

For reasons of rapid prototyping and assessment all the previously carried out tests did not involve corrosion of the substrate but rather artificial damage simulating metal loss due to corrosion. Therefore, the next step was to verify if the loss of metal due to corrosion was detectable. For this test a number of different blocking layer substrates were used as described earlier.

For this test the blocking layer sizes, in mm, were 10 by 70, 15 by 70, 10 by 75, and 15 by 75. In order to rapidly corrode the samples, they were placed in a salt spray tester in which a 35°C and 100% humidity environment of 5% NaCl solution was present. Each week, for testing, the blocking layers were removed from the chamber, allowed to dry naturally, and placed on top of an RFID tag. The test interrogation distance was kept at 25cm with a 100cm² BM. Each time the samples were removed they were photographed to visually track the degree of corrosion the sample had undergone.

6.7.1 Blackplate substrate samples

The appearance of the blackplate samples during the test is shown in *Figure 6.19*. Corrosion was clearly visible on both the coated and uncoated blackplate samples after just 1 week and this became more significant as the exposure time increased. As expected, the PVB provided a poor level of protection to the substrate although the

sample did visually appear to corrode slightly slower than the uncoated blackplate sample. The degree of corrosion in week 4 was significant and hence the test was stopped at this time.











Week	Blackplate	Blackplate coated with PVB
0		
1		
2		
3		
4		

Figure 6.19. Blackplate sample condition during testing at each measurement interval

The measured tag metrics for both blackplate substrate samples are shown in Figure 6.20, Figure 6.21 and Figure 6.22. Promisingly, the uncoated blackplate samples showed a clear decrease in the MinPow with increased time in the salt chamber, suggesting a reduction in the effectiveness of the blocking layer as the degree of corrosion increases. This trend was also indicated in the other two measurement metrics with a clear increase from the original state to the 4-week state. However, as before, these metrics did not display well the accumulation of damage for similar reasons as the previous test. Rapidly, a relatively high value was reached for these metrics which could show little further improvement even with an increased degree of corrosion. It was promising, however, to see that, for all metrics, the smallest blocking layer generally maintained the highest level of communication and the largest the least for each stage of the test. This reaffirmed the results given in the previous sections as to the effect of blocker size on communication quality.

The PVB coated blackplate provided a number of unexpected set of results. Firstly, all the blocking layers provided a response initially (0 Week) in contradiction to the similarity sized uncoated blackplate samples of which only the smallest blocking layer provided a response. It was assumed this was down to the tape layer on the reverse of the coated sample which, due to its considerable relative thickness

compared to the blackplate, reduced the effective blocking effect by introducing an insulative layer between the tag and blocker. This is a method used for decreasing the effect of metal blocking in tag design [12]. Also unexpected was that all three metrics showed little or no change throughout the course of the experiment despite the visual indication that significant corrosion had occurred. As the uncoated sample had showed that the corrosion of the metal lead to a decrease in shielding, the logical conclusion was that some other factor must be causing an increase in shielding that was balancing this out to provide little change. It was concluded that this was most likely caused by some combination of water absorption of the PVB, water penetration and blistering of the PVB and water getting trapped underneath the tape on the back side of the sample. The presence of water around an RFID tag is known to reduce communication [13,14] and hence it was thought accumulation of water in the three suggested ways was offsetting the reduction in blocking effectiveness due to corrosion. Although the samples were allowed to dry before testing it is likely water trapped in or under the coating and or tape would have remained during the testing procedure.

The results of testing these substrates therefore provide confidence that detection of corrosion was possible. However, it was also shown that additional processes occurring during the degradation of coated steel, such as the uptake of water and blistering, may adversely affect results. This may reduce the effectiveness of this technique as a detection method.

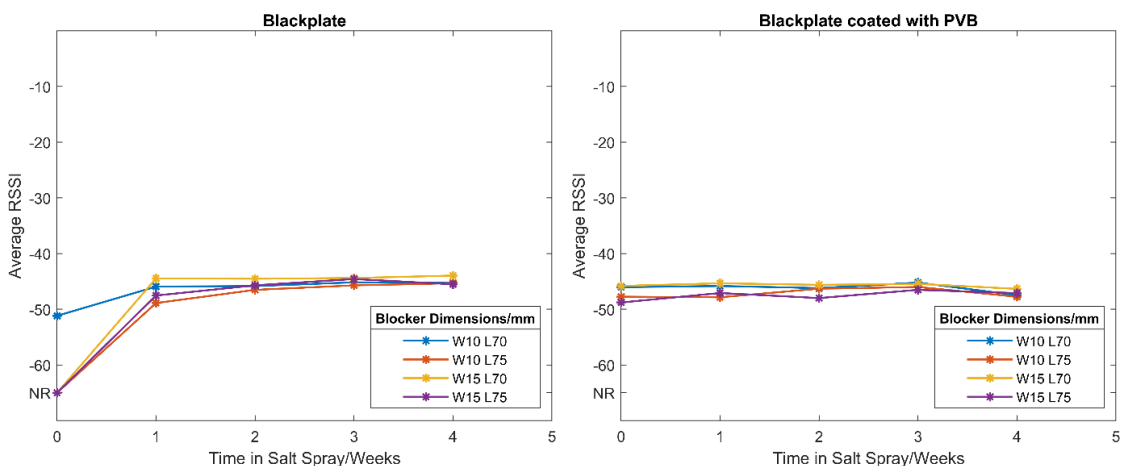


Figure 6.20. Average RSSI recorded during the corrosion test for the blackplate substrate samples

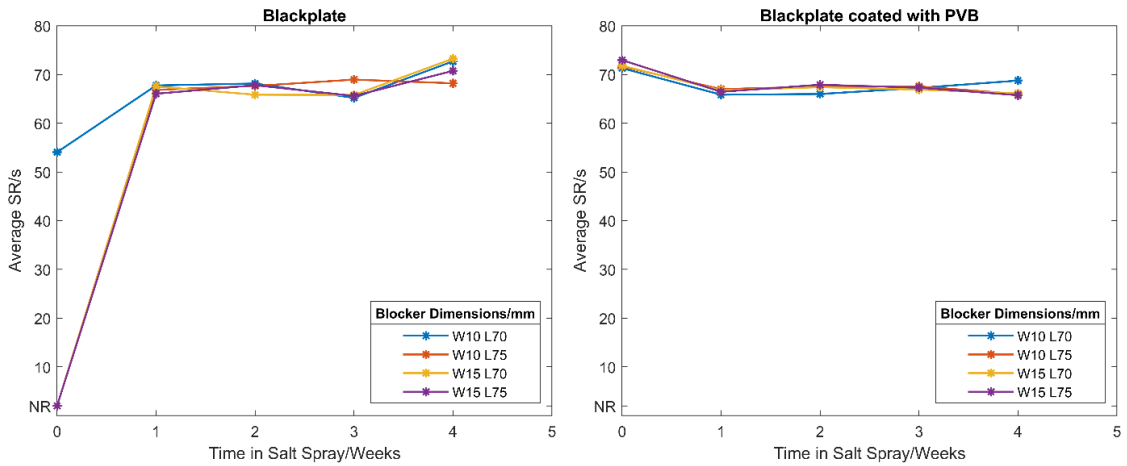


Figure 6.21. Average SR/s recorded during the corrosion test for the blackplate substrate samples

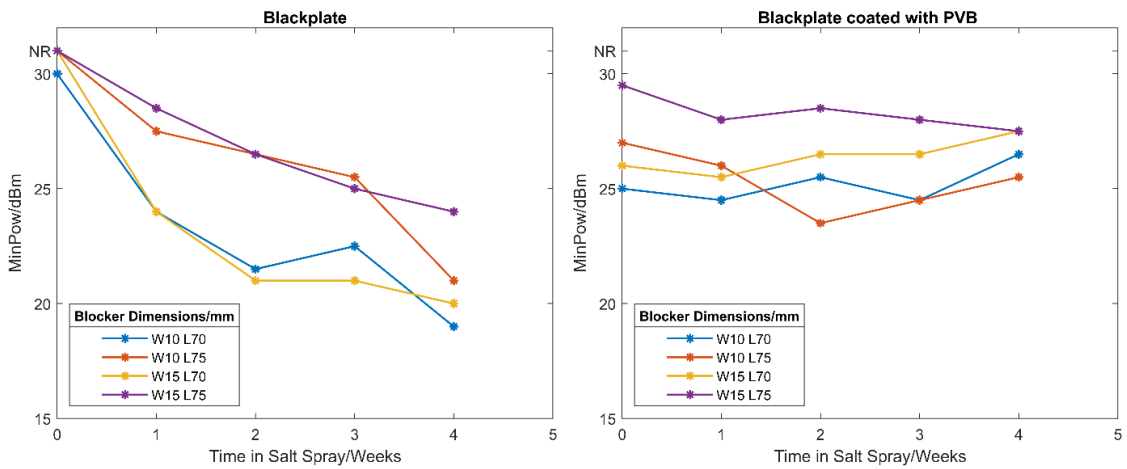


Figure 6.22. The MinPow recorded during the corrosion test for the blackplate substrate samples

6.7.2 Lacquered samples

The condition of the lacquered blackplate samples throughout the duration of the test is shown in Figure 6.23. As intended the corrosion, although still severe, was better restrained to initiate at, and propagate from, the cut edge in weeks 1 and 2. However, as the test duration increases beyond 2 weeks the severity of the corrosion was such that a majority of the sample was corroded.






Week	Blackplate coated with Lacquer
0	
1	
2	
3	
4	

Figure 6.23. Lacquered blackplate sample condition during testing at each measurement interval

The measured tag metrics for the lacquered blackplate samples are shown in Figure 6.24, Figure 6.25 and Figure 6.26. Perhaps caused by the better constraining of corrosion to the cut edge, there was a far smaller improvement in tag response across all metrics in the first 2 weeks compared to the previous blackplate samples. This was especially noticeable in the larger sized samples which only allowed a response after several weeks of corrosion. This suggests that cut edge corrosion may be detectable, however also, that the level of cut edge corrosion that must occur for detection to be possible is fairly significant. For example, by week 4 the largest tag had only just corroded enough to allow a tag response, yet the amount of red rust on the sample was significant.

It was promising that these coated sample do show a gradual improvement in tag-reader communication as a result of exposure. This suggests that the hypothesis as to why the PVB coated samples did not show this behaviour may be correct as the Lacomit does not absorb water as readily and far less entrapped water (through formed blisters) was observed. Therefore, it was thought that this technique could be used to monitor coated sample as long as water uptake is minimal.

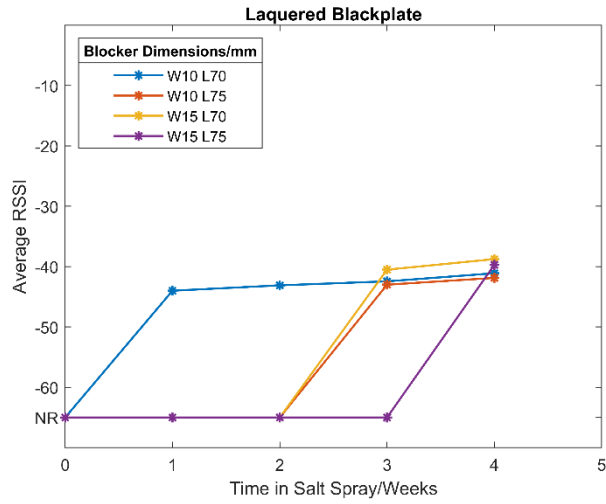


Figure 6.24. Average RSSI recorded during the corrosion test for the lacquered blackplate samples

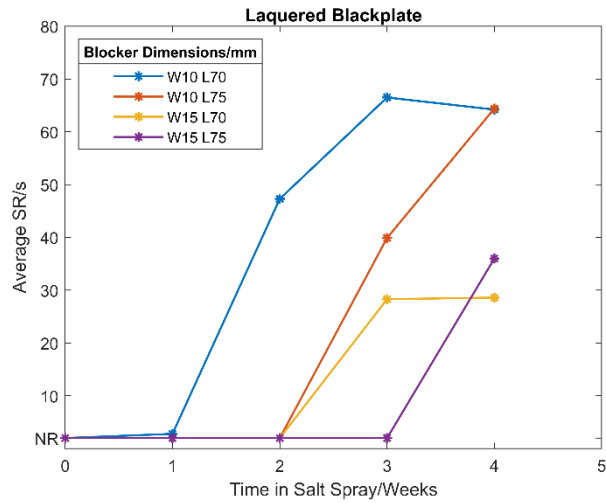


Figure 6.25. Average SR/s recorded during the corrosion test for the lacquered blackplate samples

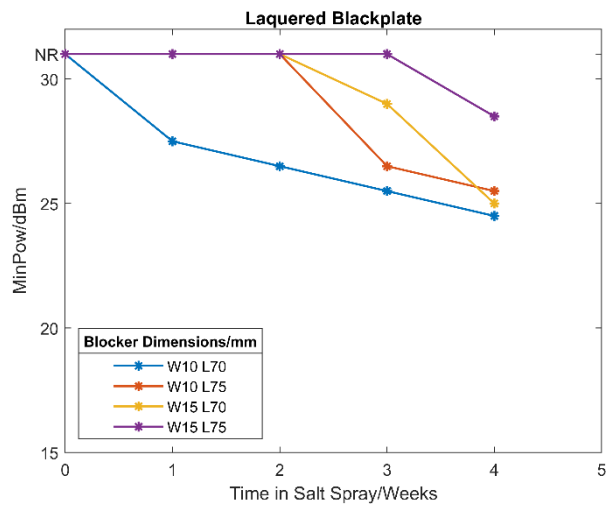


Figure 6.26. The MinPow recorded during the corrosion test for the lacquered blackplate samples

6.7.3 Metallicly coated samples

Due to the presence of the additional metallic layer both the uncoated and polyester coated steel samples mainly experienced the formation of white rust for the first 6-8 weeks. After approximately 8-10 weeks red rust was visible indicating attack of the steel substrate was occurring. The coated sample developed blistering around the cut edge at approximately week 4-6 and the blistered area increased in size for the duration of the test. At 15 weeks significant red rust was prevalent on entirely of the uncoated galvanised steel samples and the rear and edges of the polyester coated steel samples.




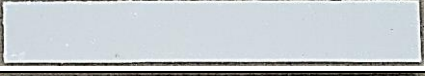










Week	Galvanised Steel	Galvanised Steel coated with polyester
0		
2		
4		
6		
8		
10		
15		

Figure 6.27. Galvanised sample condition during testing at each measurement interval

The recorded tag metrics for both these samples during the test are shown in Figure 6.28, Figure 6.29 and Figure 6.30. It was seen that for all samples there was increased tag response when comparing the 0-week sample to the 15-week sample however there was not often an incremental increase in response each week. It was interesting that the polyester coated samples took only 1-3 weeks for the values of RSSI and SR/s to increase to a maximum level and remain constant whereas the galvanised steel samples took 8-10 weeks. This was attributed to the rapid corrosion of the rear of the polyester sample which was coated with a poor performance liner coating which quickly failed. This exposed surface, which was protected to a lesser extent, by its inferior metallic coating, then proceeded to corroded faster than the Galvalloy® coated samples.

While the RSSI and SR/s did provide a degree of damage estimation, the MinPow appears to be the most comprehensive. The galvanised samples showed a consistent decrease in MinPow over time with a delay in initial response that would be expected based on the size of each sample. The polyester coated samples showed a rapid decrease in MinPow over the first 1-3 weeks but then this levelled off far more than the galvanised samples for weeks 4-10. It is possible that water uptake into the coating was limiting the effect of corrosion on the response during this period. At week 15 it is possible that sufficient corrosion has occurred that the MinPow decreased even when mitigated somewhat by the presence of water.

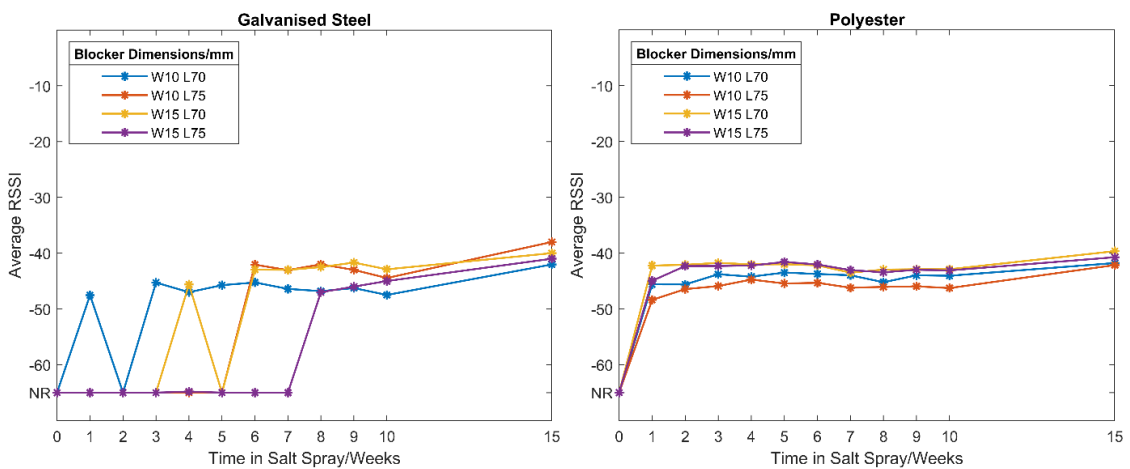


Figure 6.28. Average RSSI recorded during the corrosion test for the galvanised steel substrate samples

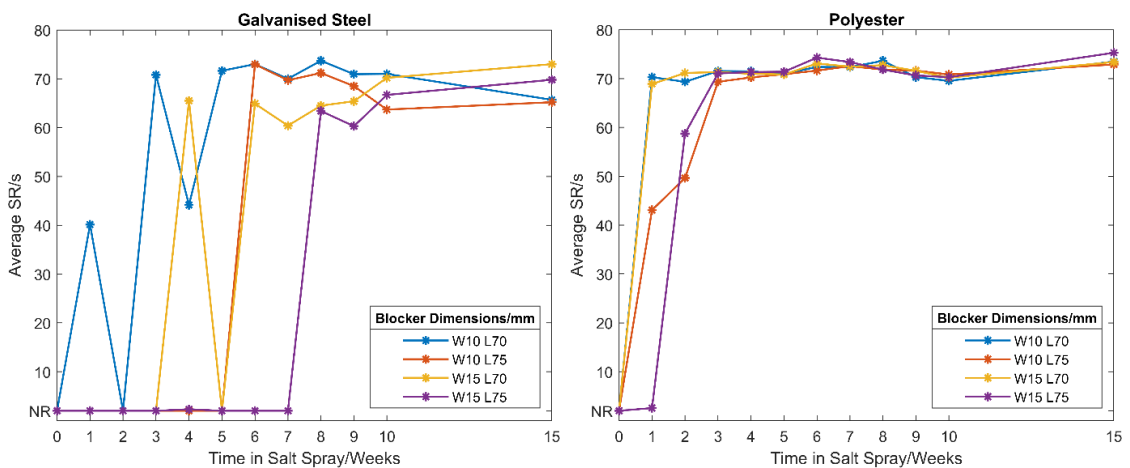


Figure 6.29. Average SR/s recorded during the corrosion test for the galvanised steel substrate samples

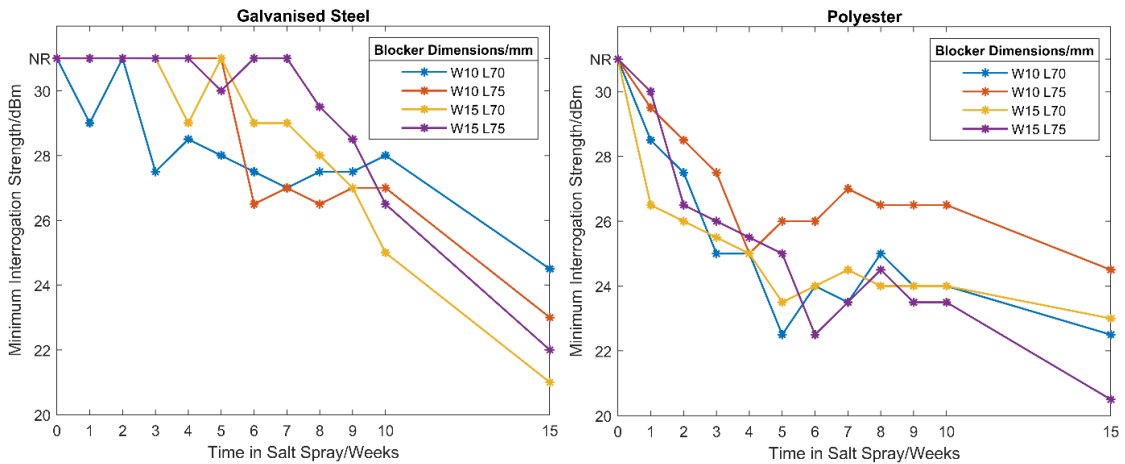


Figure 6.30. The MinPow recorded during the corrosion test for the galvanised steel substrate samples

6.7.4 Tata Steel Coated Samples

As would be expected the PVC and PU samples perform much better during salt spray exposure although began to show some blistering, especially around the cut edge, from week 2 onwards. More significant was the damage to the reverse side of the PVC and PU samples, where the less protective coating failed, and some white rust was observed within 4-6 weeks. At around 8-10 weeks the reverse side showed red rust and the front side showed significant blistering. The PVC samples generally showed larger blisters covering a reasonable area of the front surface whereas the PU samples showed smaller ones concentrated around the edges. However, compared to the rear of the sample the cut edge experienced far less corrosion. This, therefore, was not considered the most representative test of the coated product as the observed corrosion was far higher than would be expected if the front face, and cut edge, alone was exposed as in normal use.

Week	PVC	PU
0		
2		
4		
6		
8		
10		

Figure 6.31. Actual coated product sample condition during testing at each measurement interval.

The front and back of the sample is shown for each week.

Unfortunately, all the PVC samples allowed no tag response throughout the test even though there was evidence that some corrosion had occurred to the rear of the sample. The PU samples began to allow a tag response at the 2–4-week mark, depending on size, and did show some improvement in tag response from this period to the 10-week measurements. However, as has been observed previously, there was no consistent week on week improvement in response measured by any of the metrics. For example, the RSSI, Figure 6.32, showed an increase to approximately -40 to -45 by week 5 and then stayed fairly constant for the rest of the test. The SR/s, Figure 6.33, increased to week 5 and then somewhat fluctuated both up and down. Finally, the MinPow, Figure 6.34, decreased to week 5 but then remained at a similar level for the rest of the exposure for all but the largest tag which showed a fairly erratic decrease with time.

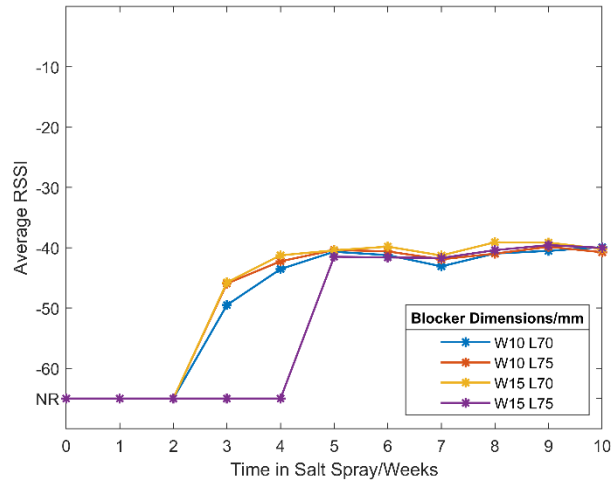


Figure 6.32. Average RSSI recorded during the corrosion test for the PU samples

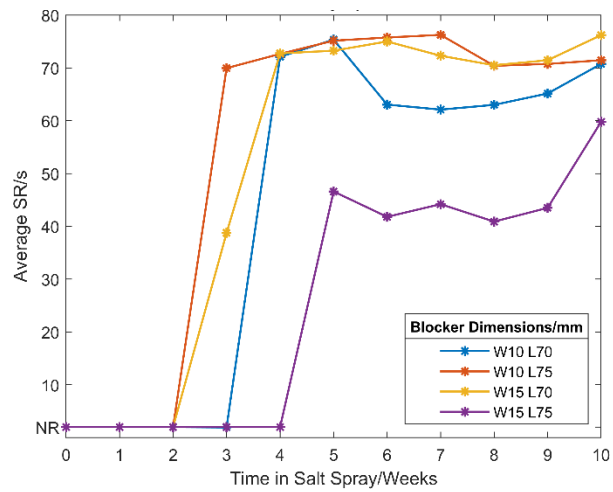


Figure 6.33. Average SR/s recorded during the corrosion test for the PU samples

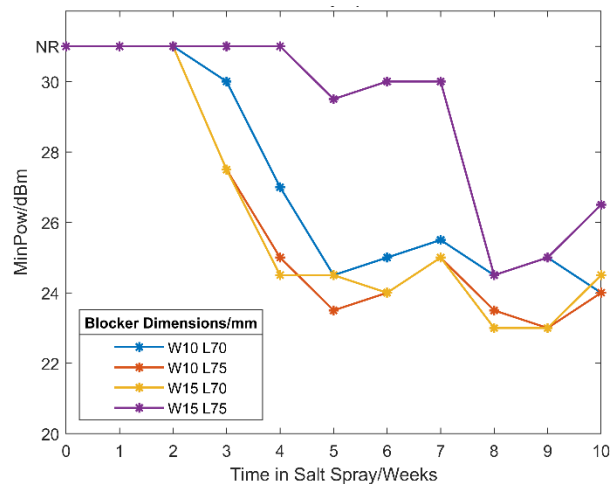


Figure 6.34. The MinPow recorded during the corrosion test for the PU samples

It is clear that these results do not tally with the model that increased corrosion of the substrate will lead to an increased tag response. Visually both samples had similar

levels of corrosion present however the PVC never allowed a response whereas the PU did. Furthermore, the PU samples did not always show an increased response with exposure time as would be expected from the model. It was suggested that both of these inconsistencies were down to some combination of water uptake and the method of exposing the blocking layers:

1. Water uptake

Water uptake was considered in previous testing as a potential disrupting factor in the measurement method as it can block RFID communication. In this test samples experienced a high degree of blistering, and it was discovered that water was often retained in these blisters, even after drying the samples. The PVC samples, especially, were observed to have sustained significant blistering across a large percentage of the sample area as shown in Figure 6.35.



Figure 6.35. PVC sample week 10 (left) with identified blister locations (right)

2. Method of testing

To allow salt spray testing the blocking layers were removed from the tag and placed in the chamber which allowed significant attack and corrosion of the, less well protected, rear of the sample as shown previously due to a lack of sealing with tape. It is thought that corrosion product produced on the rear of the sample produced an uneven surface that meant when the sample was reattached to the RFID tag there was an increased gap between the sample and tag as shown in Figure 6.36. The bigger the gap present the more reduced the blocking effect would become due to separation of the sample and tag.

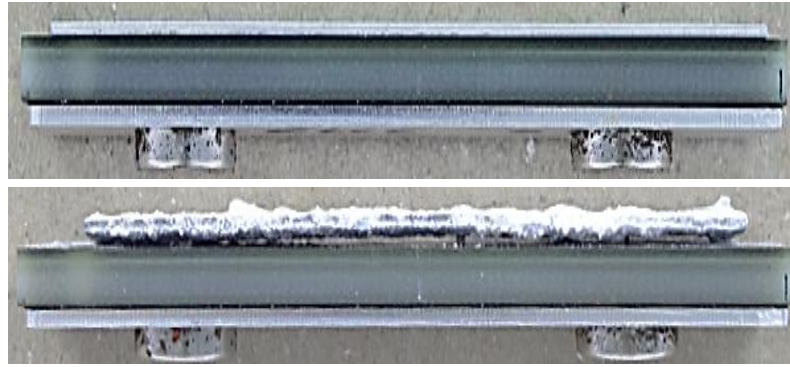


Figure 6.36. Side view of RFID tag with virgin (top) and corroded blocking layers (bottom). Note the gap produced in the corroded sample between blocking layer and tag

While it is possible that corrosion had not occurred significantly to allow a response from the PVC samples it was proposed that actually the considerable quantity of water trapped in the blisters had caused the lack of response in comparison to the PU samples. It was unsure whether the response of the PU sample was solely down to the gap produced by corrosion product or whether it had detected corrosion, but that accumulation detection was inaccurate due to the influence of water and corrosion product gap.

To investigate further this test was repeated with the samples attached permanently to the RFID tag with double sided adhesive which meant the rear of the sample was not exposed to the test environment and the sample and tag would be consistently connected. This time, even, after 10-weeks exposure there was no tag response from any of the PU and PVC samples. Therefore, it was concluded that the previous results from the PU sample were due to the emergence of corrosion product and the tag lift effect associated with this. The overall lack of response from both samples was considered to be due to a combination of insufficient corrosion and water uptake.

6.8 Improved Corrosion Testing

Previous corrosion testing showed promise in the detection of corrosion of easily corrodible substrates but presented a problem when using the actual coated product. No response was seen, potentially due to insufficient corrosion and the presence of water filled blisters. To aim to solve this a new set of samples were produced. Four 10 by 70mm samples were cut for each coating system and these were then punched

with 0, 2, 5 and 11, 2mm diameter holes. The samples were then attached to the RFID tags with adhesive to create the sample set shown in Figure 6.37.

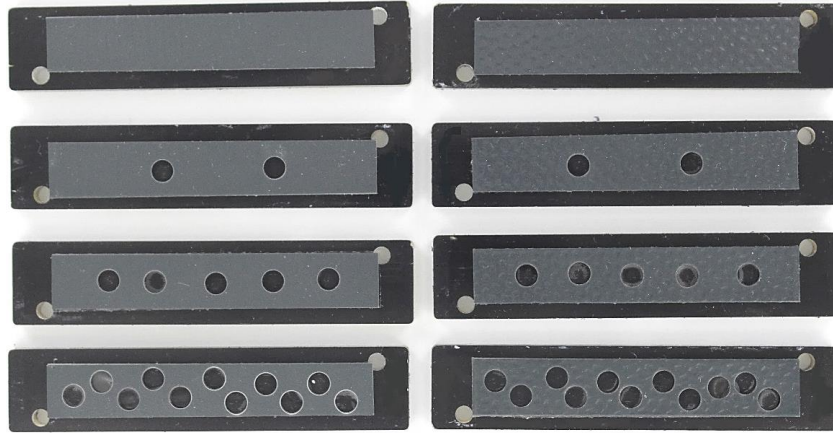


Figure 6.37. Samples used in the new corrosion test

The tag size was chosen as the smaller of the previously tested sizes to improve the chances of a response in order to ensure there was something to measure. The holes were added for two different reasons. Firstly, they increased the amount of cut edge present on the sample which would hopefully produce sufficient corrosion for a measurable change in the metrics. Secondly, it was thought that the holes would reduce the amount of water able to be trapped in the sample as blisters. Before measurement each sample would be lightly pressed face down into an absorbent towel in an attempt to drive out moisture from any blisters present and the increased holes provided more and easier paths for this water to leave the blisters.

The appearance of the 0- and 11-hole samples during the test are shown in Figure 6.38 and show a representation of the samples during testing. It is shown that the holes provide a far greater amount of exposed cut edge as intended leading to far increased white rust on the 11-hole sample compared to the 0-hole. White rust is present from week 2 and appeared to increase in prevalence with exposure. Due to the holes and the pressing of samples a far reduced number of blisters was observed on all samples compared to the previous test. It is worth noting that no red rust was observed on any of the samples even by week 15.

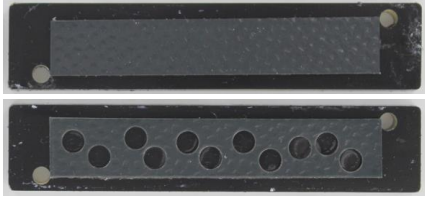



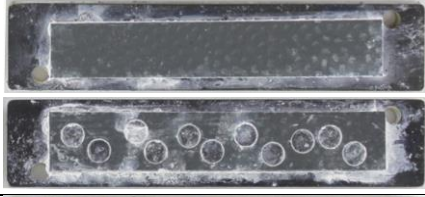







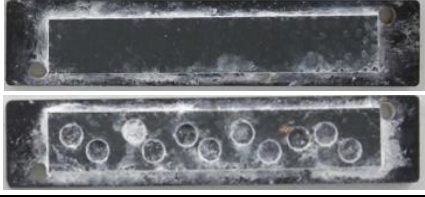

Week	PVC	PU
0		
2		
4		
6		
8		
10		
15		

Figure 6.38. Examples of the appearance of the samples during the test

The three metrics of tag response for each coating set of samples are shown below in Figure 6.39, Figure 6.40 and Figure 6.41. Unfortunately, all the metrics did not show any particularly strong trends. For the PVC samples fairly consistent values of RSSI, SR/s and MinPow were recorded throughout the test with no clear increase or decrease in tag response. The 5- and 11-hole PU samples were similar and, although it may not look to be the case so were the 0- and 2- hole samples. As these fluctuated

between little and no response the graphs show what appears to be large changes but actually if the MinPow is observed it is just the case that occasionally a signal was seen but no strong improvement was noted with time.

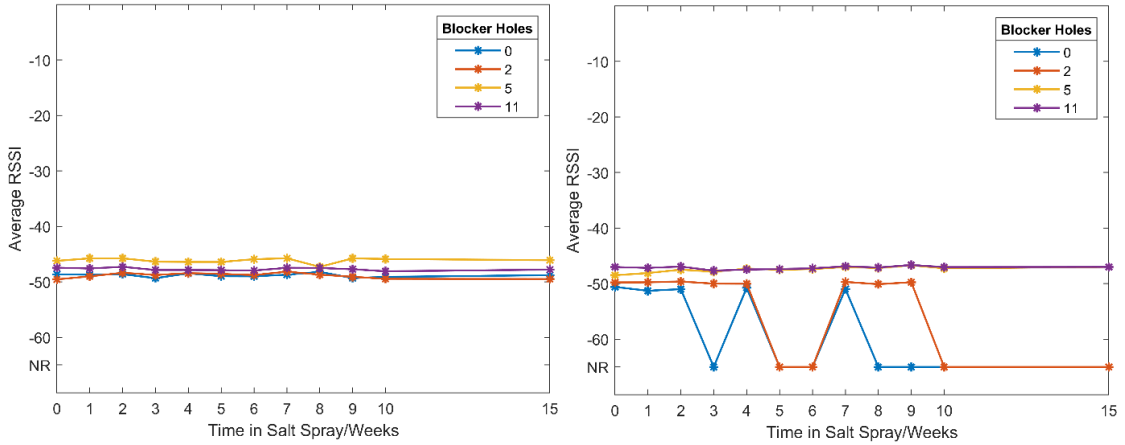


Figure 6.39. Average RSSI recorded during the corrosion test for the hole punched samples: PVC (left) and PU (right)

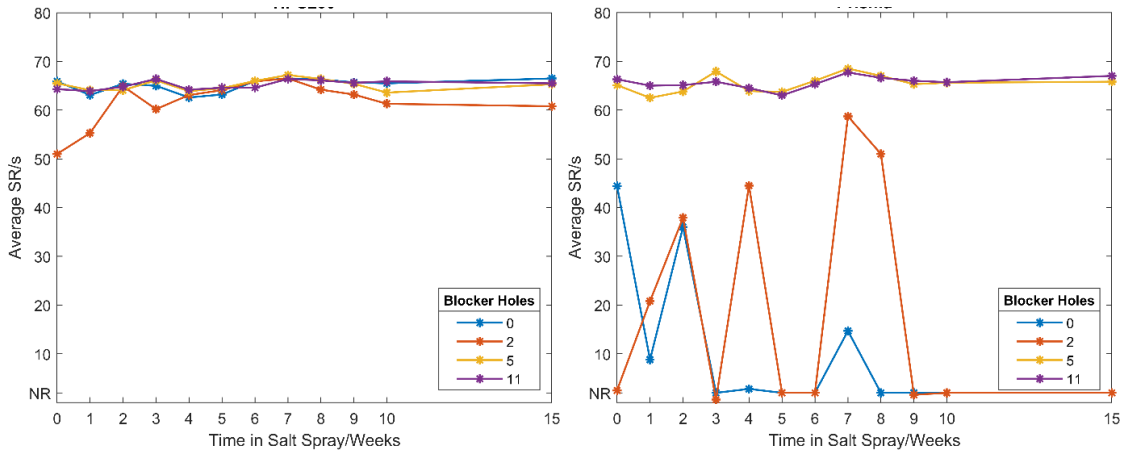


Figure 6.40. Average SR/s recorded during the corrosion test for the hole punched samples: PVC (left) and PU (right)

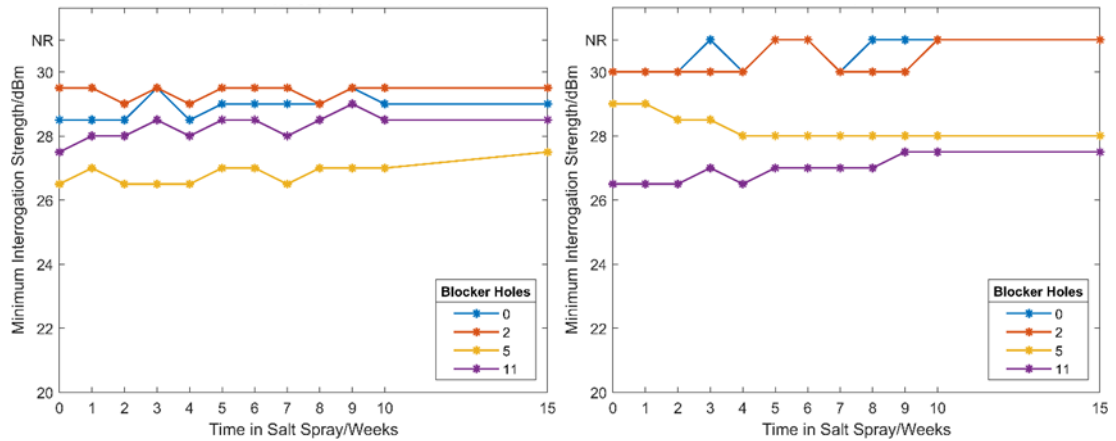


Figure 6.41. The MinPow recorded during the corrosion test for the hole punched samples: PVC (left) and PU (right)

This test was thought to be more accurate than the previous two in assessing the industrially coated samples as it was designed to remove the effect of sample lifting and reduce the effect of water ingress. However, it is clear from the results that no evidence of signal approval was detected despite the emergence of a considerable quantity of white rust indicating corrosion had occurred. As efforts have been made to ensure as little water was trapped in blisters, the samples were thoroughly dried, and it has been shown that material removal as a result of corrosion led to signal improvement it was concluded that insufficient corrosion had occurred to be detected by this method. The absence of red rust on the samples would suggest that the steel substrate had not begun to corrode significantly even at the 15-week mark. While the galvanised layer appears to have been heavily attacked, in reality this is a small proportion of the metal thickness in the sample and therefore its removal appears to be insufficient to produce a marked decrease in the blocking effectiveness of the blocking layer.

6.9 Conclusions

This work considered the application of an RFID blocking technique for the detection of substrate corrosion of coated steel. While it was clear that signal strength should increase with substrate degradation, this trend was not always observed due to other competing factors such as water ingress into the coating and tag lift due to corrosion product. However, despite these limitations, it was shown that substrate corrosion was detectable, but the severity of corrosion required was such that this was only observed strongly for test specimens which underwent a significant level of

attack. When applied to modern Tata Steel coated products under salt spray testing no detection of corrosion was provided even after 20 weeks of exposure when white rust was extremely prevalent. While it is likely, based on the previous tests, that significant red rust degradation would be detected if these samples were further exposed the technique is clearly limited in terms of early-stage detection. Arguably this technique would, therefore, be useful for detecting product failure although detection would be at a point that a simple visual inspection would suffice. While it could be deployed in locations that are harder to visually inspect, the severity required is unlikely to occur, except in exceptional circumstances, until the very end of the product lifespan. It is possible, however, that this technique could be used with less protected blocking layers to assess the aggressivity of different locations.

6.10 References

1. Wu X, Deng F, Hao Y, Fu Z, Zhang L. Design of a humidity sensor tag for passive wireless applications. *Sensors (Switzerland)*. 2015;15(10):25564–76.
2. Strangfeld C, Johann S, Bartholmai M. Smart RFID sensors embedded in building structures for early damage detection and long-term monitoring. *Sensors (Switzerland)*. 2019;19(24).
3. Gou P, Kraut ND, Feigel IM, Bai H, Morgan GJ, Chen Y, et al. Carbon nanotube chemiresistor for wireless pH sensing. *Sci Rep*. 2014;4(March).
4. Anum Satti J, Habib A, Anam H, Zeb S, Amin Y, Loo J, et al. Miniaturized humidity and temperature sensing RFID enabled tags. *Int J RF Microw Comput Eng*. 2018;28(1).
5. Shafiq Y, Henricks J, Ambulo CP, Ware TH, Georgakopoulos S V. A Battery-Free Temperature Sensor with Liquid Crystal Elastomer Switching between RFID Chips. *IEEE Access*. 2020;8:87870–83.
6. He YL, McLaughlin S, Lo JSH, Shi C, Lenos J, Vincelli A. Radio frequency identification (RFID) based corrosion monitoring sensors Part 1 – Component selection and testing. *Corros Eng Sci Technol*. 2015;50(1):63–71.
7. Reference_Designer. Shielding [Internet]. 2009 [cited 2019 Aug 13]. Available from: http://referencedesigner.com/books/si/ch15_1.php
8. He YL, McLaughlin S, Lo JSH, Shi C, Lenos J, Vincelli A. Radio frequency identification (RFID) based corrosion monitoring sensors Part 2 – Application and testing of coating materials. *Corros Eng Sci Technol*. 2014;49(8):695–704.
9. He Y. Wireless Corrosion Monitoring Sensors Based on Electromagnetic Interference Shielding of RFID Transponders. 2020;76(4):411–23.
10. Bouzaffour K, Lescop B, Talbot P, Gallee F, Rioual S. Development of an Embedded UHF-RFID Corrosion Sensor for Monitoring Corrosion of Steel in Concrete. *IEEE Sens J*. 2021;21(10):12306–12.
11. Rioual S, Lescop B, Pellé J, Radicchi GDA, Chaumat G, Bruni MD, et al. Monitoring of the environmental corrosivity in museums by rfid sensors: Application to pollution

- emitted by archeological woods. *Sustain.* 2021;13(11).
12. Park CR, Eom KH. RFID Label Tag Design for Metallic Surface Environments. *Sensors* [Internet]. 2011 Jan 17;11(1):938–48. Available from: <http://www.mdpi.com/1424-8220/11/1/938>
 13. Dobkin DM, Weigand SM. Environmental effects on RFID tag antennas. *IEEE MTT-S Int Microw Symp Dig.* 2005;2005(C):135–8.
 14. Björninen T, Elsherbeni AZ, Ukkonen L. Low-profile conformal UHF RFID tag antenna for integration with water bottles. *IEEE Antennas Wirel Propag Lett.* 2011;10:1147–50.

Chapter 7: Chipless RFID Sensor

7.1 Introduction

This chapter outlines the basics of a new passive RFID (resonant frequency identification) technique that aims to allow easy performance monitoring of organically coated steel cladding products. A passive RFID sensor presents a number of promising features for organic coating monitoring. As a cheap and ‘semi-remote’ method, it would allow for a medium range, non-destructive monitoring method of a number of assets. In fact, a significant amount of work has been carried out on developing RFID based sensors [1–3]. The approach taken by the vast majority of the sensors currently being developed is to use a so called ‘chipless’ RFID design.

Chipless RFID tags were first considered as a concept in order to allow RFID tagging to compete financially with low-cost barcode tagging [3,4]. By removing the integrated circuit, chipless RFID is greatly reduced in cost and allows consideration of fully printable tags, increasing ease and rate of production [4]. Chipless sensors offer a much simpler approach in which some of the complications of impedance matching as well as other complications are negated compared to chipped devices.

As a sensor, they are stated to have better robustness, lower radiated power, and longer life than traditional sensors [3]. Three types of chipless RFID sensors exist, namely time-domain reflectometry (TDR), frequency modulation, and phase encoded sensors [3], and these are summarized in Figure 7.1. For each of these types, different tag technologies exist, such as surface acoustic wave (SAW) and radar cross section backscatter (RCS).

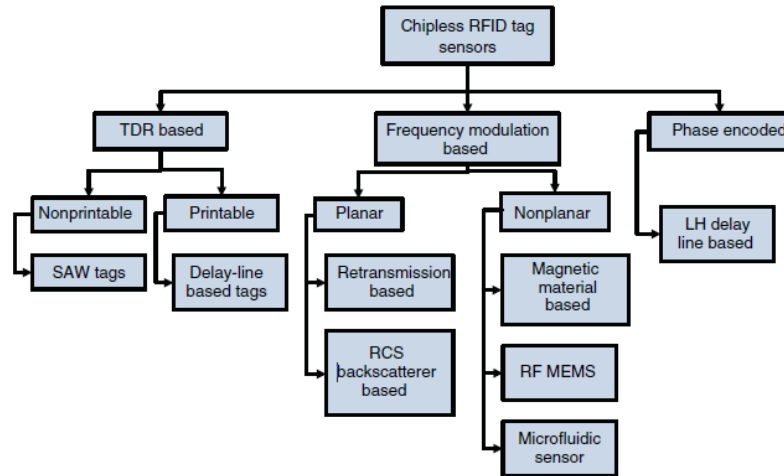


Figure 7.1. Types of chipless RFID tags [3]

7.2 Theory and Background

A recent study involved using a chipless RFID circular microstrip patch antenna (CMPA) to monitor crack growth in aluminium [5]. Microstrip antennas are commonly used in wireless communication, including in high performance situations, such as in satellites and aircraft [6]. They have advantages of low price and profile, simplicity, and versatility [6]. A basic microstrip antenna is composed of a ground plane, which is covered by a dielectric layer with a metal antenna strip on it. A microstrip patch antenna (MPA) is differentiated because it consists of relatively large sections, or patches, of metal [7]. A CMPA is simply an MPA in which the patch is circular in shape, as shown in Figure 7.2.

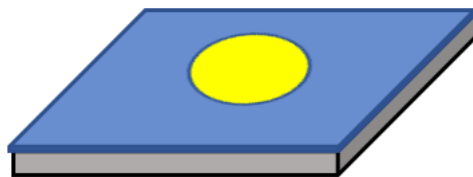


Figure 7.2. A basic CMPA.

In this paper, a similar approach was used to that in [6], which utilizes radar cross section (RCS) backscatter-based technology, which is based on frequency modulation. The principle is described visually in Figure 7.3 and involves the use of a microstrip resonator. An interrogation signal is aimed at the chipless tag which will resonate at a unique frequency and hence produce a signature backscattered signal which is received by a further antenna for analysis [3,5].

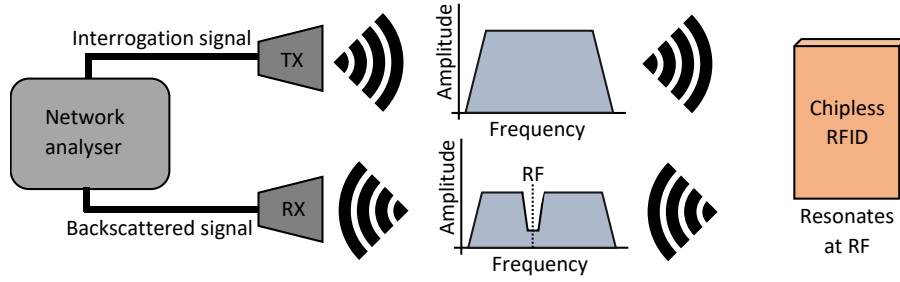


Figure 7.3. Basic working principle of an RCS backscattered RFID tag

The monitoring system developed in this paper has parallels to that designed by Marindra [5], which utilised the fact that the resonant frequency of a CMP antenna is affected by changes in the ground plane. This study aimed to use a similar antenna system to monitor changes in the dielectric layer of such a system with the dielectric layer, in this case, being an organic coating layer on a steel product.

As described in [6], the dominant TM_{mn0}^z mode for a circular microstrip patch antenna is the TM_{110} mode for which the resonant frequency is defined by:

$$(f_r)_{110} = \frac{1.8412}{2\pi a_e \sqrt{\mu\epsilon}} = \frac{1.8412v_0}{2\pi a_e \sqrt{\epsilon_r}} \quad (6.1)$$

where:

$$a_e = a \left\{ 1 + \frac{2h}{\pi a \epsilon_r} \left[\ln \left(\frac{\pi a}{2h} \right) + 1.7726 \right] \right\}^{\frac{1}{2}} \quad (6.2)$$

where a is the diameter of the circular patch, h is the thickness of the dielectric layer, ϵ_r is the relative permittivity of the dielectric layer, v_0 is the speed of light, μ is the permeability of the dielectric and ϵ is the permittivity of the dielectric layer.

Hence, it can be concluded that:

$$(f_r)_{110} \propto f(h) \quad (6.3)$$

$$(f_r)_{110} \propto f(h) \quad (6.4)$$

Therefore, the resonant frequency of a patch antenna is related to a function of both the relative permittivity (dielectric constant) and the height of the dielectric. As a result, any changes to the dielectric properties of an organically coated product could be detected via this approach. This would include degradation due to water ingress, defect formation, or paint formation failures such as chalking. This approach was

utilized by [8] to monitor the response of an epoxy coated resonator and was able to detect changes in the dielectric properties of the epoxy coating produced by the absorption and desorption of water. The proposed method differs from this method as the antenna can be placed onto, rather than under, the coating of interest which may interfere with the adhesion and/or protective properties of the coating. Furthermore, as the proposed device is solely reliant on backscatter RCS measurement, a physical wired connection to the antenna, as in [8], is not required simplifying the procedure.

The aim of the investigation was to develop the concept outlined, in order to prove its applicability to architecturally painted steel. The strategy employed used a combination of simulation and laboratory experimental techniques. The simulation provided a means of estimating the response change when variations in material properties which could be expected during degradation occurred within a purely simulation space. The simulated response could then be compared and validated using the laboratory derived experimental results. This parallel approach ensured that a greater understanding of underlying physics could be established while also proving the applicability in the real world.

7.3 Methodology

7.3.1 Simulations

The tag was designed, optimised, and initially tested in CST (Computer Simulation Technology) Design Environment 2019, a 3D electromagnetic analysis software commonly used for antenna design and analysis [9]. Two approaches, the basic design of each shown in Figure 7.4, were considered. The first approach (NS) solely used the organic coating as the dielectric layer, and the sensor patch is attached to this, while the second approach (S) used a dielectric substrate between the sensor patch and the coated steel panel.

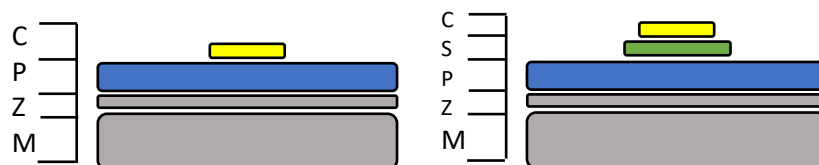


Figure 7.4. Two tag systems NS, no substrate, (left) and S, substrate, (right) showing the copper sensor (C), the substrate layer (S), the paint system (P) the zinc galvanized layer (Z) and the steel metal substrate layer (M).

Two coating systems were also considered and designed in the software based on two commonly used coated steel products composed of a steel substrate, a zinc metal coating layer, and a dielectric organic coating layer. This is referred to as coated steel in the following work. A polyvinyl chloride (PVC)-based coating with a total nominal coating thickness of 211 microns and a polyurethane (PU)-based coating with a total nominal coating thickness of 41 microns were designed. These are two commonly used coating systems for architectural steel cladding and are referred to in the following work as PVC and PU. The dimensions of the tag are displayed in Figure 7.5 and listed in Table 7.1.

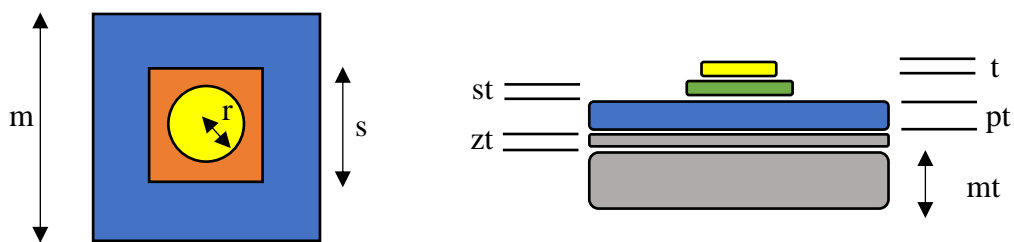


Figure 7.5. Tag systems showing key dimensions

Table 7.1. Simulation parameters

Component	Symbol	Dimension/mm
Antenna Radius	r	10
Antenna Thickness	t	0.035
Dielectric Thickness	pt	0.211 (PVC) 0.040 (PU)
Zinc Thickness	zt	0.04
Metal Thickness	mt	0.6
Dielectric Constant	e	3.5
Sample Height/Width	m	60
Substrate Thickness	st	0.00 (NS) 0.20 (S)
Substrate Height/Width	s	0.00 (NS) 22.0 (S)

In the modelling of the cladding panels, several assumptions were made for the initial testing. Firstly, the coating layers of pre-treatment, primer, and topcoats were combined into one homogenous layer with a cumulative thickness and an arbitrary dielectric constant of 3.5. The metal substrate was defined as 1010 steel and the metallic coating layer as pure zinc. The size of the cladding piece was set to 6 cm², and the substrate layer used was FR-4 (lossy). The properties for each of the materials used are shown in Table 7.2.

Table 7.2. Simulation material properties

Component	Value/Properties	Reference
Steel Conductivity (σ_s)	6.99×10^6 S/m	[10,11]
Zinc Conductivity (σ_z)	1.69×10^7 S/m	[10,11]
Fr-4 Dielectric Constant (ϵ_r)	4.3	[11]
Fr-4 Loss Tangent (δ)	0.025	[11]

Although the actual steel substrate and zinc layer are composed of either different or more complex alloys, the conductivity values used were expected to be a fair representative value. Furthermore, additional simulations, not provided in this work, showed that small deviations in these values of conductivity did not noticeably affect the resonant frequency and only produced small changes in the measured RCS.

Perhaps the largest source of uncertainty is the accuracy in modelling the coating layers as one homogenous layer, whereas in reality the pre-treatment, primer, and topcoat(s) have different requirements and hence compositions. This was mainly done for ease of modelling, and it is believed to be representative of a weighted average of the multiple dielectric layers. It is possible that experimental confirmation of this assumption may be further required. A dielectric constant of 3.5 was considered an accurate representation of both systems as the coatings are based on polyvinyl chloride chemistry, which has a stated dielectric constant of 3.4 [12,13], and polyurethane chemistry, which has a stated dielectric constant of 3.2-3.6 [14,15].

The simulation, shown in Figure 7.6, was set up with a frequency range of 2–6 GHz of plane wave excitation in the z direction. The E-plane of the excitation plane wave was oriented parallel with the y axis and the H-plane was oriented parallel with the x axis. The plane wave excitation source and an RCS Probe were set –200 mm away from the sample in z direction to provide the simulated interrogation signal and response signal measurement of the tag, respectively, at 200 mm distance. Finally, all boundaries were set to open (add space), which is used to simulate free space surrounding the set up and is recommended for antenna calculations [16].

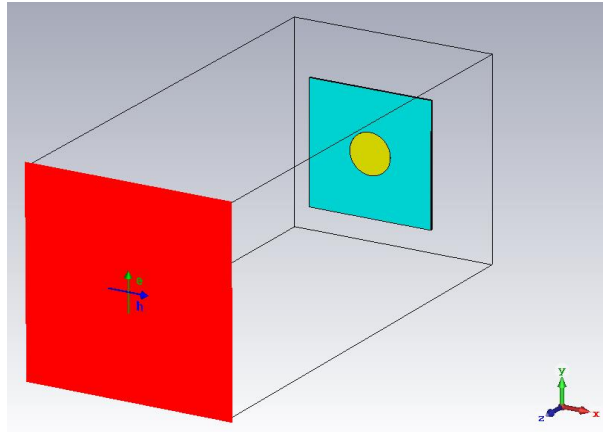


Figure 7.6. Simulation set up in CST Studio Suite

The resonant frequency of the tag was determined by measuring the frequency at the point of maximum drop of RCS amplitude. The RCS change at resonant frequency was calculated by taking the measured RCS (RCS_{RF}) away from the average of the RCS at the beginning of the valley (RCS_L) and the RCS at the end of the valley (RCS_H):

$$\Delta RCS = \frac{RCS_L + RCS_H}{2} - RCS_{RF} \quad (6.5)$$

7.3.2 Production of the Antenna

In order to validate the simulations, several tags were produced, as shown in Figure 7. The antennae were manufactured from adhesive copper tape (RS Pro foil, thickness 0.035 mm, from RS Components, Ireland) using a 20 mm paper punch. This method was initially used for simplicity and because it gave reasonable cut quality and uniformity. As copper rapidly tarnishes antennae were also produced from adhesive aluminium tape (RS Pro foil thickness 0.04 mm), this is a far more environmentally resilient substrate and hence it was considered as an alternative. The 20-mm circles were then either attached directly to the sample, or to the Fr-4 substrate, which was attached to the sample via thin double sided adhesive tape. An example of the two produced antenna systems is shown in Figure 7.7. A number of coated steel samples were used in this study with the colours used including white, anthracite, grey (PVC only), and silver (PU only). This was done to understand the effect the different coating colours may or may not have on the measured resonant frequencies. The samples used are shown in Figure 7.8.



Figure 7.7. The manufactured Chipless RFID Tag deployed onto the same without (left) and with (right) the substrate layer.



Figure 7.8. The OCS samples used in this study.

7.3.3 Antenna Measurement

To measure the antenna response, a vector network analyser (VNA) was used, connected to two horn antennas (TX and RX). A signal sweep from 4 to 6 GHz was emitted from the TX horn antenna and the resulting S_{21} from the RX antenna was recorded. To ensure similar positioning of the antenna in each test, a small acrylic stand was produced, and the position of each horn antenna was marked on the test workspace to ensure the same range was used. The distance between horn antennas was 5 cm and the distance to the sample was 20 cm as with the simulations. The test set up is shown in Figure 7.9.

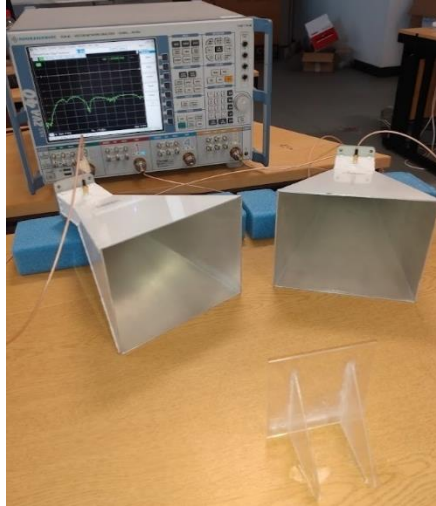


Figure 7.9. VNA and horn antennas used to interrogate the sample.

7.4 Results

7.4.1 Simulations

7.4.1.1 Antenna Radius Optimisation

In order to initially develop the concept, the first set of simulations focused on determining the optimum tag radius size for this particular application. The previous work this technique was inspired by used an antenna radius of 6 hence similar values from 4 – 12 mm were initially tested for this work. To test the effect of antenna radius the PVC (NS) system was used due to an increased response from this system for reasons explained later. When attempting to optimise the antenna radius there were two main criteria:

1. Intensity of response, the larger the RCS change at resonant frequency the easier the detection of the response.
2. Sensitivity to dielectric changes, the greater the change in resonant frequency for an identical change in dielectric properties the more useful the technique for detecting OCS changes.

The first criteria were assessed by simply recording the RCS response for each antenna radius, this is shown in Figure 7.10. It was observed that, as expected by the equation for the resonant frequency for a CMPA, an increase in antenna radius led to a decrease in the resonant frequency. The simulations showed that the antenna radius was required to be at least 8mm to give a resonant frequency between the scan range of 2-6GHz. When the RCS change at resonant frequency was measured, it was observed that the maximum RCS drop was observed for an antenna radius of 10mm

although radii of 9, 11, 12 and 13 also provided reasonable RCS changes at resonant frequency.

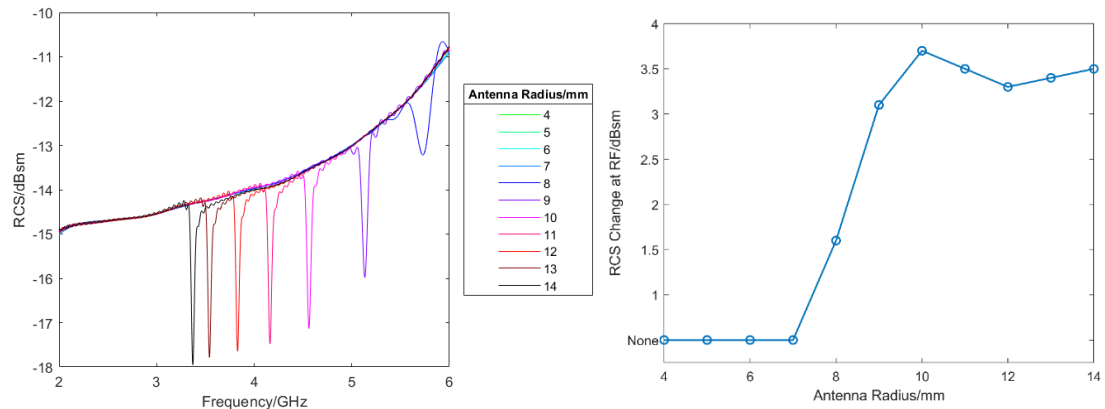


Figure 7.10. RCS response of each antenna radius (left) and the measured RCS drop (right)

To test the effect of antenna radius on sensitivity to dielectric change the best responding radii from the initial test were re-tested with a range of paint layer dielectric constants. The values chosen were 2.5, 3, 3.5, 4 and 4.5. The percentage change in resonant frequency relative to $\epsilon=3.5$ was then plotted for each radius, Figure 7.11. It was observed that all radii gave similar sensitivity to changes in dielectric constant values and there was no diameter that was clearly favourable for this criterion.

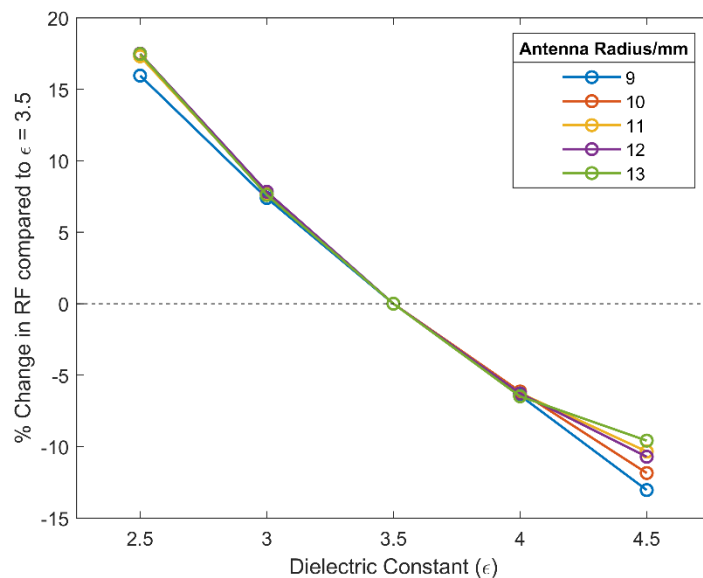


Figure 7.11. Percentage change in resonant frequency as a result of dielectric constant change from

3.5

As a result of these tests the 10mm diameter antenna was chosen due to its comparable sensitivity and large RCS drop at resonant frequency.

7.4.1.2 Initial system simulations

The simulated RCS response for each system is shown in Figure 7.12 and the main results that can be drawn from each RCS response are summarized in Table 7.3. It can be seen that the PVC system gives a similar response when the antenna is placed both directly on the coated steel and on a substrate. The PU coating system, comparatively, does not show a very significant response when the antenna is placed directly on the cladding. However, a much more prominent, albeit smaller than the PVC system, response is recorded when a substrate layer is used. Both systems show a small shift to a smaller resonant frequency when the substrate layer is used. This is expected as the substrate has a larger dielectric constant of 4.3. Adding this larger value dielectric layer has the effect of decreasing the resonant frequency of the system according to Equation (1).

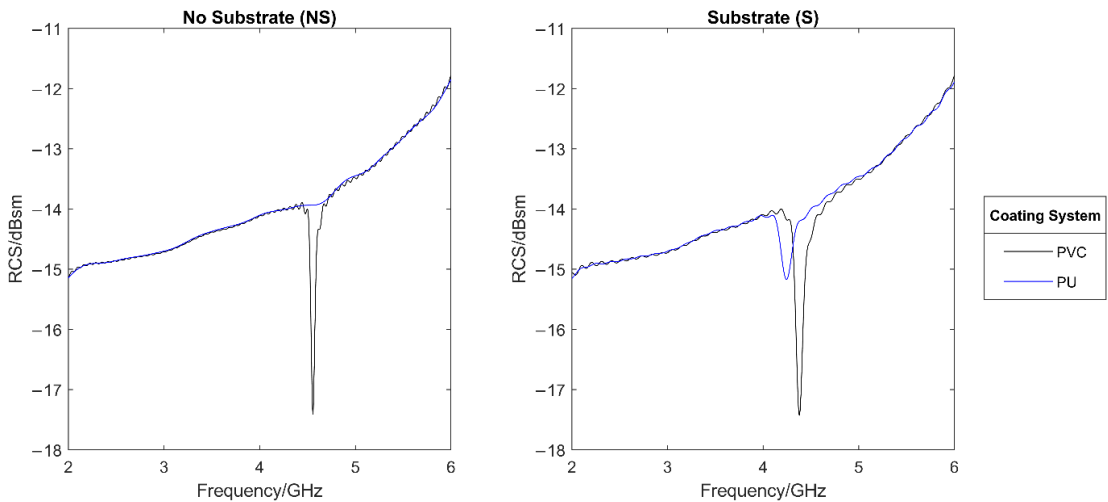


Figure 7.12. Simulated RCS response of sensors mounted directly on coated system (NS, left) and sensors mounted on an additional substrate (S, right).

Table 7.3. Results of initial simulations

System	Resonant Frequency/GHz	RCS at Resonant Frequency/dB ²	RCS change/dB ²
PVC-NS	4.556	-17.41	3.48
PU-NS	4.672	-13.87	0.03
PVC-S	4.380	-17.43	3.33
PU-S	4.244	-15.17	1.02

As the only difference in simulations between system PVC-NS and PU-NS is the paint thickness, the poor response from the PU system (PU-NS) must be caused by the change in dielectric layer thickness. It is stated in [6] that the usual dielectric substrate height h for a microstrip patch antenna with a dielectric constant between approximately 2 and 12 is:

$$0.003\lambda_0 \leq h \leq 0.05\lambda_0 \quad (6.6)$$

The calculated corresponding height range for the observed resonant frequencies seen is shown in Table 7.4. It can be concluded that the optimum range is not satisfied by the PU system paint thickness unless it is further increased with the substrate used in PU-S. As stated in [17], a decreased thickness of dielectric can lead to greater losses and a decreased efficiency, thus explaining the lack of a significant response by the PU model.

Table 7.4. Calculated optimum range of dielectric height

System	Resonant Frequency/GHz	System h/mm	h min/mm	h max/mm
PVC-NS	4.556	0.211	0.20	3.29
PU-NS	4.672	0.040	0.19	3.21
PVC-S	4.380	0.411	0.21	3.42
PU-S	4.244	0.240	0.21	3.53

This conclusion is reinforced by comparing the surface current distribution maps of each system at resonant frequency, as shown in Figure 7.13. It can be seen that the PU sample with no substrate has a significantly lower current distribution surrounding the antenna patch than any of the other systems. This is thought to be down to the poor efficiency of the antenna because of the thin dielectric layer, which causes far less resonance and hence electrical current. As a result, the backscattered RCS records far less of a change in the signal as little power has been transferred.

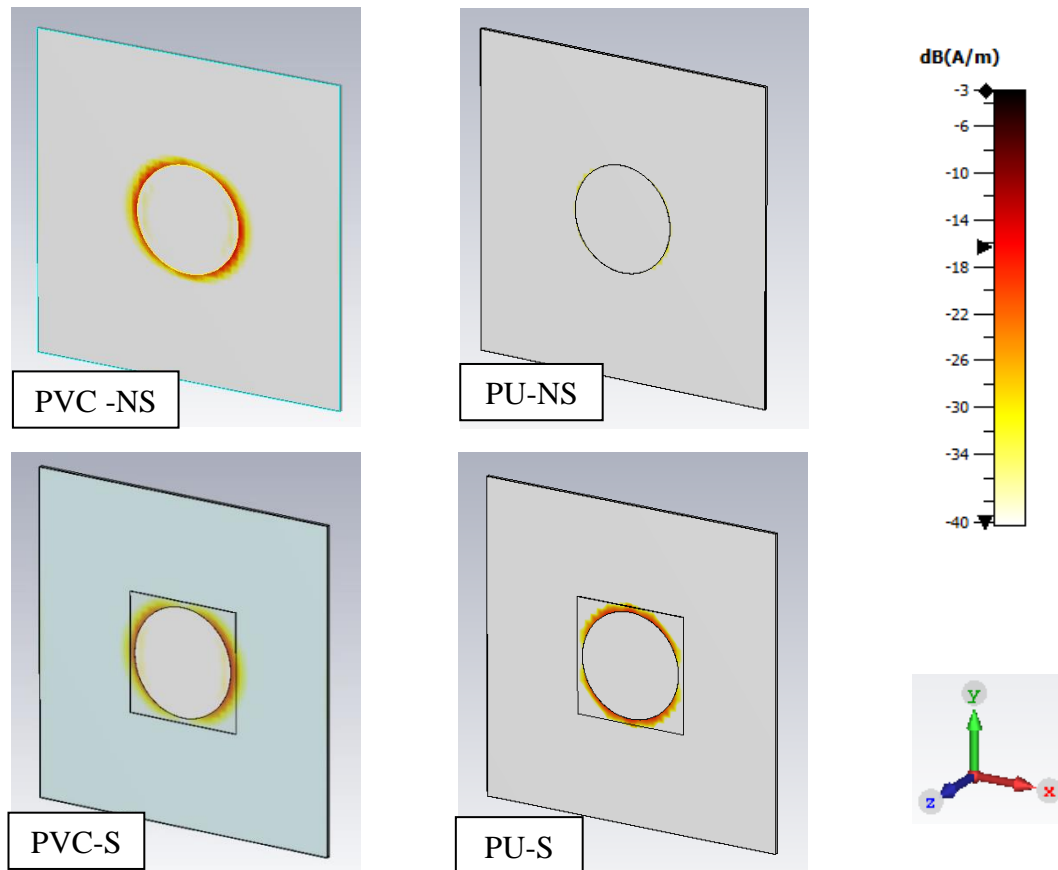


Figure 7.13. Simulated surface current distribution on each system at resonant frequency

7.4.1.3 Effect of sample size

The previous results were produced from a simulated 60mm by 60mm sample size however in reality the panels are much larger. To determine the effect, if any, of the sample size on the response simulations were carried out in which the sample size was increased from 50x50mm to 150x150mm in increments of 10x10mm. The simulated RCS response for this test is given in Figure 7.14. It was observed that, for all samples, that the sample size has little effect on the resonant frequency of the antenna however does significantly affect the magnitude of the RCS response. As the sample size increases the response is shifted to up to more positive values.

Furthermore, a smaller change (drop) in RCS at resonant frequency is seen with the larger sample size and hence it is expected that detection of the resonant frequency will be far more difficult on larger samples, especially when environmental noise is introduced. This effect was noted in [5] however was somewhat overcome during the experimental phase by isolating the metal response and subtracting this from the response of the metal and sensor.

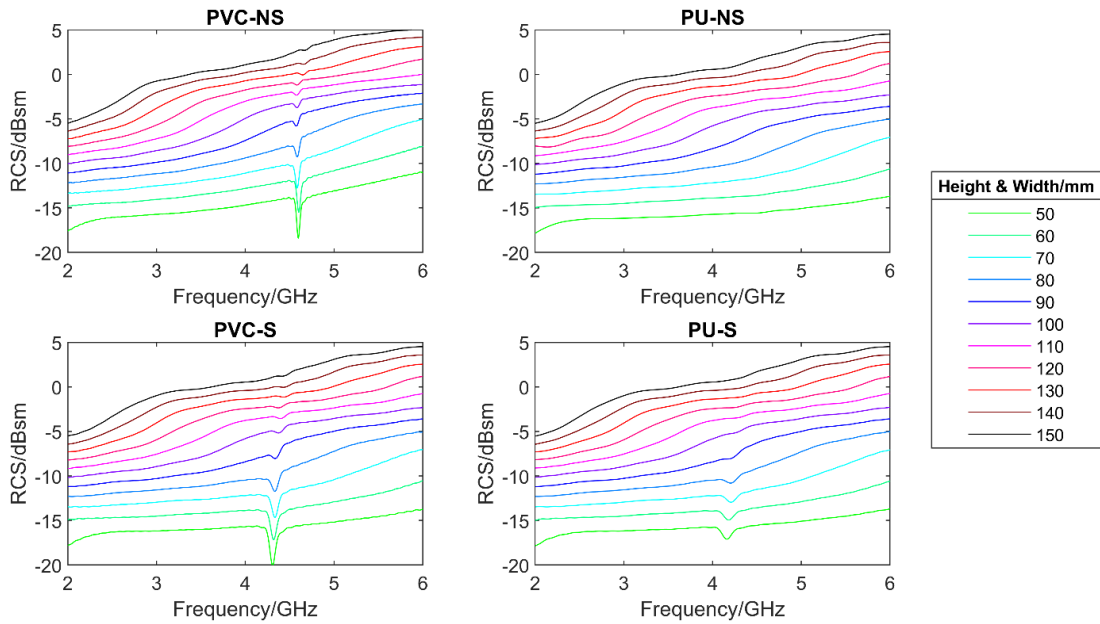


Figure 7.14. The effect of sample size on the simulated RCS response

While it is thought this limitation could affect the feasibility of the technique in assessing larger samples, given that this issue was solved to an extent by researchers in [5], the technique is still considered worth investigating. For ease of resonant frequency detection, however, the sample size of 60x60mm was maintained for the testing of the detection of organic coating changes.

7.4.1.4 Simulated Changes in Dielectric Constant

To monitor the effect of changes in the dielectric constant of the paint layer, a parametric sweep was performed in which the dielectric constant of the paint was changed from 2 to 5 in increments of 0.2.

As can be seen in Figure 7.15, for all systems, a clear trend was seen in that as the dielectric constant was increased, the resonant frequency of the system decreased. This is expected from Equations (1) and (3). However, it was also seen that the use of the substrate layer decreased the magnitude of the resonant frequency change. In Figure 7.16, it can be seen that the total change in resonant frequency for systems PVC-NS and PU-NS is far greater than that for PVC-S and PU-S. This is because the substrate has an unchanging dielectric constant and so is thought to average out some of the dielectric changes introduced.

What is perhaps more unexpected is that, by using a substrate layer, the RCS at resonant frequency showed a far clearer trend of reducing with increased value for

the dielectric constant. This can be seen by comparing the four systems against each other, as shown in Figure 13.

This set of results helps to validate the model from the assumption that a dielectric constant of 3.5 was used and hence provides more confidence in the simulation process. If the coating system used has a different dielectric constant, a result will still be expected, however it will show a shift to a lower frequency, as shown by this simulation.

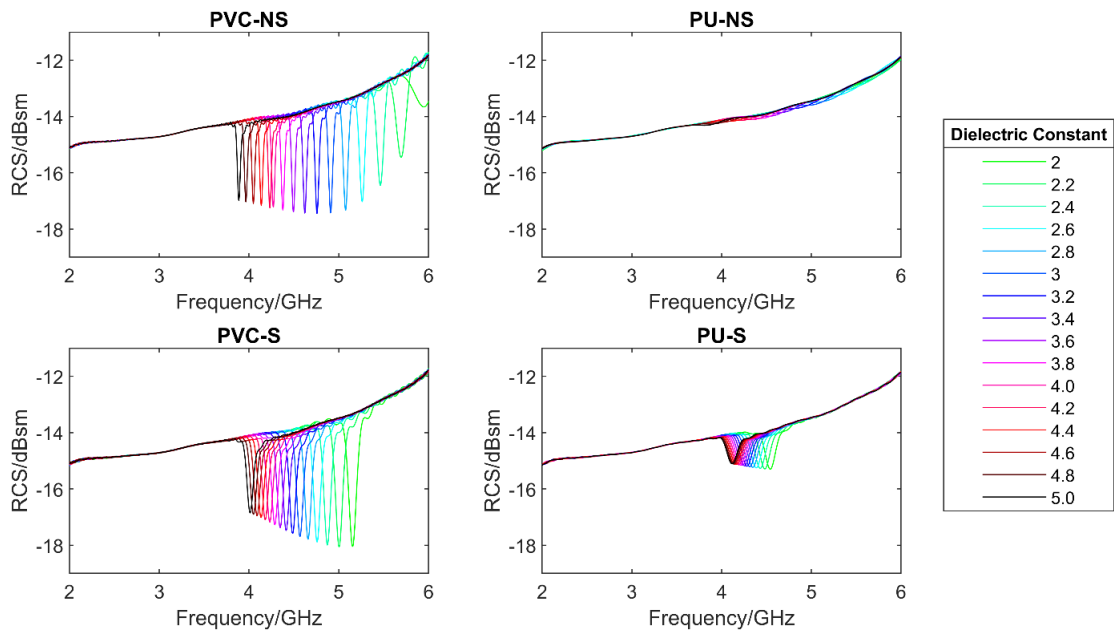


Figure 7.15. The effect of changes in the dielectric constant of the paint layer on the simulated RCS

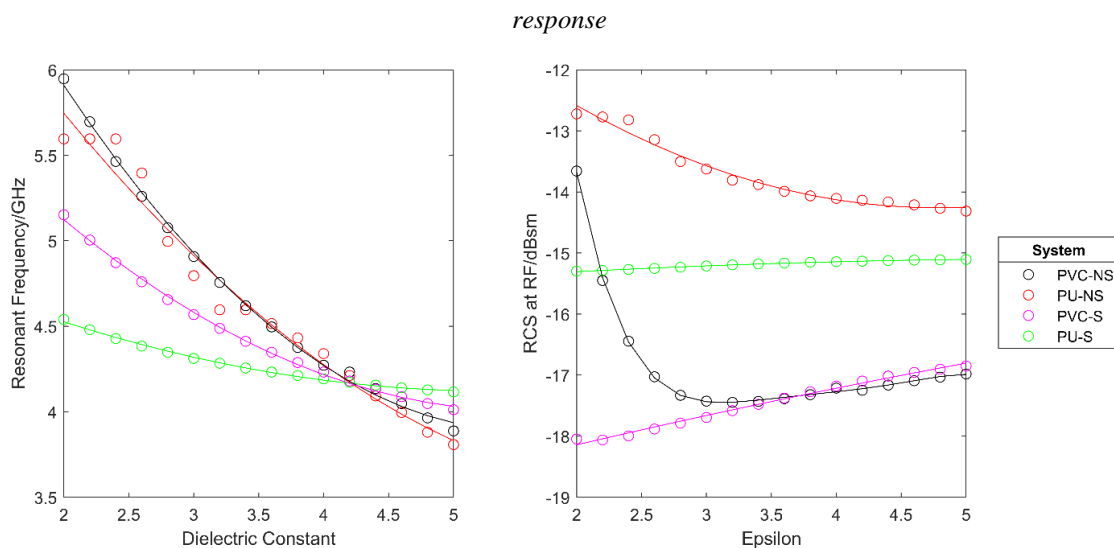


Figure 7.16. The effect of changes in the dielectric constant of the paint layer on the resonant frequency and the RCS at resonant frequency of each system

7.4.1.5 Simulated Aging/Degradation

In reality, as a coated steel sample ages, a number of the effects simulated above occur simultaneously. Hence, it is important to determine the effect of multiple expected changes on the response. It is also important to determine if the multiple effects cause the overall change in response to reduce or even cancel out. To do this, a test was performed in which aging and degradation of the coating was simulated eight times and with each iteration. As displayed in Table 7.5:

- The dielectric constant of the paint layer was increased by 0.025 to simulate water ingress. Previous work such as [8] has shown that water uptake by a coating leads to an increased dielectric constant of up to at least 8%.
- The diameter of small defect holes in the paint were increased by 0.01 mm to simulate defect growth. These were designed to be placed ‘randomly’ with no specific pattern to attempt to mimic as close as possible that which would occur in reality. The defects were placed centered on $(-4, 0)$ $(3, 3)$ $(-3, -5)$ $(-2, 7)$, with $(0, 0)$ being the centre of the CMPA. This sort of defect is a known failure method in organic coatings as a result of mechanical shock and/or aging [18].
- The paint thickness was decreased by 0.001 mm to simulated UV degradation. A decrease in organic coating thickness is known to occur through chain scission as a result of organic coating exposure to UV, oxygen, and other atmospheric contaminants [19].

Table 7.5. Parameters used for each aging severity level

Aging Severity	Dielectric Constant	Defect Diameter/mm	Paint Thickness/mm
1	3.500	0.00	0.211 (PVC) 0.040 (PU)
2	3.525	0.01	0.210 (PVC) 0.039 (PU)
3	3.550	0.02	0.209 (PVC) 0.038 (PU)
4	3.575	0.03	0.208 (PVC) 0.037 (PU)
5	3.600	0.04	0.207 (PVC) 0.036 (PU)
6	3.625	0.05	0.206 (PVC) 0.035 (PU)
7	3.650	0.06	0.205 (PVC) 0.034 (PU)
8	3.675	0.07	0.204 (PVC) 0.033 (PU)

This offered a reasonable level of replication of the real-life ageing process of a coated specimen which undergoes the changes simulated in this exercise. The simulated RCS response for each system is shown in Figure 7.17 and the effect of the aging severity on the resonant frequency and the RCS at resonant frequency are

shown in Figure 7.18. It can be seen that the resonant frequency shifts to lower frequencies as the simulated aging severity increases. Furthermore, the RCS at resonant frequency is seen to decrease in magnitude with simulated aging. Using a substrate had little effect on the change in frequency with aging. However, as before, this makes identification of resonant frequencies in the thinner paint system far easier, by increasing the depth of the trough.

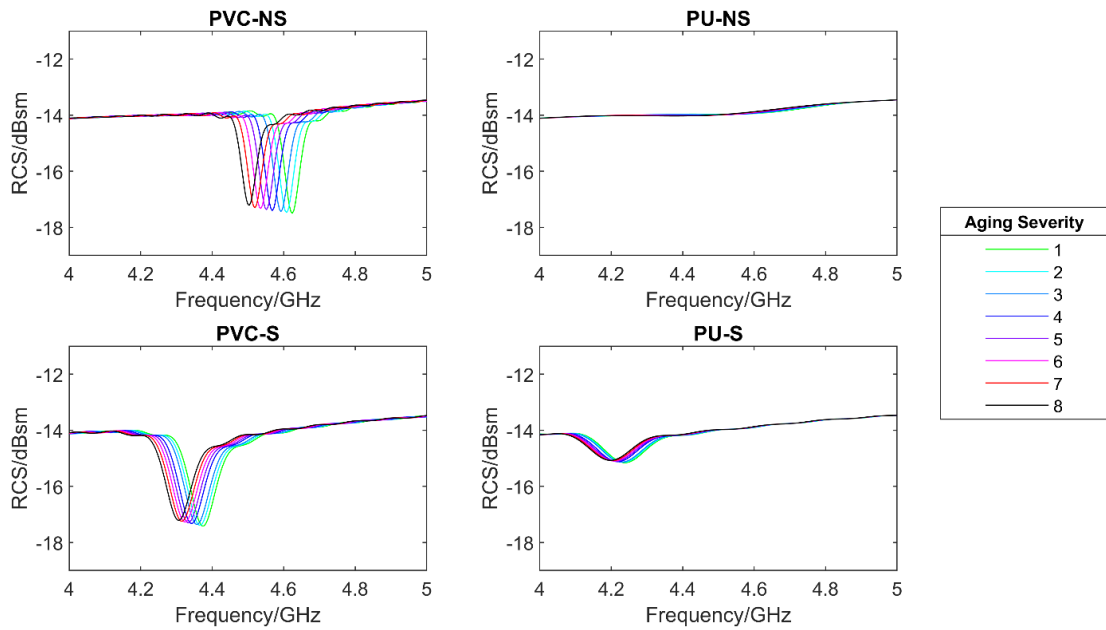


Figure 7.17. The effect of simulated aging on the simulated RCS response of each system

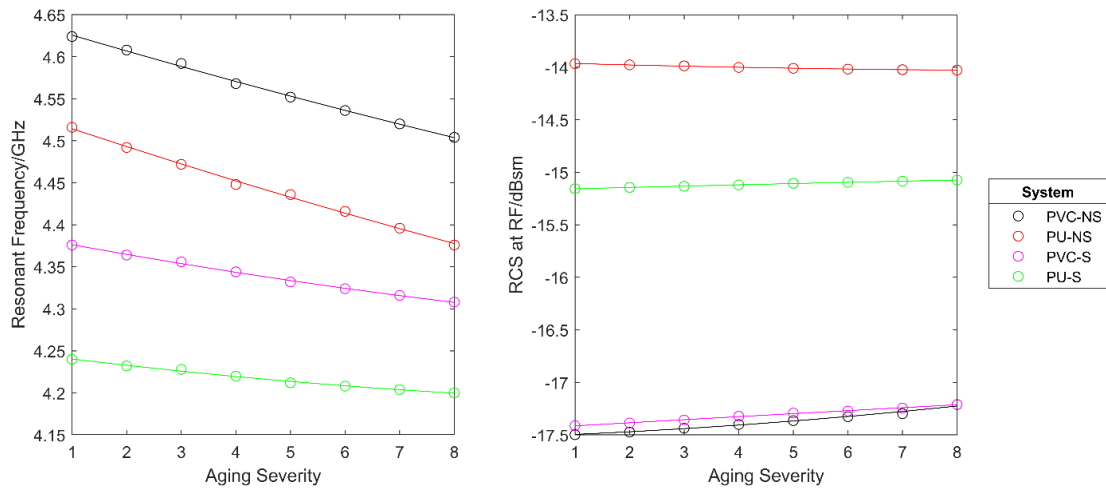


Figure 7.18. The effect of simulated aging on the resonant frequency and the RCS at resonant frequency of each system

7.4.2 Experimental

7.4.2.1 Initial test of the system

Figure 7.19 shows the comparison between the simulated and measured RCS for both paint and mounting systems. This test was carried out on virgin, white coloured samples. It can be seen that interference was captured compared to the ideal simulated scenario. This made the detection of the resonant frequencies for the NS samples (no additional substrate) impossible to determine. However, the resonant frequencies of system two (marked A and B) were detectable. These were observed to be at a higher frequency and provided a smaller RCS drop that was predicted by the simulations. However, this is not unexpected due small variations between the values and assumptions used in the simulations and the actual real values as mentioned previously in Section 7.3.1. The resonant frequency troughs did however appear in a similar position and size relative to each other when compared to the simulated results giving confidence in their correct identification. While it is true that noise would be greatly reduced through the use of an anechoic chamber, this would somewhat defeat the desire to use this technique in the field. While, due to the low simulated RCS trough, it was expected that the NS-PU sample was undetectable, it was surprising that the NS-PVC sample also produced no clear resonant frequency trough, especially as in simulations this showed a clear decrease in RCS of around 3.5 dBsm at resonant frequency. It was theorized that this discrepancy between simulation and experimental may be due to the difference between modelling the coating perfectly as a layer of set dielectric properties and measuring on what is an inhomogeneous, multi-layer, multi component, complex paint system. While in a simulation, the paint system alone can produce a resonant antenna, in real life, the addition of a small FR-4 substrate with homogenous dielectric properties is required to support the resonance of the antenna. Hence, it was concluded that the concept of attaching the circle directly to the paint without an additional substrate was insufficiently responsive to use for further testing.

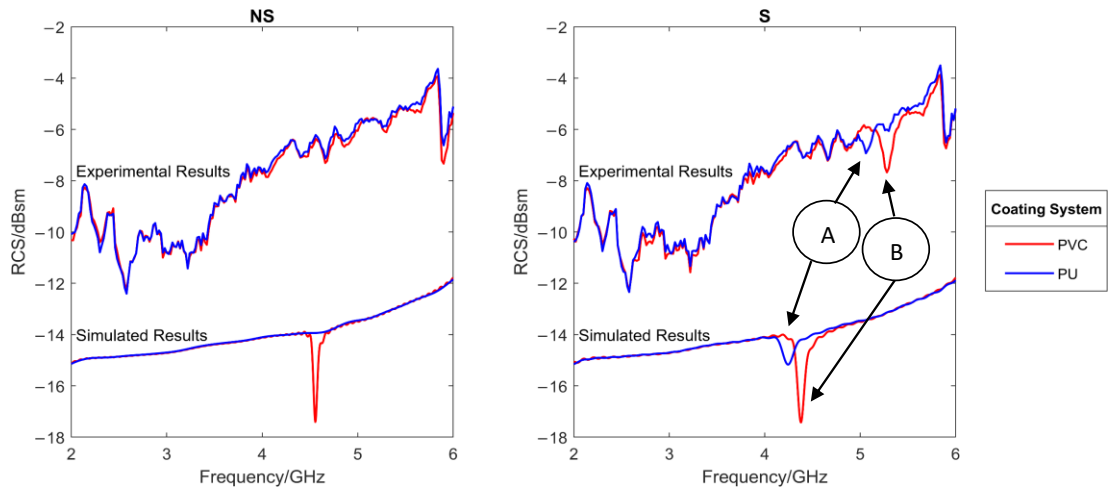


Figure 7.19. Comparison of the simulated and measured RCS response of sensors mounted directly on coated system (NS, right) and sensors mounted on an additional substrate (S, left). Identifiable peaks are matched between simulated and experimental results with designators A and B.

However, to reduce the impact of noise, the following results were calculated by subtracting the sample background RCS. This was the measured RCS of the sample without the antenna attached. As shown later, this allowed far easier trough detection and noise removal.

7.4.2.2 Detection of Artificial Weathering

Following the initial testing of the chipless RFID system, samples were produced with different artificial aging techniques. The set of samples (Salt) was produced via 10 weeks of ASTM B117 salt fog/spray exposure in a 100% humidity (5% NaCl solution, pH 7), 35 °C environment. A second set of samples (Chemical) was exposed to 50 MEK (Methyl Ethyl Ketone) double rubs, a 30 min acetone soak, and a two-hour boil. This was done as a proof of the concept of the technique to detect changes in organic coatings caused by degradation, and hence the use of common accelerated weathering techniques. The samples after exposure are shown in Figure 7.20.

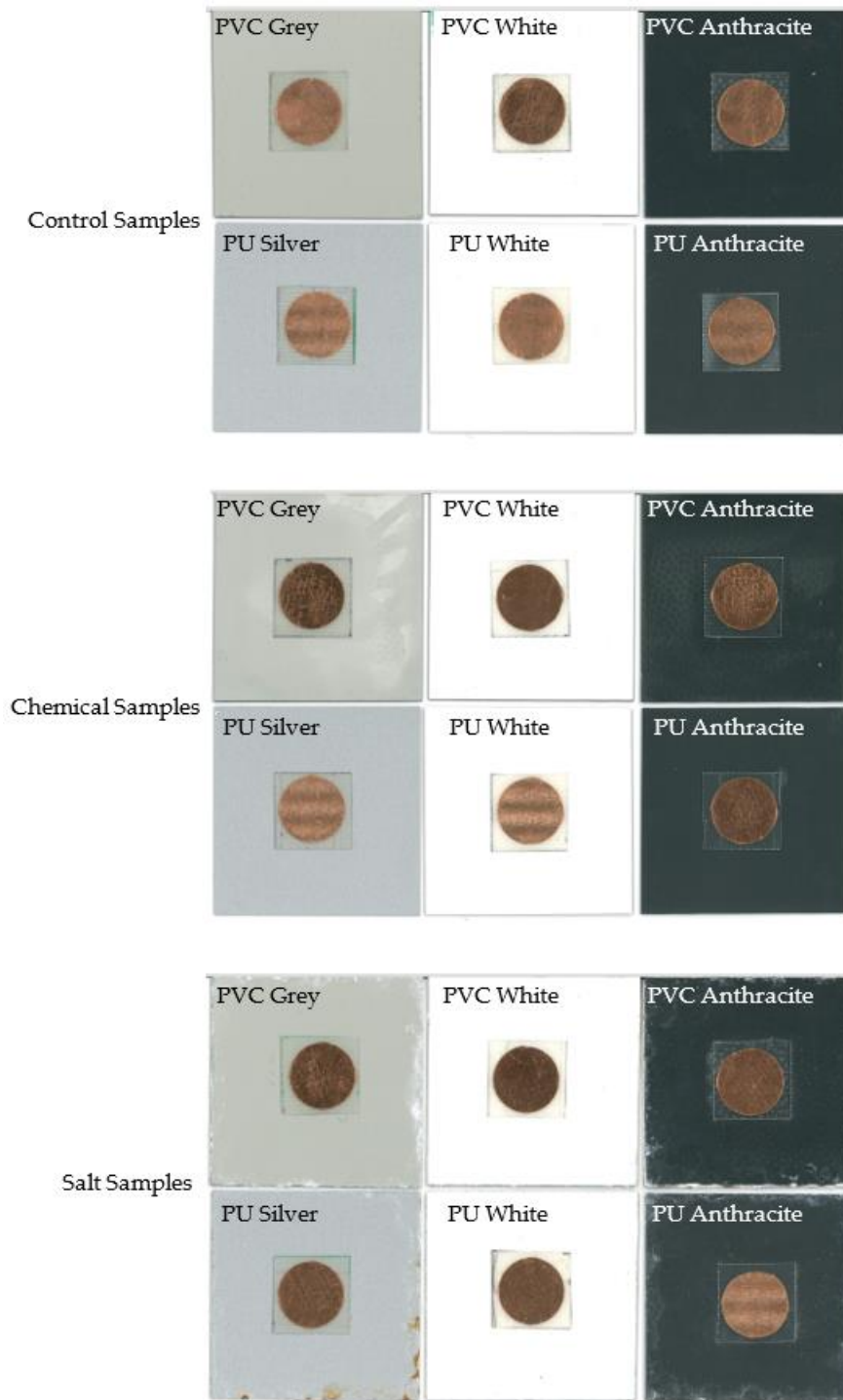


Figure 7.20. Sample appearance after no testing (control) (top), chemical (middle) and salt (bottom) exposure testing.

It can be seen that the chemical samples do not appear, visually, that different to the control samples except for slight discoloration on the PVC grey and anthracite samples. The salt exposed samples show a far greater visual level of degradation with significant blistering and corrosion at the cut edge. However, it should be noted that the sensor tag is only expected to detect changes in the coating directly

underneath where it is placed and that the middle of the samples showed little visual change to the control samples. Hence, the sensor is still monitoring an area in which degradation of the coating has not occurred significantly enough for a visual inspection to determine. After exposure to the environments, the samples were also examined using FTIR. Examples of the FTIR results are shown for a PVC and PU sample in Figure 7.21.

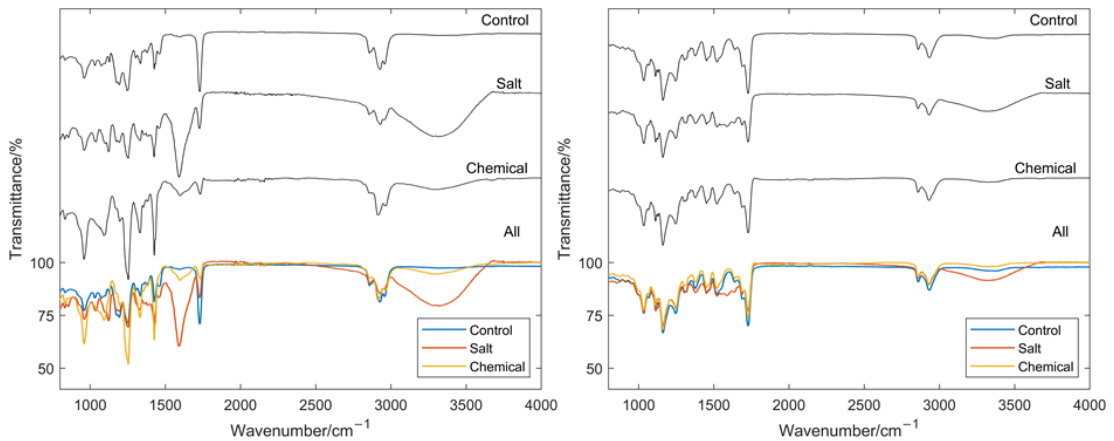


Figure 7.21. Resulting FTIR spectra for an example PVC sample (left) and example PU sample (right).

From these spectra, it is possible to see the effect the different treatments have had on the two paint systems. Perhaps most obvious is the significant emergence of the characteristic broad OH peak between approximately 3000 and 3500 cm^{-1} [20] in the samples exposed to the salt spray. This is indicative of moisture presence either in the coating itself or through the formation of micropores or blisters. While the chemically exposed samples do also perhaps show slight emergence of this peak, especially in the PVC samples, the effect is not as pronounced. From these results, therefore, it would be expected that the salt exposed samples would show a larger increase in dielectric constant compared to the chemically exposed samples as a larger quantity of water uptake is observed for these samples. The respective obtained RCS results for a PVC and PU sample are shown in Figure 7.22.

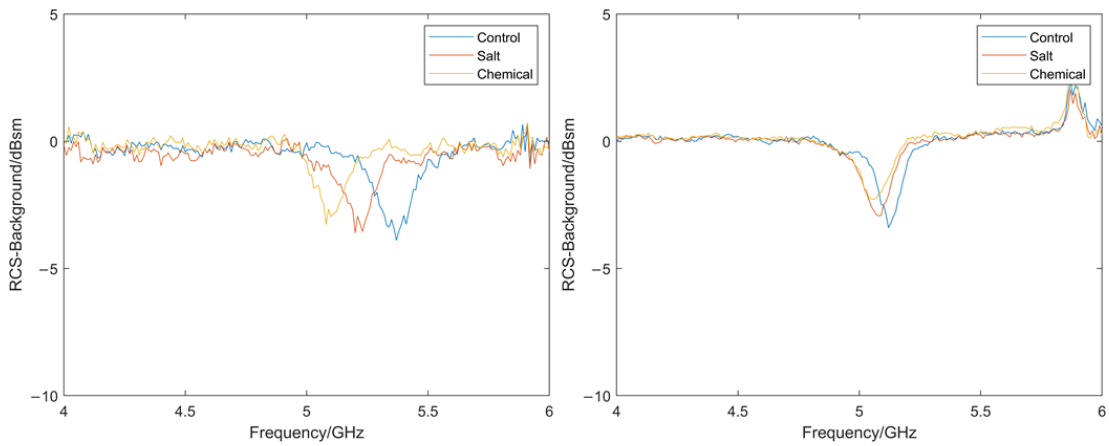


Figure 7.22. Measured RCS for a PVC coating system (left) and a PU coating system (right) samples exposed to salt and chemical degradation.

It can be observed that the salt and chemical treatment has caused the resonant frequency to shift to the left and that this shift is greater in magnitude for the PVC sample. This shift is indicative of the types of changes expected under these tests. A comparison of the resonant frequencies for all the tested samples exposed to the salt and chemical degradation can be seen in Figure 7.23 where the resonant frequency was measured using three repeats. All the samples tested show a similar trend to that of the example above, even with the variation in measurements.

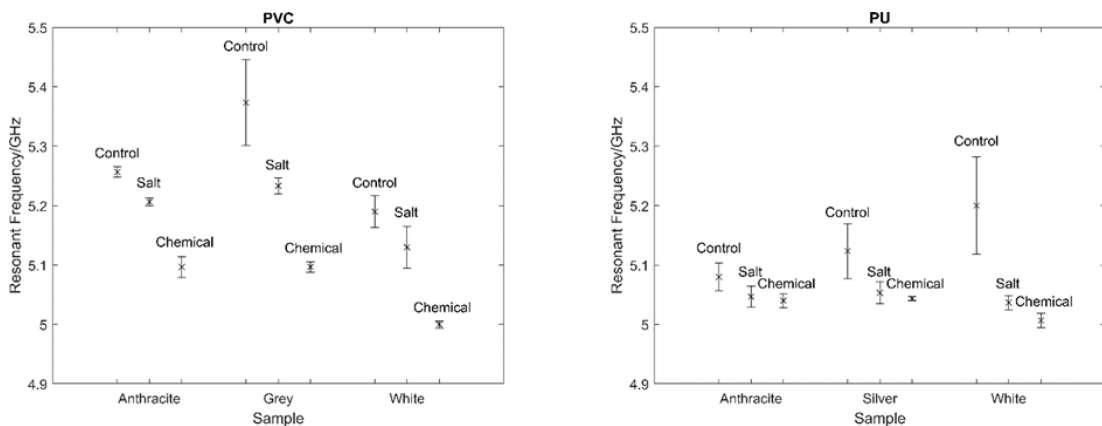


Figure 7.23. Measured resonant frequency for each PVC (left) and PU (right) sample tested and the associated standard error.

As expected, the shift in resonant frequency as a result of coating changes for the PU samples is far more reduced than for that of the PVC samples. As mentioned previously, the additional layer of FR-4 used to increase the signal for both paint systems effectively reduces the magnitude of the relative shift in resonant frequency due to its unchanging dielectric properties. The influence of this effect is far greater in the PU sample, where the FR-4 thickness (0.2 mm) constitutes a far larger

proportion of the total antenna dielectric; approximately 83% compared to 50% of the total PVC antenna dielectric. However, despite this, it is still possible to distinguish the different treatments through resonant peak identification.

7.5 Discussion

There is no doubt that the monitoring of organic coatings applied to steel cladding on buildings is a difficult proposition. The current common monitoring practices for buildings are often simple and subjective manual inspections, and generally, a ‘fix when failed’ approach is taken. This means that degradation is only detected when significant coating damage and/or corrosion has taken place, increasing the cost of rectification. Recent techniques developed for monitoring early-stage coating deterioration suffer from requirements to modify the coating layers or connect to the substrate making results less representative of the bulk and more complex to carry out in-situ.

While not a perfect solution, the novel method developed shows considerable promise for the detection of pre-failure degradation in coated steels, which could be carried out quickly and reliably at low cost. It has shown its ability to detect both water uptake by the coating/coating–metal interface and degradation of the polymer itself before a significant visual change in the sample area has occurred. The degree of degradation is expected to be semi-quantitatively assessed by considering the size of the resonant frequency shift between the virgin sample and exposed sample with a greater degree of degradation producing a larger shift.

However, to further investigate and develop the technique, a number of additional studies are required. The sensitivity of the method needs to be established such that the change in resonant frequency can be more linked to the degree of degradation. For example, UV often affects coating material integrity, and this would be expected to provide a change in the dielectric properties of the coating. Typically, the change in structure that occurs when a coating is subjected to UV arises from the breakdown of the longer polymer chains, pigment bleaching, and cracking of the coating [19]. The precise impact of this and other failure modes on the dielectric properties of the coating should be addressed. This requires multiple coated substrate samples of varied levels of degradation, through multiple degradation mechanisms to be measured and analysed.

Furthermore, the universality of the resonance value for multiple coating systems needs to be established. The absolute resonance is a function of many coating and substrate parameters. Hence, the coating systems of interest must first be tested in advance to determine the specific resonant frequency for the given coating thickness, pigmentation, polymer system and application involved. Thus, this technique would be used to monitor any resonance shift from this specific virgin sample datum, which will need to be considered as the prime indicator of coating degradation/substrate corrosion. It is therefore a relative, not an absolute measurement technique. Given the background noise observed within the laboratory, signal processing techniques may need to be refined in order to clearly identify the peaks in a consistent manner.

Finally, if the laboratory findings are positive then a simplified robust piece of hardware needs to be designed which can be used in the field. All of the hardware electronics for such a device exists and is relatively low cost, but it would need to be ruggedized for use in practice.

It is envisaged that this technique could be deployed via miniaturization into a portable handheld device, which is used to interrogate a tag that can be placed and then removed during routine inspections. The device would ensure that the interrogating antennas are fixed at a required angle and distance for measurement and a 'place and remove' testing procedure would ensure tarnishing of the tags does not impact the results and would reduce the aesthetic implications of constantly mounted tags. The resonant frequency measured could then be compared to the baseline initially measured resonant frequency and the shift related to the condition of the coating system. As each tag is only influenced by the coating directly beneath it several locations would have to be tested. However, this would allow a determination of the general condition of the coating across the building. Where the technique suggests early-stage coating degradation is occurring more rapidly than expected, maintenance and/or re-pair of the coating, via overpainting for example, would reduce the likelihood of degradation continuing to the point where replacement is required.

7.6 Conclusions

This paper has introduced a new non-contact, non-destructive method for the monitoring of organically coated steel. The design of a CMPA was achieved via

simulation and, by considering shifts in the resonant frequency of the CMPA, was shown to provide information as to the condition of an organic coating, even when the organic coating is relatively thin. It was observed that as a coating underwent simulated ageing, the expected response would be a decrease in the resonant frequency due to an increased dielectric constant and reduced thickness. For thinner coatings, the use of an additional piece of FR-4 substrate allowed a more substantial response, although it reduced the sensitivity of the method. Experimental results showed that background noise was the largest cause for concern, and hence resonant peaks could only be distinguished accurately if additional substrate thickness was used. Background removal via the measurement of the sample background RCS was also crucial to allow further ease of peak detection. However, the technique did respond as expected in the simulations when determining the resonant frequency of samples exposed to accelerated weathering conditions. These samples showed a clear decrease in resonant frequency as a result of water uptake and polymer degradation. This method shows promise as a rapid way to determine coating condition non-destructively and without contact with the product being tested.

7.7 References

1. Wiltshire BD, Zarifi T, Zarifi MH. Passive Split Ring Resonator Tag Configuration for RFID-Based Wireless Permittivity Sensing. *IEEE Sens J*. 2020;20(4):1904–11.
2. Amin EM, Karmakar NC, Jensen BW. Fully printable chipless RFID multi-parameter sensor. *Sensors Actuators, A Phys* [Internet]. 2016;248:223–32. Available from: <http://dx.doi.org/10.1016/j.sna.2016.06.014>
3. Karmakar NC, Amin EM, Saha JK. Introduction. In: *Chipless RFID Sensors*. 2016. p. 1–245.
4. Preradovic S. Chipless RFID System for Barcode Replacement [Internet]. 2009. Available from: https://www.google.com.au/url?sa=t&rct=j&q=&esrc=s&source=web&cd=1&cad=rja&ved=0CDoQFjAA&url=http://arrow.monash.edu.au/vital/access/services/Download/monash:62604/THESIS01&ei=_X8VUuSPBMm3iQfp-YHQDA&usg=AFQjCNF-9bbRZKfZK9Z95AaM8izHUfmoSw&bvm=bv.511565
5. Marindra AMJ, Tian GY. Chipless RFID Sensor Tag for Metal Crack Detection and Characterization. *IEEE Trans Microw Theory Tech* [Internet]. 2018 May;66(5):2452–62. Available from: <https://ieeexplore.ieee.org/document/8307772/>
6. Balanis CA. *Antenna theory : analysis and design*. Third edit. 2005.
7. Milligan TA. *Modern Antenna Design* [Internet]. Modern Antenna Design. Hoboken, NJ, USA: John Wiley & Sons, Inc.; 2005. Available from: <http://doi.wiley.com/10.1002/0471720615>
8. Khalifeh R, Lescop B, Gallée F, Rioual S. Development of a radio frequency

- resonator for monitoring water diffusion in organic coatings. *Sensors Actuators, A Phys* [Internet]. 2016;247:30–6. Available from: <http://dx.doi.org/10.1016/j.sna.2016.05.024>
9. DassaultSystems. CST Studio Suite [Internet]. ELECTROMAGNETIC FIELD SIMULATION SOFTWARE. 2022 [cited 2022 Apr 7]. Available from: <https://www.3ds.com/products-services/simulia/products/cst-studio-suite/>
 10. ANSYSInc. Ansys Granta EduPack software [Internet]. Cambridge, UK,. 2020. Available from: (www.ansys.com/materials).
 11. DassaultSystems. CST Material Library. CST Studio Suite. 2021.
 12. KAB_ELECTRO_ACOUSTICS. Dielectric Constants [Internet]. [cited 2020 Jun 4]. p. 1–52. Available from: <https://www.kabusa.com/Dilectric-Constants.pdf>
 13. Wroe S, Curtis-thomas C. COLORCOAT HPS200 ULTRA - APPROVAL INSPECTION TESTING CERTIFICATION. *BBA Tech Approv Constr.* 2017;1–7.
 14. MatWeb. Overview of materials for Thermoset Polyurethane [Internet]. 2020 [cited 2020 Jun 4]. Available from: <http://www.matweb.com/search/DataSheet.aspx?MatGUID=26606798bc9d4538a7c7eadf78ab082b>
 15. Wroe S, Cooper G. COLORCOAT PRISMA-APPROVAL INSPECTION TESTING CERTIFICATION. *BBA Tech Approv Constr.* 2010;1–8.
 16. CST_Microwave_Studio. Boundary Conditions - Boundaries [Internet]. 2013 [cited 2020 Jun 3]. Available from: http://www.mweda.com/cst/cst2013/mergedprojects/CST_MICROWAVE_STUDIO/special_solvopt/special_solvopt_boundary_conditions_boundaries.htm
 17. Pozar DM. MICROSTRIP ANTENNAS. *Electromagnetics* [Internet]. 1992 Jul;12(3–4):381–401. Available from: <http://www.tandfonline.com/doi/abs/10.1080/02726349208908321>
 18. de Leon A, Advincula RC. Conducting Polymers with Superhydrophobic Effects as Anticorrosion Coating [Internet]. *Intelligent Coatings for Corrosion Control*. Elsevier Inc.; 2015. 409-430 p. Available from: <http://dx.doi.org/10.1016/B978-0-12-411467-8.00011-8>
 19. Gerard Torney N, Harkin-Jones E. Investigating the recyclability of Polypropylene [Internet]. Ulster University; 2017. Available from: <https://www.researchgate.net/publication/330797824>
 20. Merck. IR Spectrum Table [Internet]. Technical Data Sheet. 2022 [cited 2022 Feb 21]. Available from: <https://www.sigmaaldrich.com/GB/en/technical-documents/technical-article/analytical-chemistry/photometry-and-reflectometry/ir-spectrum-table>

Chapter 8: Magnetic Flux Leakage Sensor

8.1 Introduction

As shown in the literature review, the magnet flux leakage (MFL) technique is a well-developed and established corrosion sensing method deployed commercially in the asset protection sector. However, the current methods of deployment are unsuitable for this application or require manual input in the operation. In this chapter, an adaptation to traditional MFL measurements is explored in an attempt to tailor the system better to the monitoring of OCS cladding. The feasibility of this new deployment concept is explored in terms of the sensitivity/ability of the corrosion detection.

8.2 Background and application of the technique

This technique, which has been explained previously, is a commonly used non-destructive technique for the detection of corrosion in pipelines and other assets. The basic concept of operation is that most steels, due to their iron content, are ferromagnetic and hence can be magnetized by an external magnetic field. Because of this when placed in a magnetic field the field lines are concentrated through the iron-based substrate [1]. This effect is shown in Figure 8.1 below.

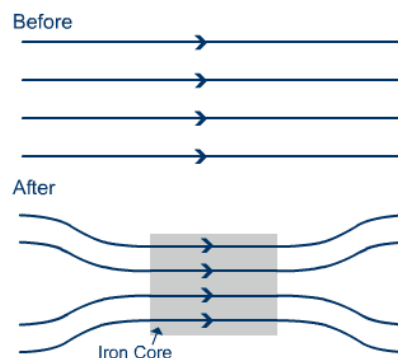


Figure 8.1. Effect of ferromagnetic iron on magnetic field lines [2]

However, as steel is corroded it forms a variety of iron oxide products which, generally speaking, are either non-ferromagnetic or less ferromagnetic. This means a corroded steel sample will be less strongly magnetised than an uncorroded sample

for the same given magnetic field. Hence, it would be expected to concentrate the magnetic field lines through it to a much lesser extent. It is therefore possible to monitor corrosion by monitoring the change of magnetic flux, or field strength, of the samples in a constant magnetic field. Most commonly this technique is used with the magnet and sensor on the same side of the sample however it is also possible to have them on different sides as is shown in Figure 8.2.

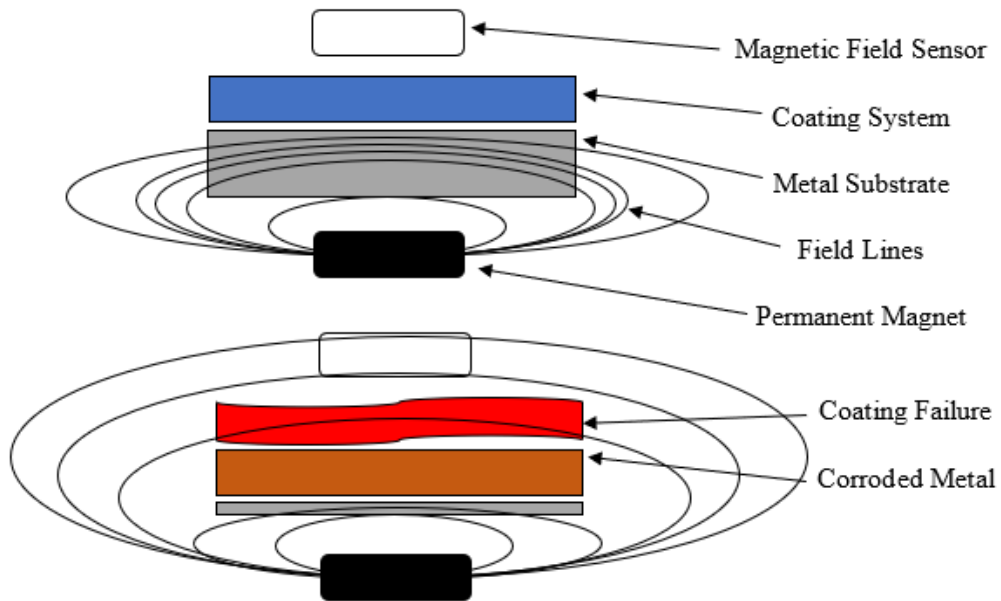


Figure 8.2. Demonstration of magnetic field testing on uncorroded (top) and corroded (bottom) coated steel

While this technique is commonly used in non-destructive testing of pipelines via autonomous ‘pigs’, autonomy of this technique is difficult on more complex, non-continuous surfaces such as façades. The majority of asset testing applications of this technique involve an operator using a handheld or portable device to manually scan over an asset or a small-scale CNC style scanning apparatus, Figure 8.3. While this is time consuming and resource demanding, this type of testing has been demonstrated a suitable technique for detecting corrosion and other defects in coated steel samples [3–6].

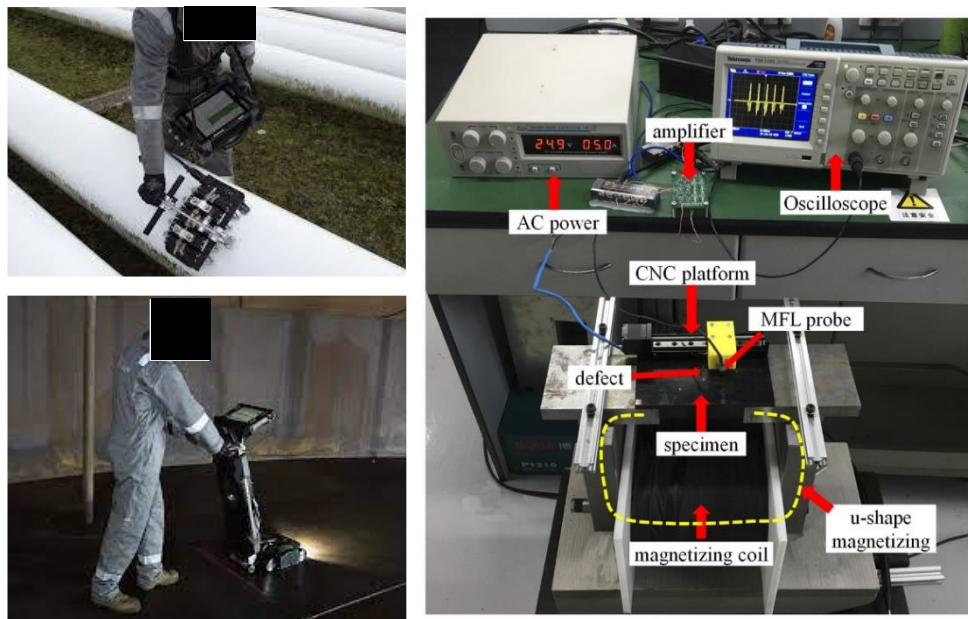


Figure 8.3. Different MFL testing methods including commercially available handheld (top left) roller (bottom left) and research-based CNC (right) [7,8]

It was theorised that this technique could be better applied to monitor OCS cladding by deploying a static array of magnets and sensors. While magnet and sensor arrays are well researched and used this is usually only to produce a more accurate measurement or larger or more specific area of measurement for a scanning device. It is not thought that this style of static array has been considered previously to passively monitor an asset over time. This system would indicate the emergence of corrosion through an increase in the measured leakage field strength from the original state, Figure 8.4. The benefit of such a system is that it would be inherently autonomous without requiring complex scanning control.

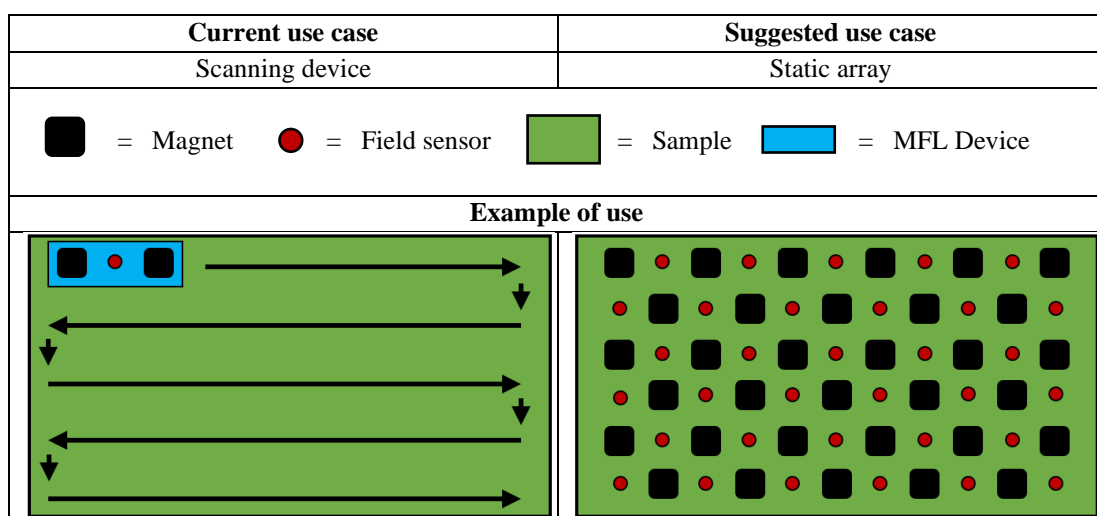


Figure 8.4. Suggested adaptation to the technique for this application.

In the current use case, the sensors and magnets can be complex and expensive as only a small number are required per device which is scanned over the surface. In the suggested use case, a large quantity of sensors and magnets are required to cover an area of sufficient size and at sufficient density to detect the formation of corrosion defects. Therefore, the sensors and magnets used need to be cost effective to deploy in moderate quantities yet still provide the required level of precision to detect changes associated with corrosion of the substrate. In this chapter, an assessment of the effectiveness of sensors of this type for corrosion detection on a number of substrates is carried out.

8.3 Methods and materials

A number of prototype measurement rigs were used to test the working principle of this concept and determine the detection abilities. Each of these prototypes had four key elements which were a magnetic field source, magnetic field sensors, measurement system and a housing.

For all the prototypes the magnetic field source was composed of rectangular neodymium magnets with a size of approximately 20x10x2mm and a rated pull strength of 2.1kg. These were chosen due to their relative strength to size ratio.

Three types of sensors were used in the prototyping state. The first was a relatively cheap, small, and simple SS495A Honeywell radiometric hall effect sensor. These had a minimum stated magnetic detection range of -600 to +600 Gauss and a sensitivity of 3.125 ± 0.125 mV/G [9]. Under a 5V supply, typical output of the sensor, from 0.5V to 4.5V, can be directly mapped to obtain the Gauss value as shown in Figure 8.5 [9].

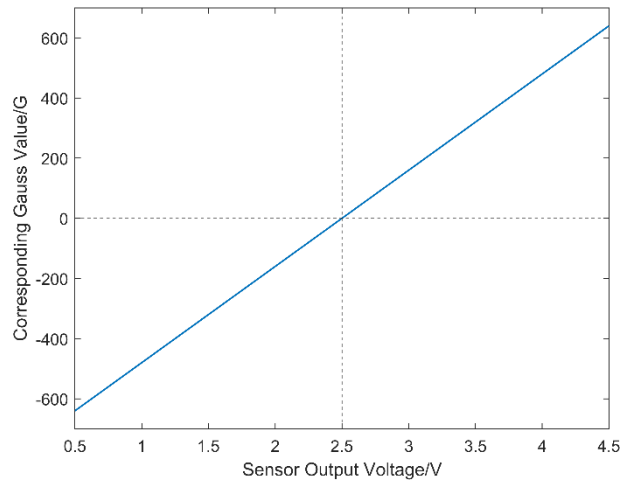


Figure 8.5. Sensor output to value relationship

The second sensor used for the second prototype was the SS495A1 Honeywell radiometric hall effect sensors which are similar to the previous sensors but had an improved sensitivity accuracy of 3.125 ± 0.075 mV/G [10].

The third sensor used in final prototype was a MLX90393 that could measure 16-bits in ranges from ± 5 mT to ± 50 mT in the x, y and z axis [11].

The measurement system for each prototype was controlled by an Arduino microcontroller which outputted data via Microsoft Excel Datastreamer. The Arduino was programmed to collect measurement data at a rate of approximately 500-1000 samples per second and output this to Datastreamer, hence each raw value recorded in Datastreamer was in itself an average of a number of measurements.

The housing for each prototype was the structure that supported either the magnets, the sensors or both. With this technique it was important that the distance between magnetic field source and sensor remains constant between tests, and this was the main reason for using a housing. These were made from laser cut 2mm acrylic sheet onto which the sensors, magnets and connecting wires were glued.

While the concept was for a large discrete array of sensors and magnets the prototypes were composed of a small linear array of magnets and sensors that could be moved to measure a number of positions on samples as if the array covered the entire sample. This was done to allow a quicker initial prototyping stage with a reduced number of sensors to connect, monitor and measure.

To test the prototypes a number of substrates were used. These included 0.221mm thick steel blackplate, polyester coated galvanised steel and 3-layer PU coated and 2-layer PVC coated samples. The blackplate was used as an easily cut and corroded starting substrate with which tests could be quickly carried out. The polyester coated galvanised steel was a more realistic and resilient substrate in terms of corrosion damage over time. The coated samples are comparable to industrially coated systems, so were used to provide the validation of this technique for use.

To test the concept several stages of tests were carried out to assess the quality of defect detection. Initially these tests aimed to conclude whether the system could detect between presence of metal and the absence of metal, then to determine the sensitivity of such detection. The ability to detect corrosion and sensitivity of such detection was then investigated. New prototypes were introduced in response to a failure of the current prototype to successfully meet requirements.

8.4 Prototype 1

This main body of the first test rig was composed of an upper sensing layer with 4 hall sensors evenly spaced and a lower magnetic field layer with 3 evenly spaced magnets, joined by a thin metal plate acting as a magnetic yoke. The gap between upper and lower layers was approximately 1cm and provided a test area of approximately 8cm by 4cm. The prototype system is shown in Figure 8.6.

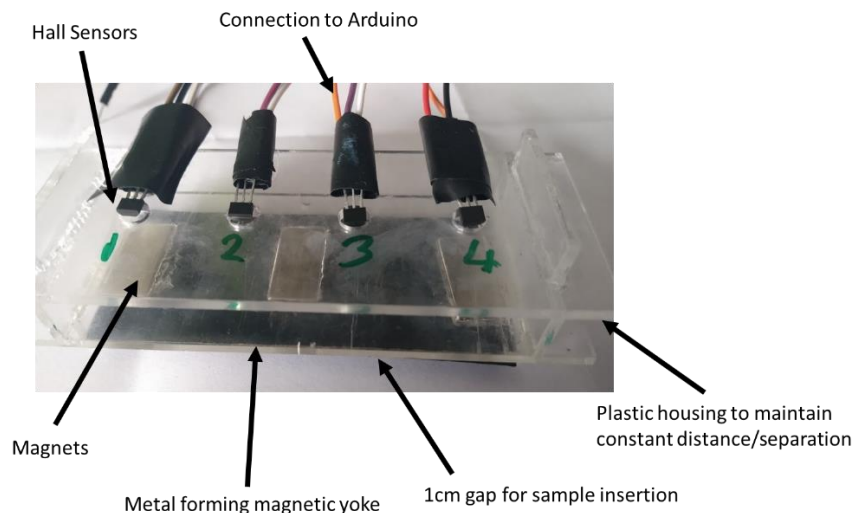


Figure 8.6. The initial test rig

8.4.1 Prototype 1 – Detection of metal presence/absence

The first test carried out using prototype 1 was used to determine if the prototype could distinguish between in the presence and absence of metal. To facilitate this an ‘s’ shaped test piece, shown in Figure 8.7, was produced out of blackplate. As the figure shows the test piece was composed of a rectangle of metal with two horizontal rectangles cut out and the bottom left corner angled off. This was done to create a number of distinct regions, and these were each measured by placing that specific section in the sensing area. At each position data was recorded for approximately 2 minutes.

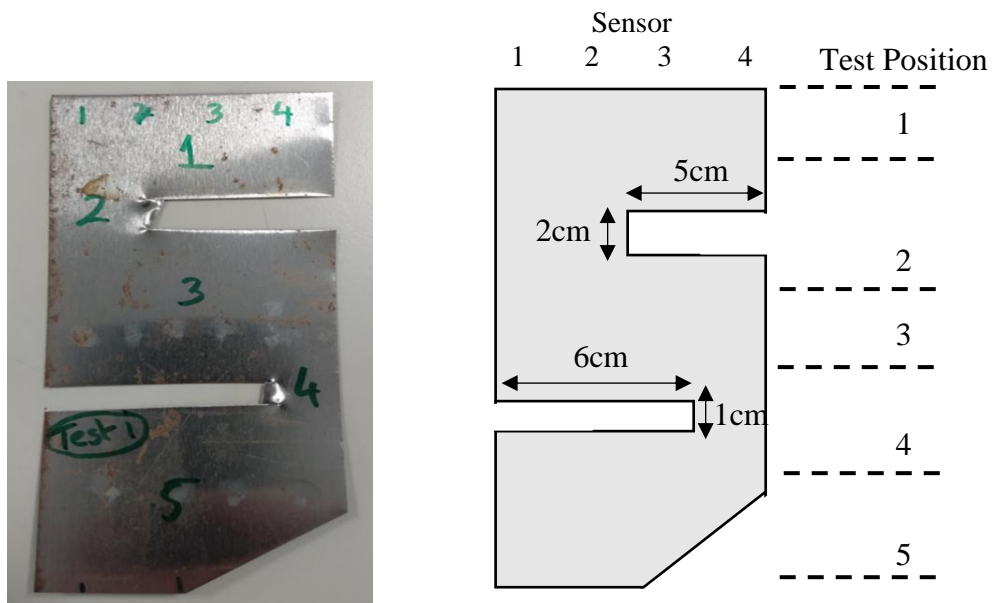


Figure 8.7. Test sample 1 image (left) and dimensions (right)

In this test, as with all, the expected trend was that when metal is present the flux measured by the hall sensors is low (as the metal contains the flux) whereas at defects or places where the amount of metal is reduced, the flux cannot be as fully contained and leaks out. Therefore, at sites of defects it was expected that the hall sensors would show an increased magnitude of measured magnetic field strength. This was shown to be the case in this initial test when considering the measured Gauss values for each sensor, Figure 8.8.

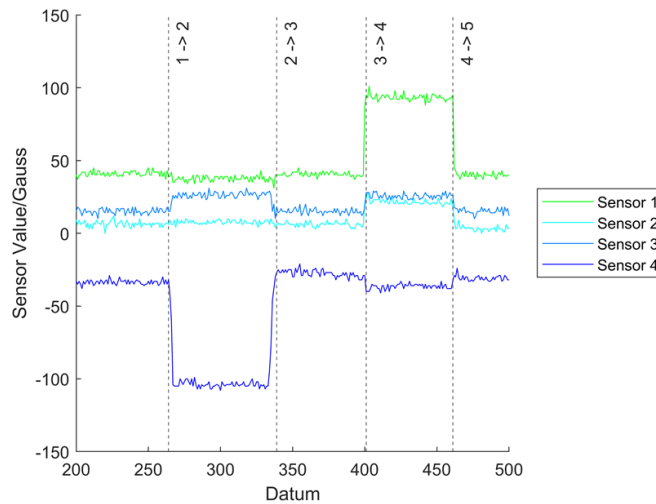


Figure 8.8. Test 1 sensor values

As the test position was changed from 1 to 2, signified by the dashed line labelled 1->2, the values from sensors 3 and 4 increased in magnitude with sensor 4 values increasing significantly. Similarly, when test position was changed from 3 to 4 the values from sensors 1,2 and 3 all increased significantly. The change for each sensor at each position was more easily observed by comparing the average sensor value at each position as is shown in Figure 8.9 where the horizontal dashed lines represent the average value for each sensor across the whole test.

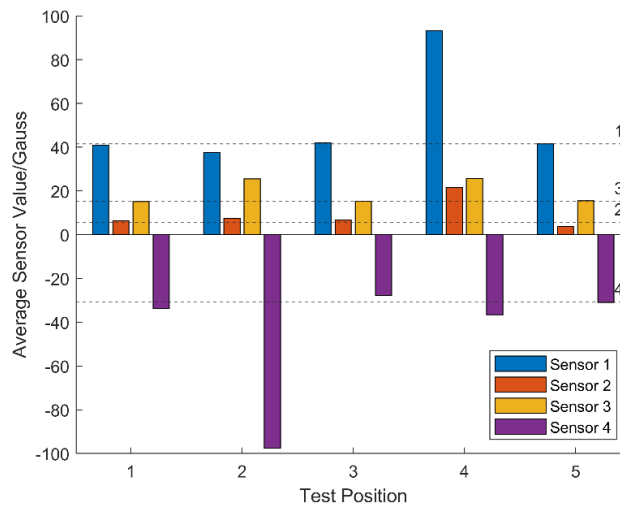


Figure 8.9. Test 1 average sensor values for each position

By taking the average value of each sensor at positions 1 and 3 where there are no defects, it was possible to compare the average sensor deviation from normal at each test position as shown in Figure 8.10A. While the graphs of the sensor values, and average deviation from the norm are useful, the aim of this work was to sense the

location, size, and severity of defects. To this aim a far more useful application of the measured data was achieved via the plotting of a 2D colour map showing the deviation in sensor value in each position, Figure 8.10B. From this visualization it was seen that the prototype has provided a reasonable representation of the tested sample.

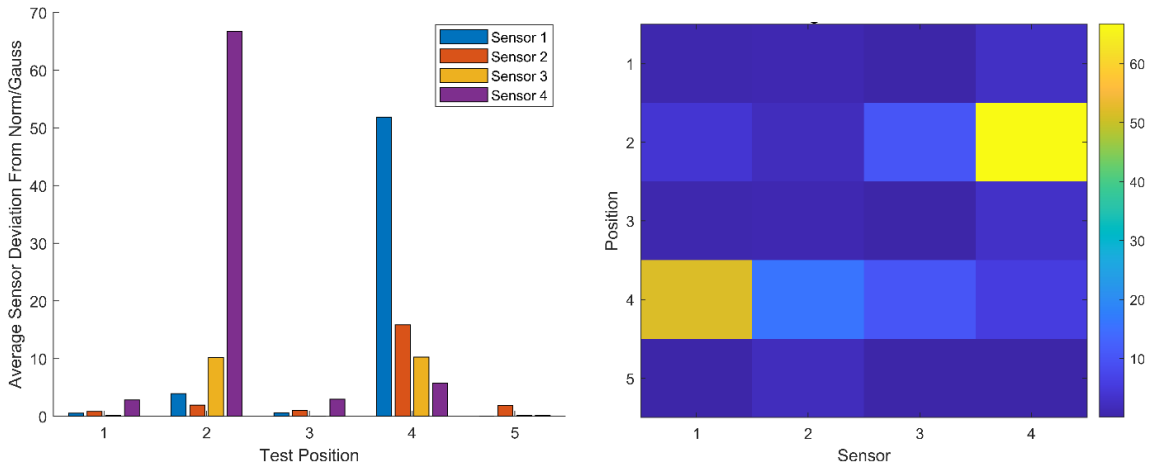


Figure 8.10. Average sensor deviation for each position (Left) and 2D Plot of the average deviation (Right)

Of particular promise is the fact that the 2D plot showed a greater deviation for sensor 4 at position 2 than for sensor 1 at position 4. This correlates with the sample dimensions, in that the cut at position 2 is double the width of that at position 4. Furthermore, the influence of the cut at position 4 was greater horizontally than that at position 2; this also correlates with the cut at position 4 being larger in length than that at position 2. Unfortunately, it appeared that the corner cut at position 5 was not adequately detected. It is possible that detection was reduced as the defect was not as orientated to the plane of magnetism and detection as the cut holes were. However, it appeared that the system generally had performed well in detecting metal presence and absence.

To confirm this conclusion a second blackplate test piece was also measured. In this case, the sample, shown in Figure 8.11, had three rectangles cut out of the same length of widths ranging from 1cm to 3cm. All the cuts were made from the right and ended directly in the middle of the sample and hence it was expected they would affect the values produced by sensors 2, 3 and 4 and leave sensor 1 unaffected.

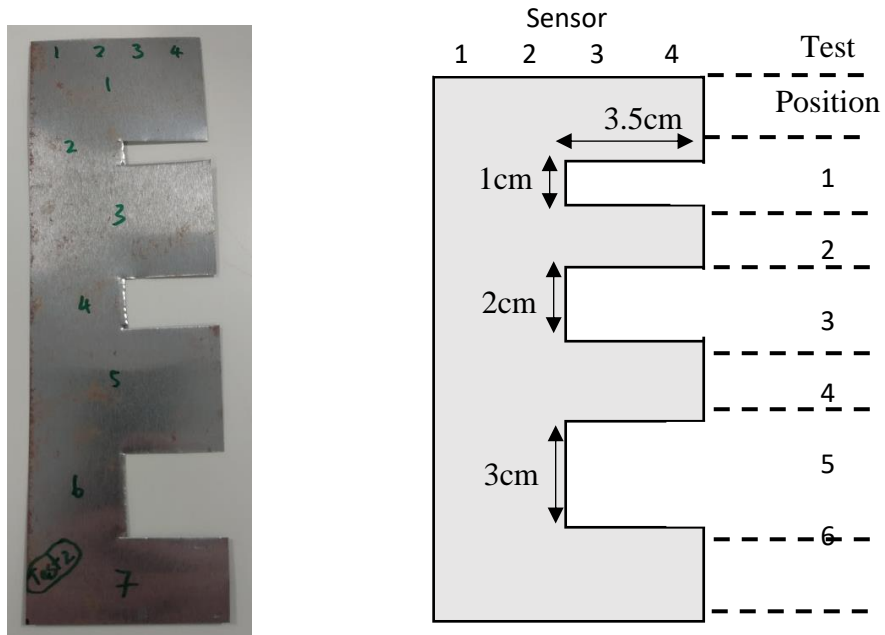


Figure 8.11. Test sample 2 image (left) and dimensions (right)

The resulting 2D colour plot, shown in Figure 8.12, again correlated well with the test sample shape and the size of each defect could be easily ranked according to relative size based on the deviation amount. It was promising to see that for all of sensors 2, 3 and 4 the deviation increased as the size of the defect being observed increased. Sensor 1 showed little to no deviation from average values indicating that the method did not produce any false positive readings during this test.

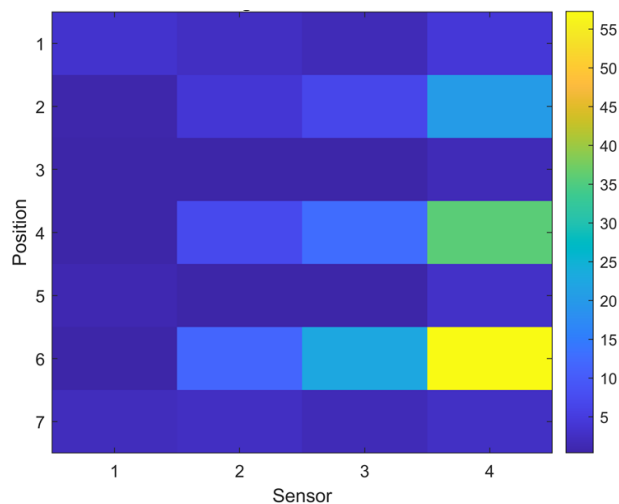


Figure 8.12. Test 2 2D Plot of the average sensor deviation for each position

From these two tests it was concluded that this set up could detect between the presence and absence of metal when large artificial defects are made in the test piece

in the direction of magnetisation. There was evidence to suggest the relative size of these defects can be determined via the size of sensor value deviation at the defect site vs normal.

8.4.2 Prototype 1 – Detection of smaller zones of metal absence

Although the previous tests proved the concept of detection, the defects used in those samples were relatively large and it was perhaps unsurprising they had a large effect on the measured magnetic field strength value. Hence it was decided to test the detection of smaller artificial defects. To do this several 5mm holes were drilled into a blackplate test piece to produce the sample shown in Figure 8.13. The holes were drilled to correspond to the position of sensor 4, 2 and 2 and 3 for test positions 2, 4 and 6 respectively.

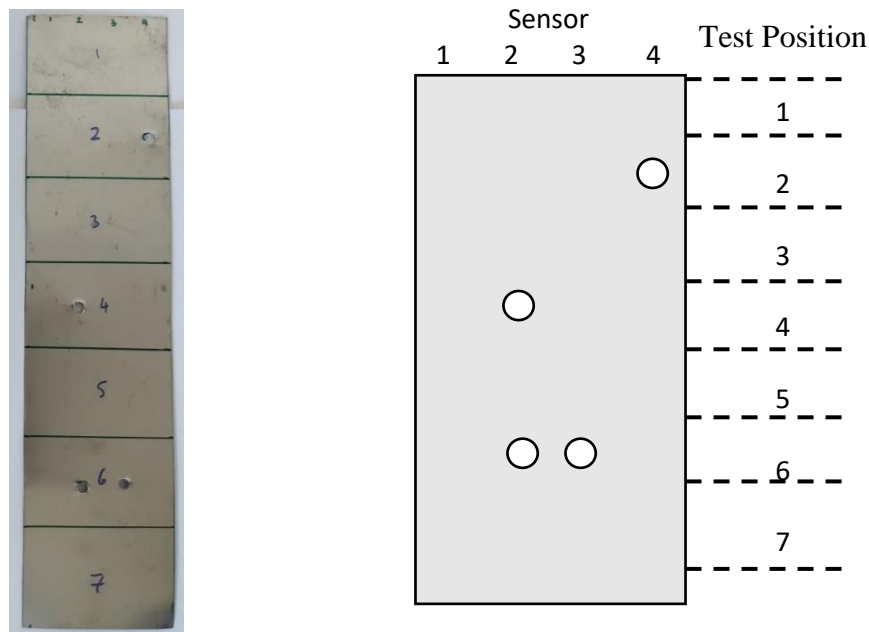


Figure 8.13. Test sample 3 image (left) and layout (right)

The resulting 2D plot of sensor value deviation, Figure 8.14, shows that there was some level of detection of these smaller defects. For example, the hole at position 2 was well detected by sensor 4 although it was strange that the holes at position 4 and 6 were detected more significantly than sensors 1 and 4 than 2 and 3 despite the latter being closer in proximity to the defect. Generally, the detection was not as accurate as the previous tests, and it was thought this was perhaps due to the reduced magnitude of the sensor deviation. The previous tests showed sensor deviations of 50+ Gauss at defects however in this test the maximum deviation at a defect was

only approximately 8 Gauss. This, therefore, suggested there may be difficulty in the separation of actual defects from general noise of measurement. However, it was concluded that this prototype does allow some detection of defects down to 5mm diameter in size, albeit with some reduced accuracy.

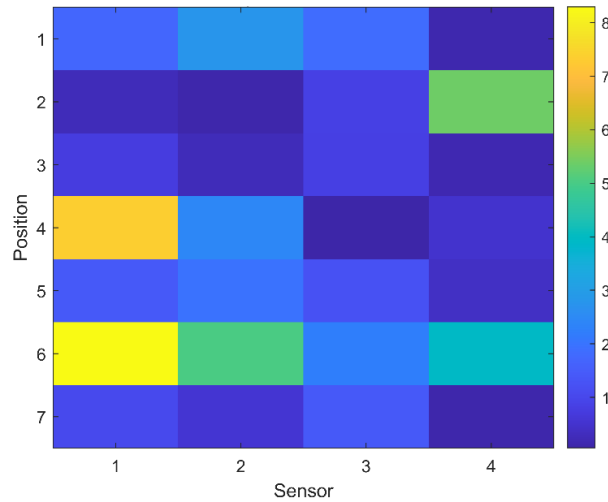


Figure 8.14. Test 3 2D Plot of the average sensor deviation for each position

8.4.3 Prototype 1 – Effect of non-metallic layer on response

All tests previously used plain sheet metal however the application required of this method is for use on coated steel samples. Therefore, a sample was produced to test if thin a non-metal layer placed on the sheet metal had any effect on measurement. This sample, shown in Figure 8.15, was coated in 0.14mm thick 3M Scotch Vinyl tape with several bare sections which would allow determination of whether the tape affects the measured Gauss value.

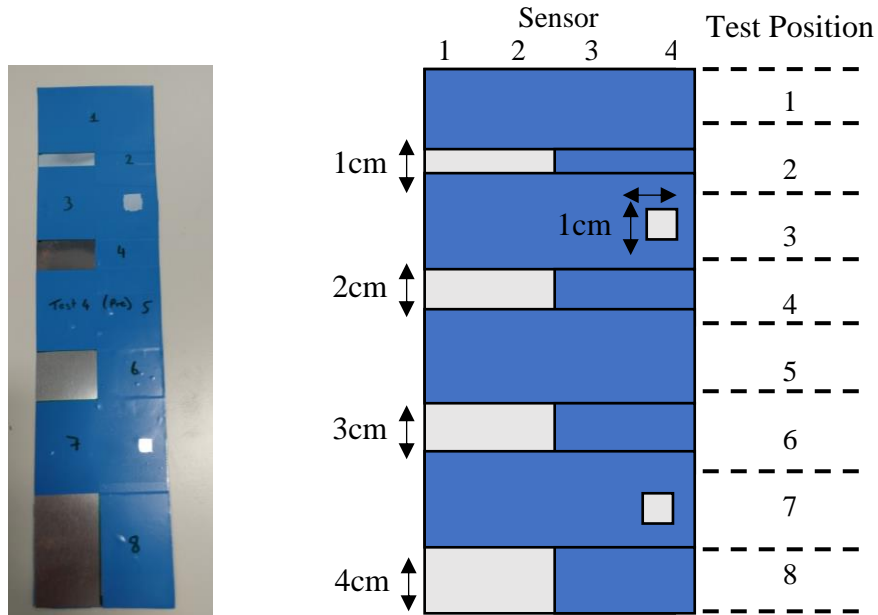


Figure 8.15. Test sample 4 image (left) and dimensions (right)

The resulting 2D plot of sensor deviation, Figure 8.16, showed that there was little correlation between deviations in the measured Gauss value and the position of the taped (coated) and bare sections. This suggested that a thin non-metal layer had little effect on the measurement and hence the previous results would be valid for a coated metal sample. This experiment can also, therefore, be considered as a test of the natural background deviation in measurement which was shown to be a maximum of approximately 3 Gauss. Therefore, for future tests this was considered; any changes in value by less than 3 Gauss were within the normal noise of the measurement method based on this test.

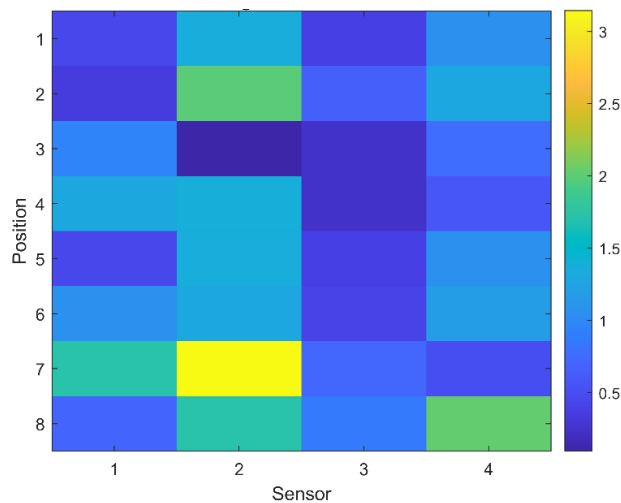


Figure 8.16. Test 4 2D Plot of the average sensor deviation for each position

8.4.4 Prototype 1 – Detection of corrosion defects

The previous testing has shown that this technique and prototype was capable of detecting artificially produced defects in steel substrates and appeared to be unaffected by thin non-metal coating layers. However, it is specifically detection of corrosion that is required for this application and hence testing was carried out on accelerated corrosion samples to determine the feasibility of detection. Theoretically, detection should be possible, as corrosion reduces the thickness of the metal substrate and the corrosion product itself is non-magnetic. Both of these factors suggest that a corroded sample or area of a sample should have a decreased ability to contain a magnetic field compared to uncorroded metal. Hence, flux should leak out at corroded sites and a greater magnetic field be detected by the hall sensors. However, it was noted that the likely change in magnetic field strength will be vastly smaller than previous tests, where it was a difference between metal or no metal as there will likely only be a relatively small reduction in metal thickness or small defects forming.

To test the ability of this prototype to detect corrosion a set of 5 samples were made of which one was a reference sample and the other 4 were samples with different sections covered with tape. These samples are shown in Figure 8.17. For each sample there were only two positions and the deviation in measurement for each sample was measured in regard to the reference sample which was fully covered in tape.

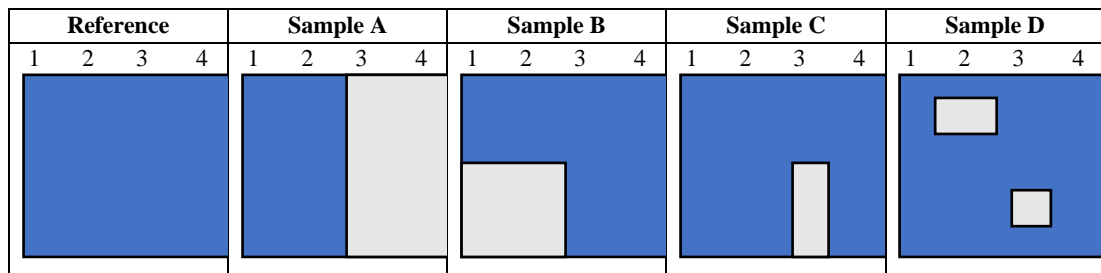


Figure 8.17. Test samples 5 Reference, A, B, C, D

In order to corrode the exposed section of each sample 5% wt NaCl solution pH 7 was placed onto the exposed area of the sample. Measurements were made after 2, 5 and 8 days of exposure to the salt solution and the samples were measured as corroded and after cleaning to remove any remaining salt crystals and corrosion product. Cleaning was achieved by gentle wiping using acetone. The appearance of each sample after exposure and cleaning is shown in Figure 8.18.

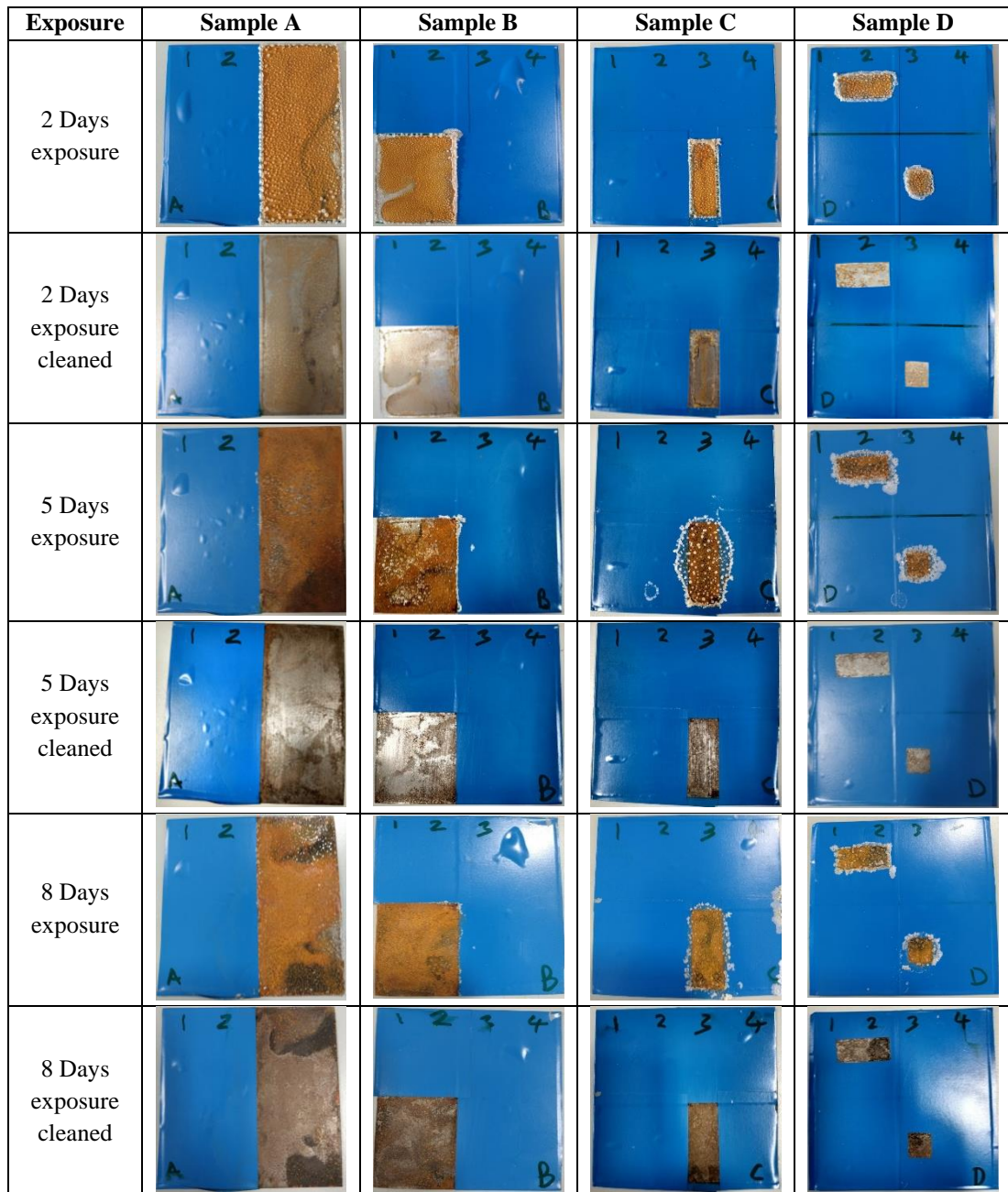


Figure 8.18. Test 5 samples after exposure/cleaning

At each stage it was observed that a reasonable quantity of corrosion product formed at the exposed metal which, when cleaned, revealed that the surface has been attacked. Visually, this confirmed that corrosion had taken place to an extent, although it was noted that this was early-stage corrosion which had not significantly affected the structural stability of the metal. Generally, there was little success at detecting the corrosion defect as shown by the 2D map of the average Gauss deviation from the, unexposed, uncorroded, reference sample for each sample at the 8-day period, Figure 8.19. This sample set is used as an example and had the greatest chance of showing detection due to it experiencing the time of corrosion.

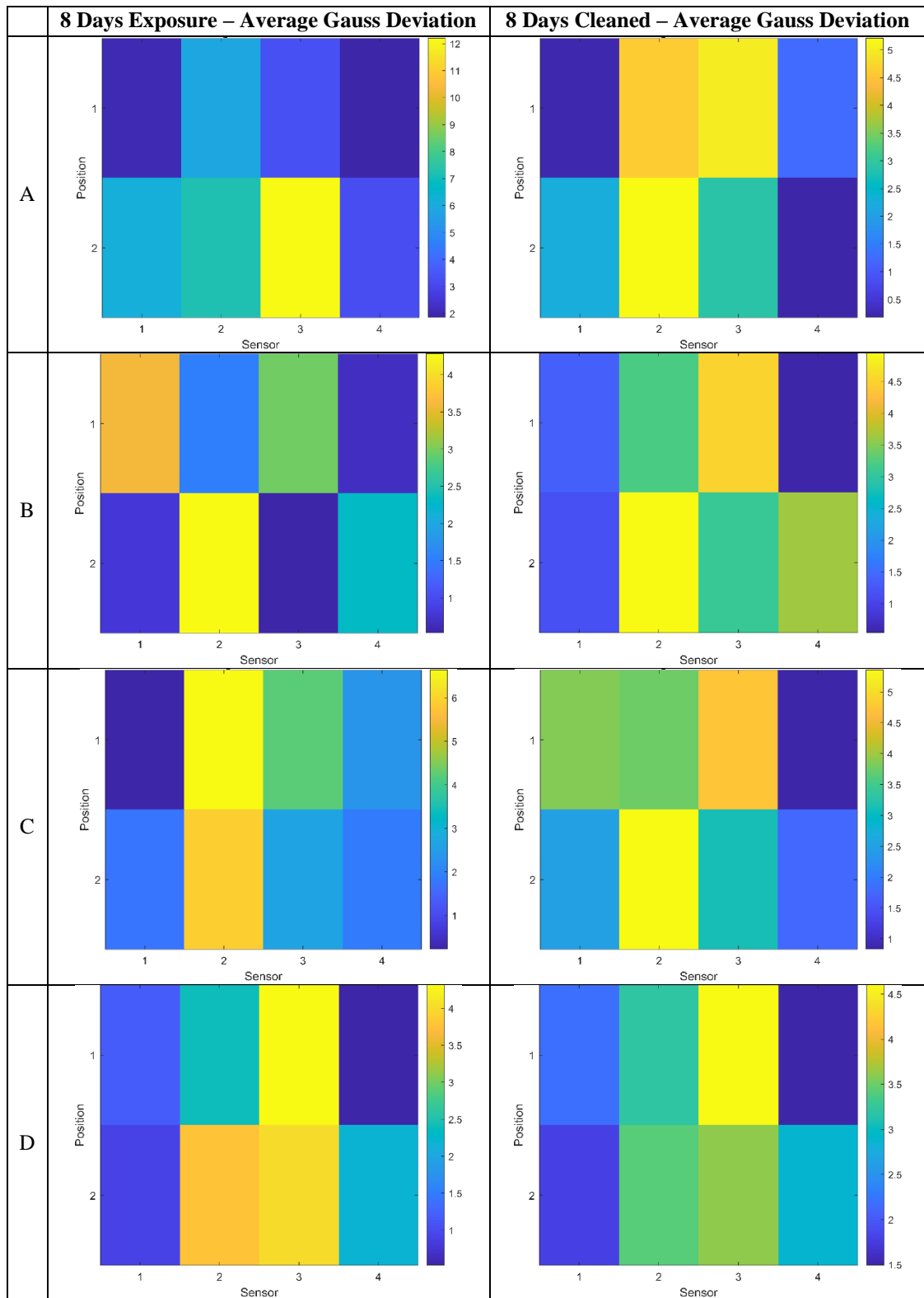


Figure 8.19. Test 5 Gauss deviations after 8 days for the uncleaned and cleaned samples

The results from this sample set were far less conclusive than any of the previous defect detection results. There appeared to be little, if any, correlation between the area of the sample that has been exposed to corrosion and the areas that show the largest change in measured Gauss value. Perhaps this was due to the generally low

values of Gauss deviation that were seen in this test with most deviations a maximum value of less than 5. As a previous test suggested that experimental noise can produce variations up to approximately 3 Gauss it was supposed that the changes due to corrosion were being lost in noise. Also, it was considered that the corrosion was not sufficient to produce a defect that is detectable by this current set up. While it was clear that a metal to no metal change was detectable, it was thought that the small reduction in the amount of metal present due to corrosion was beyond the detection limit.

8.4.5 Prototype 1 – Sensor interference check

The initial test rig used 4 sensors placed approximately 2cm apart. It was thought possible that the close proximity of the sensors could cause them to interfere with each other as their internal circuitry could theoretically create a small magnetic field. This could contribute to noise or inaccuracy in measurement. Therefore, it was decided to test if sensor proximity is a factor that could affect the quality of results. In order to determine the effect of sensor proximity four measurements were undertaken on the same sample; the sample used was the sample from the previous test 4:

1. Measurement with all sensors recording
2. Measurement with all sensors recording (repeat)
3. Measurement with only sensors 1 and 4 recording, sensors 2 and 3 disconnected
4. Measurement with only sensors 1 and 4 recording, sensors 2 and 3 disconnected (repeat)

With sensor 2 and 3 disconnected the distance between sensors was increased to approximately 6cm. By comparing the deviation between tests 1-2, 1-3 and 3-4 it was determined whether having the sensors closer together led to an increase in noise or variation in results. For example, if the sensor proximity did cause different values or noise, it was expected that the deviation between tests 1-3 would be far higher than that of tests 1-2. By comparing tests 1-2 and 3-4 it was possible to determine whether the sensors placed further apart produce more repeatable results or not.

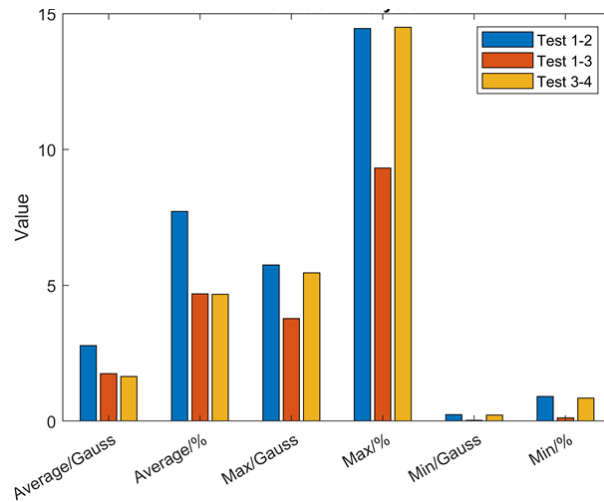


Figure 8.20. Deviation analysis for test 7

The results for this test are shown in Figure 8.20, which shows the average, max and min Gauss and percentage deviations values between tests 1-2, 1-3 and 3-4. It was shown that, generally, similar values are seen when comparing each test. Of specific importance was the fact that the values for test 1-3 were consistently lower than that for 1-2 suggesting that the difference in recorded value for 2cm and 6cm spacing was less than the natural variation in result for a 2cm spacing. This suggested similar results would be seen with a 2cm gap to a 6cm gap. It was also interesting that the test 3-4 show a lower average deviation than the test 1-2; this suggested that a 6cm gap may produce, on average, similar results but that it may have more repeatable results. However, this increase in repeatability was relatively small and it was believed that the extra resolution gained by having closer sensors offsets the small increase in repeatability offered by further spaced sensors.

8.4.6 Prototype 1 – Conclusions

The first developed prototype showed the promise of the technique and was proficient at detecting large changes in metal presence however lacked the resolution to detect smaller drilled holes fully accurately and showed little ability to detect corrosion. Because of these limitations a second test rig was produced that aimed to provide more accurate detection of corrosion and small defects.

8.5 Prototype 2

The second prototype used the higher accuracy version of the previously used sensors. In order for a greater resolution of measurement six of these sensors were

used placed approximately 1cm apart on the upper sensing layer. In order to try to produce a more consistent magnetic field in the sample only two magnets were used and were placed with alternating sides facing the sample. Initially higher strength 7.3kg pull magnets were used however it was discovered that the strength was too high and there was only a small change in measured field strength with the sample present meaning detection of defects would be more difficult. Therefore, magnets with a similar size and strength to before were used, however they were placed centered over sensors 2 and 4 rather than the edges of the sample like the previous rig. This was to try to limit the extent of magnetic flux leakage around the edge of the sample. The magnets were placed in a way to attempt to make the measured values of sensors 1 and 6 and 3 and 4 similar for ease of result interpretation.

A similar laser cut acrylic housing was used as a base for the test rig but this one was held together using nylon nuts and bolts allowing the magnet-sensor gap to be adjusted. A difficulty of taking measurements with the previous prototype was consistently carrying out measurements at the same points. In this design, a number of holes acted as test points through which nylon bolts could be placed through to act as an end to butt the sample up against. This prototype is shown in Figure 8.21.

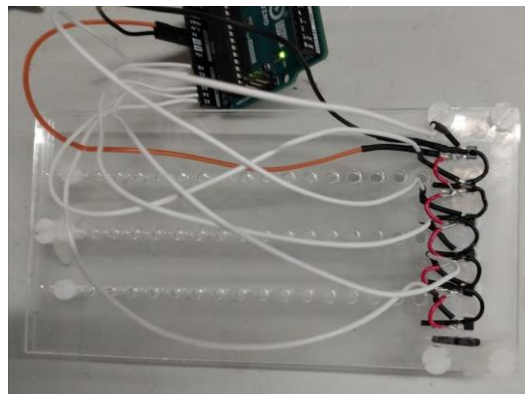


Figure 8.21. The second test rig design

8.5.1 Prototype 2 – Small defect detection

One of the limitations of the initial prototype was poor accuracy when detecting small defects. To attempt to improve this, more accurate sensors and a greater concentration of sensors were used on the second prototype. To assess if the new design was an improvement the test piece shown in Figure 8.22 was measured. This was composed of blackplate with two small 5mm holes drilled into it and a small section cut out. The previous prototype was able to detect cut outs but was limited at

detecting small, drilled holes hence the sample used in this test was produced to give a comparison between the two.

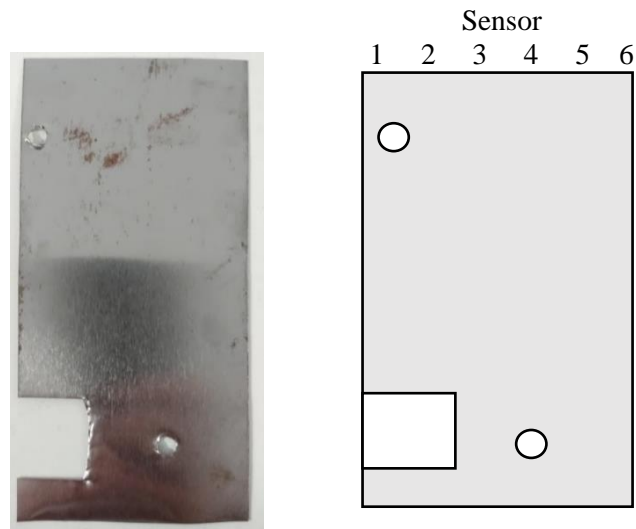


Figure 8.22. Test sample 2.1 image (left) and layout (right)

Previous tests have used raw deviations in Gauss value to produce the colour map, however, for this new prototype, additional data analysis steps were used. The percentage deviation changes in Gauss value from the original value, for each section before metal removal or corrosion, were calculated and used to plot the colour map. The percentage deviation provides a far fairer way of comparing the changes in measured Gauss at each point especially when considering there is not a consistent baseline level at each sensor due to the nature of the magnet position.

For further ease of interpretation of the colour map, a threshold value was chosen based on natural variation in results and was used to binarize the results. This allowed a determination of the points where the variation in measurement was not thought to be explained by natural variation and hence likelihood of a defect in this location was high. Initially this value was chosen as 5% as this was thought to be significant enough of a change to be notable.

Examples of these new variables are given in Figure 8.23 displaying the results of the measurement of this test piece. Even just from the percentage deviation map it was seen that the new prototype did a far better job at detecting the presence of small, drilled holes whilst maintaining the ability to detect large cut out sections. Furthermore, the new threshold map provided a better visual presentation of the

results by removing the effect of large percentage deviations which mask the smaller, but still significant, deviations in the colour scale.

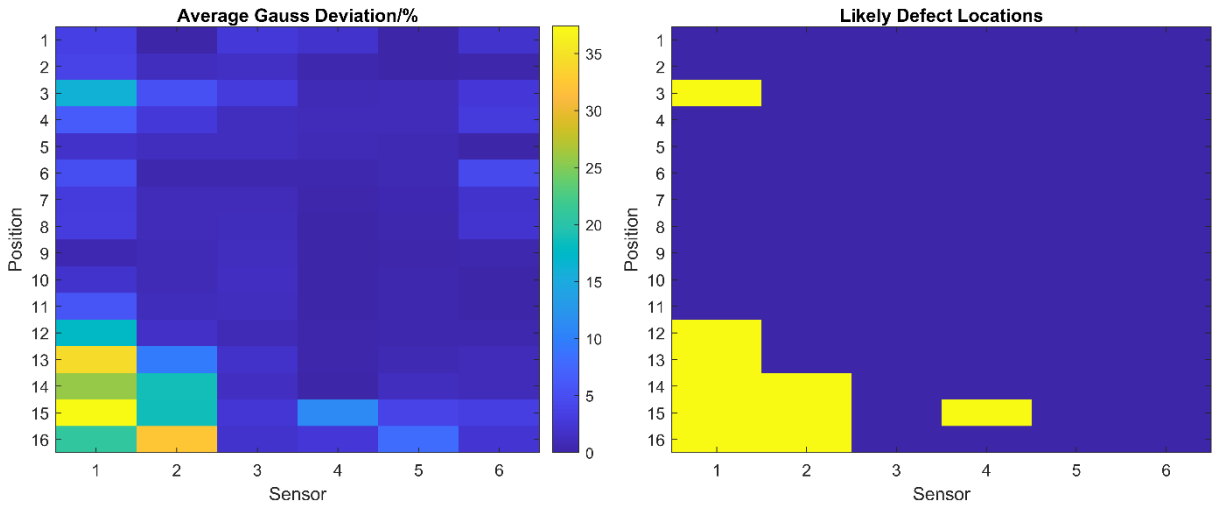


Figure 8.23. Measured Gauss percentage deviation (left) and likely defect locations based on a 5% threshold value (right)

8.5.2 Prototype 2 – Corrosion detection

Perhaps the most important aim of the second prototype was to enable the detection of corrosion. To assess the effectiveness of the new prototype on detecting corrosion two samples of blackplate with certain regions protected from corrosion by tape were used, the dimensions of them are shown in Figure 8.24.

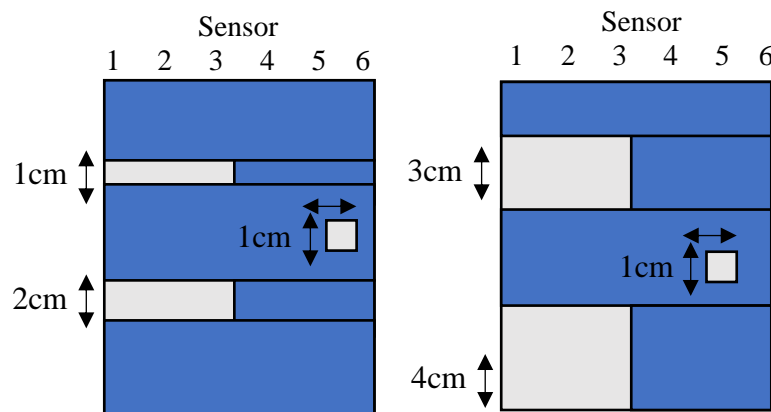


Figure 8.24. Test sample 2.2 dimensions A (left) and B (right)

Previously samples were corroded by submersion in NaCl solution, however, in order to increase the rate of corrosion, these samples were placed in a salt spray cabinet containing 5% NaCl at 35°C and 100% humidity. Measurements and pictures of the samples were taken at 7-day intervals for a 3-week period. The pictures are

shown in Figure 8.25 and show that corrosion develops slowly week by week until a heavily corroded sample was produced by 3 weeks exposure. The test was stopped at the 3 week point as it was decided that the sample was significantly corroded and if this corrosion was below the limit of detection the method was insufficiently accurate at detecting corrosion. After the final measurement was completed, the tape was removed to check if any corrosion had occurred under the tape which may have been picked up. It was seen that generally the tape did an excellent job of preventing corrosion on the covered sections with only a small amount of corrosion around tape seams and edges.

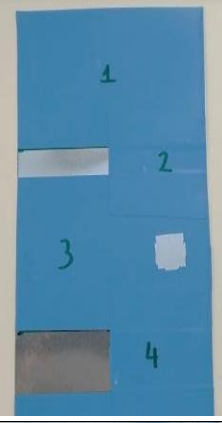
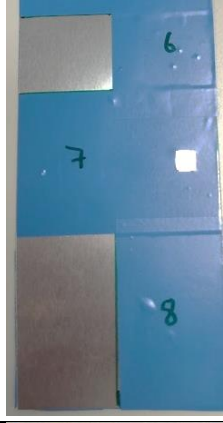






Week	Sample A	Sample B
0		
1		
2		
3		

Figure 8.25. Sample condition at each week exposure

Promisingly the Gauss deviation map taken after each week of exposure, Figure 8.26, showed a reasonable reconstruction of the areas of corrosion by week 3. Although there was a degree of noise present, the size and relative positioning of the left-hand side defects were well detected by sensor 1 and somewhat detected by sensor 2. The smaller defect on the right-hand side of both samples was not detected as well but there was some level of detection around this area although this was mostly recorded by sensor 6 rather than sensor 5 as would have been expected from positioning. It is possible there was a more limited detection by sensors 2 and 5 due to the magnets being in those positions and potentially the metal did not offer sufficient blocking even when intact to show a large increase in magnetic field strength when corrosion occurred. Although potentially a problem for thin metal samples it is thought this would be overcome by the larger substrate thicknesses that this study is aiming to monitor.

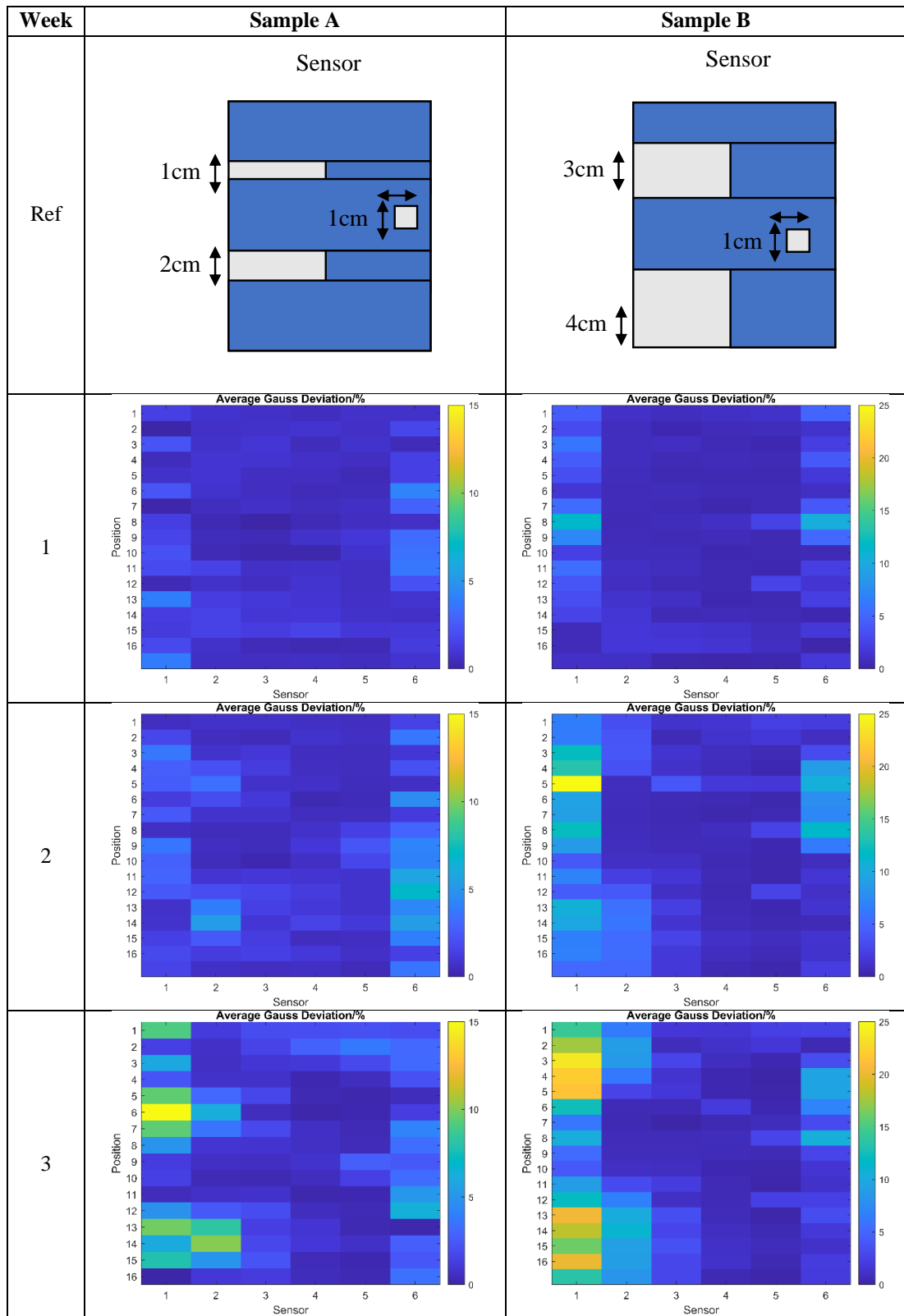


Figure 8.26. Resulting Gauss Deviation maps for samples A and B

The likely defect locations predicted by the measurements are shown in Figure 8.27. This highlights that it was only by around week 3 that a significant level of detection of the defects was possible. The technique was not sensitive enough to distinguish

the low levels of corrosion in week 1 and while week 2 does provide an indication of where corrosion is occurring it was not until week 3 that the technique could identify all the key locations. As shown in the sample images above by week 3 the sample had undergone a fairly considerable level of corrosion. This suggests that the technique was suitable for the detection of corrosion but may only detect areas where significant levels of corrosion have occurred. The level of detection, however, has been increased substantially when comparing the second prototype to the first.

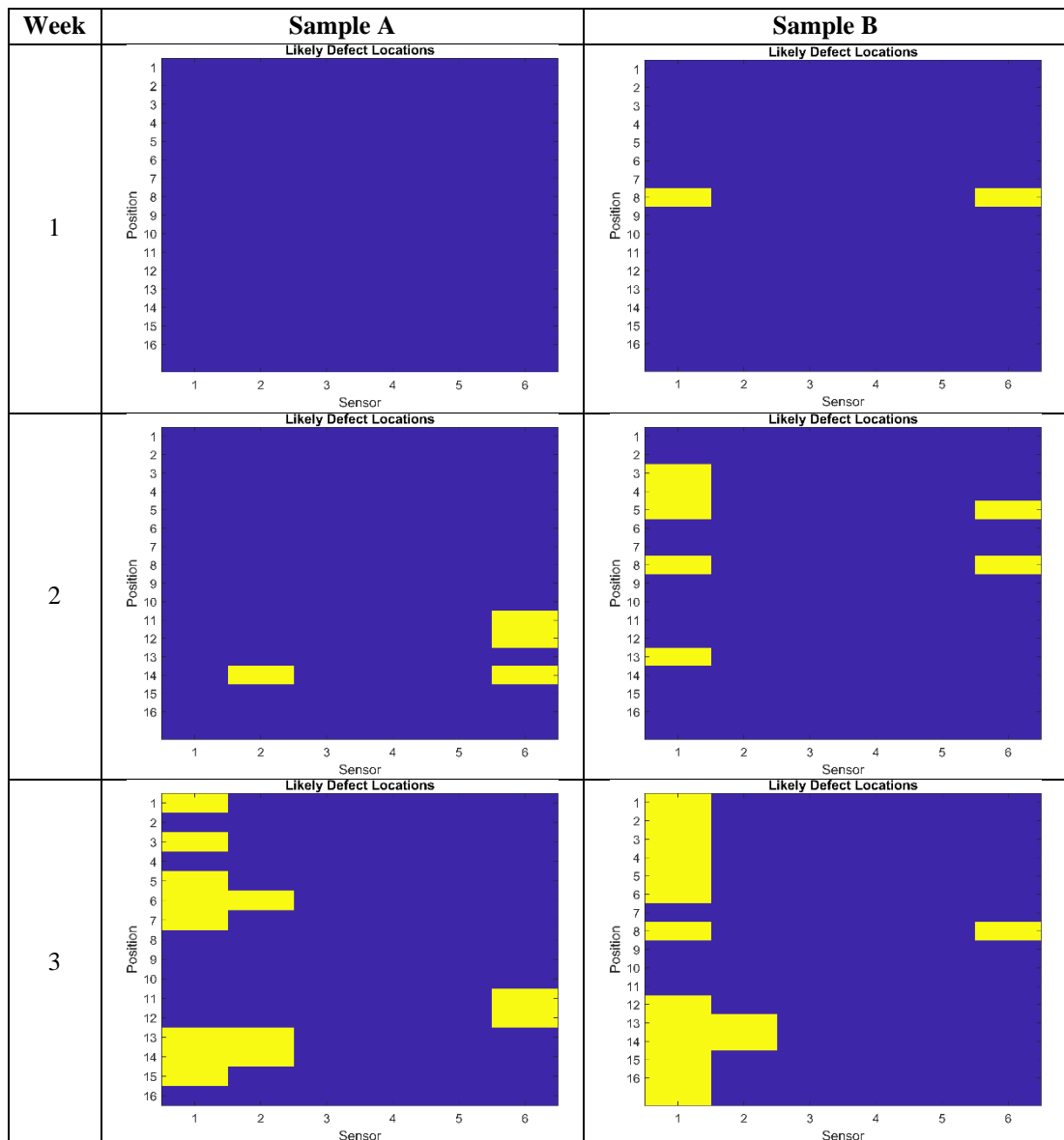


Figure 8.27. Likely defect locations based on the recorded data using a threshold value of 5%

8.5.3 Prototype 2 – Galvanised steel corrosion detection

The previous experiment used a blackplate substrate which corrodes significantly in an aggressive environment such as the salt spray chamber. In reality OCS is composed of far more corrosion resistant substrates which will degrade far slower than this. Therefore, it was important to consider if the technique can detect the early stages of corrosion of these substrates. To this aim a sample composed of polyester coated galvanised substrate was used. The edges and rear of the sample were coated with tape to prevent corrosion of these areas and a large cross was scribed in the centre of the sample. This cross would concentrate the corrosion of the substrate to this region where the coating is breached. This technique was used rather than the previous of using tape to mask of the areas to be more representative of the sorts of corrosion that occur for OCS. The sample before exposure is shown in Figure 8.28.

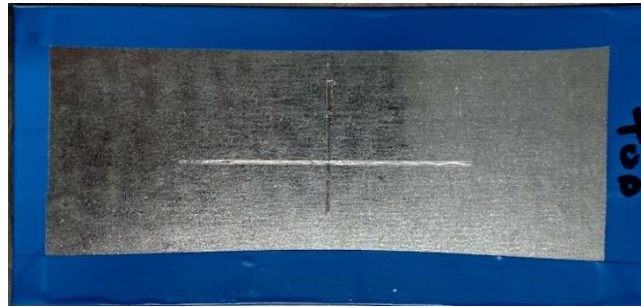


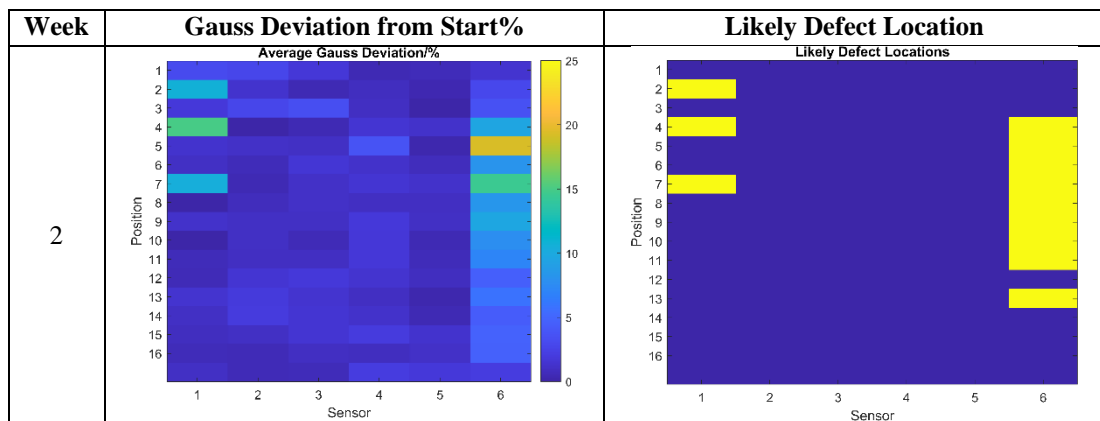
Figure 8.28. Polyester coated galvanised steel with artificial scribed cross in the centre

The sample was placed in the salt spray chamber and was tested after 1, 2, 4 and 6 weeks. The condition of the sample during the test is shown in Figure 8.29. It was observed that white rust began forming on the location of the scribe from week 1 and this progressed to significant levels of white rust by week 4. Due to its poorer protective properties, the polyester coating did not fully protect the substrate. However, significant corrosion of the coated areas was not observed until week 6 and was far less severe than the corrosion observed at the artificially introduced scribed cross. With red rust beginning to emerge from week 4-6, the levels of corrosion at week 4-6 were such that they would be considered significant for an in-service product.



Figure 8.29. Condition of the sample during the test from 1 week exposure (far left), 2-week exposure, 4-week exposure and 6-weeks exposure (far right)

A sample of the results are given in Figure 8.30. None of the results immediately provided a clear indication that there had been successful detection of the cross shaped corrosion pattern. For the threshold of 5% change there was no likely defects given in the location of the corrosion cross. In fact, for all the measured results the only large deviations in the measurements were in that of sensors 1 and 6 on the edges of the sample despite the fact no corrosion should have occurred in these regions due to the tape. It was later confirmed, post-testing, that little to no corrosion had occurred in these regions despite being identified as the likely defect regions. It was thought that this was as a result of the sample not being placed identically in the holder for each measurement and hence the edges of the samples may be shifted further towards or away from the magnets and sensors.



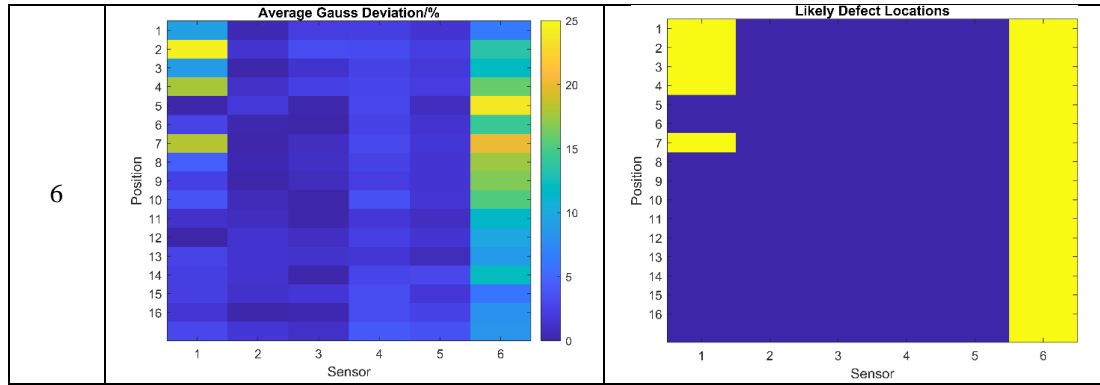


Figure 8.30. Examples of the data captured in this test for weeks 2 and 6

As a result of the large deviations measured by sensors 1 and 6 it was thought that some of the sensing data from sensors 2-4 was being drowned out. Therefore, it was decided to exclude the data from sensors 1 and 6 from the Gauss Deviation plot and the threshold for the likely defect location map was decreased to 2%. In reality the sensors would be fixed in place around the test piece and hence deviations due to positioning would be negated. It was thought, therefore, that these additional steps could be taken without compromising on the overall assessment of the technique. While decreasing the threshold may introduce more noise into the assessment of likely defect locations, it seemed required for this sample as the level of change in measurement as a result of corrosion appeared low.

The resulting data for all weeks is shown in Figure 8.31 below. Implementing the changes provided a far more promising level of detection than the original results. While there was little obvious detection in weeks 1 and 2, weeks 4 and 6 showed the emergence of a line of suspected defect on sensor 4. This was matched well with the vertical scribe line on the cross and suggests that the corrosion damage here was detected. There were some regions for sensors 3 and 5 that also suggest defects, but it was unclear if this was either noise, that is no longer filtered out by the lower threshold value, or further detection of the corrosion line. It appeared that the horizontal section of the cross was not detected, this could be due to the fact it was in the same plane as the sensors and magnets and was insufficiently sampled. There was little evidence to suggest that areas of corrosion outside of the artificial scribe were detected, although this could be due to a decreased magnitude of corrosion at these regions. Overall, this test suggested that earlier stage corrosion of galvanised substrates may be possible but that further testing was required to confirm this.

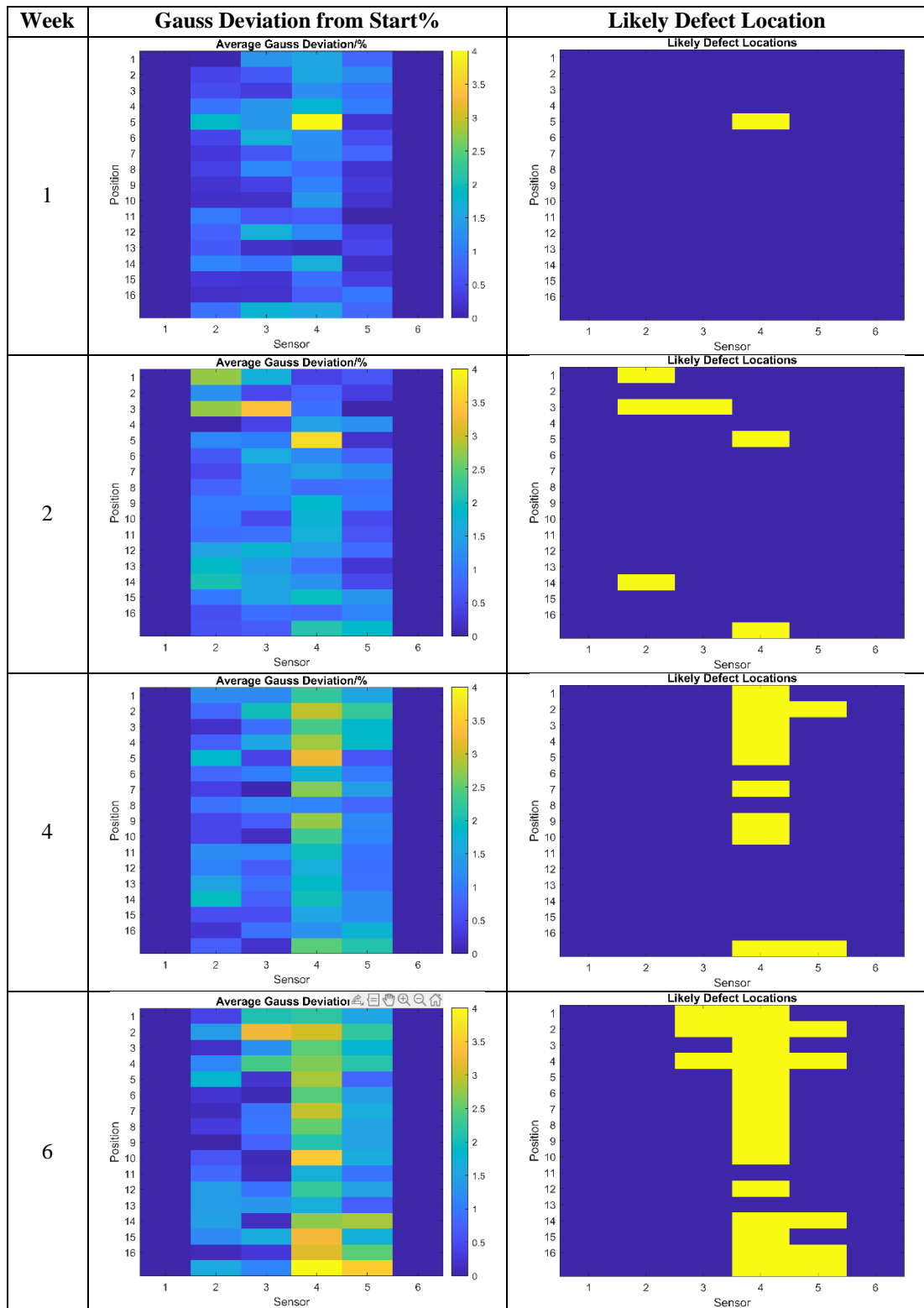


Figure 8.31. Modified data for the test period with sensor 1 and 6 removed and a new threshold of 2%

8.5.4 Prototype 2 – Coated steel corrosion detection

Given that detection of corrosion on blackplate was proven to be possible, and that there was an indication of the detection of corrosion of galvanised steel, samples of commercial OCS were tested to determine the ability of prototype two to detect

corrosion. Two samples of PU and PVC coated samples, respectively, were produced. The edges and rear of these samples were masked with tape to prevent corrosion, and, in a number of regions, the coating was removed using a spatula to expose the underlying metal and produce regions where corrosion could easily initiate. A range of sizes of regions were produced to allow a determination of the resolution limitations of the prototype. These included: two rectangular sections of 4cm by 0.5cm, two scribe marks of 4cm long and a 1cm by 1cm square. The rough outline of the sample and an example is given in Figure 8.32.

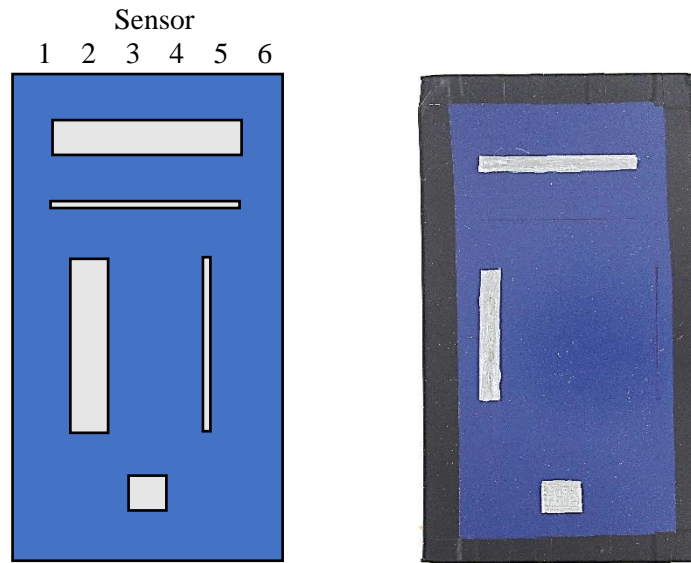


Figure 8.32. Sample outline and example used for testing the coated products

The samples were exposed to the salt spray chamber as the previous samples had been. Due to the expected resistance of the sample to corrosion, measurements were made at 4-week intervals. In Figure 8.33 the condition of the samples during the test are shown. White rust was observed to form as the test progressed, although this is at a slower rate to the previous galvanised samples due to the more resistant metallic coating present of these samples. However, by 12 weeks exposure there was a significant quantity of white rust present suggesting considerable attack; it is of note, however, that no red rust was present indicating this was still ‘early-stages’ of degradation.







Week	PU Sample	PVC Sample
4	 A photograph of a PU-coated steel sample at week 4. The sample is rectangular with a blue PU coating. It features a horizontal slot at the top, a vertical slot on the left side, and a small square label at the bottom. The coating appears relatively smooth and intact.	 A photograph of a PVC-coated steel sample at week 4. The sample is rectangular with a blue PVC coating. It features a horizontal slot at the top, a vertical slot on the left side, and a small square label at the bottom. The coating has a distinct pebbled texture.
8	 A photograph of a PU-coated steel sample at week 8. The sample is rectangular with a blue PU coating. It features a horizontal slot at the top, a vertical slot on the left side, and a small square label at the bottom. The coating shows some signs of wear and slight discoloration.	 A photograph of a PVC-coated steel sample at week 8. The sample is rectangular with a blue PVC coating. It features a horizontal slot at the top, a vertical slot on the left side, and a small square label at the bottom. The coating shows some signs of wear and slight discoloration.
12	 A photograph of a PU-coated steel sample at week 12. The sample is rectangular with a blue PU coating. It features a horizontal slot at the top, a vertical slot on the left side, and a small square label at the bottom. The coating shows significant wear, with some areas appearing darker and more textured.	 A photograph of a PVC-coated steel sample at week 12. The sample is rectangular with a blue PVC coating. It features a horizontal slot at the top, a vertical slot on the left side, and a small square label at the bottom. The coating shows significant wear, with some areas appearing darker and more textured.

Figure 8.33. Condition of the coated steel samples during the test

The results for both samples were observed to be similar and hence only those of the PU sample are given, Figure 8.34. From the results it was clear that there is considerable edge interference and generally poor detection of the areas undergoing corrosion. While it was possible to identify some of the defect regions overall the prototype was not thought to be sensitive or accurate enough to provide confidence in corrosion detection.

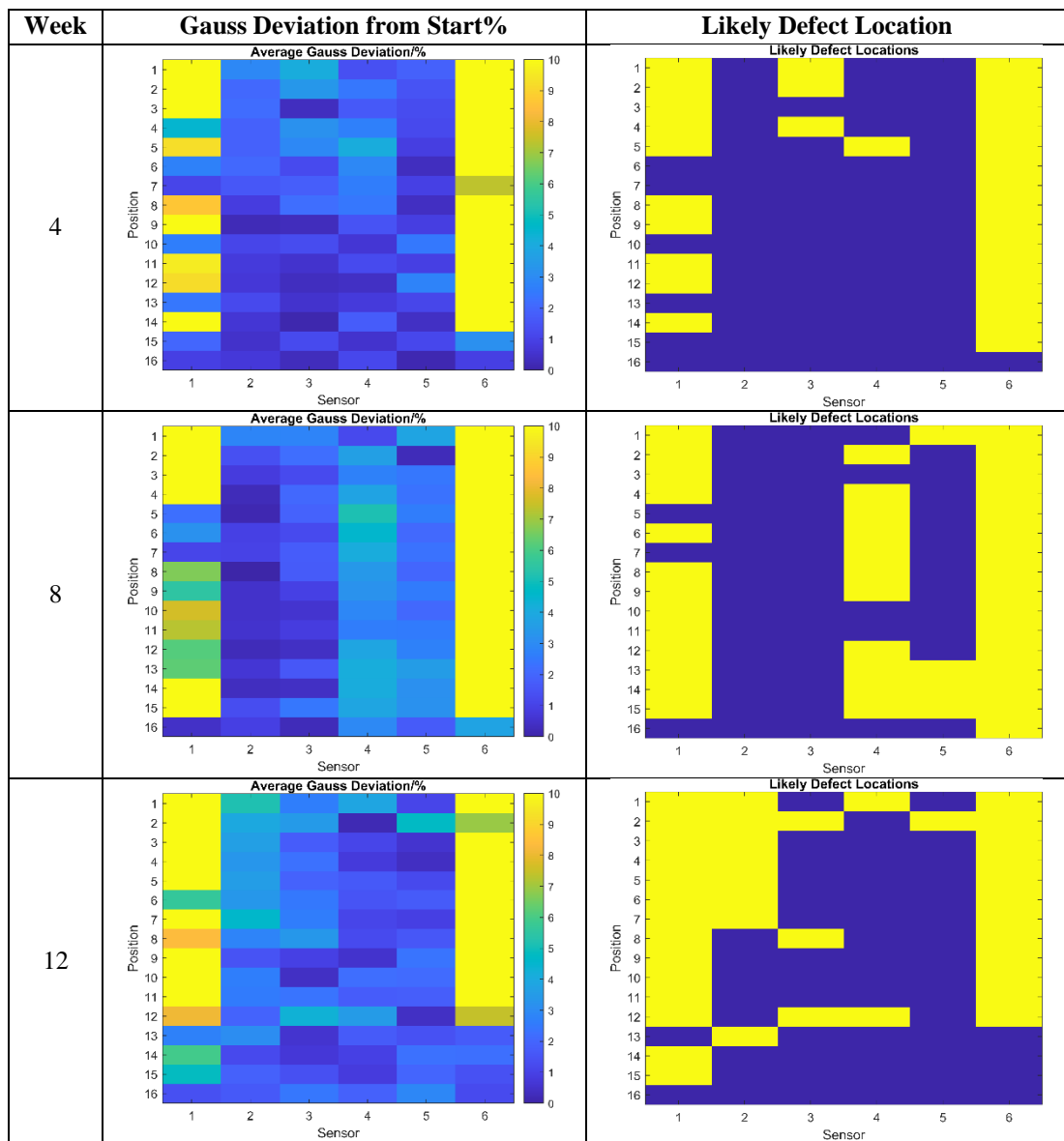


Figure 8.34. Detection pattern for the PU sample

8.5.5 Prototype 2 – Conclusions

Prototype 2 showed a clear improvement over prototype 1 in terms of detection of smaller defects and some level of detection of the corrosion metallicly coated substrates was possible. However, when applied to modern OCS substrates there was

little correlation between the areas identified as likely defects and those observed to be corroding. It is possible that this was due to a lack of severity of the corrosion however, for the sensor to be useful it has to be able to detect early-stage damage such as that present in the tests.

8.6 Prototype 3

The third and final prototype was produced using three, 3 axis magnetometers, which were thought to have an improved chance to detecting changes due to corrosion due to increased sensitivity. The sensor device design also varied slightly to allow for testing of larger samples. The magnetometers were placed on an acrylic holder with one magnet placed above and below each, Figure 8.35. It was thought this design may improve results as it better replicated the MFL sensors used in the field. It was also thought that, by placing magnet and sensor the same side of the sample, leakage fields may be stronger and magnet-sensor alignment more easily maintained on large samples.

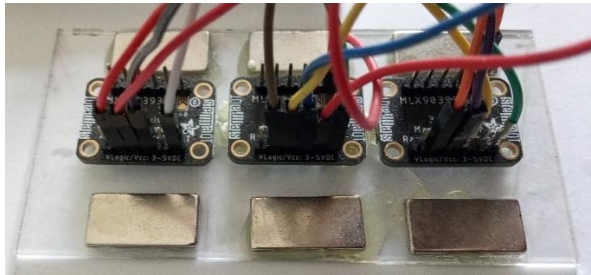


Figure 8.35. Prototype 3

8.6.1 Prototype 3 – Coated Steel Corrosion Detection

To test if the new prototype was an improvement it was tested on a A4 size sheet of PVC coated steel. This sheet was split into 13 sections that matched the size of the device, Figure 8.36. Each of these sections had different features to allow the determination of the sensors ability to detect damage. Some sections were left unaltered, some were taped off to protect them and some had a range of defects produced in them. Certain sections were sized to place a sensor/sensors over the cut edge to determine if cut edge corrosion detection was possible. Measurements were taken by placing the sensor on each section for 2 minutes and compared pre and post 10-week exposure to salt spray.

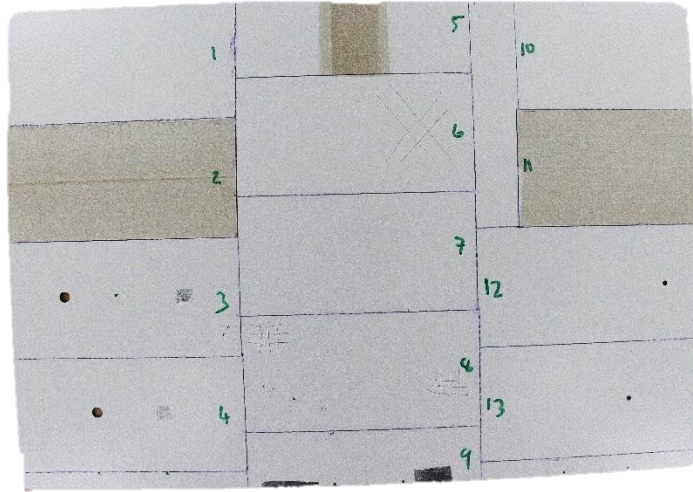


Figure 8.36. Sample used for the 3rd prototype testing

Unfortunately, the results produced from this test provided no improvement on the previous prototype in terms of the accuracy of corrosion defect detection. While it did successfully detect areas where material had been punched out there was little to no obvious detection of corrosion-based defects and hence results are not provided in any significant detail here. The sensor system is thought to be capable of detecting significant levels of corrosion however to produce that level of damage on this substrate would have required many additional weeks of exposure. This was not achievable during the project timescale and also severely limits the technique to the detection of only extremely degraded regions which are unlikely to occur frequently within the expected product lifetime.

8.7 Conclusions

MFL is clearly a suitable and powerful technique for the detection of corrosion and other defects in steel structures. However, using the technique to monitor cladding materials in-situ presents many problems that are not easily overcome. Principally, problems arise on how to monitor larger areas without using automated scanning techniques that are not feasible in this application. To attempt to solve these issues a novel, distributed sensing array approach was proposed and considered in this work. However, it has been shown that, while a number of cost-effective sensors can detect changes in metal presence, they lack the sensitivity and accuracy to detect corrosion. Due to this the MFL technique is limited to more sensitive, expensive equipment which does not lend itself to large scale arrays. It was therefore concluded that this proposed application of MFL to OCS monitoring is far less suitable than

conventional operator manipulated devices. Given that, several monitoring techniques had been considered, tested and concluded to be ineffective a different approach to the work was considered at this stage. It was considered whether a greater understanding of degradation would allow modelling and simulation of degradation rather than attempting direct monitoring. This approach is covered in the remainder of the work.

8.8 References

1. Feng B, Wu J, Tu H, Tang J, Kang Y. A Review of Magnetic Flux Leakage Nondestructive Testing. *Materials (Basel)*. 2022;15(20).
2. S-cool Limited. Effect of Ferrous Cores [Internet]. [cited 2020 Mar 30]. Available from: <https://www.s-cool.co.uk/a-level/physics/magnetic-fields/revise-it/effect-of-ferrous-cores-and-the-relationship-between-curre>
3. Tamhane D. Detection of Defect in Steel Sheets Under Coatings by Magnetic Flux Leakage Detection of Defect in Steel Sheets Under Coatings by Magnetic Flux Leakage Durgesh Tamhane. 2019.
4. Drury JC, Marino A. Comparison of the Magnetic Flux Leakage and Ultrasonic Methods in the detection and measurement of corrosion pitting in ferrous plate and pipe. In: 15th World Conference on Nondestructive Testing Roma (Italy). 2000.
5. Kawakami T, Adachi S, Wang J. Crack Detection for Welded Joint With Surface Coating Using. 2022;58(8).
6. Wu R, Zhang H, Yang R, Chen W, Chen G. Review Article Nondestructive Testing for Corrosion Evaluation of Metal under Coating. 2021;2021.
7. EddyfiTechnologies. Products [Internet]. 2022 [cited 2023 Jan 27]. Available from: <https://eddyfi.com/en>
8. Li E, Chen Y, Chen X, Wu J. Defect Width Assessment Based on the Near-Field Magnetic Flux Leakage Method. *Sensors [Internet]*. 2021 Aug 11;21(16):5424. Available from: <https://www.mdpi.com/1424-8220/21/16/5424>
9. Honeywell. Hall sensor SS495A Data Sheet [Internet]. 2020. Available from: <https://docs.rs-online.com/dc97/0900766b8009a37c.pdf>
10. International Inc H. SS490 Miniature Ratiometric Linear Hall Effect Sensor Data Sheet [Internet]. Available from: http://www.farnell.com/datasheets/1676927.pdf?_ga=2.155325819.1317214909.1558821270-2097595314.1557149251
11. Melexis. Datasheet-MLX90393 Triaxis [Internet]. Available from: <https://cdn-learn.adafruit.com/assets/assets/000/069/600/original/MLX90393-Datasheet-Melexis.pdf?1547824268>

Chapter 9: Understanding and Predicting OCS Degradation

9.1 Introduction

The previous chapters aimed to produce a sensor that could detect OCS degradation however this was shown to be a complex and non-trivial task due to various unavoidable constraints. Therefore, a different approach was considered in this section. It was thought that, if the environmental factors that affect degradation of OCS could be better understood and measured, predictions could be made as to the expected locations and severity of OCS degradation.

9.2 Background

Commonly the durability of OCS products is determined through the use of long-term natural exposure at sites with varying atmospheric conditions, and through the use of accelerated weathering techniques such as salt spray [3,4]. Despite this extensive testing, more rapid failure of coatings is occasionally seen on buildings than the estimated performance would have suggested [19].

There has been some work to suggest that this is because the current weathering tests do not well replicate the environment. For example, accelerated testing, such as salt spray or UV allow a quick analysis of performance; however, the resulting analysis has to be viewed as an extrapolated result due to the artificial nature of the test, and it is often reported that accelerated results show poor correlation with field results [15,16].

Furthermore, outdoor weathering racks, such as the ECCA T-19, expose relatively small samples at 90°, 45°, and 5° and although the 90° sample has a small overhang to produce sheltered regions, this only extends 65 mm from the sample. In comparison, buildings will have far larger overhangs and alcoves, creating a much greater sheltering effect and likely producing more extreme microclimates. This is suggested by studies that have claimed that corrosion and delamination rate of paint both occur differently on a building compared to conditions of the standard racks

[21]. Additionally, it is possible that other environmental conditions at the test sites may differ from the proposed building site.

There is limited information regarding the effect of building design and its influence on the environments to which the OCS products will be subjected. Of particular interest is the determination of whether there are certain geometries created as a result of modern building design principles and architecture that produce more localised aggressive conditions than those in standard tests, leading to accelerated failures [20].

This kind of work, considering how naturally occurring conditions affect performance, has been carried out previously for façades of different construction such as timber [22,23] and ceramic and renders [24–26]. However, it is not explored in great detail for OCS despite being highlighted as an important issue in other studies [4].

In this chapter, a single-story building is examined to determine if localised accelerated degradation rates exist, the location of these, and the severity of the acceleration. An investigation was then undertaken to determine the factors contributing to this accelerated degradation with a consideration of localised microclimatic conditions and natural fouling deposits. The overall aim was to determine if it is possible to better determine and understand the conditions that cause accelerated degradation and use this information to predict areas of concern on a building. The end goal was to test the feasibility of developing a model that can be used to predict areas of concern across buildings for the purpose of design improvement and maintenance and inspection targeting.

9.3 Methodology

The strategy employed to study the relationship between potential failure of the OCS coating and localised conditions required a suitable building to be chosen. This building served to provide experimental data necessary to understand the mechanisms of degradation such as environment (both highly localised and ambient) and the role of accumulated fouling deposited on the building. Fouled samples could subsequently be taken for immediate laboratory analysis.

9.3.1 The Building: Materials and Locational Climate Data

The building used in this study is located on the Swansea University Bay Campus, Swansea, UK, as shown in Figure 9.1 a & b, and is a one-story multipurpose teaching and office space that is mostly clad with polyvinylidene fluoride (PVDF) coated steel panels. The building has a rectangular floor plan of 18 m × 12 m. The structural elements of the building are constructed from SIPS panels manufactured by Matrix structures and incorporate a transpired solar collector for thermal energy capture on the southern aspect and building-integrated PV on the roof for electrical energy capture, Figure 9.1 a. The building was built in 2016 and the OCS is well within modern coated steel cladding lifetime warranties. The material characteristics are given in Table 9.1.

Table 9.1. Building material characteristics.

Structure	Material
Roof	Standing seam profile integrated PV and coated steel roofing
Main structure	SIPS panels attached to steel frame
External cladding (walls)	Interlocking plank profile PVDF-coated steel panels, attached via rail system
Cladding (soffit, guttering)	PVC-coated steel
Windows and doors	Glass and aluminium construction

The building is orientated slightly askew of cardinal points; however, can be said to have a north, west, east, and south aspect, as shown in Figure 9.1 c. The location of the building is determined to be extremely corrosive with a classification of C4/5 according to ISO 9223. The key features of this location that make it a highly corrosive environment are the proximity to the sea (approximately 300 m due south), the M4 motorway (approximately 2 km due north), and various heavy industries (approximately 1–7 km southeast). It is also important to note that a building site exists directly adjacent to the west and south of the building and as a result the west side of the building was inaccessible during this work. There is also a small two-story building directly north of the building of interest that somewhat shelters the north face, which is important to note for later analysis in this work.

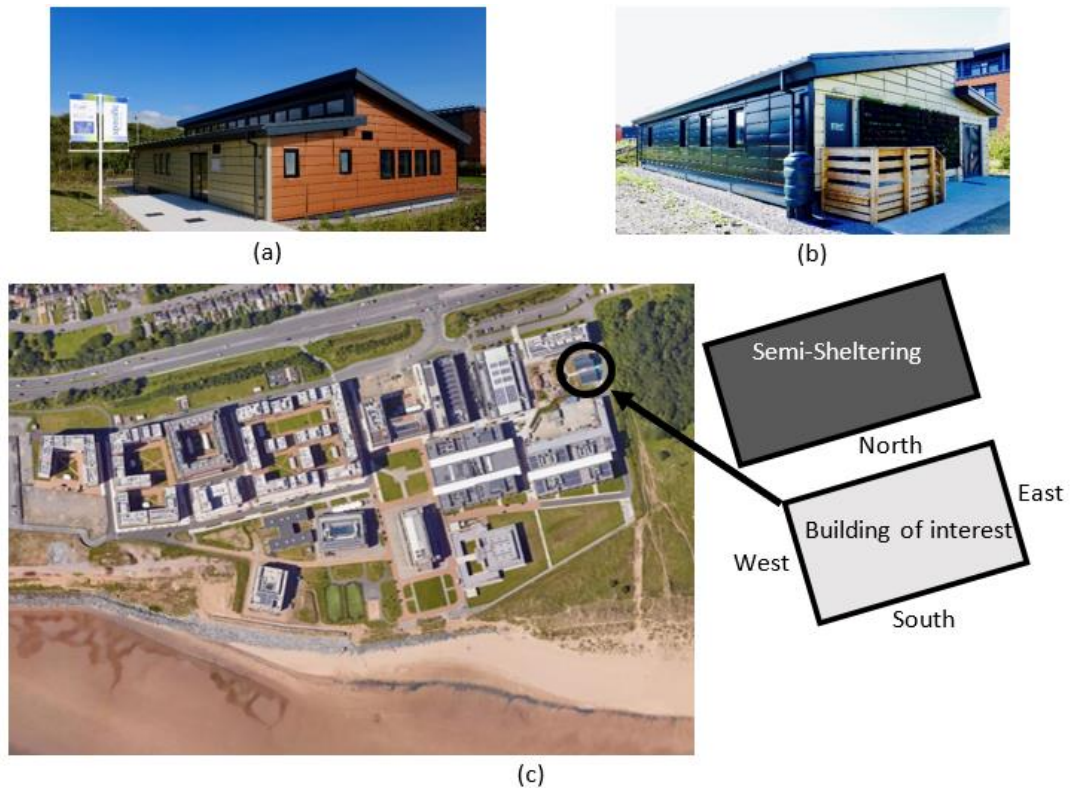
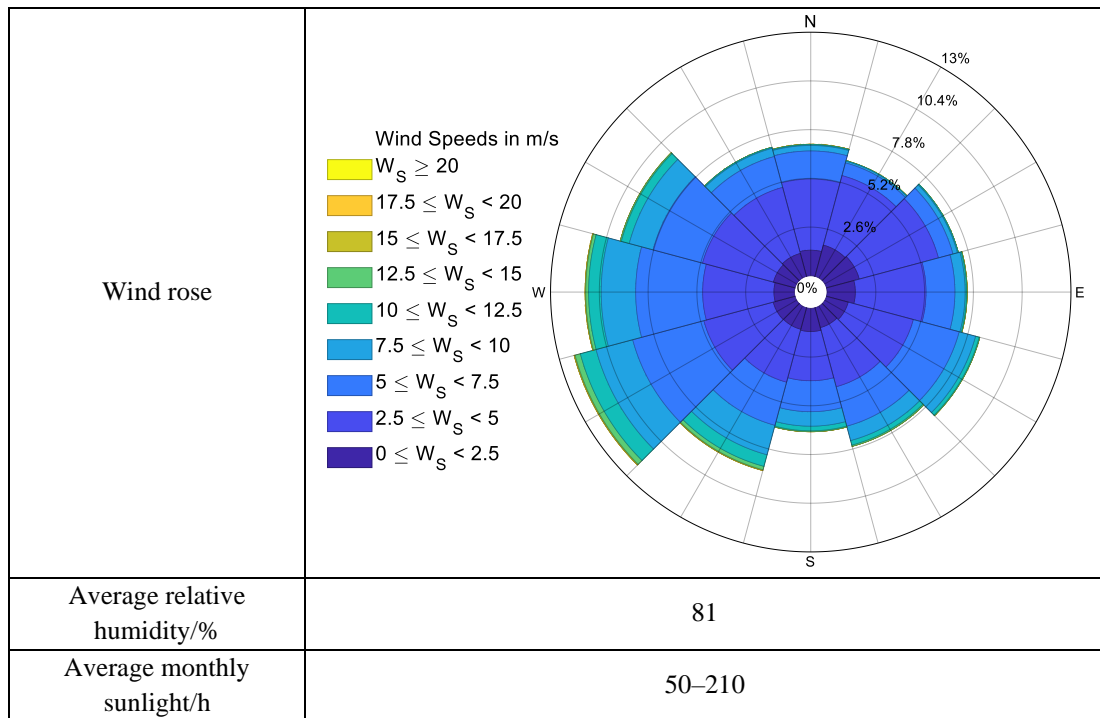


Figure 9.1. Building viewed from the (a) northwest, (b) southeast, and (c) location of the building and the façade names used for reference.

The average weather for this location (Table 9.2) indicates that this is a mixed environment that is slightly wetter and windier, yet sunnier than the UK on average.

Table 9.2. Average weather data for this location.

Metric	Location
Average temperature/°C	4.4–16.8
Average daily rainfall/mm	3
Average wind speed/ms ⁻¹	4.8–7.3



9.3.2 Experimental Tests

9.3.2.1 Measurement of Degradation

In order to measure the quantity of degradation across the classroom, a number of steps were involved with the first being a close visual inspection of the building. From this it was determined that generally the coated cladding was performing well, and, in fact, the only sign of degradation was at the cut edge. This was to be expected as modern organic coatings are unlikely to experience through coating failure within 6 years following the building’s construction, and cut edge corrosion is one of the most common routes of degradation for organically coated cladding [27]. Hence, the parameter measured to ascertain the degree of degradation was simply the distance from the cut edge that degradation had occurred. Measurement was carried out using digital callipers across a number of panels on each accessible façade of the building at different heights and locations, such as an alcove. The type of cut edge degradation was also noted with both blisters and white rust observed (both shown in Figure 9.2). Blisters are considered an early stage of cut edge coating degradation, whereas white rust is indicative of more severe metal substrate deterioration. At paint blister locations, water had penetrated the organic coating/metal interface and had reacted with the galvanised zinc surface causing a delamination separation of the metal and organic paint. This can ultimately lead to white rust formation when the zinc on the underlying galvanised metal surface is oxidised to zinc oxide.

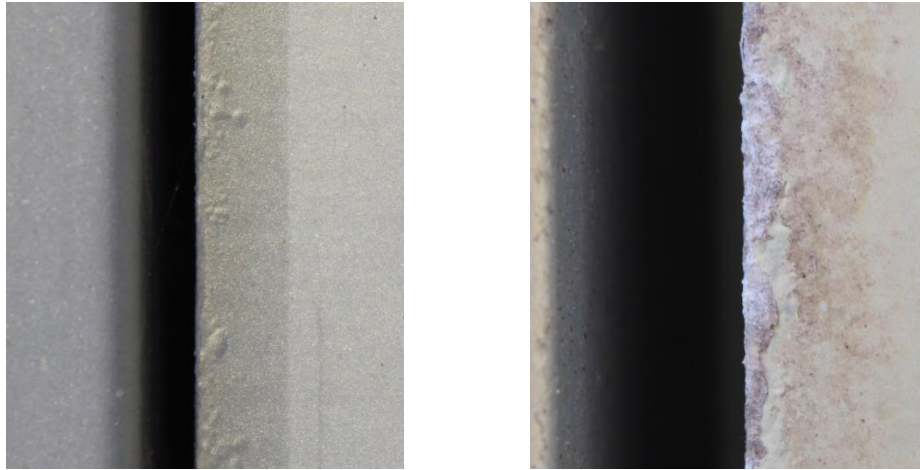


Figure 9.2. Examples of the two main types of cut edge degradation observed: blistering (left) and white rust (right).

9.3.2.2 Collection of Highly Localised Microclimatic Data

The developed multifunctional sensors, discussed in Chapter 3 and Appendix A were used to monitor the local atmospheric conditions that occur at various locations around the building façade. Each multi-function measuring unit had a footprint of only 20 cm × 10 cm × 5 cm allowing them to be magnetically attached within a small defined area on the building façade. Each unit was set to measure at 4 readings per hour for 4 weeks. Data was subsequently transferred via SD card and the battery replaced within 5 min thus allowing for continuous measurement.

Five of these multifunctional sensing boxes were used in this work and these were deployed to observe if significant variations in conditions exist between low, middle, and high locations on a façade and for different façades. To this aim, three boxes were placed on the north face of the building at ground level, mid-way up the façade, and in the eaves; two boxes were placed on the south face at mid-way up the façade and in the eaves. These locations are given in Table 9.3 and shown schematically in Figure 9.3. Data were collected from September 2020 to September 2021 at a rate of four measurements per hour.

Table 9.3. Sensing box locations and their properties.

Number	Façade	Height	Location Type
1	South	Middle	Exposed
2	South	High	Sheltered by roof overhang
3	North	Low	Exposed/semi-sheltered by 2nd building
4	North	Middle	Exposed/semi-sheltered by 2nd building
5	North	High	Sheltered by roof overhang/semi-sheltered by 2nd building

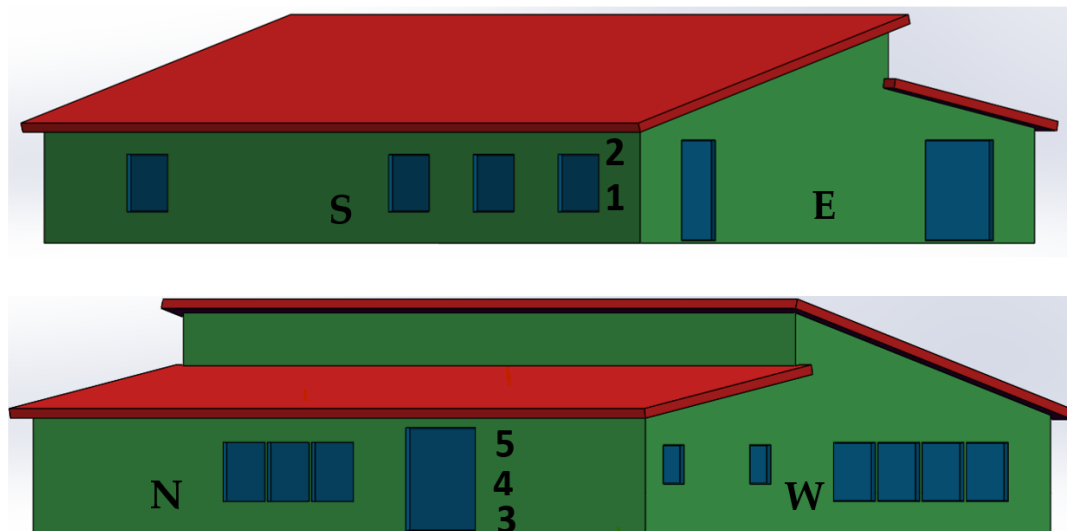


Figure 9.3. Location of the five sensing boxes on the building. The building is coloured according to materials with green indicating PVDF cladding, red indicating integrated PV roofing, blue indicating windows and doors, and dark purple indicating the soffit region composed of PVC cladding material.

9.3.2.3 Collection, Measurement, and Analysis of Accumulated Natural Deposits

The deposit accumulation was studied in two different ways. The first was to sample a fouling deposit from the building for subsequent laboratory analysis to establish the components of the deposit and hence the likely effect of its presence on OCS degradation. The second examined how the presence of the deposit on the OCS could affect the wetting and moisture retention properties leading to the creation of conditions which are amenable for degradation. This was facilitated by the production of fouled samples in the laboratory using the deposit collected from the building. Novel sampling methods were developed in order to obtain a repeatable measurement of the deposit found at each location and to distinguish between the solid matter and the soluble compounds present, both of which could contribute to the degradation of the OCS.

The procedure to measure the quantity of deposit in each location was as follows. First, a plastic sampler guide with a 5 cm × 5 cm square hole was attached to the location and this area was swabbed using a foam-tipped bud until all the deposit present had been collected. This bud was then placed in a weighing boat with 5 mL of deionised water and washed until all the deposit was transferred to the boat. The boat was then placed on a hot plate at 50 °C for 3 h at which point all the water had evaporated and only the deposit remained. The boat was then weighed, and this

weight was compared to the pre-test weight to calculate the deposit weight. For each location, three repeats were carried out and a control weight boat, with no deposit added, was used to ensure no weight loss was experienced simply by heating the weighing boat. Once an average for each location was calculated, this was converted into a value in mgm^{-2} based on the original sampling area size.

In order to analyse the composition of the deposit, $5\text{ cm} \times 5\text{ cm}$ 4-ply nonwoven sterile swabs were used to collect a significant amount of matter from the building whilst wearing nitrile gloves. The gauze was placed in 200 mL of deionised water for approximately 2 days to ensure any absorbed matter was removed. After the two days, the gauze was removed using plastic tweezers and examined to ensure that the deposit had been removed. The gauze was wrung and left to dry to allow any further matter to be extracted. The resulting solution was passed through filter paper. This filter paper was removed and placed in a Petri dish on a hot plate at $50\text{ }^{\circ}\text{C}$ for approximately 3 h to dry the powder. The powder was then collected and placed in a clean sample box. A separate swab was taken of the building and this swap was dried in a similar manner and the dry powder was then scraped off the gauze into a clean sample box. This gave two lots of dry powder for examination, one that should have any soluble components removed (P, particulates) and the other as was found on the building façade (SP, soluble compounds, and particulates).

The solid particles obtained via the collection methods were characterised using energy dispersive spectroscopy (EDS) in a Hitachi TM3000 Desktop scanning electron microscope (SEM). For each sample, three different areas were examined and an average atomic weight % calculated from these results. As there were a number of particle sizes, the three areas chosen covered a variety of particle sizes and shapes. Further analysis to determine the chemical constituents of compounds present was carried out using X-ray diffraction (XRD) [32].

The conductivity of solutions formed using the collected natural deposit was measured using the custom made solution conductivity device described in Chapter 3 and Appendix B.

9.3.2.4 Creation of Laboratory-Fouled Samples and Analysis of Moisture-Related Properties

In this work, the effect of natural deposit build-up was examined on a number of commonly used organic coating systems for steel cladding, namely a PVC-based system, a PU-based system, and a PVDF-based system. Samples 5 cm × 5 cm in size were used to create the fouled samples; 5 and 10 mg of building deposit was added to each sample to give two samples with a deposit coverage of approximately 2000 and 4000 mgm⁻², respectively. The deposit was dissolved in approximately 5 mL of deionised water and was pipetted onto the sample and allowed to dry on a hot plate at 50 °C. This produced visually similar fouling to that observed on the actual building, as shown in Figure 9.4. To ensure this process did not affect the results, the clean samples also went through the same procedure of water addition and heating.



Figure 9.4. Initially clean PVDF sample (left), PVDF sample with wet-applied 4000 mgm⁻² of deposit (middle), and observed natural deposit on the building (right).

Measurement of the wetting angle of the laboratory-fouled samples was carried out using a contact angle measurement system composed of a mounted pipette and camera. One droplet of deionised water was expelled from the pipette onto the sample surface, which was recorded using a camera and the resultant contact angle calculated using FTA 32 software (First Ten Angstroms, Newark, USA). The measurement was repeated at different sites on the sample surface three times with an average taken from these measurements.

The moisture retention of the fouling deposit from localised microclimates was considered to be a possible contributory factor in the degradation of the OCS. An experimental method was developed that allowed for this to be investigated in the laboratory by placing fouled samples in a controlled humid environment, Figure 9.5.

This was composed of a sealed tub partially filled with a 5 wt.% NaCl electrolyte to maintain a humidity of 95%. The samples were placed on a plastic stage that was supported and held out of the electrolyte by using plastic supports. The three samples of each coating system with deposits representing 0, 2000, 4000 mg m⁻² were first weighed and then placed in the chamber. They were then removed and reweighed periodically to measure weight change as a result of moisture absorption onto the surface. After the final weight was recorded, the samples were also photographed to allow visual observation of any changes.

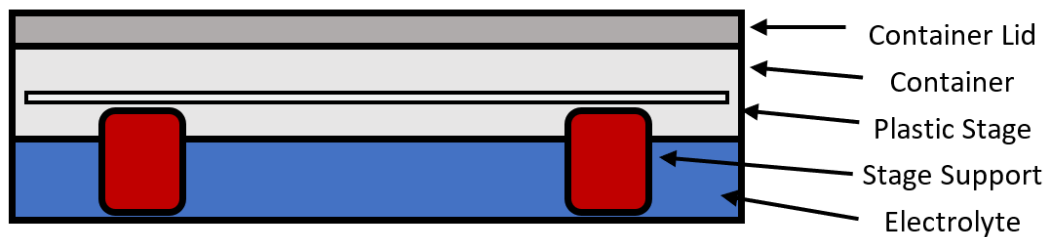


Figure 9.5. Experimental setup of the humidity testing chamber

In order to measure the effect of deposit presence on the retention of water and the drying rate of the laboratory-fouled samples, each sample was weighed and then nine 5 µL drops of deionised water were placed on the sample, as shown in Figure 9.6. The samples were left at room temperature and reweighed every 10 min until the weight of the sample returned to that of the original state. The weight of water present on the samples was then calculated for each time step.

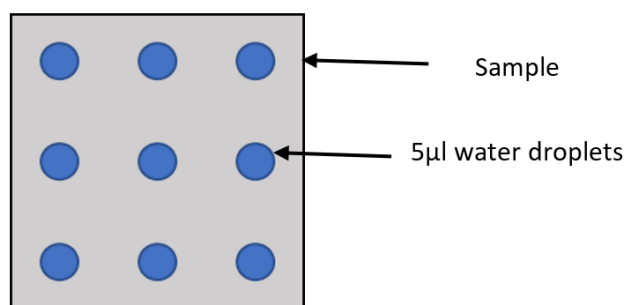


Figure 9.6. Droplet test used to measure drying/water retention.

9.3.3 Numerical Simulation of Rainfall

The aim of the rain impact simulation was to develop a theory that accurately describes the experimental observations and to identify possible mechanisms for variations in the highly localised microclimates around the building that could

influence OCS panel degradation. Potentially, those areas where air flow is limited may maintain a localised humid atmosphere, while areas which see negligible rain impact are less likely to have deposit fouling removed. Ultimately, the building simulation was seen as a means of providing a predictive tool that could be used to identify areas where potential OCS panel degradation would be accelerated. This would allow for refinements to be made at the design stage, investigate best practice for design, or apply warranty limitations for OCS used in specific areas of the building. As these are building design, local environment, and meteorologically linked, it is envisaged that such simulations would ideally be required for each location.

The building was created as a scale 1:1, 3D object in Solidworks 2022 using both the original architectural plans and physical measurements to ensure accurate building dimensions were used. To reduce the computational demand, small details such as the joints between panel sections, guttering, and other such features were not included in the model; however, larger features such as doorway and window surrounds were included. The building model is shown in Figure 9.7.

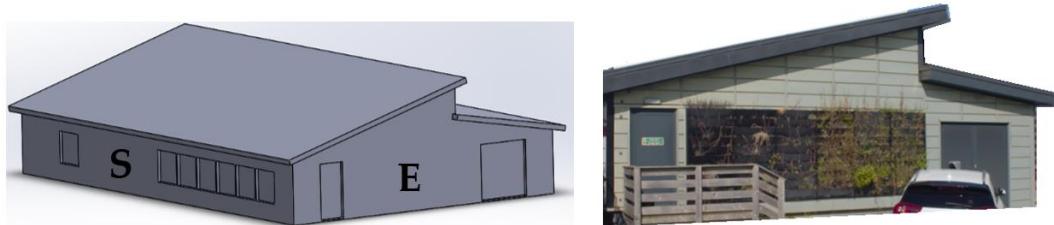


Figure 9.7. Building model (left) and actual building (right).

The nearby building providing sheltering was similarly modelled but, to reduce computational demand, less detail was used as it was only included to show the effect of a nearby sheltering building. This simple model was then, when required, placed as measured in relation to the building model, as shown in Figure 9.

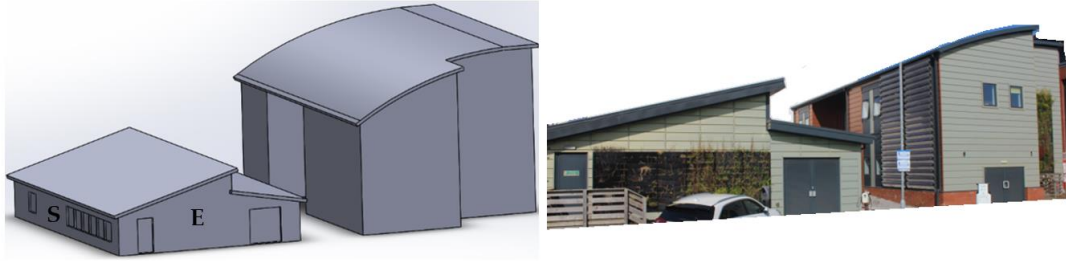


Figure 9.8. Dual building model (left) and actual buildings (right).

Both models, with and without the second building, were surrounded by a bounding box which extended in all directions by 60 m from the model and was 10 m and 20 m tall for the single and double building models, respectively. Extending the solution significantly beyond the area of interest ensures that the structures have a negligible effect on the domain boundary conditions

Meshing was carried out using ANSYS meshing with a face sizing of 150 mm on the building, a maximum size of 10 m, and a growth rate of 1.25. The final mesh had approximately 100,000–120,000 nodes, which varied for the different systems used.

The simulations were carried out using ANSYS CFX, general purpose CFD software (ANSYS, Canonsburg, USA), which utilises a finite-volume method solver and the Reynolds-averaged Navier–Stokes (RANS) equations. The k - ϵ turbulence model was used with scalable wall functions assuming a nominal 10% turbulence intensity at the inlet flow. The simulation was run isothermally (at 25 °C), but did include buoyancy effects with gravity defined in the Y direction as -9.81 ms^{-2} with a buoyancy reference density equal to that of the density of air at 25 °C, 1.19 kgm^{-3} [33]. One-way coupling was enabled so that droplet trajectories were influenced by air flow, without the change in droplet momentum influencing the air flow. Similarly, droplets did not interact with each other, so each droplet's path was considered statistically independent. A droplet drag coefficient of 0.5 was attached to the rain particles, which assumed a spherical shape for raindrops [34].

The fluid domain contained air at 25 °C that was modelled as a continuous fluid and water that was modelled as a particle transport solid with a diameter influenced by number particle distribution. This was defined using a minimum diameter of 0.1 mm and a maximum of 4 mm with a mean particle diameter of 1.5 mm and standard deviation of 1 mm. The particle diameter directly influences its trajectory through its

mass and drag. It has been show that rain particle diameter does vary as a function of rain intensity and a number of other environmental factors [35]. However, based on similar simulation work, it was thought that this provided a suitable foundation for experimental work [35]. RTP condition (25 °C) was used for the domain temperature for simplicity and because the temperature would have little effect (apart from very slight density differences), as the CFD model does not model interactions between mass transfer mechanisms between the liquid droplet and the air.

The computational domain is shown in Figure 9.9 and had the following boundary conditions set: the upper face ‘sky’ boundary was set as an opening with 0 Pa relative pressure with random injection of water particles from approximately 600,000 injection regions. The inlet location varied depending on the desired wind direction for each test; however, each inlet was defined to have a normal air velocity varying from 2 to 12 ms⁻¹, representing a range of local wind conditions (Table 9.2). All other boundaries were set as smooth walls with a restitution and parallel coefficient of 0 to draw attention to the areas that rain impacted the building, i.e., when droplets hit the surface, they stick, and their path is considered ended. No consideration was given to the droplet’s formation on the surface or the subsequent dripping through the action of gravity. The droplet flow rate was such that total droplet volume represented the annual rainfall. All other boundaries were set as smooth walls with a restitution and parallel coefficient of 0 to draw attention to the areas that rain impacted the building.

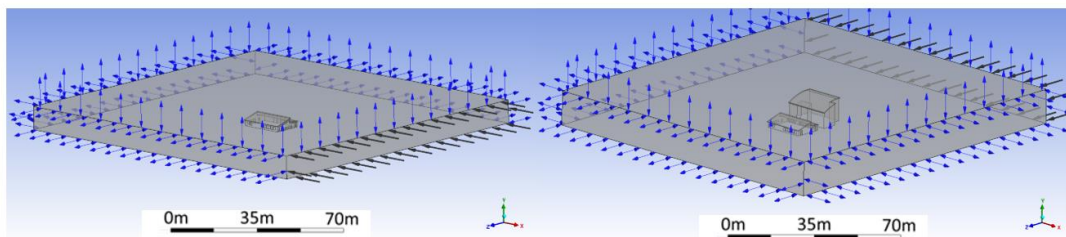


Figure 9.9. The computation domain for the single (left) and dual building (right) models. The black arrows signify an inlet boundary condition whereas the blue arrows show an open boundary condition.

The fluid simulation models were carried out in two strategic steps. Firstly, the single building model was examined with wind applied at the north, south, and east elevations to understand the effect of building geometry on rain (particulate) impact

distribution and the relationship with natural fouling. These wind directions represent approximately 19%, 22%, and 23% of the wind experienced in this location, respectively. Secondly, the effect of the adjacent, ‘semi-sheltering’, building in close proximity was then examined for the rain impact on the north face from northerly winds. The simulation scenarios are described in Table 9.4.

Table 9.4. Simulation scenarios.

Scenario	Model Used	Wind Direction	Wind Speeds Used ms ⁻¹
1–11	Single building	From east	2,3,4,5,6,7,8,9,10,11,12
12–22	Single building	From south	2,3,4,5,6,7,8,9,10,11,12
23–33	Single building	From north	2,3,4,5,6,7,8,9,10,11,12
34–44	Dual building	From north	2,3,4,5,6,7,8,9,10,11,12

Any CFD simulation is capable of producing a large volume of data on the fluid flow. However, in this instance it is the impact of the fluid flow on the rain impact density that is critical to understanding how the rain could influence the removal of fouling deposit. Semi-quantitative data were produced by sectioning the façade into a number of regions 300 mm in height to mimic the locations measured on the actual building. An example of this sectioning is shown for the south and east faces in Figure 9.10 and shows the sections numbered 1–8 increasing in height from the floor to the roof. For the east face, panel section 5 is much larger to account for the slope and presence of both roof sections; however, it gives a representation of a section approximately the correct height from both floor and roof. For each section, the quantity of rain impacting that region was recorded as an average volume fraction, averaged across the area of the section. This was to complement the visual analysis of the results.

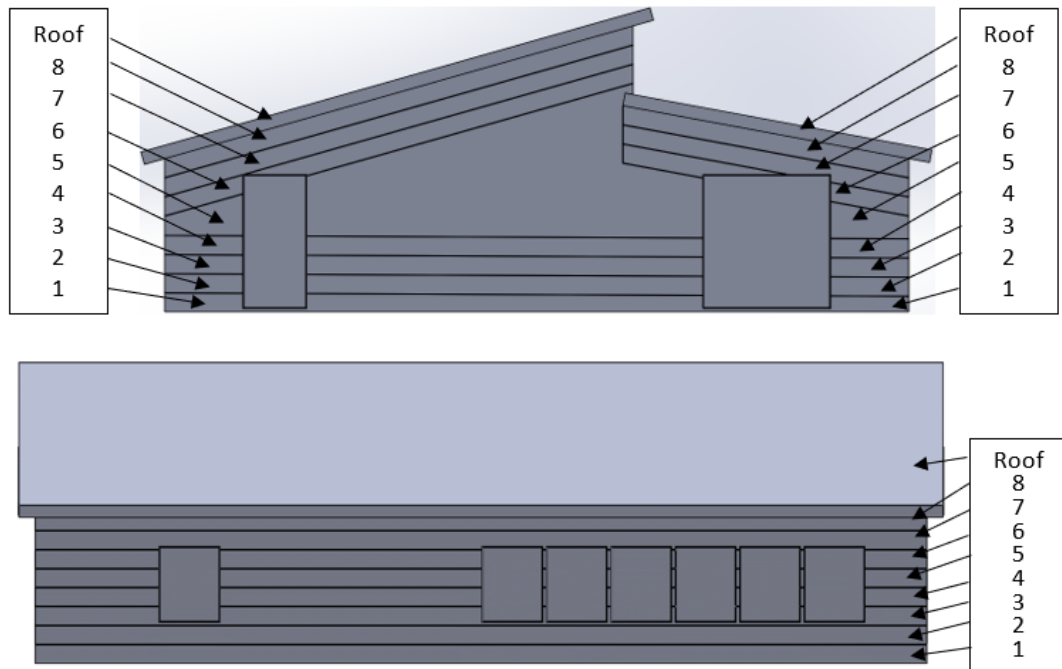


Figure 9.10. Example of façade sectioning for the east (top) and south (bottom) façades.

9.4 Results—Physical Experimental Work

The results of this work are presented in two separate sections that describe the physical measurement of the building and the simulated results. This section, covering the physical results, begins with an assessment of the measured degradation severity across the building to establish which general regions show evidence for experiencing higher degradation. The measured environmental conditions for a number of locations are then provided to discuss trends in the conditions present in different locations and suggest correlations of these conditions to the varying levels of degradation. The variation in build-up of natural fouling deposits is then presented and compared to the observed degradation levels. The likely effect of fouling on degradation is examined by presenting the constituents of the deposit and the effect of fouling on key features, such as water contact angle and time of wetness.

9.4.1 Degradation Variations Across the Building

The observed cut edge defect distance across various locations on the building is shown in Figure 9.11. Generally, the east and south façades showed similar levels of performance; however, far greater degradation was observed on the north face. Equally, it was observed that distance and severity of cut edge corrosion increased with the height of the panel with far more significant cut edge degradation occurring in the panels mounted high in the eaves of the building than those at ground level for

all observed façades. Initially, degradation is observed as blistering, which initiates corrosion and formation of white rust, which is in line with the literature [6]. This trend was also observed in door and window regions. The soffit region displayed moderate defect size, although this region was composed of more durable PVC-based coated material; hence, this may explain why it was perceived to be performing better than the highest PVDF panels that are in close proximity to the soffit region.

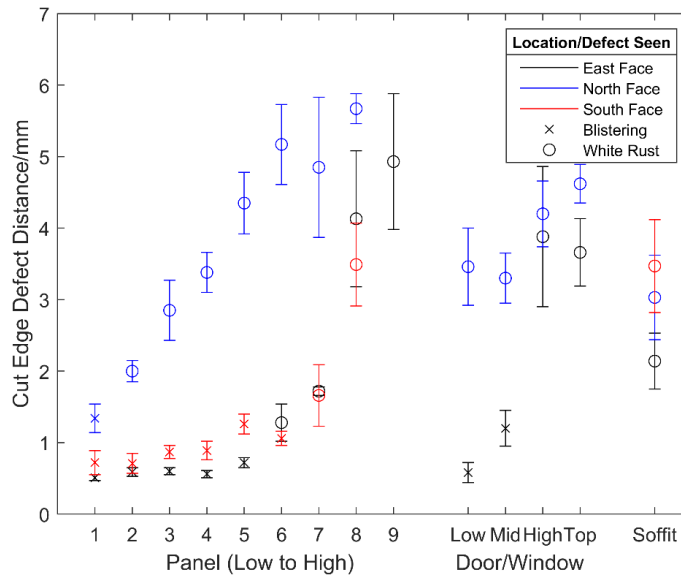


Figure 9.11. Variation in cut edge defect size and type across the building.

These results suggest that performance is significantly different across the building and even between regions separated by a few meters. When considering the age of the building, the level of degradation seen in certain locations is considerable; amounting to around 1 mm of cut edge corrosion per year. While it is possible that the discrepancy in performance is due to other factors, such as variance in workmanship or installation, the initial hypothesis was that this was a result of microclimatic aggressive localised conditions.

9.4.2 Environmental Condition Variations Across the Building

9.4.2.1 Temperature

The temperatures measured through the year reflect those which would be expected in a UK coastal location. Both the recorded ambient temperature and the panel temperatures, Figure 9.12, were generally fairly similar across all the locations with variations limited to a maximum of 3–4 °C. Location 1 (south middle) experienced

the highest temperature fluctuations due to it being on the south face and with greater sun exposure. This region also experienced some of the lower temperatures in the winter months. The panel temperatures follow a similar trend to the ambient temperature but are on average approximately 3 °C lower. This is attributed to radiative heat losses experienced during the measurement process of the IR thermopile sensor.

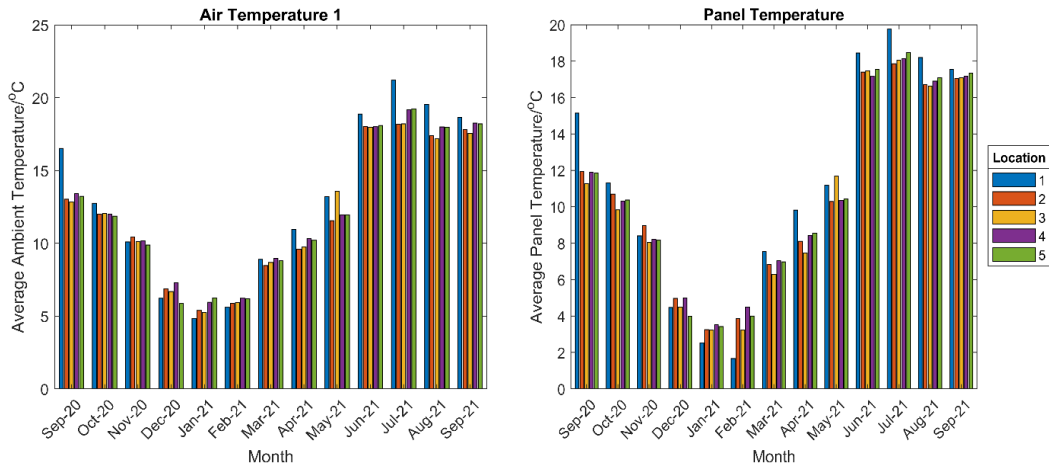


Figure 9.12. Comparison of air (left) and panel (right) temperatures recorded at each location.

9.4.2.2 Humidity

The measured humidity at each site, shown in Figure 9.13, shows much more variation among locations. Of particular interest is the difference between those locations that are high up in the eaves and are considered sheltered locations (2,5) and those lower down, which are far more exposed to the elements (1,3,4). Although there was some variation, on average these high locations recorded 4–5% increased relative humidity during the test period.

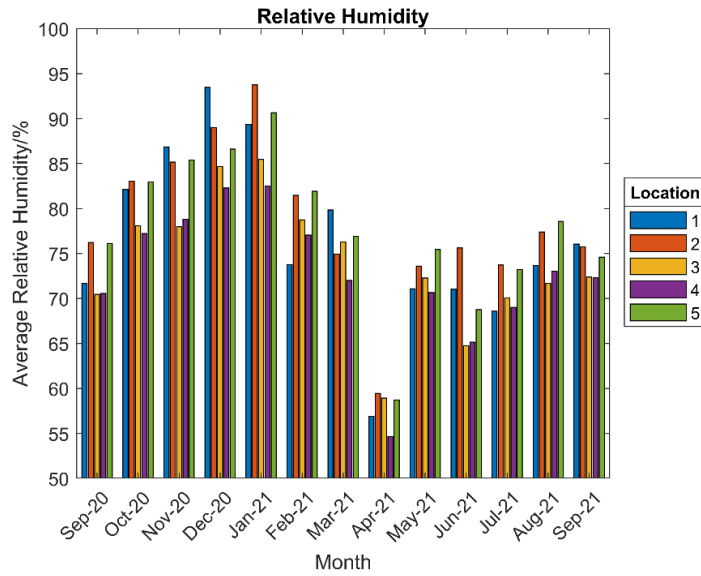


Figure 9.13. Comparison of the relative humidity recorded at each location.

9.4.2.3 UV Exposure

As expected, the recorded UVA and UVB intensity at each site, shown in Figure 9.14, shows that the high locations receive far lower irradiance by UV than the mid and low regions due to the roof overhang providing shade. Furthermore, the exposed south-facing location (1) received the highest UV exposure, which is consistent with sun movements for the northern hemisphere.

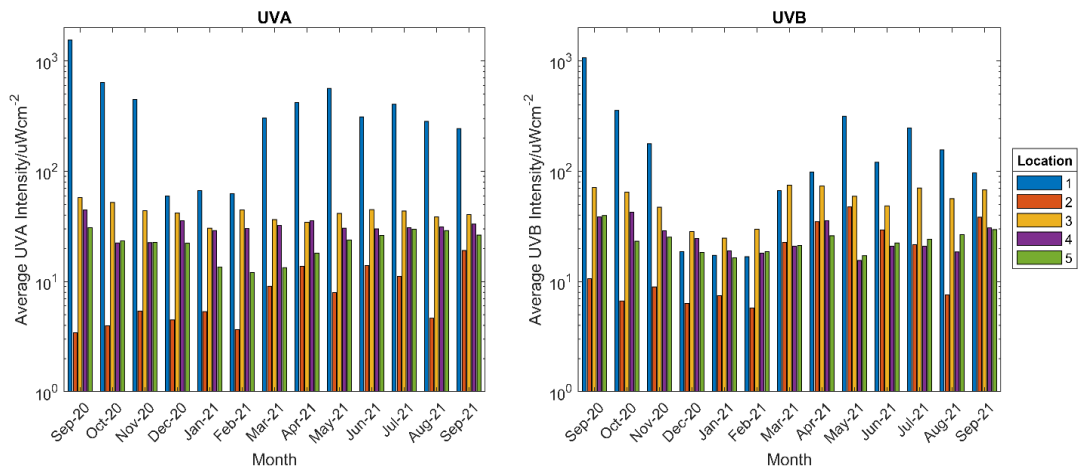


Figure 9.14. Comparison of UVA (left) and UVB (right) intensity recorded at each location.

9.4.2.4 Time of Wetness

The measured time of wetness at each location was calculated by comparing the number of readings captured suggesting probe wetness over 10% to those suggesting probe wetness under 10%. In Figure 9.15, it is observed that generally sites 1 and 2 showed greater wetness than the other sites. It is thought this is because sites 1 and 2

are more exposed to wind-driven rain than the north sites due to the semi-sheltered nature of the north face due to the building closely situated adjacent to the north. As expected, owing to increased rain exposure, comparing the mid and low sites to the counterpart high sites, the more exposed lower sites showed greater wetness. However, the high time of wetness of site 2 shows that just because a site is high and sheltered by the roof of a building does not necessarily preclude it from moisture build-up related to factors such as humidity.

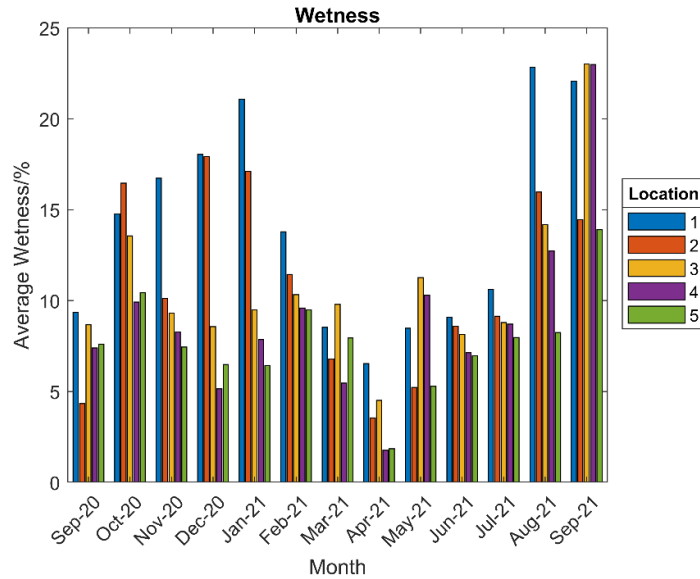


Figure 9.15. Comparison of % wetness recorded at each location.

9.4.2.5 Airborne Particulate Concentration

Figure 9.16 shows the measured particulate concentration at each location from which it is observed that there appear to be few obvious trends, although it can be said that higher average concentrations were observed on the lower, more exposed regions. It is thought this is because these locations experience the greatest exposure to wind, and hence more particles are wind-driven towards these areas. However, it is important to note that the number of particles arriving at a location does not always correlate with the amount of deposit building-up due to variations in natural washing across the building.

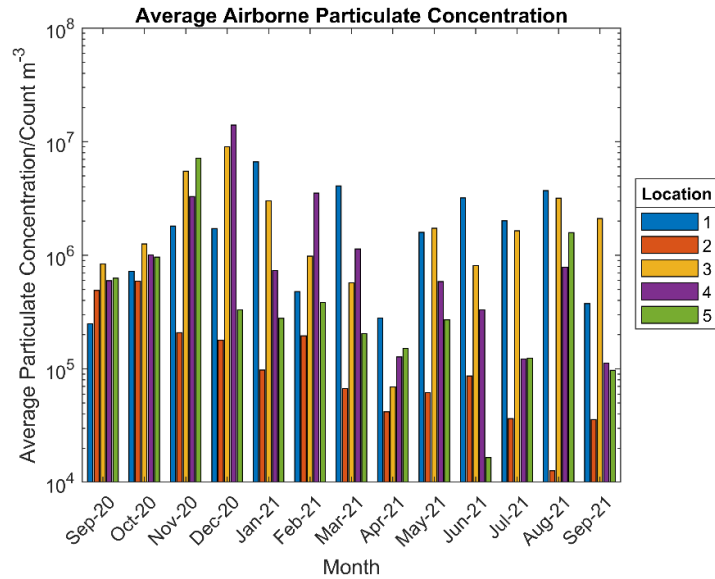


Figure 9.16. Comparison of particulate concentration recorded at each location.

9.4.3 Variations in Natural Deposit Build-Up Across the Building

The calculated weight of natural deposit built-up at each building location is shown in Figure 9.17. Generally, the north façade shows greater deposit build-up than the east and south, which show similar levels. Furthermore, the amount of deposit present increases from low at ground-level panels to the highest at the panel in the eaves of the roof and similarly increases in the door and window surrounds. The soffit regions showed relatively low levels of deposit build-up. Comparing the data presented in Figure 9.17 to that of the cut edge defect data shown in Figure 9.11, it is evident that increased natural deposits correspond to increased cut edge defects and white rust.

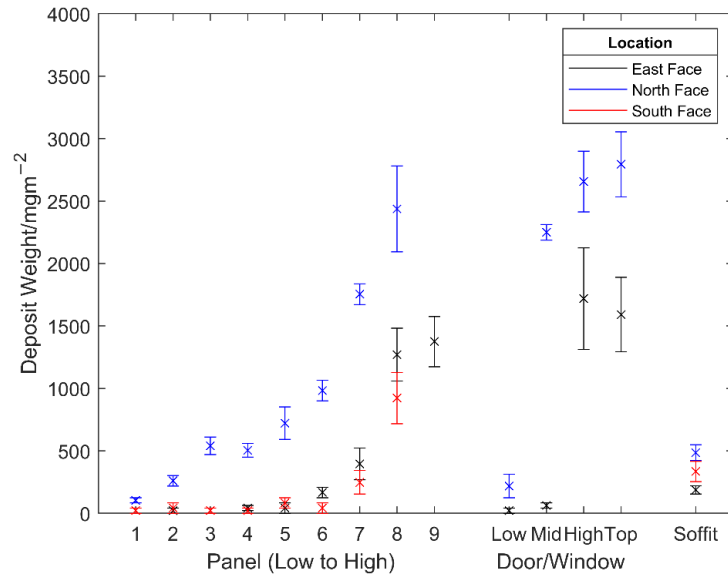


Figure 9.17. Variation in the amount of deposit present across the building.

To compare the correlation visually, the deposit weight was plotted against the cut edge defect distance, Figure 9.18, and a positive, nonlinear trend was observed. It was also observed that blistering only occurred in locations where the deposit weight was lower than approximately 250 mgm⁻², with white rust observed at all locations with larger deposit weights. Figure 9.18 also displays that the trend can be approximated to logarithmic with a calculated Pearson correlation coefficient of 0.92. The strength of the correlation led to discarding the idea that the performance variation could only be down to an additional factor such as poorer workmanship and installation in these regions.

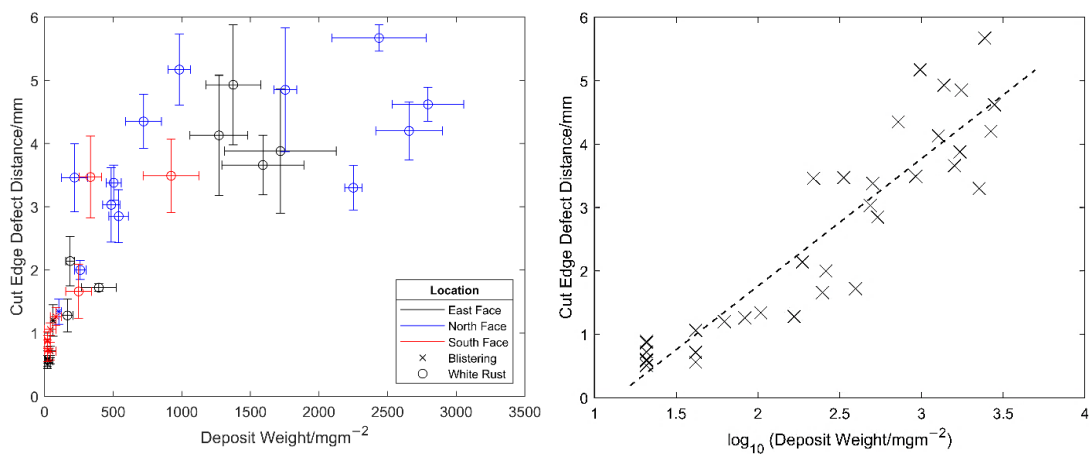


Figure 9.18. Comparison of the cut edge defect distance to the measured deposit weight in each location (left) and a demonstration of the logarithmic trend between the two factors (right).

9.4.4 Analysis of the Naturally Occurring Deposit

Figure 9.19 shows the results of the EDS analysis of the natural deposit samples SP and P. A variety of elements are present in both samples and the weight % of those often expected to be present in soluble compounds decreases in the P sample, where dissolution would have likely occurred. Of particular interest is the presence of chlorine, which appears to be soluble, presumably as Cl^- , which contributes to accelerated corrosion.

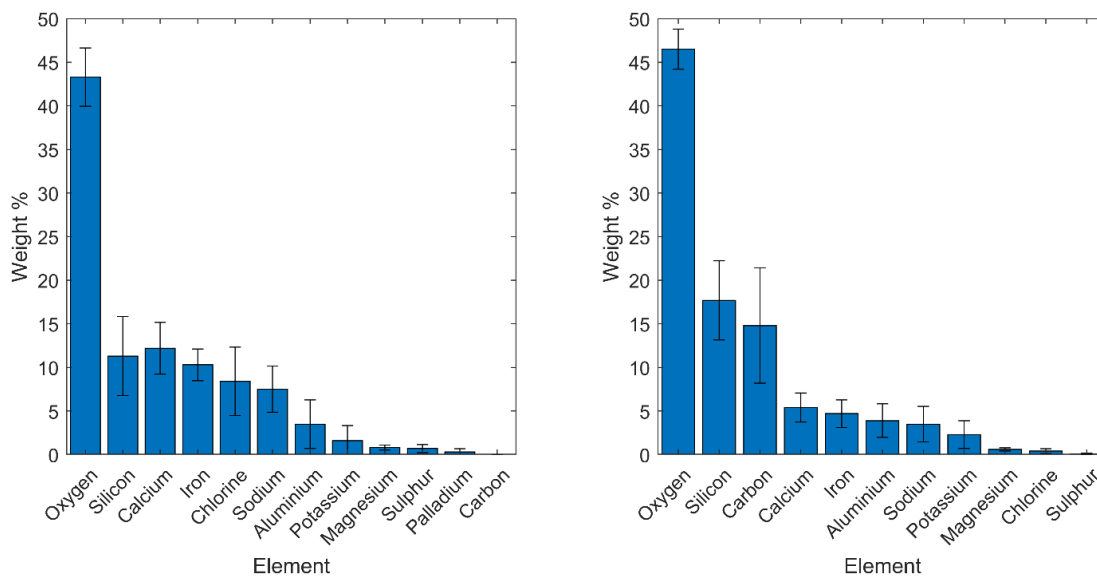


Figure 9.19. EDS analysis of the SP sample (left) and the P sample (right).

The EDS% weight data were used in combination with the likely compounds present, matched with the XRD results, Figure 9.20, to identify the compounds and the likely percentage distribution of these compounds in the two samples. The resulting data are displayed in Figure 9.21. Again, it was observed that water soluble compounds are less prevalent in the P sample, as would be expected. It is worth noting that not all elements identified in the EDS work formed part of a compound in the XRD analysis, suggesting other compounds composed of the unmatched elements may also be present. It was surprising to observe the presence of palladium and was unknown where this may have originated from.

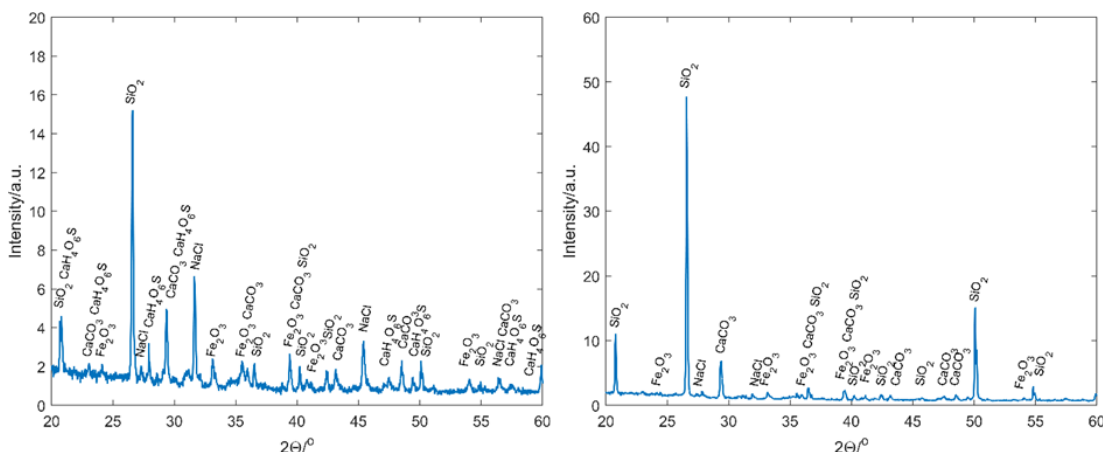


Figure 9.20. XRD analysis of the SP sample (left) and the P sample (right).

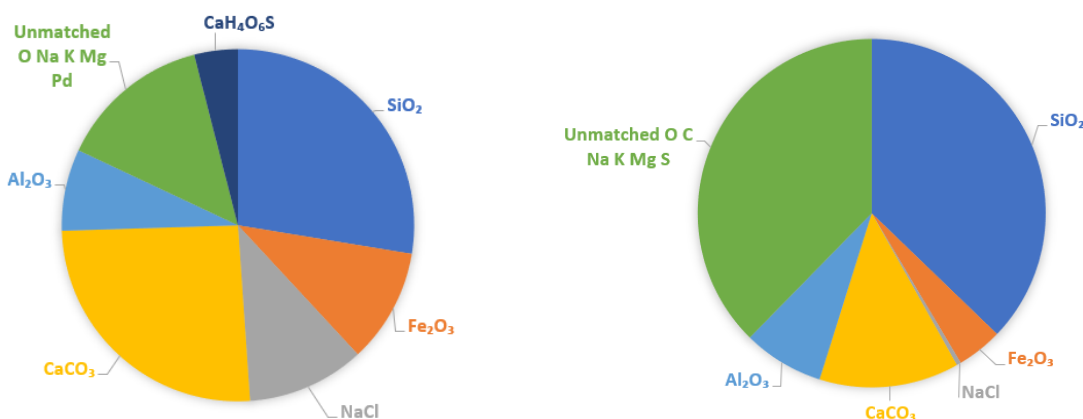


Figure 9.21. Likely constituents of the analysis of the SP sample (left) and the P sample (right).

The well-matched compounds are shown in Table 9.5 along with their more common name and the possible source of such compounds. It is immediately apparent that the identified compounds are correlated highly with the local environment. For example, at this coastal location, there is a high concentration of sand and natural salts together with building materials from the ongoing development of the university site. It is important to note, therefore, that buildings are extremely likely to observe different amounts and compositions of deposits depending on their geographical locations.

Table 9.5. Identified compounds and their likely sources.

Filtered Sample (P)		
Compound	Common Name	Found in/Possible Source
SiO ₂	Silicon dioxide/silica	Sand
Fe ₂ O ₃	Iron (III) oxide	Corrosion product
NaCl	Sodium chloride/‘salt’	Natural salt
CaCO ₃	Calcium carbonate	Natural salt
Al ₂ O ₃	Aluminium oxide	Corrosion product
Unfiltered Sample (SP)		
SiO ₂	Silicon dioxide/silica	Sand

CaH ₄ O ₆ S	Calcium sulphate dihydrate	Gypsum building materials
Fe ₂ O ₃	Iron oxide	Corrosion product
NaCl	Sodium chloride/'salt'	Natural salt
CaCO ₃	Calcium carbonate	Natural salt
Al ₂ O ₃	Aluminium oxide	Corrosion product

The effect of the deposit on the conductivity of a liquid phase was also examined by producing a solution of 1% and 5% wt. deposit in deionised water, Table 9.6. This solution was produced by using the captured deposit (SP) from previous tests and adding the required ratio of deposit to deionised water to create the desired concentrations. This was carried out using the produced conductivity device, Appendix B, and it was found that, while the conductivity of a 1 and 5% wt. deposit solution produced lower conductivity than respective concentrations of NaCl, they did produce a solution with conductivity approximately 17 and 19 times greater than that of rainwater, respectively.

Table 9.6. Measured conductivity of different electrolytes.

Sample	Measured Conductivity S/m
Deionised Water	0.00
1 wt.% NaCl	2.27
1 wt.% deposit	1.65
5 wt.% NaCl	2.75
5 wt.% deposit	1.89
Tap water	0.10
Rainwater	0.10

9.4.5 Effect of Deposit Weight on Wetting Angle

The wetting angle exhibits a significant decrease as natural deposit is applied to the originally clean samples, as shown in Figure 9.22. All three paint systems when clean have similar wetting angles of approximately 65–75°, but these decrease by 35% with the addition of 4000 mgm⁻² of deposit. In the case of the PVDF and PU samples, the decrease in wetting angle appears linear with the addition of deposit; however, the PVC sample decreases more rapidly. This clearly demonstrates that deposit built-up results in the surface becoming more hydrophilic. In practice, this would lead to less water runoff, greater spreading of the water droplets, and longer exposure times of the paint to the conductive water.

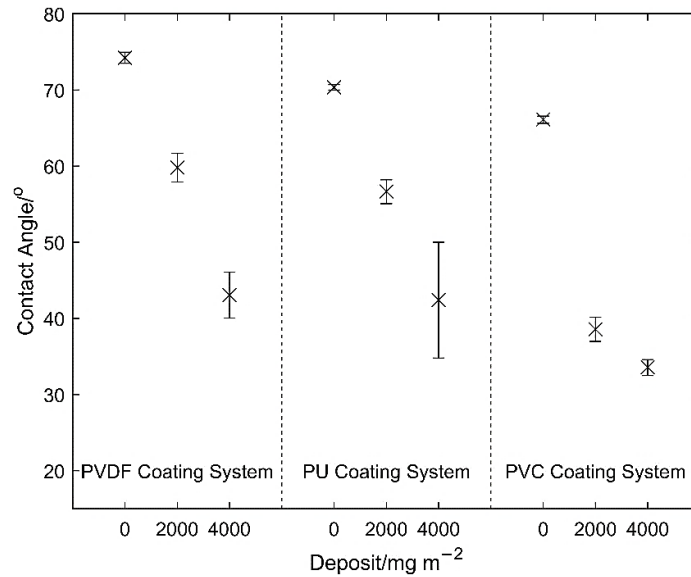


Figure 9.22. The effect of increased deposit build-up on the wetting angle measurements for the three different coating systems.

9.4.6 Effect of Deposit Weight on Water Absorption and Retention

The results of the humidity chamber test for the PVDF coating system are shown in Figure 9.23. It can be observed that the samples with applied deposit increased in mass through time in the humidity chamber, and that the greater the deposit weight applied, the greater this increase. The control sample gained a small amount of weight after approximately 2 hours and levelled, representing some condensation due to initial sample temperature. The mean increase in mass per $\text{mg/m}^2/\text{day}$ at 95% humidity was determined to be $5 \pm 0.5 \mu\text{g}$. Thus, any surface fouling plays a key role in maintaining moisture on the paint surface, increasing water diffusion through coating to the substrate below. Increased presence of hygroscopic compounds in such fouling will likely increase the magnitude of this effect.

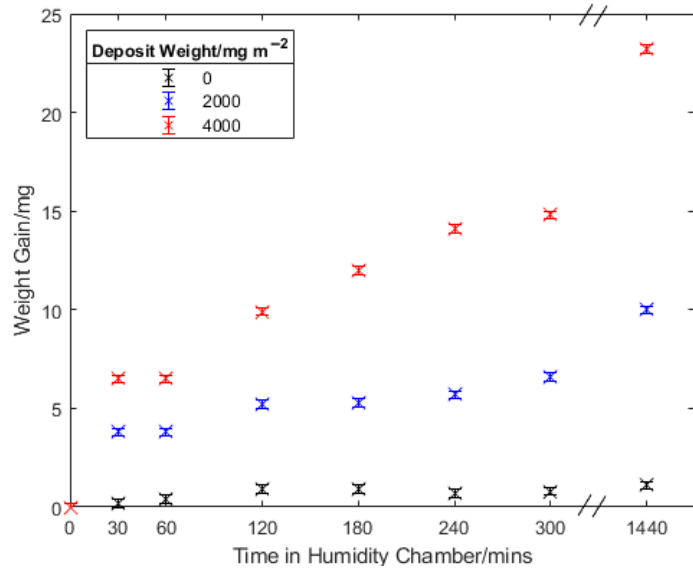


Figure 9.23. Water adsorption as a result of deposit weight and time in a humidity chamber for the PVDF-coated samples.

These trends were also observed with the other coating systems. For all coating systems, the weight gain with time, per mgm⁻² of deposit vs. the clean samples, is given in Figure 9.24. It is displayed that all the three coating systems perform similarly, suggesting that independent of the coating system used the sample will gain approximately 4–5 μg of H₂O per mgm⁻² of deposit present, per day, in a 95% humidity environment.

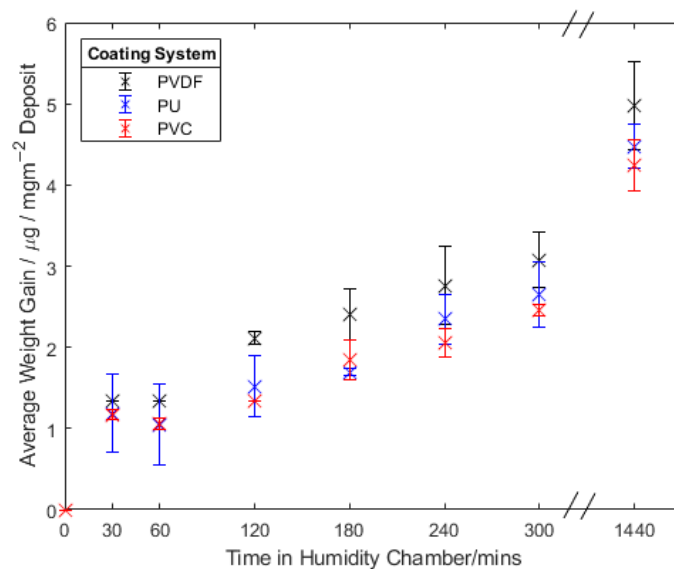


Figure 9.24. Water adsorption per mgm⁻² of deposit weight as a result of time in the humidity chamber for each coating system.

When subjected to a lower relative humidity, moisture leaves the surface, Figure 9.25. The consistency of the mass loss suggests that the deposit build-up has little effect on the ability of the sample to dry. However, it has to be considered that the deposit-applied samples do have a reduced contact angle and hence the droplets covered a larger area. Therefore, it would be expected that the droplets on the lower contact angle samples would evaporate faster due to increased surface area to volume ratio. Hence, the fact that all the samples showed similar drying rates suggests that there is an element of the deposit retaining the water, somewhat. It is difficult, however, to conclude that amount of deposit has a significant effect on the drying rate for this sample.

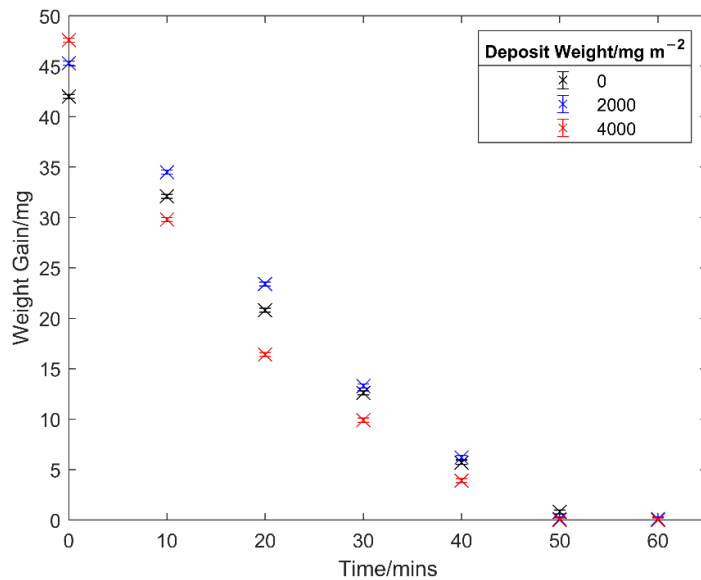


Figure 9.25. Effect of deposit weight on the drying of applied water droplets for the PVDF-coated samples.

Similar results were observed for the other coating systems, as shown in Figure 9.26. There appears to be little trend in terms of drying rate, again suggesting that the competing factors of contact angle and water retention by the deposit mean there is little difference in the drying rate observed using this testing method.

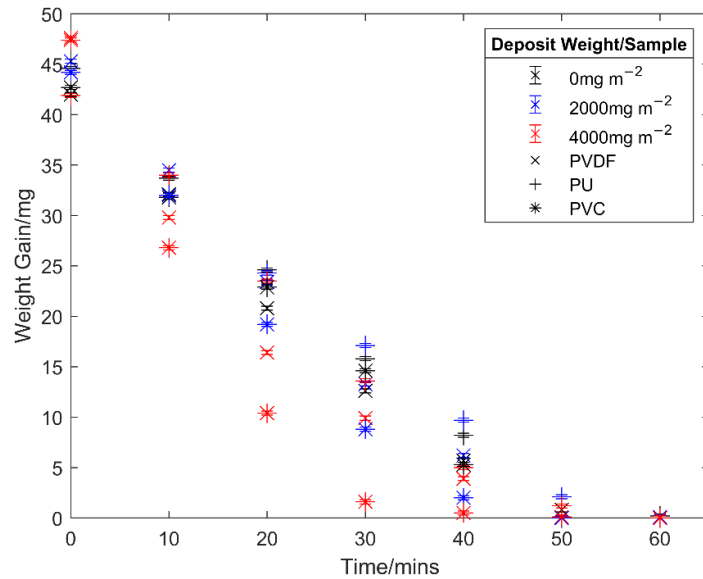


Figure 9.26. Effect of deposit weight on the drying of applied water droplets for all coating systems.

9.5 Results—Simulated Measurements

Given that the build-up of fouling deposits has been shown to be well correlated with degradation, simulations were carried out to attempt to predict locations of deposit build-up specifically by considering areas of the building that are naturally washed. These are presented along with semi-quantitative analysis and then compared to the measured fouling build-up to determine the usefulness of the model in determining the regions of fouling and therefore increased degradation concern.

9.5.1 Single Building Only—‘Visual’ Analysis

Simulations were carried out to understand the rain impact of each façade under different wind speeds. The contour plots discussed below show what can be considered a probability plot of the likelihood of rain particles impacting the building in each specific area, with those in blue the least likely to experience direct rain fall and those in red the most likely. Visual examination of the single building model for the east, south, and north faces, shown in Figure 9.27, Figure 9.28, Figure 9.29, shows some clearly identifiable trends.

Firstly, it is observed that the greatest barrier preventing natural washing of the façade via rain impact is the roof soffit overlap. This creates a shielded region which is protected to an extent from the wind-driven rain particles. The extent to which this occurs is a function of the wind speed; when the wind speed is low, then the sheltered area is large, but as the wind speed increases, the particle trajectory is

increased in the horizontal direction reducing the sheltering effect of the roof overlap. However, even at high wind speeds of $10\text{--}12\text{ ms}^{-1}$, the roof soffit still maintains a sheltering effect to some extent. At lower speeds ($4\text{--}6\text{ ms}^{-1}$), it is also possible to see that the doorway and window inset surrounds also produce a sheltering effect to some extent with greater sheltering observed in the higher regions of the surrounding area.

It is worth noting that the regions that are shown to have a low probability of natural washing are well correlated to those that have a high quantity of natural deposits. This provided some confidence that the model may be able to predict regions likely to be subjected to fouling and therefore higher degradation rates. The exception to this is the north face where this model predicts that similar rain impact occurs on the south and north faces, suggesting that similar deposit levels should be seen on the actual building. However, this is thought to be due to the lack of the second sheltering building in this model.

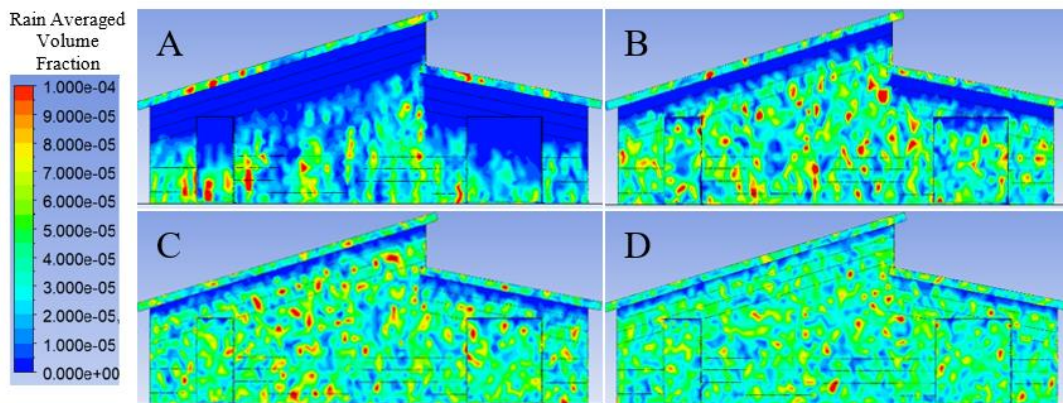


Figure 9.27. Predicted rain impact density for the east elevation under 2 (A), 4 (B), 6 (C), and 8 (D) ms^{-1} wind speed applied normal to the east elevation.

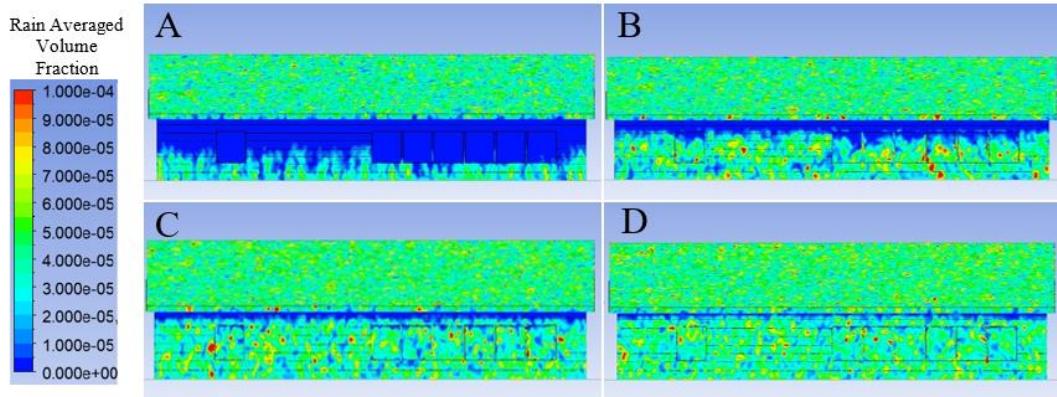


Figure 9.28. Predicted rain impact density for the south elevation under 2 (A), 4 (B), 6 (C), and 8 (D) ms^{-1} wind speed applied normal to the south elevation.

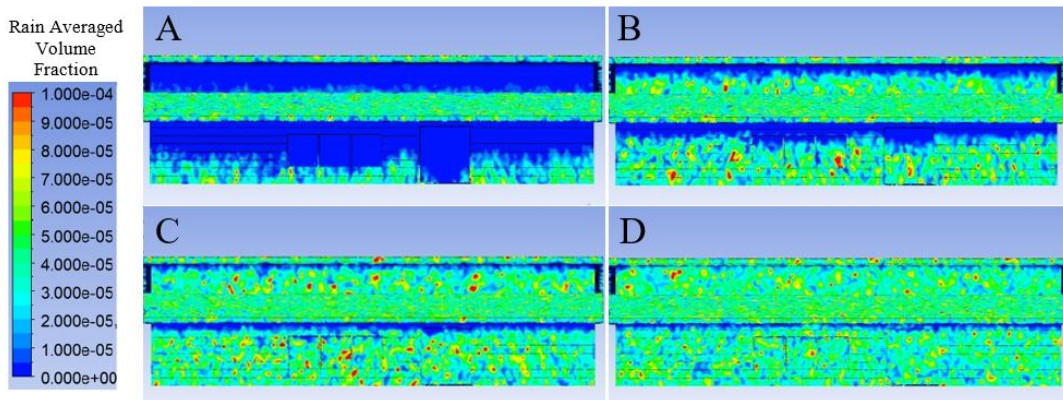


Figure 9.29. Predicted rain impact density for the north elevation under 2 (A), 4 (B), 6 (C), and 8 (D) ms^{-1} wind speed applied normal to the north elevation.

9.5.2 Single Building Only—Semi-Quantitative Analysis

The measured average rain volume fraction for each location identified in Figure 11 can be seen in Figure 9.30. This provides further evidence to corroborate the visual observation that the roof soffit provides a sheltering effect that decreases with increased wind speed. It is also apparent just how significant that sheltering effect is on the higher panels (6–8), suggesting a very low probability of direct rainfall contacting these panels unless a high normal wind speed is present.

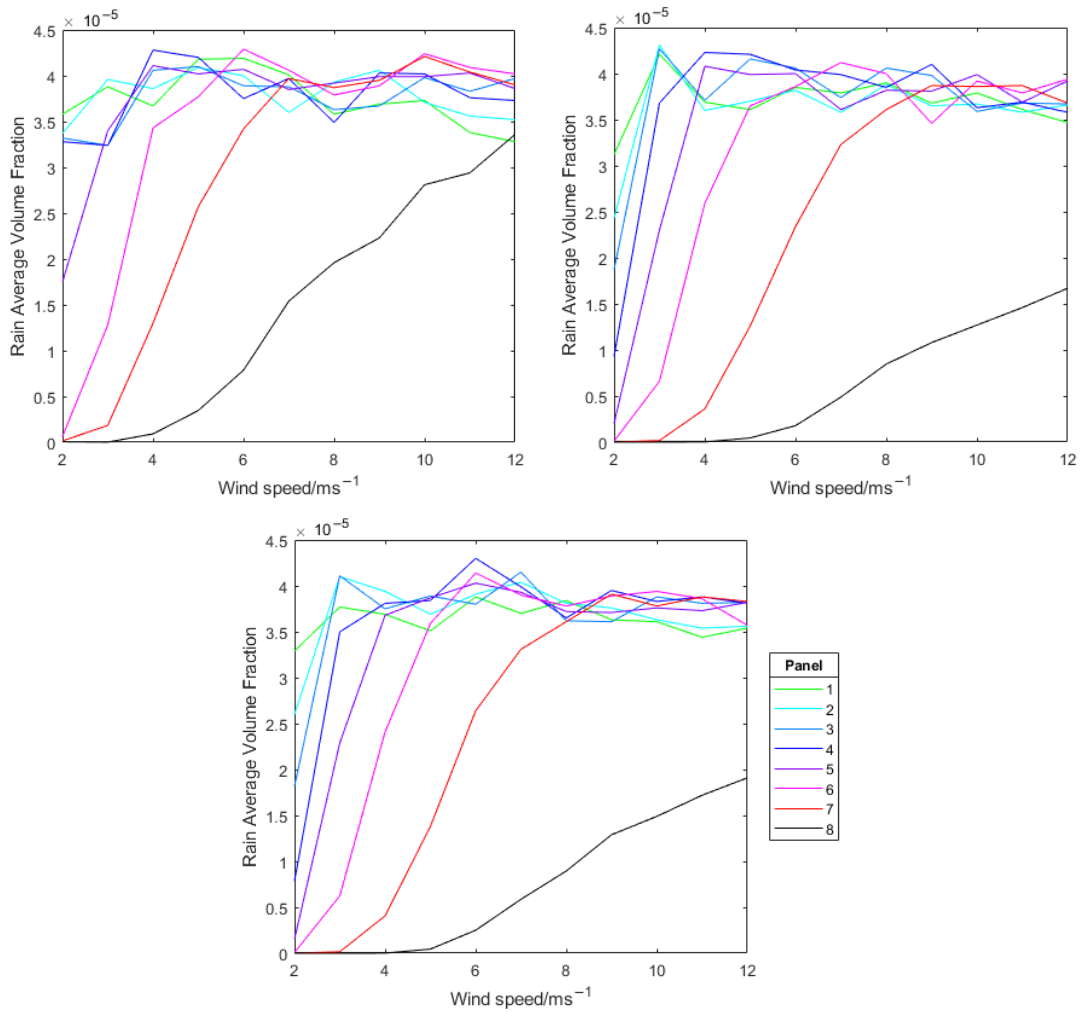


Figure 9.30. Measured average rain volume fraction at each location for the east (top left), south (top right), and north (bottom) façade.

In order to compare these results to the measured fouling, for each panel the values of rain average volume fraction for each wind speed were converted into a single value using a weighted average corresponding to the likely windspeed probability shown in Figure 9.31. It was thought that the windspeed probability was suitable for the location tested given the previously mentioned average weather conditions.

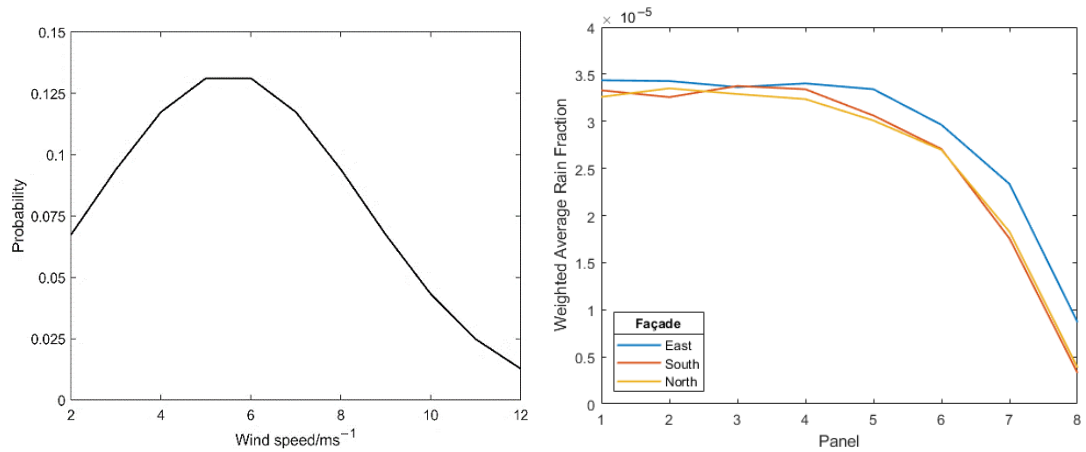


Figure 9.31. Wind-speed probability distribution used (left) to calculate wind-speed weighted averaged rain fraction for each panel on each façade (right).

When this value was plotted against the measured deposit fouling, Figure 9.32, the results show that, as expected, the extent of fouling increases as the quantity of model-predicted rain impact decreases. While the east and south faces generally show similar behaviour, the north face, however, is observed to show far greater fouling for a similar weighted average rain fraction. It is thought this is due to the importance of considering other nearby buildings on the effect of natural building washing and not solely the geometry of the building of interest.

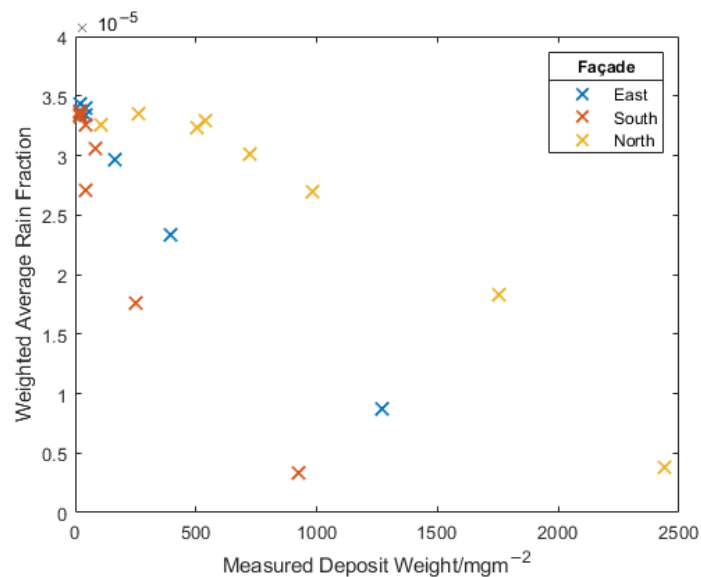


Figure 9.32. Comparison between measured deposit fouling intensity and model predicted rain impact density.

9.5.3 Adjacent Building Model—‘Visual’ Analysis

The model above provided an accurate representation of the naturally washed regions of the east and south face; however, it did not accurately represent the north face in terms of the measured deposit build-up. This was attributed to the omission of the second semi-sheltering adjacent building, which may provide a significant change to the predicted rain impact density on the north face it overlooks. The second model included this adjacent building and the resulting contour map of rain impact the north face, shown in Figure 9.33, displays this effect. It is clear that, when compared to the single building model, the dual building model predicts far less natural rain impact on the north face. This correlates far better to the measured deposit build-up shown previously with high levels of deposit observed on the lower panels.

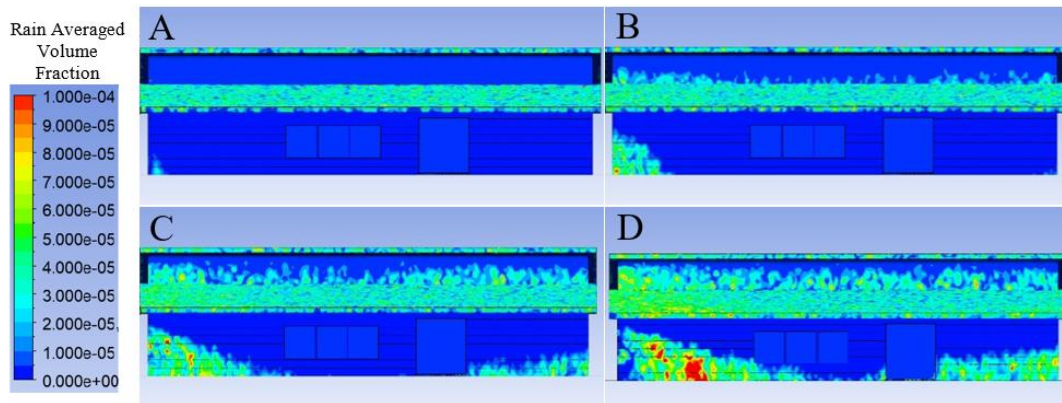


Figure 9.33. Effect of the semi-shielding building on the predicted rain impact density for the north elevation under 2 (A), 4 (B), 6 (C), and 8 (D) ms^{-1} wind speed applied normal to the north elevation.

9.5.4 Adjacent Building Model—Semi-Quantitative Analysis

It is observed in Figure 9.34 that with the adjacent building included in the model all the panels on the north façade record far lower averaged volume fractions of rain at the lower wind speeds (2–8 ms^{-1}). In fact, it is observed that a wind speed of 8 ms^{-1} is required just for panel 1 to receive a similar rain average volume fraction to panel 1 in the single building model at just 2–4 ms^{-1} . While panels 1–4 do experience slightly higher volume fractions at high wind speeds 8–12 ms^{-1} , it should be noted that panels 5–8 never record similar volume fractions to those in the single building model, even at high wind speeds. This difference in the predicted north façade rain impact density in the two models is further shown by the wind-speed weighted average rain fraction, also shown in Figure 9.34.

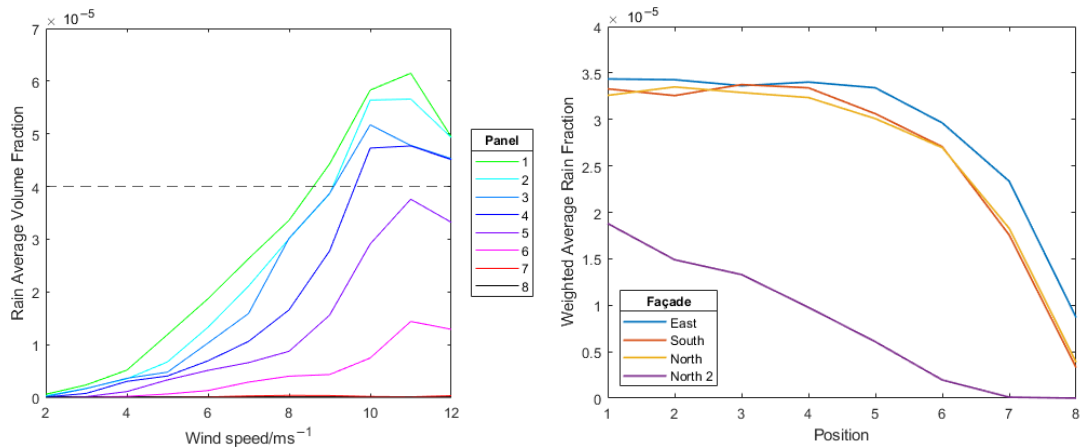


Figure 9.34. (Left) Measured average rain volume fraction at each location for the north façade in the dual building model. The dashed line represents the maximum volume fraction achieved in the single building model. (Right) Comparison between the wind-speed-weight

The improvement on the north face model by adding the adjacent building is further evidenced when again comparing the model-predicted rain impact density against the measured deposit fouling, Figure 9.35. When considering the trend line provided by the east and south façade data, the north façade data provided by the second (with the adjacent building) fit far better than that of the original model (without the adjacent building). These results build on the previous visual results to highlight the importance of the adjacent building on the expected natural washing of the building leading to increased deposit build-up in regions that would otherwise be considered to be naturally washed. Given the effect that natural deposit fouling appears to have on degradation, this is a significant consideration.

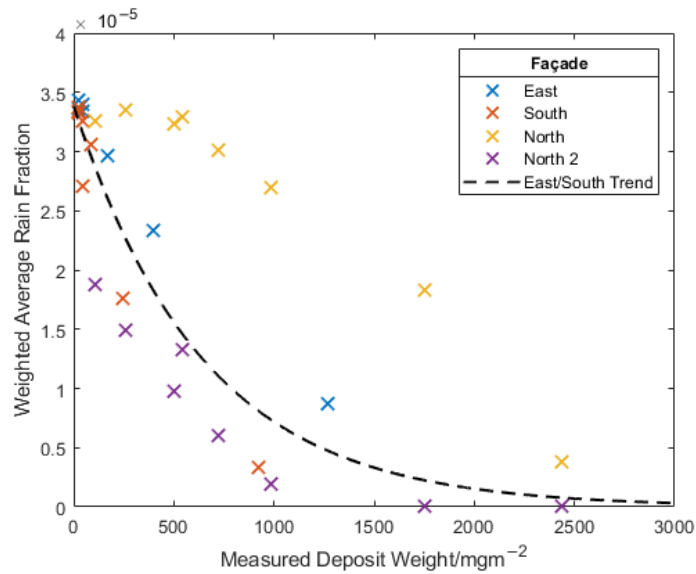


Figure 9.35. Comparison of the fitting of north façade data from each model to the trend given by the east and south façade data.

9.5.5 Using the Simulation to Predict Degradation Rates

While it is promising to see a clear correlation between the simulations and the deposit fouling intensity, the far more important factor is the measured distance of the cut edge corrosion defect. The result of plotting this against the wind-speed weighted average rain fraction for all façades and panels, Figure 9.36, is a highly correlated exponential trend between the two factors, providing an R^2 value of 0.94. The exponential decay of the cut edge defect distance with simulated rain fraction was thought to be explainable through the effect of cleaning and therefore the relative influence of deposits. As the rain impact density increases, the fouling decreases, which leads to an ever-smaller contribution of the fouling deposit to the degradation. This suggests the simulations could accurately be used to determine likely areas of concern.

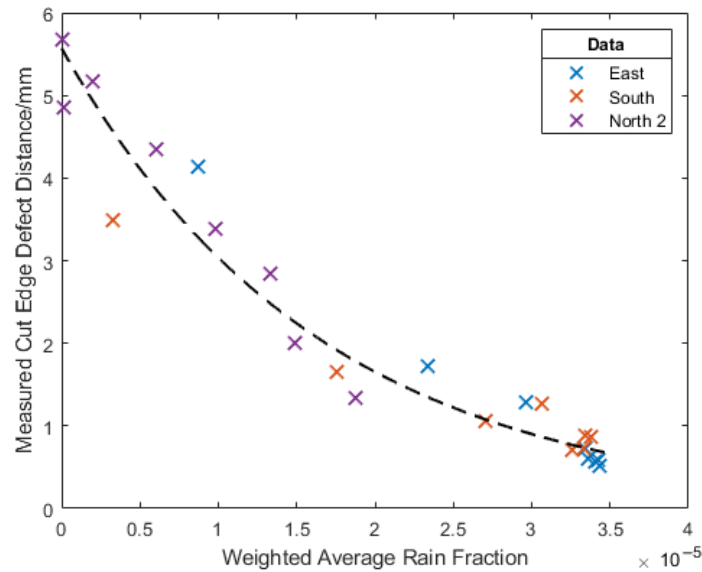


Figure 9.36. Comparison of measured cut edge defect distance and the model-predicted rain impact density.

9.6 Discussion

It was shown that significant variations in the degradation of steel architectural cladding can be experienced around a building, and that this caused by the formation of microclimates due to building geometries. Regions separated by less than 30 cm can experience significantly different degradation. What was observed in this work builds on research claims [20], that it is the more sheltered regions of the building that often receive far lower exposure to rain and sunlight, which appear to show the greatest levels of degradation. These regions generally only experience high levels of a single conventional aggressive condition—humidity; however, in the present example, it appears that OCS performance is more highly correlated with the build-up of natural fouling deposits than any other measured factor. Significantly, even regions with relatively similar humidity levels show vastly different levels of degradation when the amount of deposit is varied. Natural deposits (although usually only specifically pollutants) have been shown previously to be key accelerators of degradation for façades of other construction materials, such as paint, concrete, and ceramic [24,36,37], but have often not been examined or measured in great detail as factors when comparing discrepancies between natural and accelerated weathering of OCS [4,38].

The present investigation builds on an understanding that has emerged in the OCS research field that the unprofessional concept ‘more exposure is worse’ is outdated as

the performance of coatings has improved [20]. The significant development of coating resistance to UV (requiring the new Ruv5 classification of BS EN 10169:2022 [39]) and water (5000 h+ humidity testing by BS EN 13523-25 [39]) means that generally OCS is very durable to high exposure to sun and rain, and very rarely is degradation experienced in the centre of a panel unless a significant defect, such as a scratch, is produced as a result of, for example, poor installation. Owing to this, the most commonly seen defect is caused by corrosion at the cut edge where exposure of the substrate is inevitable [19]. What is shown in this work is that cut edge corrosion occurs far faster in sheltered regions due to the increased humidity combined with aggressive salty deposits that naturally absorb water and hence maintain a highly corrosive environment. In comparison, exposed areas frequently experience a natural cycle of washing and drying and are therefore subjected overall to less corrosive conditions.

While our work above focuses on a single building, it is important to consider generally the implications of these results on current testing methods. While sheltered regions that are not naturally washed do exist on outdoor weathering testing racks (BS EN 13523-19 [39]), due to the small size of the sample and overhang, this region is less likely to show significantly increased fouling and humidity compared to the bulk to the same extent as was measured on the present building. Furthermore, it is important to consider the highly localised nature of the deposit constituents. Depending on the weathering site used, a representative deposit may be formed; however, it is likely that the exact composition, and therefore the effect on degradation, will vary between test site and the eventual site of product use. Two of the most common testing standards for outdoor weathering, EN 13523-19 and ISO 2810, make no specification as to the debris environment and no significant recommendations are made concerning any analysis of fouling during testing except general, mostly visual, qualitative comparisons such as those described in BS EN 13523-29 [39,40]. This means that a key factor shown to be highly correlated with the degradation rate of OCS is insufficiently defined during natural exposure testing. This is similarly true for accelerated weathering tests, while there are tests for high UV and saline exposure, there is no such test for accelerated fouling-induced degradation.

Hence, it is unlikely that the determination of performance purely from standard tests is fully representative for in-service use, especially concerning regions sheltered from natural washing. Identification of where these regions occur is therefore important.

The simulation work supports this understanding of the importance of the natural washing of panels on the likely rate of fouling and therefore degradation. It was shown that an indication of sheltered regions can be created using a computational model such as the one presented here. This can, therefore, act as a simple way to determine likely areas of accelerated degradation, especially those caused by a nearby sheltering building and/or other structures. The authors believe that similar models could be used in the building design process to highlight the effect certain building geometries may have on the likely size of highly aggressive, unwashed areas. While this may not be significantly important to alter building design, it could be used by the cladding supplier to highlight areas to the installation team where cladding solutions should be used that do not expose the cut edge. Furthermore, if any maintenance or inspection is to be carried out, the model could provide areas on which to focus, thus leading to reduced cost and time.

The limitations of this work are that it was carried out on a single building in a single location. The degradation effects of fouling deposits in this region were significant; however, this may not be representative of all building locations due to variations in the deposit constituents. Coastal regions will inevitably produce aggressive salty deposits, but other locations such as rural or urban may also produce deposits with other potential accelerants, such as ammonia, acid rain, or pollutants. This is noted in [38] as a possible reason for differences in electrochemical measurements of naturally weathered samples in coastal, urban, and mountainous regions. Further work is required to assess several locations to determine the aggressiveness of the deposit in each. Although the simulations did determine the areas where degradation was occurring fastest on the building considered, the investigation and simulation of other buildings of different sizes and shapes is required to determine the effectiveness and accuracy of this method.

9.7 Conclusions

The performance of identical OCS cladding across a building was shown to vary significantly as a result of localised environmental factors. This work agrees with other studies that show most degradation occurs at the cut edge, but reinforces suggestions that the greatest concern should be regions that are less exposed to the elements and less likely to be naturally washed.

Quantitatively, areas that were unwashed produced cut edge defects that had propagated six times farther (1 mm compared to 6 mm) into the cladding compared to those areas most naturally washed.

This work suggests this is because these regions suffer from significant build-up of locationally correlated deposits which, in coastal regions, seem to be exceptionally aggressive. Under the increased humidity also present in unwashed locations, these deposits create a wet, corrosive environment, accelerating cut edge corrosion.

In comparison, although the more exposed areas of a building are subject to higher levels of UV and rain, modern coatings are adequately durable and increased natural cleaning and drying reduces cut edge corrosion in these regions.

This work identified that sheltered regions of concern exist in the eaves of the buildings and enclosed doorways and windows, but can also be produced on a larger scale by the sheltering effect of nearby buildings.

However, it seems that fairly simple simulations of areas likely to be washed are possible, leading to the identification of areas likely to face harsher conditions. The information gathered from these simulations allow for better design, more appropriate product deployment, and targeting of maintenance and inspection work. The identification of rain-washing as a key parameter inspired the final chapter of work which returned the focus to live monitoring. While live monitoring of degradation had proved complicated it was thought that rain sensing could be feasibly achieved.

9.8 References

1. Eurofer. European Steel in Figures 2021 [Internet]. Statistical guide. 2020 [cited 2022 Nov 11]. Available from: <https://www.eurofer.eu/assets/publications/brochures-booklets-and-factsheets/european-steel-in-figures-2021/European-Steel-in-Figures-2021.pdf>

2. TATA Steel. THE CONFIDEX® GUARANTEE [Internet]. 2022 [cited 2022 Jul 4]. Available from: <https://www.tatasteeleurope.com/construction/services/guarantees/confidex>
3. Deflorian F, Rossi S, Fedrizzi L. Advanced Testing Procedures for High Performance Coatings. *J Coatings Technol.* 2000;72(908):81–7.
4. Deflorian F, Rossi S, Fedrizzi L, Zanella C. Comparison of organic coating accelerated tests and natural weathering considering meteorological data. *Prog Org Coatings.* 2007;59(3):244–50.
5. Savill T, Jewell E. Techniques for in situ monitoring the performance of organic coatings and their applicability to the pre-finished steel industry: A review. *Sensors.* 2021;21(19).
6. Buchheit RG. Corrosion resistant coatings and paints [Internet]. Third Edit. *Handbook of Environmental Degradation of Materials.* Elsevier Inc.; 2005. 367-385 p. Available from: <http://dx.doi.org/10.1016/B978-0-323-52472-8.00022-8>
7. Tator KB. Coating Deterioration. In: *Protective Organic Coatings* [Internet]. ASM International; 2015. p. 462–73. Available from: <https://dl.asminternational.org/books/book/13/chapter/143061/coating-deterioration>
8. Knudsen O., Forsgren A. *Corrosion Control Through Organic Coatings.* 2nd ed. Schweitzer P, editor. CRC Press; 2017.
9. Munger CG. Causes and Prevention of Paint Failure. In: *Good Painting Practice, Steel Structures Paint Manual.* 2014. p. 1–21.
10. Nazarov A, Thierry D. Influence of electrochemical conditions in a defect on the mode of paint corrosion delamination from a steel surface. *Corrosion.* 2010;66(2):0250041–02500410.
11. Walch M, Mitchell R. Biological Aspects of Corrosion of Offshore Structures. *NavalResearchReviews.* 1894;16.
12. ASTM International. ASTM B117-19 Standard Practice for Operating Salt Spray (Fog) Apparatus [Internet]. 2019. Available from: <https://www.astm.org/b0117-19.html>
13. Standard I. ISO 4618 Paints and varnishes — Terms and definitions [Internet]. 2014. Available from: <https://www.iso.org/obp/ui/#iso:std:iso:4618:ed-2:v1:en%0D>
14. InternationalOrganizationforStandardization. ISO 11507:2007 Paints and varnishes — Exposure of coatings to artificial weathering — Exposure to fluorescent UV lamps and water [Internet]. 2007. Available from: <https://www.iso.org/standard/37489.html>
15. Appleman B. Predicting exterior performance of organic coatings from salt spray: Two types of errors. *J Prot Coatings Linings.* 1992;135.
16. Skilbred AWB, Arntzen OA, Aamodt T, Løken A. Field Testing - on the Correlation Between Accelerated Laboratory Tests and Field Testing. *CORROSION 2019.* 2019. p. NACE-2019-13154.
17. Dean Trombetta. Outdoor Weathering Rack [Internet]. 2016 [cited 2020 Apr 20]. Available from: <https://weekypellet.com/2016/07/08/plastic-weathering-demysitfied/https://weekypellet.com/2016/07/08/plastic-weathering-demysitfied/>
18. Q-Lab. Q-FOG SSP & CCT Cyclic Corrosion Testers [Internet]. 2020 [cited 2020 Apr 20]. Available from: <https://www.q-lab.com/en-gb/products/q-fog-cyclic-corrosion-chamber/q-fog-ssp-cct>

19. Ryan PA, Wolstenholme RP. Durability, maintenance and lifespan. In: DURABILITY OF CLADDING A STATE OF THE ART REPORT. 1994. p. 35–72.
20. Lebozec N, Thierry D. Corrosion Performance of coil coated steel : model buildings vs ECCA panels. In: 4th International Symposium on Coil Coated Steel. Paris; 2016. p. 1–23.
21. Prosek T, Nazarov A, Thierry D. Role of steel and zinc coating thickness in cut edge corrosion of coil coated materials in atmospheric weathering conditions; Part 2: Field data and model. Prog Org Coatings [Internet]. 2016;101:45–50. Available from: <http://dx.doi.org/10.1016/j.porgcoat.2016.06.019>
22. Prieto AJ, Silva A. Service life prediction and environmental exposure conditions of timber claddings in South Chile. Build Res Inf [Internet]. 2020;48(2):191–206. Available from: <https://doi.org/10.1080/09613218.2019.1631143>
23. Silva A, Prieto AJ. Probabilistic Approach to the Service Life Prediction of Timber Claddings. Curr Top Trends Durab Build Mater Components - Proc 15th Int Conf Durab Build Mater Components, DBMC 2020. 2020;1925–32.
24. Barreлас J, Dias IS, Silva A, de Brito J, Flores-Colen I, Tadeu A. Impact of environmental exposure on the service life of façade claddings—A statistical analysis. Buildings. 2021;11(12):1–20.
25. Ferreira C, Barreлас J, Silva A, de Brito J, Dias IS, Flores-Colen I. Impact of environmental exposure conditions on the maintenance of facades' claddings. Buildings. 2021;11(4):1–31.
26. Prieto AJ, Silva A, de Brito J, Macias-Bernal JM. Serviceability of facade claddings. Build Res Inf [Internet]. 2018;46(2):179–90. Available from: <https://doi.org/10.1080/09613218.2016.1264808>
27. Ryan PA, Wolstenholme RP, Howell DM. Durability of Cladding, A State of the Art Report. 1994.
28. Adafruit. Adafruit BME680 - Temperature, Humidity, Pressure and Gas Sensor [Internet]. [cited 2020 Apr 7]. Available from: <https://www.adafruit.com/product/3660>
29. Texas Instruments. Infrared Thermopile Sensor in Chip-Scale Package. 2012;(December). Available from: <http://www.ti.com/product/TMP006/description>
30. vishay. VEML6075 Vishay Semiconductors Not for New Designs UVA and UVB Light Sensor with I 2 C Interface. 2019;1–11. Available from: www.vishay.com/doc?91000
31. Shinyei Corporation. Particle Sensor Model PPD42NS. 2010;2010:3. Available from: http://www.seeedstudio.com/wiki/images/4/4c/Grove_-_Dust_sensor.pdf
32. Bunaciu AA, Udriștioiu E gabriela, Aboul-Enein HY. X-Ray Diffraction: Instrumentation and Applications. Crit Rev Anal Chem. 2015;45(4):289–99.
33. EngineeringToolBox. Air - Density, Specific Weight and Thermal Expansion Coefficient vs. Temperature and Pressure. [Internet]. 2003 [cited 2022 Jun 21]. Available from: https://www.engineeringtoolbox.com/air-density-specific-weight-d_600.html
34. EngineeringToolBox. Drag Coefficient. [Internet]. 2004 [cited 2022 Jun 21]. Available from: https://www.engineeringtoolbox.com/drag-coefficient-d_627.html
35. Kubilay A, Derome D, Blocken B, Carmeliet J. CFD simulation and validation of

- wind-driven rain on a building facade with an Eulerian multiphase model. *Build Environ* [Internet]. 2013;61:69–81. Available from: <http://dx.doi.org/10.1016/j.buildenv.2012.12.005>
36. Grøntoft T. Estimation of damage cost to building facades per kilo emission of air pollution in Norway. *Atmosphere (Basel)*. 2020;11(7).
 37. Sousa V, Almeida N, Meireles I, De Brito J. Anomalies in wall renders: Overview of the main causes of degradation. *Int J Archit Herit*. 2011;5(2):198–218.
 38. Deflorian F, Rossi S, Fedel M. Organic coatings degradation: Comparison between natural and artificial weathering. *Corros Sci* [Internet]. 2008;50(8):2360–6. Available from: <http://dx.doi.org/10.1016/j.corsci.2008.06.009>
 39. BSI. International Standard: BS EN 13523 - Coil coated metals. Test methods [Internet]. Available from: <https://www.bsigroup.com/en-GB/>
 40. International Organization for Standardization. ISO 2810:202 Paints and varnishes — Natural weathering of coatings — Exposure and assessment [Internet]. 2020. Available from: <https://www.iso.org/standard/76042.html>

Chapter 10: Wetness Sensing

10.1 Introduction

In the previous chapter, natural washing was identified as a key metric which can indicate the likely severity of OCS cladding degradation. While it has been shown that sensing the direct degradation of cladding is a complex problem, the sensing of natural washing is a far simpler affair. Hence, due to the strong correlation identified between washing and degradation, it was thought that wetness sensors could be used as identifiers of areas of concern and ‘second order’ degradation sensors. In this chapter, current wetness sensors are briefly examined in terms of their applicability and ultimately a sensor, which aims to be more representative, is proposed, produced, and tested.

10.2 Current Wetness Sensing

A number of wetness sensors exist commercially both at a hobbyist and professional measurement level and examples of four such systems are given in Table 10.1. The majority of these systems are based on a PCB sensing element and utilise either capacitive or resistive measurements. However, a large quantity of these sensors are designed to specifically measure leaf wetness, atmospheric time of wetness, or soil moisture content. Hence, despite their widespread availability they often suffer from certain problems that reduce their effectiveness for use monitoring the wetness, and therefore washing, of cladding panels.

Table 10.1. Examples of four commercially available wetness sensors

No.	Sensor	Manufacturer	Price	Measurement
1	Leaf Wetness 6420 [1]	DAVIS	£100-150	Resistive
2	Industrial Leaf Wetness [2]	SEED	£80-120	Capacitive
3	Raindrop Sensor Module	Numerous	£2-10	Resistive
4	Capacitive Soil Moisture	Numerous	£4-15	Capacitive

One of these issues is the difficulty of flush mounting commercially available wetness sensors. They often are or contain thick components meaning water cannot easily run onto the sensor from above limiting the representability of the results. Examples of this is shown in Figure 10.1.

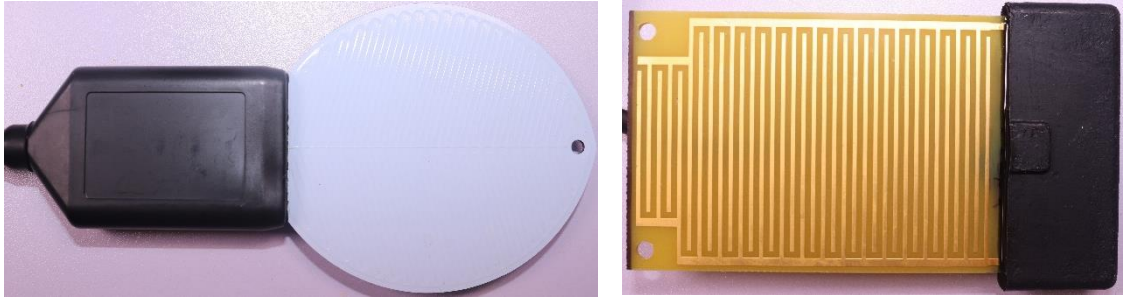


Figure 10.1. Examples of wetness sensors with elements that prevent flush mounting and wetting from water run off

Furthermore, resistive moisture sensors require an exposed set of electrodes which do often corrode overtime limiting the lifespan and accuracy of monitoring [3]. An example of the extent of corrosion that can occur is shown in Figure 10.2. The corrosion of the tracks reduces the accuracy of results and changes the surface properties, significantly changing the wetting characteristics.

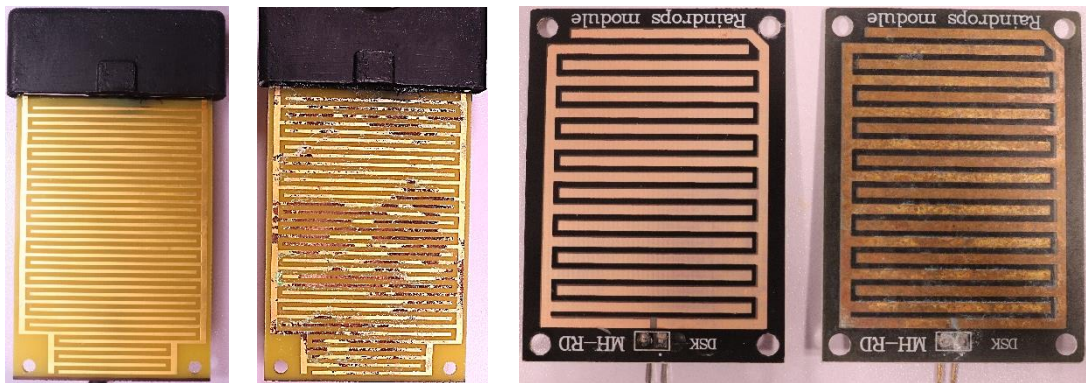


Figure 10.2. Corrosion of resistive sensors after just 6 months of exposure

Finally, the materials that make up the sensing element do not always accurately represent the wetting characteristics of the paint systems and the wetting properties of the element can often change significantly as a result of exposure. This is shown in Figure 10.3. Using a sensor overcoated with the actual paint system would produce far more accurate wetting properties both initially and throughout the lifetime of the moisture sensor. This approach is often used for leaf wetness monitoring in which sensors are produced with a latex covering which better replicates leaf wetting characteristics [4]. However this is not common practising in the corrosion community [5].

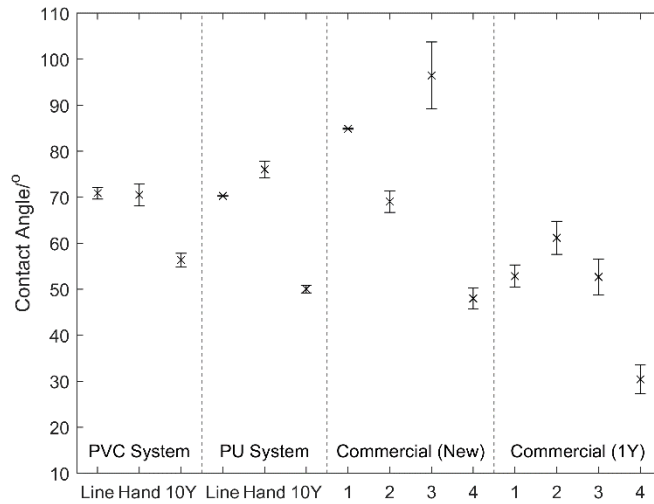


Figure 10.3. Contact angle measurements of two commercial coating systems and a number of commercial sensors

10.3 Wetness Sensor Design

10.3.1 Concept

It is well documented that a capacitive sensor is far superior in terms of long-term lifespan when compared to the resistive style sensors [3,6]. Therefore, the concept was to create a capacitive track system that could then be overcoated by the paint system to ensure representative wetting characteristics. Initially a system similar to that introduced in Chapter 5 was considered, Figure 10.4, however ultimately this would suffer from the durability issues shown to arise from the introduction of the embedded electronic paint.

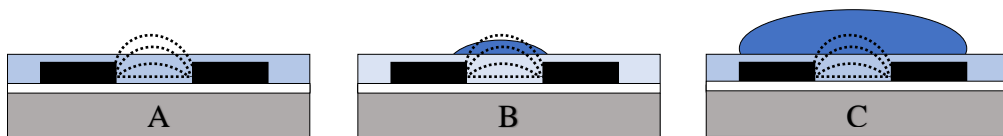


Figure 10.4. An embedded wetness sensor (A) for detecting moisture levels (B & C)

As this sensor only aims to detect moisture presence then different substrates could be used. Therefore, it allows the use of PCBs, which can be designed with intricate tracks more easily, and are less likely to affect the durability of the paint system. The concept of capacitive detection, Figure 10.5, is identical but this approach may be, easier to produce samples and avoid the issues of embedding electrically conductive paint in the system. Overcoating of PCBs with organic coatings has been previously

presented for degradation monitoring with no mention of significant compatibility issues [7,8].

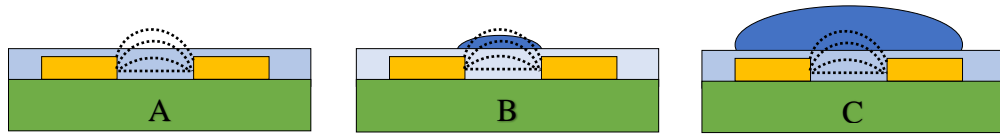


Figure 10.5. A PCB based wetness sensor (A) for detecting moisture levels (B & C)

There were several reasons for taking this approach rather than simply overcoating an existing wetness sensor with the coating system. Firstly, it allows control over the sensor size, thickness and design which can then be optimised for the application and allow flusher mounting. Secondly the existing wetness sensors are precoated with a protective layer which may not bond sufficiently to the coating system. Also due to this pre-existing coating, the sensitivity of the sensor would be reduced as the overall coating system would be thicker.

10.3.2 PCB Designs

Two designs, Figure 10.6 (A and B), were created using EAGLE PCB design software and were composed of a series of interlocking PCB traces. These were produced by a third party PCB manufacturer JLC PCB. While the designs were in no way optimised it was considered suitable for testing the concept. Design A used less, but thicker, overlapping traces than design B as it was thought that while an increased number of smaller tracks would give improved resolution, this would produce a rougher surface for coating application. Design A was produced on both a 0.6mm FR-4 substrate (1) and a 1mm aluminium substrate (1a) whereas design B was produced on a 0.6mm FR-4 (2). This was to investigate if the aluminium substrate provided any benefits over the FR-4. Both these substrates were significantly thinner than the commercially available wetness sensors which ranged from 2-7mm.

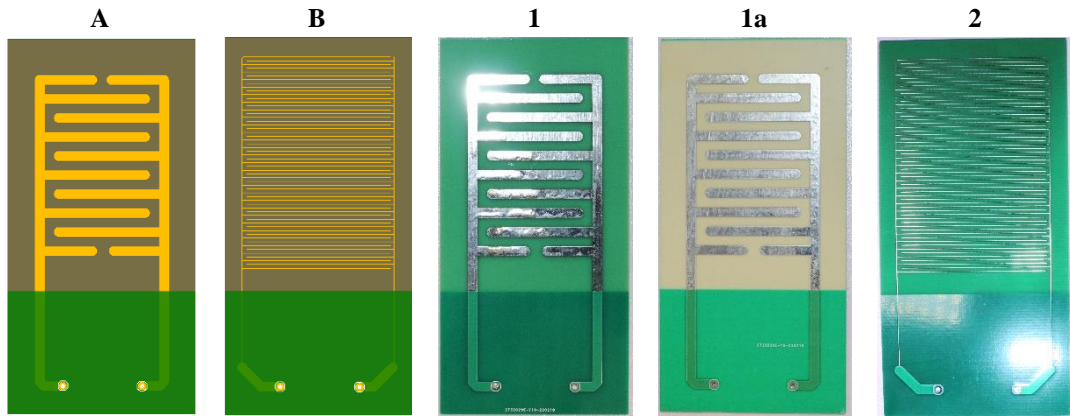


Figure 10.6. The designed PCB boards including designs (A/B) and produced boards on FR-4 (1/2) and aluminium (1a)

10.4 Paint Compatibility

While PCBs have been previously overcoated with organic coatings successfully the quality of coating produced is often not well examined. Hence, studies were conducted to assess the properties of two of the common OCS coatings applied to PCBs.

10.4.1 Three-layer PU system

Generally, the three-layer PU system appeared to coat well over the PCB board with no obvious de-wetting, blistering or delamination during the application or curing process of any of the three layers. The appearance at each stage of coating application is shown for sample 1 in Figure 10.7. From a visual inspection, most of the resulting samples appeared similar to the hand coated steel samples produced previously giving confidence that the system could be applied to this substrate. The exception to this was sample 2 where it was observed that there was a significant amount of blistering around the smaller tracks on curing of the primer, Figure 10.8, perhaps due to greater air entrapment or poorer wetting of the very thin trace. These blisters affected the appearance of the final sample. Due to the thin nature of the PU system, even though the protruding traces were fully coated, they were not fully embedded into the coating system and still visible as topographic features.

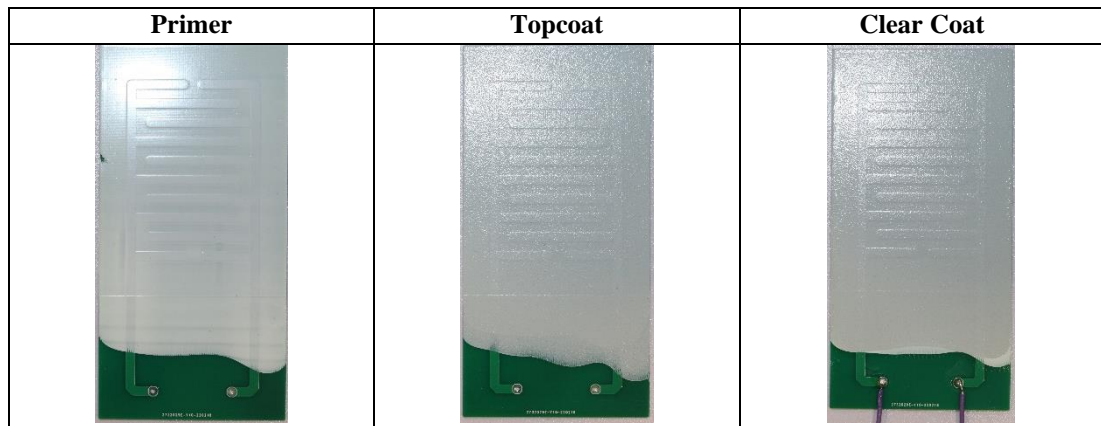


Figure 10.7. Appearance of sample 1 after application and curing of each PU coating layer



Figure 10.8. Appearance of the traces after primer application and cure for samples 1 (top) and 2 (bottom).

On examination of the samples under a microscope, Figure 10.9, it appeared that they had a similar surface appearance at a microscopic level to the hand samples. The traces were easily identifiable as raised areas however the boundaries appeared to be well coated and there were no obvious defects present. The coating applied over the traces did not differ considerable to that of the bulk and the previously produced hand samples and hence it was concluded that the overall compatibility of the PCB's was good.

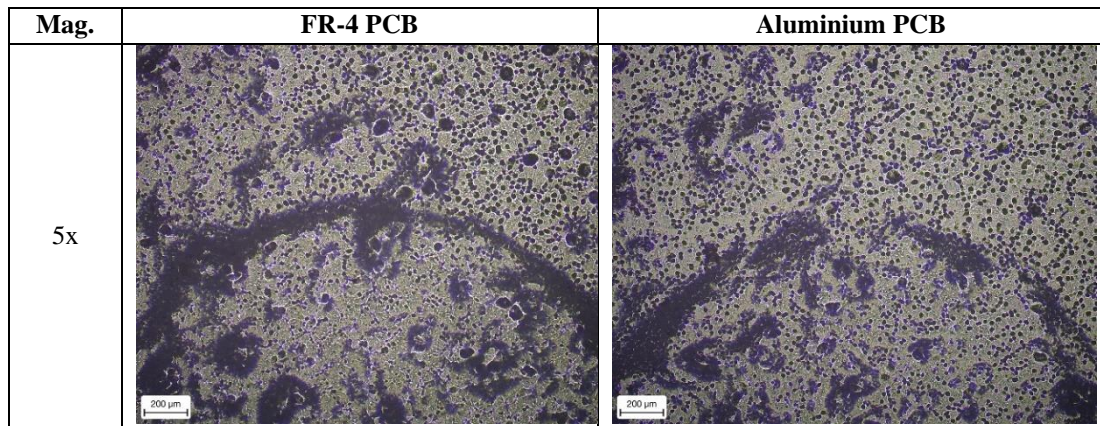


Figure 10.9. Appearance of the PU PCB samples under microscope focussing on the end of a trace

When comparing the properties of the PU coated PCB samples to that of the line sample, shown in Table 10.2, it was observed that similar properties were measured. All the samples had similar gloss values within the specification of the system and samples 1 and 1a showed very little colour difference to the line sample. Sample 2 did show a noticeable colour difference to the line sample although this was attributed to a slight over-curing of this sample leading to yellowing of the paint as shown by shift in b^* value towards yellow. The scratch resistance was reduced compared to the line sample however the adhesion of the coatings were measured to be comparable. It was thought that the reduced scratch resistance was due to the topography of the sample with the traces as failure occurred when the scribe hit the raised section.

Table 10.2. Comparison of the PCB PU coated samples to the line sample

Property	Line Sample	PCB 1 Sample	PCB 1a Sample	PCB 2 Sample
Colour (L^*)	77.8 ± 0.3	77.7 ± 0.1	77.3 ± 0.1	77.3 ± 0.2
Colour (a^*)	-1.7 ± 0.0	-1.8 ± 0.0	-1.7 ± 0.0	-1.9 ± 0.1
Colour (b^*)	-2.62 ± 0.0	-1.9 ± 0.2	-2.6 ± 0.0	-1.2 ± 0.2
Colour difference (ΔE^*_{ab})	N/A	0.8	0.6	1.6
Scratch Resistance	3200g	2350g	2800g	2300g
Gloss @ 60°	$28.8 \pm 0.5 \%$	23.2 ± 0.6	29.7 ± 3	22.8 ± 0.6
Water Contact Angle	$70.3 \pm 0.1^\circ$	$76.8 \pm 1.8^\circ$	$71.3 \pm 0.5^\circ$	$70.6 \pm 1.1^\circ$
Adhesion Cross Hatch (T)	100%	100%	100%	100%

10.4.2 Two-layer PVC system

The PVC coatings, similarly, did not provide any particularly serious issues of compatibility when coating and curing on the PCBs. The thinner primer layer did tend to pool slightly more around the raised traces however this did not appear to affect the final coated product. On visual inspection of the sample there was no obvious repeating defects and generally the appearance matched that of previous

hand coated samples. Due to the thickness of the topcoat the traces were far more embedded in the coating system and only just, or not at all, visible or able to be felt. Again, sample 2 showed poorer curing and the emergence of some blistered regions in the primer layer surrounding the thin traces, thought to be due to the inability to fully wet the whole of the thin track. However, this was to a lesser extent than the PU samples. The appearance of the samples during each coating process is shown in Figure 10.10 for sample 1.

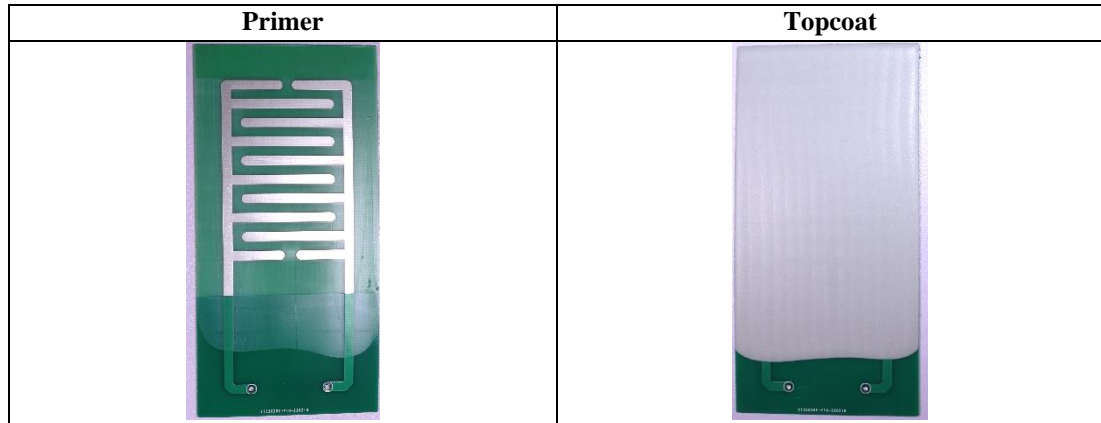


Figure 10.10. Appearance of sample 1 during the PVC coating process

The appearance of the coated samples under a microscope is shown in Figure 10.11. As before, due to the increased thickness of the PVC topcoat it is difficult to make out the traces and the system has been full encapsulated. The overall appearance of the FR-4 sample was very similar to the previously produced hand sample however the aluminium PCB did appear slightly more mottled. This is perhaps due to slight over or under curing, while the substrate temperature reached was identical to that in the FR-4 and steel samples perhaps the high heat transfer qualities of aluminium have somewhat affected the cure.

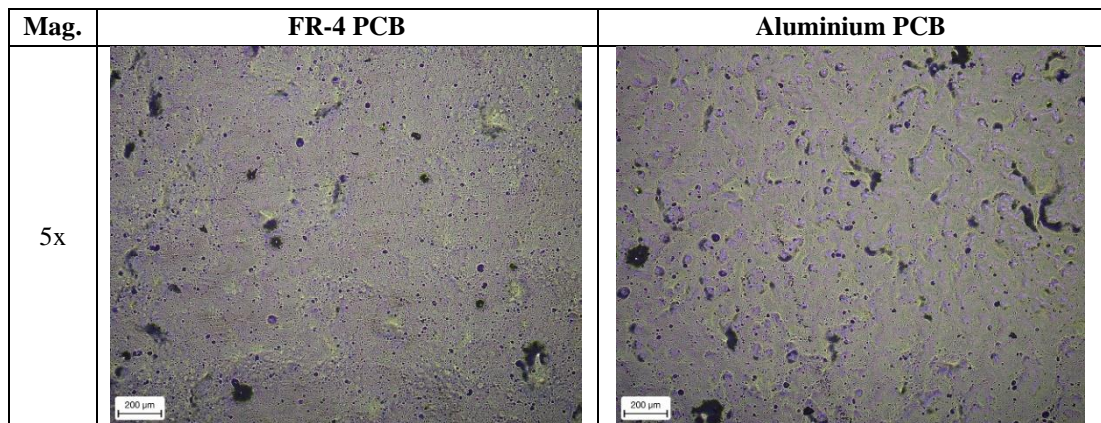


Figure 10.11. Appearance of the PVC PCB samples under microscope focussing on the end of a trace

A comparison of the coating properties of the three PCB samples and the line sample is given in Table 10.3. All samples were a very similar colour with similar levels of scratch resistance and adhesion. While gloss did vary it always remained within the specification. Therefore, it was considered that a representative coating with similar properties was produced.

Table 10.3. Comparison of the PCB PVC coated samples to the line sample

Property	Line Sample	PCB 1 Sample	PCB 1a Sample	PCB 2 Sample
Colour (L*)	72.8 ± 0.1	73.0 ± 0.5	72.9 ± 0.1	72.9 ± 0.1
Colour (a*)	-1.0 ± 0.0	-1.1 ± 0.0	-1.1 ± 0.0	-1.1 ± 0.0
Colour (b*)	3.8 ± 0.0	3.4 ± 0.1	3.3 ± 0.1	3.4 ± 0.0
Colour difference (ΔE^*_{ab})	N/A	0.2	0.2	0.1
Scratch Resistance	>4200g	>4200g	>4200g	>4200g
Gloss @ 60°	31.7 ± 0.2 %	37.8 ± 1.6 %	49.2 ± 3.8 %	26.3 ± 7.2 %
Water Contact Angle	70.9 ± 1.3 °	73.4 ± 1.5 °	70.1 ± 1.4 °	65.7 ± 3.3 °
Adhesion Cross Hatch (T)	100%	100%	100%	100%

10.4.3 Durability assessment

To determine the durability of the PCB coated wetness sensor each sensor was placed in an ASTM B117 salt spray cabinet for 5 weeks. After 5 weeks the samples were removed, photographed, Figure 10.12, and examined as to their condition. It was found that minimal evidence of degradation was observed on samples 1 and 1a for both coating systems. Sample 2 showed blistering around some of the tracks, though to be as a result of the small blister defects in these regions that were difficult to avoid in the production process.







System	PCB 1 Sample	PCB 1a Sample	PCB 2 Sample
PU			
System	PCB 1 Sample	PCB 1a Sample	PCB 2 Sample
PVC			

Figure 10.12. Appearance of the samples after the salt spray test

10.4.4 Compatibility Conclusions

Generally, the coating of PCB substrates appears suitable, and coatings are produced with similar mechanical and aesthetic qualities when compared to line produced samples. The wetting properties, as displayed by the contact angle, of the completed wetness sensor is also far similar to that of the line samples when compared to the commercial sensors, Figure 10.13. This, combined with a decreased thickness of sensor, is thought to increase the accuracy of the wetness measurement.

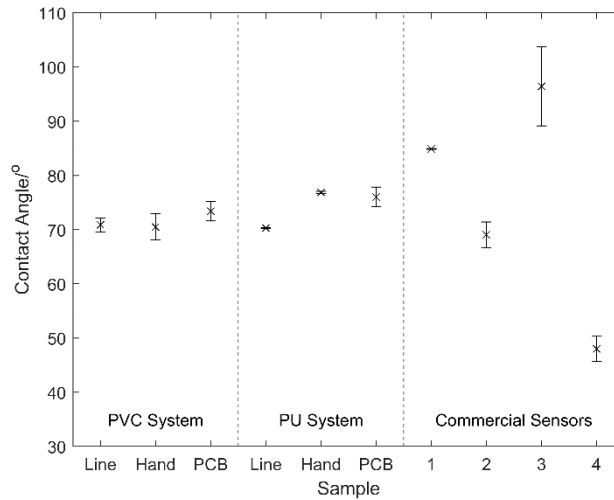


Figure 10.13. Comparison of the water contact angle of the produced wetness sensor and commercial sensors to line and hand produced samples

It does appear, however, that using thinner traces on the PCB can lead to wetting issues leading to the production of coatings with many small defects which reduce durability. This effect is minimised when using larger, but still relatively thin (1mm) traces. Therefore, unless thinner tracks are improved from a measurement standpoint, the recommendation would be to create designs with larger tracks.

10.5 Initial proof of concept

To test the moisture sensing concept the PCB sensors were first coated with epoxy, Figure 10.14, and then de-ionised water was applied in a controlled manner to the sensor while the capacitance was measured and recorded.

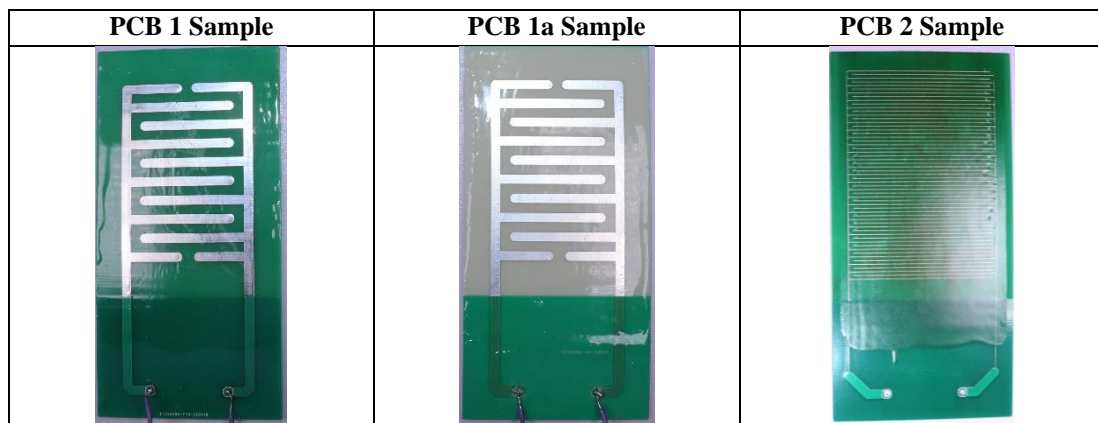


Figure 10.14. The epoxy coated wetness sensors

Thirteen different test conditions of varying moisture presence were used to measure the effect of water concentration on the capacitance, and these are shown in Figure 10.15. The general moisture trend was a gradual increase from dry to almost fully

wet and then a more rapid decrease back to dry again. While efforts were made to maintain consistency across all the tested samples it was likely that there was some minor variation in drop size and location.

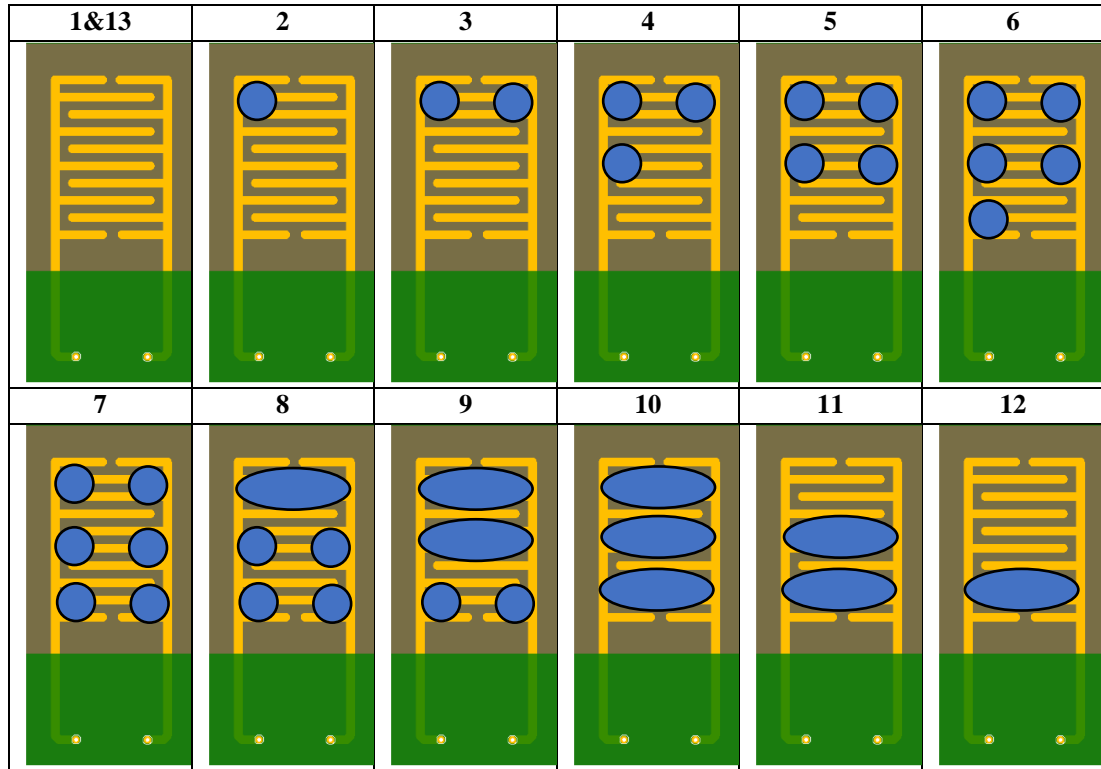


Figure 10.15. Each test condition for the moisture test, the blue regions indicate de-ionised water was placed in these regions

The measured capacitance of the three PCB sensors during the test are shown in Figure 10.16. The raw data and the average value for each test condition are given. All three sensors showed an increase in capacitance with the addition of moisture and the degree of the increase was related to the quantity of water added for each condition. When water was fully removed the measured capacitance dropped to a similar value to the pre-test value. The slight increase shown on condition 13 compared to 1 was thought to be due to small amounts of moisture remaining even once the bulk of the water was removed. Interestingly the PCB 2 sample did not show a vastly improved sensitivity over the other two samples despite its design however it was thought that this may be down to variations in the coating thickness applied to each sample. If the PCB 2 sample had a slightly thicker coating it would reduce the sensitivity perhaps cancelling out the design improvement.

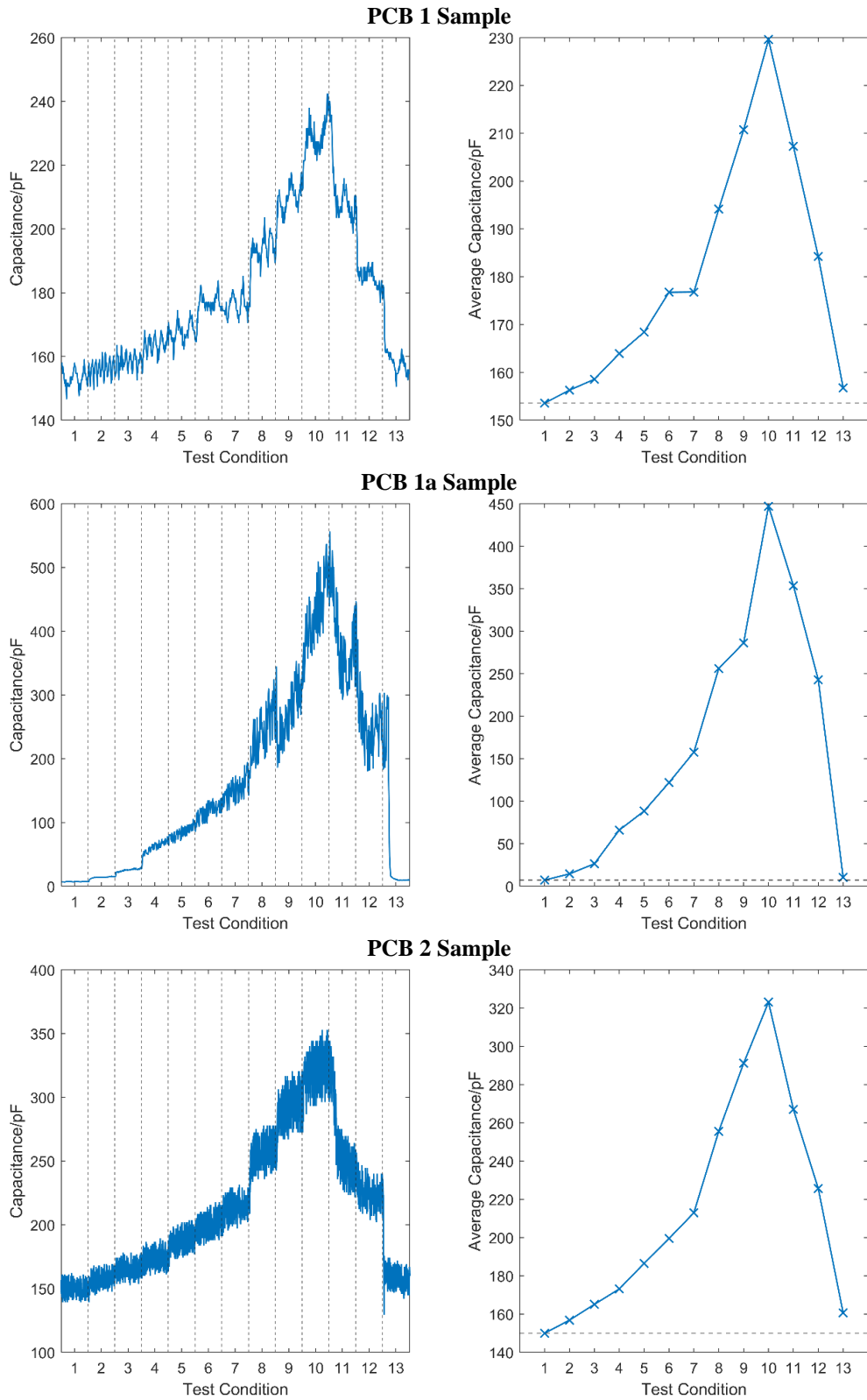


Figure 10.16. Measured capacitance (left) and average values (right) for each condition during the epoxy coated PCB moisture test

10.6 Testing of actual paint system

Given the promising results shown by the epoxy coated sensors the same test was carried out on the industrially coated sensors. The results are given in Figure 10.17. It was observed that all three sensors responded as would be expected to the increase in moisture present. As has been noted throughout this chapter, due to the increased thickness of the PVC system there was a far reduced sensitivity compared to the PU system. This led to very small changes in capacitance between test conditions 1-2-3-4-5-6-7 for samples 1 and 1a and although the sensitivity was improved in sample 2 it was still limited. The PU sample 2 did, however, show improved sensitivity for small changes in moisture presence. All samples could detect well the larger changes in moisture presence and had a very clear difference between the measured capacitance of the dry and fully wet conditions. This suggests that these PCB sensors could accurately be used as quantitative or semi-quantitative moisture sensors.

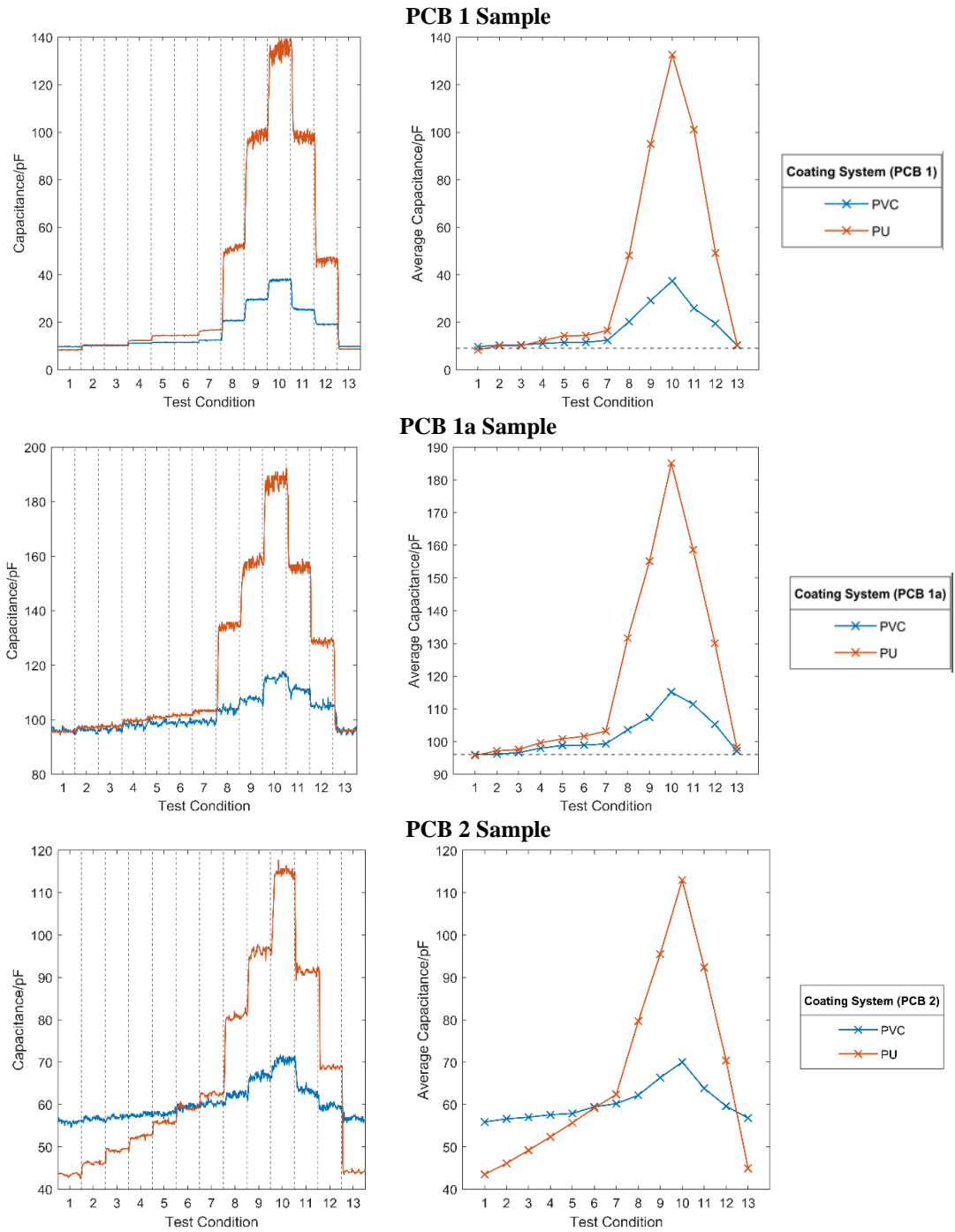


Figure 10.17. Measured capacitance of the coated PCB sensors during the moisture test (left) and the average value for each condition (right)

10.7 Conclusions

Current solutions for measuring wetness and time of wetness have limitations when used for determining the natural washing of OCS cladding. It has been shown, however, that measurements can be made far more representative by producing simple PCB based wetness sensors which are overcoated with the coating system of interest. PCBs both composed of aluminium and FR-4 were shown to survive the

coating process with little change to their properties and coating systems with similar properties to line coated steel substrate were formed. All the produced sensors were able to detect changes in moisture levels present on the surface of the sample. It was also shown that, by decreasing the distance between PCB traces and increasing the number of traces, smaller droplets of water could be detected, and sensitivity was increased. However, as the PCB trace size decreased full wetting of the trace became problematic leading to increase prevalence of micropores surrounding traces. Hence, further design work should consider the balance between sensitivity and wettability when producing the trace layout of the capacitive sensor. As a concept however, this seems viable for the monitoring of natural washing and therefore an indicator of likely deposit build-up and ultimately expected degradation rate.

10.8 References

1. Davis_Instruments. Leaf Wetness Sensor Data Sheet [Internet]. 2011. p. 1. Available from: https://cdn.shopify.com/s/files/1/0515/5992/3873/files/6420_SS.pdf
2. SEED. Leaf Wetness and Temperature Sensor User Guide [Internet]. 2020. p. 1–18. Available from: <https://files.seeedstudio.com/products/314990737/doc/LeafWetnessandTemperatureSensor-UserGuide.pdf>
3. Mukhlisin M, Yunanto B, Suharjono A, Martono M, Apriantoro R, Kusumawardani R. Monitoring rainfall intensity and moisture water content using soil column experiment. *IOP Conf Ser Mater Sci Eng.* 2021;1108(1):012007.
4. Sentelhas PC, Monteiro JEBA, Gillespie TJ. Electronic leaf wetness duration sensor: Why it should be painted. *Int J Biometeorol.* 2004;48(4):202–5.
5. Schindelholz E, Kelly RG, Cole IS, Ganther WD, Muster TH. Comparability and accuracy of time of wetness sensing methods relevant for atmospheric corrosion. *Corros Sci* [Internet]. 2013;67:233–41. Available from: <http://dx.doi.org/10.1016/j.corsci.2012.10.026>
6. Duric J, Matijevic M, Mahmutovic A, Ivankic M. Monitoring of Plant Growth Using Soil Moisture and Temperature Sensor and Camera. 2022 45th Jubil Int Conv Information, Commun Electron Technol MIPRO 2022 - Proc. 2022;835–40.
7. Zajec B, Bajt Leban M, Lenart S, Gavin K, Legat A. Electrochemical impedance and electrical resistance sensors for the evaluation of anticorrosive coating degradation. *Corros Rev.* 2017;35(2):65–74.
8. Diler E, Lédan F, LeBozec N, Thierry D. Real-time monitoring of the degradation of metallic and organic coatings using electrical resistance sensors. *Mater Corros.* 2017;68(12):1365–76.

Summary, Conclusions and Recommendations

Conclusions

This work has examined a number of different techniques and methods for the monitoring the performance and degradation of OCS cladding. The following conclusions, outlined below, were reached.

A number of techniques exist for corrosion and/or coating monitoring however commercially available deployable systems are limited to those for manually operated NDT or specific sector-based applications such as pipeline inspection. Emerging technology in embedded and wireless sensing were highlighted as key areas of interest as was the increased use of computer modelling and simulation for determining corrosion.

Initial investigation of techniques determined the complexity of the research task and identified that the solution would have to be static. Embedded sensors were shown to only be feasible on laboratory produced samples due to the high line speeds of coating lines, and the reluctance to, and complication of, changing manufacturing lines and difficulty connecting the sensor. Totally embedded wireless sensors were considered but, due to thickness constraints and complications arising from communication methods, these were also not considered a practical approach. The use of any realistic embedded technology was found to be limited to passive printed embedded element connected to by wires.

Two embedded sensing concepts were developed and tested using industrial coating systems. These aimed to detect cut edge corrosion and coating property changes respectively and were constructed using both, water-based, carbon and, polyurethane-based, silver electrical paints. Compatibility of the electrical paint layer in the industrial paint system was highlighted as a key issue with poor adhesion achieved by the carbon paint. While the silver paint seemed far more compatible, durability of the system was noted to be decreased as a result of embedding. It was clear that investigation into different electrical paints was required to ensure a

representative sample. Of the sensing concepts produced the cut edge sensor, while simple in nature, proved promising at providing an indication of the rate and severity of defect spread and its performance was only limited by paint compatibility issues. The embedded capacitive coating sensor was less effective; this was thought to be due to competing factors influencing the measurement simultaneously and a diminished sensitivity. While large changes in properties were detectable it was not clear that gradual deterioration would be adequately distinguishable from noise.

Detection of corrosion via increased communication of an RFID tag shielded by the sample undergoing degradation was considered next. It was shown that detection of large artificial defects and considerable red rust corrosion was possible. Detection of degradation of a modern OCS sample was less effective with little to no trend of increased signal with degradation up to the emergence of red rust. Sensitivity was thought to be inherently limited by the technique but also hampered by the formation of water filled blisters which were thought to negate the decrease in blocking ability due to corrosion.

A novel dielectric monitoring method was then proposed, designed, optimised via software modelling, produced and tested. This technique was attractive due to the semi-remote nature of the measurement and the expected ability to detect early-stage changes in coating properties preceding failure. Simulations showed that the expected change in dielectric properties from water ingress, defect generation and UV degradation produced a noticeable shift in the resonant frequency of the antenna. For thin coating systems it was discovered that determination of the resonant frequency was more difficult due to decreased resonance. This issue was overcome by using a thin substrate layer to increase the overall dielectric layer thickness and increase resonance. However, the use of such a substrate was found to negatively affect sensitivity to changes in the dielectric properties of the coating system. The antenna system was tested on two common coating systems and found to detect changes caused by both salt spray exposure (water ingress) and chemical attack (polymer degradation).

Adaptations to magnetic flux leakage, a common non-destructive corrosion testing method were trialled in an attempt to produce a static array-based monitoring method. Three iterations of device were used to test a range of small, inexpensive

magnetic field sensors that would be crucial to allow widescale array deployment. It was shown that detection of changes in the presence of metal due to removal of material or significant, red rust, corrosion were easily detectable. However, the sensitivity was insufficient to detect corrosion of modern OCS samples due to their inherent increased corrosion protection and durability. Ultimately it was concluded that damage would have to be so significant for detection that it was unlikely to realistically occur during the expected lifespan of the cladding.

It was evident that, these monitoring techniques showed promise but required significant additional work or lacked sensitivity, accuracy, or repeatability. Hence a different approach was considered and investigations into a real-life building were carried out to aim to better understand degradation rates and the environmental conditions affecting them. It was found that a combination of the build-up of aggressive natural fouling deposits and higher humidity levels led to significantly increased degradation in sheltered regions of the building. It was concluded that, in this case, the salty and hygroscopic nature of the deposits, formed, and maintained, a corrosive aqueous environment. In comparison washed regions, while exposed to greater exposure to rain and sun, were periodically cleaned and dried. This work highlighted a limitation of current outdoor exposure techniques which often use small, or no sheltering regions. Using this experimental information rain-washing computer simulations of the building were then produced which showed that it was possible to directly estimate the respective level of degradation faced by OCS on a specific building from the modelled rain impact density.

As a result of these field measurements, computer modelling and simulation work, rain-washing was identified as a key parameter of interest. Although the simulation studies allowed an estimation of un-washed regions the focus returned for live monitoring to the more easily measurable parameter of wetness. It was shown that there are limitations to using currently existing wetness sensors and that custom PCB coated variants can provide more realistic wetting parameters and better mounting options. While further optimisation of the PCB design would be possible, the present concept was shown to accurately measure wetness and could be easily and cheaply affixed post-construction to buildings to support computer simulation and modelling.

Recommendations for further work

Several recommendations for further work have been made in earlier chapters, which are summarized below:

Of all the techniques considered, the cut edge embedded sensor and the computer simulative work are considered the most promising for further exploration.

As mentioned previously, for the cut edge corrosion sensor to be advanced, further work is required to determine an electrical paint system that can be embedded with no effect on system durability. Some consideration must also be given to the device monitoring the sensor, encapsulation of the connecting wires, and long-term stability testing.

Correlation of simulated rainfall to OCS cladding degradation has only been carried out on one test building. To fully validate the sensor concept, further work is required, looking at a range of buildings and locations. Such studies are also required to determine if the effect of fouling deposits is increased or decreased in different locations. It may well be the case that locations inland generate less aggressive fouling deposits and hence there is a lesser correlation between degradation severity and natural washing. This would have to be determined experimentally. Depending on the results, further optimisation of the modelling methods may be warranted, and provide a driver for further work on representative wetness sensors such as those presented in Chapter 10.

While the other sensing techniques examined have been deemed less promising, some further work is still recommended to fully understand the capability of each technique.

In particular for the RFID blocking technique, it is possible that other RFID tags or antenna measuring systems may provide increased sensitivity. One area that should be considered is the use of active tags which have much improved range. While their use for the monitoring of OCS directly may not be suitable, it is possible that this method could be used to measure the rate of corrosion of a more corrodible layer. With experimentation it may be possible to correlate the condition of the layer to that of the OCS.

Further investigation of the chipless RF antenna for dielectric sensing is also recommended, particularly study of the rate of change in resonant frequency with increased artificial and natural weathering. A study of the effect of UV exposure is also recommended as this was not possible within the timeframe of the present project. Finally, while deployment of the chipless antenna method for OCS monitoring is complex it may have other benefits as a non-destructive technique in the coatings industry. For example, it could potentially be examined as a method for determining level of cure.

Appendix

A. Development of a localised condition sensor

A.I Requirement of the device

As covered in the literature review coating degradation and corrosion are complex processes which are affected by a large number of environmental parameters. To establish how these parameters vary across a building a device was required to measure as many of these factors as accurately as possible. Such a system would also be required to have certain features to facilitate use and to simplify this process the required specification of hypothetical best-case system, shown in Table A.I, was drawn up.

Table A.I. Design requirements of the system

Requirements	Justification
Easy secure mounting to building facades	The system must allow non-intrusive attachment to a variety of building envelope geometries to avoid damaging panels and allow all area monitoring. Mounting must be secure enough to ensure safety.
Ability to change components easily if required	In the case that components become uncalibrated or less accurate with time these can be changed without affecting the overall system to lower costs and decrease downtime.
Long term weather resistance	The system will be exposed outdoors for long durations and hence will require considerable resistance to water ingress as well as temperatures ranging from sub-zero to 40°C+.
Data acquisition rate of several points per hour	A datalogging style of results is required to have meaningful long-term data acquisition.
Long term battery life	Mains power will not always be easily available on building exteriors and hence the system should have a battery which is suitable for long term measurements.
Live data monitoring and acquisition	Live data allows instantaneous analysis and would allow better monitoring of the system effectiveness.
Easy interface to commercial sensors	Commercially available sensors for measuring certain parameters will be incorporated into the system.
Compact size	The requirement to be placed in a variety of building locations means the system should be smaller than A4

Measurements	Justification and Requirements
Ambient temperature	A number of temperature driven failure methods were mentioned previously. Higher temperature often leads to accelerated rates of reactions however can allow better drying.
Ambient humidity	Humidity often accelerates corrosion rate and leads to greater prevalence of moisture to produce moisture driven coating failure methods.
Panel temperature	The temperature of the panel will likely vary from ambient and hence is important to consider when determining temperature effects.
UV intensity	UV is known to attack organic coatings leading to colour fade and other more damaging effects.

Time/cycle of wetness	Moisture presence can cause coating failure via a number of methods and facilitates aqueous corrosion. Cyclic wetting however can reduce contaminant build up protecting the coating.
Contaminant build up	Soiling of the coating surface can produce differential aeration cells and may lead to aggressive compounds being held close to the coating.
Contaminant composition	Some contaminants are far more damaging than others for example the presence of acidic or saline compounds.
Aqueous conditions	The conditions present, such as concentration of salts or other dissolved compounds, can affect the rate of coating degradation and failure.
Gaseous conditions	Different concentrations of local gases, for example oxygen, can cause greater likelihood of some failure modes.
Local pH	Both acidic and alkaline conditions attack coatings and can be important in establishing corrosion.
Windspeed	Erosion of coatings can occur by wind driven particles
Biological build up	The build-up of biological matter can directly damage coatings or can cause products that lead to degradation. Ideally measurement of the different rate of build-up of contaminant in both area and mass would be possible.

A.II Prototype 1

Some of the key features and parameters mentioned were far easier to implement than others. For the first design prototype, it was decided it to aim to measure the easier parameters of temperature, humidity, panel temperature and UV intensity. To meet the specification, it was also decided that the method of powering would be via a portable phone battery pack and the communication of data would be via WIFI.

A.II.I Design and production

It was decided that, initially, the system would be based around and controlled with an Arduino Uno, an easy-to-use microcontroller which is designed to be able to interface with a large number of components to perform a variety of tasks at temperatures from -40 to 85°C. The benefit of a system like this is that it contains key a number of key components to allow easy modular building through addition of units such as commercial sensors.

A BME280 based sensor was determined to be a good choice for measuring temperature and relative humidity. This small chip is designed by Bosch is stated to be well suited to low power applications and has a fast response time with high accuracy and low noise and has interface capability with Arduino. [1] Adafruit, a company who produce breakout boards with the BME280 which, state it has an accuracy of $\pm 3\%$ relative humidity and $\pm 1.0^\circ\text{C}$ temperature. [2] Furthermore, an operational range of -40 to 80°C and 0-100% RH and a response time of 1 second make this sensor attractive to the required specification.

Measuring panel temperature presented more of a challenge as most temperature sensors measure the temperature of the environment, the ambient temperature, rather than that of a specific object. Contact temperature sensors were considered but were rejected due to the requirement to maintain contact to the panel at all times and difficulties occurred when trying to attach them securely to the wall. In the end a non-contact IR sensor was chosen, the TMP006 sensor by Adafruit, which works on the principle of detecting IR radiation from an object via a sensitive thermopile and using this to calculate the temperature of said object. This sensor has an operating range of -40 to 125°C with low supply current with a typical accuracy of $\pm 1-3^\circ\text{C}$.

A number of UV sensors exist on the market but many of these do not have an actual UV sensor in them and instead use calculations based on the measured IR and visible light recorded in order to give an estimate of the UV index [3]. The VEML6075 produced by Vishay is much more accurate option than these sensors as it has both an actual UVA and UVB sensor and hence can accurately indicate the intensity of these bands as well as calculating the UV index. The benefit of this is ability to determine much more data than just the UV index and knowing the band intensities may be of interest. An operating range of -40 to 85°C ensures that it can operate accurately in the conditions present.

It was desirable for the eventual system to be self-sufficient, and this meant that a battery system would have to be included. A number of options were considered but eventually a simple rechargeable phone power bank of 10,000 mAh capacity was chosen due to ease of use. This had the benefit of being an all-in-one system with no complicated charging/discharging circuitry to be designed. Furthermore, it provided a 5v output which was required for the Uno to function.

Concept of live monitoring was a key idea of this initial sensor development. Two options were considered to facilitate this, RF communication and WIFI communication. WIFI communication was chosen as it required only one device to function suffers less from interference if multiple sensor systems and is easier to use within regulations. An ESP8266 WIFI module was used for the device which is a very popular module for sending and receiving data. For data receiving the website Thingspeak was used which is a website specifically for enabling storage and retrieval of data from Internet of Things (IoT) devices.

In order to protect the components from the environment a simple housing was produced. This was 3D printed from ABS and had a number of simple features to allow the internal sensors to function accurately, such as a small 1mm PEG window above the UV sensor and a rear facing opening so the IR sensor could record panel temperature. The housing was composed to two sections that bolted together to seal and contained small mounts for each sensor and the battery and control system. A set of magnets were glued on the rear to allow easy mounting and removal on OCS. The completed prototype is shown in Figure A.I and Figure A.II

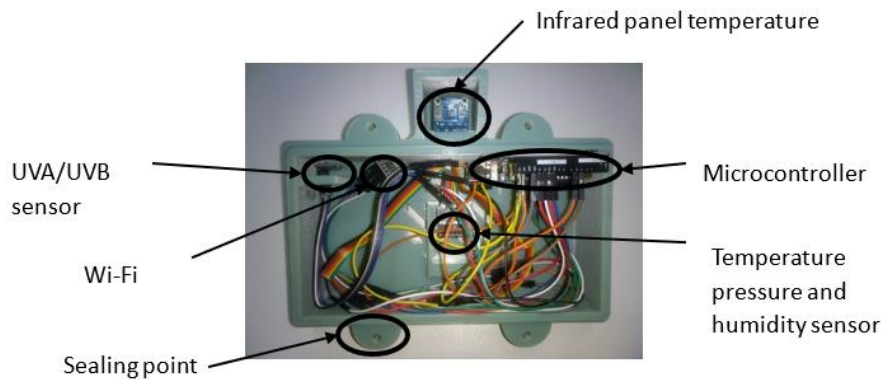


Figure A.I. Internals of the System Box (Front)

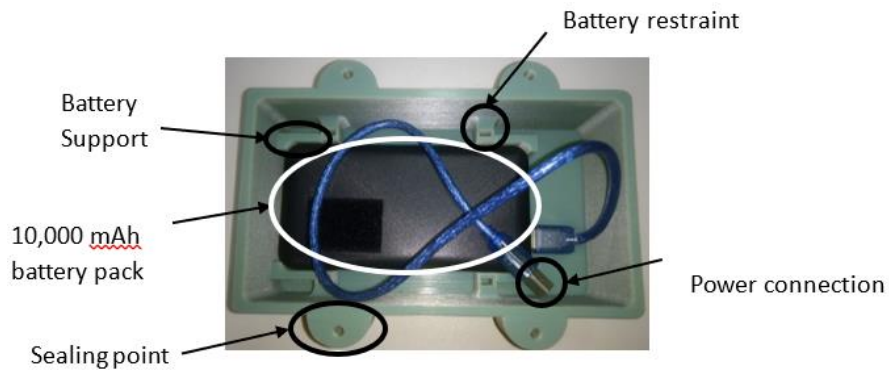


Figure A.II. Internals of the System Box (Back)

A.II.II Testing

Battery life was a key feature of the device which is dependent on the current draw. The average current draw of the device A_{av} , in mAh, can be calculated through the time weighted average of the awake and asleep current:

$$A_{av} = \frac{(A_s \times T_s) + (A_w \times T_w) + (A_t \times T_t)}{3600} \quad (A. I)$$

Where, A_s , A_w and A_t are the respective current draw for the device in sleep, wake and transmit mode and T_s , T_w and T_t are similarly the approximate seconds per hour the device spends in each mode. This allows calculation of the expected battery life (T_{Bat}) in days:

$$T_{Bat} = \frac{C_{Bat}}{A_{av} \times 24} \quad (\text{A. II})$$

Where C_{Bat} is the capacity of the battery in mAh. By using a power supply, the current draw of the developed sensor was measured in each mode and the estimated battery life was calculated for the intended battery system used. This data is shown in Table A.II in which the expected battery life is shown for each mode individually and the whole system in operation.

Table A.II. Battery life calculations for the device

Mode	Duration per hour/s	Current Draw/mA	Expected Battery Life
Sleep	N/A	N/A	N/A
Wake	3520	52	8 Days
Transmit	80	105	4 Days
Operation	3600	53	7.8 Days

From the calculations a battery life of 7.8 days was expected. This was fairly poor for the first prototype however this system aimed to test the operation of the sensors and such like and hence battery life was less of a design consideration at this stage.

In order to determine the accuracy of the sensors, tests were undertaken in which the sensor box was placed upon the Active Classroom at Swansea University, the first of which took place between the 14th and 16th of June 2019. The sensor box was placed on the panel façade of the east elevation of the building.

The accuracy of temperature and humidity measurement of the sensor used was assessed by comparison to, Figure A.III and Figure A.IV, a commercially available temperature and humidity logger; an EL-USB-2 made by EasyLog which has a stated manufacturers tolerance of $\pm 0.55^\circ\text{C}$ and $\pm 2.25\% \text{ RH}$ [4]. It was observed that developed sensor provided an almost identical response curve giving confidence to the temperature trends recorded by the developed sensor. Quantitatively there was a small amount of variation between the two devices however generally the developed sensor appeared to have performed very well.

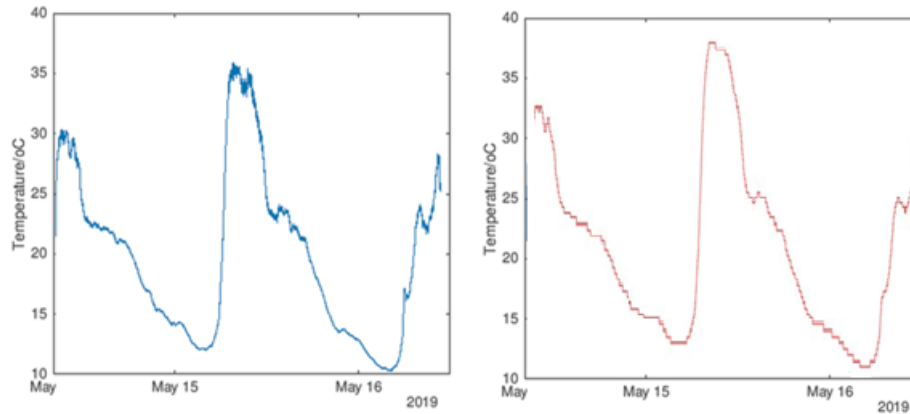


Figure A.III. Comparison between the temperature measured by the developed sensor (left) and the commercially available sensor (right)

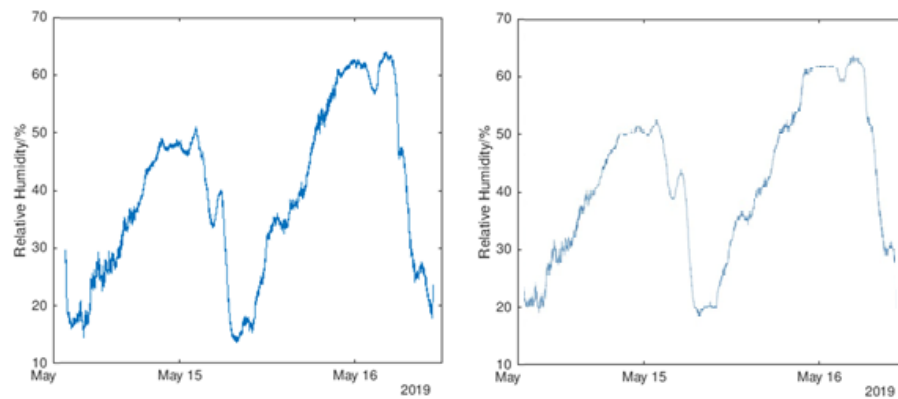


Figure A.IV. Comparison between the relative humidity measured by the developed sensor (left) and the commercially available sensor (right)

Analysis of the discrepancy between device and commercial sensor was undertaken and in terms of temperature the max discrepancy recorded was approximately 3.5°C and the average discrepancy was 0.7°C . The humidity measurements showed more variation with a maximum of 10.5% RH and an average of 1.5% RH. It is worth noting that the 10.5% RH discrepancy occurred during a rapid change in relative humidity and hence was disregarded somewhat. Generally, the discrepancy was smaller than the total inherent uncertainty in both devices, $\pm 1.55^{\circ}\text{C}$ and $\pm 5.25\% \text{RH}$, indicating agreement within the level of accuracy for these devices.

The accuracy of the UV sensing capability was compared against two temperature compensated thermopile pyranometers which were present on the Active Classroom and measure solar radiation flux density through the difference in temperature of an exposed plate to a shielded plate[5]. While the UVA-UVB band fits approximately in the 280-400nm range the pyranometers are stated to detect radiation intensity of

wavelengths between 280-2800nm and hence will detect far more of a range of wavelengths than the developed sensor will as shown in Figure A.V [5].

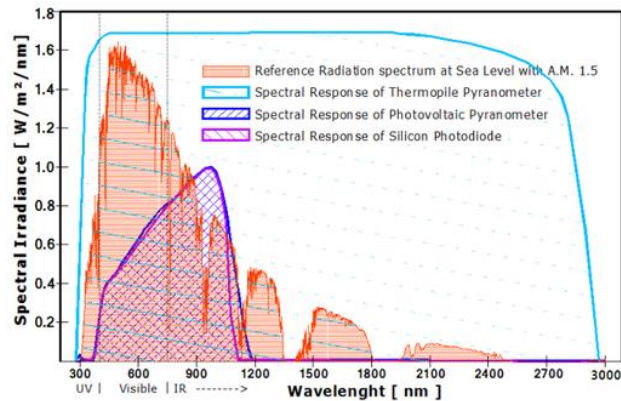


Figure A.V. Response of a thermopile pyranometer to spectral wavelength[5]

When compared to the measured UVA, shown in Figure A.VI, it was seen that at the times where the pyranometers recorded little or no solar irradiance the prototype also recorded little or no UVA. Furthermore, both systems detect increases in both solar irradiance and UVA intensity at similar times indicating a good response to the rising of the sun at the start of the day. The measured UVA appeared to rapidly decrease at approximately midday however investigation showed that this was due to the location of the developed sensor. The test location was shaded by a soffit after approximately 1pm and hence a drop off in solar radiation was recorded compared to the roof mounted pyranometer. The point at which the developed sensor was shaded is labelled (*) on the figure below. It is worth noting that the absolute values recorded were not considered directly comparable due to the measurement differences.

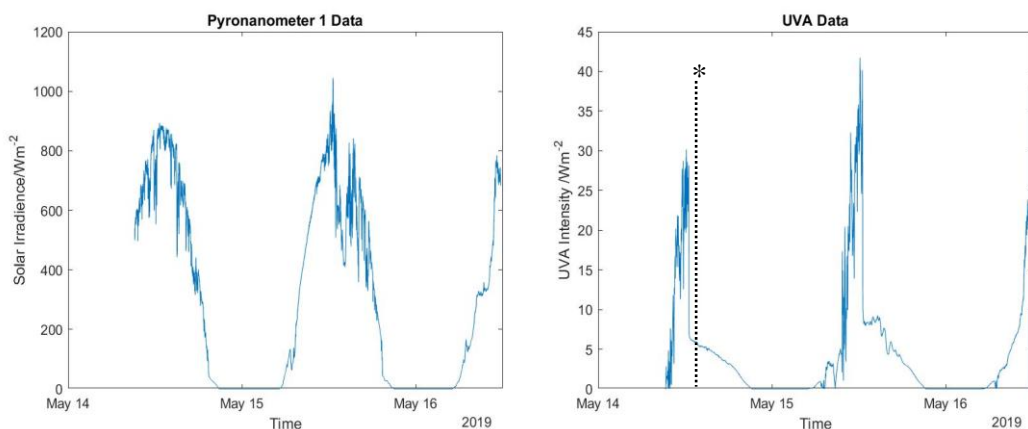


Figure A.VI. Comparison between pyranometer data (left) and developed sensor UVA (right)

The measured UVB was similar to the measured UVA when compared to the pyranometer data. It showed low values of UVB when the pyranometer measured no

solar radiation and also began to show increased in UVB intensity with increasing light intensity in the morning. While the overall trend does not match as well as the UVA, this may be because the UVB spectrum is at the lowest end of the pyranometer data and hence the rest of the detected pyranometer spectrum, from 320-2800nm is dominating the response. However, it was possible to conclude that the UVB sensor was responding correctly to increasing and decreasing levels of sunlight due to the overall similar trends seen.

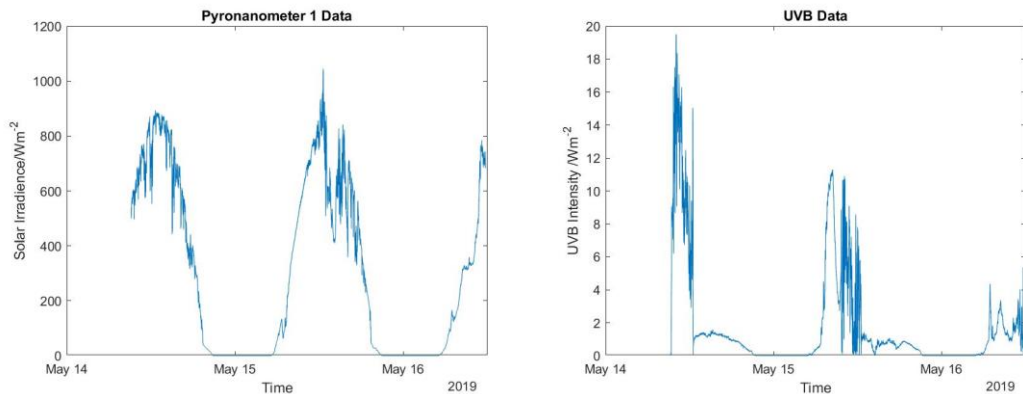


Figure A.VII. Comparison between pyranometer data (left) and developed UVB (right)

The data recorded by the IR contactless panel temperature sensor is shown in Figure A.VIII below. While there was no easy way to assess the accuracy a level of confidence in the trend of data recorded was observed with the panel temperature measured to be warmer when there is a high ambient temperature and solar irradiance and cooler when there is a lower ambient temperature and solar irradiance. The sensor did seem to measure temperatures on the higher end of would be expected and while quantitative analysis was not possible from this test it was investigated later on.

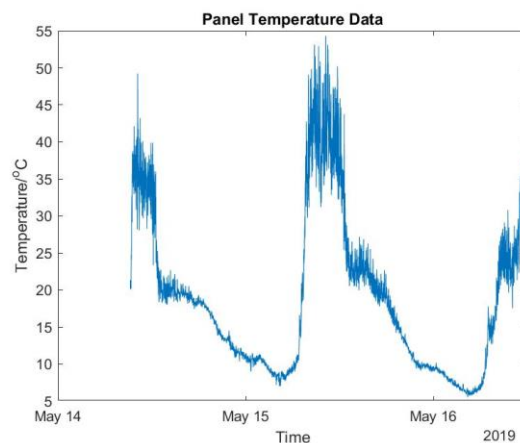


Figure A.VIII. Recorded Panel Temperatures

A.II.III Conclusions

The system prototype proved that environmental data capture was possible however there are significant changes that would improve the effectiveness of this system in light of the design specification. The initial system was analysed against the design specification and further improvements were suggested, Table A.III. While the system did meet some of the specification requirements it is clear it could be improved to fulfil more.

Table A.III. Design Specification Comparison

Requirements	Met	Current solution	Possible improvements
Easy secure mounting to building facades	Yes	Magnetic mounting to allow non-permanent mounting.	Embedding the magnets to ensure the box is flusher to the façade.
Ability to change components easily if required	Yes	Arduino block-based building allows easy component removal	Non-wire-based system to reduce the number of connection changes.
Long term weather resistance	Yes	3D Printed box housing with PETG windows for external sensing. Components are rated for expected temperature ranges.	Drainage holes for removing condensation and placing all sensors internally.
Data acquisition rate of several points per hour	Yes	Ability to select any data acquisition rate via programming.	None Required
Long term battery life	No	Use of a 10,000mAh battery pack	A larger battery or a more efficient system reducing current draw.
Live data monitoring and acquisition	Yes	WIFI connectivity facilitates real time monitoring.	None Required
Easy interface to numerous commercial sensors	Yes	Arduino system allows easy interface and system updating.	Remove wired connections to slimline the design and make production easier.
Compact size		Current 3D box is approximately	Reduce battery size as this is limiting factor.

Measurements	Met	Solution
Ambient temperature	Yes	Measured to a stated instrument accuracy of $\pm 1^{\circ}\text{C}$. Agreement with calibration testing.
Ambient humidity	Yes	Measured to a stated instrument accuracy of $\pm 3\% \text{RH}$. Agreement with calibration testing.
Panel temperature	Yes	Measured to a stated instrument accuracy of $\pm 1-3^{\circ}\text{C}$. Further calibration testing required.
UV intensity	Yes	UVA, UVB and UVI measured with agreement to calibration testing.
Time/cycle of wetness	No	
Contaminant build up	No	
Contaminant composition	No	
Aqueous conditions	No	
Gaseous conditions	No	
Local pH	No	
Windspeed	No	

Biological build up	No	
---------------------	----	--

A.III Prototype 2

The battery life of prototype 1 was found to be approximately 3 days which is significantly shorter than ideal. It was found that a key contributor to the low battery life was the WIFI module which requires a significant current draw (120+mA) to transmit data. Hence to improve the battery life other data storage options were considered. Furthermore, additional sensing was considered including time of wetness and contaminant build up.

A.III.I Design and production

In order to measure the time of wetness and washing cycle of the panel a rain and moisture sensor was selected. A YL-83 resistance-based moisture sensor was chosen due to the ability to perform such a task and the suitable operating temperature of -15 to 55°C. This sensor works by measuring the resistance between two unconnected conductive tracks and the decrease in resistance due to moisture present allows an estimation of the percentage of the sample that is wet.

Attempting to measure contaminant build up proved complicated and the approach taken was to measure airborne particulate concentration. For this use a Grove dust sensor by Seed Studio was selected as the method of choice. This is an all-in-one manufactured sensor and hence it was expected to be better than any developed method. It works by using an infrared led and photodiode detector and assumes that any increase in opacity detected is due to interference from dust or other airborne particulate. Particles down to 2.5 microns are stated to be detected and the number of particles per unit volume can be extracted via calculation.

While WIFI capability was considered interesting, for reasons of simplicity, battery life and expected use case this prototype switched to SD card based off-grid style datalogger via an Adafruit SD shield. This shield has a built-in real-time clock (RTC) which has a separate battery supply and hence the datalogger can extract the current date and time regardless of whether it has been powered off. This was important for timestamping the data recorded in order to give meaningful results but was also used as an alarm to sleep and wake the system to save power between readings.

In order to reduce the overall size of the prototype and increase the ease of manufacturing a (Printed Circuit Board) PCB based system was considered. The PCB was designed on Autodesk Eagle and sized so that it would stack with the microcontroller and the SD card shield for a reduced sensor size. Furthermore, the sensors were positioned on the board so that they would be in the correct position for their use. However, because of the reliance on the large battery pack, even though the new PCB design would allow a far smaller housing, the same housing was used as previously.

A.III.II Testing

The battery life calculations, shown in Table A.IV show that the second device had a slightly improved expected battery life compared to the previous prototype. As the device did not transmit through Wi-Fi the transmit mode was changed to the data write mode although all calculations followed the same principles as before.

Table A.IV. Battery life comparisons between the second device (S2) and the previous device (S1)

Mode	Duration per hour/s	Current Draw/mA	Expected Battery Life
(S1) Sleep	N/A	N/A	N/A
(S1) Wake	3520	52	8 Days
(S1) Transmit	80	105	4 Days
(S1) Operation	3600	53	7.8 Days
(S2) Sleep	3520	44	9.5 Days
(S2) Wake	70	75	5.5 Days
(S2) Transmit	10	100	4.1 Days
(S2) Operation	3600	45	9.3 Days

As the UV, temperature and humidity were previously tested, their effectiveness was not analysed beyond their ability to function for the duration of the system test.

Hence system testing focused mainly on determining the quality of the data recorded by the wetness and dust sensors. To test these the prototype system was again placed on east elevation façade of the active classroom and was left out from the 23rd to the 26th of October. For calibration the wetness data would be compared to the expected rain fall from weather reports and observation however there was no easy way to determine the accuracy of the dust sensor.

Observation of the data recorded by the dust sensor, shown in Figure A.IX, shows that it did indeed seem to detect dust concentrations. However, it can be seen that, while at night-time there is consistent measurement of dust particulates, no measurement appears to be being taken during the day. This may be due to the

measurement method which is reliant on a photodiode which is perhaps being flooded by daylight and hence assuming there is no dust opacity from the laser. While this is not ideal it was thought that this sensor could provide useful data to supplement manual measurements.

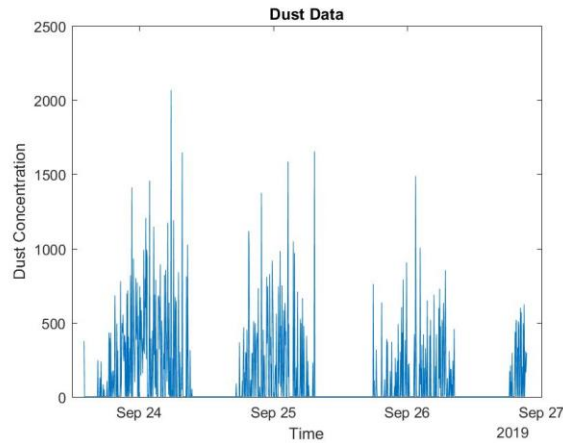


Figure A.IX. Recorded data from the dust sensor

The data recorded by the wetness sensor is shown in Figure A.X. It appeared that little measured rain was detected even though rain was falling for a large majority of the test, and the sensor was visibly observed to be wet. On close inspection of the sensor, after the test was completed, it was decided this was caused by rapid corrosion of both the sensing element and wire connections in the harsh marine environment that it had been placed in. Unfortunately, due to the working principle of the sensor, the electrical tracks must be exposed to the environment and hence it is believed a resistive sensor, such as this, will not be suitable for use.

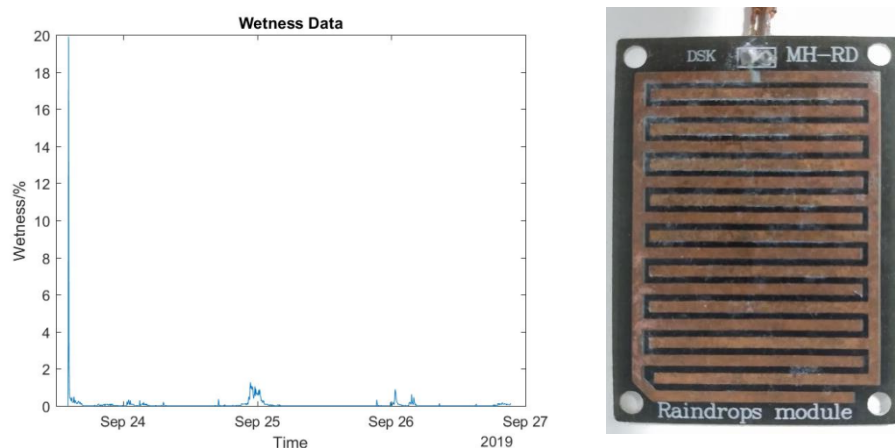


Figure A.X. Recorded wetness data (left) and corroded wetness sensor (right)

Further testing of the accuracy of the infrared thermopile sensor was also carried out in a separate test. The IR sensor was held in a clamp stand approximately 10cm above a beaker of water which was placed on a hot plate with built in magnetic

stirring. The temperature of the water was increased from 20 to 40°C and monitored simultaneously using a waterproof high accuracy DS18B20 water temperature sensor and the IR thermopile. The results, displayed in Figure A.XI, show that, although noisy, the results produced by the IR sensor match the measured water temperature well. Although the IR measurements were consistently lower than the actual water temp, the average discrepancy across the whole set of results was only approximately 6.4% and the vast majority of these discrepancies fall within the stated $\pm 1-3^{\circ}\text{C}$ instrument accuracy. This suggested the IR sensor could, with a reasonable degree of accuracy, measure object temperatures.

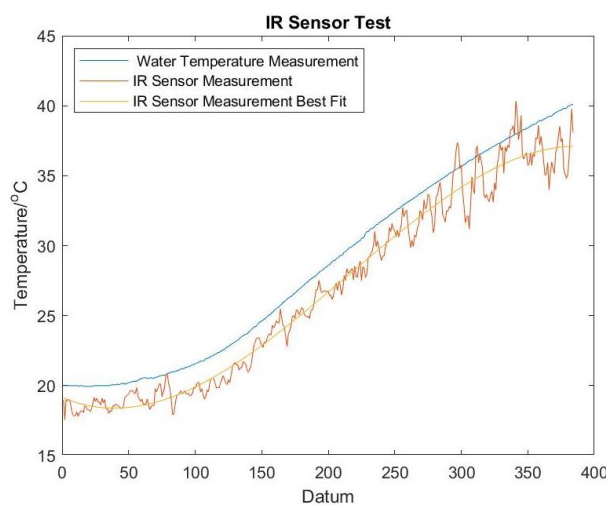


Figure A.XI. Accuracy of the IR sensor compared to actual object temperature

A.III.III Conclusions

The improvements to the design were evaluated against the specification in Table A.V. Although the improvements attempted to satisfy more of the criteria it was clear further work was required in order to improve the design.

Table A.V. Design specification analysis on improved design

Requirements	Met	Current solution	Possible improvements
Easy secure mounting to building facades	Yes	Embedding the magnets to ensure the box is flusher to the façade.	None Required
Ability to change components easily if required	Yes	PCB based design allows easy manufacture and repair.	None Required
Long term weather resistance	Yes	New 3D box design with greater waterproofing.	Redesign windows to ensure better glue sealing.
Data acquisition rate of several points per hour	Yes	Ability to select any data acquisition rate via programming.	None Required
Long term battery life	No	SD based system to reduce WIFI current requirements	Redesign from the ground up for a more efficient control system

Live data monitoring and acquisition	No	No longer considered a key requirement	None Required
Easy interface to numerous commercial sensors	Yes	PCB design allows easy interfacing without wired connections.	Sourcing of further sensors to interface.
Compact size		Current 3D box is approximately	Reduce current requirement to allow smaller battery system.

Measurements	Met	Solution
Ambient temperature	Yes	Measured to a stated instrument accuracy of $\pm 1^\circ\text{C}$. Agreement with calibration testing.
Ambient humidity	Yes	Measured to a stated instrument accuracy of $\pm 3\% \text{RH}$. Agreement with calibration testing.
Panel temperature	Yes	Measured to a stated instrument accuracy of $\pm 1-3^\circ\text{C}$. Agreement with calibration testing.
UV intensity	Yes	UVA, UVB and UVI measured with agreement to calibration testing.
Time/cycle of wetness	No	Resistive based solution ineffective for long term testing due to corrosion. New system required
Contaminant build up	No	Dust sensor may give relative air particle pollutant concentration however further testing is required. Measurement of actual contaminant build up on the panels.
Contaminant composition	No	
Aqueous conditions	No	
Gaseous conditions	No	
Local pH	No	
Windspeed	No	
Biological build up	No	

A.IV Prototype 3

It was clear the prototype design needed to be optimised from the point of view of battery life to ensure a long-term test is feasible. Hence improvement at this stage focused on redesigning the system to this end.

A.IV.I Design and production

While the sensors in the system are difficult to optimise for low power the control system was possible to improve. To this end an Arduino Pro Mini 5V replaced the Uno as the microcontroller to operate the sensor system. This is a much more power efficient device than the previously used Uno for example, in ‘awake mode’ the Uno used approximately 50mA whereas a Pro Mini used approximately 25mA, a large saving.

To reduce power consumption during sleep a transistor was incorporated into the system to allow components to be turned off between measurements to save battery life. The transistor could be easily used as a switch applying a voltage to the gate. In

this system the transistors were NPN transistors, specifically PN2222. These were combined with a smaller microSD card breakout board that was sourced from Adafruit and a separate DS3231 RTC. This RTC has a small internal battery that could trigger an interrupt to allowed all the components to be turned off and on when required [6].

A number of options were considered to replace the resistance-based wetness sensor, but the chosen solution was a capacitive moisture sensor. This measures the wetness as a relation to the capacitance between two tracks on the probe and hence the tracks can be coated and thus protected from the environment. The size and shape of the sensor also meant that it was easily positioned near to the façade being monitored and hence monitor the correct conditions.

Though the temperature and humidity sensor that had been previously used had performed well, the new design used a BME680 sensor. This has the same capabilities and sensors for temperature and humidity sensing but also has the ability to give an indication of volatile organic compounds (VOC) content. The resistance of a metal oxide (MOX) sensor changes due to reactions with VOCs in the local environment although differentiation between different gasses is not possible [7]. It is possible this may be more of a comparative technique than one capable of measuring absolute values, but it added an additional sensing element to the system.

A smaller less bulky battery system was implemented due to the expected decrease in current draw and increased efficiency of the device. This was also required as the sleep current from the device was below the shut off current of the battery pack and hence the battery pack was unable to power the device while it slept. 2800mAh NiMH batteries were chosen as these have a reasonably high capacity, power density and are much safer to recharge and use than other alternative such as Li-Ion batteries. As the voltage of each of these batteries is 1.2V, 5 were required in series in order to provide a voltage sufficient to power the Arduino mini.

Although the dust sensor has the ability to measure airborne particles this does not fully meet the specification to measure the rate of accumulation of matter on the cladding and also of what composition the matter is. It appeared that this was too complex a measurement to automate and hence it was concluded that this type of work would be carried out manually.

Due to reduced battery size of the new system a reduced size housing was produced. This design was similar to the first design with a few improvements for example the magnets were inset into the box by a few millimetres to allow the box to be mounted as flush as possible to prevent wind and rain getting behind it and forcing it away from the wall. Two spaces for PETG window sections were created for the panel temperature and UV sensor and a separate housing for the dust sensor was placed on the front of the device with a large cut out section exposing the sensing element. A slit in the side of the device box allowed placement of the capacitive moisture sensor. The final design is shown in Figure A.XII.

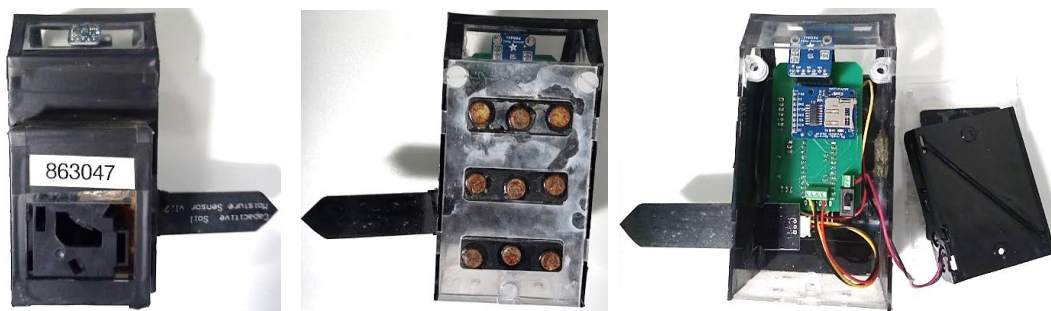


Figure A.XII. The final sensor device front (left) back (middle) and internals (right)

Even though the new system used a lower capacity battery system a far greater expected battery life was calculated for this new prototype as shown in Table A.VI. This is due to the significantly reduced sleep current and wake current draw.

Table A.VI. Battery life calculations between the three system design iterations (S1,2,3)

Mode	Duration per hour/s	Current Draw/mA	Expected Battery Life
(S1) Sleep	N/A	N/A	N/A
(S1) Wake	3520	52	8 Days
(S1) Transmit	80	105	4 Days
(S1) Operation	3600	53	7.8 Days
(S2) Sleep	3520	44	9.5 Days
(S2) Wake	70	75	5.5 Days
(S2) Transmit	10	100	4.1 Days
(S2) Operation	3600	45	9.3 Days
(S3) Sleep	3520	2.8	42 Days
(S3) Wake	70	16	7.3 Days
(S3) Transmit	10	88	1.3 Days
(S3) Operation	3600	3.3	35.4 Days

A.IV.II Testing

As the biggest aim of this improvement iteration was to improve battery life, testing of the system involved leaving the sensor in an indoor environment until battery depletion occurred. A considerable increase in battery life was seen, even with the

reduced capacity of the batteries, with the sensor running from the 9th of December til the 21st of January; a duration of 43 days. This is similar to the previously calculated expected battery life of the sensor of and represents an improvement of over ten times on the previous design. For the duration of the test the sensors appeared to work as expected and reasonable data was recorded at every sampling point.

The capacitive moisture sensor was tested separately to determine its accuracy in detecting wetness. It was first calibrated based on a measurement when the element was completely dry and immersed in water and then the measured percentage wetness was monitored as drops of de-ionised water were added and then removed incrementally. At the maximum of 8 drops on the sensor approximately 60-70% of the element was wet. The results of this test are shown in Figure A.XIII and show that the sensor accurately detects the addition and removal of water droplets. It did somewhat underestimate the percentage cover of water however for determining the likely time of wetness the exact quantity of water present is not required. Hence the wetness sensor appears suitable for the device.

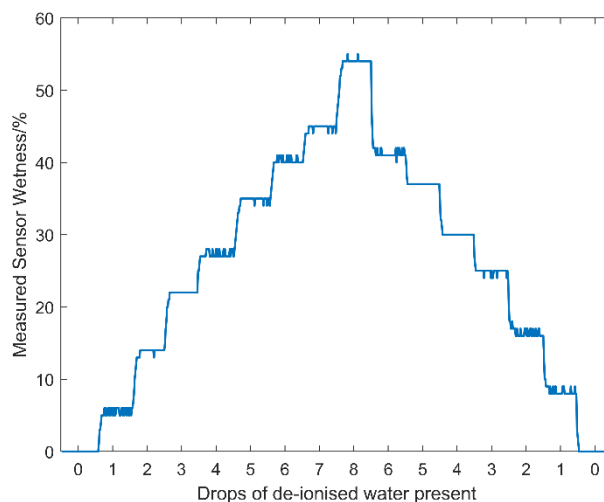


Figure A.XIII. Detection of water addition and removal by the capacitive wetness sensor

A.IV.III Conclusions

Comparison of the improved design to the specification is shown in Table A.VII. It was realised that the requirements of the system were mainly fulfilled and although the system could of course be improved it was considered to meet the specification. Although there were, however, still measurement criteria that were not met by the current system, the specification was viewed as an ideal system that may not be

feasible. The feasibility of the measurements not currently implemented in discussed in Table A.VII.

Table A.VII. Design specification analysis on further improvements

Requirements	Met	Current solution	Possible improvements
Easy secure mounting to building facades	Yes	Smaller lighter design with more secure mounting	None Required
Ability to change components easily if required	Yes	As before	None Required
Long term weather resistance	Yes	More secure box sealing and better component fitting	None Required
Data acquisition rate of several points per hour	Yes	As before	None Required
Long term battery life	Yes	Redesigned control system with new battery system of up to 40-day life.	Further remove non-essential components.
Live data monitoring and acquisition	No	No longer considered a key requirement	None Required
Easy interface to numerous commercial sensors	Yes		
Compact size	Yes	Current 3D box is approximately	None Required

Measurements	Met	Solution/Justification
Ambient temperature	Yes	Measured to a stated instrument accuracy of $\pm 1^{\circ}\text{C}$. Agreement with calibration testing.
Ambient humidity	Yes	Measured to a stated instrument accuracy of $\pm 3\% \text{RH}$. Agreement with calibration testing.
Panel temperature	Yes	Measured to a stated instrument accuracy of $\pm 1-3^{\circ}\text{C}$. Agreement with calibration testing.
UV intensity	Yes	UVA, UVB and UVI measured with agreement to calibration testing.
Time/cycle of wetness	Yes	Capacitive moisture sensor which provides % wetness output.
Contaminant build up	Yes	Dust sensor Measurement of actual contaminant build up via manual measurement
Contaminant composition	Yes	Accurate in-situ measurement considered too complicated so will be carried out in the lab post collection.
Aqueous conditions	No	Not considered possible to automate due to the complication of collecting, analysing and releasing liquids. Human measurement at discrete intervals would be far easier and more efficient as it is not expected to vary on an hourly basis.
Gaseous conditions	Yes	Accurate in-situ measurement considered too complicated to automate however VOC measurement (indication) facilitated.
Local pH	No	No considered possible to automate due to the complication of collecting, analysing and releasing liquids. Human measurement at discrete intervals would be far easier and more efficient as it is not expected to vary on an hourly basis.
Windspeed	No	Although possible the size of the system would be adversely affected. Human measurement at discrete intervals would be far easier and more efficient.
Biological build up	Yes	Difficult to distinguish biological matter from other contaminants and classify automatically. Measurement can be taken via manual analysis if required.

The remaining measurements that were not been considered possible were aqueous conditions, pH and windspeed. Windspeed can be easy measured with a handheld commercial device held in close proximity to the test site, if needed. pH can be measured with a standard lab-based probe by either collecting rainwater coming off the test site or washing the test site with pH 7 deionised water and collecting the resulting liquid.

The aqueous conditions of each location are more complicated but essentially what was required was some sort of device that can determine which locations of a building are most susceptible to aqueous corrosion and one way to achieve this is through the detection of the conductivity which is indicative of the dissolved salts in an aqueous system. By creating a standalone device many of the complications to the initial system is removed human operation removes complication of liquid management.

B. Development of an electrical conductivity device

B.I Background

Electrical conductivity (EC) is often used to measure, amongst other things, the presence of sea water and the quantity of TDS (total dissolved solid) [8]. It is a cheap and rapid method that allows continuous measurement of solutions [8]. For this work it is believed that measurement of electrical conductivity will give an indication of the aggressivity of the aqueous environment. This is because it is expected that an increased electrical conductivity in an electrolyte is likely due to a greater ionic concentration in said electrolyte as conductivity can be calculated by considering the number of charge carriers available (n), the charge carrier mobility (μ), the charge on the carriers (q) their average drift velocity (\tilde{v}) and the present electrical field (E) [9] [8]:

$$\sigma = nq \frac{\tilde{v}}{E} = nq\mu \quad (\text{B.I})$$

Ionic current is one of the four components of the electrochemical cell that must be present for corrosion to occur. Hence, if the ionic current is more easily able to flow, due to an increased number of charge carriers in the electrolyte, the greater the likely rate of corrosion in this environment.

EC varies with temperature and hence a standard temperature is used when quoting the EC of a solution [8]. The most common standard is 25°C and, therefore, measurements of solutions at different temperatures require conversion to a value that would be expected at 25°C [8]. This is especially important for accurately comparing results as it is stated that the electrical conductivity of a solution will increase by 2% under a temperature increase of 1°C [8].

Although it is reported that the relationship between EC and temperature is non-linear, commonly a linear relationship is used to calibrate for temperature [8] as the deviation from linearity is stated to be small between common monitoring conditions up to 30°C. Sorensen and Glass [10] derived the following equation for converting an EC measurement at a temperature t to the corresponding EC at 25°C (EC_{25}):

$$EC_t = EC_{25}[1 + a(t - 25)] \quad (\text{B.II})$$

Where a is a temperature coefficient which was stated by Sorensen and Glass to be 0.022 for their specific experiment [10]. There is a range of values that have been used for 'a' in various further work although 0.0191 or 0.02 appear to be the most commonly used and recommended [8,10].

If non-linear temperature compensation is required, this can be derived from the equations for the viscosity of water as a function of temperature and the diffusion of water. The full derivation is not covered in any detail here but is explained in [11] and [12]. The resulting equation is [12]:

$$EC_t = 0.889 \times 10^{\frac{A}{B}} \times EC_{25} \quad (\text{B.III})$$

Where [12]:

$$A = 1.37023(t - 20) + 8.36 \times 10^{-4}(t - 20)^2 \quad (\text{B.IV})$$

$$B = 109 + t \quad (\text{B.V})$$

B.II Device design

The easiest way to measure conductivity is to model the liquid, or part of the liquid, as a resistor in an electrical circuit by using two probes of a known size. If the resistance of the liquid can be measured it is then fairly trivial to convert this to the

conductivity using the dimensions of the probe. A simplified example of such a circuit is shown in Figure B.I [13].

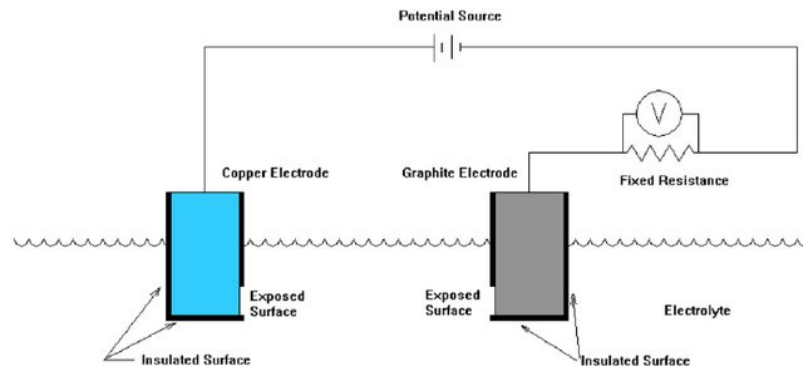


Figure B.I. Simplified electrical conductivity circuit [13]

For simplicity the device will measure conductivity via a DC current. Generally electrical conductivity devices will use AC current as there is the potential with DC to polarize the electrolyte which can lead to poor accuracy of results. To avoid this the DC current will be applied for a very short time (ms range) to take a sample and then removed for up to 10 seconds before repeating. Furthermore, to prevent capacitive effects two readings per sample will be taken with the first ignored.

Based on this approach a simple design was produced which is shown below in Figure B.II. It was decided that two 1cm diameter graphite electrodes placed 1cm apart would be used as these are inert to the intended electrolyte and should not significantly degrade with time or electrical current. An acrylic box was chosen as the vessel as this would not conduct electricity itself and also would not react with any solutions placed inside. A waterproof high accuracy DS18B20 temperature probe was used in order to allow temperature compensation and an Arduino and fixed resistor were chosen to take the voltage measurements. The fixed resistor was chosen at 430 Ohms as initial testing suggested this would give the best sensitivity.

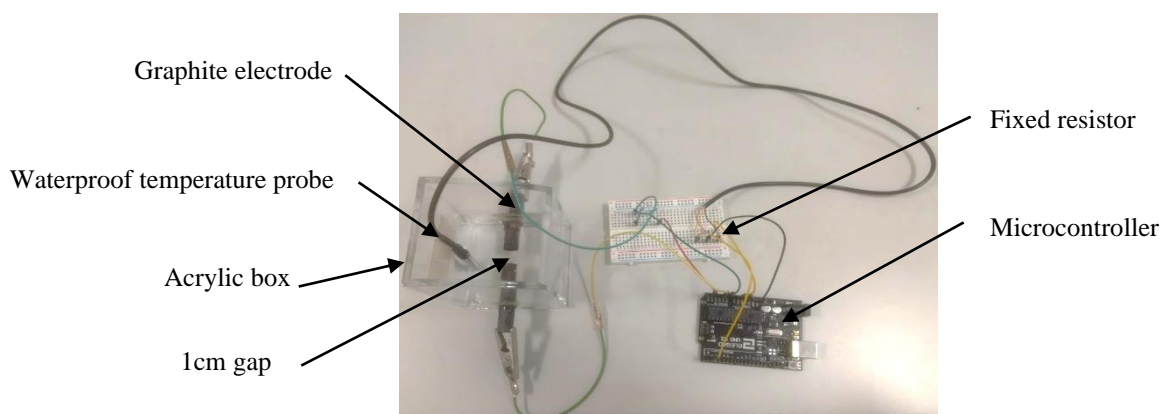


Figure B.II. Initial electrical conductivity device

B.III Initial device tests

In order to test the effectiveness and overall functionality of the device some initial basic testing was undertaken. The first test involved using four different concentration salt solutions which were produced by addition of NaCl to 250ml of deionised water. It is known that increased NaCl content increases the conductivity of an electrolyte and hence this test would test the basic response given. The solutions that were tested were 250ml of deionised water with 0, 1, 2 and 3 grams of NaCl. The results of this test are shown in Figure B.III and show that the sensor responded as expected to the increase in NaCl concentration by detecting an increased electrical conductivity. The results also showed, as expected at temperatures between 10-30°C, that both the linear and non-linear temperature adjustment gave very similar values for electrical conductivity.

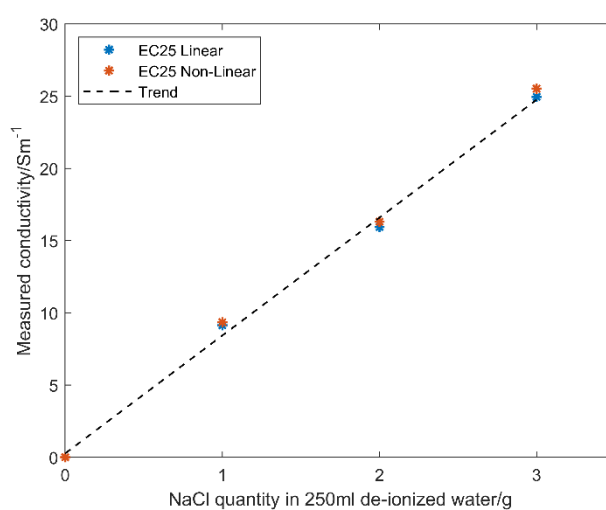


Figure B.III. Effect of NaCl addition on electrical conductivity of initially deionised water

A second test was then designed which aimed to test the device on a more continuous basis. The test started with purely deionised water present in the device but at regular 5-minute intervals approximately 1ml of a concentrated 10% wt NaCl solution was added. The results of this test are shown in Figure B.IV and clearly show that the device is responding as would be expected to the increase in ionic presence. As each increase in conductivity appears fairly similar, this would suggest that the device is responding accurately to identical additions of concentrated salt solution.

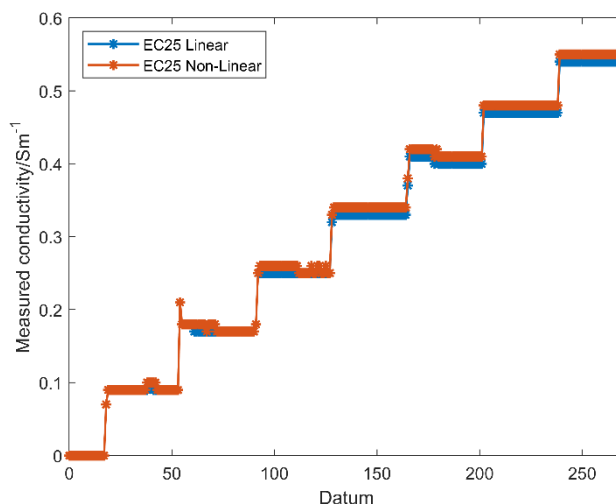


Figure B.IV. The effect on measured conductivity of addition of concentrated salt solution to initially deionised water at regular intervals

Both these tests confirmed that the developed device was responding correctly to changes in conductivity and it was decided that the next stage would be to attempt to calibrate the device to give accurate quantitative data.

B.IV Device calibration

In order to calibrate this device a set of standard solutions were produced. Vernier [14] and Golnabi [15] have both published information as to the expected electrical conductivity for certain concentrations of NaCl in deionised water and based on this work the solutions shown in Table B.I were prepared.

Table B.I. Calibration concentrations and the expected electrical conductivity values

Solution	NaCl Concentration/gL ⁻¹	Expected Value of Conductivity/μScm ⁻¹
1	0.500	1020
2	1.005	2000
3	1.451	2808
4	2.000	3860
5	2.922	5250

6	5.556	10000
---	-------	-------

Each solution was tested in the device until approximately 25 results were recorded. These results were then averaged to give the device measured value of conductivity. These values are shown in Table B.II.

Table B.II. Measured conductivity for each solution compared to the expected conductivity

Solution	Expected Conductivity/ μScm^{-1}	Measured Linear Conductivity/ μScm^{-1}	Measured Non-Linear Conductivity/ μScm^{-1}
1	1020	6200	6327
2	2000	14471	14781
3	2808	18562	18962
4	3860	25763	26356
5	5250	47538	48608
6	10000	188633	192829

It was immediately apparent that the measured values differ from the expected value by a significant factor ranging from approximately 6 for solution 1 to 20 for solution 2. The next step, therefore, was to compare the deviation factor against the measured conductivity in order to attempt to find a correction equation to bring the measured values in line with the expected values. The graph for the linear temperature adjusted values is shown as an example in Figure B.V below.

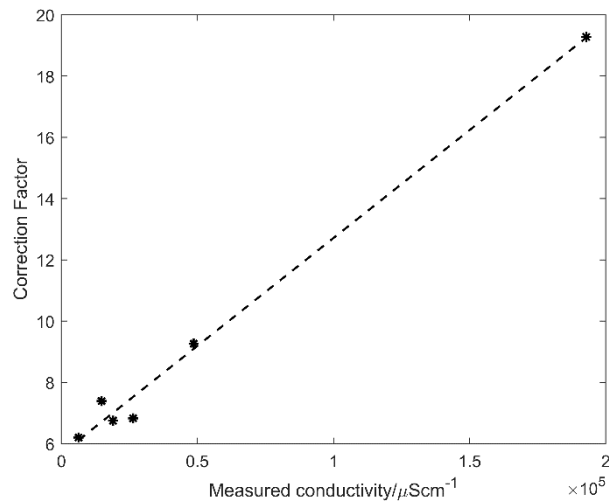


Figure B.V. Relationship between measured conductivity and the correction factor

It was seen that a linear relationship existed between the device measured conductivity and the correction factor, that is the factor the measured value differed from the expected. This trend was strong with a calculated R value of 0.992 and

suggests that the measured values could be adjusted by the linear equation defining this relationship which was.

$$y = 7 \times 10^{-5}x + 5.5504 \quad (\text{B.VI})$$

By using this formula resulted in the values shown in Table B.III being produced for the calibrated measured conductivity values.

Table B.III. Effect of calibration on the measured conductivity values

Solution	Expected Value of Conductivity/μScm^{-1}	Calibrated Measured Linear Conductivity/μScm^{-1}	Calibrated Measured Non-Linear Conductivity/μScm^{-1}
1	1020	1036	1035
2	2000	2205	2204
3	2808	2710	2710
4	3860	3503	3507
5	5250	5355	5357
6	10000	10058	10060

Analysis of these new values showed they had an average deviation from the expected values of only approximately 4.5% for both the linearly and non-linearly temperature compensated values. Therefore, the device was considered to be calibrated accurately.

B.V The final device

To streamline the initial device for ease of use the components were soldered to a Veroboard and an OLED screen was added to allow measurements to be read without a computer. By attaching a small 9V battery the device became portable and capable of taking and providing measurements in the field if required. A small tube acting as a syphon allowed excess electrolyte to be easily drained. Finally, a second set of electrodes were added which were used to determine if sufficient electrolyte was present for a measurement to be taken. This device was tested and re-calibrated as before to ensure accuracy. The completed device used in this work is shown in Figure B.VI below.

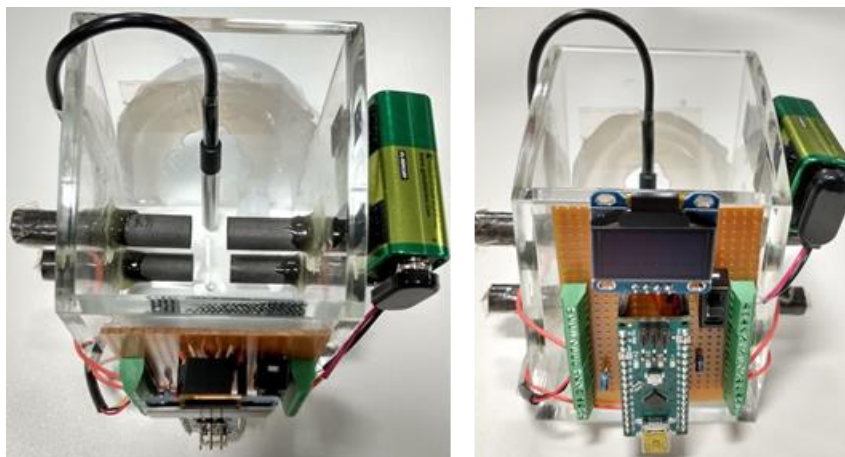


Figure B.VI. The final electrical conductivity device

Appendix References

1. Bosch. BME280 [Internet]. 2019 [cited 2019 Oct 2]. Available from: https://www.bosch-sensortec.com/bst/products/all_products/bme280%0D
2. Adafruit. Adafruit BME280 I2C or SPI Temperature Humidity Pressure Sensor [Internet]. [cited 2019 Oct 2]. Available from: <https://www.adafruit.com/product/2652%0D>
3. Adafruit. Adafruit VEML6075 UVA UVB and UV Index Sensor Breakout [Internet]. [cited 2019 Oct 2]. Available from: <https://www.adafruit.com/product/3964%0D>
4. EasyLog. Easy Log EL-USB-2 [Internet]. [cited 2019 Oct 2]. Available from: <https://www.lascarelectronics.com/easylog-data-logger-el-usb-2/>
5. US_Solar_Institute. Pyranometer [Internet]. 2018 [cited 2019 Oct 3]. Available from: <https://www.myussi.com/glossary/pyranometer/>
6. Adafruit. Adafruit DS3231 Precision RTC Breakout [Internet]. [cited 2020 Apr 7]. Available from: <https://www.adafruit.com/product/3013>
7. Adafruit. Adafruit BME680 - Temperature, Humidity, Pressure and Gas Sensor [Internet]. [cited 2020 Apr 7]. Available from: <https://www.adafruit.com/product/3660>
8. Hayashi M. Temperature-Electrical Conductivity Relation of Water for Environmental Monitoring and Geophysical Data Inversion. *Environ Monit Assess* [Internet]. 2004 Aug;96(1-3):119-28. Available from: <https://doi.org/10.1016/j.physleta.2017.10.039%0Ahttp://dx.doi.org/10.1016/j.epsl.2015.04.028%0Ahttp://dx.doi.org/10.1016/j.desal.2012.06.001%0Ahttps://www.omicsonline.com/open-access/temperature-effects-on-conductivity-of-seawater-and-physiologic-salinem>
9. Taherian R. The Theory of Electrical Conductivity. In: *Electrical Conductivity in Polymer-Based Composites: Experiments, Modelling and Applications* [Internet]. Elsevier; 2019. p. 1-18. Available from: <http://dx.doi.org/10.1016/B978-0-12-812541-0.00001-X>
10. Sorensen JA, Glass GE. Ion and temperature dependence of electrical conductance for natural waters. *Anal Chem* [Internet]. 1987 Jul;59(13):1594-7. Available from: <http://pubs.acs.org/doi/abs/10.1021/ac00140a003>

11. Atkins PW, J. de Paula PW. Atkins' Physical Chemistry [Internet]. 8th Editio. W.H. Freeman; 2006. Available from:
<https://linkinghub.elsevier.com/retrieve/pii/S0013468606009509>
12. Aquion. Temperature Compensation for Conductivity [Internet]. 2018 [cited 2019 May 29]. Available from: <http://www.aqion.de/site/112>
13. Butler BM, Kassab AJ, Chopra MB, Chaitanya V. Boundary element model of electrochemical dissolution with geometric non-linearities. Eng Anal Bound Elem [Internet]. 2010;34(8):714–20. Available from:
<http://dx.doi.org/10.1016/j.enganabound.2010.03.007>
14. Vernier. Conductivity Probe. Vernier Softw Technol. 2006;1–12.
15. Golnabi H, Matloob, M R, Bahar M, Sharifian M. Investigation of electrical conductivity of different water liquids and electrolyte solutions. Iran Phys J. 2009;3(November 2014):24–8.